Lecture Notes in Electrical Engineering 680

Zhongliang Jing
Xingqun Zhan *Editors*

Proceedings of the International Conference on Aerospace System Science and Engineering 2020

Springer

Lecture Notes in Electrical Engineering

Volume 680

The book series *Lecture Notes in Electrical Engineering* (LNEE) publishes the latest developments in Electrical Engineering - quickly, informally and in high quality. While original research reported in proceedings and monographs has traditionally formed the core of LNEE, we also encourage authors to submit books devoted to supporting student education and professional training in the various fields and applications areas of electrical engineering. The series cover classical and emerging topics concerning:

- Communication Engineering, Information Theory and Networks
- Electronics Engineering and Microelectronics
- Signal, Image and Speech Processing
- Wireless and Mobile Communication
- Circuits and Systems
- Energy Systems, Power Electronics and Electrical Machines
- Electro-optical Engineering
- Instrumentation Engineering
- Avionics Engineering
- Control Systems
- Internet-of-Things and Cybersecurity
- Biomedical Devices, MEMS and NEMS

For general information about this book series, comments or suggestions, please contact leontina.dicecco@springer.com.

To submit a proposal or request further information, please contact the Publishing Editor in your country:

China

Jasmine Dou, Editor (jasmine.dou@springer.com)

India, Japan, Rest of Asia

Swati Meherishi, Editorial Director (Swati.Meherishi@springer.com)

Southeast Asia, Australia, New Zealand

Ramesh Nath Premnath, Editor (ramesh.premnath@springernature.com)

USA, Canada:

Michael Luby, Senior Editor (michael.luby@springer.com)

All other Countries:

Leontina Di Cecco, Senior Editor (leontina.dicecco@springer.com)

**** This series is indexed by EI Compendex and Scopus databases. ****

More information about this series at http://www.springer.com/series/7818

Zhongliang Jing · Xingqun Zhan
Editors

Proceedings of the International Conference on Aerospace System Science and Engineering 2020

Springer

Editors
Zhongliang Jing
Shanghai Jiao Tong University
Shanghai, China

Xingqun Zhan
Shanghai Jiao Tong University
Shanghai, China

ISSN 1876-1100 ISSN 1876-1119 (electronic)
Lecture Notes in Electrical Engineering
ISBN 978-981-33-6059-4 ISBN 978-981-33-6060-0 (eBook)
https://doi.org/10.1007/978-981-33-6060-0

This Springer imprint is published by the registered company Springer Nature Singapore Pte Ltd.
The registered company address is: 152 Beach Road, #21-01/04 Gateway East, Singapore 189721, Singapore

Contents

Test Research and Finite Element Analysis on Extension Performance of Civil Aircraft Flaps Subjected to Extreme Temperature 1
Jingtao Wu, Sibo Zhou, Wenliang Deng, and Yunwen Feng

Mathematical Modeling of an Environment Control System in the Framework of Creating a Comprehensive Mathematical Model of Aircraft On-Board Systems 13
R. S. Savelev, K. S. Napreenko, and A. V. Lamtyugina

Investigation on the Effects of Atwood Number on the Combustion Performance of Hydrogen-Oxygen Supersonic Mixing Layer 23
Chengcheng Liu, Zi'ang Wang, Bin Yu, Bin Zhang, and Hong Liu

Analysis of Supersonic Axisymmetric Air Intake in Off-Design Mode 43
Svetlana Koval

Parameter-Orientated Functional Modeling Method Based on Flight Process 55
Yuqian Wu, Zoutao Xue, Gang Xiao, Ke Gong, Xiaoxu Dong, and Yue Luo

Experimental Study on Ice Shear Strength Evolution 71
Gong Chen, Weiling Kong, and Fuxin Wang

Investigation of the Effect of Electron-Beam Processing on the Surface of Samples Obtained by Additive Technologies from Cobalt-Chromium and Stainless Steel Powders 91
E. E. Dzhafarov, K. M. Erikov, O. A. Bytsenko, and A. V. Ionov

The Use of Basalt Plastic for the Manufacture of Sound Insulation Panels of an Aircraft Engine 101
E. D. Moskvicheva and V. I. Reznichenko

Contour Segmentation of Image Damage Detection Based on Fully Convolutional Neural Network 115
Xuesong Zhong and Xiuhua Chen

A Study on Aerodynamic Interference for Truss Braced Wing Configuration 129
Lizhen Liu and Xiongqing Yu

Research on the Mechanism of Resistance Generation in Disc Acceleration Based on Lagrangian Method 153
Shujia Lin, Fuxin Wang, Zhuoqi Li, and Yang Xiang

A Review of Supersonic Turbines Based on Constant Volume Combustion Cycle 169
Liangjun Su and Fengbo Wen

An Application of QFD in Aircraft Conceptual Design 193
Shiyu Wang, Zhouwei Fan, and Xiongqing Yu

Parametric Optimization of the PCM Caisson Structural Strength Elements 217
Aleksandr Bolshikh and Valentin Eremin

Influence and Correction of Satellite Phase Center Offsets for RNSS Performance of BDS-3 225
Cheng Liu, Weiguang Gao, Chengpan Tang, and Wei Wang

Effects of Tube Wall Thickness on Combustion and Growth Rate of Supersonic Reacting Mixing Layer 243
Di Lu and Fang Chen

An Investigation for Effective Thermal Properties of Titanium Alloy Lattice Sandwich Panels 253
Junpeng Li and Zhibin Yang

Modeling and Analysis of Gate to Gate Flight Process Based on SysML in Commercial Aircraft 265
Hongyu Li, Miao Wang, Gang Xiao, Guoqing Wang, Bei Tian, and Zihang Chen

Research of Commercial Aircraft's Battery Layout Design Method Based on Ditching Situation 283
Li Wen Wu

Model-Based Surface Trajectory-Based Operations Analysis in Airport Surface Management 293
Wenhao Zhao, Miao Wang, Gang Xiao, and Guoqing Wang

Development and Application of a Functional Analysis Method for Aero Engine Requirement Management 305
Yan Ji, Zhenyu Sun, and Zhimin Li

Research on Civil Aero Engine Requirements Development and Management 317
Zhenyu Sun, Yan Ji, and Zhimin Li

Investigations on the Acoustic Resonance in Aeroengine Multi-Stage Compressor 329
Zihao Wu and Xiaohua Liu

Computational Method in the Throughflow Simulation of Aeroengine Compressor 345
Qitian Tao, Hailiang Jin, and Xiaohua Liu

Rotating Beamforming in the Frequency Domain for an Incomplete Microphone Array 359
Mengxuan Li, Wei Ma, and Wei Zhou

Comprehensive BDS-3 Signal Simulating for Strong Ionospheric Scintillation Studies 369
Jihong Huang, Xingqun Zhan, and Rong Yang

Fan Broadband Noise Localization and Mode Identification Technology in Turbofan Engine 387
Jingnan Chen and Wei Ma

Performance Evaluation of Robust GPS Signal Tracking with Moving Horizon Estimation in Urban Environment 403
Jiawei Xu, Rong Yang, and Xingqun Zhan

Feasibility Exploration on Simulation Study Based on Peridynamic for the Bio-Inspired Nacre Nano Composite Against the Impact 419
Zhiwei Zhou, Shufan Wu, Zhongcheng Mu, Wei Wang, and Ningjing Jiang

An Interface Management Approach for Civil Aircraft Design 435
Dake Guo, Xinai Zhang, Jiejing Zhang, and Haomin Li

Finite Elements Modeling of Randomly Oriented Short Fiber-Reinforced Composite Materials 447
Daniil Lupachev and Yile Hu

Capturing and Defining Interface Requirements in Commercial Aircraft Development Program 455
Jiejing Zhang, Xinai Zhang, Haomin Li, Dake Guo, Yong Chen, and Kaili Zhang

Features of the Use of Damper Supports of Various Designs in a Gas Turbine Engine 463
N. S. Konoplev, L. V. Farsiian, A. V. Davidov, and M. K. Leontiev

Research on Integration Technology of Stereoscopic Environment Monitoring System Based on UAV 473
Weigang An, Liu Liu, Yanping Wang, Wei Zeng, and Le Wang

Effects of Transition on Aerodynamic Characteristics of Laminar Airfoil Based on CFD 485
Yanping Zhao, Lianghua Xiao, Yao Chen, and Rui Chen

4D Trajectory and Controller Command Generation Based on Schedule Time of Arrival 495
Jie Liu, Shuoyan Zhang, and Jizhi Mao

The Mechanisms of Albatrosses' Energy-Extraction During the Dynamic Soaring 507
Wei Wang, Weigang An, and Bifeng Song

Aerodynamic Design and Optimization of Bionic Wing Based on Wandering Albatross 517
Weigang An, Fuzhen Shi, Shibei He, Wei Wang, Hang Zhang, and Liu Liu

Effect of Aspect Ratio on Wake Patterns and Thrust Characteristics of Pitching Wings 537
Dechuan Ma, Zhan Qiu, Gaohua Li, and Fuxin Wang

Research on Negative Turbulent Kinetic Energy Production in Supersonic Channel Flow 553
Hang Zhou and Fang Chen

Design and Experimental Study of Automatic Docking and Undocking Robot System for Launch Vehicle Propellant Filling 565
Jiawei You, Yue Huang, and Xiangming Dun

Adaptive Fading Factor Unscented Kalman Filter with Application to Target Tracking 579
Peng Gu, Zhongliang Jing, and Liangbin Wu

A Function Analysis Methodology Applied in Civil Aircraft Design 589
Chao Tang, Xinai Zhang, Haomin Li, Dongsheng Chen, Jian Wang, and Yong Chen

Test Research and Finite Element Analysis on Extension Performance of Civil Aircraft Flaps Subjected to Extreme Temperature

Jingtao Wu, Sibo Zhou, Wenliang Deng, and Yunwen Feng

Abstract Aircraft climate test was conducted to investigate the effect of extreme temperature on extension performance of civil aircraft flaps in aircraft climate laboratory. Test results show extending the flaps to 10° requires 9.5 s, 7.8 s, 7.6 s when the standard equipped aircraft was kept at −40 °C, 20 °C and 40 °C for the stipulated time, respectively. The lower the temperature is, the more difficult it is to extend the flaps. Furthermore, a finite element analysis (FEA) mode of the flap motion mechanism was proposed to reveal the influence of extreme temperature on deformation and drive torque of the flaps. Actual motion law of flap motion mechanism was adopted to describe behavior of flap motion mechanism under extreme temperature. The numerical research shows the drive torque decreases from -0.51×10^4 to -4.52×10^4 N mm when temperature rises from 20 to 74 °C; conversely the drive torque increases from -0.51×10^4 to 27.5×10^4 N mm when temperature drops from 2 to −55 °C. In addition, the lower the temperature is, the more obvious the deformation mismatch of the flap mechanism is, which may cause the friction to increase. The increasing friction due to the temperature drop results in the higher drive torque required to extend the flaps, which is also the reason that the time for extending the flaps to 10° increases with the decrease of temperature. The numerical results are observed to mutually agree with the test results mentioned above that the low temperature makes it difficult to extend the flaps.

Keywords Aircraft climate test · Standard equipped aircraft · Civil aircraft flaps · Finite element analysis · Extreme temperature

J. Wu (✉) · S. Zhou · W. Deng
AVIC Aircraft Strength Research Institute, Xi'an, China
e-mail: ASRI_cetf@163.com

S. Zhou
e-mail: zhouyinwpu@163.com

Y. Feng
Northwestern Polytechnical University, Xi'an, China
e-mail: fengyunwen@nwpu.edu.cn

Z. Jing and X. Zhan (eds.), *Proceedings of the International Conference on Aerospace System Science and Engineering 2020*, Lecture Notes in Electrical Engineering 680,
https://doi.org/10.1007/978-981-33-6060-0_1

1 Introduction

The performance of the wing should be considered during cruise, landing and takeoff periods. Therefore, high-lift devices must be used on the original surface of the wing. A typical cross section of the wing is shown in Fig. 1 [1], in which the flaps exist. During the cruise, the flaps retract to reduce the drag of the aircraft. The flap extension increases the camber and the area of the wing to improve the lift coefficient, and shorten the distance during take-off and landing periods. Flap motion mechanism consists of a large number of motion pairs. It not only needs to bear and transfer loads, but also realize the relative movement between the flap and wing [2–4].

For the flap motion mechanism, it inevitably suffers all kinds of damages during life time, such as load parameters, extreme climate, dimensional error and abrasive wear. Some of the factors give rise to failure of movement mechanism [5–9]. The performance of flaps influences the reliability and safety of an aircraft directly during cruise, landing and takeoff periods. Once its movement mechanism fails and the flap can't deploy or retract, the aerodynamic performance will be greatly affected [10, 11]. Even worse, the Even worse, the deployment or retraction of flap fails, leading to a crash of an aircraft. According to the statistics of aviation accidents, accidents caused by damage of flap motion mechanism had occurred. As a result, many studies have focused on researches of the reliability of the flap mechanism. High-lift mechanisms were analyzed in combination with test data, mathematic model and simulation technology in recent years. As the occurrence of drive strut rupture is the main failure mode of the flap, Yoshida T. et al. used MSC Adams to establish the parametric model of the high-lift system. Dynamical response were analyzed to facilitate understanding of the normal case and fault case, after validating the simulation model based on the test data [1, 12, 13]. With regard to flap fault simulation, Huan Pang et al. builded the rigid and flexible coupling model of the flap mechanism, using the virtual prototyping technology, and analyzed the reliability of flap seizure [6, 14]. Reliability analysises of the flap mechanism were conducted, considering the manufacturing errors, aerodynamic loads, component damage and other factors [6,

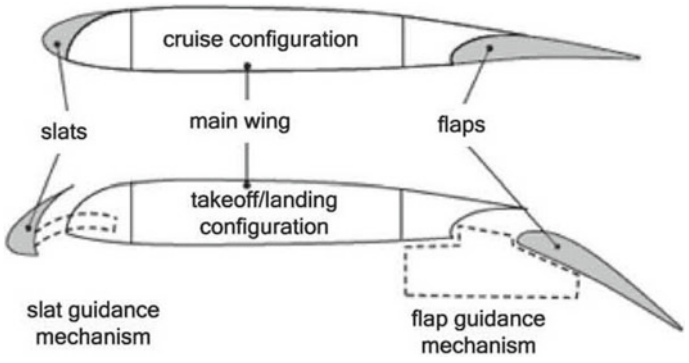

Fig. 1 Schematic of wing cross section with high-lift devices [1]

15, 16]. In addition, important sampling method was used to analyze the structure reliability of the flap, taking into considerarion of randomness of the elastic modulus, shear modulus and aerodynamic loads [17].

Under extreme temperature, the components of the flap motion mechanism may produce a certain amount of deformation. If the deformation amount is too large, the movement of relevant components may not be in place, which will affect the flap extension performance. In serious cases, it will also cause flaps to jam, which has a great impact on the flight safety of civil aircraft. The damage of flap motion mechanism has caused several accidents. However, the effects of extreme temperature on extension performance of civil aircraft flaps have not been globally and adequately researched. In order to reduce the risk and analyze the failure mechanism and reliability of the flap mechanism clearly, in this paper, a finite element analysis (FEA) mode of the flap motion mechanism was proposed to reveal influence of extreme temperature on extension performance of civil aircraft flaps. After validating the simulation model based on the test data, deformation, friction torque and drive torque of the flaps are fully analyzed at extreme temperature. Then, aircraft climate test was conducted to investigate effect of extreme temperature on extension performance of civil aircraft flaps in aircraft climate laboratory. The calculated performance simulation data were compared with the experimental data.

2 Simulation Model Building of the Flap

The finite model of the flap mechanism is comprised of the flap structure, rocker arm, rotation and slide rail mechanism. A typical flap motion mechanism is shown in Fig. 2. The coordinate system assembly method is used to establish the motion pairs between the components according to the motion relationship and the corresponding friction coefficient was set at the motion pairs. Load and drive are added to the model to complete the multi-rigid body modeling. Based on the simulation model, the influence of extreme temperature on deformation and extension performance of the flap is analyzed.

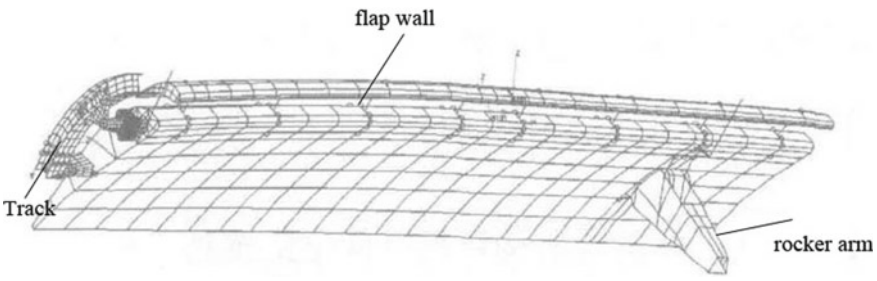

Fig. 2 Typical flap motion mechanism

3 Change Law of Rotation Angle of Rocker Arm with Time

The extreme temperature influences the extension performance of the flap motion mechanism, so it is necessary to analyze the influence of the extreme temperature on the drive torque. In the model, the temperature affects the magnitude of the friction torque by changing the friction coefficient, which in turn affects the drive torque. Method for calculating the law of rotation angle of rocker arm with time is showed in Fig. 3. M_r, M_d, M_g and M_f are the resultent torque, drive torque,

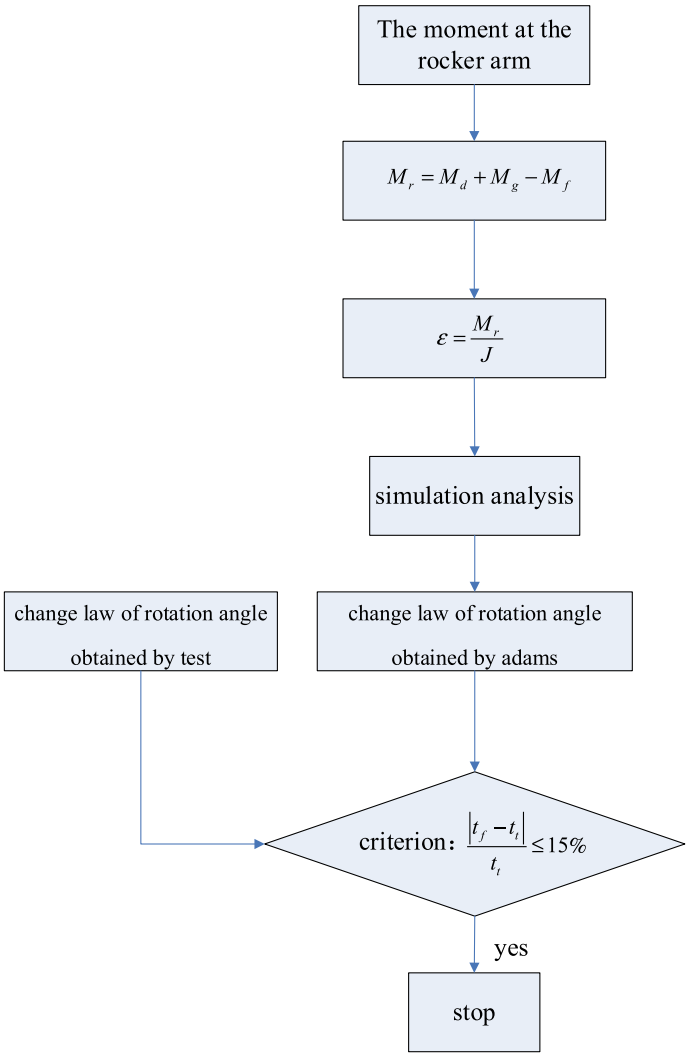

Fig. 3 Dynamic simulation program based on test data

gravity torque and friction torque of the rocker arm shaft during the extension of flap motion mechanism, respectively. J is moment of inertia of flap motion mechanism. ε represents the angular acceleration of flap motion mechanism. Time required to rotate the same angle in simulation analysis and test is t_f and t_t, respectively.

The resultant torque is obtained by the following formula:

$$M_r = M_d + M_g - M_f \tag{1}$$

The angular acceleration is calculated by the following formula:

$$\varepsilon = \frac{M_r}{J} \tag{2}$$

The variation law of angular acceleration can be obtained through simulation analysis. The variation law of angular acceleration is taken as the input of simulation. Furthermore, through the comparison test and simulation analysis, the error between the simulation analysis and test results is expressed:

$$\delta = \frac{\left|t_f - t_t\right|}{t_t} \tag{3}$$

if the error does not exceed 15%. Simulation stop is generated.

4 Deformation Analysis of Flap Motion Mechanism at Extreme Temperature

A certain amount of deformation may occur when flap motion mechanism is subjected to extreme temperature. Figure 4 presents the deformation of the flap wall and the flap motion mechanism subjected to extreme temperature load. Flap wall-L and and Flap wall-H in Fig. 4 represent the deformation of flap wall at low temperature and high temperature, respectively. Deformation representation method of mechanism is similar to that of flap wall. As can be found in Fig. 4, the deformation at high temperature is greater than the deformation at low temperature. The maximum deformation of the flap wall and flap motion mechanism occur at high temperature. The deformation of the flap wall, rocker arm and connecting rod decreases as the flap extends, while the deformation of the support arm and track increases as the rotation angle of the flap increases. The maximum deformation of flap wall, rocker arm, connecting rod, support arm and track are 4.42 mm, 3.57 mm, 3.39 mm, 1.27 mm and 1.10 mm, respectively. What's more, the thermal elongation of the connecting rod intensifies the compressive stress along the connecting rod, resulting in the bending and rupture of connecting rod. The increasing friction due to the misfit of deformation may result in the higher drive torque required to extend the flaps.

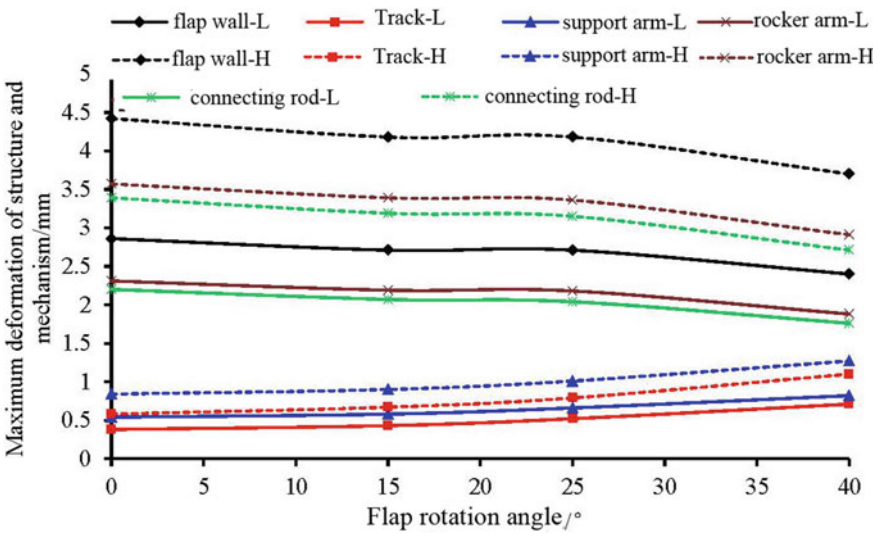

Fig. 4 Variation of maximum deformation with the rotation angle

In recent years, failure modes of flap motion mechanism have been investigated. As can be seen obviously in Fig. 5, the bending and rupture of connecting rod occur. The thermal deformation on the flap motion mechanism will aggravate the wear and stagnation of the flap motion mechanism, resulting in larger drive torque to extend the flap. When the driving torque is large enough, the connecting rod bends or breaks.

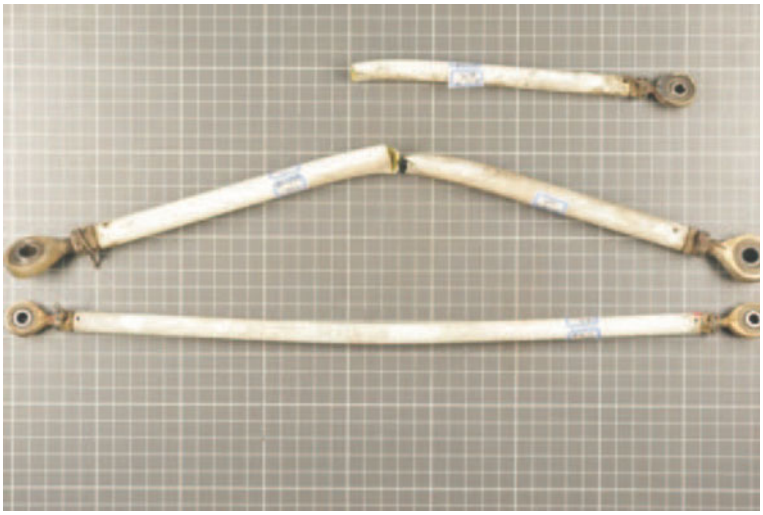

Fig. 5 Bending and rupture of connecting rod

The phenomenon agrees very well with the result above that compressive stress along the connecting rod leads to the bending and rupture of connecting rod.

5 Extension Performance Analysis of Flap Motion Mechanism

The drive shaft is subjected to drive torque, gravity torque and friction torque during the extension of the flap motion mechanism. Herein, the changes of the driving torque, gravity torque and friction torque at the drive shaft of the flap motion mechanism at 20 °C (room temperature), −55 °C (low temperature) and 74 °C (high temperature) can be obtained through simulation analysis, respectively.

5.1 Extension Performance Analysis at Room Temperature

The evolution of the gravity moment during the extension of the flap motion mechanism is shown in Fig. 6a. Gravity moment increases with the extension angle. During the extension of the flap motion mechanism, the distance from the center of mass of flap motion mechanism to the drive shaft gets increased, which in turn causes the gravity moment to increase continuously with the extension angle. As also can be found in Figs. 6a, 7a and 8a, temperature has no effect on the moment of gravity. The value of gravity moment only depends on the distance from the center of mass of flap motion mechanism to the drive shaft.

Figure 6b presents the change of the friction torque during the extension of the flap motion mechanism. The friction torque increases rapidly when the flap starts to extend, then becomes almost invariant in magnitudes during the extension of the flap motion mechanism. Whereas the friction torque increases as the temperature decreases. The increasing friction coefficient due to the temperature drop results in the higher friction torque.

Figure 6c shows the variations of the drive torque during the extension of the flap motion mechanism. The drive torque of the flap motion mechanism decreases first, then increases as the flap extends. During extension performance of civil aircraft flaps the angular acceleration of the flap mechanism increases from 0 to a certain value in a short time. A larger total torque is required to overcome the inertial force when the flaps start to extend. So the drive torque decreases to -0.51×10^4 N.

Gravity moment increases as the flap extends, while the friction torque remains invariant in magnitudes at the subsequent extension of civil aircraft flaps. The drive torque also needs to increase continuously to maintain the torque balance of the flap motion mechanism.

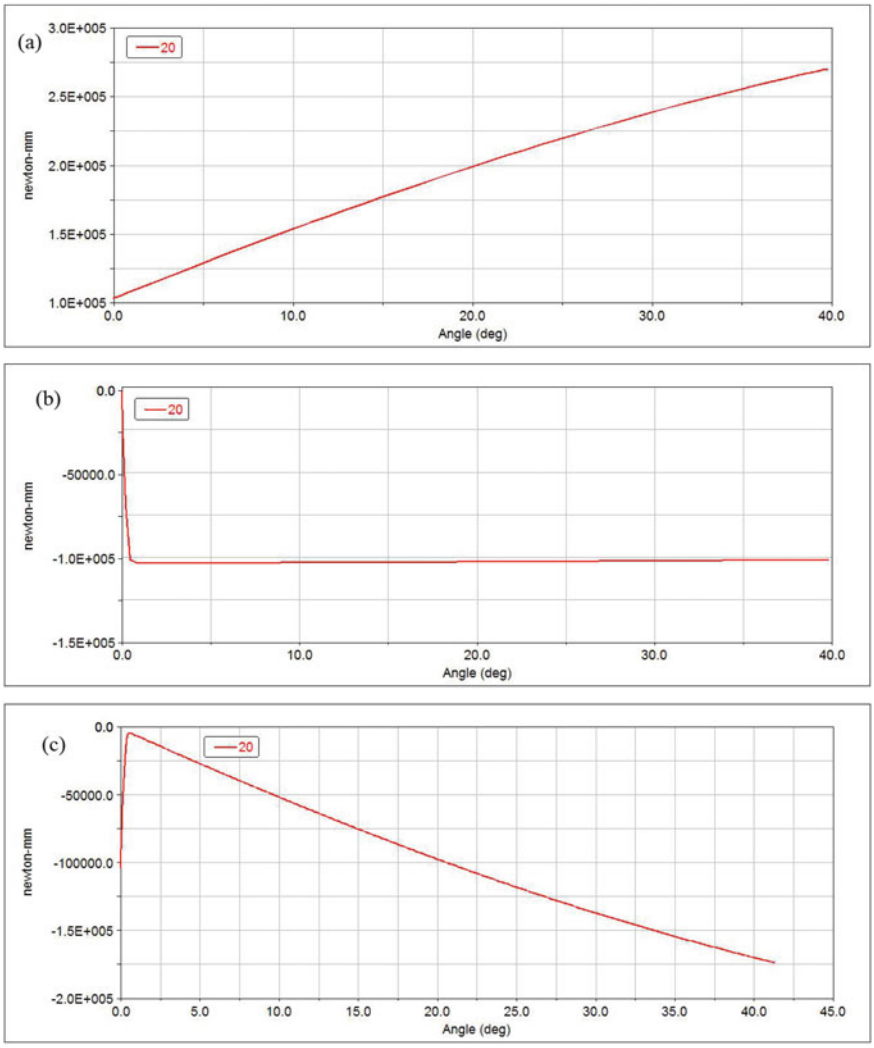

Fig. 6 Variation of moment with the rotation angle of flap motion mechanism at room temperature: **a** gravity moment; **b** friction moment and **c** drive gravity

5.2 Extension Performance Analysis at High Temperature

The variation of moment with the rotation angle of flap motion mechanism is shown in Fig. 7. As can be seen obviously in Fig. 7a, b, the gravity moment of the flap motion mechanism is greater than the friction torque when flap motion mechanism is at high temperature, so the drive torque and the friction torque are used together to balance the gravity moment.We can find that in Fig. 7c, the drive torque of the flap

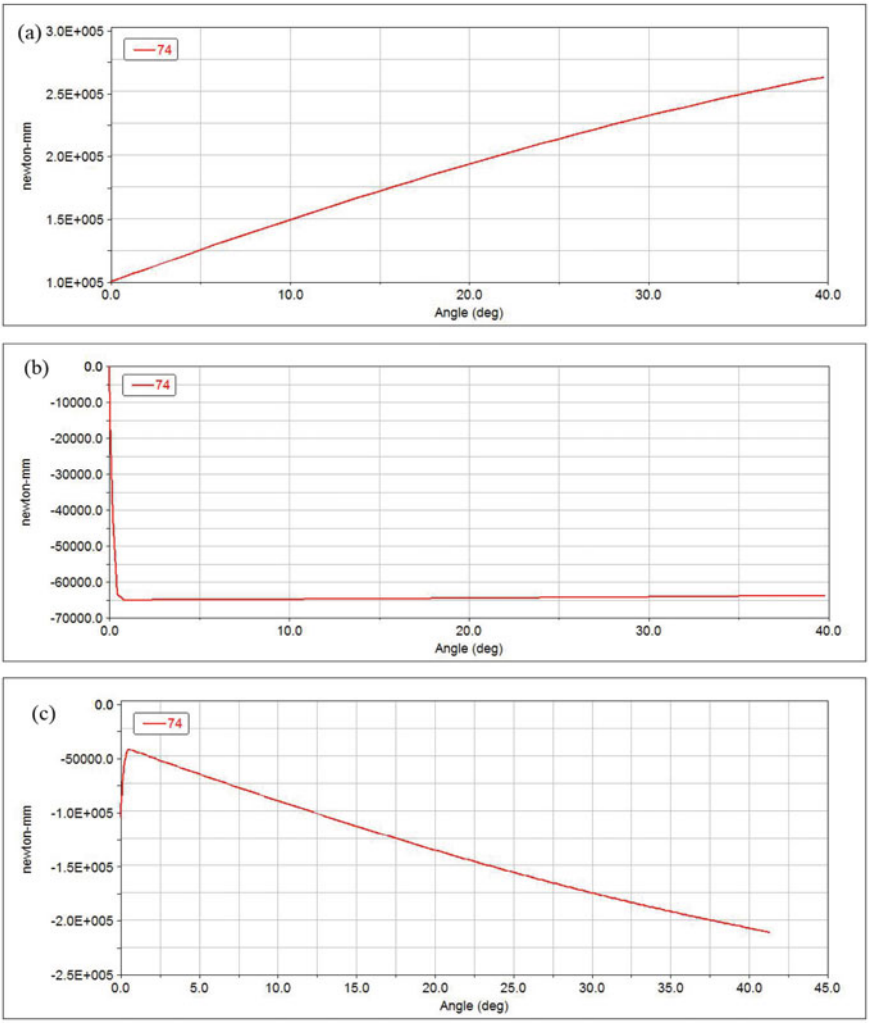

Fig. 7 Variation of moment with the rotation angle of flap motion mechanism at high temperature: **a** gravity moment; **b** friction moment and **c** drive gravity

motion mechanism decreases first, then increases as the flap extends. The change trend of gravity moment and friction moment is similar to that at room temperature.

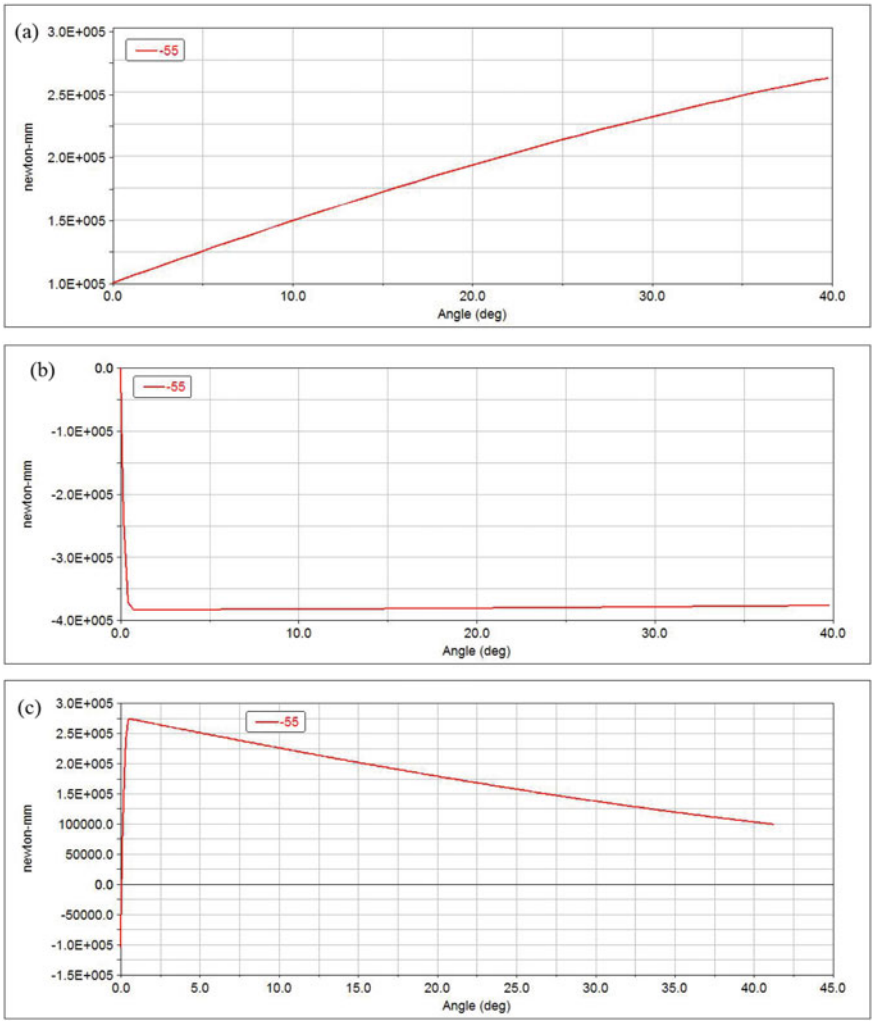

Fig. 8 Variation of moment with the rotation angle of flap motion mechanism at low temperature: **a** gravity moment; **b** friction moment and **c** drive gravity

5.3 Extension Performance Analysis at Low Temperature

The evolution of the drive torque during the extension of the flap motion mechanism is shown in Fig. 8c. Nevertheless, negative value of drive torque is converted to positive value when temperature drops to −55°C, suggesting the increasing friction due to the temperature drop results in the higher drive torque required to extend the flaps. Futhermore, drive torque decreases as the flap extends. The gavity torque of the flap mechanism keeps increasing while the friction torque stay basically unchanged.

Consequently, the drive torque needs to decrease to maintain the torque balance of the flap mechanism. As shown in Fig. 8a, b, the change trend of gravity moment and friction moment is similar to that at room temperature.

It is manifest in the contrast among Figs. 6c, 7c and 8c, that the drive torque decreases from -0.51×10^4 to -4.52×10^4 N mm when temperature rises from 20 to 74°C; conversely the drive torque increases from -0.51×10^4 to 27.5×10^4 N mm when temperature drops from 20 to −55°C. The lower the temperature resultes in greater friction, implying the larger drive torque is needed to extend the flaps. It is concluded that the low temperature makes it difficult to extend the flaps. The extreme temperature influence the friction force of each motion pair of flap motion mechanism. Especially, the drive torque of the flap motion mechanism will be affected to some extent by low temperature, which will increase the risk of jamming or even rupture of the motion mechanism.

5.4 Test Verification of Flap Motion Mechanism Simulation Model

Aircraft climate test was conducted to investigate the effect of extreme temperature on extension performance of civil aircraft flaps in aircraft climate laboratory. The tests were performed with the non-contact measurement under the stated test conditions. The time for extending the flaps to 10° is used to characterize difficulty of starting to extend the flaps. Test results show extending the flaps to 10° requires 9.5 s, 7.8 s, 7.6 s when the standard equipped aircraft was kept at −40°C, 20°C and 40°C for the stipulated time, respectively. The lower the temperature is, the more difficult it is to extend the flaps.

The numerical results are observed to mutually agree with the test results mentioned above that the low temperature makes it difficult to extend the flaps. The larger drive torque is needed to extend the flaps when temperature decreases. It demonstrates accuracy of the method proposed in the paper.

6 Conclusions

The present study focuses on deformation analysis and effect of extreme temperature on extension performance of civil aircraft flaps. What's more, drive torque, gravity torque and friction torque are fully analyzed when the flap motion mechanism is subjected to extreme temperature, and simulation model is validated by test. The major conclusions are summarized as follows:

(1) The maximum deformation of the flap wall and flap motion mechanism occur at high temperature.

(2) The deformation misfit of flap motion mechanism will aggravate the wear and stagnation of the flap motion mechanism, resulting in larger drive torque to extend the flap.
(3) The increasing friction due to the temperature drop results in the higher drive torque required to extend the flaps. What's more, negative value of drive torque is converted to positive value due to the decrease of temperature.

Acknowledgements The authors gratefully acknowledge the support for this work from civil aircraft environmental adaptability research team.

References

1. Heyden T Elastic multibody models of transport aircraft high-lift mechanisms. J Aircraft 46(5):1513–1524
2. Chunlin G et al (2018) Numerical investigation of the effects of different parameters on the thrust performance of three dimensional flapping wings. Aerospace Sci Technol
3. Song Q (2017) Analysis of flap mechanism reliability. In: International conference on mechatronics engineering & information technology
4. Renukumar B et al Effect of flap and slat riggings on 2-D high-lift aerodynamics. J Aircraft. 43(5):1259–1271
5. Cui L, Lu Z, Hao W Importance analysis of the aircraft flap mechanism movement failure. J Aircraft 48(2):606–611
6. Pang H et al (2011) Reliability analysis of the flap mechanism with multi-pivots. Inf Japan 15(12)
7. Rehwald S (2007) Analysis of the performance potential of a single aisle transport aircraft with a new high-lift differential flap system. J Ethnic Migration Stud 33(6):1003–1016
8. Song B (2011) Reliability analysis of the flap mechanism with multi-pivots. In: International conference on quality
9. Tang Z (2015) Nonprobabilistic reliability analysis for an inside flap of an aircraft. J Aircraft 49(1):250–256
10. Liu P (2017) Aerodynamic optimization and mechanism design of flexible variable camber trailing-edge flap. 中国航空学报(英文版) 30(3):988–1003
11. Yang L Reliability analysis of structure and control mechanism of aircraft flap. Comput Struct 38(1):21–24
12. Winter E, Woernle C (2013) Multibody modelling of high-lift mechanisms of modern transport aircraft. In: Mechanisms and machine science
13. Yoshida T, Mizusaki Y, Taki T (2004) Analysis and rig test in EMB170 flap mechanism development. In: 24th international congress of the aeronautical sciences (ICAS), pp 1–4
14. Cui L et al (2009) Dynamic response reliability analysis of airplane inner-flap mechanism. Gaojishu Tongxin/Chin High Technol Lett 19(12):1299–1304
15. Luo X et al (2020) The feasibility and survival mechanism of a large free flap supported by a novel hybrid perfusion mode. Oral Oncol 101:104506
16. Song B (2011) Reliability analysis of the flap mechanism with multi-pivots. Inf Japan 15(12)
17. Tang HM et al (2012) Expression of NPY and 5-HT in rat model of diarrhea-predominant irritable bowel syndrome. Chin Pharmacol Bull 28(7):916–920

Mathematical Modeling of an Environment Control System in the Framework of Creating a Comprehensive Mathematical Model of Aircraft On-Board Systems

R. S. Savelev, K. S. Napreenko, and A. V. Lamtyugina

Abstract The development and creation of modern aircraft is a complex technical process consisting of many iterations. Successful design and further operation of the developed aircraft models can be achieved only if there is the required amount of research at the design stage and when carrying out the full volume of tests. Also, when developing aviation technology, it is necessary to apply an integrated approach, for example, it is necessary to consider aircraft systems as a complex of interconnected systems, and not as separate, unrelated components. When developing technically complex aircraft systems, it is advisable to use mathematical modeling methods. The main aircraft systems of interest from the point of view of mathematical modeling (determination of the mutual influence of systems, maximum energy loads, optimization of aggregate parameters, etc.) and the formation of a complex of interrelated mathematical models are the following systems: power supply system (PSS), hydraulic system (HS); environment control system (ECS) and fuel system (FS). The study of the joint operation of these systems will allow not only an assessment of the parameters of the units and components of the systems, but also an assessment of the operation of the systems as a whole at various operating modes of the aircraft; working out the basic algorithms for controlling systems under various airplane operating modes, to determine the effect of failures of one system on the operation of other systems. In this paper, we consider in more detail the mathematical model of ECS. The main simulated characteristics in the mathematical model of ECS are: change in pressure and temperature in the system through pipelines and on key units (heat exchangers, turbomachine, shutters, etc.); changing the bleed air flow rate in bleed system in case of various operation mods, as well as at different values of the supported pressure in the cabin; change in air flow in the branches of the pipelines of the system with a mixture of hot air in accordance with the algorithms of operation of the valves, etc. A mathematical model of the key node of ECS—an air-cooling unit—is considered, simulation results for various operating modes are shown (airplane parking on the ground on a hot day, flying near the ground and flying at altitude). The developed mathematical model of ECS allows to use it both

R. S. Savelev (✉) · K. S. Napreenko · A. V. Lamtyugina
Moscow Aviation Institute (National Research University), Moscow, Russia
e-mail: r_sr@inbox.ru

Z. Jing and X. Zhan (eds.), *Proceedings of the International Conference on Aerospace System Science and Engineering 2020*, Lecture Notes in Electrical Engineering 680,
https://doi.org/10.1007/978-981-33-6060-0_2

for evaluating the operation of nodes and units of the ECS, and for use as part of a set of interconnected mathematical models of the aircraft.

Keywords Mathematical model · Complex on-board systems · Environment control system · Heat exchanger · Turbomachine

1 Introduction

The development and creation of modern aircraft is a complex technical process consisting of many iterations. Successful design and further operation of the developed aircraft models can be achieved only if there is the required amount of research at the design stage and when carrying out the full volume of tests. Also, when developing aviation technology, it is necessary to apply an integrated approach, for example, it is necessary to consider aircraft systems as a complex of interconnected systems, and not as separate, unrelated components.

When developing technically complex aircraft systems, it is advisable to use mathematical modeling methods. The main aircraft systems of interest from the point of view of mathematical modeling (determination of the mutual influence of systems, maximum energy loads, optimization of aggregate parameters, etc.) and the formation of a complex of interrelated mathematical models are the following systems: power supply system (PSS), hydraulic system (HS); environment control system (ECS) and fuel system (FS).

Mathematical modeling is a relatively new and rapidly developing method for studying the behavior of complex systems [1–5].

The use of mathematical modeling for the design of aircraft systems allows to:

- Reduce system design time;
- Optimize the system architecture according to the criteria of weight and energy perfection;
- Create requirements for suppliers of nodes and aggregates;
- Develop and optimize control algorithms for onboard systems;
- Evaluate the reliability of onboard systems, fault safety.

2 Building a Mathematical Model of a Technical Object

Consider the sequence and relations of stages of building a mathematical model of an object. Figure 1 shows a flowchart for creating a mathematical model of a technical system.

The real object when creating a mathematical model can be a complex of aircraft onboard systems, any separate system or a specific node of this system.

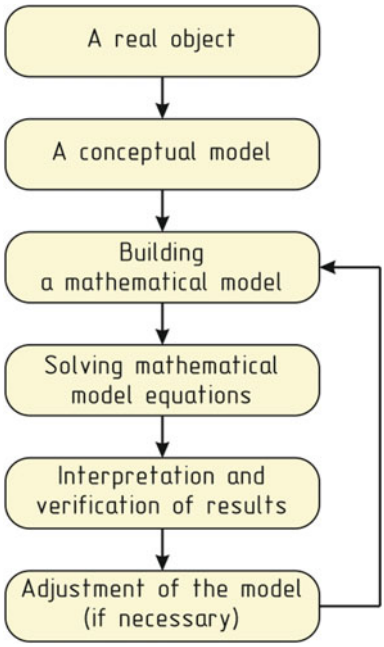

Fig. 1 Sequence and relations of stages of building a mathematical model of an object

The conceptual model formulates the properties of an object that are of interest for building a mathematical model, for example, thermal and gas-dynamic processes that occur during the operation of objects.

The stage of building a mathematical model consists in forming a complex of mathematical dependencies that describe the functioning of the object in general. These dependencies are formed in general terms and contain a complex of values (coefficients) that are not defined at this stage.

The stage of solving the equations of a mathematical model involves determining the coefficients of the equations for a specific type of product and allows to calculate the output parameters or product characteristics that are of interest to us at known values of the input parameters.

The next stage is to analyze the results obtained from the point of view of their reliability by comparing them with other known facts, for example, with experimental data or results obtained from other computational studies. Here it may be necessary to adjust the model and repeat the cycle of its formation.

3 Creating a Comprehensive Mathematical Model of Aircraft On-Board Systems

When developing aviation technology, it is necessary to apply an integrated approach, for example, aircraft systems should be considered as a complex of interconnected systems, and not as separate, unrelated components. Therefore, a promising direction in the development of aircrafts is currently the creation of a complex mathematical model of onboard systems. A complex mathematical model of aircraft onboard systems is a combination of all power and mechanical systems that ensure the implementation of the main goals and objectives of the designed aircraft. Figure 2 shows the structure of a comprehensive mathematical model of on-board systems functioning. The structure shows that the aircraft systems are connected to each other by a common connection (electrical energy) through the PSS. PSS is a system that allows to combine several aircraft systems within a complex of interconnected onboard systems [6].

On this structure of the complex mathematical model different types of energy, due to which the interaction of mathematical models of individual systems occurs, are indicated with different colors: red—electrical energy, black—mechanical energy, blue—pneumatic energy, green—hydraulic energy, light green-fuel. The use of the electrical power supply system and electric energy as the basic and unifying system is not accidental. First, it provides operation of aggregates of other systems (power supply of sensors, dampers, shutoff valves, etc.). And also electric energy to date has a number of advantages over other types of energy (for example, in terms of reliability, speed, automation and operation), which has led to the trend of creating aircraft with an increased level of electrification in the aircraft industry [7–10] and replacing traditional types of energy with electric in other areas of industry [11–14].

The main aircraft systems that are of interest for mathematical modeling (determining the mutual influence of systems, maximum energy loads, optimizing

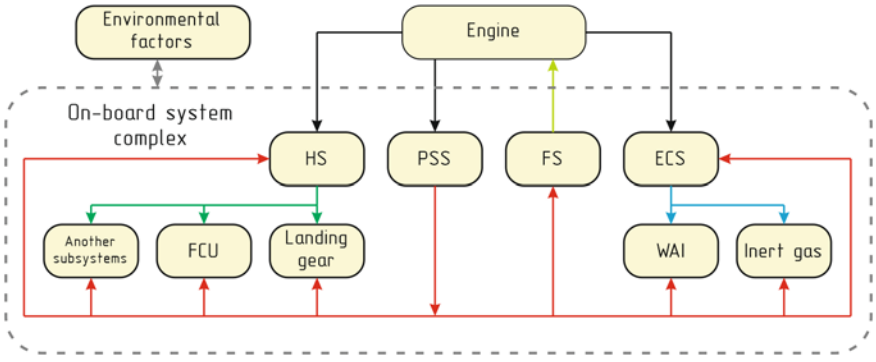

Fig. 2 Structure of a comprehensive mathematical model of on-board systems functioning

the parameters of aggregates, etc.) and forming a complex of interconnected mathematical models are the following systems:

– Power supply system;
– Hydraulic system;
– Environment control system;
– Fuel system.

In addition to these systems, it is also worth noting that to create a digital twin of the aircraft, it is also necessary to consider an inert gas generation system, an anti-icing system, and others.

Research collaboration onboard systems will allow:

– To hold not only the estimation of the parameters of assemblies and units of systems, but also the evaluation of work systems in general in different modes of operation of the developed aircraft;
– Development of the main algorithms for controlling systems in various modes of operation of the aircraft, to determine the impact of failures of one system on the operation of other systems.

4 Mathematical Model of an Environment Control System

When designing and researching environment control system, the method of mathematical modeling is widely used [15–18].

The mathematical model of the ECS contains both the thermohydraulic part (pipelines, heat exchangers, dampers, etc.) and the control system (algorithms of the ECS).

The main input parameters for the mathematical model of the ECS are the characteristics of its operating mode (Mach number, height, setting the temperature parameters in a cockpit, data on cooling electronic units, rates required for other systems (an anti-icing system, an accumulator tank pressurization system-tank pressurization system, etc.)). The input parameters of the ECS should also include data on the selection from the engine stage (pressure, selection temperature).

The main output parameters of the mathematical model are the parameters of the cooling air (pressure, temperature, flow rate) downstream of the ECS or at the entrance to the air intake sources from the ECS. The output parameters also include sensor signals (temperature, pressure, flow rates, and failure information).

Main modeled characteristics:

– Pressure changes in the system on pipelines and on key units (heat exchangers, turbomachines, dampers, etc.);
– Temperature changes in the system on pipelines and on key units (heat exchangers, turbomachines, dampers, etc.);
– Flow rate changes in the engine bleed system for different modes of operation of the aircraft and for different values of the maintained cabin pressure;

– Change in the air flow rate in the branches of the system pipelines when mixing hot air in accordance with the algorithms of the dampers, etc.

The key node of the system is the air cooling unit (ACU), which includes heat exchangers, turbomachines and other units.

The basic equation for calculating heat exchange effectiveness is Eq. 1:

$$\varepsilon_{steady} = \frac{\left|\phi_{steady}\right|}{\left|C_{\min} \cdot (T_{hot,in} - T_{cold,in})\right|} \tag{1}$$

where:

ε_{steady}	the effectiveness in steady state,
ϕ_{steady}	the heat exchanged in the heat exchanger in steady state,
$C_{\min}$	the minimal heat capacity rate,
$T_{hot,in}$—$T_{cold,in}$	the temperature difference between the inlet hot stream and the inlet cold stream of the heat exchanger.

Consider a mathematical model of the environment control system of an advanced aircraft.

Figure 3 shows a block-scheme of the Environment control system of an advanced passenger aircraft, which consists of two key components—the air bleed system (ABS) and the air cooling unit, as well as pipelines, etc.

The main elements of the air bleed system from the power plant are a pre-heat exchanger; a pressure regulator; a shutoff valve that provides air bleed from a higher or lower engine stage; sensors, control system, etc. The air cooling unit consists of a primary heat exchanger, a secondary heat exchanger, a condenser heat exchanger, a reheater heat exchanger, an air dryer, a three-wheeled turbomachine, sensors, regulating dampers, and control system.

In the Simcenter Amesim software package, the ECS was simulated in various operating modes. One of the key advantages of the developed ECS model is the ability to dynamically model the behavior of the system in the event of various failures in the selection system, which are the most critical in terms of ensuring the normalized air parameters in the passenger compartment. The model calculates the amplitudes of changes in air parameters in the bleed system, as well as the duration of the transition mode, in which there may be no air flow rate in the failed subsystem.

Figure 4 shows how the system works in a failure situation according to the following scenario:

Step 1-Failure of the pressure regulator in one of the two air bleed systems (ABS).
Step 2-Opening the cross-selection tap, air supply to the two subsystems from the same engine.

As an example, the following situation is considered: the regular operation of the environment control system is shown at the beginning, then at 15th second there is a failure of the pressure regulator of one of the ABS, as a result of which the

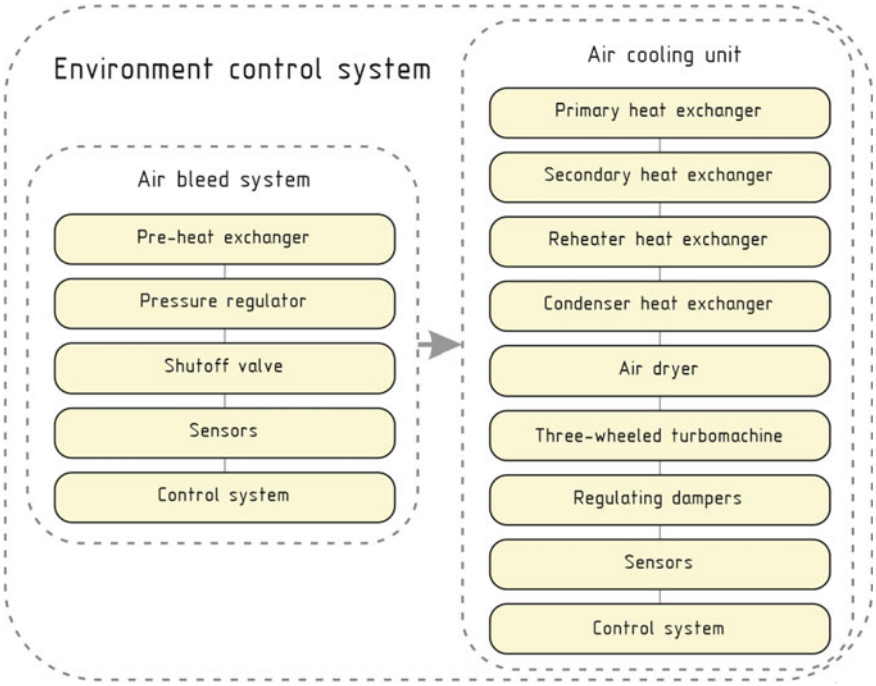

Fig. 3 Block-scheme of the ECS

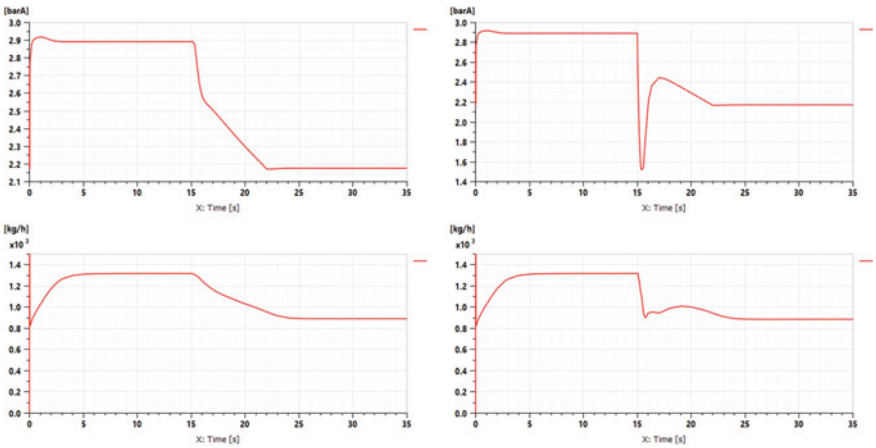

Fig. 4 Simulation of a failure situation

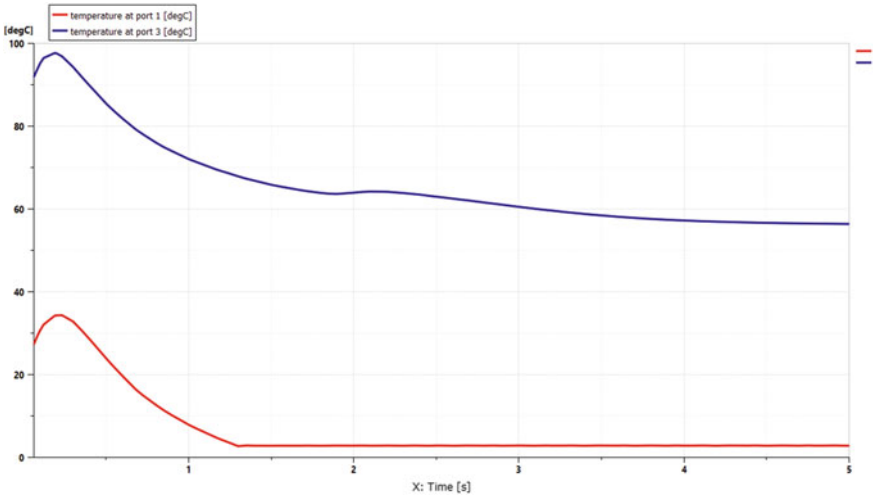

Fig. 5 The temperature at the inlet and the outlet of the turbine

cross-selection tap is opened and two air cooling units are powered from one of the ABS. The graphs (Fig. 4) on the left show the pressure and flow rate in the ACU for one side, and on the right the same parameters for the side where the ACU failure occurred. The mathematical model allows to evaluate not only the nature of changes in the parameters under study, but also to numerically estimate the values during transients.

The operation of the ECS on the ground, which ensures that there is no icing at the exit of the turbine due to the mixing of hot air, was also modeled. Thus, using a mathematical model, you can create a control law and select its parameters for the correct operation of the system.

The characteristics of the external environment correspond to the mode of Parking the aircraft in the parking on a hot day (Fig. 5).

It is worth noting that the correspondence of the mathematical model to the real object and, as a result, obtaining correct results in the study of various modes of operation of the system is possible only when filling and refining the model with a sufficient amount of initial data, which include local pipeline resistances, characteristics of aggregates, operating conditions, etc.

The developed mathematical model of the environment control system (as well as other onboard systems) and the entire complex of onboard systems can be used at all stages of the product life cycle. For example, the developed mathematical models of onboard systems that are validated based on the results of bench and flight tests can be refined, for example, during the modernization of the aircraft (Fig. 6).

The addition of the existing onboard system complex with initial data on key system nodes and aggregates provided by suppliers and developers during its modernization will reduce time and resources at this stage of the life cycle, as well as improve the quality of calculations.

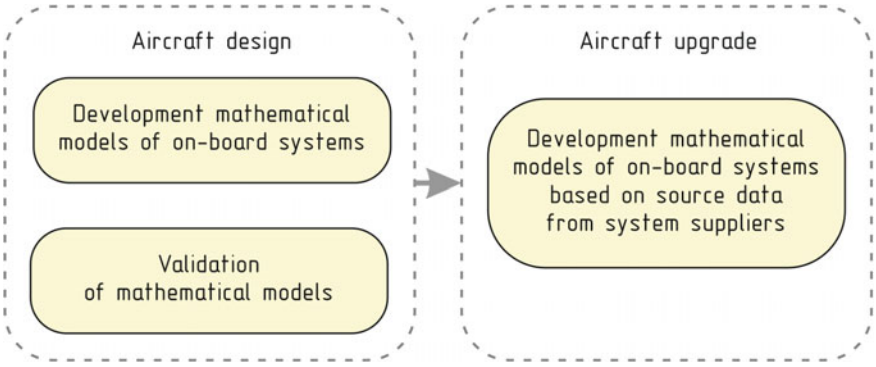

Fig. 6 Example of application of mathematical models of on-board systems at various stages of the product life cycle

5 Conclusion

As a result of the research, a mathematical model of the environment control system is developed, which allows determining the main parameters of the system. It is also worth noting that the developed model can be used in the future to create a complex mathematical model of the aircraft, adding connections with other systems (for example, PSS) and combining into one thermal model. It can also be used at all stages of the product life cycle, both during testing and when upgrading the system. This approach to the creation of new aircraft models will not only allow us to study the issues of mutual influence of systems on each other, including in the case of failure situations, but will also significantly reduce the costs spent on testing and refining on-board systems.

References

1. Satin A, Savelev R, Smagin D, Napreenko K, Neveshkina A (2019) Application simintech software for optimization fuel system parameters of the perspective helicopter. MATEC Web Conf 304:04016
2. Jian FU, Jean-Charles MARE, Liming YU, Yongling FU (2018) Multi-level virtual prototyping of electromechanical actuation system for more electric aircraft. Chin J Aeronaut 31(5):892–913. https://doi.org/10.1016/j.cja.2017.12.009
3. Wang H, Shang Y, Jia J, Jiao Z (2016) Simulation and analysis for users flow requirements of aircraft hydraulic system based on AMESim. In: Conference: 2016 IEEE/CSAA international conference on aircraft utility systems (AUS). https://doi.org/10.1109/AUS.2016.7748165
4. Tang J, Liu Q, Hu J, Huo J, Wang L (2018) Leakage fault diagnosis method of aircraft landing gear hydraulic cylinder based on wavelet packet. J Eng. https://doi.org/10.1049/joe.2018.9037
5. Maia Neto M, Goes L (2017) Use of LMS Amesim model to predict behavior impacts of typical failures in an aircraft hydraulic brake system. In: Proceedings of 15th Scandinavian international conference on fluid power. https://doi.org/10.3384/ecp1714429

6. Schettini F, Denti E, Di Rito G (2017) Development of a simulation platform of all-electric aircraft on-board systems for energy management studies. Aeronaut J New Ser 121(1239):1–10. https://doi.org/10.1017/aer.2017.16
7. Zhao Y, Che Y, Lin T, Wang C, Liu J, Jianmei Xu, Zhou J (2018) Minimal cut sets-based reliability evaluation of the more electric aircraft power system. Math Probl Eng. https://doi.org/10.1155/2018/9461823
8. Bozhko S, Hill CI, Yang Y More electric aircraft: systems and modeling. In: Wiley encyclopedia of electrical and electronics engineering, pp 1–31. https://doi.org/10.1002/047134608x.w8367
9. Ni K, Liu Y, Mei Z, Wu T, Hu Y, Wen H, Wang Y (2019) Electrical and electronic technologies in more- electric aircraft: a review. IEEE Access 7:2169–3536. https://doi.org/10.1109/ACCESS.2019.2921622
10. Rosero J, Romeral JL, Cusido J, Ortega JA, Garcia A (2007) Moving towards a more electric aircraft. IEEE Aerosp Electron Syst Mag 22(3):3–9. https://doi.org/10.1109/MAES.2007.340500
11. Smagin DI, Trofimov AA, Napreenko KS, Neveshkina AR (2020) Mathematical model of lithium-ion battery cell and battery (Lib) on its basis. In: IOP Conf Ser Mater Sci Eng 714:012027. https://doi.org/10.1088/1757-899X/714/1/012027
12. AVCI GZ, Özener O (2019) An electric public transportation vehicle modelling and comparison with conventional diesel vehicle. Int J Eng Res Adv Technol (IJERAT) 5. https://doi.org/10.31695/IJERAT.2019.3439
13. Gelmanova ZS, Zhabalova GG, Sivyakova GA, Lelikova ON, Onishchenko ON, Smailova AA, Kamarova SN (2018) Electric cars. Advantages and disadvantages. IOP Conf Ser J Phys Conf Ser 1015:052029. https://doi.org/10.1088/1742-6596/1015/5/052029
14. Hamilton H, Schulz N (2007) DC protection on the electric ship. In: Electric ship technologies symposium, 2007 ESTS'07 IEEE. https://doi.org/10.1109/ESTS.2007.372101
15. Unlu D, Cappuzzo F, Broca O, Borrelli P (2016) Minimizing aircraft ECS bleed off-take—virtual integrated aircraft applications. SAE Int J Aerosp 9(1):2016. https://doi.org/10.4271/2016-01-2054
16. Chen X, Yang S, Sun X, Wang L (2015) Research on 1D–2D Co-simulation for cabin air environment accident. Proc Eng 121:1983–1989. https://doi.org/10.1016/j.proeng.2015.09.196
17. Cappuzzo F, Broca O, Leboi J (2017) Simulation of aircraft virtual architecture—bleed off-take and ECS. SAE Technical Paper 2017-01-2159. https://doi.org/10.4271/2017-01-2159
18. Jordan P, Schmitz G A Modelica library for scalable modelling of aircraft environmental control systems. In: Modelica conference, at Lund, vol 15. https://doi.org/10.3384/ecp14096599

Investigation on the Effects of Atwood Number on the Combustion Performance of Hydrogen-Oxygen Supersonic Mixing Layer

Chengcheng Liu, Zi'ang Wang, Bin Yu, Bin Zhang, and Hong Liu

Abstract Combustion enhancement strategies are needed to improve the combustion efficiency of the supersonic shear layer. A 2D hydrogen-air supersonic shear layer with central jet filled of hydrogen and inert gas mixture under different Atwood (At) numbers is simulated, based on Navier-Stokes equations. The main purpose is to study whether optimal combustion enhancement can be obtained by changing fluid properties (At number). The Euler method cannot effectively identify the hidden flow field structure. Thus, the Lagrangian coherent structure method (LCS) is adopted to visualize the evolution process of vortex. Different Atwood numbers are adjusted by different inert gas (N_2, Ar, and He, corresponding to At = 0.14, 0.26, 0.57) with identical mass flow of hydrogen. The obtained results show that combustion efficiency of the reacting cases tends to increase and then decrease, as At number increases. At = 0.26 has the best combustion efficiency which is mainly measured by the normalized mass production of water. Combustion efficiency of At = 0.26 is higher than that of other two cases because of the shorter vortex shedding distance and resulting larger burning area. Combustion performance is controlled by the mixing process. Vortex shedding position is found to play an important role in entrainment process which directly decides the combustion efficiency. The entrained oxygen can be completely

C. Liu · Z. Wang · B. Yu · B. Zhang (✉) · H. Liu
School of Aeronautics and Astronautics, Shanghai Jiao Tong University, Shanghai, China
e-mail: zhangbin1983@sjtu.edu.cn

C. Liu
e-mail: liuchengcheng611@sjtu.edu.cn

Z. Wang
e-mail: wangziang@sjtu.edu.cn

B. Yu
e-mail: kianyu@sjtu.edu.cn

H. Liu
e-mail: hongliu@sjtu.edu.cn

B. Zhang
Sichuan Research Institute, Shanghai Jiao Tong University, Chengdu, China

Z. Jing and X. Zhan (eds.), *Proceedings of the International Conference on Aerospace System Science and Engineering 2020*, Lecture Notes in Electrical Engineering 680,
https://doi.org/10.1007/978-981-33-6060-0_3

consumed because of the excess hydrogen. In conclusion, shortening vortex shedding position helps improve mixing and combustion efficiency, which can be achieved by adjusting Atwood Number.

Keywords Atwood number · Supersonic shear layer · Combustion efficiency · Mixing enhancement · Vortex shedding

1 Introduction

The supersonic shear layer is a universal flow structure in engineering problem, for example, the mixing phenomena between the fuel injected through a strut and the inlet air in the combustion chamber of scramjet engine. Enhancing the mixing and combustion of the supersonic shear layers is important in the design of the combustion chambers. Inlet flow conditions significantly affect the combustion efficiency of these problems. Exploring the optimal inlet flow conditions helps improve combustion performance and understand the physical mechanism behind.

Interface instabilities including Rayleigh–Taylor instability (RTI), Richtmyer–Meshkov instability (RMI), and Kelvin–Helmholtz instability (KHI) are of great significance in studying mixing process. Extensive works have studied how interface instabilities influence the mixing between two fluids to explore proper fluid conditions [1–4]. The Atwood number is an important dimensionless number that is proposed to study the RTI and RMI of the density stratified flows. The RTI phenomenon appears when a light fluid is accelerated into a heavy fluid according to [5]. Any perturbation along the interface between the two fluids grows continuously. The mixing rate between the two fluids are determined by the effective viscosity of the two fluids. Wang et al. [6] found the ratio value of the nonlinear saturation amplitude η_s and the perturbation wavelength λ were determined by the Atwood number. When impulsively accelerating the interface between two fluids of differing densities, the RMI phenomenon occurs, for example, by the passage of a shock wave [7]. The instability begins with small amplitude perturbations which initially grow linearly with time. Lombardini et al. [8] carried out a systematic study of the Atwood dependence of shock-driven mixing under reshock conditions, the asymmetry of post-reshock mixing zone width was more pronounced with the Atwood number increasing.

As above research shows, the At number associated with density ratio is closely related to the interface instability, thus, changing the properties of the fluid can effectively affect the mixing process. The density ratio of the upper and lower stream has been found to effectively affect the growth rate of the mixing layers. In the high-speed case (Mc = 0.7), Pantano et al. [9] studied the effect of different free-stream densities parameterized by the density ratio. With the density ratio varying, the growth rate of momentum thickness was found to decreases substantially as a function of density ratio. Soteriou1 et al. [10] invested the effect of the density ratio on free and forced spatially developing shear layers. In the high-amplitude external forcing case, the growth rate of mixing layer non-monotonically varied with the

free-stream density ratio increasing. It strongly depended on the momentum ratio and could be expressed by a function, and reached a minimum at a momentum ratio of unity. Lesshafft et al. [11] described the convective character of the linear instability of axisymmetric jets under a wide range of parallel velocity and density profiles. When the density ratios is above the assumed threshold value 0.72, the jets without counterflow were found to be absolutely unstably.

Combustion enhancement through active control is more complicated [12]. When considering different At numbers or density ratio in the shear layers, it is worth exploring whether additional combustion enhancement can be obtained due to interface instabilities. The main purpose of this paper is to explore how much combustion enhancement can be obtained by changing the fuel properties. Whether there is an optimal At number to maximize the combustion efficiency of the reactive shear layer, and why this At number has the best combustion efficiency are also investigate.

The roll-up and interaction of vortices in the shear layer have a great influence on the mixing process. To represent the entrainment formation process, visualization method are necessary. The LCS method proposed by Haller and Yuan [13] is particularly suitable for identifying flow field structure. The finite-time Lyapunov exponent (FTLE) method belongs to LCS algorithms is widely adopted to obtain the hidden flow field structure in low-speed flow. Relevant study demonstrates that the LCS method is superior to the Euler method in the identification of the hidden flow structure [14]. The entrainment characteristic can be evaluated by the hidden structure. The LCS method has been applied to compressible mixing layer [15], and the same algorithm is used in this work.

In order to improve the combustion efficiency of shear layers by changing the fuel properties, nonreacting and reacting cases under At = 0.14, 0.26, and 0.57 are simulated in present work. This article is organized as follows. In Sect. 2, the physical model, governing equation, and numerical method are presented. The validation of CFD algorithm adopted herein and independence study of different grids are also included. In Sect. 3, the influence of the Atwood numbers on the shear layer is discussed and explained. A LCS method is used to represent the entrainment formation process. In Sect. 4, the main conclusions drawn from the results.

2 Numerical Method and Computational Setup

2.1 Physical Model

A two dimensional (2D) supersonic mixing layer with a pulsed central jet is numerically investigated in present work. The inlet flow conditions of the ambient air and fuel mixture are similar to that of case 3 in Chen et al. [16]. The detailed descriptions about computational conditions are shown in Fig. 1. The length and height of the computational domain are taken as $X_l = 0.5$ m, $Y_l = 0.15$ m, while the diameter of the injection orifice where fuel is injected into the flow field is D = 0.03 m. According

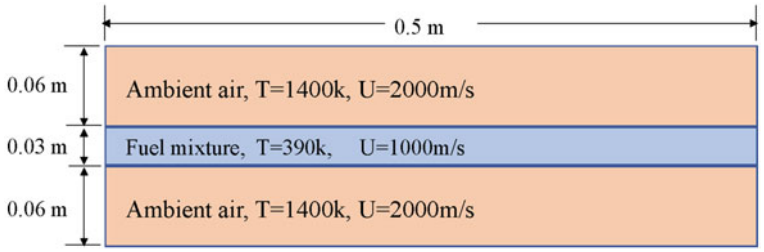

Fig. 1 Computational domain

to the computational setup in [16] both lower and upper boundaries of the computational domain are regarded as non-reflective conditions, to avoid the reflect from boundaries back to calculation domain. The extrapolation operation is applied to each primitive variable in the outflow.

The central fuel jet injected in the flow filed is composed of H_2, N_2, Ar, and He. The pressures of the inlet ambient air and fuel mixture are 1 atm. Other information about the fuel mixture can be found in Table 1. To achieve the autoignition of fuel mixture in supersonic conditions, the temperature of inlet air is taken as 1400 K. The velocities of the fuel mixture and the ambient air are U_1 = 1000 m/s and U_2 = 2000 m/s, respectively.

The definition of Atwood number (At) is given by

$$At = \frac{\rho_1 - \rho_2}{\rho_1 + \rho_2} = \frac{\rho_1/\rho_2 - 1}{\rho_1/\rho_2 + 1} = \frac{s-1}{s+1} \tag{1}$$

where ρ_1 and ρ_2 are the densities of ambient air and central jet fuel, respectively. s refers to the density ratio. Thus, At can be adjusted by changing the density of central fuel jet.

To ensure the mass flux of hydrogen of central fuel jet maintains the same, the inert gas in the center jet is selected from N_2, Ar, and He, respectively. If only one kind of inert gas is used, the hydrogen mass flow rate cannot maintain the same. The mass fractions of mixture components are specially adjusted, so that the equivalence ratio between oxygen of ambient air and hydrogen of fuel jet are the same.

Table 1 Inlet flow conditions

	$T[K]$	$\rho[kg/m^3]$	U[m/s]	At	Y_{H_2}	Y_{O_2}	Y_{Ar}	Y_{N_2}	Y_{He}
Air	1400	0.2511	2000		0.000	0.233	0.000	0.767	0.000
Case 1	390	0.1879	1000	0.1442	0.300	0.000	0.700	0.000	0.000
Case 2	390	0.1486	1000	0.2566	0.3793	0.000	0.000	0.6207	0.000
Case 3	390	0.0695	1000	0.5663	0.8105	0.000	0.000	0.000	0.1895

The detailed species information is listed in Table 1. The At number calculated using Eq. (1) is approximately 0.14, 0.26, 0.57, correspond to the inert gas N_2, Ar, and He.

2.2 Governing Equation

When chemical reactions are considered in supersonic mixing layer, two dimensional compressible Navier–Stokes equations are taken as the governing equations. The two dimensional conservation form in Cartesian coordinates is given by:

$$\frac{\partial U}{\partial t} + \frac{\partial G_i}{\partial x_i} = \frac{\partial G_{vi}}{\partial x_i} + S, \tag{2}$$

where U is on behalf of the variable vector in conserved form. $i = 1, 2$ represents the spatial subscript of coordinate variables. G_i denotes the convective flux vectors, and G_{vi} denotes the diffusive flux vectors. S is taken as the chemical source term because of chemical reactions between mixture components. The vectors are defined as follows:

$$U = \begin{bmatrix} \rho \\ \rho u_j \\ \rho E \\ \rho Y_s \end{bmatrix} G_i = \begin{bmatrix} \rho u_i \\ \rho u_i u_j + \delta_{ij} p \\ u_i(\rho E + p) \\ \rho u_i Y_s \end{bmatrix} G_{vi} = \begin{bmatrix} 0 \\ \tau_{ij} \\ u_j \tau_{ij} - q_i \\ -\rho D_s \frac{\partial Y_s}{\partial x_i} \end{bmatrix} S = \begin{bmatrix} 0 \\ 0 \\ 0 \\ \omega_s \end{bmatrix}, \tag{3}$$

where i, j, and k refer to the subscripts of coordinate variables in 2D Cartesian coordinates system (i, j, and $k = 1, 2$) and s represents the index of mixture component ($s = 1, 2, \cdots, Ns$ and Ns the number of mixture components). δ_{ij} refers to the Kronecker delta which is as the discrete version of the delta function. E, p, and ρ are the total energy per mass, pressure, and mixture density, respectively. u_i refers to the movement velocity in the i coordinate direction. Y_s and ρ_s are the mass fraction and density of species s. ω_s refers to the mass production rate of species s because of the chemical reactions. The heat flux q and viscous stress tensor τ are defined as follows:

$$q_k = \lambda \frac{\partial T}{\partial x_k} + \rho \sum_{s=1}^{NS} D_s h_s \frac{\partial Y_s}{\partial x_k}, \tag{4}$$

$$\tau_{ij} = -\frac{2}{3}\delta_{ij}\mu \frac{\partial u_k}{\partial x_k} + \mu\left(\frac{\partial u_i}{\partial x_j} + \frac{\partial u_j}{\partial x_i}\right), \tag{5}$$

where T refers to the temperature of the gas mixture and h represents the specific enthalpy of gas mixture. μ is the shear viscosity, and λ stands for the gas mixture thermal conductivity. Shear viscosity μ in the flow field and is calculated according to the Wilke's semiempirical formula [17]. After the evaluation of μ, through Wilke's equation, λ can be calculated based on Prandtl number $Pr = 0.72$ [18].

For the supersonic shear layer investigated in this work, thermal diffusion and pressure diffusion is removed to simplify the calculation of mass diffusion, and the binary diffusivity D_{ij} is assumed to be equal among all components [19]. D_i represents the diffusion coefficient and is given by

$$D_i = \frac{1 - X_j}{\sum_{j \neq i} D_{ij}}; \quad D_{ij} = \frac{\mu}{\rho Sc}, \tag{6}$$

where i, $j = 1, Ns$ represents the index of component in the gas mixture. X_j is the mole fraction of the species j in gas mixture. The Schmidt number $Sc = 0.5$ for all species is adopted in this work [17]. The ideal gas state equation is applied in the following calculation and is given by:

$$p = \rho R_u T \sum_{i=1}^{Ns} \frac{Y_i}{M_i}, \tag{7}$$

where R_u stands for the universal gas constant of gas mixture and M_i is the molecular weight of species i. The total energy E per unit mass is given as

$$E = \sum_{i=1}^{Ns} Y_i \left(h_{fi}^0 + \int_{T_0}^{T} \frac{C_{pi}}{M_i} dT \right) - \frac{p}{\rho} + \frac{1}{2} \left(u^2 + v^2 \right), \tag{8}$$

where h_{fi}^0 means the specific enthalpy of species i during chemical formation at the reference temperature T_0. C_{pi} is stands for the specific heat capacity under constant-pressure conditions and is taken as the polynomial functions of reference temperature, and is given by

$$C_{pi} = R_u \left(p_{1i} T^{-2} + p_{2i} T^{-1} + p_{3i} + p_{4i} T + p_{5i} T^2 + p_{6i} T^3 + p_{7i} T^4 \right), \tag{9}$$

where $p_{1i}, ..., p_{7i}$ refer to the polynomial expansion coefficients and can be found in the detailed descriptions of NASA thermochemical data [20].

The mass production rate of species i is calculated as follows:

$$\omega_i = M_i \sum_{r=1}^{Nr} v_{ir} \left[M \right]_r \left(k_{fr} \prod_{i=1}^{Ns} \left[X_i \right]^{v'ir} - k_{br} \prod_{i=1}^{Ns} \left[X_i \right]^{v''ir} \right), \tag{10}$$

where Nr refers to the total elemental chemical reaction number. $[M]_r$ stands for the molar concentration of mixture components when taking third body coefficient of r

th reaction into consideration. v'_{sr} and v''_{sr} are the forward and backward molecular stoichiometric coefficients of reaction r, respectively. $v_{ir} = v''_{ir} - v'_{ir}$ measures the stoichiometric coefficients variation of the species during reaction r. $[X_i]$ represents the molar concentration of i th species in gas mixture. k_{fr} and k_{br} mean the forward and backward chemical reaction rate, respectively. The forward reaction rates can be calculate by Arrhenius equation.

$$k_{fr} = A_{fr} T^{\beta_{fr}} \exp\left(\frac{E_{fr}}{R_u T}\right), \tag{11}$$

where A_{fr} refers to the pre-exponential factor, β_{fr} stands for the temperature exponent, and E_{fr} represents the activation energy of r th elementary reaction. According to the equilibrium constant k_{cr}, the backward reaction rates k_{br} is expressed as $k_{br} = k_{fr}/k_{cr}$.

2.3 Numerical Method

In supersonic reactive shear layers, the stiffness of the main control equations is increased because of the smaller characteristic time scale of the chemical reactions. Thus, the practical implicit methods are suitable for solving the governing equations. The semi-implicit methods implemented in [21] are applied to the simulations in the present work. The corresponding ordinary partial equation Eq. (12) is expressed as following:

$$\frac{dV}{dt} = \underbrace{m(V)}_{\text{non-stiff term}} + \underbrace{n(V)}_{\text{stiff term}}, \tag{12}$$

where m stands for the spatial discretization vector of the flow equations without considering chemical reactions and n is the reaction source terms vector originating from chemical reactions. The universal r-stage additive semi-implicit Runge-Kutta (ASIRK) method [22] that calculates n implicitly and m explicitly is adopted in present work to improve the numerical simulation accuracy

$$\begin{cases} V^{n+1} = V^n + \sum_{j=1}^{r} w_j k_j \\ K_1 k_i = \Delta t (K_2 + K_3), i = 1, 2 \cdots r \\ K_1 = \left[I - \Delta t a_i J \left(V^n + \sum_{j=1}^{i-1} d_{ij} k_j \right) \right] \\ K_2 = m \left(V^n + \sum_{j=1}^{i-1} b_{ij} k_j \right) \\ K_3 = n \left(V^n + \sum_{j=1}^{i-1} c_{ij} k_j \right) \end{cases}, \tag{13}$$

where $J = \frac{\partial n}{\partial V}$ is the Jacobian matrix of the stiff chemical source term n and Δt is the integral time step. A diagonal matrix (approximate Jacobian matrix) is adopted

in present work to achieve higher computational efficiency. Such approximation for Jacobian matrix has been widely used [23].

The ASIRK-2 method has been proved to be suitable for the numerical simulation of the reactive flows because of its secondary-order accuracy and L-stability. The central difference [24] and fifth-order Weighted Essentially Non Oscillatory (WENO) scheme are utilized in present work to discrete the diffusive and convective terms.

2.4 Lagrangian Coherent Structures LCS

To analyse the vortex structures of the supersonic compressible mixing layer, the LCS method is adopted in present work. The detailed features of LCS method used here can be found in [15]. The physical meaning of the LCS method helps compare and analyze the flow field characteristic. The LCS method suitable to calculate the Lagrangian integral [20–21] (time integral) in the flow field as in Eq. (14)

$$\boldsymbol{x}_{t_1}^{t_1+T} = \int_{t_1}^{t_1+T} \boldsymbol{u}\left(\boldsymbol{x}_{t_1}^{t}\right) \mathrm{d}t \tag{14}$$

where t_1 stands for the starting time of Lagrangian integral, T represents the total integral time from t_1, and $\boldsymbol{x}_{t_1}^{t_1+T}$ refers to the integral result when the integration is accomplished.

While the transfer matrix corresponding to the initial and final position is expressed as follows.

$$\begin{gathered} \boldsymbol{F}_T\left(\boldsymbol{x}_{t_1}^{t_1}\right) = \left(\partial \boldsymbol{x}_{t_1}^{t_1+T}\right) / \left(\partial \boldsymbol{x}_{t_1}^{t_1}\right), \\ \boldsymbol{x}_{t_1}^{t_1} = \boldsymbol{x}_0, \boldsymbol{x}_{t_1}^{t_1+T} = \boldsymbol{x}_T, \\ \boldsymbol{F}_T\left(\boldsymbol{x}_{t_1}^{t_1}\right) = \boldsymbol{F}_{t_1}^{t_1+T}\left(\boldsymbol{x}_0\right). \end{gathered} \tag{15}$$

Taking the 2D case as an example, the following formula is obtained.

$$\boldsymbol{F}_{t_1}^{t_1+T}\left(\boldsymbol{x}_0\right) = \begin{bmatrix} \frac{\partial x_T}{\partial x_0} & \frac{\partial x_T}{\partial y_0} \\ \frac{\partial y_T}{\partial x_0} & \frac{\partial y_T}{\partial y_0} \end{bmatrix} \tag{16}$$

Finally, the Cauchy–Green tensor can be obtained to measure the deformation process of the line element in the flow filed.

$$C_{t_1}^{t_1+T}\left(x_0\right) = \left[\boldsymbol{F}_{t_1}^{t_1+T}\left(\boldsymbol{x}_0\right)\right]^{\mathrm{T}} \left[\boldsymbol{F}_{t_1}^{t_1+T}\left(\boldsymbol{x}_0\right)\right] \tag{17}$$

The eigenvector of the Cauchy–Green tensor which is a positive and symmetric matrix can be used to describe the maximum or minimum deformation direction in the flow field. On basis of the maximum eigenvalue of the Cauchy–Green tensor, we can finally obtain the finite time Lyapunov exponent (FTLE). The finite-time Lya-

Table 2 Inlet flow conditions of Goebel's experiment

Mixing layer	Ma	U[m/s]	$T[K]$	$P[kPa]$	δ[mm]
Low-speed stream	1.37	403.0	295.0	49.0	2.5
High-speed stream	1.91	700.0	578.0	49.0	3.0

punov exponent is calculated using the Cauchy–Green tensor. The flow property, for example, the separation characteristics which is measured by the average exponential divergence rate, can be measured by the FTLE number.

$$\text{FTLE}\,(t_1, T, \boldsymbol{x}_0) = \frac{\ln\left[\lambda_{\max}\,(t_1, T, \boldsymbol{x}_0)\right]}{2T} \tag{18}$$

In conclusions, the FTLE number can be used to identify the maximum stretch location of the fluid micelle. And the maximum stretch location is usually associated with the vortex motion, which helps to identify the vortex boundary.

2.5 Code Validation

The in-house CFD program, namely *ParNS3D*, has integrated the numerical calculation method described above. The accuracy and reliability of this in-house CFD program have been proved in many shear layer studies [15, 25]. To compare with the experiment results obtained by Goebel and Dutton [26], the similar inlet flow conditions are adopted for following numerical simulations. A supersonic mixing layer is simulated to examine the accuracy of *ParNS3D* for shear layers problem. The detailed inlet conditions are listed in Table 2.

Here, the computational domain is taken as 0.3 m $\times$ 0.048 m, and the grid size is 900 $\times$ 150 cells and the time step is 1×10^{-8} s. The timeaveraged velocity profile of flow field is obtained by using numerical simulation data from 1 ms to 2 ms, then, this numerical results is compared with that of the experiment result at the flow direction position X = 200 mm. As shown in Fig. 2, a good agreement is achieved with the experimental results, thereby demonstrating the accuracy of the program used. Such algorithm is adopted for following simulations. Because of the lack of experimental data on reacting H_2/O_2 mixing layer flows, it is hard to implement the validation which considers the chemical reactions as mentioned by [16].

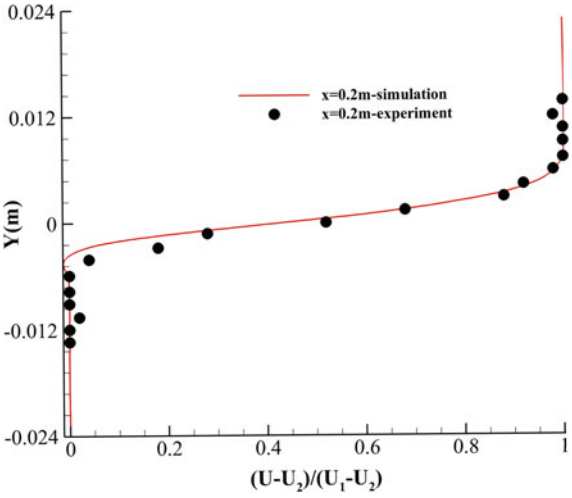

Fig. 2 Reliability verification of the numerical algorithm by comparing time-averaged velocity profiles from 1 ms to 2 ms at X = 200 mm. U_1 = 700 m/s, U_2 = 403 m/s

2.6 Chemical Reaction Kinetics

As the accuracy of the reaction mechanism greatly influences the combustion characteristics, such as ignition delay time, etc., a detailed reaction mechanism describing the H_2/O_2 reaction process is essential to calculate the complex process. In current work, a middle size chemical mechanism with 9 reaction species (H_2, O_2, H_2O, OH, H, O, HO_2, H_2O_2, N_2) and 20 elemental chemical reactions, namely Jachimowski model [27] is adopted herein. This chemical reactions model is found to keep a balance between the calculation accuracy and computational cost. Thus, this reaction mechanism is generally adopted in numerical simulation concerning supersonic combustion problems [28].

2.7 Mesh Independence Study

The gird independence test are performed using three grids with different elements. The At = 0.26 case (inert gas is N_2) is simulated with 480,000 elements (1200 × [150 + 100 + 150], coarse mesh), 825,000 (1500 × [200 + 150 + 200], medium mesh), and 960,000 (1600 × [220 + 160 + 220], fine mesh) elements, respectively. There are three mesh blocks in every gird used in this work, because the inlet flow conditions are different, which can be found in Fig. 1. The mesh is refined in different ways according to the flow direction. In the x direction, the mesh is refined backward to the inlet boundary, to properly match the inlet flow conditions. In the y direction, the junctions of these blocks are regarded as essential in simulation because of fluid shear, thus, the grid is refined towards these junctions. The minimum cell located at the inlet of all the grid is $\Delta x_{\min} = 4 \times 10^{-5}$ m, $\Delta y_{\min} = 4 \times 10^{-5}$ m. The validation

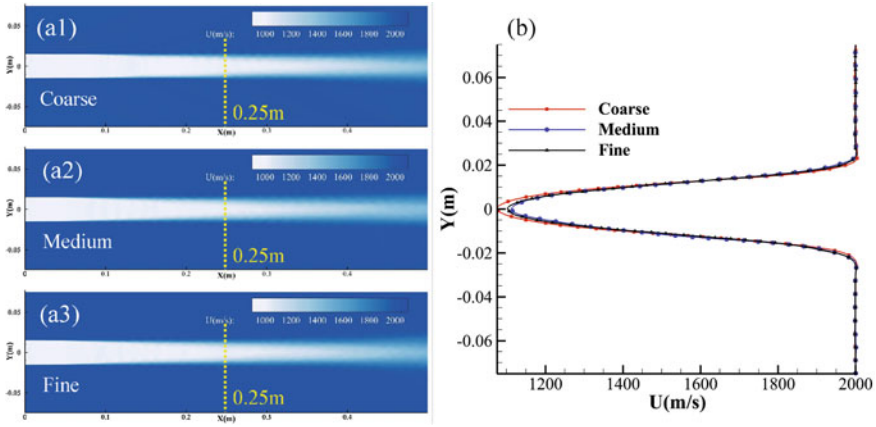

Fig. 3 The distribution of the time-averaged velocity at X = 400 mm with different grids

simulations are implemented using three different meshes (coarse, medium, fine mesh). The distribution of time-averaged velocity at x = 0.40 m is plotted in Fig. 3. The results indicate that the solution remains constant after 825,000 elements. Thus, the medium mesh with 825000 elements is adopted for following calculations.

3 Results and Discussions

3.1 Combustion Performance

For the reacting cases simulated, the density of the central fuel jet gradually decreases as the At number increases, which can found in Table 1. The flow field stability of At = 0.14 case is obviously higher than that of At = 0.26 and At = 0.57 cases as shown in Fig. 4a1–a3. When At = 0.14, the mixing region only appears at the interface of fuel jet and ambient air. The middle region of fuel jet does not mix with hydrogen. Besides, the flow field structure of At = 0.14 still maintains symmetry. While when At = 0.26 and At = 0.57, due to the smaller density of the central jet compared with that of At = 0.14, the disturbance caused by the vortex roll-up has larger effects on the growth of mixing layers. The asymmetry of the flow field structure becomes more and more obvious. With At number increasing, the central jet is more unstable, so that more oxygen can be entrained from the surrounding air to promote mixing and combustion.

The instantaneous distributions of the water mass fraction can be found in Fig. 4b1–b3. The water generation area is consistent with the hydrogen-oxygen mixing area. In the area where water is generated, the mass fraction of hydrogen has decreased significantly. As the At number increases, the jet hydrogen is obviously

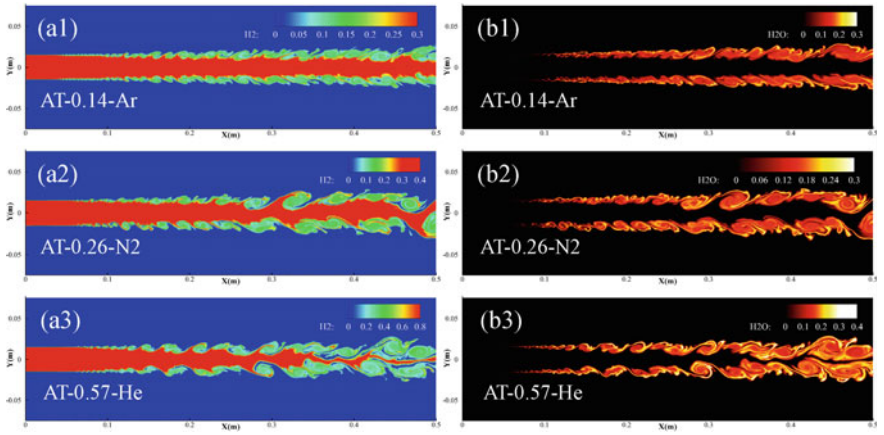

Fig. 4 Distributions of the instantaneous hydrogen mass fraction (left, a1–a3) and water mass fraction of reacting cases (right, b1–b3) of reacting cases under different At numbers (At = 0.14, 0.26, 0.57) at t = 1.8 ms

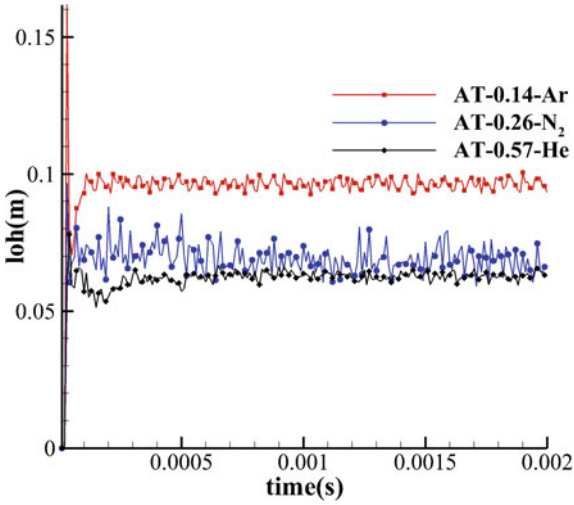

Fig. 5 Ignition position corresponding to temperature exceeding 2000 K

consumed in the range of 0.4–0.5 m. Although the same mass flow rate of hydrogen in the inlet flow is ensured in present work, the ignition position *loh* (defined as x position where temperature exceeds 2000 K) is more close to injection orifice as the mass fraction of hydrogen in the central jet increase. The corresponding ignition position of At = 0.26 and At = 0.57 cases are greatly advanced compared to that of At = 0.14 case, as shown in Fig. 5. At the same time, there is a certain degree of fluctuation in the ignition position in Fig. 5. The fluctuation of calculation results at At = 0.26 are much higher than that of At = 0.56 and At = 0.14 cases, which is considered to be related to the fluctuation of the vortex roll-up position.

In the combustion problem, combustion efficiency is an important indicator to measure combustion performance. There are many selection about criteria for combustion efficiency. Since the mass flux of hydrogen is controlled to be the same in this work, the mass production of water normalized by hydrogen mass is selected as the criterion for measuring the combustion efficiency. η_c is defined as the production of water normalized by hydrogen, and is given by Eq. (19). In supersonic shear layer problems, the mixing efficiency is also an important factor that measures mixing process. The definitions of mixing efficiency are quit different as shown [29–31]. These definitions usually study the mixing efficiency of the cross section along the streamwise for 3D problems, which are not suitable for present work. The original definition adopted in [30] is adjusted by removing the velocity term to fit the 2D cases. The formulation of mixing efficiency η_m is written as Eq. (20).

$$\eta_c = \frac{\int_A \rho_{\mathrm{H_2O}} dA}{\dot{m}_{\mathrm{H_2}} * L_x / U_{cj}}, \tag{19}$$

$$\eta_m = \frac{\int \alpha_{\mathrm{react}} \rho dA}{\int \alpha \rho dA} - \eta_m|_{t=0}, \tag{20}$$

$$\alpha_{\mathrm{react}} = \begin{cases} \alpha, \alpha \le \alpha_{\mathrm{stoic}} \\ \alpha(1-\alpha)/\left(1-\alpha_{\mathrm{stoic}}\right), \alpha > \alpha_{\mathrm{stoic}} \end{cases}, \tag{21}$$

Many mixing efficiency criteria are invalid in combustion problems because of the consumption of oxygen or fuel. Due to the lack of a standard definition of for mixing efficiency measuring the mixing extent of combustion problems, a new definition of equivalent mixing efficiency is proposed in this work. By dividing the mass of H_2O into H_2 and O_2, the formula Eq. (20) can used to calculate mixing efficiency η_m to describe mixing performance in combustion problems.

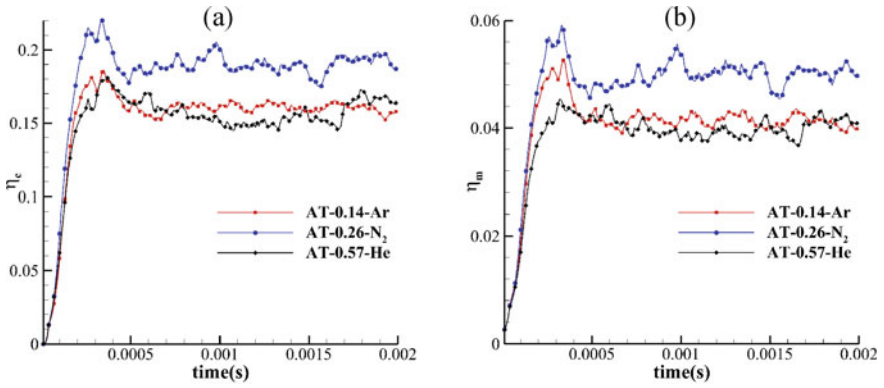

Fig. 6 Variation of η_c and η_m with time under different at numbers

As shown in Fig. 6, At = 0.26 case has the highest mixing efficiency and combustion efficiency. As the At number increases, the combustion efficiency and mixing efficiency both increase first and then decrease. Because the production of water is closely related to the consumption of hydrogen or oxygen, changes in components mass in the flow field require attention.

3.2 Variation of Components

Since the boundary conditions of simulation cases are the open boundary conditions, thus, mass-exchange occurs at the boundary of the computing domain, which leads to the difference of the remaining mass of oxygen or hydrogen in the flow field at different At numbers. Although the inlet hydrogen and oxygen mass flux is the same when setting the boundary conditions in this work, the mass of oxygen and hydrogen

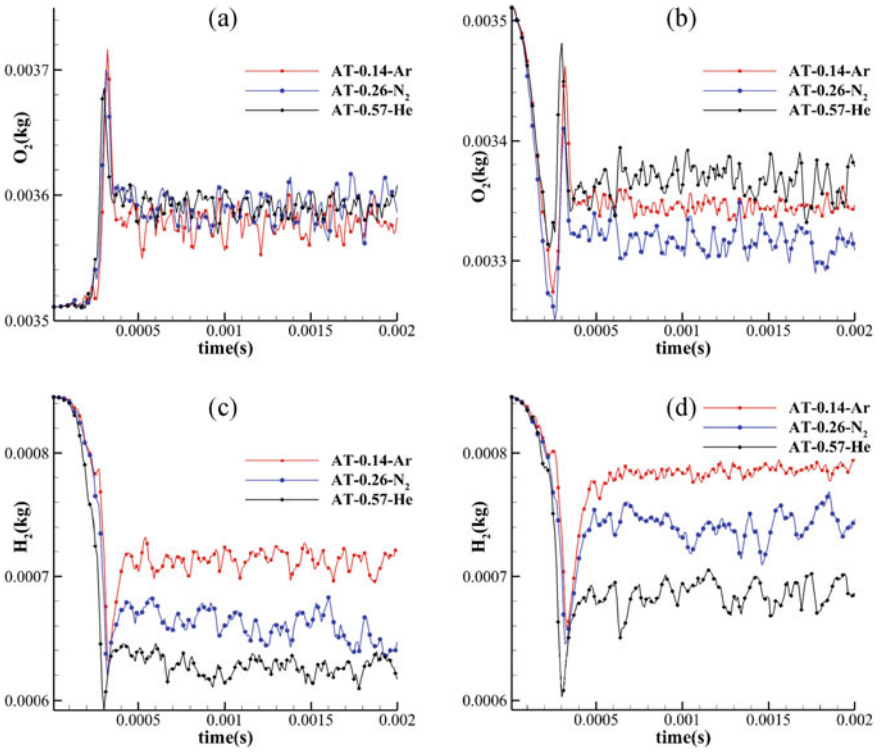

Fig. 7 Variation of mass of O_2 and H_2 with time under different At numbers. **a** O_2 mass of nonreacting cases; **b** O_2 mass of reacting cases; **c** H_2 mass of nonreacting cases; **d** H_2 mass of reacting cases

allowed in the flow field has changed, during the evolution process of fluid field from its initial status to when the combustion efficiency and mixing efficiency are stable.

For nonreacting cases (Fig. 7a, c), the variation trend of hydrogen and oxygen mass is opposite to each other. The oxygen mass is relatively close to each other under the three At numbers, and the difference in hydrogen mass is greater due to its smaller mass fraction compared with that of oxygen. With the evolution of the flow field, the oxygen mass allowed the flow field increases significantly at first, and then decreases. The variation trend of hydrogen mass is just opposite to that of oxygen. From 0 to 0.3 ms, a large amount of central fuel jet is pushed out of the flow field, thus, the mass fraction of oxygen rises and the hydrogen mass fraction decreases. While from 0.3 to 0.5 ms, the flow field begins to stabilize when considering components mass. The central fuel jet is continuously injected into the flow field, as a result, the mass fraction hydrogen begin to increases.

For reacting cases (Fig. 7b, d), the consumption of oxygen is in accordance with the production of water (Fig. 6a). While the trend of hydrogen mass maintains the same compared with that of nonreacting cases. These results indicate that the hydrogen mass in the above cases is excessive to be consumed. The oxygen entrained into the central fuel jet can be completely consumed, so the reduction in oxygen mass determines the amount of water production. The remaining hydrogen mass is consistent with the central jet density, indicating that the smaller the central jet density, the more hydrogen is "squeezed out" by oxygen during the evolution process.

The oxygen mass is found to decreases quickly from 0 to 0.2 ms by comparing the variation trend of oxygen mass between the nonreacting and reacting cases. Such results indicate that the temperature of the surrounding air is high enough for H_2 to autoignite even if hydrogen and oxygen in the interface are not efficiently mixed. From 0 to 0.3 ms, the flow field evolves from the initial stage to the stable stage

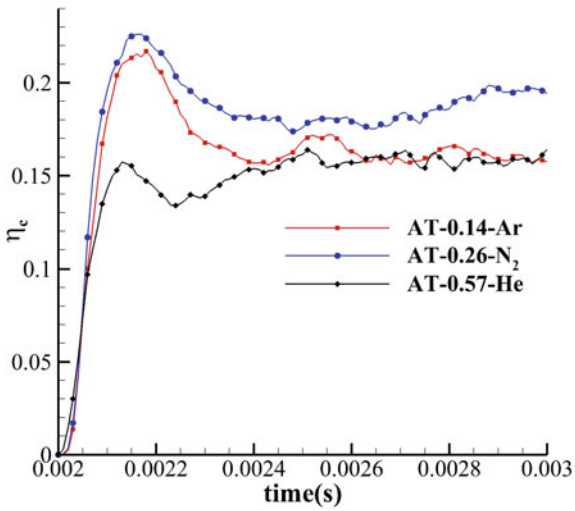

Fig. 8 Variation of η_c with time under different At numbers. These cases use the final flow field of nonreacting cases as initial conditions and consider chemical reactions

measuring by η_c and η_m, the consumption of oxygen entrained into the central jet basically determines the amount of water produced, that is, the combustion efficiency.

To further discuss the impact of the initialization of the flow field on combustion efficiency, this work also calculates cases that use the final flow field status of non-reacting cases as initial status, but then considers chemical reactions. As shown in Fig. 8, At = 0.26 case has highest mixing efficiency and the corresponding highest combustion efficiency. This results show that the problem is controlled by the mixing process. The mixing performance determines the combustion performance.

3.3 Evolution of Shear Layers

The vortex roll-up and interaction determine the mixing process of the shear layers. The LCS method is used to study the roll-up and interaction processes of vortex in this work. The computation results of LCS field are considerably different with that of the Eulerian field near the boundary of the vortex (Fig. 9). The FTLE results calculated through LCS method reflects the variation of the flow field over a period of time. The characteristics of the Lagrangian method contribute to the difference between Eulerian and Lagrangian field.

The instantaneous distributions of vorticity and FTLE number plotted in Fig. 9 show that the LCS method can reveal the hidden structure of the shear layers. In the yellow rectangular region of vorticity field, no vortex roll-up or evolution is observed. While for the FTLE distributions, the shearing phenomenon in interface between air and hydrogen has occurred. As shown by the red arrow, the hidden structure is more obvious in the vortex interaction region.

As shown in the green rectangular region of Fig. 9, The rolled-up position of the vortex gradually moves along the flow direction with At number increasing or the density of central jet decreasing. However, the vortex interaction of At = 0.14 is significantly weaker than that of At = 0.26 and At = 0.57 cases. When At = 0.14, although the vortex roll-up position is shortest compared with other cases, the evolution of the vortex is slower. The distance between vortex roll-up position and vortex shedding position of At = 0.14 case is much larger. On the contrary, At = 0.26 and At = 0.57 cases have longer roll-up distance, but stronger vortex interaction.

The ignition position in Fig. 5 is in accordance with the vortex shedding position, not the roll-up position. This result shows that in the vortex interaction region, the mixing between air and hydrogen is more adequate. In this supersonic shear layers, the the roll-up position is not the key factor that affects combustion performance. The ignition positions under At = 0.26 and At = 0.57 are obviously shorter than that of At = 0.14, which explains the poor combustion performance of At = 0.14 case. However, the reasons for better performance of At = 0.26 case compared with that of At = 0.57 need more discussion.

Comparing the distribution of vorticity and FTLE number, it can be found that the longer the vortex roll-up position is, the less the number of vortices in the flow field is. At At = 0.26 and At = 0.57, the evolution of vortices is more adequate, but

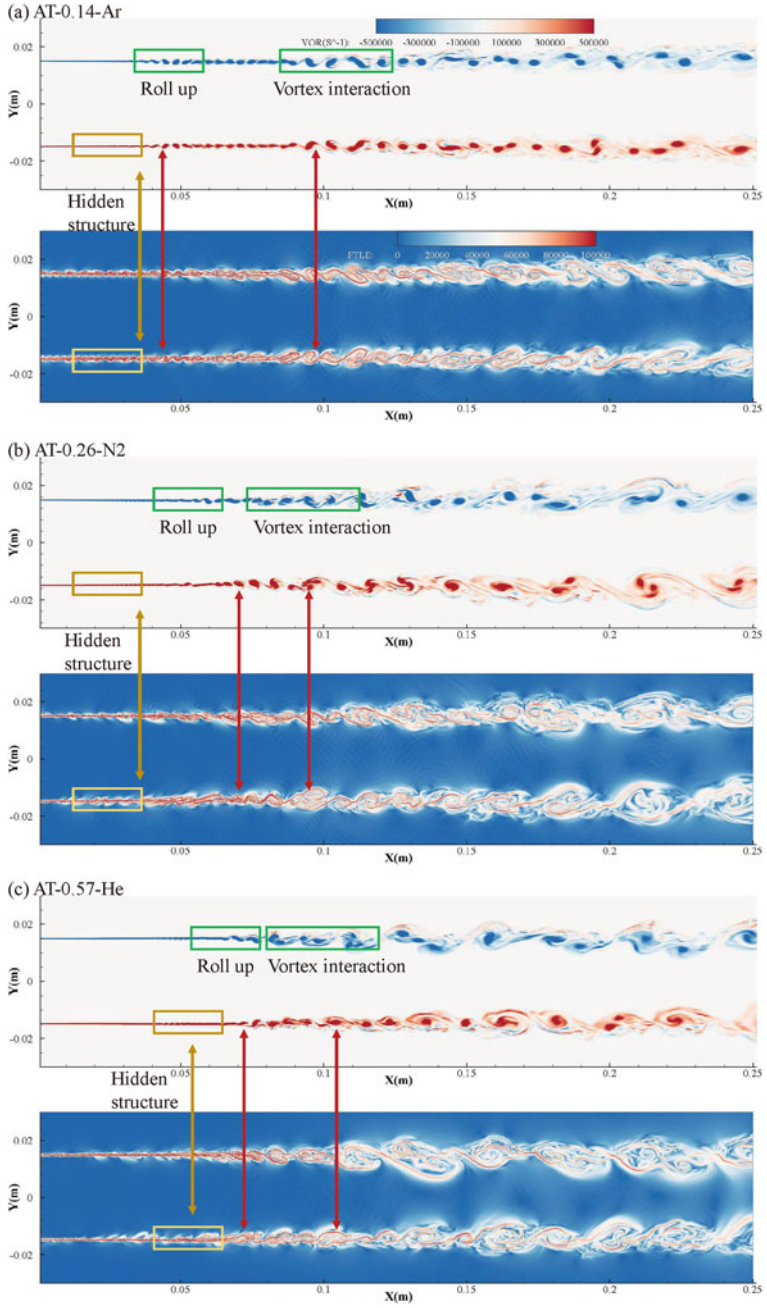

Fig. 9 Distributions of the instantaneous vorticity and FTLE number of reacting cases under different At numbers (At = 0.14, 0.26, 0.57) at t = 1.8 ms

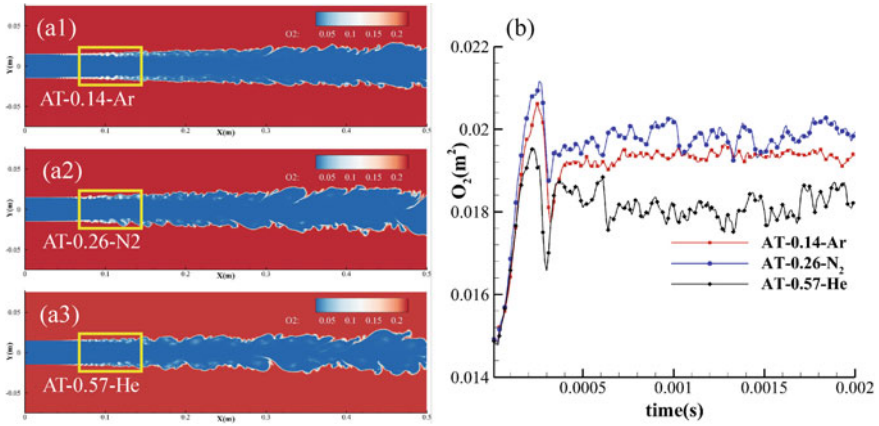

Fig. 10 Variation of the consumption area of O_2 with time

relatively, the number of vortices is also decreasing. When At = 0.26, the rolled-up distance is shorter than that of At = 0.57 case, so the mixing of shear layer is more sufficient. At the same time, the consumption area of oxygen is defined as where the oxygen mass fraction in the flow field is less than 0.1 to roughly represent the oxygen entrained by the vortex into the central jet. The results of At = 0.26 cases are larger than that of other two cases as shown in Fig. 10, which also shows that the evolution of vortices in the At = 0.26 cases is more adequate, which is consistent with the vortex roll-up position.

4 Conclusions

The influence of At numbers on combustion performance are studied in this work. The optimal At = 0.26 is revealed through the comparison of combustion and mixing efficiencies under different At numbers. The analysis of the variation of component mass shows that this problem is dominated by mixing process. The ignition position defined as where the temperature exceeds 2000 K of At = 0.26 and At = 0.57 cases are much shorter than that of At = 0.14. The differences of ignition position are also in accordance with the vortex shedding position presented by LCS method. The number of vortices in the flow field decreases with the increase of At number. The vortex structure is also more plump at At = 0.26, so the combustion efficiency of At = 0.26 is higher than that of At = 0.57. These results explains the existence of the optimal At number.

Acknowledgements This work is partially supported by Key Research and Development project of Sichuan Province (Grant No. 2019ZYZF0002) and the National Natural Science Foundation of

China (Grant No. 91741113). We thank the Center for High Performance Computing of SJTU for providing a super computer to support this research.

References

1. Abarzhi SI (2010) Review of theoretical modelling approaches of Rayleigh–Taylor instabilities and turbulent mixing. Philos Trans Roy Soc Math Phys Eng Sci 368(1916):1809-1828. https://doi.org/10.1098/rsta.2010.0020
2. Brouillette M (2002) The richtmyer-meshkov instability. Ann Rev Fluid Mech 34(1):445–468. https://doi.org/10.1146/annurev.fluid.34.090101.162238
3. Gan Y, Xu A, Zhang G et al (2011) Lattice Boltzmann study on Kelvin-Helmholtz instability: roles of velocity and density gradients. Phys Rev E 83(5):056704. https://doi.org/10.1103/PhysRevE.83.056704
4. Zhou Y (2017) Rayleigh–Taylor and Richtmyer–Meshkov instability induced flow, turbulence, and mixing. II. Phys Rep 723:1–160. https://doi.org/10.1016/j.physrep.2017.07.008
5. Goncharov VN (2002) Analytical model of nonlinear, single-mode, classical Rayleigh-Taylor instability at arbitrary Atwood numbers. Phys Rev Lett 88(13):134502. https://doi.org/10.1103/PhysRevLett.88.134502
6. Li-Feng W, Wen-Hua Y, Ying-Jun L (2010) Two-dimensional Rayleigh-Taylor instability in incompressible fluids at arbitrary Atwood numbers. Chin Phys Lett 27(2):025203
7. Ding J, Si T, Yang J et al (2017) Measurement of a Richtmyer-Meshkov instability at an air-SF 6 interface in a semiannular shock tube. Phys Rev Lett 119(1):014501. https://doi.org/10.1103/PhysRevLett.119.014501
8. Lombardini M, Hill D J, Pullin DI et al (2011) Atwood ratio dependence of Richtmyer–Meshkov flows under reshock conditions using large-eddy simulations. J Fluid Mech 670:439–480. https://doi.org/10.1017/S0022112010005367
9. Pantano C, Sarkar S (2002) A study of compressibility effects in the high-speed turbulent shear layer using direct simulation. J Fluid Mech 451:329-371. https://doi.org/10.1017/S0022112001006978
10. Soteriou MC, Ghoniem AF (1995) Effects of the free-stream density ratio on free and forced spatially developing shear layers. Phys Fluids 7(8):2036–2051. https://doi.org/10.1063/1.868451
11. Lesshafft L, Marquet O (2010) Optimal velocity and density profiles for the onset of absolute instability in jets. J Fluid Mech 662:398–408. https://doi.org/10.1017/S0022112010004246
12. Milton BE, Pianthong K (2005) Pulsed, supersonic fuel jets—a review of their characteristics and potential for fuel injection. Int J Heat Fluid Flow 26(4):656–671. https://doi.org/10.1016/j.ijheatfluidflow.2005.03.002
13. Haller G, Yuan G (2000) Lagrangian coherent structures and mixing in two-dimensional turbulence. Phys D Nonlinear Phenom 147(3–4):352–370. https://doi.org/10.1016/S0167-2789(00)00142-1
14. Peacock T, Haller G (2013) Lagrangian coherent structures: The hidden skeleton of fluid flows. Phys Today 66(2):41–47. https://doi.org/10.1063/PT.3.1886
15. Liang G, Yu B, Zhang B et al (2019) Hidden flow structures in compressible mixing layer and a quantitative analysis of entrainment based on Lagrangian method. J Hydrodyn 31(2):256–265. http://dx.doi.org/10.1007/s42241-019-0027-z
16. Qian C, Bing W, Huiqiang Z et al (2016) Numerical investigation of H2/air combustion instability driven by large scale vortex in supersonic mixing layers. Int J Hydrogen Energy 41(4):3171–3184. http://dx.doi.org/10.1016/j.ijhydene.2015.11.029
17. Gupta RN, Yos JM, Thompson RA et al (1990) A review of reaction rates and thermodynamic and transport properties for an 11-species air model for chemical and thermal nonequilibrium calculations to 30000 K

18. Houim RW, Kuo KK (2011) A low-dissipation and time-accurate method for compressible multi-component flow with variable specific heat ratios. J Comput Phys 230(23):8527–8553. http://dx.doi.org/10.1016/j.jcp.2011.07.031
19. Yuan L, Tang T (2007) Resolving the shock-induced combustion by an adaptive mesh redistribution method. J Computat Phys 224(2):587–600. http://dx.doi.org/10.1016/j.jcp.2006.10.006
20. McBride BJ (2002) NASA Glenn coefficients for calculating thermodynamic properties of individual species. John H. Glenn Research Center at Lewis Field, National Aeronautics and Space Administration
21. Zhong X (1996) Additive semi-implicit Runge–Kutta methods for computing high-speed nonequilibrium reactive flows. J Comput Phys 128(1):19–31. http://dx.doi.org/10.1006/jcph.1996.0193
22. Rosenbrock HH (1963) Some general implicit processes for the numerical solution of differential equations. Comput J 5(4):329–330. http://dx.doi.org/10.1093/comjnl/5.4.329
23. Kim SL, Choi JY, Jeung IS et al (2001) Application of approximate chemical Jacobians for constant volume reaction and shock-induced combustion. Appl Numer Math 39(1):87–104. http://dx.doi.org/10.1016/S0168-9274(01)00054-X
24. Liu XD, Osher S, Chan T (1994) Weighted essentially non-oscillatory schemes. J Comput Phys 115(1):200–212. http://dx.doi.org/10.1006/jcph.1994.1187
25. Wang Z, Yu B, Chen H et al (2018) Scaling vortex breakdown mechanism based on viscous effect in shock cylindrical bubble interaction. Phys Fluids 30(12):126103. http://dx.doi.org/10.1063/1.5051463
26. Goebel SG, Dutton JC, Krier H et al (1994) Mean and turbulent velocity measurements of supersonic mixing layers. Miner Deposita 29(1):263–272. http://dx.doi.org/10.1007/BF01816689
27. Choi JY, Jeung IS, Yoon Y (2000) Computational fluid dynamics algorithms for unsteady shock-induced combustion, part 1: validation. AIAA J 38(7):1179–1187. http://dx.doi.org/10.2514/2.1112
28. Clutter J, Mikolaitis D, Shyy W (1998) Effect of reaction mechanism in shock-induced combustion simulations. In: 36th AIAA aerospace sciences meeting and exhibit p 274. http://dx.doi.org/10.2514/6.1998-274
29. Gerlinger P, Stoll P, Kindler M et al (2008) Numerical investigation of mixing and combustion enhancement in supersonic combustors by strut induced streamwise vorticity. Aerosp Sci Technol 12(2):159–168. http://dx.doi.org/10.1016/j.ast.2007.04.003
30. Li L, Huang W, Yan L et al (2017) Mixing enhancement and penetration improvement induced by pulsed gaseous jet and a vortex generator in supersonic flows. Int J Hydrogen Energy 42(30):19318–19330. http://dx.doi.org/10.1016/j.ijhydene.2017.06.014
31. Gong C, Jangi M, Bai XS et al (2017) Large eddy simulation of hydrogen combustion in supersonic flows using an Eulerian stochastic fields method. Int J Hydrogen Energy 42(2):1264–1275. http://dx.doi.org/10.1016/j.ijhydene.2016.09.017

Analysis of Supersonic Axisymmetric Air Intake in Off-Design Mode

Svetlana Koval

Abstract The most important issue in the design of a perspective aircraft is the development of a highly efficient power plant. One of the factors affecting its efficiency is the choice of air intake. The interest in this task is due to the fact that the operation of the air intake control program in various flight modes has a huge impact on the performance of the air intake device and, as a result, the power plant as a whole. The choice of the regulatory program is one of the most important types of work at the stage of forming the initial data when designing the power plants of aircraft (Bakulev et al. in Theory, calculation and design of aircraft engines and power plants, MAI, Moscow, 2013). The use of numerical modeling to solve various gas-dynamic problems allows us to expand the research range, and therefore, significantly reduce the number of experiments when practicing an air intake device. One of these tasks is to determine the characteristics of an air intake device in a wide range of flight speeds of aircraft. In this paper, we consider a supersonic axisymmetric three-shock air intake device of an external type of compression, numerical simulation of which was carried out in an application package for various operating modes. Based on the results of numerical modeling of the air intake device, a comparison is made to verify the design model, a solution is obtained to determine the optimum point for minimum losses in the off-design operation mode of the air intake device by changing the position of the central body without changing its geometry.

Keywords Shock wave · Air intake · CFD

1 Introduction

The engine inlets are designed to slow down the flow of air entering the engine. The main requirements [2] imposed on input devices are:

– Ensuring high values of the total pressure retention coefficient;

S. Koval (✉)
Moscow Aviation Institute, Moscow, Russia
e-mail: koval-svetlana@ro.ru

Z. Jing and X. Zhan (eds.), *Proceedings of the International Conference on Aerospace System Science and Engineering 2020*, Lecture Notes in Electrical Engineering 680,
https://doi.org/10.1007/978-981-33-6060-0_4

– Creating a uniform flow at the engine inlet or the desired (permissible) irregularity;
– Minimal aerodynamic drag;
– Minimum dimensions and weight;
– Ensuring stable and efficient operation in the entire required range of flight modes and engine operating modes.

Modern aircraft input devices are characterized by the presence of a large number of controls to ensure optimal operation, as well as strong integration with the body and systems of the aircraft.

Modern software systems make it possible to reliably calculate the three-dimensional flow around an air intake in a stationary setting, considering viscous effects and with a duct through the internal channels of air intakes and engine cavities.

The main objective of this work was to calculate and optimize the shock wave system in a supersonic input device. By optimal we mean a system that has the maximum possible value of the total pressure retention coefficient [3]. The position of the first shock wave due to the shift of the air intake cone in axial movement is considered as an optimization parameter.

As a result of the calculation, it is possible to optimize the flow part of the air intake, which has the optimum position of the shock system, or specify the geometry of the flow part of the inlet device that will best meet the requirements.

2 Engine Air Intake

2.1 Purpose and Classification of Air Intakes

Air intake devices are designed to take air from the surrounding atmosphere, supply it to the engine with the least losses and the process of compressing this air from the high-speed head.

Input devices used on various aircraft differ in a wide variety of types and structural forms. The range of flight speeds of the aircraft and the requirements for its maneuverable properties have the greatest impact on the appearance of the input device. Accordingly, the airplane air intake device is divided into:

Subsonic—M numbers of cruising flight not exceeding 0.8…0.9. Installed on civil aviation aircraft, helicopters. In the power plants of these aircraft, air compression is carried out mainly by the compressor, and the pressure increase from the high-speed head is small.

Transonic—large subsonic cruising and relatively small supersonic maximum flight speeds (M < 1.5…1.7). The pressure increase due to the high-speed head in such input devices is more significant. Air intake input devices of these aircraft are simple in design, as they are usually performed unregulated.

Supersonic—installed on aircraft with high values of the maximum number of M flight (usually at M > 2.0). They are usually performed adjustable (Fig. 1).

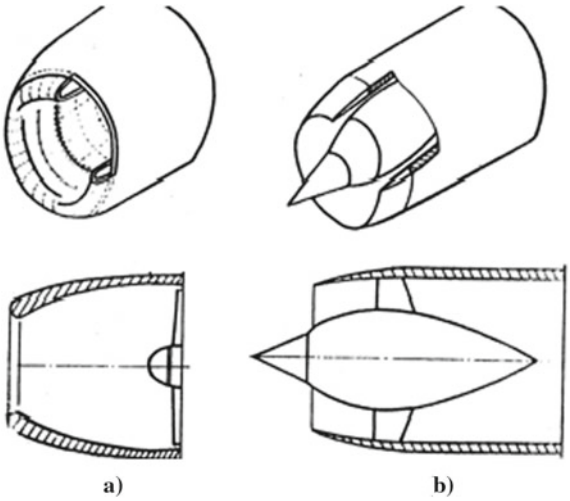

Fig. 1 Scheme of the air intake device: **a** subsonic; **b** supersonic

The numerical calculation of the gas-dynamic characteristics of the air intake supersonic air intakes is characterized by a wide variety of types and schemes. They are classified according to the signs:

1. The number of shocks—single-shock multishock intake:

The braking of supersonic flow to subsonic speed occurs in shock waves. The simplest case—a single straight shock wave. But it cannot provide effective air compression due to the increase in its intensity and loss of full pressure at high flight speeds. To reduce the intensity of the direct jump, the airflow in front of it is pre-braked in several oblique shock waves of low intensity.

To create a system of shock waves, a special profiled surface, called the braking surface, is used. Its forming is a broken line with one or another number of fractures. When this surface is flowed around by a supersonic flow, oblique shock waves are formed at its fractures, in which the supersonic flow is pre-compressed before the closing direct shock [4] (Fig. 2).

1. By the location of the shock waves relative to the entry plane:

At the supersonic input external compression device, all the shock waves formed during the flow around the braking surface are located in front of the input plane of the input device. The area of the smallest section of the internal channel (“throat”) is close to the plane of the entrance.

In the supersonic input internal compression device, all oblique shock waves are located behind the input plane, and compression is carried out inside the channel.

In the supersonic input device of mixed compression, one part of the oblique jumps is placed in front of the input plane, and the other part—in the internal channel. In this case, the inner channel from the input plane to the “throat” has a significant

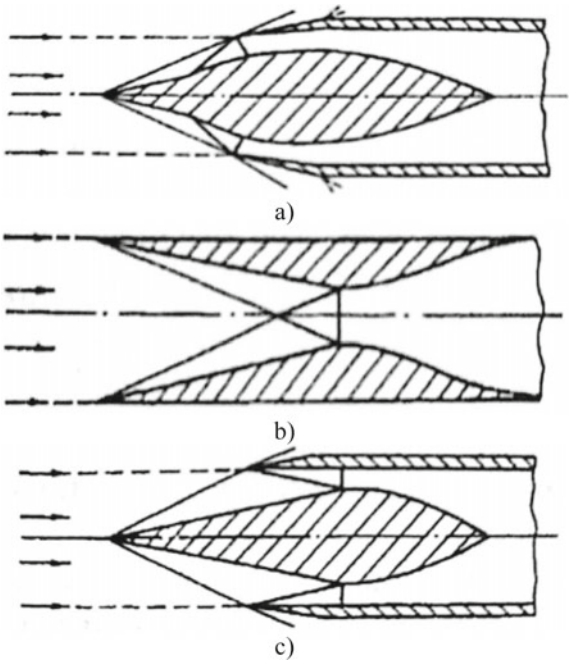

Fig. 2 Types of supersonic diffusers: **a** external compression; **b** internal compression; **c** external—internal compression

narrowing, and the minimum cross-section of the channel, called "throat", is located at some distance from the input plane.

Currently, supersonic external compression input devices are used in aviation. The supersonic input device of mixed and especially internal compression can in principle provide a more efficient process of compression of the supersonic flow at high m flight numbers, but there are some difficulties in their practical use (Fig. 3).

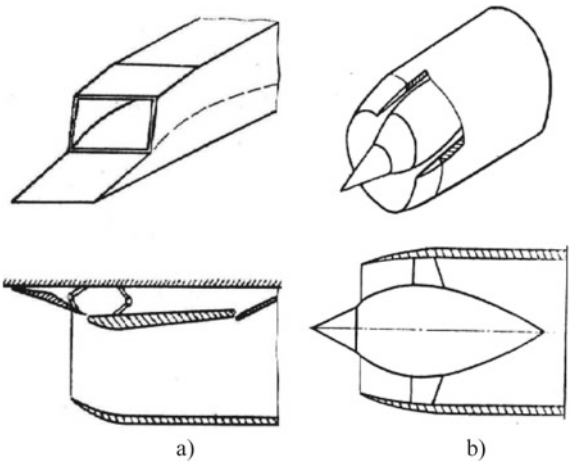

Fig. 3 Air intake devices: **a** two-dimensional; **b** axisymmetric

2. According to the shape of the braking surface and the inlet section, there are flat and axisymmetric supersonic air intake devices.

3 Numerical Simulation of the Operation of a Three-Shock Air Intake Device

To conduct a numerical study, we chose a model of an axisymmetric triple-shock intake device of the external compression type in Fig. 4 in the range of Mach numbers (M = 1.5–2.5), corresponding to the experimental model described above.

The work presents the results of calculating the flow characteristics along the inlet device path, namely, throttle (dependences of the total pressure recovery coefficient σ on the flow coefficient φ) and speed characteristics at the calculated and non-calculated operation modes of the air intake under consideration are determined.

For numerical modeling, the original geometric model was modified by adding further volumes for simulate air flow and simulate outflow from the air intake device for various throttling modes.

As a result, the geometric model of the computational domain looks according in Fig. 5. It can be seen from the model that a cylindrical region is added at the inlet, the geometrical dimensions of which are sufficient to form a flow at the air

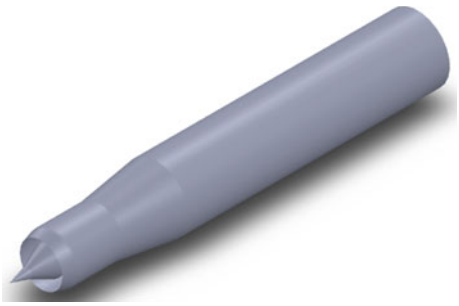

Fig.4 Geometric model of the considered air intake device

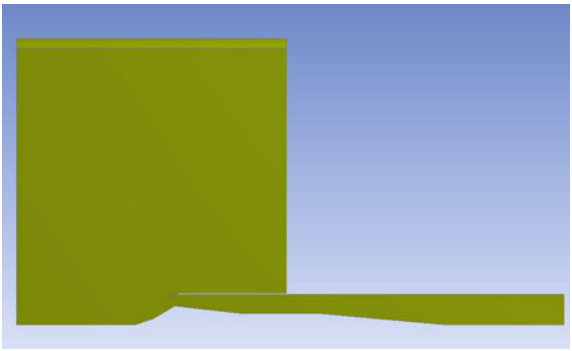

Fig. 5 Geometric model of the computational domain

intake device inlet, while the system of shock waves realized on the shell does not affect the flow in the air intake device channel. At the exit of the air intake device channel, a subsonic nozzle with a supercritical differential with a small opening angle is installed. This is done to obtain the throttle characteristics of the air intake device by solving a parametric problem, in which the diameter of the nozzle exit section, which determines the flow through the device, acts as a parameter. Attached to the nozzle area for the free flow of the jet from the nozzle by the condition of supercritical differential. The size of this area is chosen arbitrarily [5, 6].

3.1 Mathematical Model of the Air Intake

The Navier–Stokes Equations are the basic governing equations for a viscous, heat conducting fluid. It is a vector equation obtained by applying Second Newton's Law of Motion to a fluid element and is also called the momentum equation. It is supplemented by the mass conservation equation, also called continuity equation and the energy equation. Usually, the term Navier–Stokes equations is used to refer to all of these equations [7].

Navier–Stokes Equations are the governing equations of Computational Fluid Dynamics (CFD). Computational Fluid Dynamics is the simulation of fluids engineering systems using modeling (mathematical physical problem formulation) and numerical methods (discretization methods, solvers, numerical parameters, and meah generations, etc.) [8, 9].

To solve this problem, we used a numerical method that allows calculating spatial viscous three-dimensional turbulent gas flows of the gas in the time-based process. The system of Reynolds-averaged Navier–Stokes's equations describing the spatial flow of a viscous compressible gas in the Cartesian coordinate system is as follows:

$$\partial\rho/\partial t + \partial\left(\rho u_j\right)/\partial x_j = 0 \tag{3.1}$$

$$\partial(\rho u_i)/\partial t + \partial\left(\rho u_i u_j - \tau_{ij}\right)/\partial x_j + \partial p/\partial x_i = 0 \tag{3.2}$$

$$\partial(\rho e)/\partial t + \partial\left(\rho u_i H - u_j \tau_{ij} - q_i\right)/\partial x_i = 0, \tag{3.3}$$

where: $i, j = 1,2,3$.

The stress tensor τ and the heat flux vector q are related to the parameters of the averaged flow by means of the relations:

$$\begin{aligned}\tau_{ij} = \tau_{lij} - \rho\overline{u_i u_j} =& (\nu + \nu_t)[\left(\partial u_i\ /\partial u_i \partial x_j\ - \partial x_j + \partial u_j/\partial u_j \partial x_i\ - \partial x_i\right) \\ & - \tfrac{2}{3}\delta_{ij}\partial u_k \partial u_k \partial x_k - \partial x_k]\end{aligned} \tag{3.4}$$

$$q_i = -C_p\left(\nu/\mathrm{Pr} + \nu_t\Big/\underset{t}{\mathrm{Pr}}\right)\partial T/\partial x_i, \tag{3.5}$$

where: $\nu = \mu/\rho$ is the laminar kinematic viscosity; μ is the molecular viscosity determined by the Sutherland's law; $\nu_t = \mu_t/\rho$ is the turbulent kinematic viscosity.

In the above equations, p, ρ, T, u_i are the pressure, density, temperature, and components of the velocity vector U in the Cartesian coordinate system, respectively; $e = \varepsilon + 0.5\ u_i\ u_i$ is the total specific energy and $H = e + p/\rho$ is the total specific enthalpy. Specific internal energy ε, is defined as $\varepsilon = p/(-1)/\rho$, where æ is the ratio of specific heats, C_p is the specific heat at constant pressure, P_r and P_{rt} are ordinary and turbulent Prandtl's numbers, respectively 0.72 and 0.90.

For viscous flows on the walls, the following conditions should be specified:

$$q_w = 0, (\nu_t)_w = 0,$$

where $q_{w,}(\nu_t)_w$ is the velocity vector and turbulent viscosity on the wall and, in addition to the above conditions, at the boundaries of the computational domain, the normal derivatives of the flow parameters and the setting of values ν_t (at the boundaries through which the gas flows into the computational domain).

As initial, for all types of flow, it is necessary to set parameters of the flow in the entire computational domain. The main assumptions were considered to be that the calculation was carried out under the assumption of thermally insulated walls for a three-dimensional stationary statement [10, 11].

3.2 Statement of the Problem. Calculated Mesh. Boundary Conditions

To carry out numerical modeling of gas-dynamic processes, an unstructured mesh of the computational domain with thickening to the walls was constructed, which provides the necessary accuracy in determining the parameters of the boundary layer.

The characteristics of the configuration of the diffuser are determined above by numerical simulation of gas-dynamic processes, based on the solution of the system Navier-Stokese's equations. The calculation was carried out for the following values of the parameters of the oncoming flow: flight Mach number M = 2.5 [12, 13] (Fig. 6).

Assignment of boundary conditions for calculation

To provide the necessary input data for the calculation of the aerodynamic characteristics of the air intake, it is necessary to assign boundary conditions to all surfaces of the calculated volume, in order to fully simulate the most accurate gas flow. The following boundary conditions are specified in the calculation:

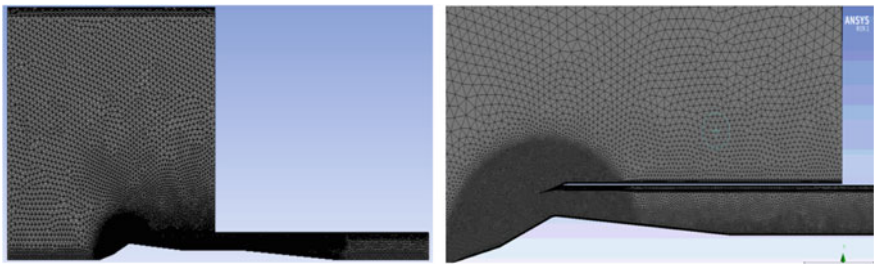

Fig.6 Computational mesh

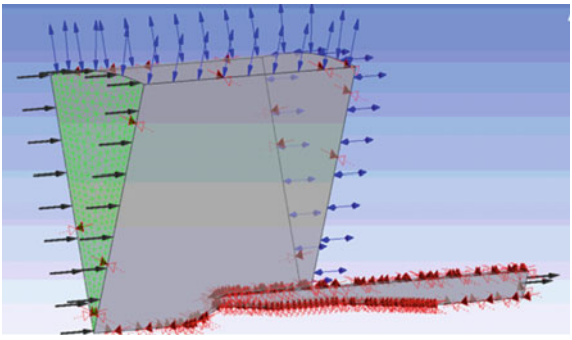

Fig. 7 Boundary conditions for solving the Inlet problem

1. At the entrance to the computational domain (inlet), the oncoming flow velocity (with the corresponding value Mn), static pressure (P = 101,325 Pa) and static temperature (T = 288 K), corresponding to the flight at height H = 0 km in Fig. 7.
2. On all other surfaces (excluding the walls of the air intake) (opening)—static pressure (P = 101,325 Pa) and temperature (T = 288 K), corresponding to a given flight altitude H = 0 km in Fig. 8.

In addition, when solving the problem in the calculation model, the following options are set:

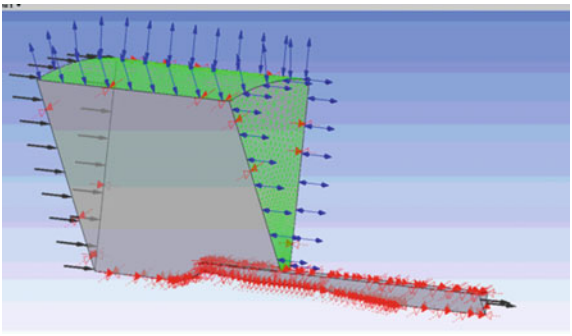

Fig. 8 Boundary conditions for solving the opening problem

– All air intake surfaces are specified as non-slip surfaces, however, the roughness affecting at parameters of the boundary layer wasn't taken into account;
– The Reference Pressure = Ph parameter was set to reduce rounding errors when the dynamic pressure changes in the computational area are small compared with the absolute pressure value;
– As the working substance was chosen—air as an ideal gas (Air Ideal Gas);
– Heat transfer calculation option—total energy (Total Energy) [14, 15].

3.3 Results of Numerical Simulation

As a result of a series of calculations, the distribution fields of the main gas-dynamic parameters of the air flow were obtained, which clearly illustrate the change in the position of the system of oblique jumps and the closing normal shock depending on the flight Mach number and the backpressure value. In Fig. 9 the fields of the distribution of the Mach number over the computational domain when flying at Mach number is presented 2.5 at pressures at the outlet of the diffuser corresponding to the maximum value of the total pressure recovery coefficient. In Fig. 9 also clearly demonstrates the position of oblique shock waves and the closing direct shock, which corresponds to the theory, namely, on the estimated flight Mach number, oblique shock converges on the air intake shell, which ensures maximum air flow and the absence of additional wave resistance [16].

The calculation was performed in the ANSYS CFX environment in automatic mode using ANSYS WORKBENCH.

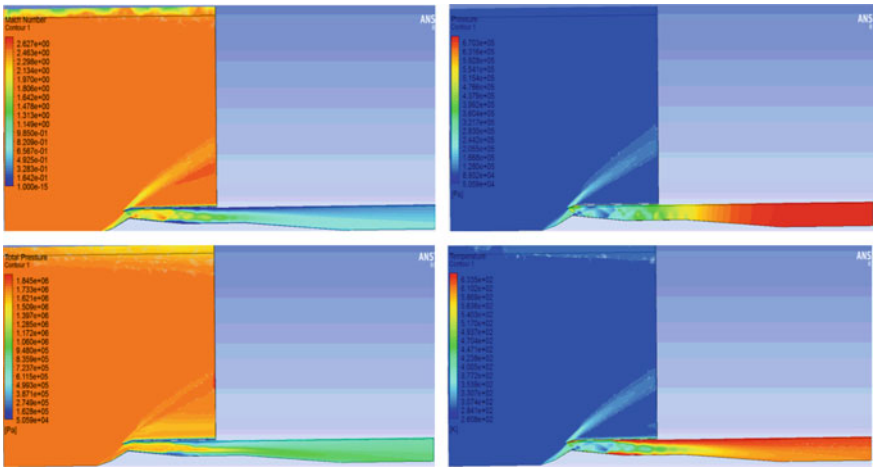

Fig. 9 Fields of static pressure, total pressure, static temperature and the Mach number of the air intake in the mode M = 2.5

In Fig. 9 shows the fields of static, total pressure, static temperature and Mach number of the input device in the mode M = 2.5. It can be seen that the shock system has gone inside the input device, which corresponds to the experimental data of this mode, therefore, the device doesn't work in the calculated mode. According to the results of the analysis, it can be said that the real design mode for the input device of this geometry is located in the region M = 2.

4 Conclusion

This paper provides an overview of classic and promising input devices of the power plant of a supersonic aircraft is presented. As a test sample, we selected a three-shocks air intake with a central body for the estimated flight Mach number M = 2 of the external compression types. Based on the selected model, numerical modeling was performed in the range of Mach numbers (M = 2.5) and compared with experimental results in order to verify the calculation model, which allows us to draw the following conclusions:

1. As the flight Mach number increases, the maximum value of the total pressure recovery coefficient decreases, while the flow coefficient increases. Thus, the operating mode of the investigated input device is not always optimal. So, the flight at M = 2.5 is characterized by the operation of the diffuser at a lower recovery coefficient of the total pressure ($\sigma_{max} = 0.73637$);
2. Comparison of experimental data with the results of numerical calculation allows us to conclude that the constructed calculation model is adequate, the selected boundary conditions, as well as the modeling technique.

References

1. Bakulev VI, Golubev VA, Nechaev YN (2013) Theory, calculation and design of aircraft engines and power plants. MAI, Moscow, p 688
2. Sazonov AI (2011) Design and operation of aircraft engines, lecture notes. UVAU GA (I), p 8
3. Nechaev YK, Fedorov RM, Kotovsky VKh, Polyak VA (2005) Theory of aircraft engines. VVIA named prof. Zhukovskiy NE, pp 47–64
4. Akopov MG, Snipes BI, Dolgachev VG. Gas dynamics. Mashinostroenie, pp 56–712
5. Kandasamy R, Gunasekaran K, Sulaiman HH (2011) Scaling group transformation on fluid flow with varible steam conditions. Int J Non-Linear Mech 46(7):976–985
6. Luers AS (2003) Flow control techniques in a Serpentine inlet. Springer, V.25(5):325
7. Gea LM, Nyugen S (2015) CFD simulation of S-duct test case using overset meshes. Springer 35(2):569
8. Andersson B, Andersson R, Sudio R. Computational fluid dynamics for engineers. Cambridge University Press, p 86
9. Molchanov AM (2019) Thermophysics and fluid dynamics. OSF Preprints, p 160
10. Molchanov AM (2019) Numerical method for solving the Navier-Stokes equations. OSF Preprints, p 139

11. Tarik AS (2010) Engineering thermodynamics. Publishing ApS, p 104
12. Nag PK (2006) Basic and applied thermodynamics. McGraw Hill, p 81
13. ANSYS Inc. (2010) ANSYS modeling and meshing guide. ANSYS release 13.0. Documentation Inc., p 280
14. Fletcher K (1991) Computational methods in fluid dynamics: part 2. Mir, p 512
15. Farrashkhalvat M, Miles JP (2003) Basic structured grid generation with an introduction to unstructured grid generation. Laserwords Private Limited, Oxford (India), p 242
16. Egorov IN, Kuzmenko ML, Shmotin YN (2005) Increasing of air engine efficiency basing on optimization technology. Int Semin—Aero India 2005, Bangalore 57(1):58–72

Parameter-Orientated Functional Modeling Method Based on Flight Process

Yuqian Wu, Zoutao Xue, Gang Xiao, Ke Gong, Xiaoxu Dong, and Yue Luo

Abstract The system function execution intimately couples with the flight process, which is regarded as a critical factor to evaluate the system design comprehensively and precisely. Intending to establish the flight process-oriented functional model, this paper proposed a functional modeling method centering on parameter relationships, establishing the functional architecture of the system in multiple scenarios from the perspective of the flight process. Foremost, the functions of aircraft systems are categorized according to the application, then the system functional blocks of each category are further decomposed, with functional parameters and performance parameters embedded respectively. Progressively, the function completion status is constrained through the functional parameter relationships considering the dimensions of control demand, input parameters, physical components, etc., as well as the logic gates setting forth configuration relevance, and the specific blocks regarding the flight scenario collectively., rendering a comprehensive system-level functional architecture. The paper modeled the concrete functional flows of typical avionics systems, and evaluated functional completion status in various scenarios via Enterprise Architect, verified the efficiency and correctness of the method. The method facilitates the combination of the function model with the flight process, which is

Y. Wu (✉) · Z. Xue · G. Xiao · K. Gong · X. Dong · Y. Luo
Shanghai Jiao Tong University, Shanghai, China
e-mail: wuyuqian@sjtu.edu.cn

Z. Xue
e-mail: xzt0407@sjtu.edu.cn

G. Xiao
e-mail: xiaogang@sjtu.edu.cn

K. Gong
e-mail: Dark_sky@sjtu.edu.cn

X. Dong
e-mail: dongxiaoxu@sjtu.edu.cn

Y. Luo
e-mail: luoyue@sjtu.edu.cn

Z. Jing and X. Zhan (eds.), *Proceedings of the International Conference on Aerospace System Science and Engineering 2020*, Lecture Notes in Electrical Engineering 680,
https://doi.org/10.1007/978-981-33-6060-0_5

capable of measuring the rationality of the functional mechanism from an overall perspective in the early development stage.

Keywords Model based system engineering · Functional modeling · Flight process · SysML

1 Introduction

Functional models depict the intentions of designer [1], showing how the general goal of a system is achieved by realization of subgoals via the subfunctions in the system [2], which acts as a significant role in the system development by bridging the requirements of stakeholders with the physical components assignment.

The safety critical complex systems, especially aircraft systems are the combination of mechanical, structural, pneumatic, electronic, software, hardware domains and so forth. Therefore, the multidisciplinary of various domains induces integration challenges in terms of predicting system functional interactions in the early development process, raising the need of function modelling.

The theoretical framework is the prerequisite of function modelling, aiming at sorting out the relationships among functions. In literature, there are various approaches of function framework establishment. The well-established function modeling schemes include system decomposition analysis [3], and flow-based functional framework by interpreting the function into material, energy, and information through the system [4–6].

Furthermore, the emphasis lies in how to implement the existing function framework in system design process under the multidiscipline characters. SysML [7, 8] is regarded as a standard graphical method to describe the lifelong operational process of the system, capable of capturing functional interactions from the operational perspective of the system, as well as connecting with requirement traceability, system architecture, behavioral analysis, performance analysis, and simulation verification.

Model-based systems engineering (MBSE) [9], is the practice of SysML language. When it comes to model based function modeling method, behavior modeling is one of the branches of function modelling, such as the function–behavior–structure (FBS) model [10] and the structure–behavior–function (SBF) model [11], which focuses on the mapping among function, the intended behavior and the physical architecture of the system.

Besides, state flow contributes to the function interaction presentation towards the multiple operational modes of the systems [12]. Article [13] introduces a rigorous modeling framework of multidisciplinary systems utilizing the system state flow diagram (SSFD). Research [14] identifies fault propagation paths and the combined effect that cross disciplinary boundaries based on functional models.

The above methods highlight the internal operational process of systems. However, the aircraft function execution is coherent with the aircraft operational process, thus pose the limitation of the function interaction evaluation accuracy.

The work presented in this paper focuses on the challenge of developing an effective function modeling framework that supports the comprehensive evaluation of the aircraft functional status by combining the internal function with the external environment, namely the practical flight process of the aircraft, which is scalable across the system abstraction levels.

The method realized early-stage simulation of functional correlation, contributing to better understand the operational mechanisms of multiple systems considering the flight process, which facilitates the function decomposition and optimization in the following development process.

The second section of the paper represents the framework of parameter-oriented functional modeling method. Furthermore, the steps of the parameter-oriented functional modeling and simulation are introduced respectively. In the third section of the paper, the integrated surveillance system of the aircraft is taken as the object, verifying the proposed method combing the flight process.

2 Method Description

The parameter-oriented functional modeling method based on the flight process mainly includes the following steps: All the functions in the system should be analyzed at first to establish a functional operational framework composed of main functions. Then the elements in the framework can be connected from different dimensions through logical parameters, combining with flight process to show the impact of different constraint factors on the function completion.

Above all, the basic elements of the functional model framework will be introduced. Then, the functional decomposition, functional framework establishment, and functional parameter simulation are described sequentially.

2.1 Functional Model Framework

The functional operation model framework can be expressed as a combination of functional organization, behavioral organization, and physical component mapping.

Function: Abstract behaviors to achieve the task or requirement, which can be divided into more specific activities layer by layer.
Behavior: A series of specific activities carried out to meet the objectives of upper-level functions.
Physical components: Specific physical components to conduct the behaviour (Fig. 1).

The behavior model is the medium in the framework to carry out the mapping of functions to physical components, achieving the transfer from abstract functions to concrete behaviors. The differences between function and behavior are that function

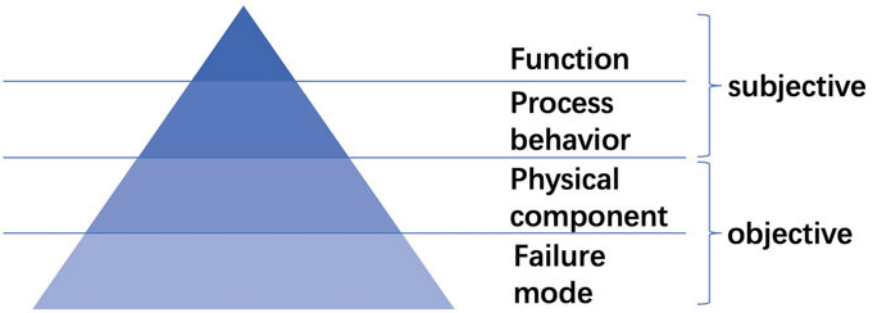

Fig. 1 Functional operation model framework

has no subject, while behavior has a specific subject. Generally speaking, function can be expressed in the form of "verb + noun", indicating that function is abstract definition which does not possess a specific execution object. Secondly, physical behavior can be understood in the form of "subject + predicate + object", which defines the objective initiator and executor of the action. Therefore, the subjective function can be refined into the specific objective behavior chains to realize the linkage of the function, behavior and physical components based on the functional target.

Besides, the state of physical components is affected by the failure modes. Specifically, FMEA can be used to analyze the failure effects and extract the parameter changes caused by the failure modes, so that the specific impact on the upper layer behavior can be indicated through the state derivation from bottom to up.

2.2 Function Extraction and Decomposition

The functional relationships are organized according to the purpose and the application similarity of each function. Accordingly, sub-functions/behaviors are divided into four categories to sort out and combine the different types of functions.

- **To provide**: Provide energy, resources, data and other parameters to the external systems
- **To maintain**: Ensure that each characteristic parameter/performance index involved in the functional operational process is within the normal range, which can be divided into two sub-types.
  - Positive: Positive measures in normal conditions to maintain the operating conditions (e.g. state monitoring).
  - Negative: Negative measures in abnormal conditions to return to the operating conditions (e.g. overheat protection, overvoltage protection).

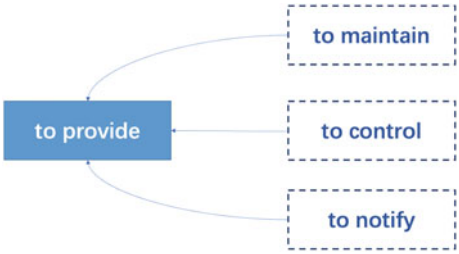

Fig. 2 Relationships of different function categories

- **To control**: Provide control to the functional operation, which can be gradually refined to specific physical components.
- **To notify**: Provide the necessary information to the pilot and external systems, such as the abnormal state of the system (Fig. 2).

In further, the main functions and auxiliary functions can be extracted to establish the system functional framework according to the functional classification. Generally, the "to provide" functions are the main functions in the functional framework. The other three types of functions provide support for the main functions, the states of which will influence the state of the main functions.

2.3 Functional Operation Framework Establishment

Functional model organization. The functional framework includes the combination of the main functions and the auxiliary functions. The main functions are the basic elements in the framework establishment process, which can exist in the form of a chain or a loop. Furthermore, the auxiliary functions are embedded in the upstream and downstream of the main function model according to the actual operating relationship. The connections between the functions are established through the directional lines as well as the logical symbol such as AND gates, and OR gates (Fig. 3).

Operational parameter expression. The information transmitted among functional modules in the framework can be expressed through operational parameters.

The focus in the system operational process is whether the expected function is achieved under the specified conditions. In specific, the output parameter state of the function module is set as the main criterion for measuring the abnormal situations of the system. Furthermore, the failure state of the physical component will be mapped to the abnormal state of the functional parameter, achieving the mapping from the physical layer to the logical layer. Therefore, the key parameters in the system operational process can be the transfer variables among the functional modules.

As for the modeling of operational parameters, the parameters can be divided into the energy material, control commands, data parameter, and state variables according

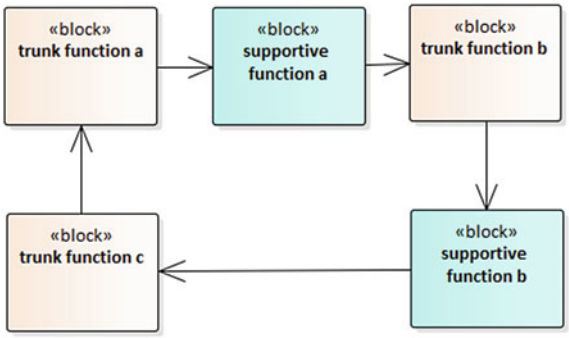

Fig. 3 Functional operation framework depiction

to the application of the function module, which can be embedded in the operational process model in the form of properties. In addition, the operational parameters can be expressed in the form of performance parameters for the key performance systems, expressing the effects of different failure modes of physical components on the functional operational process more accurately.

Furthermore, the output parameters of a functional module depend on the external influence and the internal state of the functional module.

$$output\_par = f(func\_status) * f\left(\sum_{i=1}^{n} input\_par\right) \tag{1}$$

Specifically, the transfer of functional operational process parameters is affected by factors such as upstream input parameters, control commands, energy supply, physical components, and so forth.

The input parameters are the parameters transmitted from the upstream and the external system. The control commands may originate from the automatic control mechanism in the system or the manual control buttons in the cockpit panel. Energy is the required electrical energy, mechanical energy and other substances for the operational process. The physical components are the specific objects for the operational process execution.

The internal state of the module depends on the state of the underlying behavior or the state of the physical component performing the behavior. The internal functional state and the input parameters are combined to affect the output parameters of the module, and the output parameters of the module will act as the input parameters of other modules to propagate the effect through the functional parameter flow (Fig. 4).

Flight phase modeling. The flight phase should be integrated with the functional operational process as the function execution has a strong correlation with the flight process. The flight phases of the aircraft include scenarios such as taxiing, takeoff, climb, cruise, approach, and landing. The flight phases can be expressed as one of the judging conditions for the functional parameter passing down, embedded in the operational process chains through the logic gate such as AND gate, OR gate.

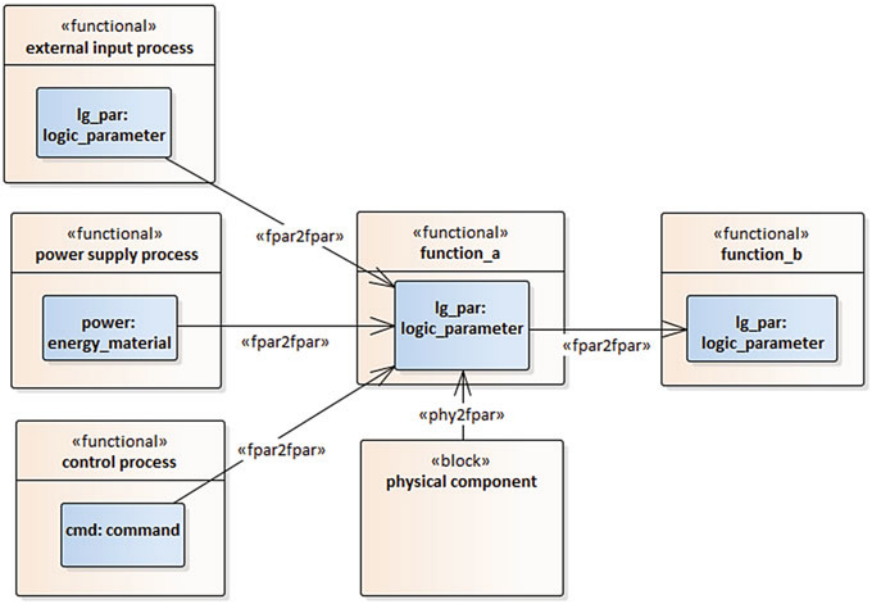

Fig. 4 Determinants of operational parameters

The AND gate shows that all the premises must be met to realize the parameter transmission. The OR gate shows that the parameter transmission can be realized if any one of the premises is met. Then the current flight phase will be set through user input or software, to determine the evolution direction of the functional chain combining with the judgment of logic gates (Fig. 5).

2.4 Parameter Propagation Simulation

The simulation of the functional parameter relationship is carried out by traversing the functional relationship chain from bottom to top. Firstly, the failure mode of the physical component is coded, establishing the logical relationship with the state of the physical component. And then the state of the physical component is passed to the internal state of the behavior module. Progressively, the deviation of the output parameters of the behavior module is transferred to the functional parameter network by the behavior chain, so that abnormal upstream parameter will be transmitted downwards through the functional parameter network, resulting in the anomaly of the functional logic chain of other systems, which is ultimately reflected in the anomaly of the downstream system functions (Fig. 6).

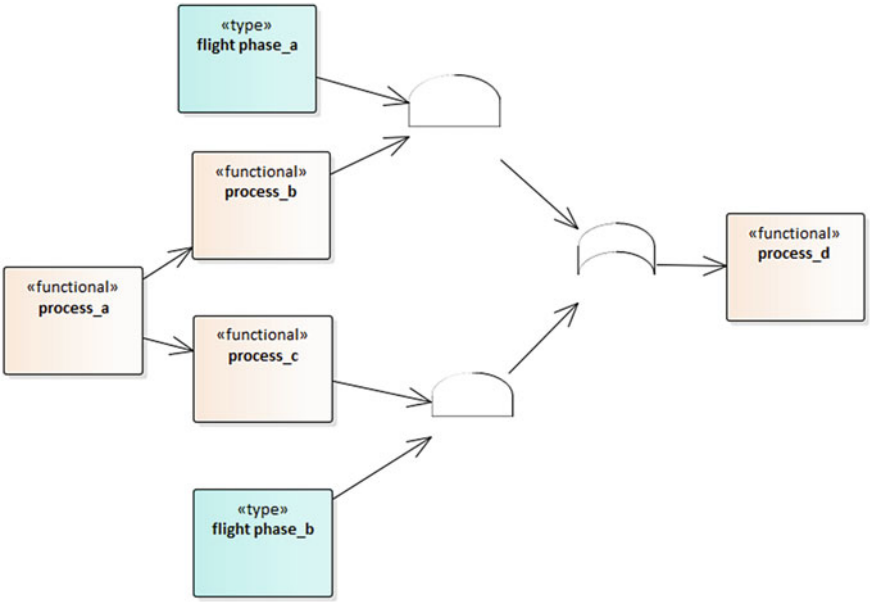

Fig. 5 Flight phase expression depiction

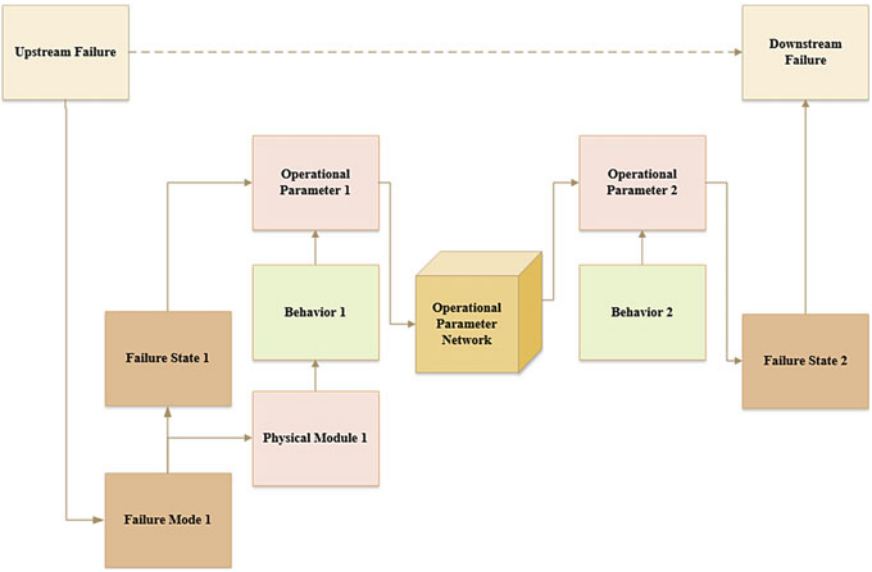

Fig. 6 Searching network of functional state relationship based on operational parameters

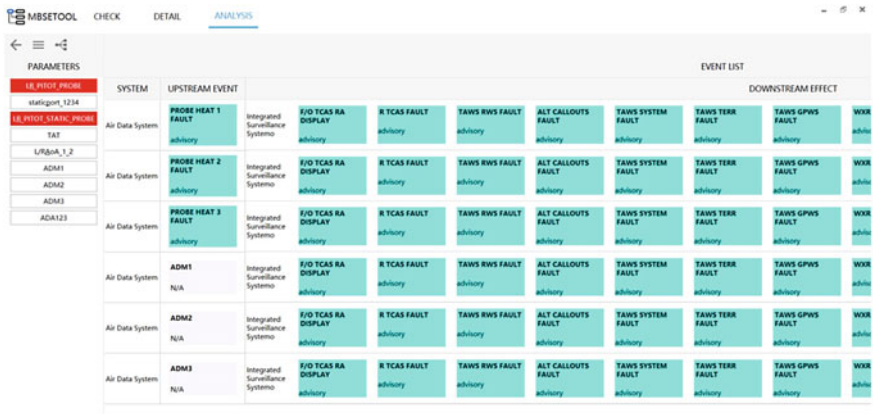

Fig. 7 User interface of functional state relationship search

The simulation is implemented by the functional relationship search algorithm. Taking some present underlying failure events of the selected upstream and downstream systems as the starting point of the searching process, the failure will be traced back to the corresponding system-level function through the mapping relationship between physical components and behaviors. Furthermore, the cascade relationship diagrams between the systems are established according to the existing function diagrams of each system. Then the depth-first search (DFS) algorithm is utilized to traverse the cascade relationship diagrams recursively until the state-associated chain from the upstream failure state to the downstream failure state is established, The nodes in the chain represent the various parameters in the functional propagation process.

Furthermore, the user-interface of the state association chain is realized by C#. The state parameters of the physical components of upstream system can be set on the left side of the interface to simulate the upstream root failure state, and the cascade failure of downstream system can be displayed on the right side of the interface. The transmission chain between the upstream and downstream functional states can be visualized by right-click the downstream cascade abnormal state, which records each parameter node in the parameter transmission process (Fig. 7).

3 Simulation Verification of Functional State Relationship

To verify the efficiency of the method, the paper selected the aircraft integrated surveillance system as the object to demonstrate the function state relationship. The integrated surveillance system plays an important role in the safe operation of the aircraft, which monitors dangerous environments such as traffic, weather, and terrain

around the aircraft, and transmits dangerous situations to the crew. Moreover, the inherent fault of the system will be displayed through the cockpit alert system.

3.1 Functional Model Establishment

According to the integrated surveillance system function list of certain aircraft, the system functions can be expressed as meteorological surveillance function and surveillance control function. The meteorological surveillance function is categorized as "to provide" function, which can provide meteorological condition and threat alerts. The surveillance control function belongs to "to control" category, which provides the support for the surveillance function realization.

In the simulation environment, the meteorological surveillance function includes two sub-functions, namely the meteorological condition display function and the wind shear detection function. The meteorological condition display function can display all important meteorological information in the range of 320 nm around the aircraft automatically according to the radar echo. The wind shear detection function can monitor and predict the wind shear at low altitude to provide the corresponding warning to the crew.

In order to realize the display of meteorological information, the meteorological surveillance function are further decomposed into a series of operational processes, combined with the auxiliary surveillance control function to establish the functional logic chains.

(1) Transmit and receive antenna signals: Send and receive radio frequency pulses.
(2) Control antenna scanning direction: Control the antenna scanning direction and range through the antenna scanning angle.
(3) Process radar signals: Generate and send radar pulses based on surveillance instructions, as well as process the received pulses into digital signals, which are then transmitted to the threat calculation process.
(4) Calculate meteorological condition and threats: Combine the parameters transmitted by external systems with the parameters from radar echo data to calculate meteorological condition and meteorological r threat warning information.
(5) Transmit information to the cockpit: Transmit meteorological information and warning information to the cockpit display system to inform pilots of the relevant meteorological conditions and wind shear threats.

The difference of functional operational process between the wind shear detection function and the meteorological condition display function is that the wind shear detection function needs to receive vertical speed, radio altitude and other information to judge the wind shear scenario, which is appliable at the takeoff and landing phases below a specific altitude range (radio altitude 2300 ft). Consequently, those two functions result in different parameter transfer branches at the operational level as shown in Fig. 8.

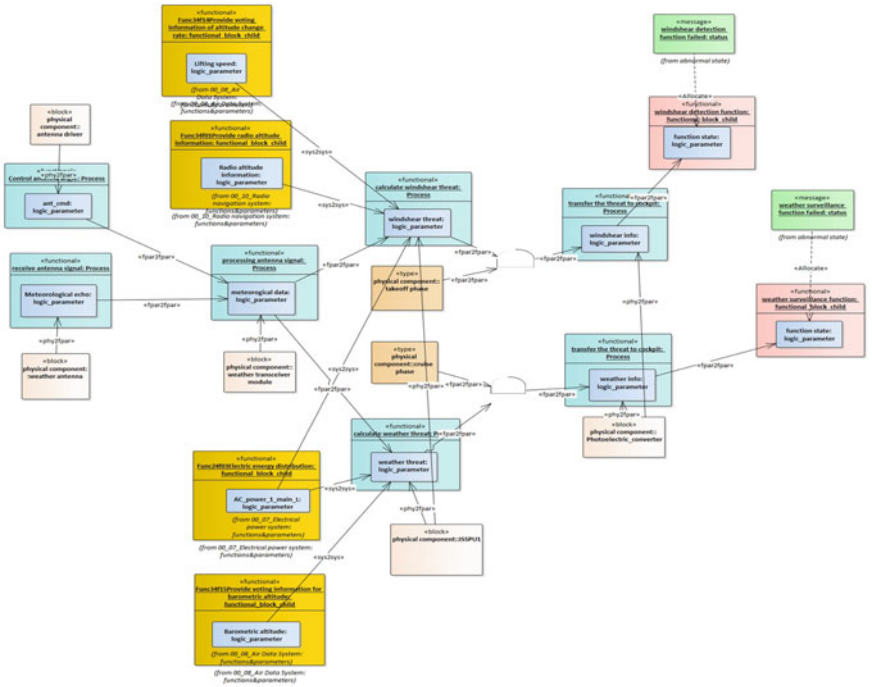

Fig. 8 Functional operation models of meteorological surveillance function

Physical components related to the meteorological surveillance functions include weather radar antenna (ANT), antenna driver (DRV), transceiver module (RTM), integrated surveillance system processing unit (ISSPU), and photoelectric convertor.

The antenna driver controls the antenna through the antenna scanning angle. The transceiver module generates and sends radar pulses according to the ISSPU instruction, and transmits the received data to the ISSPU. The ISSPU processes the data to generate meteorological condition and predictive wind shear warning information. The information is transmitted to the cockpit for display and alert through a photoelectric convertor.

Above all, the operational process of meteorological surveillance function is depended on the inner factors, the as well as the upstream system parameters, including atmospheric altitude, vertical velocity, radio altitude and other parameters. In addition, the completion of the function requires the electrical system to supply energy. Therefore, the models of the air data system and the electrical system were built according to the simulation purpose. Here presents a brief introduction to the operational process models of the air data system, including the pressure and temperature signals measured by a series of sensors such as pitot tubes, static pressure holes, and total temperature probes, which are then converted into barometric altitude, vertical speed and so on through the Air Data Module (ADM) Then the parameters are passed to the corresponding functions of the downstream system.

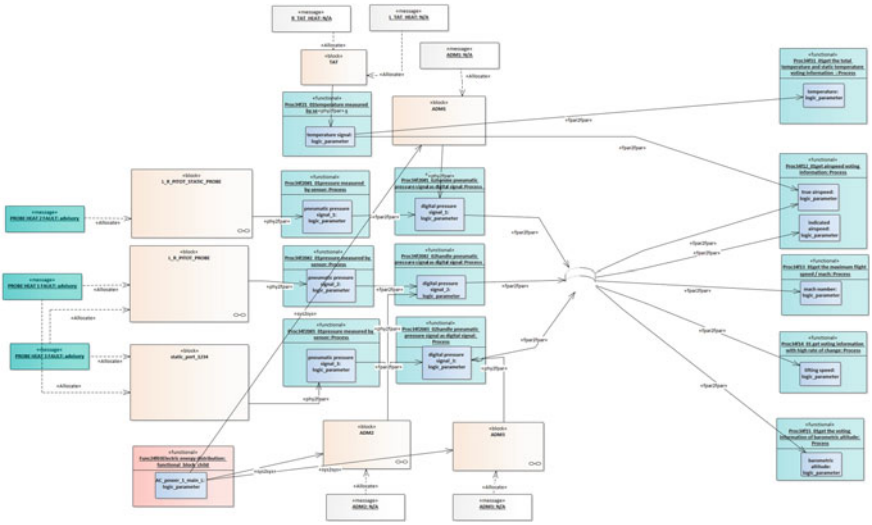

Fig. 9 Functional operation models of Air data system

Moreover, the operational process of the Air data system is affected by the power system (Fig. 9).

3.2 Simulation Results Discussion

Since the function acts on the specific flight phase, the same upstream system failure in different phases will result in different downstream abnormal states. Thereby, two typical flight phases are selected as the scenarios, where the corresponding upstream system failure were triggered and led to the abnormal state of different downstream functions.

Input error in the take-off phase. In the take-off phase the enabled state of the wind shear detection function is determined by the parameters of the radio altimeter, and then the wind shear condition is determined based on the altitude and speed changes of the flight status.

Under the premise of the take-off phase, the abnormal state of physical component probe heat sensor which facilitates the collection of air pressure was set, resulting in the error of vertical velocity information transmitted by the air data system which led to the abnormal state of wind shear calculation process through the transmission of two functional parameter chains in Fig. 10

Power supply error in the cruise phase. In the cruise phase, the system performs meteorological surveillance functions. The meteorological calculation process will obtain energy from the electrical power system. Therefore, the left generator failure

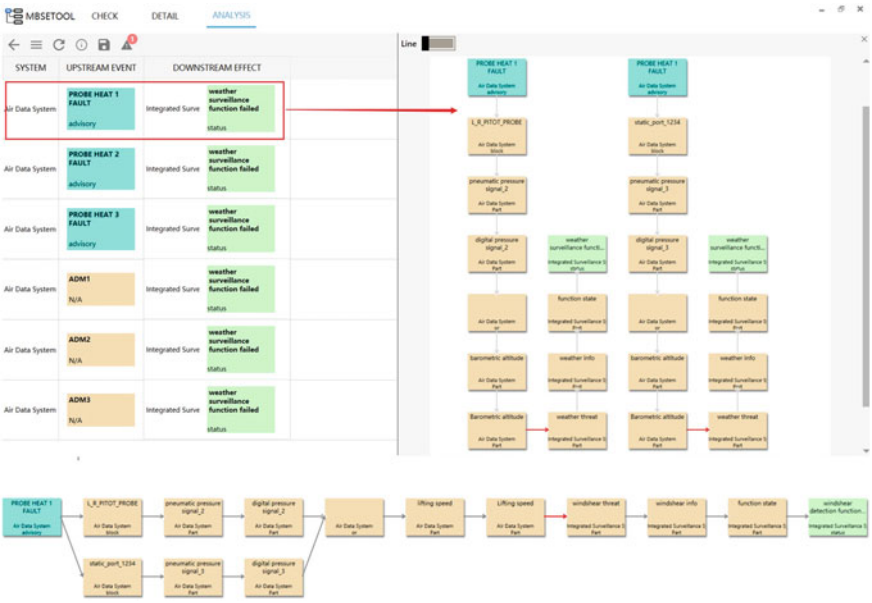

Fig. 10 Searching results of input error in the take-off phase

of the electrical power system in the cruise phase led to the power supply abnormal, resulting in the meteorological surveillance function abnormal depicted by Fig. 11.

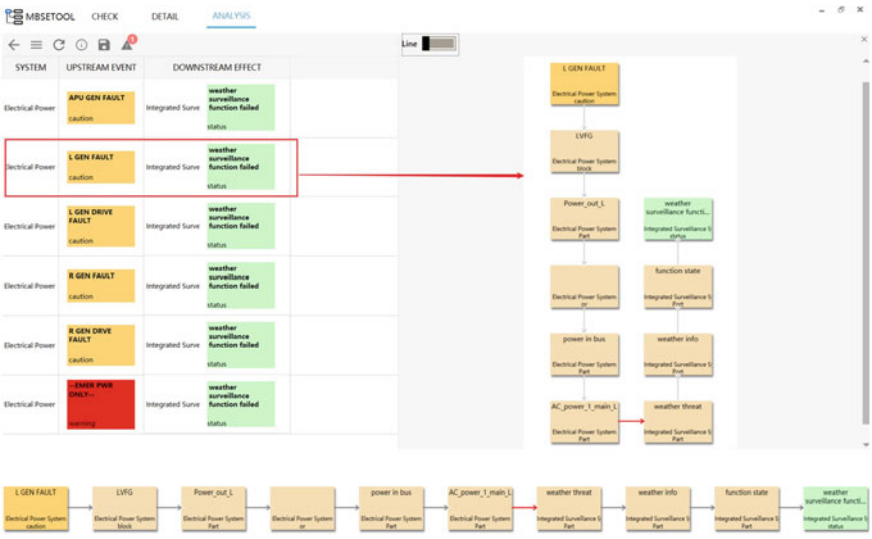

Fig. 11 Searching results of power supply error in the cruise phase

However, since the wind shear detection function is only activated below a certain radio altitude, the upstream failure did not cause the abnormal state of the wind shear detection function in the cruise phase.

4 Conclusion

To address the gap between the existing functional modeling method of aircraft systems and the practical flight application, a functional modeling method based on flight process is proposed centralized on the operational parameter relationships between the functional states of multiple systems. The efficiency of the method was verified by aircraft integrated surveillance system with several failure scenarios considering the flight process.

The method realizes the evaluation of the functional state correlation under the premise of the joint operation of the functional process and the flight process. The future research directions include quantitative evaluation of the functional state correlation in combination with the actual operational parameters of the system.

The method can be applied in the early stage of design, which contributes to further understand the operational mechanism of complex systems and provides support for functional decomposition and design optimization.

Acknowledgements The project is supported by National Program on Key Basic Research Project (2014CB744903), National Natural Science Foundation of China (61673270), New Young Teachers Launch Program of Shanghai Jiaotong University (20X100040036), Shanghai Pujiang Program (16PJD028), Shanghai Industrial Strengthening Project (GYQJ-2017-5-08), Shanghai Science and Technology Committee Research Project (17DZ1204304) and Shanghai Engineering Research Center of Civil Aircraft Flight Testing.

References

1. Kitamura Y, Kashiwase M (2004) Masayoshi fuse: deployment of an ontological framework of functional design knowledge. Adv Eng Informat 18(2):115–127
2. Erden MS, Komoto H, Van Beek TJ et al (2008) A review of function modeling: approaches and applications. AI EDAM 22(02)
3. Komoto H, Tomiyama T (2011) A theory of decomposition in system architecting. Proc Int Conf Eng Des. Technical University of Denmark
4. Stone RB, Wood KL (2000) Development of a functional basis for design. J Mech Des 122(4):359–370
5. Ulrich KT, Eppinger SD (2003) Product design and development, 3rd edn. McGraw-Hill/Irwin, New York
6. Pahl G, Beitz W, Feldhusen J, Grote KH (2007) Engineering design: a systematic approach, 3rd ed Springer, London. Tomiyama T (2016) Function allocation theory for creative design. Proc CIRP 50:210–215
7. Hoffmann H-P (2011) Systems engineering best practices with the rational solution for systems and software engineering. IBM Corporation, Somers NY

8. Friedenthal S, Moore A, Steiner R (2008) A practical guide to SysML: the systems modeling language. Kaufmann, Burlington, VT
9. Fisher J (1988) Model-based systems engineering: a new paradigm. OR Insight 1(3):1502–1644
10. Beek TJV, Erden MS, Tomiyama T (2010) Modular design of mechatronic systems with function modeling. Mechatronics 20(8):850–863
11. Goel A, Rugaber S, Vattam S (2009) Structure, behaviour, and function of complex systems: the structure, behaviour, and function modelling language. Artif Intell Eng Des Anal Manuf 23(1):23–35
12. Yildirim U (2015) Function modelling of complex multidisciplinary systems: development of a system state flow diagram methodology for function decomposition of complex multidisciplinary systems. Ph.D. Thesis University of Bradford
13. Yildirim U, Campean F, Williams H (2017) Function modeling using the system state flow diagram. Artif Intell Eng Des Anal Manuf 31(4):413–435
14. Sierla S, Tumer I, Papakonstantinou N et al (2012) Early integration of safety to the mechatronic system design process by the functional failure identification and propagation framework. Mechatronics 22(2):137–151

Experimental Study on Ice Shear Strength Evolution

Gong Chen, Weiling Kong, and Fuxin Wang

Abstract Prediction of ice shearing performance on aluminum substrate is significant to develop de-icing technology for engineering problems. Ice shearing stress, which involves both adhesion and cohesion, varies with progression of substrate-icing both in temporal and spatial. Thus, study on evolution of both during substrate icing helps comprehensive understanding regularity of shearing performance. In this research, an experiment is designed to measure both ice adhesive and cohesive strength. Afterward, the evolutionary law is discussed with both physical and thermal theories. Experiment results show that substrate icing could be divided into several stage in sequence as "freezing", "cooling" and "equilibrium". Both adhesive and cohesive strength increases obviously in the freezing and cooling stage, while finally converges in the equilibrium stage. Such evolution of ice adhesive and cohesive strength are contribute to gradual change of temperature during vertical growing of ice layer. Finally, A model is established to evaluate the adhesive and cohesive strength via given initial temperature, time and position.

Keywords Substrate-icing · Ice adhesive strength · Thermal diffusion

1 Introduction

Ice shedding is a common physical phenomenon which bring serious engineering problems, especially in the field of aviation and aerospace. For instance, ice cube shed from aircraft surface might be sucked into the air-turbo-engine and causes damage to engine component [1]. Also, irregular geometric configuration of turbo-blade front edge after ice shedding might result in aerodynamics deterioration.

G. Chen · W. Kong (✉) · F. Wang
School of Aeronautic and Astronautic, Shanghai Jiao Tong University, Shanghai, China
e-mail: kongwl@sjtu.com

G. Chen
Department of Advanced Vehicle Development and Vehicle Integration, Pan-Asia Technical Automotive Center Co, Ltd., Shanghai, China

Z. Jing and X. Zhan (eds.), *Proceedings of the International Conference on Aerospace System Science and Engineering 2020*, Lecture Notes in Electrical Engineering 680,
https://doi.org/10.1007/978-981-33-6060-0_6

In essences, ice shedding happens as long as external load, such as aerodynamics load, centrifugal inertial force, or even gravity, exceed its attaching force to substrate. Such attaching force could be either "adhesion" or "cohesion" according to their mechanism. Ice adhesion is defined as the molecular force on the interface between ice and substrate. In contrast, ice cohesion is defined as the inter-molecular force of ice. Ice adhesion and cohesion could be either shearing or normal. In most case, shearing performance is more focused in ice shedding problem.

It has been found that both adhesion and cohesion are influenced by many factors according to the research in recent years. Kraj [2], Zou [3], Kulinich [4] find ice adhesion is sensitive to physical and chemical properties of substrate surface. Ice adhesion to substrate ranges from 0.05Mpa to 0.5Mpa with different surface roughness and coating treatment. Jellinek [5], Guerin [6], Janjua [7] and Archer [8] find that both ice adhesive and cohesive strength are temperature-dependent. Chu [9] also points out adhesion and cohesion also related to the geometry and configuration of the water before freezing.

However, In most of the literatures above, both ice adhesion and cohesion are regarded as steady state parameters after complete substrate-icing. There is few attention has been paid on the evolution of ice adhesion and cohesion during ice progression. However, in reality, adhesion or cohesion failure usually occurs before complete ice formation. For instance, larger aerodynamic load leads to ice shedding or breaking from the front edge of airfoil as soon as ice is partly accumulated. Also, ice shedding usually occurs with a little residual ice remains on the surface of aircraft fuselage. Thus, temporal and spatial evolution during freezing deserves more study for comprehensive prediction and effective prevention of ice shedding.

In this research, experiment is designed to measure the both ice adhesive strength and cohesive strength at each significant moment within a substrate icing process. Afterward, both mechanical and thermal effect are discussed respectively to find the main cause of the experimental results. Finally, a analytical model is established for qualitative description of such evolutionary law.

2 Research Method

2.1 Experiment Apparatus and Strategy

The arrangement of experimental apparatus is shown in Fig. 1. It includes three main part: cooling box, icing specimen and force measuring system. The cooling box is filled with glycol ethylene as the coolant for temperature controlling by an external refrigerator with bump. An icing specimen is located in the space inside cooling box. The specimen is composed by a basement and a slider. A thermal couple is embedded into the slider for monitoring temperature while a electric vibrator is attached on the basement for icing-triggering. The horizontal translation of the slider inside groove

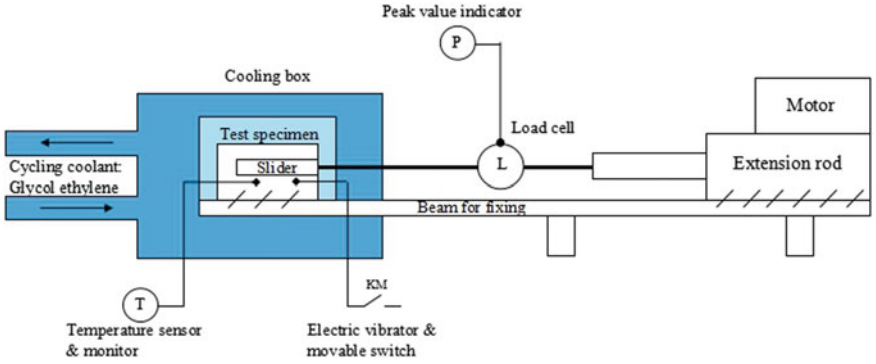

Fig. 1 Arrangement of experiment apparatus

is achieved by an electric extendable rod. Between slider and the rod, a load cell is installed for measuring the load.

The structure and function of the icing specimen is shown in Fig. 2. Both of the basement and slider are made of 6061 aluminium, which is widely used in aviation engineering. The slider, on which there is groove, is inserted in the tunnel of the basement. Vaseline is coated in clearance between basement and slider for sealing, lubrication and preventing unexpected freezing. The ultra-purred water used in experiment is prepared by a purifier (RS2200QUV, Rephile Bioscience, Ltd) in order to satisfy the laboratory standard. The water is filled in the cuboid hollow composed of the slider and basement. The length l and width w of the hollow cross section are 10 mm and 12 mm respectively while the depth d of the hollow is variable.

As shown in Fig. 2, icing is triggered by switching on the vibrator at particular temperature. An increasing load F is applied on the slider in horizontal direction to pull out the slider until displacement occurs. The payload is recorded by the peak value indicator.

As shown in Fig. 3, force-measurement on section planes with different distance to substrate is achieved by alternating a group of individual slider with different deep hollow. Slider with no hollow (d_0) is applicable for measurement of adhesive strength between ice and substrate. While for cohesive strength measurement, the distance of the tested section to substrate is numerically equal to the depth, d, of slider hollow.

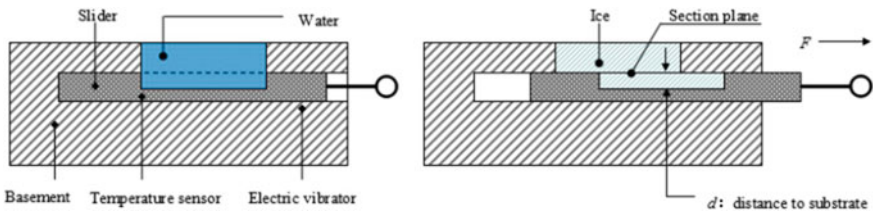

Fig. 2 Structure and principle of the ice specimen

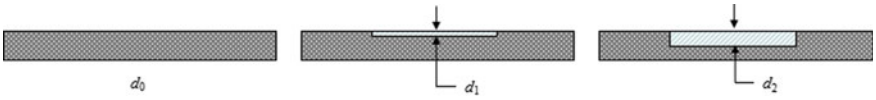

Fig. 3 Slider for measurement on different section plane

The shear stress F_τ of ice on the section is numerically equal to the payload F when the displacement occurs. The shear strength τ is then calculated with section plane area A of the hollow.

$$F_\tau = F \tag{1}$$

$$\begin{cases} \tau = \dfrac{F_\tau}{A} = \begin{cases} \tau_{\text{adheison}}(\tau_{ad}) & (d = 0) \\ \tau_{\text{coheison}}(\tau_{co}) & (d \neq 0) \end{cases} \end{cases} \tag{2}$$

Measurement of adhesive strength τ_{ad} or cohesion strength τ_{co} on different distant sections is alternated easily by changing different slider.

2.2 Experiment Condition and Variables

As mentioned above, evolution of either adhesive or cohesive strength happens in both spatial or temporal, and it also sensitive to ambient temperature. Therefore, three variables are involved in this experiment: freezing time t, distance from shear section to substrate d and initial ambient temperature T.

Freezing time, t

Five moments are followed for the same experiment condition to reflect status at each icing stage. The specific selection of moment is shown in Sect. 3.1.

Position of shear section, d

Three sections with different short distance d: $d_0 = 0$ mm, $d_1 = 1$ mm, $d_2 = 2$ mm is selected to identify the spatial evolutionary trend of shearing performance.

Initial temperature, T_∞

Effect of temperature is always concerned for all the icing problem. For substrate-icing, ice shearing performance is still changeable and unclear within the temperature range of [271.15, 267.15 K] in previous study by our colleague [10]. Thus, $T_\infty = 27.015$ K and $T_\infty = 267.65$ K are selected as the two variables for the experiment. For better illumination, relative initial temperature to equilibrium freezing point $\Delta T_\infty (\Delta T_\infty = |T_\infty - T_m|)$ is also used besides absolute value in following discussion.

3 Experiment Results

3.1 Changing History of Substrate Temperature

Before shearing stress measurement, temperature near substrate is monitored every minute for tracing its changing history during substrate-icing process. Two temperature history curves, which are corresponding to the two initial temperature $T_{\infty 1} = 27.015$ K and $T_{\infty 2} = 267.65$ K, are plotted in Fig. 4. Each curve is numerically fitted by averaging the values from at least four repeated attempts.

The result shows the temperature history of the two conditions are qualitatively similar. Both curves of $\Delta T(t)$ are in accord with the freezing principle of supercooled water [6]. According to feature of the curves, the progression of substrate-icing could be divided into four stages.

Stage 0: Triggering. As soon as external impulse is applied on the ice specimen, icing is immediately triggered from the substrate surface and the temperature suddenly re-calescence to the equilibrium freezing point. This stage usually lasts less than 1 s so that it could be regarded as instantaneous.

Stage I: Freezing. Phase transition of water from liquid to solid occurs right after sudden temperature re-calescence. Latent heat due to continuous phase transition releases from the substrate so that freezing field almost remains at equilibrium freezing point T_m. This process lasts until the phase transition is absolutely accomplished.

Stage II: Cooling. Phase transition is absolutely completed and no latent heat released anymore. Then, ice domain is cooled continuously until it reaches to initial temperature T_∞.

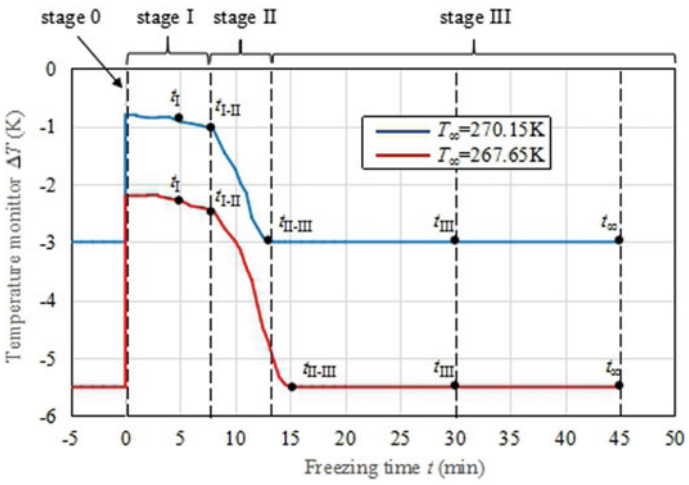

Fig. 4 Temperature history monitored from substrate

Table 1 Time duration of each icing stage

T_∞(K)	Stage I	Stage II	Stage III
270.15	[0.0, 8.0 min]	[8.0, 13.5 min]	[13.5 min,∞]
267.65	[0.0, 8.0 min]	[8.0, 15.0 min]	[15.0 min,∞]

Table 2 Time point for ice adhesion/cohesion measurement

T_∞(K)	t_{I}	$t_{\mathrm{I–II}}$	$t_{\mathrm{II–III}}$	t_{III}	t_∞
270.15	≈3 min	≈8.0 min	13.5 min	30 min	45 min
267.65	≈3 min	≈8.0 min	15.0 min	30 min	45 min

Stage III: Equilibrium. No more energy conversion and heat conduction occurs so that thermodynamic equilibrium is achieved.

It is notable that freezing stage and cooling stage are divided here for better illumination of substrate-icing progression. In reality, however, these stages usually process simultaneously without any clear boundary. It means the cooling of the ice layer occurs as soon as it is formed from supercooled water under the effect of substrate-heat conduction.

Time duration of each icing stage is listed in Table 1. It shows that they are slightly different with the conditions of two initial temperature. Icing in the condition with lower initial temperature requires a bit longer time for finishing stage II and III.

As marked in Fig. 4 as well as listed in Table 2, t_{I}, $t_{\mathrm{I–II}}$, $t_{\mathrm{II–III}}$, t_{III}, t_∞ are set as "critical icing moment" for force measurement. $t_{\mathrm{I–II}}$ and $t_{\mathrm{II–III}}$ are the transition moment from stage I to stage II and from stage II to stage III. While t_{I} and t_{III} are the interpolated moment for stage I and stage III. t_∞ is the moment that stage III lasts for enough time. Measurements are made at these five moment to trace the evolution.

3.2 *Results of Ice Adhesive Strength, τ_{ad}*

Measurements of adhesive strength τ_{ad} are made at each of the five critical moments of both two temperature conditions. The results are illustrated in Fig. 5a, b respectively.

According to the result in each figure, it is noticeable that τ_{ad} increases gradually in stage I and stage II while such increment reduces in following period and finally tend to convergent at the end of stage III. Comparing to the result in both of the two figure, it is also notable that the final converged value of τ_{ad} when $T_\infty = 267.65\,\mathrm{K}$ is slightly higher than that when $T_\infty = 270.15\,\mathrm{K}$.

Table 3 listed the statistical data of adhesion as the supplement to that in Fig. 5. It is obvious that large dispersion of measurement occurs at first moment and then reduces for the rest. Such status indicates that ice-adhesion is unstable at the early stage of icing while it tend to be stable in the end.

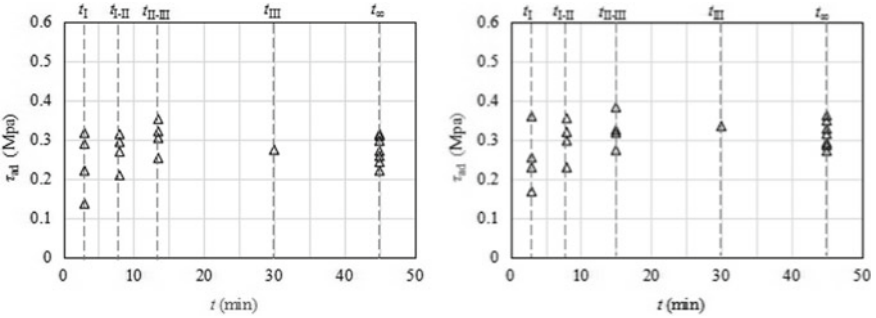

(a) T_∞=270.15K **(b) T_∞=267.65K**

Fig. 5 Evolution of ice adhesion during substrate icing

Table 3 Statistical data of adhesion measurement (Mpa)

T_∞(K)	t_I		$t_{I–II}$		$t_{II–III}$		t_{III}		t_∞	
	Mean	Stdv	Mean	Stdv	Mean	Stdv	Mean	Stdv	Mean	Stdv
270.15	0.241	0.080	0.272	0.045	0.308	0.041	0.274	/	0.273	0.035
267.65	0.252	0.081	0.299	0.052	0.324	0.045	0.334	/	0.314	0.029

3.3 *Results of Ice Cohesive Strength, τ_{co}*

Measurements of cohesive strength τ_{co} are made at each of the five critical moments of both two temperature conditions at the two certain sections. The results are illustrated in Fig. 6a–d respectively.

As shown in Fig. 6a, b, the evolutionary trend of cohesive strength at the closer section is illustrated. Tremendous increasing of τ_{co} is observed during stage I and stage II, which is dramatically larger than that of ice adhesion at same period as that in Fig. 5a, b. In stage III, cohesive strength is converged gradually, of which the value is negatively related to initial temperature $\boldsymbol{\Delta T_\infty}$.

As shown in Fig. 6c, d, the situation of cohesive strength at a more distant section is similar to that in Fig. 6a, b. The only difference is that the value at moment t_I is extremely low, some of which is even lower than the minimum sensitivity of the instrument. In fact, the measurement of cohesive strength is not always available at such early moment. Only about one-fourth attempts are able to produce effective results.

The statistic data in Table 4 reflects numerical characteristics of cohesion. Compare to that of adhesion in Table 3, the increasing trend of cohesion at the given two sections is much more obvious. In addition, it is similar that lower initial temperature leads to higher convergent value of cohesion at the end of substrate icing progression. It is also noteworthy that, especially in stage I and II, the cohesive strength at a closer section to substrate is lightly larger than that at a more distant. Such status is diminished in stage III.

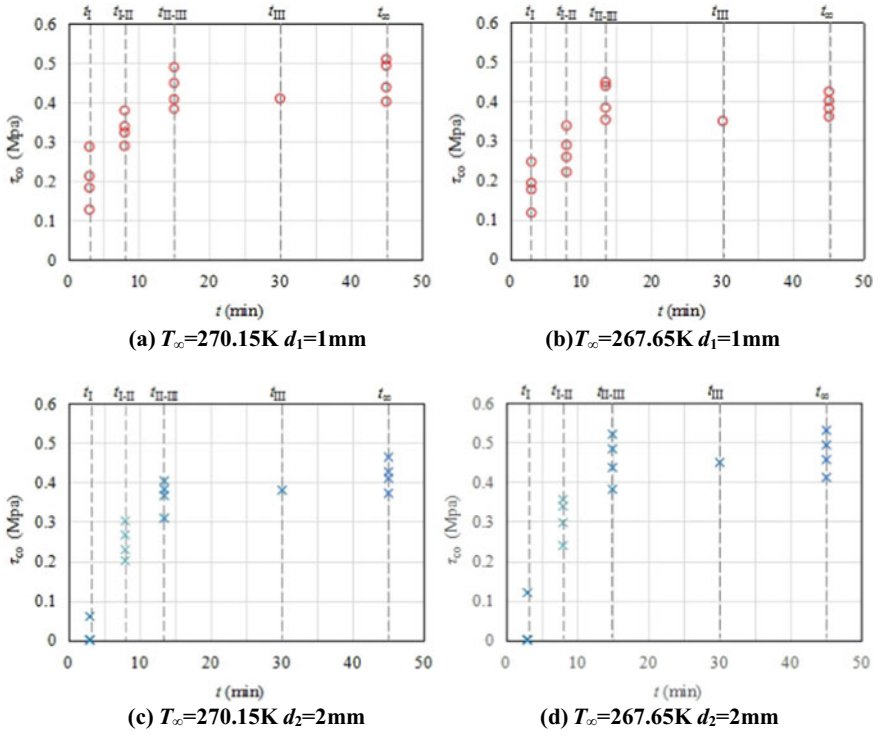

(a) T_∞**=270.15K** d_1**=1mm** **(b)** T_∞**=267.65K** d_1**=1mm**

(c) T_∞**=270.15K** d_2**=2mm** **(d)** T_∞**=267.65K** d_2**=2mm**

Fig. 6 Evolution of ice cohesion during substrate icing

Table 4 Statistical data of cohesion measurement (Mpa)

T_∞(K)	t_I		$t_{I–II}$		$t_{II–III}$		t_{III}		t_∞	
$d_1 = 1$ mm										
	Mean	Stdv	Mean	Stdv	Mean	Stdv	Mean	Stdv	Mean	Stdv
270.15	0.183	0.054	0.276	0.049	0.406	0.046	0350	/	0.392	0.027
267.65	0.206	0.067	0.332	0.037	0.432	0.046	0.409	/	0.461	0.049
$d_2 = 2$ mm										
	Mean	Stdv	Mean	Stdv	Mean	Stdv	Mean	Stdv	Mean	Stdv
270.15	/	/	0.249	0.044	0.365	0.041	0.379	/	0.419	0.038
267.65	/	/	0.308	0.052	0.456	0.060	0.449	/	0.473	0.051

3.4 Summary of Experiment Results

The general evolutionary trend of both ice adhesion and cohesion in each stage during substrate icing could be summarized according to the experiment result in 3.2 and 3.3 respectively as follow:

(1) Both adhesion and cohesion increase during the substrate icing progression. Both of the increment are large in stage I and stage II, and then they reduce in stage III and final converge at the end of the icing process.

$$\text{Stage I\&II}: \begin{cases} \tau_{ad}(t_1) < \tau_{ad}(t_2) \\ \tau_{co}(t_1) < \tau_{co}(t_2) \end{cases} \quad 0 < t_1 < t_2 < t_{\text{II–III}} \tag{3}$$

$$\text{Stage III}: \begin{cases} \lim\limits_{t\to\infty} \tau_{ad}(t) = [\tau_{ad}] \\ \lim\limits_{t\to\infty} \tau_{co}(t) = [\tau_{co}] \end{cases} \quad t_{\text{II–III}} < t < \infty \tag{4}$$

(2) The final converged value of both adhesion and cohesion at the end of icing process are negatively relative to initial temperature.

$$\begin{cases} [\tau_{ad}(T_1)] < [\tau_{ad}(T_2)] \\ [\tau_{co}(T_1)] < [\tau_{co}(T_2)] \end{cases} \quad (T_1 > T_2) \tag{5}$$

(3) With the condition of the same initial temperature, ice adhesive strength is numerically different to cohesive strength. In general, the final converged value of cohesive strength is usually larger than that of the adhesive strength.

$$[\tau_{ad}(T_1)] < [\tau_{co}(T_1)] \tag{6}$$

(4) Evolution of ice cohesion has been identified in spatial. It is earlier for ice cohesion to generate and develop at a closer section to substrate while there is a delay in time for such generation and development at a more distant section. With the icing progression, cohesion at different section tend to be uniform at last.

$$\begin{cases} \tau_{co}(d_1) < \tau_{co}(d_2) \\ \lim\limits_{t\to\infty} [\tau_{co}(d_1) - \tau_{co}(d_2)] \to 0 \end{cases} \quad (d_1 > d_2) \tag{7}$$

In summary, we find a gradually-convergent increasing trend of both ice adhesion and cohesion in temporal and spatial. And such evolution is strongly related to substrate icing progression.

4 Evolution of Thermal Condition During Substrate Icing

It has been summarized in Sect. 3.4 that evolution of ice adhesion and cohesion is coupled with substrate-icing. Moreover, according to the results obtained from previous research of our group [11, 12], thermal condition, especially the transient local temperature of on growing ice layer, changes continuously. Since temperature is regarded as the significant factor which affect both ice adhesion and cohesion

as mentioned in the introduction, it is necessary to focus the law and principle of temperature variation during substrate icing progression.

4.1 Principle of Thermal Condition During Substrate Icing

Referring to the monitored temperature changing history in Sect. 3.1, a simplified illustration is assumed to describe thermal condition during a substrate icing. As shown in Fig. 7, a "finite element" is introduced to illustrate thermal status of ice formation near the substrate.

Firstly, before ice growing, the entire finite element, which includes both supercooled water and substrate surface, remains at equilibrium freezing point T_{m}.

Afterward, phase transition from liquid to solid begins as soon as ice being triggered. Ice layer grows continuously in vertical direction, which represents upward moving of the ice-water interface. Simultaneously, the temperature of the frozen ice layer is gradually cooling down from equilibrium freezing point T_m to initial temperature T_∞ again due to the high heat conductivity of the aluminium substrate.

Finally, since substrate icing is entirely complete and temperature difference between substrate and ice layer is absolutely eliminated, neither latent heat dissipation nor heat conduction occurs so that the system tends to equilibrium.

In summary, temperature variation mainly occurs during the vertical growth of ice layer. Hence, analytical solution of dynamic temperature field should be considered with relevant icing principles.

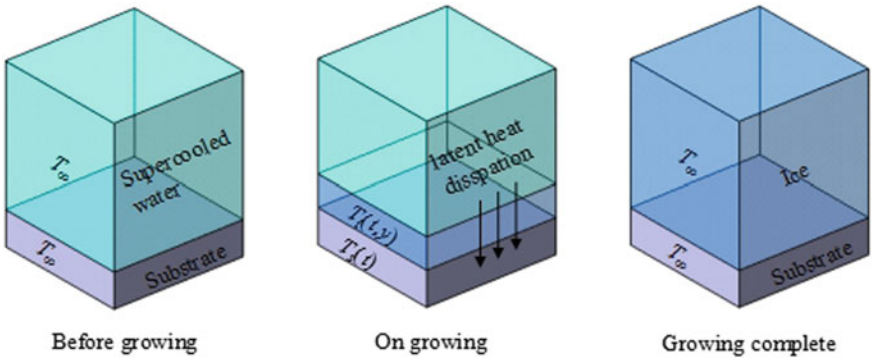

Fig. 7 Thermal status of "finite element" during substrate icing

4.2 Analytical Solution of Temperature Field

Usually, "unsteady state heat transfer theory" is commonly used to solve the problem of temperature variation within different media. The system, which is composed of substrate and supercooled water or ice could be treated as "semi infinite body" and the time/position-dependent temperature field $T_i(t, y)$ is consequently derived by the unsteady state heat transfer equation as shown (8).

$$\frac{\partial T_i}{dt} - a_i \frac{\partial^2 T_i}{dy^2} = 0 \quad 0 < y < h_i(t) \tag{8}$$

In which a_i is the diffusive coefficient of ice. t and y are the time and position dependent variable of the temperature filed. *hi(t)* is the dynamic range of temperature field, which is physically equal to transient thickness of on growing ice layer. Generally speaking, compared to the aluminium substrate, ice is not an effective heat conductor due to its lower heat conductivity. In this situation, temperature gradient within the range of on growing ice layer is reasonable to simplified as linear. Hence, transient local temperature $T(t, y)$ within the ice layer could be analytically solved with two available boundary condition of temperature. They are the temperature of ice-water interface $T_{i-w}(t)$ and the temperature of substrate-ice interface, $T_{i-s}(t)$.

$$T = \begin{cases} T_{i-w}(t, y) & y = h_i \\ T_{i-s}(t, y) & y = 0 \end{cases} \tag{9}$$

In addition, the range of linear temperature gradient is also need be considered as a time-dependent function.

$$y = h_i = h_i(t) \tag{10}$$

The analytical solution of Eqs. (9) and (10) is determined by ice vertical growing mode as well as the specific structure of the ice layer.

According to our previous research [11, 12], the structure of ice layer and its growing mode are all sensitive to initial thermal condition. When $T_\infty > 269.15$ K, ice grows smoothly in vertical direction and absolute solid ice layer forms from bottom to up. When $T_\infty < 268.15$ K, ice vertical growing is more complex, which is further divided in two sub-progression: spongy-ice growing and "filling of the spongy ice". The difference in structure and growing mode is contribute to the thermal stability of the interface between substrate and supercooled water [13]. Correspondingly, temperature field should be solved in accord with them respectively.

Dynamic temperature field of simple ice layer

When initial temperature $T_\infty > 269.15$ K, structure of the simple ice layer and temperature filed are shown in Fig. 8a, b.

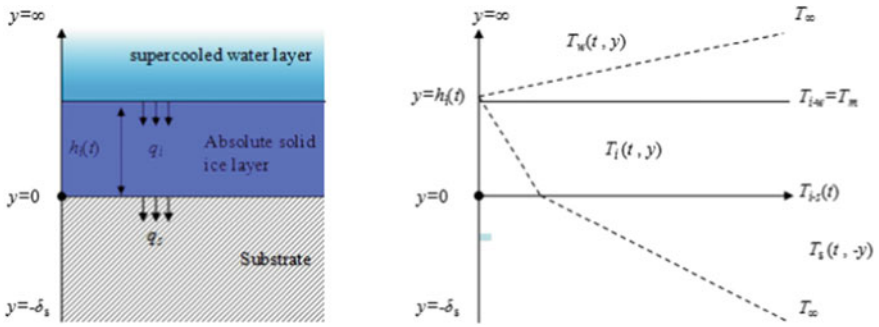

Fig. 8 Structure and temperature field of simple ice layer $T_\infty > 269.15$ K

As shown in Fig. 8a, as soon as ice being triggered, phase transition occurs smoothly from bottom to up and the latent heat due releases from substrate. In this situation, ice layer grows as an absolutely solid media, in which the temperature field of the on growing ice layer is linearly continuous as shown in Fig. 8b. To derive the analytical solution of transient local temperature of ice layer, three variables $T_{i-w}(t)$, $T_{i-s}(t)$ and *hi(t)* need be identified.

The boundary temperature $T_{i-w}(t)$ is always numerically equal to the equivalent freezing point T_m due to its status of water–ice existence.

$$T_{i-w} \equiv T_m \tag{11}$$

The transient thickness of the layer *hi(t)* at given time t is derived by Eq. (12), which is positive proportional to the square root of time variable t.

$$h_i(t) = 2\eta_i\sqrt{a_i t} \tag{12}$$

In which, η_i is "moving boundary coefficient", which could be derived by the "Stefan approximate solution", as expressed in Eqs. (13) and (14).

$$\eta\sqrt{\pi} = \frac{St_i}{\exp(\eta^2)erf(\eta)} + \frac{St_w}{v\exp(v^2\eta^2)erfc(v\eta)} \tag{13}$$

$$St_i = \frac{c_i \cdot \Delta T_\infty}{L_i} \quad St_w = \frac{c_w \Delta T_\infty}{L_i} \quad v = \sqrt{\frac{a_w}{a_i}} \tag{14}$$

St_i and St_w are the "Stefan number" of ice and supercooled water respectively. In which c_i, c_w are the specific heat capacity of ice and water while a_i, a_w are their heat-diffusion rate. Beside, L_i is the latent heat of ice.

The other boundary temperature $T_{i-s}(t)$ is related to the heat conductivity of the substrate. Since both ice and substrate are solid media at the moment, the heat

conduction and internal temperature field could be described by "multi-wall heat conduction model" [14]. Assume that $T_{i-w}(t)$ at $y = hi(t)$ is T_m and the temperature at the bottom boundary of substrate $y = -\delta_s$ remains at T_∞ constantly. Thus, the boundary temperature at ice-substrate interface could be expressed as Eqs. (15) and (16).

$$T_{i-s}(t) = T_\infty - q\prime(t)\frac{\delta_s}{\lambda_s} \tag{15}$$

$$q\prime(t) = \frac{T_\infty - T_m}{\frac{\delta_s}{\lambda_s} + \frac{h_i(t)}{\lambda_i}} \tag{16}$$

In which $q'(t)$ is the heat flux during heat transfer throughout the "multi-wall" composed of substrate and ice. λ_s, λ_i are the heat transfer coefficient of substrate and ice respectively. Hence, the boundary condition of $T_{i-s}(t)$ is obtained by substituting Eq. (15) into Eq. (16), as shown in Eq. (17).

$$T_{i-s}(t) = T_\infty - \frac{\delta_s \lambda_i (T_\infty - T_m)}{\lambda_i \delta_s + \lambda_s h_i(t)} \tag{17}$$

Above all, since the two boundary condition temperature, $T_{i-s}(t)$,$T_{i-w}(t)$,and the "moving boundary" *hi(t)* are all identified, the temperature field within the on growing ice layer is then expressed by Eq. (17).

$$T_i(t, y) = \frac{T_{i-s}(t) - T_m}{h(t)} \cdot y \tag{18}$$

With such equation, transient local temperature within ice layer is able to be estimated with given freezing time t and position y.

Dynamic temperature field of complex ice layer

When initial temperature $T_\infty < 268.15$ K, structure of "complex" ice layer and temperature filed are shown in Fig. 9a, b.

As shown in Fig. 9a, the structure of ice layer is much complicated than the condition of lower initial temperature. Ice layer could be further divided into three sub-component: as ice crystal layer, spongy ice layer and solid ice layer.

As soon as being triggered, ice crystal grows immediately from substrate towards the water field. Afterward, these ice crystal develops with a plenty of side branches and then links with each other so as to construct spongy ice. Spongy ice is the ice network, which still contains unfrozen liquid component. In following period, freezing of residual liquid component occurs to fill the "cave" of spongy ice and transit it to absolute solid ice layer from bottom to up. The consequential growing of different part construct a complex ice layer. Corresponding to its complex construction, the temperature field could also be divided into three section as shown in Fig. 9b. The

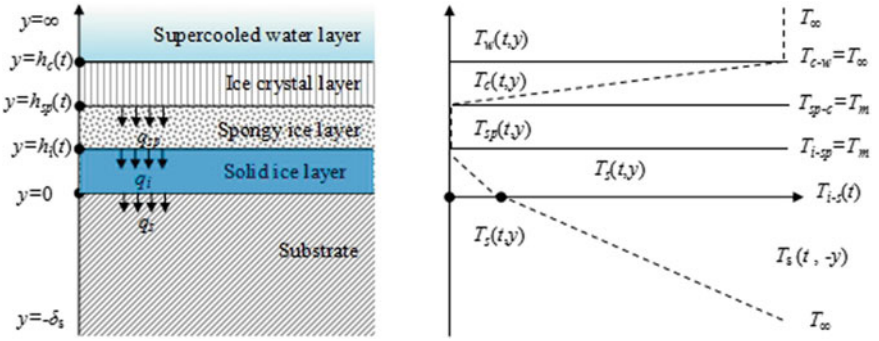

(a) Structure **(b) temperature field**

Fig. 9 Structure and temperature field of "multiple" ice layer $T_\infty < 268.15\,\mathrm{K}$

analytical solution of temperature $T_i(t, y)$ of each section are expressed in following section.

Temperature field of bottom solid ice layer

As shown in Eq. (18, 19), within the absolute ice layer at bottom, temperature changes linearly, which is similar to that in simple ice vertical growing. The two boundary condition temperature is derived similarly to that of simple ice layer.

$$\begin{cases} T_i(t, y) = \frac{T_{i-s}(t) - T_{i-w}}{h\prime_i(t)} \cdot y \qquad 0 < y < h\prime_i(t) \\ T_{i-w} \equiv T_m \\ T_{i-s}(t) = T_\infty - \frac{\delta_s \lambda_i (T_\infty - T_m)}{\lambda_i \delta_s + \lambda_s h\prime_i(t)} \end{cases} \tag{19}$$

While the analytical solution for moving boundary layer of bottom solid layer is somewhat different to that of simple ice layer.

$$\begin{cases} h\prime_i(t) = 2\eta\prime_i \sqrt{a_i t} \\ \eta\prime_i = \sqrt{\frac{(T_m - T_\infty)c_i}{2 \cdot L\prime_i}} = \sqrt{\frac{(T_m - T_\infty)c_i}{2 \cdot (1-f) \cdot L_i}} \end{cases} \tag{20}$$

In which, L_i'is the latent heat released by the freezing of those residual liquid component, where f is the dimensionless solid component fraction of the spongy ice. According to Makkonen [15], f is negatively relate to initial temperature. For $T_\infty > 273.15 - 263.15\,\mathrm{K}$, $f \approx 0.56$–0.7.

Temperature field of bottom solid ice layer

As shown in Eq. (21), within the range of spongy ice layer, temperature is constantly numerically equal to equilibrium freezing point T_m due to the status of ice-water coexistence.

$$T_{sp}(t, y) \equiv T_m \quad h\prime_i(t) \le y \le h_{sp}(t) \tag{21}$$

The moving boundary of spongy ice $h_{sp}(t)$ could also be derived by "Stefan approximate solution". However, the difference is that the thermal-physical properties of spongy ice-layer should be used to replace that of absolute solid ice layer with solid fraction f as expressed in Eq. (22).

$$\begin{cases} T_{sp}(t, y) \equiv T_m \quad h\prime_i(t) \le y \le h_{sp}(t) \\ h_{sp}(t) \approx \sqrt{\frac{|T_m - T_\infty| \cdot c_{sp}}{2 f L_i}} \sqrt{4 a_{sp} t} \end{cases} \tag{22}$$

c_{sp}, a_{sp} and λ_{sp} are the specific heat, heat diffusion coefficient and heat conductivity of spongy ice. They are calculated by consideration the solid fraction f as well as corresponding thermal-physical properties of water and ice respectively as shown Eqs. (23a)–(23c).

$$c_{sp} = f \times c_i + (1 - f) \times c_w \tag{23a}$$

$$\frac{1}{\lambda_{sp}} = \frac{f}{\lambda_i} \times + \frac{1 - f}{\lambda_w} \tag{23b}$$

$$\begin{cases} \rho_{sp} = f \cdot \rho_i \\ a_{sp} = \frac{\lambda_{sp}}{c_{sp} \cdot \rho_{sp}} \end{cases} \tag{23c}$$

By piecewise function of Eqs. (18)–(23a, 23b, 23c), the temperature field of such complex on growing ice layer is also analytically solved.

5 Model for Ice Adhesion/Cohesion Evolution

In Sect. 4.2, the variation of temperature fields of both solid ice layer during its simple vertical growing and complex ice layer during its composite vertical growing are both identified by analytical solution. Since the temperature is the important factor for both ice adhesion and cohesion, their evolution during substrate-icing progression could be modeled based on temperature variation.

5.1 Model of Ice Adhesion Evolution

Ice adhesive strength τ_{ad} is regarded as the function of freezing temperature in most of the researches. Guerin's [6] result of steady static adhesion is quoted as the reference for establishing the relationship between initial temperature and adhesive stress.

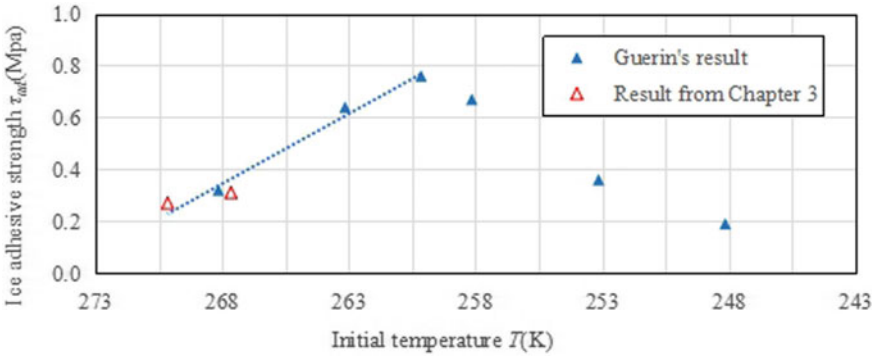

Fig. 10 Relationship between temperature and steady static ice adhesive strength

As shown in Fig. 10, steady static τ_{ad} is negatively proportional to initial temperature within the interval of [273.15, 261.15 K] while it turns positively proportional in the interval of [261.15, 248.15 K]. By linear data fitting, the relationship between τ_{ad} and T within the interval [261.15, 273.15 K] is best expressed by Eq. (24).

$$\tau_{ad}(T_\infty) = 0.612 \times |T_\infty - 273.15\,\mathrm{K}| \quad T_\infty \in [261.15\,\mathrm{K}, 273.15\,\mathrm{K}] \tag{24}$$

In the equation above, temperature is regarded as constant. However, as discussed in Chap. "Analysis of Supersonic Axisymmetric Air Intake in Off-Design Mode", temperature at substrate-ice layer interface changes over time. Therefore, τ_{ad} accordingly turns to a time-dependent variable $\tau_{ad}(t)$ with given initial temperature T_∞. The evolutionary law of $\tau_{ad}(t)$ is expressed as Eq. (25).

$$\tau_{ad}(t) = 0.612 \times \left| T_\infty - \frac{\delta_s \lambda_i (T_\infty - T_m)}{\lambda_i \delta_s + \lambda_s h_i(t)} - 273.15\,\mathrm{K} \right| \tag{25}$$

In Eq. (25), λ_s, λ_i, c_i, L_i, a_i are the constant of physical or thermal properties of substrate and ice, while *hi(t)* refer to Eqs. (12)–(14).

5.2 Model of Ice Adhesion Evolution

Referring to the early result of Han [16], ice cohesive strength τ_{co} is expressed as the power function of the relative temperature ΔT as shown in Eq. (26).

$$[\tau_{co}] = 0.258 \times |\Delta T|^{0.78} \quad |\Delta T| \in [0\,\mathrm{K}, 30\,\mathrm{K}] \tag{26}$$

Table 5 Ice cohesion within different temperature in relevant literature

$\|\Delta T\|$ (K)	≈0	2	5	10
τ_{co}(Mpa)	≈0.28	≈0.31	0.34	0.35

According to Bernard's induction, however, ice cohesion is null at freezing point T_m, which is not reasonable in reality. Therefore, an intercept, $\tau_{co}(\Delta T = 0)$, at freezing point is necessary to create a more comprehensive description.

To obtain the corrected equation for "$T-\tau_{co}$" relationship, "indefinite coefficient algorithm" is used by carrying over the power function as shown in Eq. (27) and then referring to a series of discrete results of τ_{co} (ΔT) as shown in Table 5 [17].

$$[\tau_{co}] = b_0 + b_n|\Delta T|^n \tag{27}$$

The corrected equation is shown in Eq. (28), which represents the relationship between static ice cohesive strength and temperature.

$$\tau_{co}(\Delta T) = \tau_{co}(\Delta T = 0) + b|\Delta T|^n = 0.28 + 0.0219|\Delta T|^{0.5385} \tag{28}$$

In Sect. 4, the temperature is expressed with both variable for time t and position y during the progression of ice vertical growing. Thus, evolution of ice cohesive strength is identified by using temperature variation as the "transfer function".

For those growing of absolute solid ice layer when $T_\infty < 269.15\,\mathrm{K}$, τ_{co} is expressed as Eq. (29). In which the transient local temperature of the ice layer refers to Eq. (17).

$$\tau_{co}(t) = \begin{cases} 0.28 + 0.0219|T_i(t, y) - T_m|^{0.5385} & 0 < y < h_i(t) \\ 0 & y > h_i(t) \end{cases} \tag{29}$$

Here *hi(t)* and $T_i(t, y)$ refer to Eqs. (12) and (19). Within the range of the transient solid ice layer, the evolution of τ_{co} could be roughly estimated by corresponding time t and position y.

For those growing of complex ice layer with lower initial temperature, τ_{co} is expressed as Eq. (30).

$$\tau_{co}(t) = \begin{cases} 0.28 + 0.0219|T_i(t, y) - T_m|^{0.5385} & 0 < y < h\prime_i(t) \\ f \cdot \tau_{co}[\Delta T = 0] = 0.7 \times 0.28 \approx 0.2 & h\prime_i(t) < y < h_{sp}(t) \\ 0 & y > h_{sp}(t) \end{cases} \tag{30}$$

Evaluation of τ_{co} is more complicated for complex ice layer. The transient range of solid ice layer *hi'*(t) and spongy ice layer $h_{sp}(t)$ should be calculated with the given t to identify whether the given position y is in the solid ice layer or spongy ice layer. Therefore, the evolution of τ_{co} could be evaluated by corresponding part of the piece-wise functions as expressed in Eq. (30).

Here $h'_i(t)$, $h_{sp}(t)$ and $T_i(t, y)$ refer to Eqs. (18), (19), (20) and (22) Within the range of solid ice layer, τ_{co} is power functional with the evolutionary local temperature $T(t, y)$. Within the range of spongy ice layer, τ_{co} is constant equal to the ice cohesive strength at equilibrium freezing point, which consider the effect of solid fraction.

6 Conclusion

In this paper, the evolutionary principle of both adhesive strength τ_{ad} and cohesive strength τ_{co} during substrate icing are validated experimentally and analyzed theoretically. Evolution due to both physical properties as well as thermal condition are presented. The following conclusions are drawn:

(1) Ice adhesion and cohesion are two totally different ice mechanical performance, which could not be replaced by each other.
(2) In the condition with a constant initial temperature, both ice adhesion and cohesion increase obviously with freezing time especially at the early stage of substrate-icing progression and then become convergent in the end.
(3) The evolutionary trend of both ice adhesion and cohesion are strongly relate to the temperature variation of the ice layer, which is determined by their structure of as well as their growing pattern.
(4) A model expressed by piece-wise functions is established to predict the evolutionary of ice adhesion and cohesion in both temporal and spatial. By this model, adhesive strength and cohesive strength could be quickly estimated with given variables of initial temperature, time and position.

Acknowledgements The project is not supported by any Foundation.

References

1. Chen G, Yang K, Wang LP et al (2018) Test of ice shedding on turbofan engine blade in refrigeratory environment. J Beijing Univ Aeronaut Astronaut 44(010):2106–2114
2. Kraj AG, Bibeau EL (2010) Measurement method and results of ice adhesion force on the curved surface of a wind turbine blade. Renew Energy 35:741–746
3. Zou M, Beckford S, Wei R et al (2011) Effects of surface roughness and energy on ice adhesion strength. Appl Surf Sci 257:3786–3792
4. Kulinich SA, Farzaneh M (2009) Ice adhesion on super-hydrophobic surfaces. Appl Surf Sci 255:8153–8157
5. Jellinek HHG (1962) Ice adhesion. Can J Phys 40(10):1294–1309
6. Guerin F, Laforte C, Farinas MI et al (2016) Analytical model based on experimental data of centrifuge ice adhesion tests with different substrates. Cold Reg Sci Technol 121:93–99
7. Janjua ZA (2017) The influence of freezing and ambient temperature on the adhesion strength of ice. Cold Reg Sci Technol 140:14–19

8. Archer P, Gupta V (1999) Measurement and control of ice adhesion to aluminum 6061 alloy. J Mech Phys Solids 46(10):1745–1771
9. Scavuzzo RJ, Chu ML, Kellackey CJ (1996) Impact ice stresses in rotating airfoils. J Aircr 28(7):450–455
10. Liu Z, Kong WL, Liu H (2018) Experimental study for effect of mean volumetric diameter on ice adhesion strength. J Exp Fluid Mechan 32:35–39
11. Kong WL, Liu H (2018) Unified icing theory based on phase transition of supercooled water on a substrate. Int J Heat Mass Transf 123:896–910
12. Chen G, Kong WL, Wang LP, Wang FX (2020) On the experimental and theoretical model for ice crystal characteristics near a substrate. Int J Heat Mass Transf 152:119462
13. Kong WL (2015) Mechanism and fundamental theory of supercooled water solidification on the abnormal aircraft icing. Dissertation, Shanghai Jiao Tong university
14. Tao WQ (2018) Heat transfer. Higher Education Press, Beijing
15. Makkonen L (2010) Solid fraction in dendritic solidification of a liquid. Appl Phys Lett 96:091910
16. Bernard M (1978) The strength of polycrystalline ice. Can J Civ Eng 5(3):285–300
17. Jia Q, Li ZJ (2015) Experimental study on shear strength of freshwater Ice in a Reservoir. Math Pract Theory 45(5):132–137
18. Tirmizi SH, Gill WN (1987) Effect of natural convection on growth velocity and morphology of dendritic ice crystals. J Cryst Growth 85:488–502

Investigation of the Effect of Electron-Beam Processing on the Surface of Samples Obtained by Additive Technologies from Cobalt-Chromium and Stainless Steel Powders

E. E. Dzhafarov, K. M. Erikov, O. A. Bytsenko, and A. V. Ionov

Abstract Products made of cobalt-chromium and stainless steel made by additive manufacturing methods are widely used in many branches of modern industry (aviation, mechanical engineering, shipbuilding and instrumentation, energy, medicine, etc.). Surface treatment with high-current pulsed electron beams (HPEB) is a promising method for further expanding the scope of these alloys. The article presents studies of the structural and phase state of the surface layer of samples before and after treatment with high-current pulsed electron beams, as well as the results of roughness measurements before and after irradiation with high-current pulsed electron beams.

Keywords Irradiation with high-current pulsed electron beams · Selective laser melting · Additive technologies · Modification · Surface layer · Structure · Properties

1 Introduction

Development and improvement of methods for surface treatment of parts and workpieces using concentrated pulsed energy flows (CPEF) has a number of advantages over classical methods of surface mechanical, chemical and thermomechanical treatments: formation of a unique physical and chemical state of the surface layer material; achievement of record manufacturing accuracy (at the nanometer level) and surface roughness (Ra∼0.05–0.06 microns); environmental cleanliness; high performance

E. E. Dzhafarov · K. M. Erikov · O. A. Bytsenko · A. V. Ionov (✉)
Institute №2 "Aviation Rocket Engines and Power Plants", Moscow Aviation Institute, Volokolamsk highway.4, Moscow 125993, Russia
e-mail: woln@mail.ru

E. E. Dzhafarov · K. M. Erikov
School of Aeronautics and Astronautics, Shanghai Jiao Tong University, 800 Dongchuan Road, Shanghai 200240, China

Z. Jing and X. Zhan (eds.), *Proceedings of the International Conference on Aerospace System Science and Engineering 2020*, Lecture Notes in Electrical Engineering 680,
https://doi.org/10.1007/978-981-33-6060-0_7

(the cross-sectional area of energy flows varies from 30 cm^2 to 1 m^2, and the pulse duration is from 10 ns' to several tens of microseconds).

The use of CPEF has in fact only one drawback: the high science intensity of the developed technologies, due to the need to conduct long-term and expensive studies of the influence of irradiation modes on the physical and chemical state of the material in the surface layers of parts [1].

Relevance of the work. The problem of improving the performance properties of materials, in particular cobalt-chromium and stainless steel alloys, is one of the most complex in modern materials science. Having high specific mechanical characteristics, these alloys are difficult to form material. This disadvantage can be overcome by using various types of surface hardening associated with the use of concentrated energy flows, which can be used to create nanostructured States with a high set of properties in the surface layer. One of the effective and fairly common methods of such structure modification is HPEB. The experience of using this method accumulated to date shows that its wide implementation in practice is hindered by the existing gaps in the study of the regularities of the electron-beam effect on the structural and phase state of the processed layer of the product manufactured using additive technologies and its influence on the mechanical properties of these materials. Thus, the topic devoted to the need to obtain basic knowledge about the influence of high-current pulsed electron beam processing modes on the physical nature of changes in the structural and phase states of surface layers of cobalt-chromium and stainless steel alloys obtained by additive technologies.

2 Materials and Research Methods

The research was carried out on cylindrical samples made by additive technologies from cobalt-chromium powder and stainless steel. Before irradiation, samples from cobalt-chromium powder were cut into six equal parts, and samples from stainless steel powder were cut into five equal parts in order to be able to irradiate the same sample under different modes. Processing with high-current pulsed electron beams was carried out from the outer surface, the roughness of which corresponds to the roughness after creating the samples.

Irradiation of samples was carried out on a vacuum pulsed electron beam installation "GEZA-MMP" designed for smoothing the microrelief by melting the surface layer of parts and surface modification of metals by pulse quenching, at the following values of the main parameters: W = 25–37 J/cm^2, n = 1–6 pulses. The appearance of the installation is shown in Fig. 1. At the end of the beam pulse, the heated layer is quickly cooled by the process of thermal conductivity into the depth of the material. As a result, the properties of the surface layer change [2]:

- The microstructure changes—the grain size decreases from hundreds of microns to fractions of a micron, the transition to an amorphous state and the formation of nanostructures is possible;

Fig. 1 Appearance of the "GEZA-MMP" installation

- The phase composition changes, and metastable phases and compounds may appear that cannot be formed under conventional heat treatment methods;
- The phase composition is homogenized, for example, carbides in steels are crushed and uniformly distributed.

Practical consequences of these changes is to increase the hardness, corrosion resistance and wear resistance of the materials surface, reducing the coefficient of friction, increasing the dynamic strength of the products.

The state of the surface layers of the samples was analyzed using optical microscopy and roughness measurement in mass production. Using these methods, it was possible to determine the thickness of the modified layer, obtain the microstructure of samples, and also establish the dependence of surface roughness on irradiation modes.

3 Experimental Data and Their Discussion

As object of research used samples obtained by the method of additive manufacturing (AM) a powder of cobalt-chromium and stainless steel. Irradiation of samples was performed after etching on a complex automated electron-beam installation "GEZA-MMP" at various modes and the number of pulses. The appearance of samples made of cobalt-chromium after exposure to HPEB, as well as samples made of stainless steel before and after exposure to HPEB, are shown in Figs. 2 and 3.

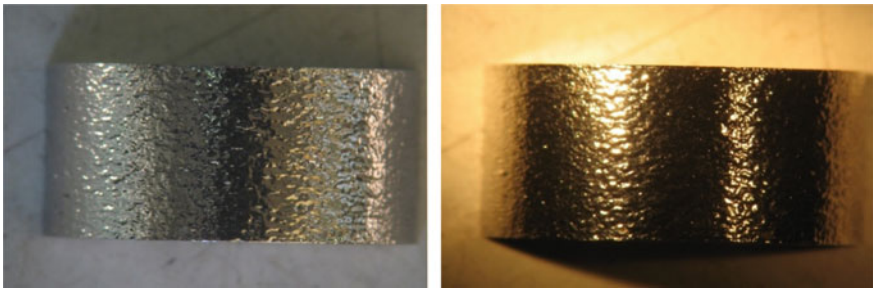

Fig. 2 Appearance of cobalt-chromium powder samples after irradiation

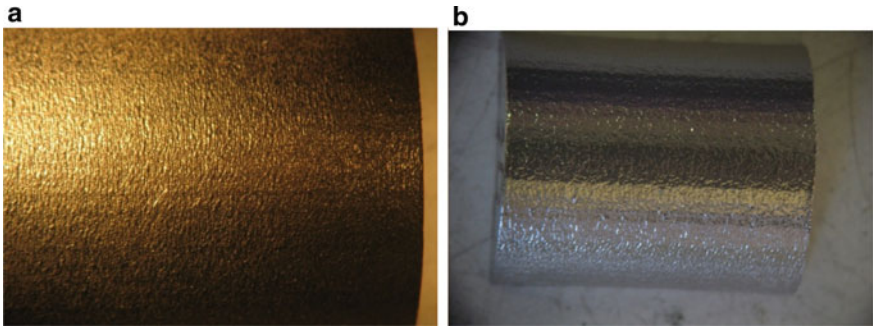

Fig. 3 Appearance of stainless steel powder samples **a** before irradiation, **b** after irradiation

It is well known that this treatment leads to a redistribution of elements during irradiation, which is carried out strictly in accordance with the values of equilibrium distribution coefficients of impurities, according to the basic provisions of the theory of directional solidification: an impurity with a distribution coefficient $K_0 < 1$ is pushed by the solidification front to the surface for cobalt-chromium, carbon, iron, cobalt, and stainless steel chromium and nickel. While the components with $K_0 > 1$ for cobalt chromium are molybdenum, silicon, chromium, and for stainless steel, molybdenum must be concentrated in the zone of the "recrystallized material-matrix alloy" interface.

This process usually occurs at low crystallization rates (several centimeters per minute [2]). When processing HPEB, we are dealing with very high crystallization rates V–10^7 K/s. It should be taken into account that for conventional directional crystallization and conventional zone melting, the thickness of the molten zone L_m is several tens of millimeters. When irradiated with HPEB at "GEZA-MMP", the L_m values of cobalt-chromium do not exceed 25 m km (Fig. 4), while the L_m values of stainless steel do not exceed 27 m km (Fig. 5) therefore, the redistribution of elements during the crystallization of the material in the molten electron beam zone is quite possible.

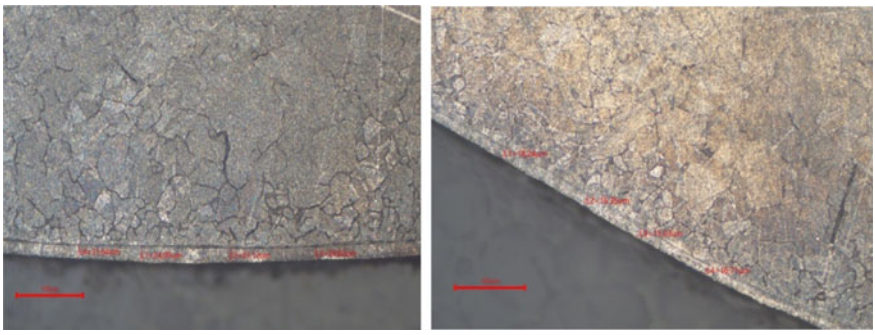

Fig. 4 Optical microscopy of cobalt-chromium samples irradiated at "GEZA-MMP"

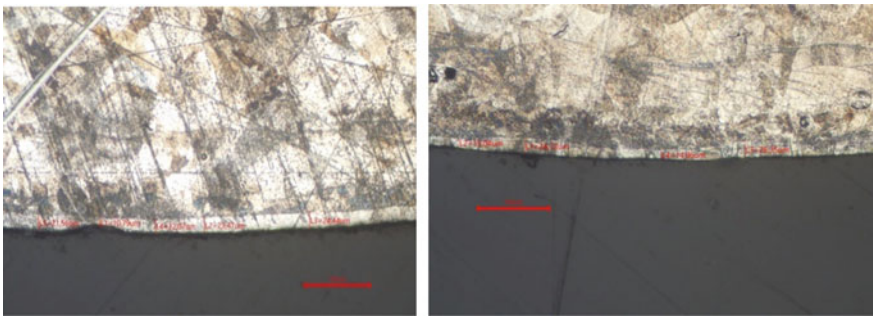

Fig. 5 Optical microscopy of stainless steel samples irradiated at "GEZA-MMP"

The obtained results of the study of the influence of irradiation modes on the chemical composition of the surface layers of samples made by the AM from cobalt-chromium powder and stainless steel allow us to draw preliminary conclusions about the most promising modes of electron-beam processing at this stage of the study.

Rather specific conclusions can be drawn on the choice of the energy density in the pulse. These conclusions are based on the following considerations. When irradiating samples made by an AM from cobalt-chromium powder and stainless steel, it is advisable to obtain a surface that does not contain macro—and microdefects, which are stress concentrators under fatigue loading. This requirement is met by the surface of a cobalt-chromium sample irradiated in the mode W = 31–35 J/cm^2 and a stainless steel sample irradiated in the mode W = 33–37 J/cm^2. The microstructure in the surface layer of cobalt-chromium and stainless steel samples is shown in Figs. 6 and 7.

In addition, it is desirable to achieve optimal redistribution of elements in the surface layer of targets. As you know, cobalt alloys owe their heat resistance to the formation of refractory carbides. These carbides do not dissolve in a solid solution. They also have low diffusive mobility. However, the advantages of such alloys over nickel appear only at temperatures from 1038 °C and higher. The latter should not be

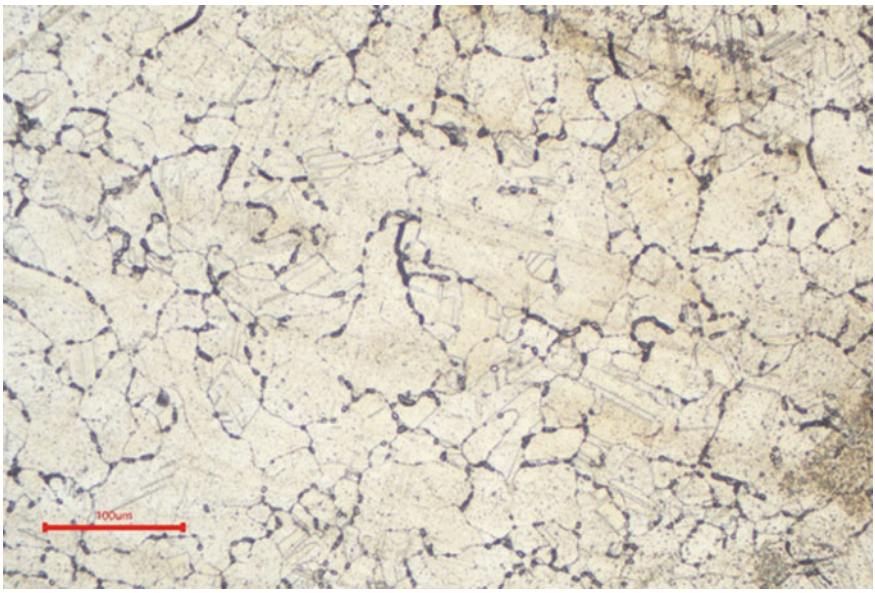

Fig. 6 Microstructure of a cobalt-chromium sample irradiated in the mode W = 31–35 J/cm^2 on "GEZA-MMP"

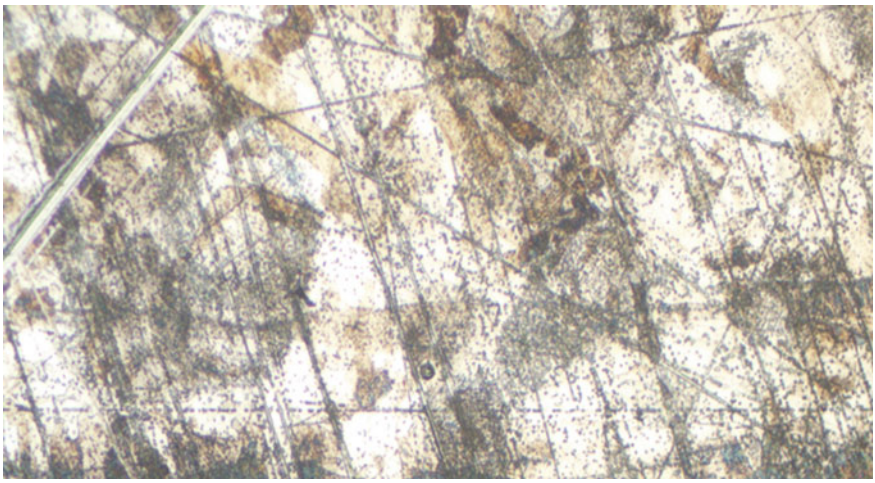

Fig. 7 Microstructure of a stainless steel sample irradiated in the mode W = 33–37 J/cm^2 on "GEZA-MMP"

confused: it is known that the higher the temperature developing in the engine, the greater its efficiency. Cobalt alloys are good for the most efficient high-temperature engines. From the data obtained, processing a sample of cobalt-chromium with high-intensity pulsed electron beams in the mode W = 31–35 J/cm^2 allows to achieve a preferential yield to the surface of carbon, which contributes to the formation of carbides on the surface, which in turn should lead to an increase in such important performance characteristics as wear resistance, hardness, and corrosion resistance. It is worth noting that before the advent of additive technologies, alloys based on cobalt-chromium were rarely used for the manufacture of parts of the hot path of gas turbine engines. It's because it doesn't flow well. Due to the low fluidity of the material when casting thin-walled parts and parts of complex shapes made of cobalt alloys [3]. Additive technologies not only save us from this problem, but also help us implement complex designs that cannot be performed using traditional manufacturing technologies, such as stamping, casting, or machining [4].

Processing of a stainless steel sample with high-intensity pulsed electron beams in the mode W = 33–37 J/cm^2 allows to achieve a preferential yield to the surface of chromium, which increases the ability of steels to thermal hardening, their resistance to corrosion and oxidation, provides increased strength at elevated temperatures, and also increases the resistance to abrasive wear. The introduction of innovative processes, such as selective laser melting (SLM) technology, into modern aircraft engine manufacturing will significantly reduce the traditional manufacturing process of blades, as well as allow obtaining complex-profile designs of stainless steel blades.

The influence of HPEB irradiation modes on the surface roughness of samples made of cobalt-chromium powder and stainless steel was studied in order to select the energy density and number of pulses that reduce the initial surface roughness.

Another important conclusion about the choice of irradiation modes for samples, in particular the conclusion about the choice of the required number of pulses, can be made on the basis of these results. Since the surface of irradiated samples is characterized by a high heterogeneity of the structure-phase state distribution, namely, the dislocation density values, these values will differ after the first pulse, which is associated with the loss of part of the energy for relaxation processes in the surface layer. Thus, from the point of view of the structural-phase state, the optimal number of pulses during electron-beam processing should be n > 2 pulses.

The study of the microstructure of samples before and after irradiation with high-current pulsed electron beams revealed a significant decrease in roughness. When irradiated with "GEZA-MMP", it is approximately 3 times for cobalt-chromium and 3,5 times for stainless steel (Table 1).

4 Conclusion

It is shown that a high-current pulsed electron beam of microsecond duration is a highly effective tool for modifying the surface of alloys obtained by additive technologies from cobalt-chromium and stainless steel powders. In the study of

Table 1 The roughness of the samples during irradiation on the "GEZA-MMP"

Cobalt-chromium				
№ sample's	Irradiation modes		Roughness R_a	
	W, J/cm^2	n, pulse	min	max
1	25–28	1–3	1,7	2,3
2	28–31	1–3	2,4	2,5
3	31–35	1–3	2	2,2
4	25–28	3–6	1,1	2,5
5	28–31	3–6	1,2	2,3
6	31–35	3–6	1,2	2,2
Initial			5,8	
Stainless steel				
№ sample's	Irradiation modes		Roughness R_a	
	W, J/cm^2	n, pulse	min	max
1	25–28	1–3	2,8	2,9
2	28–31	1–3	2,2	2,3
3	31–35	1–3	2,4	2,5
4	28–31	3–6	2,4	2,5
5	33–37	1–3	1,6	1,7
Initial			5,4	

microstructure of selected samples before and after irradiation of HPEB revealed the absence of cracks that are inherent to traditional methods of treatment and revealed a significant reduction in surface roughness of samples, and for samples of powdered cobalt-chromium, surface roughness decreased about 3 times, and for samples of stainless steel powder of about 3.5 times.

References

1. Shulov VA, Teryaev DA, Shirvanyants GG, Engelko VI, Gromov AN, Bytsenko OA (2015) Application of high-current pulsed electron beams for the restoration of properties of the blades of gas-turbine engines. Russian J Non-Ferrous Metals (56):333–338. https://doi.org/10.3103/S1067821215030190
2. Pavlov YuS (2020) Russian electron beam technologies. Institution of physical chemistry and electrochemistry. https://old.phyche.ac.ru/wp-content/uploads/010.pdf, last accessed 10 Aug 2020
3. Bytsenko OA, Filonova EV, Markov AB, Belova NA (2016) Influence of irradiation by high-temperature Nickel alloys with ion-plasma coatings of various compositions. Proc All-Russian Res Inst Aviat Mater 6(42):85–92. https://doi.org/10.18577/2307-6046-2016-0-6-10-10

4. Shein E (2020) Modern materials for additive manufacturing. Additive technologies: present and future. In: Proceedings of the IV international conference, https://viam.ru/review/5942, last accessed 10 Aug 2020
5. Starikov P, Ionov A, Seliverstov S, Borovik I, Matushkin A (2018) Mathematical modeling of heat transfer processes in a wall with a regular pseudo-pore structure. ICASSE 549:155–168. https://doi.org/10.1007/978-981-13-6061-9_10

The Use of Basalt Plastic for the Manufacture of Sound Insulation Panels of an Aircraft Engine

E. D. Moskvicheva and V. I. Reznichenko

Abstract The paper presents some information about the problems of noise produced by the engines. Recently, the international standards of the ICAO standard for aircraft noise reduction are constantly being tightened. The solution to this problem, in recent years, is the use of resonant sound-absorbing honeycomb panels installed in the air intake channel and in the external circuit of the engine. Today, due to the discrepancy in noise level, Russian aircrafts cannot fly on international lines with a full load. The reason for this is the lack of sound-absorbing characteristics of carbon fiber, as well as carbon fiber is quite fragile and not shock-resistant material, which also affects the operation of aircraft engines. In order to increase the acoustic efficiency and increase the strength characteristics of the aircraft engine hood, a variant of a three-layer honeycomb panel using basalt fabric and basalt-plastic fiber is being developed.

Keywords Noise · ICAO · Engines · Basalt plastic · Honey comb panels · Technology · Basalt fiber · Sound-absorbing characteristics · Basalt fiber reinforced polymer (BFRP)

1 Introduction

Civil aviation is one of the most modern transport systems and is a high-tech sector of the world economy. Recently, the international standards of the ICAO standard for aircraft noise reduction are constantly being tightened.

Despite many years of experience in creating aircraft engines, reducing their noise remains an urgent problem, which is very complex and must be solved by implementing a set of measures.

E. D. Moskvicheva (✉) · V. I. Reznichenko
Moscow Aviation Institute, Volokolamskoe highway, 4, Moscow 125993, Russia
e-mail: moskvich.ekaterina13@yandex.ru

E. D. Moskvicheva
School of Aeronautics and Astronautics, Shanghai Jiao Tong University, 800 Dongchuan Road, Shanghai 200240, China

Z. Jing and X. Zhan (eds.), *Proceedings of the International Conference on Aerospace System Science and Engineering 2020*, Lecture Notes in Electrical Engineering 680,
https://doi.org/10.1007/978-981-33-6060-0_8

The noise produced by the engines has a wide range of frequencies and intensity. The overall GTE noise index depends on the degree of engine double-circuit and the properties of sound-absorbing structures (SAS) used in the engine channels and engine nacelles [1].

The solution to this problem, in recent years, is the use of resonant sound-absorbing honeycomb panels installed in the air intake channel and in the external circuit of the engine.

In passenger aircraft that are currently being manufactured, cellular sound-absorbing structures are widely used, consisting of a perforated sheet, a rigid impermeable base and an air cavity between them, divided into separate cells by a cellular filler. Analysis of the structural features of aircraft engine nacelles showed that three—and five-layer panels with honeycomb and tubular filler and composite sheathing are used as SAS. Carbon and glass fiber are used as a composite material [2].

The disadvantages of carbon and glass composites:

- Inefficient noise suppression;
- A significant share of manual labor in manufacturing;
- Huge costs for auxiliary materials, in particular for molding consumes rubber for one-time use.

To date, domestic passenger aircraft do not meet the requirements of Chapter 4 of the ICAO standard. Thus, the ability of domestic aircraft to get on European airlines is significantly limited. Solving the problems faced by domestic civil aviation is necessary to preserve the Russian sector of the international passenger and cargo transportation market. Today, due to the discrepancy in noise level, Russian aircraft cannot fly on international lines with full load.

In addition to the lack of sound-absorbing characteristics, carbon fiber is quite fragile and not shock-resistant material, which also affects the operation of aircraft engines, since the structure loses its ability to resist high loads during impacts or other damages.

In order to increase the acoustic efficiency and increase the strength characteristics of the aircraft engine hood.

The noise produced by the engines has a wide range of frequencies and intensity. The overall GTE noise index depends on the degree of engine double-circuit and the propebeing developed.

2 Methods of Reduction of the Aircraft Engine Noise

The major sources of the aircraft engine noise are as follows: a fan, a compressor, a combustion chamber, a turbine and a jet stream.

The information search resulted in the identification of the fact, that at the high degree of double-point (involved) the defining contribution to the overall noise level from the aircraft engines is caused by the fan, and according to the estimates

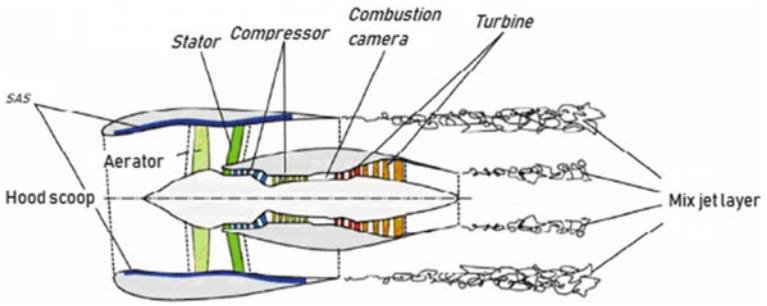

Fig. 1 Turbofan engine noise sources representation scheme

confirmed by the experimental studies, the sound intensity of the other noise sources accounts for no more than 10% of the engine noise intensity.

One of the most effective passive methods of reducing discrete noise from the fan is, the lining of air intake's inner surfaces by using SAS [3] (Fig. 1).

Sound-absorbing structures named specially designed structures that have the ability to significantly absorb the sound energy falling on them.

The sound absorbing structure can be characterized by its specific acoustic impedance:

$$Z = \frac{P}{u_n} * \frac{1}{\rho_0 * c} = R + iX \tag{1}$$

where u_n—is the normal component of the acoustic velocity, $\rho_0 * c$—state wave resistance.

SAS installed in the channels of aircraft engines must meet a number of requirements: they must have a minimum thickness and weight, low hydraulic losses, withstand high pressures and temperatures, good strength, and of course, have a high sound absorption capacity (namely, absorption in a wide frequency band).

They have gone from single-layer resonant structures with a narrow sound absorption band to multi-layer wide-band structures that can extinguish engine noise in a wide frequency range (from 500 to 10,000 Hz).

The most promising sound-absorbing structures are multi-layer structures with high rigidity and low weight.

This is especially true for three-layer structures with honeycomb filler. It is known that a three-layer structure consists of two external, relatively thin layers and a thick middle layer (filler) Fig. 2.

Load-bearing layers take longitudinal loads (tension, compression, shear) in its plane and transverse bending moments.

Filler takes transverse forces when bending and ensures joint operation and stability of the bearing layers. Filler sensing ability the load in the plane of the bearing layers depends on the design of the aggregate and its stiffness characteristics.

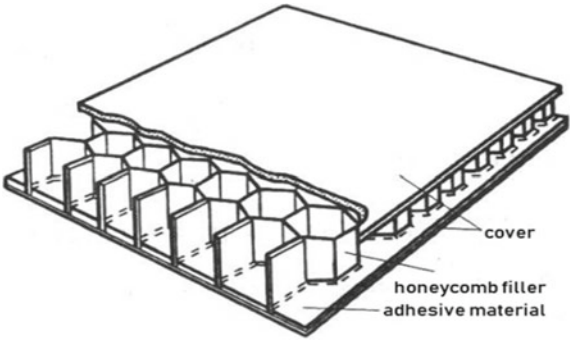

Fig. 2 Honeycomb filler structure

The choice of honeycomb shape depends on the shape of the three-layer structure and the function it performs. Mechanical properties of honeycomb filler they depend mainly on the thickness of the walls and the size of the cell faces.

As a sound-absorbing material often is taken cork, glass fiber, mineral plates, various foams.

The main parameters of the SAS that determine the frequency and maximum sound absorption are the panel thickness, the length of the lining channel, the degree of perforation and the Mach number of the bearing flow [4].

3 Russian-Made Engines Well-Known Sound-Absorbing Panels Analysis

The most famous prototype in Russia is the SAS for the PS-90 engine, which is installed on such aircraft as the TU-204 and IL-96-300 (Fig. 3).

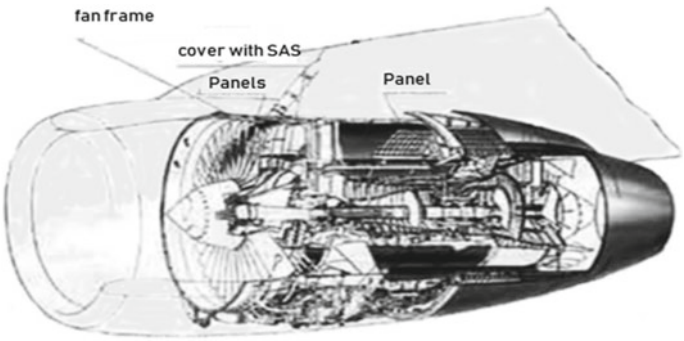

Fig. 3 PS-90 engine with perspective SAS

Analysis of the design features of the engine nacelles of the TU-204 and IL-96-300 aircraft showed that three—and five-layer panels with honeycomb and tubular filler and composite skinning are used as SAS.

For panels installed in the channel, fiberglass on a heat-resistant adhesive material EDT-69 N is used. All SAS have perforation of the skin with holes with a diameter of 2–2.5 mm with a degree of perforation of 5%.

From the analysis of the SAS structures of the TU-204, it was revealed that the T-10-80 prepreg on the EDT-69 N binder is used as the material for the skin. The thickness of the skin is 1.3 mm (3 layers of prepreg with the layout scheme (0-90-0), as fillers honeycomb SP-1-2.5 (N = 20 mm).

Dimensions of the SAS PS-90 engine: d = 1950, l = a = 854.5 mm.

These aircraft were certified in accordance with the ICAO standard, but with a minimum margin, after the installation of the new SAS.

To improve the sound-absorbing characteristics of the acoustic panel, it is proposed to change the geometry and material of the structure [5].

4 Development of SAS with a Folded Filler Using Basaltplastic

The structure of the proposed panel includes the upper and lower skin, consisting of basalt plastic, a folded filler, the material of which is also basalt fabric BT-13 or BT-11, impregnated with polyimide binder SP-97 K (Fig. 4).

Basalt-a natural material of volcanic origin-is increasingly used in various branches of technology.

Basalt fibers in all their main characteristics are significantly superior to those made of traditional aluminosilicate glass, approaching the more expensive high-modulus fibers made of magnesium silicate glass Table 1.

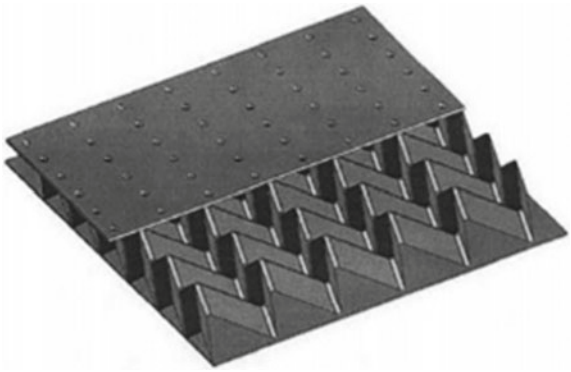

Fig. 4 Basaltplastic SAS with a folder filler

Table 1 Comparative properties of basalt and glass fibers

Properties	Basalt fiber	Glass fiber
Thermal		
Operating temperature, °C Sintering temperature, °C Coefficient of thermal conductivity	From −200 to +700 1050 0,031–0,038	From −60 to +460 600 0,034–0,040
Physical		
Density, kg/m^3 Modulus of elasticity, MPa	2600 910–1100	2540 To 720
Maintaining the tensile strength after heat treatment, %		
at 200 °C at 400 °C	95 82	92 52
Acoustic Normal sound absorption coefficient	0,9–0,99	0,8–0,92

Basalt plastics are polymer composite materials, the use of basalt filler in comparison with glass fiber will reduce the cost of the composite material, its hygroscopicity, and increase the operating temperature.

Based on basalt fabric BT-11 and polyamide binder SP-97 K, basalt plastic was produced, the mechanical properties of which are indicated in Table 2 [6].

To calculate the thickness of the bearing layers of the skin, the following loading scheme is considered Fig. 5

The sound-absorbing acoustic panel of the air intake is affected by a distributed load—the pressure of the air flow, which depends on the value of the dynamic pressure and the degree of pressure increase in the fan ($\Pi_к$), namely

$$P = q = \Pi_к * p_д, \tag{2}$$

where

Table 2 Mechanical properties of basalt plastic

Parameters	Basalt plastic (BT-11 + polyimide binder)
Density kg/m^3	1880
Strength, MPa	
In tension In bending At compression	390 480 380
Tensile modulus of elasticity, MPa	37,000
The thickness of the fabric	0.27
Poisson ratio	0.28

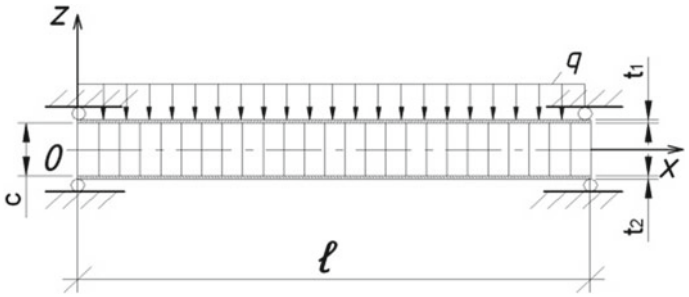

Fig. 5 Loading scheme

$$\Pi_к = 1.75, \text{а } p_д = 1.73047 \text{ Па}$$

Find the angle the optimal thickness and the angle of reinforcement of this acoustic panel [7].

Maximum bending moment:

$$\mathrm{M} = \frac{ql^2}{8} \tag{3}$$

Maximum shear load:

$$Q = \frac{ql}{2} \tag{4}$$

Height of the filler:

$$h = \frac{Q}{\tau} \tag{5}$$

Force in the covers from the action of M:

$$P = \frac{M}{h} \tag{6}$$

The thickness of the cover:

$$\delta_C = \frac{P}{10 * \sigma} \tag{7}$$

Number of layers:

$$n = \frac{\delta_C}{\delta_1} \tag{8}$$

Acting stress for the package:

$$\sigma_{\mathrm{Y}}^{\mathrm{CM}} = \frac{\mathrm{P}}{10 * \sum \delta_{\mathrm{CM}}} \tag{9}$$

Tensile strength:

$$[\sigma_y^{CM}] = Ky * \sigma_B \tag{10}$$

A condition must be met:

$$\sigma_y^{CM} < [\sigma_y^{CM}] \tag{11}$$

Perform a design calculation of the three-layer shell [8] Table 3:

$$\delta = \left[\frac{\mathrm{B} * \mathrm{a} * \mathrm{R}^{3/2}}{(1 + \lambda_{0\pi\mathrm{T}})^{3/2}} \right]^{0.4} \tag{12}$$

$$\mathrm{h} = \delta * \lambda_{\mathrm{o}\pi\mathrm{T}} \tag{13}$$

where

$$\mathrm{B} = \frac{\mathrm{p}}{4.18 * \mathrm{k} * \mathrm{E}} \tag{14}$$

$$\lambda_{0\pi\mathrm{T}} = \frac{3}{\mu} - 2,5 + 1.12 * \mathrm{d}_{0\pi\mathrm{T}} \tag{15}$$

$$\alpha = 1 - \frac{0.708\mathrm{d}^{3/4}}{[\lambda(1 + \lambda)]^{3/8}} \tag{16}$$

$$d = \frac{1.88h^{3/2}}{lR^{1/2}G} \tag{17}$$

Prove that the rigidity of an acoustic panel reinforced along the main stress paths is significantly higher than when reinforced along diagonals.

Deflection for an orthotropic plate [9]:

Table 3 Parameters of the proposed design

Parameters	$\delta_C \delta_C$, mm	*nn*	Reinforcement placement	h, mm
Basaltplastic covering based on BT11 + polyimide binder	1.2	8	6-unidirectional layer 0° 2-layers directed at 90°	6

$$w = \frac{16qa^4}{\pi^6} \frac{\sin\frac{\pi x}{a} \sin\frac{\pi y}{a}}{[D_{11} + 2(D_{12} + 2D_{33}) + D_{22}]} \tag{18}$$

The maximum deflection value is at the point at x = y = l/2(if the fibers are located along the coordinate axes)

$$w_{max} = \frac{16qa^4}{\pi^6[D_{11} + 2(D_{12} + 2D_{33}) + D_{22}]} = \frac{8qa^4}{\pi^6 D} \frac{1}{\left[1 + \mu + \frac{2G(1-\mu^2)}{E}\right]} \tag{19}$$

We will find the optimal direction of the reinforcement placement using the formula:

$$tg2\theta = \frac{2\tau_{xy}}{\sigma_x - \sigma_y} \tag{20}$$

If the fibers are directed diagonally, the maximum deflection value is found by the formula:

$$w_{max(2)} = \frac{4qa^4}{\pi^6 D} \tag{21}$$

Find the ratio of maximum deflections for basalt plastic:

$$\frac{w_{max(2)}}{w_{max}} = 0.855 \tag{22}$$

This proves that the stiffness of the plates reinforced along the paths of the main stresses is significantly higher.

The degree of perforation of the SAS facing sheet has an optimal value, which depends mainly on the flow rate. The following dependence obtained empirically can be used for subsonic flows [10].

$$S = 20\sqrt{M + 5} \tag{23}$$

The degree of perforation of the proposed acoustic panel will be equal to S = 18%, dhole = 2.5 mm (Fig. 6).

The density of the filler will be based on the formula:

$$A = 1 - \frac{\sin\frac{\alpha}{2} * \sin\frac{\beta}{2}}{\sqrt{1 - (\sin\frac{\alpha}{2} * \cos\frac{\beta}{2})}} \tag{24}$$

Determining the height of a folded filler:

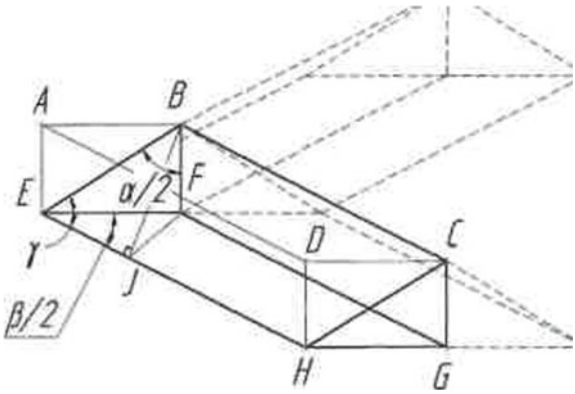

Fig. 6 The unit cell of the filler

Table 4 Filler parameters

A	d, mm	α	β	b = EH (edge length of the folded filler), mm
0.74	6	30°	135°	0.02

$$d = \frac{c * d_{\text{OTB}}}{4 * f * \sqrt{\pi (t + 4d_{\text{OTB}}) * 0.5b * tg\frac{\alpha}{2} * \sin\frac{\beta}{2}}} * \sqrt[3]{1 - \frac{\sin\frac{\alpha}{2} * \sin\frac{\beta}{2}}{\sqrt{1 - (\sin\frac{\alpha}{2} * \sin\frac{\beta}{2})^2}}} \tag{25}$$

The resonant frequency of the mass-elasticity-mass system of a three-layer panel is determined by the formula Table 4:

$$\mathrm{f} = 0.16 * \sqrt{\frac{\mathrm{E}(\mu_1 + \mu_2)}{\mathrm{d}\mu_1\mu_2}} \tag{26}$$

In the standard calculation method, when deriving the main calculation formulas for the impedance and absorption coefficient, the full sound absorption condition kM = ctg(kL) is used, where the effective mass of air in the panel openings is expressed as follows:

$$\mathrm{M} = \frac{\mathrm{h}}{\mathrm{n}}[1 + \frac{\pi d}{4\mathrm{hF}(\sqrt{\mathrm{n}})} \tag{27}$$

Formulas for calculating the impedance of multilayer structures:

$$\mathrm{Z_i} = 1 + \mathrm{i}^*\left\{\frac{2\pi}{\mathrm{c}}{}^*\mathrm{f}^*\frac{\delta}{\mathrm{S}}{}^*\left[1 + \frac{\delta\pi d_{\mathrm{h}}}{4{}^*\mathrm{F}\sqrt{\mathrm{S}}}\right] - \mathrm{ctg}\left(\frac{2\pi}{\mathrm{c}}\mathrm{fd}\right)\right\} \tag{28}$$

$$Z_{3layers} = Z_1 + \frac{1}{\sin^2(\frac{2\pi}{c} fd) * [Z_2 + \frac{1}{\sin^2(\frac{2\pi}{c} fd) Z_3}]} \tag{29}$$

Sound absorption coefficient:

$$t = 1 - \left| \frac{Z - 1}{Z + 1} \right|^2 \tag{30}$$

Analysis of existing methods for assessing noise absorption has shown that the main characteristics of the SAS, which determine its sound absorption capacity, are: the frequency characteristic of the sound absorption coefficient-t, and the impedance Z, which determines the wave resistance of the material.

Modification of the materials, the type and parameters of the SAS should lead to a quantitative and qualitative change in the spectrum of sound absorption and structural weight.

When using honeycomb instead of folded filler type Z—corrugations, expanding the band absorption, as in contrast to the honeycomb there are no resonators with a fixed height of the cavity, and the variability of the height of the resonators in the transverse and longitudinal direction should smooth out the sharp peak of attenuation at the resonant frequency.

5 Manufacturing Technology of the Proposed Design

The technological process of manufacturing cellular structures has a determining influence on the quality of cellular structures, on the weight and strength efficiency of the joint zone of the skin and filler.

Today, traditional technology is preferred in the manufacture of cellular panels.

Traditional technology refers to a technology in which all elements are delivered to the Assembly in a cured form, and the final operation is their Assembly—gluing.

Existing quality control methods determine the presence or absence of gaps between the parts to be glued (between the panels and the honeycombs, between the edging profiles and the honeycombs (along the bevels) and with the panels), but do not answer the question of the strength of the connection.

Therefore, this technological process, especially for structures of double curvature, does not guarantee high-quality (in terms of strength) bonding of panels with honeycombs and edging profiles with honeycombs and sheaths. Traditional technological process of manufacturing cellular structures with composite materials covering:

- Requires a large number of precisely matched tooling;
- It is a labor-intensive and energy-intensive process, which increases the cost design;
- Does not provide guaranteed product quality;

- Creates significant difficulties when creating a connection zone;
- Limits the scope of cellular composite structures

A combined technology was used to produce a sound-absorbing structure (SAS) made of basalt plastic.

Combined technology refers to a technology in which the polymerization of the skin, gluing them with honeycombs and among themselves, and the formation of a joint zone occurs in a single operation.

Simultaneous polymerization of the shells and their bonding with the cells provide a guaranteed quality of the product.

Combined technological process of manufacturing cellular structures with composite materials covering:

- Requires one snap-in;
- It is a productive process;
- Guarantees the quality of the product;
- Allows you to use new effective types of detachable and non-removable connections (in the design of panels, needle connections in the form of spikes are used);
- Allows you to expand the scope of cellular applications indefinitely composite structures.

An important component that affects the quality of the SAS is also the connection between them. Traditionally, the joint zone of composite parts is formed by mechanical connections (bolted, riveted, etc.), but when holes are formed in the composite by drilling, the reinforcing fibers are cut, thus the joint zone is weakened. For the developed SAS, it is proposed to use the method of extending the fibers to the composite material polymerization process with subsequent molding of the cover.

The use of needles in the form of spikes in the connection zone allows you to connect the panels without breaking the reinforcing fibers [11].

6 Conclusion

The aim of this work was to create a new-and-improved three-tier cellular panel made of basalt plastics with a folded filler in order to increase the acoustic effectiveness, durability and shock-resistant characteristics of the hood of the aircraft engine. The presented materials show that this (the given) SAS has higher durability and (as well as) the absorption coefficient. According to the completed experimental studies, the replacement of the existing fiberglass and carbon fiber SAS with basalt plastics can provide the best (most optimal) acoustic effects in the air intake channel which allows to increase the ability of domestically produced aircrafts to access European airlines (market).

References

1. Dekalin AA, Nechaeva OA (2019) Impact of aviation noise on the environment
2. Zhelezina GF, Beyder EA, Raskutin AE, Migunov VP, Stolyankov UV (2011) Materials for sound-absorbing structures for aircraft
3. Munin AG (1986) Aviation acoustics: in 2 parts/ed. by. Part 1. Noise on the ground—news of subsonic passenger planes and helicopters. Mashinostroenie, Moscow, p 243
4. Samokhin V Course of lectures (Introduction to aviation acoustics)
5. Postnov VI, Vyatkin VN, Veshkin EA (2011) Research and optimization of the choice of cound absorbing structures
6. Vasiliev VV, Protasov VD, Bolotin VV, etc.; Under the General editorship of Vasiliev V. V., Tarnopolsky Y. M. (1990) Composite materials: reference
7. Akimenko AA (1997) Engineering methods for designing aircraft structures made of composite materials
8. Lizin VT, Pyatkin VA (1976) Design of thin-walled structures
9. Dudchenko AA (2007) Strength and design of elements of aircraft structures made of composite material
10. Bogdanov SA (2007) The development of SAS for reducing gas turbine noise engines and power plants
11. Krysin VN, Krysin MV (1989) Technological processes of molding, winding and gluing structures

Contour Segmentation of Image Damage Detection Based on Fully Convolutional Neural Network

Xuesong Zhong and Xiuhua Chen

Abstract Damage detection is a critical task in monitoring and inspection for aircraft internal structures. In the actual situation, most were nondestructive evaluation, such as ultrasonic inspection, which scan the internal structure of the aircraft, to obtain the damage inside for the testing parts. However, there is still no accurate standard for damage assessment and quantification on the scanned images by ultrasonic, due to the low image resolution, or the complicated scan result. The traditional contour detection algorithms, such as Canny Edge Detection (CED), color threshold, are difficult to apply on the damage contour segmentation for such images. In view of the progress of deep learning methods, the current study proposes a damage detection method based on Fully Convolutional Network (FCN), for the contour segmentation on ultrasonic detection of damage images. The whole FCN network for contour segmentation with the Visual Geometry Group (VGG) based is trained end-to-end on a set of 2000 256 × 256 pixels damage-labeled scanned images of a certain alloy which can be made for fan blade, another 400 images are used to test the FCN method. The contour extracted by FCN are qualitatively similar to the ground truth, achieve over 92% average precision. The FCN performance is better than the traditional algorithm, and the training model can be used for transfer learning to adapt to the extraction of different damage types. The results of segmentation can be further used for quantitative analysis of damage area.

Keywords Damage detection · Fully convolutional network · Contour segmentation · Transfer learning

X. Zhong · X. Chen (✉)
School of Aeronautics and Astronautics, Shanghai Jiao Tong University, No. 800, Dongchuan Road, Shanghai 200240, China
e-mail: chenxiuhua@sjtu.edu.cn

X. Zhong
e-mail: zhongxuesong@sjtu.edu.cn

Z. Jing and X. Zhan (eds.), *Proceedings of the International Conference on Aerospace System Science and Engineering 2020*, Lecture Notes in Electrical Engineering 680,
https://doi.org/10.1007/978-981-33-6060-0_9

1 Introduction

Damage detection of critical load-carrying parts in the aircraft will greatly ensure the safety of the flight [1]. For the inspection and maintenance of key components, such as landing gear, fan blade, inside checking results can be obtained by ultrasonic scanning, which can greatly assist the mechanic to judge the state of the components [2]. As is shown in Fig. 1a, the maintainer uses ultrasonic phased array instruments to detect blade damage. Figure 1b shows the results of ultrasonic testing. The results can qualitatively reflect the damage, and the maintainer can briefly evaluate the blade. One more way, after impact experiment on aircraft parts such as laminates, skins, etc., analyzing external and internal damage also helps researchers accurately assess the performance of parts and improve the material structure, as Fig. 2 shows. Above all, the internal damage is usually not directly visible, so it is necessary to use nondestructive testing like ultrasonic scan, to obtain the damage image and analyze it. However, the ultrasonic scanned image has low resolution and contains noise, can only be analyzed qualitatively [3]. If the size of the damage needs to be further quantified, the contour of the damage image needs to be segmented and extracted to further quantification. So far, the quantification of the size of the damage has mainly

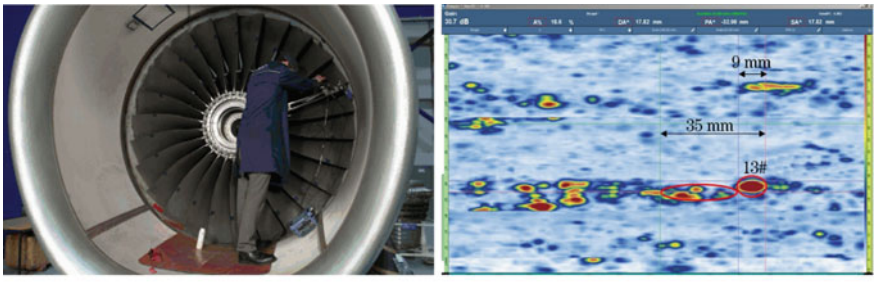

Fig. 1 **a** Ultrasonic inspection of engine blades, **b** result of blade inspection

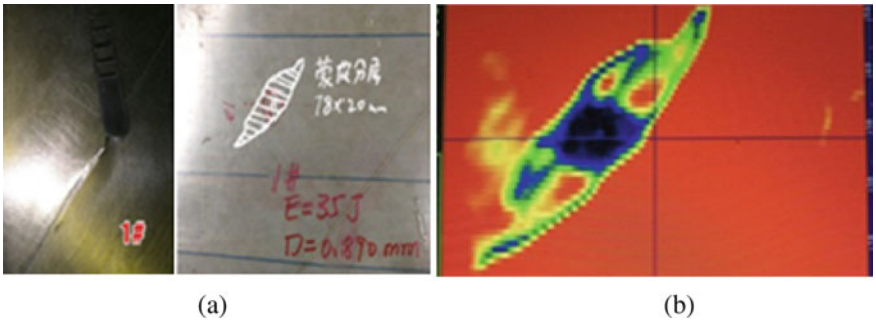

Fig. 2 **a** Impact experiment on aircraft skin, **b** ultrasonic scan inspection result

relied on the manual evaluation of experts. Therefore, it is very important to get the accurate segmentation of damage for quantitative calculation, and this type of segmentation task belongs to the target detection.

Traditional target detection mostly uses methods based on template matching or traditional machine learning [4]. Due to the lack of effective image representation, only a classifier with complex features is designed to classify the target. For example, an edge detection algorithm is used to extract crack information by setting a threshold. Another named Histogram of Oriented Gradients [5] combination with Support Vector Machine [6] are used to automatically identify cracks. However, the performance of these algorithms depends heavily on the quality of the data. For ultrasonic scan images with a complex background and a lot of noise, the detection task is difficult, the model generalization performance is poor, and the effect is not good [7].

In recent years, with the help of Graphics Processing Unit (GPU) high-performance computing, classification models based on deep learning have been widely used in the field of image detection. Among them, Convolutional Neural Networks (CNN) has significant effect in the field of image processing, mainly because convolution can extract the key features of the image. In 2012, the Hinton team won the championship in the Image-net classification competition, relying on the CNN. The accuracy rate was 10% higher than the second. At the same time, the accuracy rate of the classification finally exceeded the manual classification [8]. Girshick et al. proposed a Region with CNN features (RCNN) for target detection in 2014 [9], and the detection accuracy has been greatly improved compared with traditional detection methods. Inspired by the success of CNN for image classification tasks, Long et al. proposed Fully Convolutional Networks (FCN) for image segmentation [10]. FCN has been applied to solve problems in multidisciplinary fields, such as road detection to assist autonomous vehicles [11] and drawing image contours in aerial imagery [12]. At the same time, the combination of FCN method and residual network can currently achieve complex scenes of segmentation tasks.

In order to extract the damage contour more accurately, this paper uses FCN to segment the damage image. The whole FCN network is trained, an end-to-end for image segmentation on a set of annotated ultrasonic scan images. Finally, the performance of the FCN method is verified using 400 images. At the same time, in order to test the generalization of the model, based on the already trained model, we conducted a simple transfer learning test and used the trained model on the damage extraction of the ultrasonic scan image on web plate and skin. The results show that FCN can accurately segment the damage contour, thereby helping researchers to accurately judge the damage of parts or evaluate the performance of test parts.

2 Neural Network Structure Theory

Since CNN can efficiently extract image features, we use it to extract damage features as the input to the FCN. VGG is a CNN model introduced by the Visual Geometry Group from the University of Oxford. They proposed various models and configurations of deep CNNs. A widely used model is known as VGG16 due to the fact that it is composed by 16 weight layers, with an achievement of 92.7% TOP-5 test accuracy, ranked first in the positioning task and second in the classification task in ILSVRC-2014 [13]. The feature extraction of the first half in the FCN is VGG16, shown as Fig. 3.

The VGG16 process for feature extraction is as follows:

1. Input is a picture of 224 × 224 × 3, and using convolution + ReLU operation by 64 3 × 3 convolution kernels, the size after convolution becomes 224 × 224 × 64.
2. Max pooling, the size of the pooling unit is 2 × 2 (the effect is to reduce the image size by half), and the size after pooling becomes 112 × 112 × 64.
3. After 128 convolution kernels of 3 × 3 for two convolutions + ReLU, the size becomes 112 × 112 × 128, and 2 × 2 max pooling, the size becomes 56 × 56 × 128.
4. 256 3 × 3 convolution kernels are used three times for convolution + ReLU, the image size becomes 56 × 56 × 256, and 2 × 2 max pooling, the size becomes 28 × 28 × 256.
5. After 512 3 × 3 convolution kernels for three convolutions + ReLU, the size becomes 28 × 28 × 512, and 2 × 2 max pooling, the size becomes 14 × 14 × 512.
6. After 512 3 × 3 convolution kernels for three convolutions + ReLU, the size becomes 14 × 14 × 512, and make 2 × 2 max pooling, the size becomes 7 × 7 × 512.

Finally, Convolution operation with 4096 × 1 × 1 kernels, instead of full connection in VGG16, and because all layers are related to convolution, so it is named as fully convolution neural network, shortly FCN.

The last half of FCN aims to get the segmentation of the input image. After multiple convolutions and poolings, the image is getting smaller and smaller, and

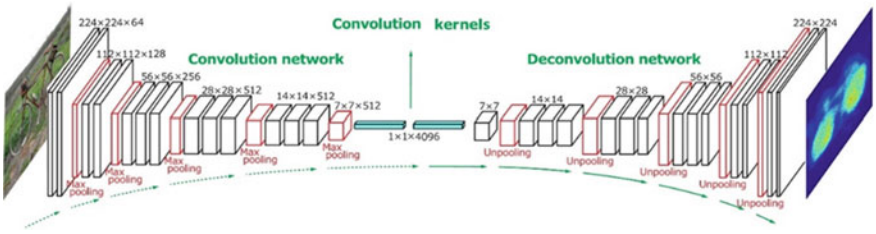

Fig. 3 Fully convolutional neural network architecture

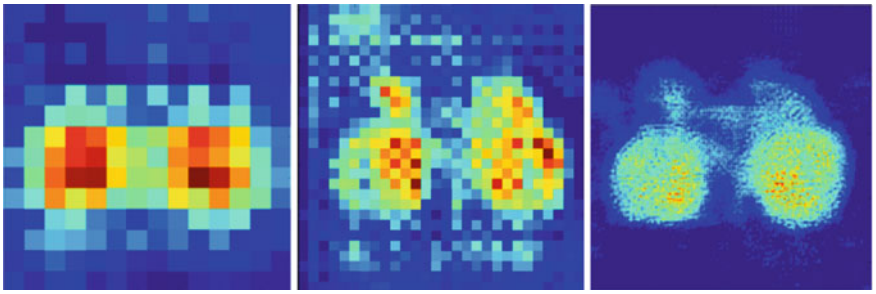

Fig. 4 Upsampling and deconvolution of a heatmap

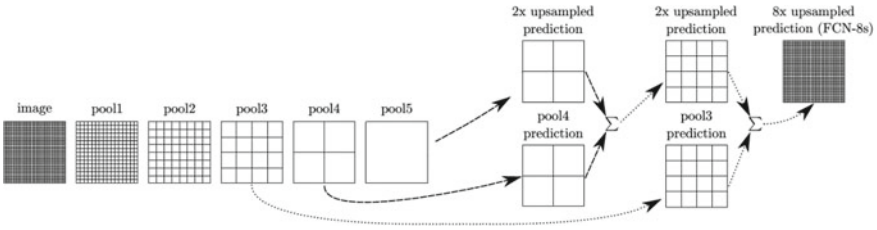

Fig. 5 Skip architecture

the resolution is getting lower and lower. When the image reaches H/32 × W/32 (here is 7 × 7), the generated picture is called a heatmap. The heatmap keeps the main features of the image and we want to enlarge the heatmap to restore the original size, so can achieve pixel-level classification and get the contour segmentation [14] (Fig. 4).

In FCN, deconvolution and upsampling are used on the heatmap image to restore original image size and obtain the contour segmentation of the original image.

In actual operation, it is necessary to balance the number of convolution operations and the depth of feature extraction, one tip is using the Skip Architecture in FCN, as Fig. 5 shows. This structure is mainly used to optimize the final result. The idea is to restore the pooling results from different convolutional layers respectively, and then merge these results to optimize the output, avoiding the rough output caused by direct upsampling the heatmap that generated by the last layer of convolution operation.

3 Experiment Based on Fully Convolutional Network

In the impact experiment, for the damage inside, we use the ultrasonic nondestructive evaluation to detect the damage. The damage size can be judged qualitatively from the scan results. But in many situations, the damage contour needs to be extracted

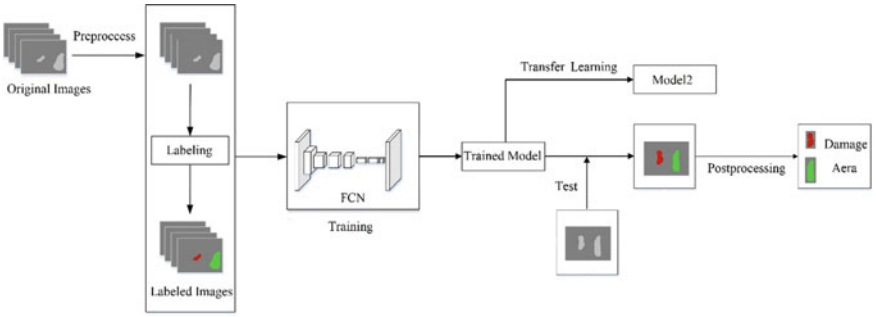

Fig. 6 Damage segmentation flow chart

for quantitative analysis. The FCN-based image segmentation algorithm can learn the general characteristic of damage from a large number of damage images, and then segment the outline of the damage, so as to accurately assess the area of the damage. The algorithm uses image preprocessing to reduce the noise relatively in the original image data and then performs labeling processing, then puts the labeled data into FCN for iterative training and test verification; at the same time, it uses transfer learning to apply the trained model to another category. The recognition results are finally optimized by postprocessing. The whole process is shown in Fig. 6.

3.1 Damage Image Dataset

With annotating 2000 images scanned by ultrasonic, we obtain a dataset for training. These images are obtained from the impact experiment of a certain type of alloy. The alloy can be used for a fan blade. The resolution of the image is low, the contour boundary is blurred. The red part indicates the severe damage area, and the yellow-green part indicates the light damage.

Image damages are divided into 3 categories, shown in Fig. 7, the first category is only light damage area, the second category is only severe damage area, and the third category is the mixed damage area.

3.2 Experiment Setup and Training Process

Using the deep learning framework TensorFlow, we construct a FCN structure suitable for damage contour extraction. First, randomly initialize the network, input the samples and labeled map into the network, and after the first to fifth convolution and pooling operations, the image becomes 1/2, 1/4, 1/8, 1/16 and 1/32 of the original image size. Through the convolution operation, it extracts the main features of

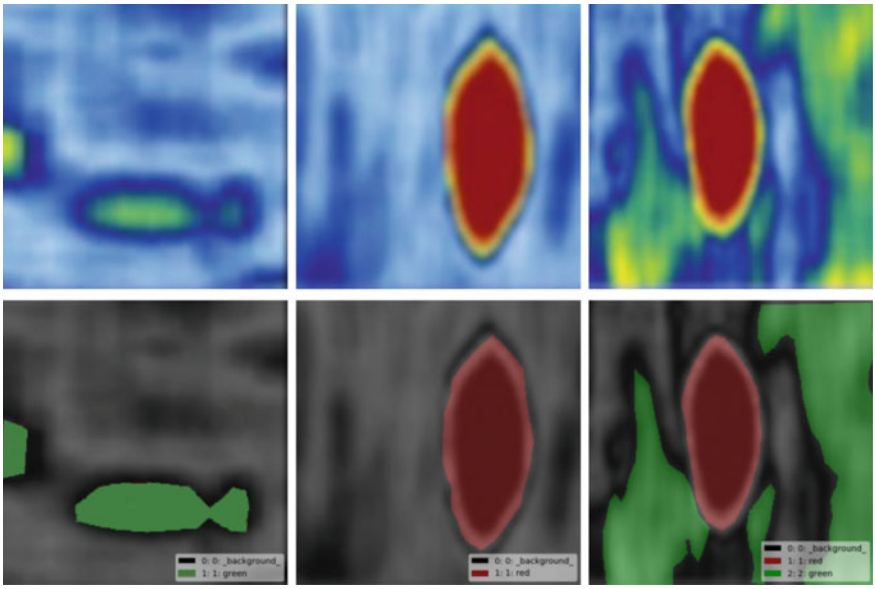

(a) light (b) severe (c) mixed

Fig. 7 Labeled image of three damage categories

the image layer by layer. Then we use the tip Skip Architecture, merge the image after the third convolution operation and pooling operation layer, the image after the fourth convolution operation and pooling operation layer, and the image after the fifth convolution operation layer and conduct the deconvolution operation, enlarged to the same size as the original image, to get the result of image segmentation.

FCN's loss calculation is equivalent to a classification loss for every pixel of the whole image, so once the loss is finally calculated on all pixels, the total loss is obtained. We calculate the loss from the labeled image and minimize the overall loss of the network through the back-propagation algorithm. We use the following formula to calculate the total loss

$$L = \sum_{i=0}^{w-1} \sum_{j=0}^{h-1} p_{ij}^{*} \times Inp_{ij} \tag{1}$$

w and h represent the width and height of the image, p_{ij}^{*} is the probability distribution vector on the real category at point (i, j), p_{ij} is the probability distribution vector on the predicted category at point (i, j).

After 20,000 iterations, the pixel matching error tends to converge (Fig. 8). We get a set of optimal parameter matrix values that match the labeled image within the least tolerant error and save the final parameter values to get the trained model. By

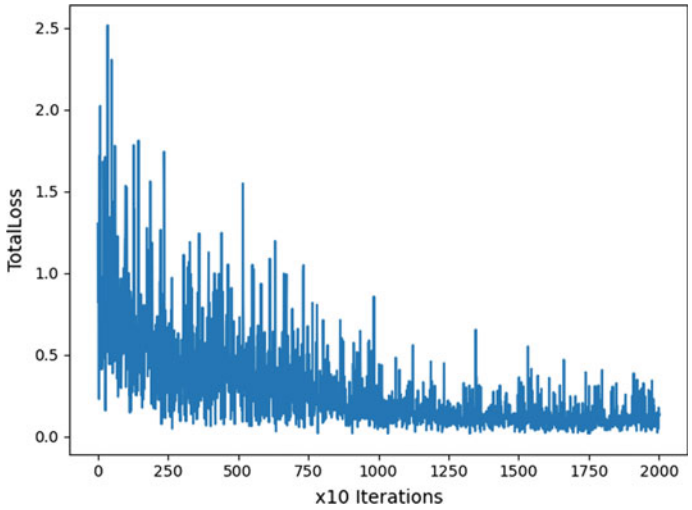

Fig. 8 Total loss during training process

calling the trained model, we can segment and extract the damage contour of the image that needs to be segmented.

3.3 Results and Discussion

After the model training is completed, the generalization performance of the model needs to be evaluated on the test set. Segmentation of damaged images is essentially a problem of binary classification of pixels. For binary classification problems, the samples can be divided into TP (true positive, Fig. 9a), FP (false positive, Fig. 9b), TN (true negative, Fig. 9c), and FN (false negative, Fig. 9d) examples, totally four cases according to the distribution of the real category and the learning prediction category. TP means that damaged pixels are correctly predicted as damaged pixels, FP means that non-damaged pixels are incorrectly predicted as damaged pixels, TN means that non-damaged pixels are correctly predicted as non-damaged pixels, and FN means that damaged pixels are incorrectly predicted as non-damaged pixels damage pixels.

We introduce classification accuracy as the evaluation criterion, that is, the numbers of the correct predict samples to all samples, it is defined as:

$$Acc = \frac{TP + TN}{TP + TN + FP + FN} \tag{2}$$

In an image, for the connected damage, we record it as a test, for the non-connected damage area, each damage is counted as a test result separately, as shown in Fig. 10c. We record the damage as a positive value and the background as a negative value. On

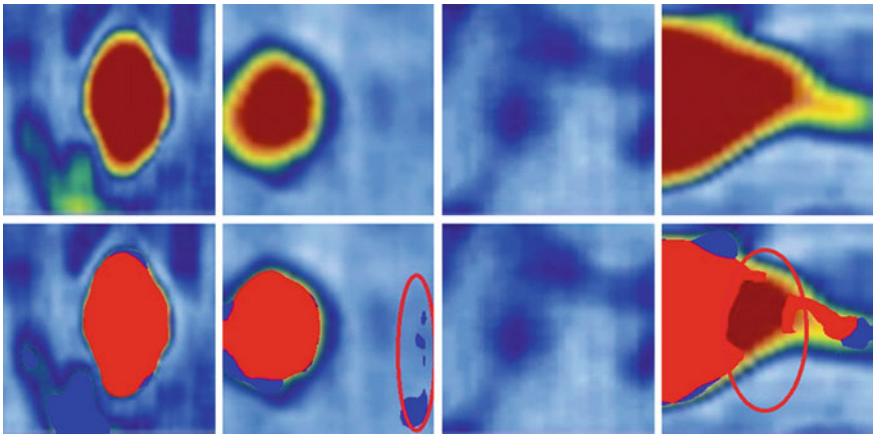

Fig. 9 Samples of four cases

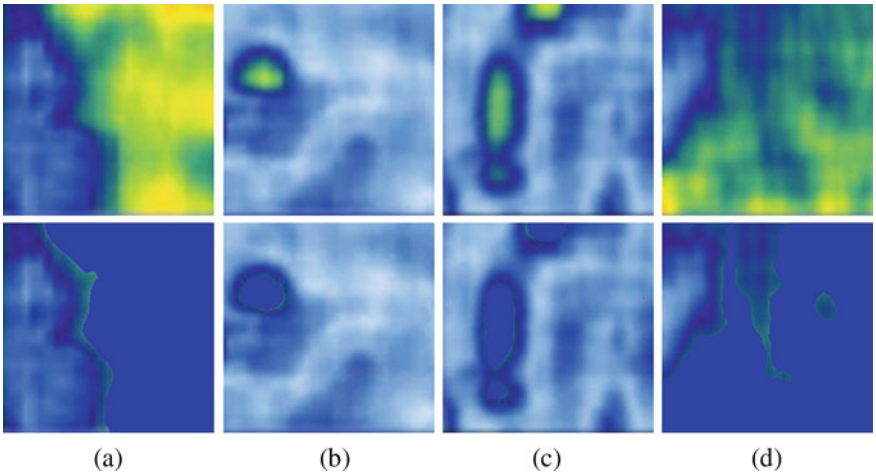

Fig. 10 Segmentation of light damage

the 400 test images, three types of damage are counted. 80 light damage images with total 103 damages, 80 severe damage images with total 85 damages, and 240 mixed damage images with total 265 damages, the test results are in Table 1, the FCN can reach a total weight accuracy of 92.1%.

It can be seen from the experimental results that, for light damage, severe damage, and mixed damage, FCN can accurately segment the damage contour.

The training model can be used for transfer learning to adapt to the extraction of different damage contours. The images are the skin impact test. The scanned damage

Table 1 Test result on 400 images test set

Category	Item	TP	TN	FP	FN	Acc (%)
Light	Truth	103	80	0	0	92.9
	Prediction	97	73	5	7	
Severe	Truth	85	80			94.5
	Prediction	81	75	4	5	
Mixed	Truth	265	240			91.1
	Prediction	241	219	24	21	

image is similar to the previous. The damage it reflects can also be divided into severe and light injuries. The image representation here is slightly different. Through the transfer learning method, the previously trained model is applied to the segmentation of this type of scanned image, and the effect is also very good.

For the impact experiment of the aircraft skin, we obtained the damage image after the impact through ultrasonic inspection. For images with complex color changing, although the traditional contour extraction method can extract the damaged contour, it needs to adjust the color threshold multiple times, and also have several mistakes since the noise maybe close to the result in a range of threshold, shown in Fig. 13c. And for color filter method, shown in Fig. 13d, if you want to extract all the damaged contours, it needs multiple times design for different color filters. However, the FCN method learns the characteristics of different damages from the annotated images, so can be directly used to extract the contour information of the damages after training. Here we use a transform learning to deal with this problem, and the segmentation result is good for further analysis.

We can calculate the damage contour based on the FCN method extraction because it simplifies the noise and keeps the main information of the ultrasonic inspection image, also proposes a definite color boundary. The image size is uniformed to 256 $\times$ 256 pixels. The calculation is very useful for quantitative analysis of damage (Table 2).

Table 2 Damage pixel area analysis

Item	Source	Light	Severe	Light percentage (%)	Severe percentage (%)
1	Figure 10d	46,572		71.1	
2	Figure 11d		22,061		33.7
3	Figure 12d	12,650	6868	19.3	10.5
4	Figure 13e1	23,033	2267	35.1	3.5
5	Figure 13e2	5524	3819	8.4	5.8

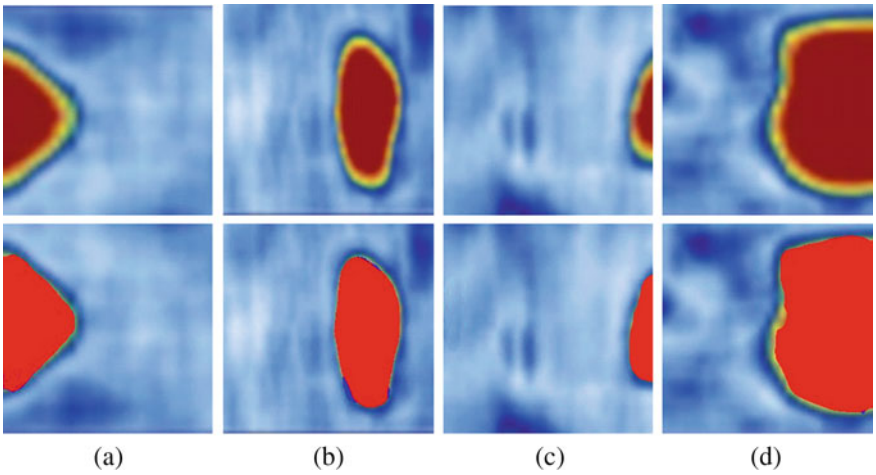

Fig. 11 Segmentation of severe damage

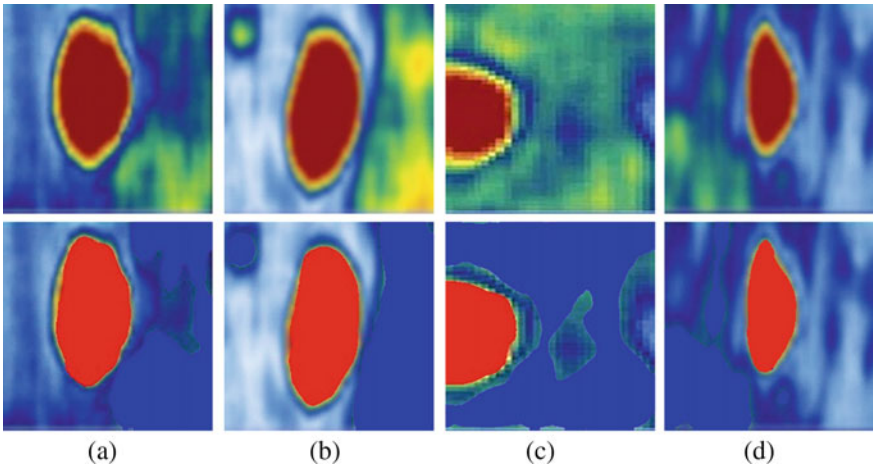

Fig. 12 Segmentation of mixed damage

4 Conclusion

Ultrasonic detection of damaged image segmentation is a key step in damage quantification, which is great significance to further judge the damage of fan blades or other parts. Due to the noise in the image, the traditional segmentation method cannot effectively segment all types of damage and can only segment the specific with manually selected threshold. The most important thing is that it cannot achieve automatic image segmentation. This paper uses FCN to automatically segment image contours, which solves the problem of inspectors manually selecting damage contours and improves

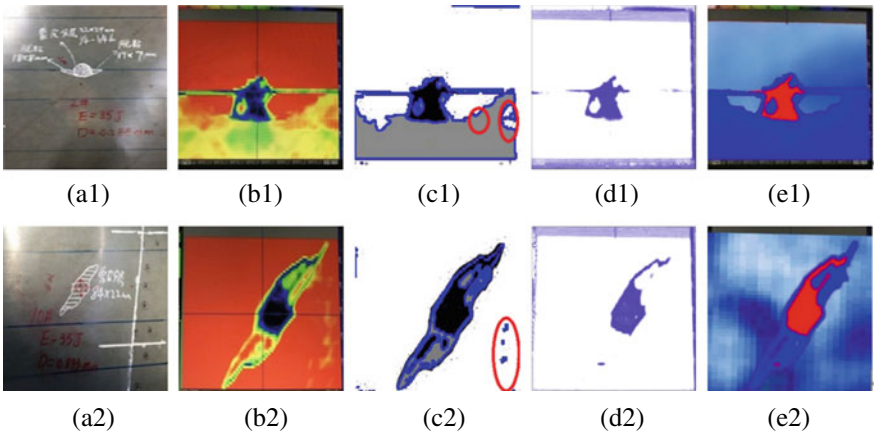

Fig. 13 **a1**, **a2** Impact experiment on airrcraft skin; **b1**, **b2** damage scan results of ultrasonic; **c1**, **c2** combination of threshold and Canny Edge Detection algrithms; **d1**, **d2** color filter method; **e1**, **e2** transfer learning based on FCN

detection efficiency. The damage boundaries extracted by FCN can be directly used for further area calculations. The accuracy can reach an average 92.1%. The damage contour extraction method based on fully convolutional neural network is more adaptable. The test results show that the method can provide strong engineering support for actual projects and has significant application value. However, the edge detection and contour extraction methods based on FCN need a huge dataset support, which is the deficiency of this method. The neural network should be optimized so that it can get good performance on a small training dataset and reach a high recognition accuracy, which is a problem that needs to be solved.

References

1. Xuyun FU et al (2019) Aircraft engine fault detection based on grouped convolutional denoising autoencoders. Chin J Aeronaut 32(02):296–307
2. Yousef G et al (2008) Modelling of guided ultrasonic wave in aircraft wiring, p 1
3. Katayama K, Shibata K, Horita Y (2017) Noise reduction and enhancement of contour for median nerve detection in ultrasonic image. In: IEEE international conference on signal and image processing applications (ICSIPA), pp 341–344
4. Sonkamble BA, Doye DD (2008) An overview of speech recognition system based on the support vector machines. In: International conference on computer and communication engineering, pp 768–771
5. Dalal N, Triggs B (2005) Histograms of oriented gradients for human detection. In: IEEE computer society conference on computer vision and pattern recognition (CVPR'05), vol 1, pp 886–893
6. Mavroforakis ME, Theodoridis S (2005) Support vector machine (SVM) classification through geometry. In: 13th European signal processing conference, pp 1–4

7. Sewak M, Sahay SK, Rathore H (2018) Comparison of deep learning and the classical machine learning algorithm for the malware detection. In: 19th IEEE/ACIS international conference on software engineering, artificial intelligence, networking and parallel/distributed computing (SNPD), pp 293–296
8. Krizhevsky A, Sutskever I, Hinton GE (2012) ImageNet classification with deep convolutional neural networks. In: Annual conference on neural information processing systems, Lake Tahoe, pp 1097–1105
9. Girshick R et al (2014) Rich feature hierarchies for accurate object detection and semantic segmentation. In: IEEE conference on computer vision and pattern recognition, pp 580–587
10. Long J, Shelhamer E, Darrell T (2015) Fully convolutional networks for semantic segmentation. In: IEEE conference on computer vision and pattern recognition (CVPR), pp 3431–3440
11. Murata D, Motoya T, Ito H (2019) Automatic CNN compression system for autonomous driving. In: 18th IEEE international conference on machine learning and applications (ICMLA), pp 838–843
12. Gevaert CM et al (2018) A deep learning approach to DTM extraction from imagery using rule-based training labels. ISPRS J Photogramm Remote Sens 142:106–123
13. Karen S (2015) Very deep convolutional networks for large-scale image recognition. In: ICLR
14. Noh H, Hong S, Han B (2015) Learning deconvolution network for semantic segmentation. In: IEEE international conference on computer vision (ICCV), pp 1520–1528

A Study on Aerodynamic Interference for Truss Braced Wing Configuration

Lizhen Liu and Xiongqing Yu

Abstract Truss Braced Wing (TBW) is one of the most promising configurations for future single-aisle commercial aircraft. The additional strut and jury in TBW endow the structure with better stiffness and strength, which enables a wing with larger aspect-ratio, thinner thickness and smaller swept angle, and even equipped with laminar flow airfoil. Theoretically, TBW configuration has the advantage of higher lift-to-drag ratio. However, one of potential problems for TBW is that severe disturbance may exist at the junction of truss and wing, which will reduce the aerodynamic benefit of TBW. To deal with this issue, this paper investigates influence of truss geometry on aerodynamic characteristics by numerical simulations of CFD. The Reynolds-averaged Navier–Stokes (RANS) method with the S-A turbulence model is used to compute the aerodynamic force and observe flow phenomenon of TBW in flight speed of Mach 0.73. The simulation results show that the geometric parameters that have large impacts on the cross section shape around the junction tend to have greater influences on aerodynamic characteristics (The Cross Section in this paper represents the cross section of air flow tunnel between the wing and truss). To analyze the impact of cross section geometry at the junction on the interference drag, we introduce a specific term, namely 'flow section compression ratio' that is the decreased rate of the cross section area from the entrance to the throat. The analysis indicates that the transonic disturbance will be considerable weaken when the 'flow section compression ratio' around the junction is under 16%, and the drag due to transonic disturbance accounts for only about 25% of the total interference drag. In order to further decrease the interference drag at the junction, we also investigate influences of the cross section geometry and airfoil thickness at the junction on the profile drag. The results from this paper can be helpful for TBW configuration design.

Keywords Truss braced wing · Aerodynamics · Interference drag · Computational fluid dynamics

L. Liu (✉) · X. Yu
College of Aerospace Engineering, Nanjing University of Aeronautics and Astronautics, Nanjing, China
e-mail: 592599344@qq.com

Z. Jing and X. Zhan (eds.), *Proceedings of the International Conference on Aerospace System Science and Engineering 2020*, Lecture Notes in Electrical Engineering 680,
https://doi.org/10.1007/978-981-33-6060-0_10

1 Introduction

As modern society pays more attention to environmental issues, carbon emission, noise and economic needs have become the main indicators of the next generation commercial aircraft [1–4], which is bringing challenges to civil aviation. In order to meet the challenge, aviation research institutions and suppliers in the world have proposed a lot innovative aerodynamic configuration. Among them, Truss Braced Wing (TBW), proposed by Boeing and NASA, is one of the most promising configurations for future single-aisle commercial aircraft [5–7]. Researches has proved that the additional strut and jury in TBW endow the structure with better stiffness and strength, which enables a wing with larger aspect-ratio, thinner thickness and smaller swept angle, and even equipped with laminar flow airfoil [7–9]. At present, the TBW configuration air-craft project under the codename SUGAR carried out by Boeing and NASA has achieved three stages of success [9]. The German Aerospace Center (DLR), COMAC and other R & D institutions showed great concern for the TBW configuration aircraft too [10–12]. Domestic and foreign universities have also conducted considerable re-search on TBW configuration aircraft [12–15].

However, researchers have found that severe disturbance may exist at the junction of truss and wing in high subsonic flow, which will reduce the aerodynamic benefit of TBW [9, 16]. To deal with this issue, researchers have made a lot of investigations. Using CFD method, Ko et al. gave the mechanism of supersonic flow between the strut and the wing, proposed a solution to weaken the disturbance using negative camber airfoil [16]; Ivaldi [17] and Ney [18] optimized the aerodynamic shape of TBW using RANS based CFD method respectively. They both used the profile shape of wing and strut as design variables, and both eliminated the supersonic flow between strut and wing. By their optimization, Ivaldi achieved 28% drag decrease of TBW, while Ney achieved 10% drag decrease. However, Ney doesn't consider it a satisfactory result in the solution [17]. What's more, a lot early researchers had made investigations about flow disturbance between surfaces. Knight et al. discussed aerodynamic interference caused by wings mounted vertically on a flat plate [19]. Tetrault discussed the influence of dihedral of a wing mounted on a vertical plate [20]. Duggirala discussed the influence of dihedral of a wing mounted on another vertical wing [21]. Tetrault and Duggirala drew a same conclusion that, the bigger the dihedral is, the severer supersonic flow will occur, the more interference drag will appear.

Throughout the above studies about aerodynamic disturbance of TBW, Ko's solution compromised a lot on lift performance using negative camber airfoil. Ivaldi eliminated the supersonic flow disturbance successfully by optimization, but his final solution is somewhat similar to that of Ko's research. Moreover, although studies have found supersonic flow between strut and wing do correlated with influence drag strongly, the conclusion of Ivaldi's research still hinted that there might exist other factor to cause severe interference drag of TBW.

To deal with these issues, this paper carried out RANS based CFD simulation to investigate influence of truss geometry on aerodynamic characteristics, which tries to

provide more idea for supersonic flow disturbance eliminating. Further re-search is also carried out by this paper to investigate influences of the cross section geometry on profile drag (The Cross Section in this paper represents the cross section of air flow tunnel between the wing and truss), which tries to figure out some other causes for severe interference drag.

2 Model and Methods

The shape and size of the wing model used in this paper is referred to that of Yu Xing's research [13]. The planform of the wing is shown in Fig. 1, whose parameters' value is shown in Table 1. Common form of TBW in current research can be classified by whether they have jury or not. There are two different kinds of jury for TBW. One locates at the junction of wing and strut, playing a transition role in the connection between the wing and strut (shown as red in Fig. 2a). It will be simply referred to as the first jury. The other jury connects the strut to the wing from the middle of the strut. It will be simply referred to as the second jury.

Research shows that setting the first jury is beneficial to delay the emergence of local supersonic flow and improve the wing drag characteristics [16]. And setting of the second jury will improve the structural rigidity of the wing and increase the flutter speed [13]. So in recently TBW study, re-searchers generally adopt the configuration

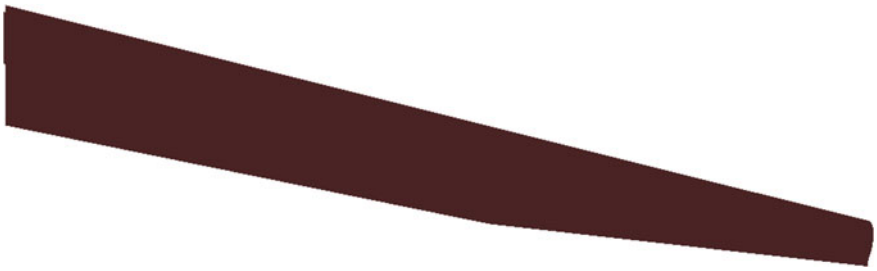

Fig. 1 Planform of the wing

Table 1 Geometric parameters of the wing used in this paper

Parameters	Values
Sref (m^2)	137.2
Cref (m)	3.3
AR	19.56
$\wedge_{1/4}^{inner}$ (°)	13.3
$\wedge_{1/4}^{outer}$ (°)	12.5
b/2(m)	24.745

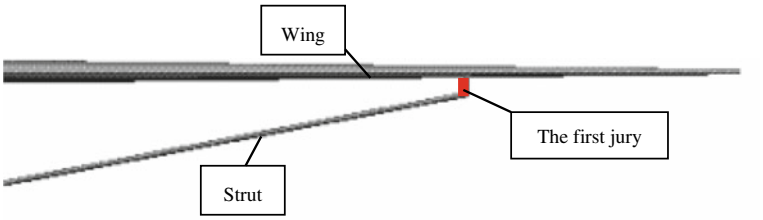

(a) TBW with the first jury only

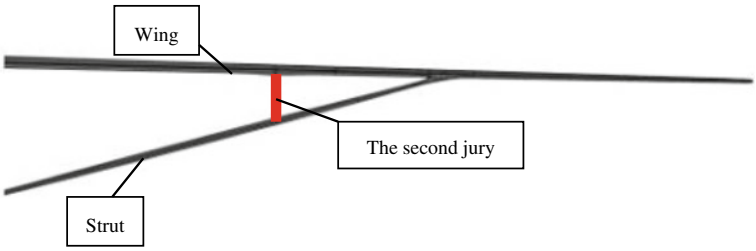

(b) TBW with the second jury only

Fig. 2 General configuration of TBW classification

with both the first jury and the second jury [13]. The TBW in this study also adopt this configuration. Its geo-metric parameter is shown in Fig. 3 and Table 2.

This paper focuses on the influence of geometric parameters of the truss on aerodynamic characteristics. Influence of wing shape or strut profile is not the core topic of this paper. Refer to previous researches, this paper selected five geometric parameters in Table 2 that may have a greater impact on the local flow field as design variables. In the study, the influence of each design variable on the flow field and

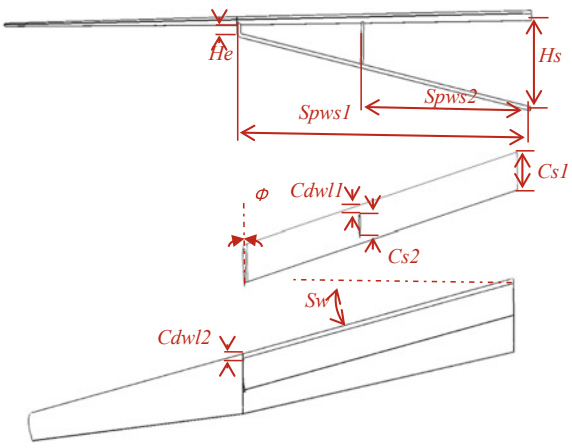

Fig. 3 The geometric parameters of TBW in this paper

Table 2 The geometric parameters of TBW

Parameters	Symbol	Values
Chordwise location of the second jury (mm)	*Cdwl1*	600
Chordwise location of strut (mm)	*Cdwl2*	100
Height of the first jury (mm)	*He*	750
Vertical distance between wing root and strut root (mm)	*Hs*	40,000
Chord length of strut (mm)	*Cs1*	1460
Chord length of the second jury (mm)	*Cs2*	850
Sweep back of strut (deg)	*Sw*	13.7
Spanwise location of the first jury (mm)	*Spws1*	13,632
Spanwise location of the second jury (mm)	*Spws2*	7875
Initial angle of the first jury (deg)	Φ	0

Table 3 The design variables concerned in this paper and their values

Parameters	Symbol	Values
Chordwise location of strut (mm)	*Cdwl2*	***100***, 150, 200, 400, 1000
Height of the first jury (mm)	*He*	***750***, 850, 950, 1150, 1350
Sweep back of strut (deg)	*Sw*	12, 13, ***13.7***, 14.5, 15
Spanwise location of the second jury (mm)	*Spws2*	6000, 7000, ***7875***, 8500, 9000
Initial angle of the first jury (deg)	Φ	−1.5°, ***0***°, 1.5°

aerodynamic performance are discussed separately. The value of design variables adopted in this study is shown in Table 3.

Using commercial software FLUENT, this paper analyzed the flow around the TBW based on the SA method. Cruise height is set 13411 m, Mach number is set 0.73. The simulation used unstructured grid with quadrilateral prismatic boundary layer. The grid is shown in Fig. 4. In order to intuitively reflect the impact of the

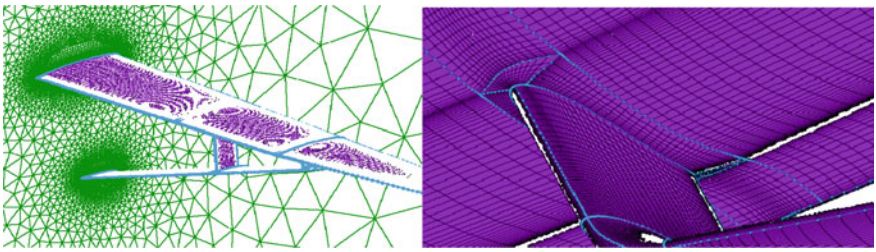

Fig. 4 Grid used in simulation

Table 4 The performance of pure wing

AOA	Turbulence model	Cell num	CL	CD	L/D
1.25	SA	3,200,000	0.817	0.03186	25.64
1.25	SA	4,000,000	0.808	0.03190	25.34

Table 5 Result of independence verification for the standard TBW model

AOA	Turbulence model	Unsteady	Cell num	CL	CD	L/D
0	SA	On	6,000,000	0.535	0.02162	24.76
0	SA	Off	5,000,000	0.538	0.02141	25.12
0	SA	Off	6,000,000	0.535	0.02147	24.91

truss on the performance of the wing, the aerodynamic performance of the pure wing was first analyzed. The performance of pure wing is shown in Table 4 together with independence verification result. In addition, in order to intuitively reflect the influence of the change of design variable on the aerodynamic performance, a set of design variables' value is selected to form a standard TBW model. The selected value for each design variable is marked italic and bold in Table 3. Result of independence verification for the standard TBW model is shown in Table 5.

Table 4 shows that the simulation result of wing barely affected by grid, and the result is reliable enough to be used as a reference in later research. Table 5 shows mesh of 5,000,000–6,000,000 elements is precision enough to describe the flow around the standard TBW model. And Table 5 also shows that, even some partial separation is caused by supersonic flow occasionally (see Fig. 5), a steady method is still suitable for the simulation.

3 Simulation and Analysis

3.1 Influence of Truss on Wing Aerodynamic Characteristic

Aerodynamic performance of the standard TBW model and the wing-only model at the same AOA is calculated. The comparison between their results is shown in Table 6. It can be seen that after the truss is used, the drag coefficient has increased by 17 counts, accounting for 5% of that of the wing-only model. And meanwhile the lift coefficient is reduced by 0.1, accounting for 12% of the total lift coefficient. Obviously, in addition to the drag characteristics concerned in previous studies, the truss also causes a negative impact on lift characteristics. The situation of pressure distribution may tell us why.

For ease of discussion, the region near the first jury and between the wing and the strut (shown in Fig. 6) is named 'armpit'. Pressure distribution on the wing at the

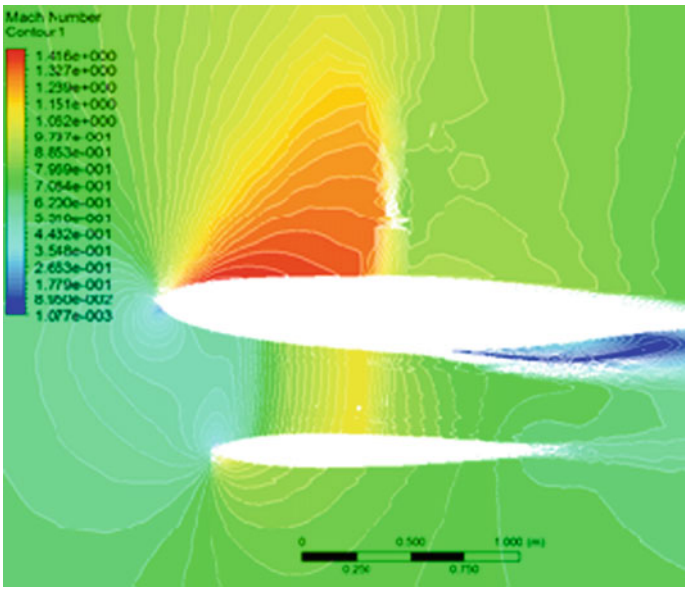

Fig. 5 Local separation caused by changes of design variables

Table 6 Comparison between result of TBW model and wing-only model

Geometric model	AOA	CL	CD	L/D
Wing-only	1.25	0.808	0.03190	25.34
Truss braced wing	1.25	0.712	0.03359	21.19

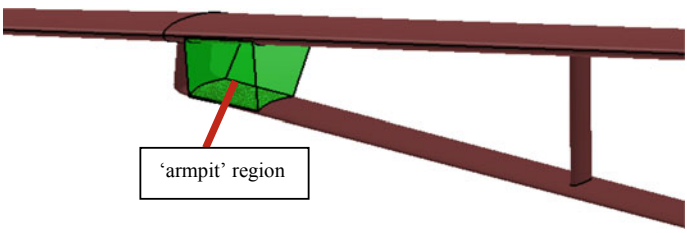

Fig. 6 The 'armpit' region

'armpit' of the two model is drawn in Fig. 7. The airflow acceleration effect between the strut and the wing, caused by Laval nozzle effect [16], creates a negative pressure region on the lower surface of the wing (hereinafter referred to as Nozzle pressure region). Under certain value of design variable, the strut can even affect the trailing edge loading of the supercritical wing (as shown in Fig. 8). They both caused a loss of lift on the wing.

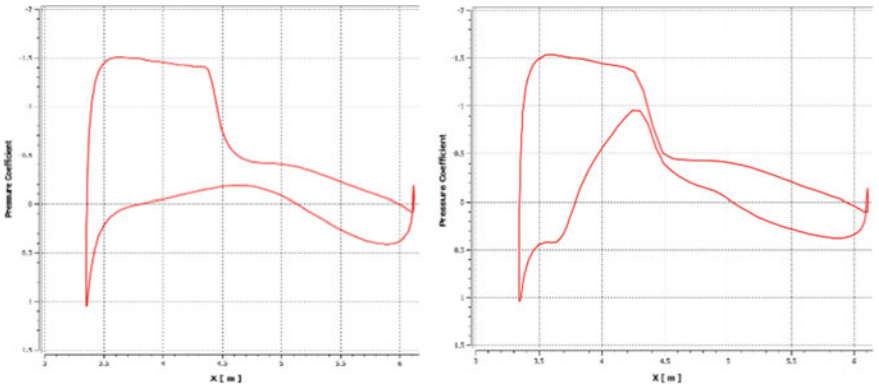

(a) Wing-only model (b) Standard TBW model

Fig. 7 Comparison of wing pressure distribution at the 'armpit' region

Fig. 8 Effect of design variables on trailing edge load of wing

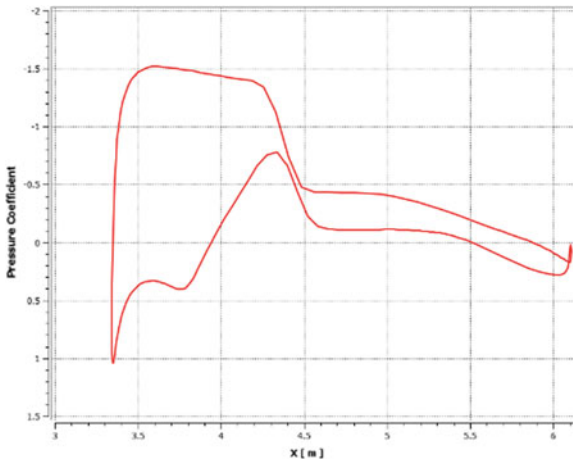

A more interesting thing is, the strut can produce negative lift load even at positive AOA with a symmetrical airfoil. Figure 9a, b shows the pressure distribution on the strut profile which is 0.2 m or 1 m away from the first jury respectively. From the figure we can see two key phenomena.

The first phenomenon is, due to the influence of the wing wash, the suck pressure on the upper leading edge of the strut is greatly weakened. While the suck pressure on the lower leading edge of the strut is less disturbed, resulting in a certain negative lift load at the leading edge of the strut. The effect of wing wash is less affected by the spanwise location.

The second phenomenon is, the nozzle effect also forms a 'Nozzle pressure region' at the middle of the upper strut, which generates a positive lift load on the strut. While the strut profile is close to the first jury, the wing and the strut is very close, so the

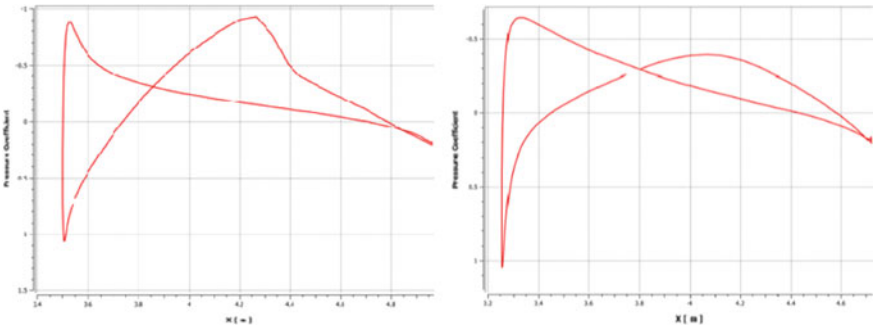

(a) 0.2m away from the first jury (b) 1m away from the first jury

Fig. 9 Pressure distribution on different profile of strut

nozzle effect is strong. If the strut profile goes further away from the first jury, the nozzle effect will weaken steeply.

By analyze, above two phenomena turn out to load a negative lift on the strut. Considering that the lift on the wing is also decreased, the truss does have a considerable negative impact on the lift performance.

3.2 Influence of Design Variables on Aerodynamic Performance

Figure 10 shows that aerodynamic performance of TBW model affected by design variables. It can be seen that *Cdwl2* and *He* have greater influence on the aerodynamic characteristics in the range of exploration, while *Spws2*, *Sw* and Φ have limited impact on aerodynamic performance. In order to be more intuitive, the effects of *Cdwl2* and *He* on aerodynamic characteristics are now shown in Figs. 11, 12, 13, 14, 15 and 16, respectively.

Figure 11 shows that as the strut gradually move backwards, the lift coefficient of the TBW model shows a significant downward trend. The drop of lift co-efficient is 0.1 within the scope of investigation. And the drag coefficient shows a trend of increasing first then decreasing with the backward translation of the strut. The variation range of drag coefficient is 6.5 counts, accounting for about 25% of the interference drag of the truss.

Next, let's discuss the effect on the flow field. Figure 12 shows the size of super-sonic flow area changing in the front view by the moving backward of strut. The supersonic flow in the 'armpit' region is limited to about 0.5 m in the spanwise, and gradually decreases as the strut translates backwards. The super-sonic flow in the 'armpit' region disappears quickly when strut moves to the rear-most position. The Mach number distribution of the cross section at the 'armpit' region changing with *Cdwl2* is shown in Fig. 13. As the strut translates back-ward, the shock wave in the

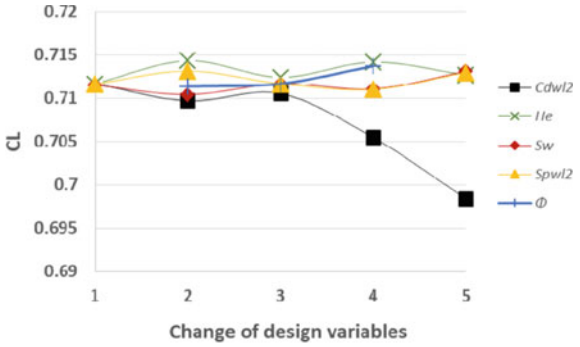

(a) Lift performance

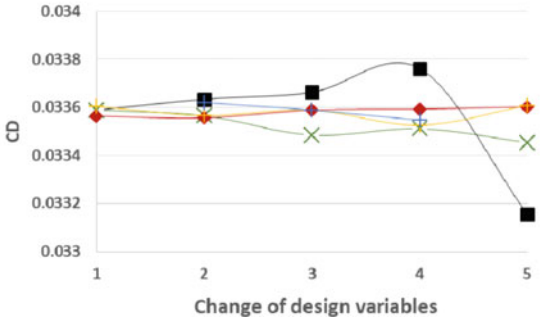

(b) Drag performance

Fig. 10 Aerodynamic performance of TBW model affected by design variables

'armpit' region gradually weaken, and a strong local separation gradually appears on the lower trailing edge of wing.

The above flow field changes reflect in the pressure distribution. Figures 14 and 15 show the variation of the pressure distribution on the wing and strut with *Cdwl2*, respectively.

As the strut moving backward, the peak of the 'Nozzle pressure region' on the wing gradually weakens, and the peak position gradually moves backward. Due to the occurrence of local separation, the load at the trailing edge of supercritical wing is gradually shrinking.

At the same time, the peak of 'Nozzle pressure region' on the strut is also gradually reducing, while the suck peak on the lower leading edge of strut is gradually increasing.

In summary, the backward movement of the strut caused considerable change in most of the negative pressure region, which lead to an impact on the lift characteristics. And the movement of the negative pressure region and the change of the pressure peak value cause the variation of the drag characteristics.

Figure 16 shows the effect of the height of the first jury on the aerodynamic characteristics. The lift performance of TBW model do not change a lot with He,

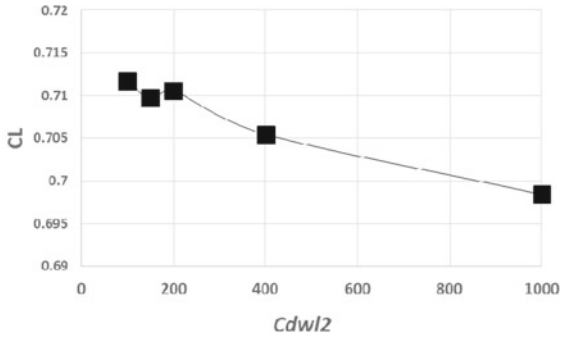

(a) Lift performance

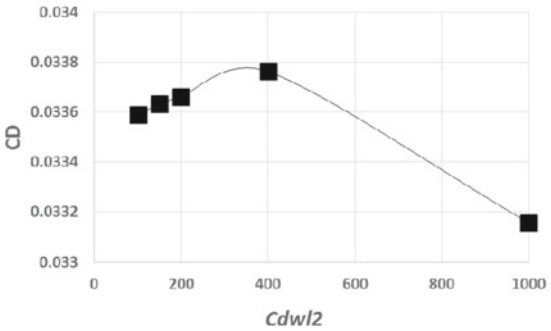

(b) Drag performance

Fig. 11 Effect of chordwise location of strut on aerodynamic performance

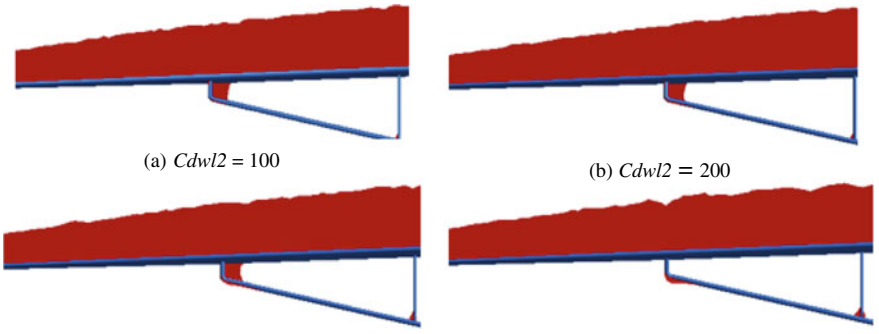

(a) *Cdwl2* = 100

(b) *Cdwl2* = 200

(c) *Cdwl2* = 400

(d) *Cdwl2* = 1000

Fig. 12 Influence of *Cdwl2* on the supersonic flow range from the front view

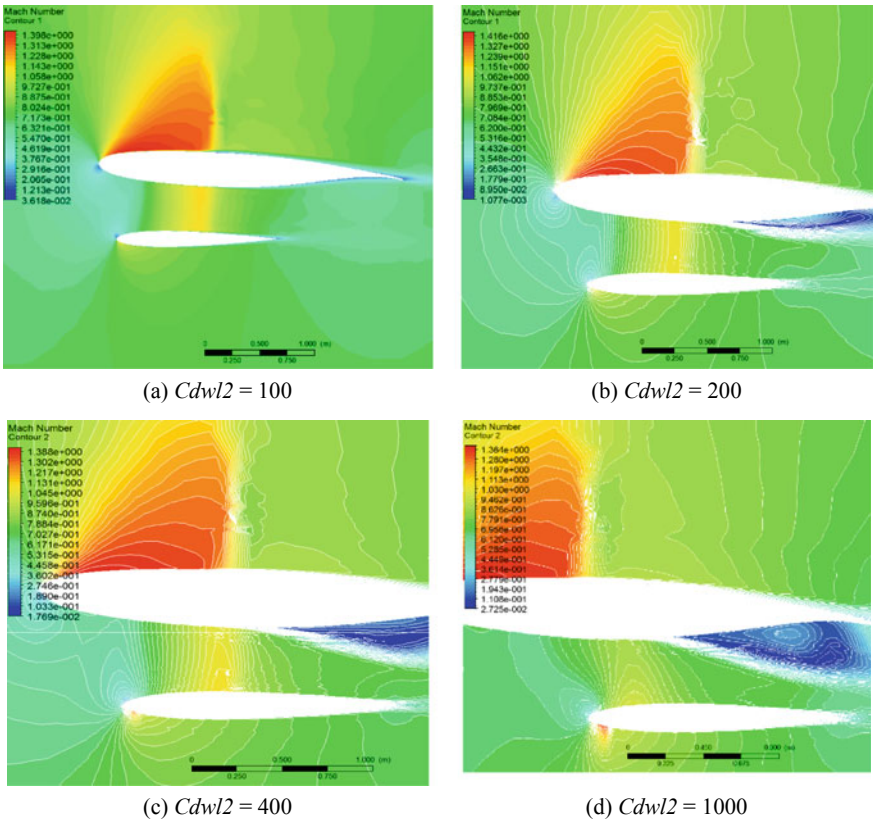

(a) *Cdwl2* = 100 (b) *Cdwl2* = 200

(c) *Cdwl2* = 400 (d) *Cdwl2* = 1000

Fig. 13 Effect of *Cdwl2* on Mach number distribution in 'armpit' region

while the drag performance shows a decreasing trend as *He* increasing. The variation range of drag performance was 1.5 counts within the scope of investigation.

Figure 17 shows the size of supersonic flow area changing in the front view against *He*. As the height of the first jury increasing, the supersonic flow between the strut and the wing decreased rapidly. The Mach number distribution in the 'armpit' region also reflects the same situation (see Fig. 18).

The effect of the *He* on the pressure distribution of the wing and the strut is shown in Figs. 19 and 20, respectively. The main effect of the height of The First Strut on the pressure distribution is the decreasing of 'Nozzle pressure region'. Because the changes of the 'Nozzle pressure region' on wing and strut cancelled each other, the lift performance did not change significantly. But the drag performance was greatly affected.

It should be noted that, other design variables that have little effect on the aerodynamic performance (*Spws2, Sw and Φ*) have no significant effect in 'armpit' region. For there is stronger nozzle effect in the 'armpit' region, and it is the most sensitive area of aerodynamic character while the design variable changes, we can infer that the

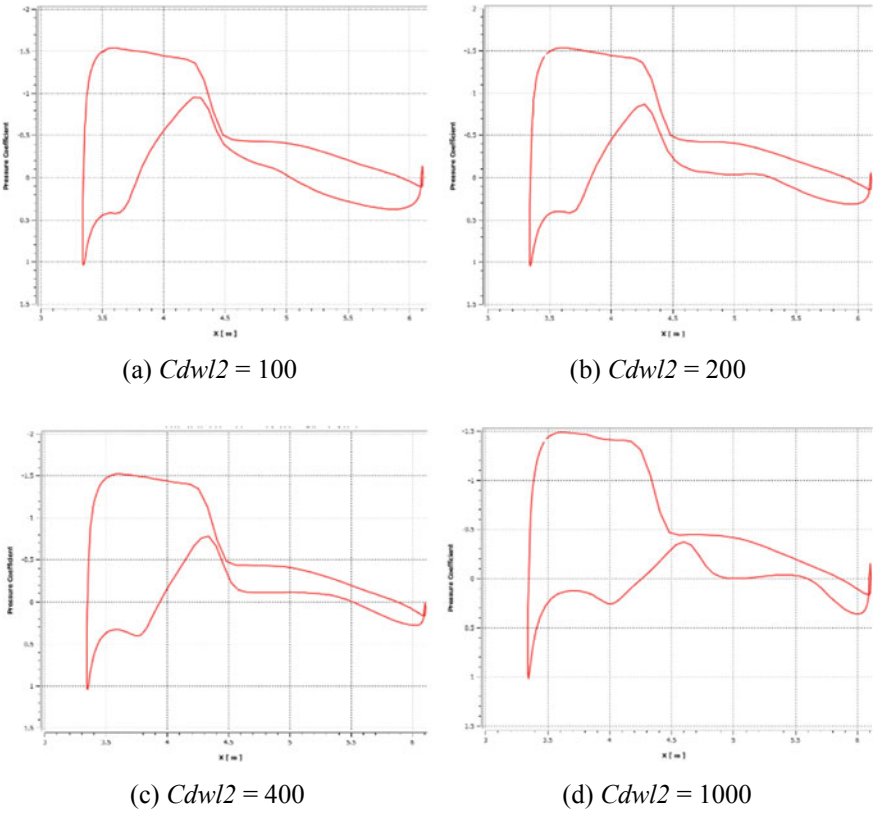

(a) *Cdwl2* = 100 (b) *Cdwl2* = 200

(c) *Cdwl2* = 400 (d) *Cdwl2* = 1000

Fig. 14 Effect of *Cdwl2* on wing pressure distribution in the 'armpit' region

design variables that have greater impact on the cross section in the 'armpit' region are more likely to have a greater impact on the overall aero-dynamic performance.

In addition, the previous study pointed out that the supersonic flow in the 'armpit' region does show a strong correlation with the drag performance. When the supersonic flow is significantly weakened, the drag of the TBW model will also be reduced. And the supersonic flow in 'armpit' region results from the nozzle effect. Therefore, the shape of the cross section near the 'armpit' is likely to have greater impact on the strength of supersonic flow.

The shape of the cross section at 'armpit' region under variation of design variables is shown in Fig. 21. The parameter is shown in Table 7. It can be seen that the 'flow section compression ratio' does have a strong correlation with the strength of supersonic flow ('flow section compression ratio' in this paper represent the decreased rate of the cross section area from the entrance to the throat). Despite the differences in shape of the cross section, supersonic flow can be eliminated both by variable *Cdwl2* and variable *He* when the 'flow section compression ratio' is around 16%.

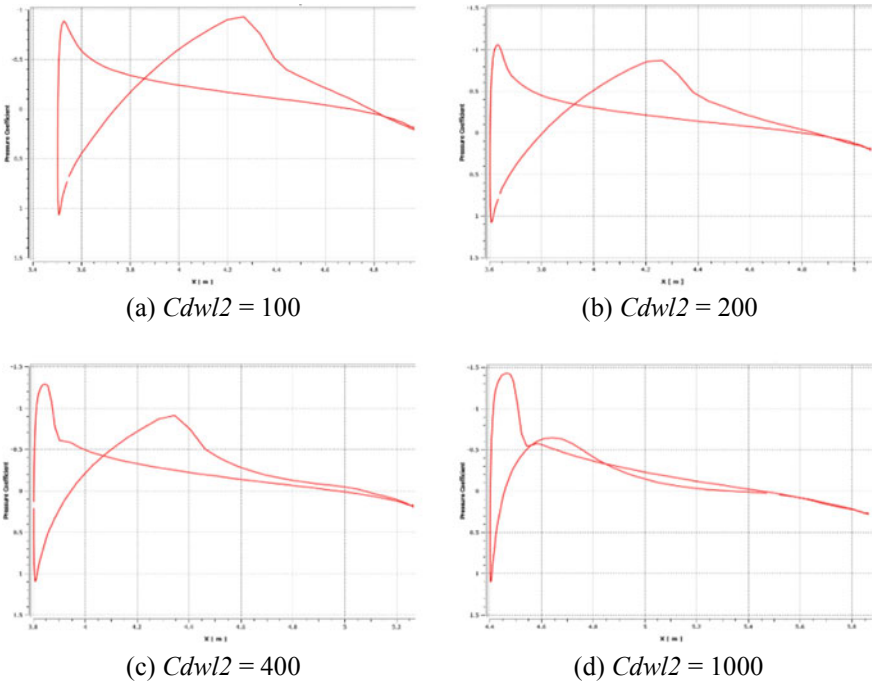

(a) *Cdwl2* = 100 (b) *Cdwl2* = 200

(c) *Cdwl2* = 400 (d) *Cdwl2* = 1000

Fig. 15 Effect of *Cdwl2* on strut pressure distribution in the 'armpit' region

This shows that the 'flow section compression ratio' can be used as an independent design reference to characterize the supersonic flow strength in 'armpit' region in a way.

3.3 Interference Drag

Next, with the help of the pressure distribution, let's focus on the drag performance. According to the previous study, the impact of design variables on aero-dynamic force is mainly reflected in the peak size and peak position of the 'Nozzle pressure region'. The nozzle consists of the wing's lower surface and the strut's upper surface. And it is easy to cause a situation where the position of pressure peak is inconsistent with the position of maximum thickness of the profile. When the suction pressure peak resides behind the maximum thickness, there will be additional profile drag coefficient (shown in Fig. 22). If supersonic flow has occurred in the 'armpit' region, the peak of airflow velocity will increase, the peak's position will move backward, and so will the peak of pressure. Therefore, the drag coefficient of the TBW model usually increases with the supersonic flow in the 'armpit' region.

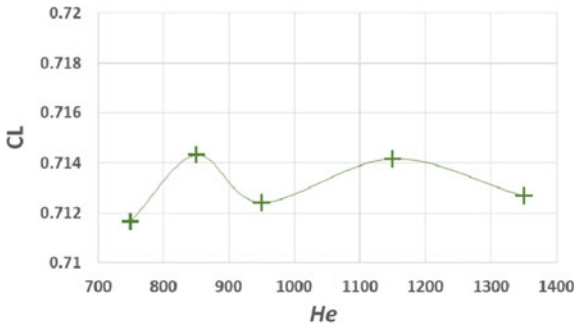

(a) Lift coefficient

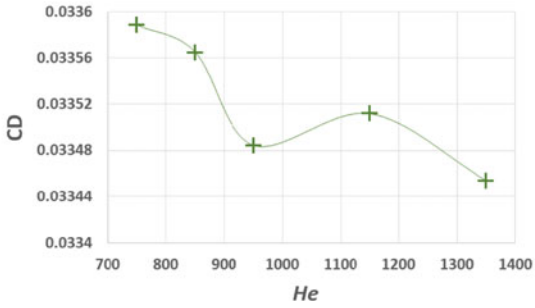

(b) Drag coefficient

Fig. 16 Effect of *He* on aerodynamic characteristics

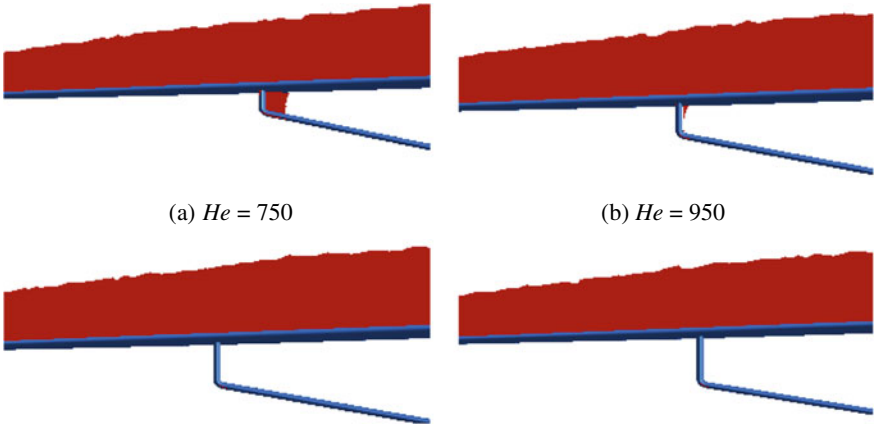

(a) *He* = 750 (b) *He* = 950

(c) *He* = 1150 (d) *He* = 1350

Fig. 17 Influence of *He* on the supersonic flow range from the front view

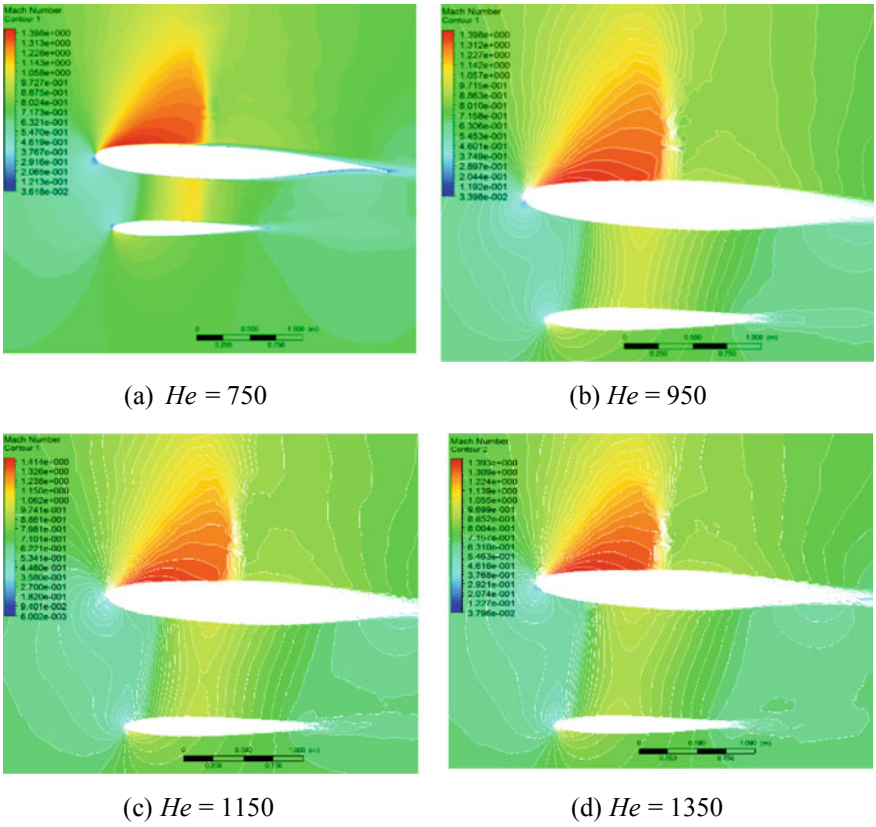

(a) *He* = 750 (b) *He* = 950

(c) *He* = 1150 (d) *He* = 1350

Fig. 18 Effect of *He* on Mach number distribution in 'armpit' region

However, when there is no supersonic flow in the 'armpit' region, the negative pressure zone between the wing and the strut will still be generated by Continuity Equation (hereinafter referred to as Venturi pressure region). And the peak's position the Venturi pressure region may not be consistent with the maximum thick-ness of profile either due to the shape of the cross section, which in turn creates additional profile drag (shown in Fig. 23).

In order to discuss this part of drag, this paper simplified the flow into two dimensions, and carried out an analysis about the influence of maximum thickness position of strut profile. Figure 24 shows the drag performance of the result. Figure 25 shows the pressure distribution. Figure 26 shows the Mach number distribution.

It can be seen that the peak of Venturi pressure region is obviously behind the maximum thickness position of strut when the maximum thickness of the strut is at the front, but the Venturi pressure region is weak due to a low 'flow section compression ratio'. Therefore, the profile drag is low at this situation.

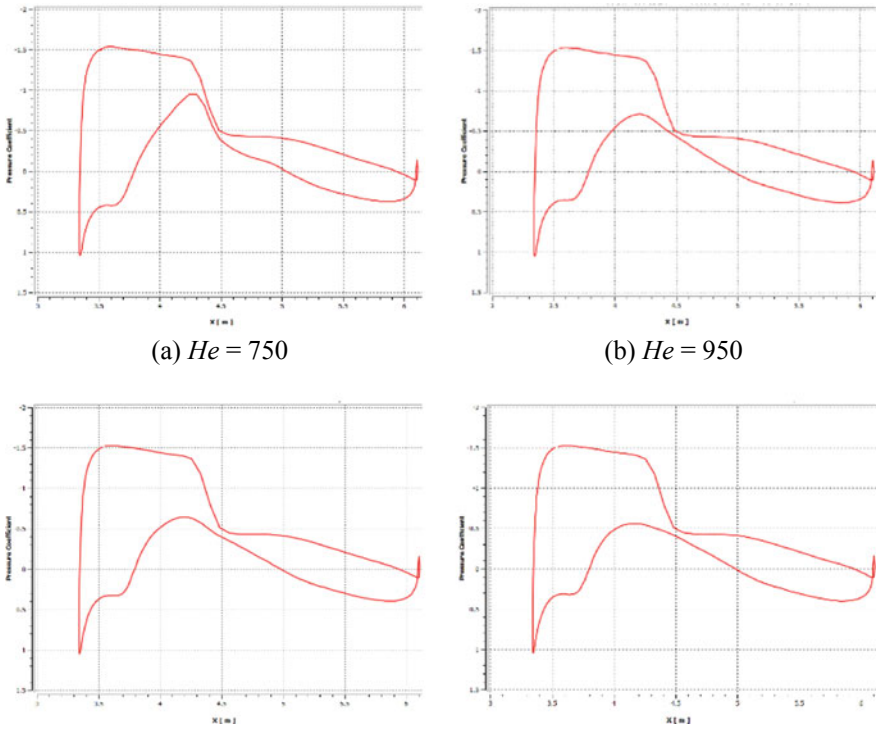

(a) *He* = 750 (b) *He* = 950

(c) *He* = 1150 (d) *He* = 1350

Fig. 19 Effect of *He* on wing pressure distribution in the 'armpit' region

As the maximum thickness position moves backward, the peak of Venturi pressure region increases, and its position is still behind the maximum thickness position, so the profile drag trend to increase.

When the maximum thickness position moves back to a certain degree, the maximum thickness position couples with the peak of Venturi pressure region, and the profile drag is significantly reduced.

According to the research in this part, the misalignment between the peak of 'Venturi/Nozzle pressure region' and the peak of thickness is the key factor leading to a large interference drag. The additional drag caused by supersonic flow is also due to this phenomenon. Aligning the maximum thickness of strut with which of the lower surface of wing may have a better effect, but this approach has the risk of inducing supersonic interference. In the actual design, the position of the maximum thickness and the 'flow section compression ratio' had better be comprehensively considered.

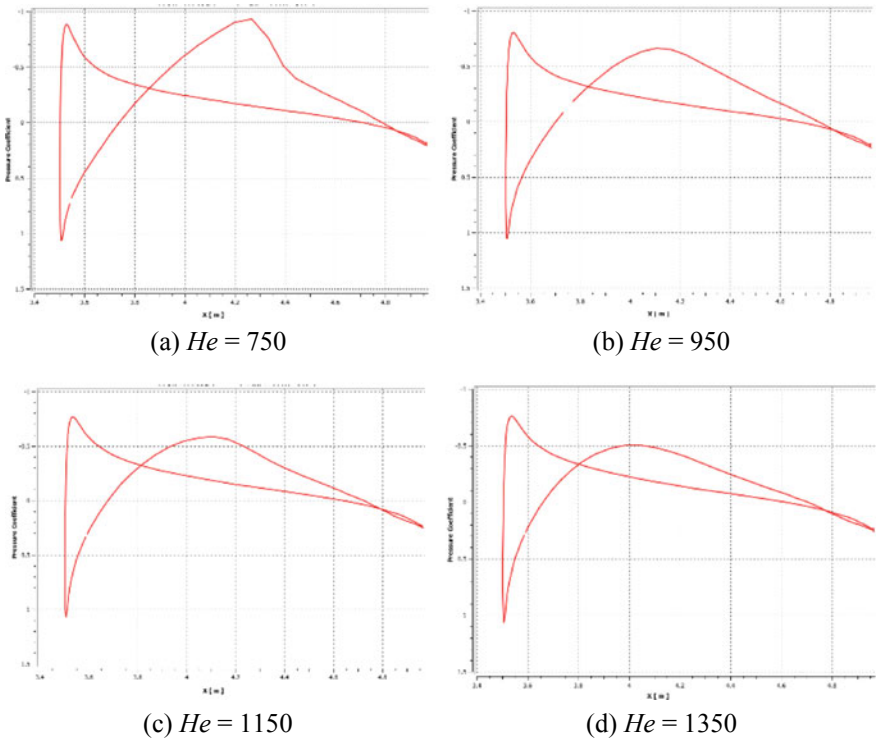

(a) *He* = 750 (b) *He* = 950

(c) *He* = 1150 (d) *He* = 1350

Fig. 20 Effect of *He* on strut pressure distribution in the 'armpit' region

4 Conclusion

Base on the above simulation and analysis on the aerodynamic interference of the TBW configuration, the conclusions are summarized as follows:

(1) In addition to the drag characteristics concerned in previous studies, the truss also causes a negative impact on lift characteristics.
(2) The design variables that have greater impact on the cross section in the 'armpit' region are more likely to have a greater impact on the overall aerodynamic performance.
(3) The supersonic flow in the 'armpit' region does show a strong correlation with the drag performance. The'flow section compression ratio' can be used as an in-dependent design reference to characterize the supersonic flow strength in 'arm-pit' region in a way.
(4) The misalignment between the peak of 'Venturi/Nozzle pressure region' and the peak of thickness is the key factor leading to a large interference drag. Aligning the maximum thickness of strut with which of the lower surface of wing may have a better effect, but this approach has the risk of inducing supersonic interference. In the actual design, the position of the maximum thickness and the 'flow section compression ratio' had better be comprehensively considered.

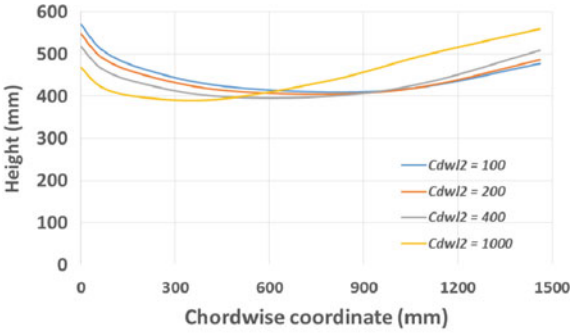

(a) The cross section shape influenced by *Cdwl2*

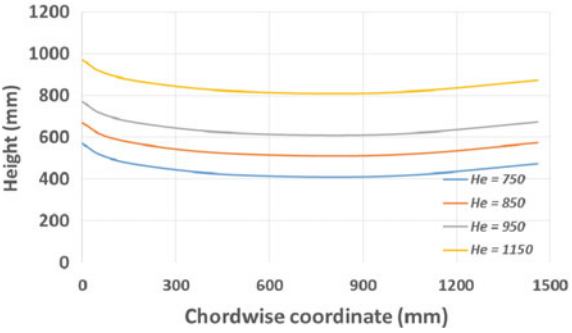

(b) The cross section shape influenced by *He*

Fig. 21 The cross section shape at 'armpit' region influenced by design variables

Table 7 The cross section parameter at 'armpit' region influenced by design variables

Design variable	Values	'Flow section compression ratio' (%)	Mach number peak @ 'armpit'
Cdwl2	100	28.2	1.10
Cdwl2	200	26.1	1.08
Cdwl2	400	22.9	1.05
Cdwl2	1000	16.1	0.99
He	750	28.2	1.10
He	850	23.9	1.06
He	950	20.7	1.02
He	1150	16.5	0.98

This paper provided an auxiliary decision for TBW configuration sizing. Aerodynamic optimization based on this research may be further carried out in future work.

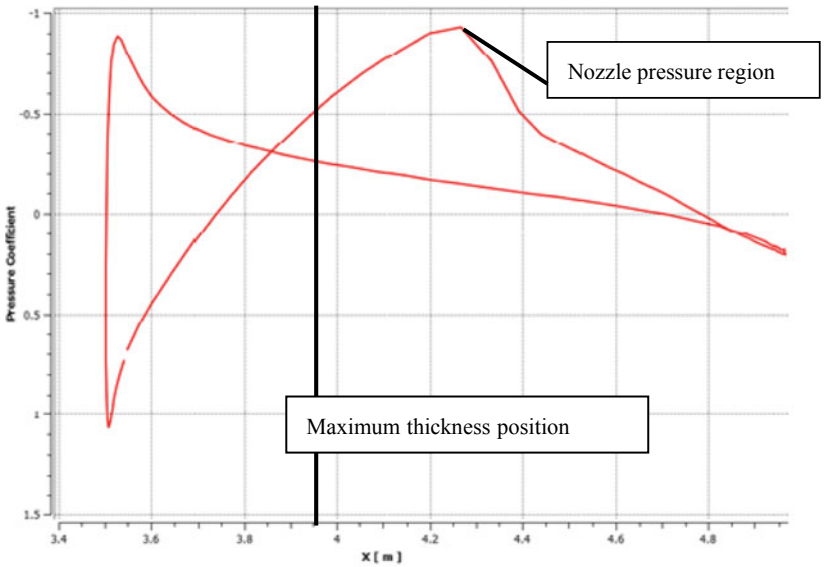

(a) Chordwise pressure distribution along

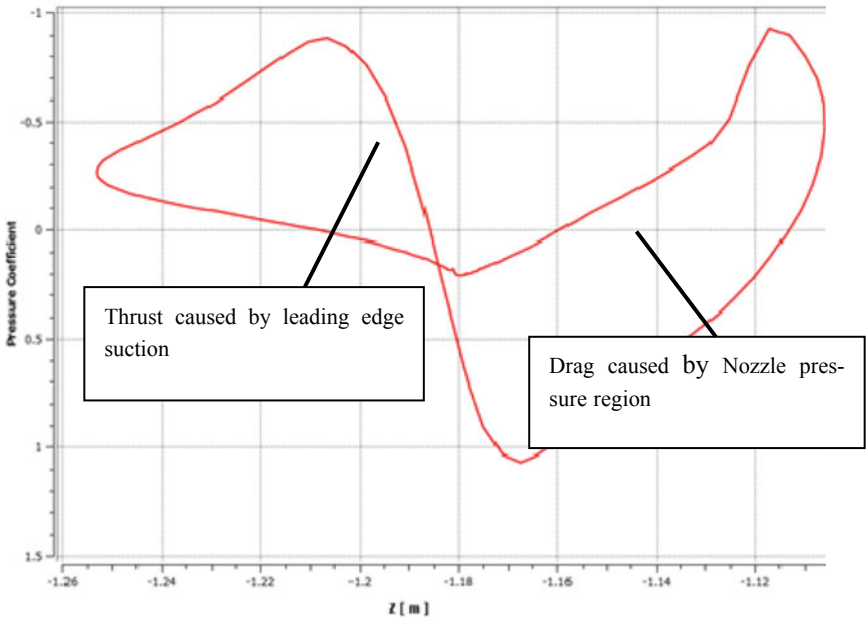

(b) Pressure distribution along the thickness

Fig. 22 Additional profile drag caused by nozzle effect

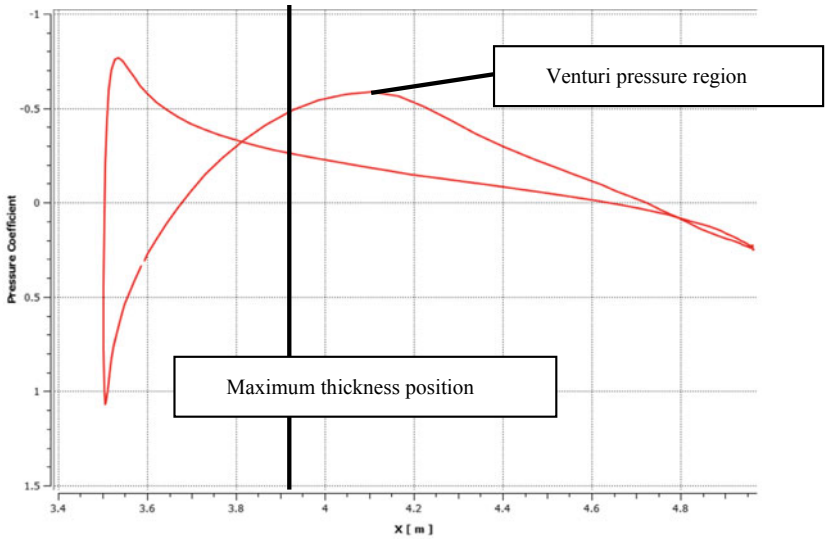

(a) Chordwise pressure distribution

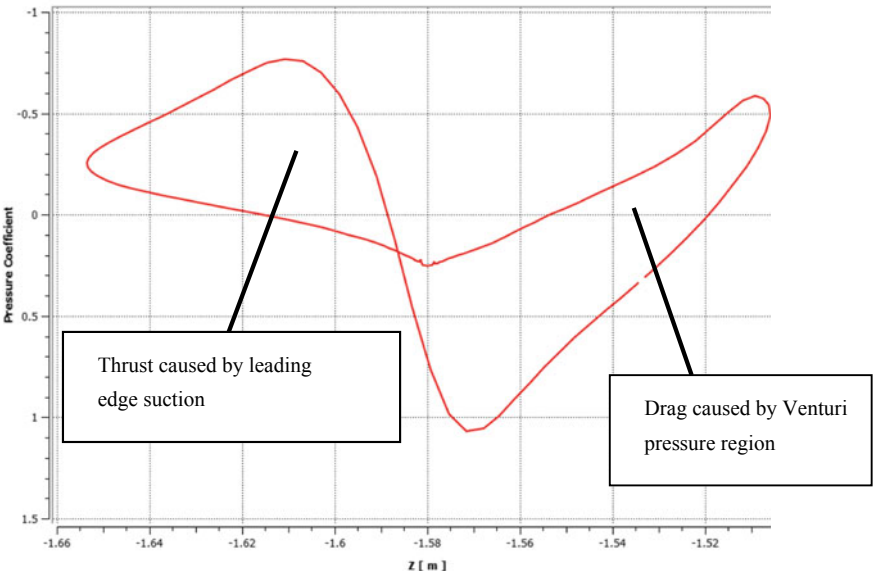

(b) Pressure distribution along the thickness

Fig. 23 Additional profile drag caused by continuity equation

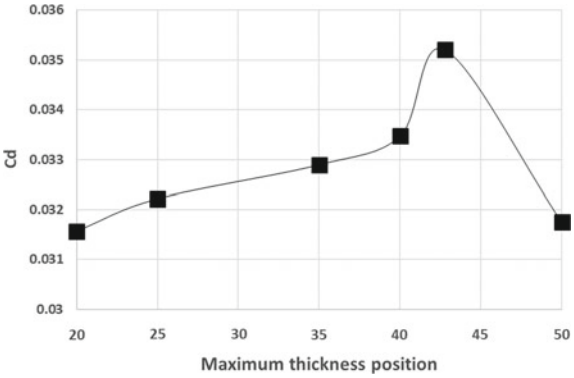

Fig. 24 Profile drag against Maximum thickness position of strut

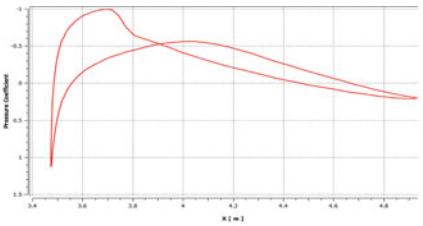

(a) Maximum thickness position of strut = 20% chordwise

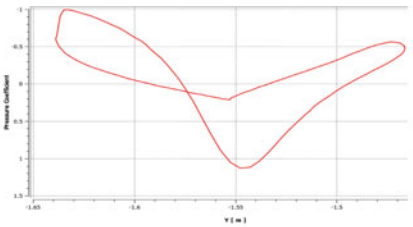

(b) Maximum thickness position of strut = 20% along the thickness

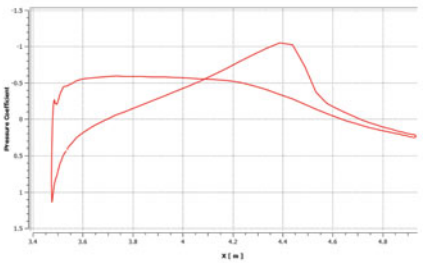

(c) Maximum thickness position of strut = 43% chordwise

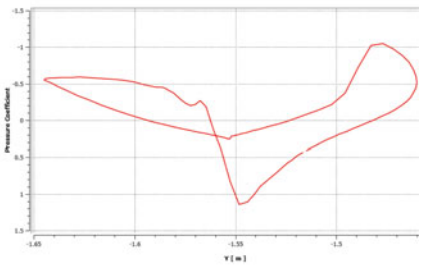

(d) Maximum thickness position of strut = 43% along the thickness

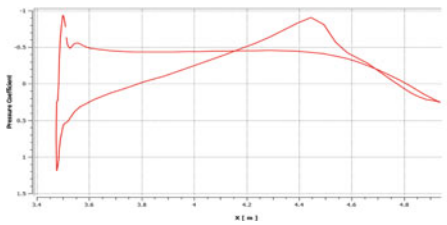

(e) Maximum thickness position of strut = 50% chordwise

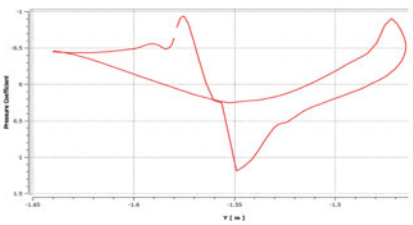

(f) Maximum thickness position of strut = 50% along the thickness

Fig. 25 Pressure distribution of strut in two-dimension simulation

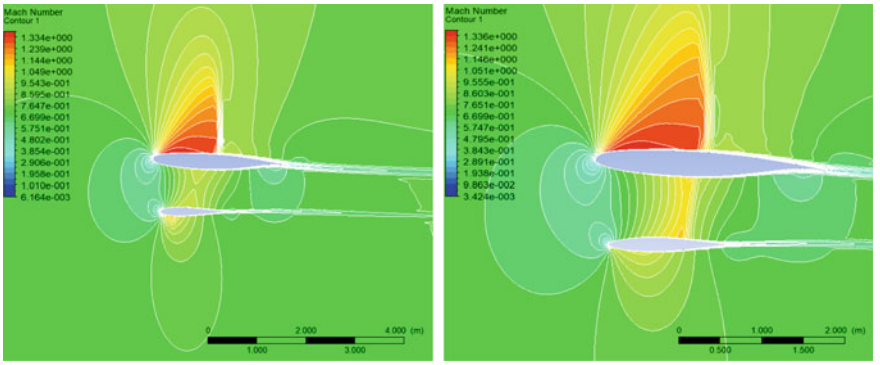

(a) Maximum thickness position of strut = 20% (b) Maximum thickness position of strut = 35%

(c) Maximum thickness position of strut = 43% (d) Maximum thickness position of strut = 50%

Fig. 26 Mach number distribution in two-dimension simulation

Acknowledgements This work is supported by National defense key discipline laboratory of advanced aircraft design technology, NUAA. Great gratitude giving to all the professors and companions of research group MDO305 for their help during the re-search. The authors also gratefully acknowledge the helpful comments and suggestions of the reviewers, which have improved the presentation.

References

1. Xu DF (2010) US' N+3-generation airliner program into phase 1. Int Aviat. (6):49–51. Chinese
2. Zeng JF, Qu JS (2012) EU aviation carbon tax and its international influences. Clim Change Res 8(4):292–296. Chinese
3. Lu ZF (2014) ICAO-based aviation carbon emission calculation and low-carbon countermeasures. Resour Economization Environ Prot (9):129–130. Chinese
4. Hardman AF (2014) Measures for international aviation to respond to global carbon emissions. China Civ Aviat (6):27–28. Chinese
5. Xu DF (2015) Truss-braced wing shows promise. Int Aviat (2), 79–79. Chinese

6. Bradley KF, Droney KS (2012) Subsonic ultra green aircraft research phase II. NASA/CR-2012-217556
7. Zhu ZF (2009) Multi-disciplinary optimization of strut-braced wing transonic transport. Acta Aeronautica et Astronautica Sinica 30(1):1–11. Chinese
8. Gern FF, Ko AS (2000) Transport weight reduction through MDO: the strut-braced wing transonic transport. In: 35th AIAA fluid dynamics conference and exhibit
9. Wang YF (2016) The adventure of truss-braced wing. World Flight (6):54–57. Chinese
10. Moerland EF, Pfeiffer S, Daniel T (2017) On the design of a strut-braced wing configuration in a collaborative design environment. In: 17th AIAA aviation technology, integration, and operations conference
11. Wang GF, Zeng JS, Lee JT (2015) Preliminary design of a truss-braced natural-laminar-flow composite wing via aeroelastic tailoring. ASD J (3):1–17
12. Xing YF, Yu XS (2018) The wing mass estimation for commercial aircraft with truss-braced wing configuration. Mach Des Manuf Eng (2):83–86. Chinese
13. Xing YF (2018) Integrated analysis and optimization in conceptual design of airliners with truss braced wing configuration. Doctor, Nanjing University of Aeronautic and Astronautic. Chinese
14. Zhang SF, Ji BS, Bakar AT (2012) Multidisciplinary evaluation of truss-braced wing for future green aircraft. In: 28th international congress of the aeronautical sciences, Bonn, Germany
15. Locatelli DF, Riggins KS, Kapania KT (2015) A physics-based methodology for cantilever and strut-braced wing weight estimation. In: AIAA aerospace sciences meeting
16. Ko AF, Mason WS, Grossman BT (2003) Transonic aerodynamics of a wing/pylon/strut juncture. In: 21st AIAA applied aerodynamics conference, AIAA-2003-4062
17. Ivaldi DF, Secco NRS, Chen ST (2015) Aerodynamic shape optimization of a truss-braced-wing aircraft. In: 16th AIAA/ISSMO multidisciplinary analysis and optimization conference
18. Ney RF (2019) RANS-based aerodynamic shape optimization of a strut-braced wing with overset meshes. J Aircr 56(1):217–227
19. Knight KF (2011) Assessment of RANS turbulence models for strut-wing junctions. Master, Virginia Polytechnic Institute and State University
20. Tetrault AF, Schetz JS, Grossman BT (2013) Numerical prediction of the interference drag of a streamlined strut intersecting a surface in transonic flow. In: Aerospace sciences meeting & exhibit
21. Duggirala KF, Roy JS, Schetz AT (2011) Analysis of interference drag for strut-strut interaction in transonic flow. AIAA J 49(3):449–462

Research on the Mechanism of Resistance Generation in Disc Acceleration Based on Lagrangian Method

Shujia Lin, Fuxin Wang, Zhuoqi Li, and Yang Xiang

Abstract During flapping wing flight or fish swimming, a large-scale vortex structure is in general generated by each stroke motion of the wing or the trail, and contributes most of the lift and thrust. As a fundamental model to characterize the wake structures of flapping flight and fish swimming, the disc vortex ring (DVR) generated by the impulsive motion of a disc contains numerous unsteady aerodynamic mechanisms. In this paper, an experimental set-up was designed to produce DVRs with different acceleration, particle image velocimetry (PIV) technique was used to measure the growth and evolution process of wake vortices, and force sensor was used to measure the instantaneous change in drag directly. PIV results show that a DVR is formed in the wake during the disc starting, and the circulation growth of DVR satisfies the Logistic growth model. Using the Lagrangian coherent structure (LCS) to analyze the formation of DVR shows that, under the interaction of the add-mass effects of disc and DVR, the vortex flow shows a significant Lagrangian drift, which contributes a significant increase of the drag. Besides, the results of the drag measurement show that the formation process of the vortex ring consists of three phases, including a peak and a valley. Based on the vorticity-moment theorem, the evolution of drag is explained in terms of the dynamics of DVR and the added-mass effects. Moreover, the findings of this paper provide a new Lagrangian perspective for understanding the mechanism of lift and thrust during flapping wing flight and fish swimming.

Keywords Disc vortex ring · Acceleration · Added-mass · PIV · LCS

S. Lin · F. Wang (✉) · Z. Li · Y. Xiang
School of Aeronautics and Astronautics, Shanghai Jiao Tong University, Shanghai, China
e-mail: fuxinwang@sjtu.edu.cn

S. Lin
e-mail: linshujia@sjtu.edu.cn

Z. Li
e-mail: LIZhuoqi@sjtu.edu.cn

Y. Xiang
e-mail: xiangyang@sjtu.edu.cn

Z. Jing and X. Zhan (eds.), *Proceedings of the International Conference on Aerospace System Science and Engineering 2020*, Lecture Notes in Electrical Engineering 680,
https://doi.org/10.1007/978-981-33-6060-0_11

1 Introduction

Vortex rings are one of the fundamental flow structures in nature and act as the consistent feature in the wake of biological propulsion [8]. Pulsatile jet propulsions (like Jellyfish, Salps and Medusa) create obvious vortex ring structures, which are similar with the vortex rings generated by a starting jet from a nozzle or orifice [6, 9, 10]. This vortex ring is termed as jet vortex ring (JVR). For flapping wings, their bound vortices can also be characterized a vortex ring structure, which consists of a leading edge vortex (LEV) on top of the wing, connected to a start vortex shed in the wake via a tip vortex (TPV) and a root vortex (RTV) [29]. Moreover, the wake of flapping wing is modelled by a chain of coaxial small cored circular vortex rings [3, 13, 35]. Applying vortex ring model, the stroke-average lift forces is expressed as the function of the dynamics of these vortex rings [44, 45]. This type of vortex ring has a more similarly topological structure with the disc vortex ring (DVR) that is generated by an impulsively started disc rather than the JVR. In addition, a vortex ring model can provide a more holistic and comprehensive perspective to investigate the unsteady mechanisms associated with the vortices (LEV, TEV, and RTV) around a flapping wing, because interactions and vorticity transports between these vortices are ver8 complex. Therefore, this paper focuses on the formation of DVRs that can be a canonical problem to investigate the formation of the vortex structures around a flapping wing.

For the studies of JVRs, massive studies have been performed particularly including two comprehensive reviews [8, 39] and one specific book [2]. Compared with the formation of JVRs, the formation of DVRs is intrinsically different and less studied. In 1953, Taylor [43] theoretically investigated the formation of a vortex ring by giving an impulse to a circular lawdisk and then dissolving it away in a perfect fluid without separation of flow. According to Taylor's derivations, the ratio of the vortex translational speed (W) to the disc speed (U) is 0.436, the dimensionless core radius ($\varepsilon = a/R$) is 0.186, the ratio of vortex radius (R) to disc radius (C) is 0.816, and the circulation of DVR is $4Uc/\pi$. Besides, Sallet [38] made a comparison between experimental results and theoretical approximations. The results showed there were discrepancies. In 2012, Yang et al. [49] performed an experimental study on the formation of DVRs. Based on the dimensionless time ($T^* = L/D$, L is the stroke length of the disc and D is the disc diameter), they found that the formation of the vortex ring basically includes three phase: a rapid growth phase ($0 < T^* < 0.2$), a stable growth phase ($0.2 < T^* < 4$) and a non-axisymmetric phase ($4 < T^*$). In the first phase, the physical features of DVR satisfy Taylor's inviscid estimation. In the second phase, DVR entrains fluids and grows gradually. Then, DVR loses axisymmetry due to instability when $T^* > 4$. Yang et al. [49] also quantitatively investigated the circulation, energy, and impulse formation of DVR.

Compared with JVRs generated by a piston-cylinder apparatus, the formation and physics of DVRs exhibit some obvious discrepancies. For JVRs, their formation can be predicted by the slug model [14, 41], although the overpressure at nozzle exit plane also contributes to their formation [23, 24]. During the formation process,

JVRs freely propagates downstream due to self-induced velocity and entrains fluids significantly. By contrast, the formation of DVRs strongly depends on the motion of disc. The vorticity flux enters into the JVR along the symmetry axis, whereas the vorticity flux enters into the DVR from the outer edges. For the formation of JVR, one most fascinating mechanism is the vortex pinch-off. In 1998, Gharib et al. [19] conducted JVR experiments and firstly found that JVRs cannot grow indefinitely but rather there is a physical limit to their size. Beyond this limit, JVRs no longer grow but pinch off at this timescale. Furthermore, the timescale when JVRs pinch off is found to stay in a narrow range and exhibits a universal formation number that is approximately 4.0. Once the JVR pinches off, a trailing vortex rolls up owing to shear-layer instability [17, 18]. It should be noted that this formation number (also called pinch-off time) may vary by some parameters, such as the velocity programs of piston [42], external background flow [24], and temporal-varying exit diameter [11]. Gharib et al. [19] explained the formation number based on the limiting effect of the energy implied by the Kelvin-Benjamin variational principle [5, 19, 22]. In particular, vortex pinch-off hints the principle of optimal vortex formation, which is applied by biological propulsions [8, 19, 26]. The idea of vortex pinch-off has been widely applied to investigate some canonical vortices separated from a body, such as, the flow generated by a starting circular cylinder [21], the vortex wake of an oscillating flat plate [28], and the LEV formation in bio-inspired flight [4, 36]. However, these vortices are two-dimensional, and we must emphasize that the pinch-off and the universal formation number are not observed during the formation of two-dimensional vortex generated by the two-dimensional orifice [1, 32]. Therefore, whether the formation of DVRs involves the pinch-off mechanism or not is a remained question and should be identified.

The main purpose of the present study is to investigate the formation of DVRs. The discrepancies between the formation of DVR and JVR are also analysed. The rest of the paper is organized as follows: Both experimental methods and the computations of Lagrangian coherent structures (LCSs) are introduced in Sect. 2. Section 3 attempts to reveal the body-linked effects on DVR formation by investigating the formation process of DVR and the circulation production mechanism. And further analyses the formation and pinch-off process of DVR by investigating the Lagrangian coherent structures. In Sect. 4, a balanced formation mode for DVRs is proposed by comparing with the formation of JVRs. Section 5 concludes the paper with a brief discussion.

2 Methods

2.1 Experimental Set-up

A circular disc with diameter $D = 50$ mm and thickness $\delta = 3$ mm is immersed in a water tank with dimensions of 4 m $\times$ 1 m $\times$ 1 m. Figure 1 shows a schematic of the experimental setup. The disc was driven by a linear slider, which was connected

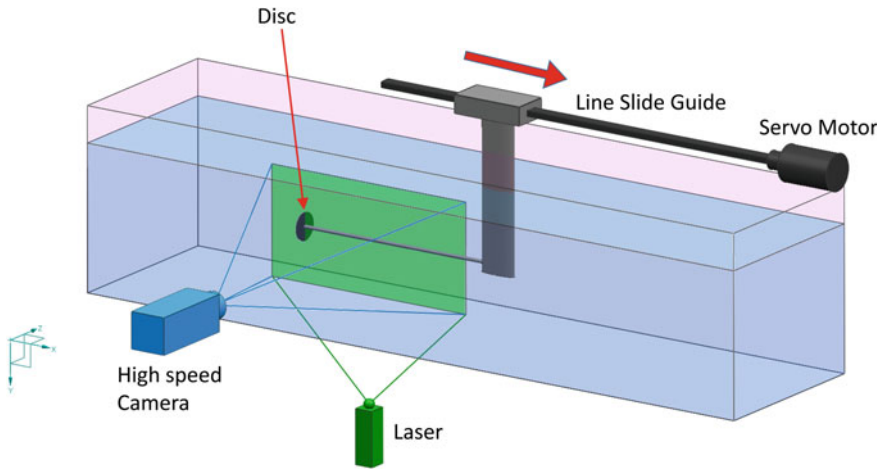

Fig. 1 Schematic of the experimental set-up

with a servo motor controlled by a programmable microcontroller called Arduino. The disc is connected with a circular rod, which has a diameter of 5 mm and is fixed with a plate. This plate is designed to have a airfoil section to avoid flow separation and reduce the perturbation brought by the motion of plate. In addition, the disc moves very smoothly and the experiments have very good repeatability (the same experimental is repeated five times, $\Delta L/L < 0.1\%$, L represents the given stroke length of the disc, and ΔL represents maximal discrepancy of the real stroke length between the five runs).

In order to measure the flow field of DVRs, the digital particle image velocimetry (DPIV) technique is applied. A kind of hollow glass beads, which have a mean diameter of 20–50 μm and a density of 1.02 g/m^3, are chosen as the seeding particles. In addition, the particles are illuminated by a thin laser sheet conducted by a continuous laser with the power of 10 W and a wavelength of 532 nm. The laser sheet is placed at the symmetry plane of the disc, which is termed as z-r plane. Then, a high-speed camera is positioned normal to the laser sheet and records the images of the particle field. The recorded filed has 2336 × 1200 pixels spatial with a 380 mm × 195 mm field of view. Besides, the camera operates at 200 frames per second. The obtained images are paired and processed by the standard cross-correlation algorithm. Using an interrogation area of 32 × 32 pixels and a step size for the moving average of 16 × 16 pixels (50% window overlap), the processing can construct a flow field of 231 × 117 velocity vector. In order to yield more accurate results, the multi-pass processing method is applied. According to calculated velocity fields, the vorticity fields are also calculated using finite differences of the velocity data at eight neighbouring points via a second-order accurate scheme. By satisfying the constraints of PIV measurements (interval time, particle size, and particle concentration), the uncertainty in the velocity measurement an vorticity calculation were considered to be 1% and 3%, respectively [34, 49]. In our study, the driven velocity of disc is

sinusoidal and is $U = 0.1\sin\left(\frac{\pi}{5.5}t\right)$ m/s, respectively. The corresponding Reynolds number ranges from 2500 to 5000 based on the disc velocity and diameter.

2.2 Lagrangian Coherent Structures

As the Lagrangian skeleton of flow, Lagrangian coherent structures (LCSs) not only provide a geometrical view of flow structures, but also characterize fluid transport and deformation over a certain period of time. This paper applies FTLE ridges to analyse the fluid transport, as well as uses elliptic LCSs to identify the boundary of coherent Lagrangian vortices.

The efficient approaches for computing the FTLE ridges and elliptic LCSs have been developed by Onu et al. [30] and applied by Xiang et al. [48]; David et al. [12]. The concept and computation of FTLE ridges and elliptic LCSs are presented as follows.

Applying $\phi_{t_0}^{t_0+T} : x(t) \rightarrow x(t+T)$ to denote the flow map of a material point located at x(t) at time t to its position at time (t + T), the deformation gradient is

$$\nabla\phi_t^{t+T}(\boldsymbol{x}) = \frac{d\phi_t^{t+T}(\boldsymbol{x})}{d\boldsymbol{x}} \tag{1}$$

Defining the finite-time Cauchy Green deformation tensor as:

$$\Delta(x, t, T) = \left[\nabla\phi_t^{t+T}(\boldsymbol{x})\right] * \nabla\phi_t^{t+T}(\boldsymbol{x}) \tag{2}$$

Then, FTLE is computed by

$$\sigma_{t_0}^{T}(x) = \frac{1}{|T|} ln\sqrt{\lambda_{\max}[\Delta(x, t_0, T)]} \tag{3}$$

where, $\lambda_{\max}[\Delta(x, t_0, T)]$ is the maximum eigenvalue of $\Delta(x, t_0, T)$. $|T|$ is used because FTLE can be computed for T > 0 and T < 0. Regions of maximum fluid particle separation (for T > 0) or maximum fluid particle attraction (for T < 0) produce local maximizing curves known as "ridges" in the FTLE. The ridges in forward-time FTLE (T > 0) reveal repelling hyperbolic LCSs (r-LCSs) and the ridges (T > 0) in backward time FTLE T < 0 reveal attracting hyperbolic LCSs (a-LCSs).

In our study, at a given time of interest t, we detect the FTLE ridges and the region enclosed by the elliptic LCS. Then, we distribute numerous particles in the region to trace the trajectory of these particles, and advect the elliptic LCS to investigate the evolution of coherent Lagrangian vortex. For particle advection in backward time and elliptic LCS advection in forward time, we used the fourth-order Runge-Kutta scheme to integrate in time. In addition, cubic interpolation in space and linear

interpolation in time were used to obtain the fluid velocity at the particle locations. By examining the repeatability of elliptic LCSs detection and particle advection, the results presented in Sect. 5 have sufficient accuracy within error less than 3%.

3 Formation of DVRs Based on the Lagrangian Analysis

3.1 Formation Process of DVRs

In general, a non-dimensional time, defined as $T_n = \frac{L}{D}$ where L is the stroke length of the disc, is applied to parameterize the formation of DVRs [43, 49]. In terms of the results of Yang et al. [49], for $T_n < 0.2$, the fluids separate from the edge of disc to form a DVR, which satisfies the description of Taylor's inviscid theories [43]. In the present study, the formation process of DVR for $T_n > 0.2$ is mainly investigated.

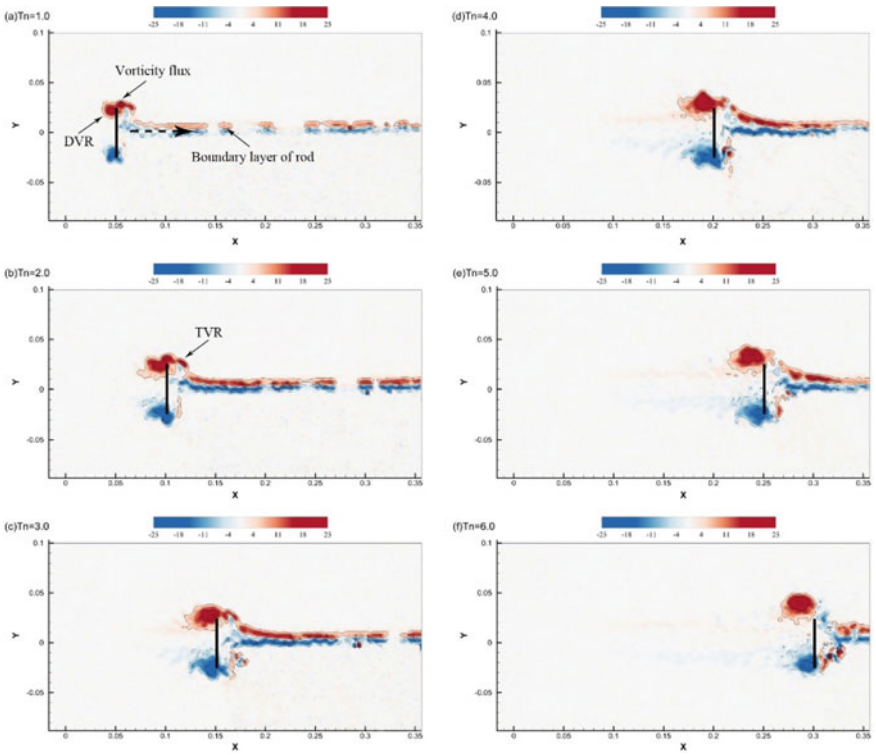

Fig. 2 Temporal evolution of vorticity field: **a** $T_n = 1.0$; **b** $T_n = 2.0$; **c** $T_n = 3.0$; **d** $T_n = 4.0$; **e** $T_n = 5.0$; **f** $T_n = 6.0$. Dashed lines indicate negative vorticity, disc moves from left to right

As shown in Fig. 2, the formation process from $T_n = 1.0$ to $T_n = 6.0$ for the case of $U = 0.1\sin\left(\frac{\pi}{5.5}t\right)$ m/s is presented.

As the disc moves, the vorticity flux from the disc edge rolls up to form a DVR. When $T_n = 1.0$, DVR has been formed with considerable strength. According to the Biot-Savart law, DVR has its own self-induced velocity, whose direction is consistent with that of disc moving. Note that, the propagating velocity of DVR depends on not only its self-induced velocity, but also the driving velocity of disc. By contrast, the velocity of JVRs generated by a piston-cylinder apparatus largely depends on their self-induction velocity. As the disc moves, the DVR continues to grow in size and the vorticity flux continues to feed DVR. When $T_n = 3.0$, DVR is sufficiently formed, and remains symmetrical and keeps attachment on the disc. Comparison of DVR patterns at $T_n = 3.0$ and $T_n = 4.0$ demonstrates that the growth of DVR is very slight. In addition, the fluids ahead of the disc perform a circular motion, which forms a trailing vortex ring (labelled TVR). The formation of TVR is also because of the corner flow between the disc and the rod. After $T_n = 4.0$, the DVR no longer grows and gradually becomes asymmetrical, as shown in Fig. 2e, f. During $T_n = 6.0$, DVR cannot keep complete attachment on the disc and becomes non-axisymmetric. If the disc continues to move for a sufficiently long time, DVR should separate from the disc and becomes a hairpin-shaped vortex structure [40].

In general, the occurrence of asymmetry is due to the growth of one perturbation, which causes the instability of the symmetrical flow. Moreover, an alternative mechanism is suggested to explain the occurrence of instability by Gao and Yu [18] and Jeon and Gharib [21]. They found that the vortex growth can actually exert a stabilizing effect on the growth of perturbation. In particular, Gao and Yu [18] found that when the JVRs no longer grow, the first secondary trailing vortex rolls up owing to the Kelvin-Helmholtz shear layer instability.

With the qualitative observation of DVR formation, we tend to investigate the circulation production mechanism. The circulation of DVR is calculated based on the PIV measurements. Figure 3 shows the variation of the dimensionless circulation Γ^*, defined as $\Gamma^* = \Gamma/(UD/2)$, against the non-dimensional time T_n. As shown in Fig. 3, the circulation evolution of DVR performs a rapid increase at the initial stage, and then slowly grows with the decreased growth rate after the initial stage until the circulation nearly no longer grows. The growth of DVR circulation satisfies the Logistic law originating from the biological populations. That is, the circulation evolution of DVRs includes an accelerated growth phase, a decelerated growth phase, and a saturation phase. This growth process is quite different from that of JVRs. For JVRs, their circulation exhibits a nearly linear increase with the non-dimensional time and can be estimated on the basis of the slug model [14, 19], despite that the overpressure at the exit of nozzle has a considerable contribution to the circulation of JVRs [23].

The motion of ambient fluids is largely attributed to the added-mass effects of DVR, which induces the Lagrangian drift [7, 27, 47]. As DVRs grow, their propagating velocity increases and the ambient velocity around DVRs also increases.

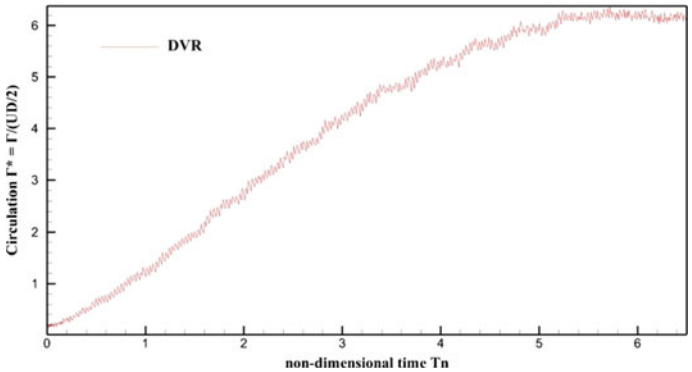

Fig. 3 Normalized circulation of DVR as a function of the non-dimensional time T_n. The variation of the dimensionless circulation Γ^*, defined as $\Gamma^* = \Gamma/(UD/2)$. The integral region for calculating the circulation of DVR is behind the disc

3.2 Lagrangian Analysis of the Formation of DVR

For JVRs, the onset of pinch-off coincides with the initial rollup of the secondary trailing vortex and the appearance of a trailing pressure maximum (TPM) behind the JVR [18, 25, 31]. Based on the Lagrangian analysis, O'Farrell and Dabiri [31] and Lawson and Dawson [25] identified the formation of secondary trailing vortex and appearance of TPM, respectively. Thus, the signals and changes of DVR formation brought by vortex pinch-off are investigated based on the Lagrangian analysis.

Figure 4 shows the contours of vorticity and FTLE for the cases of $U = 0.1\sin\left(\frac{\pi}{5.5}t\right)$ m/s, at six separate time instants $T_n = 1.0$, 2.0, 3.0, 4.0, 5.0, and 6.0. The forward-time and backward-time FTLE fields are represented in the form of contours ranging from white to red and white to blue. The ridges in forward-time and backward-time FTLE fields denote the repelling LCSs (r-LCSs) and attracting LCSs (a-LCSs). As shown in Fig. 4a, e, DVRs have grown with a sufficient size at $T_n = 1.0$ and the rear boundary of DVR (denoted by the r-LCS) is formed, however, the front boundary of DVR (denoted by the a-LCS) has not completed. In particular, a channel is observed between the r-LCS and a-LCS. This channel is referred to as the "flux window" and also observed by Yang et al. [49]. The vorticity flux is fed by the shear layer from this flux window. When $T_n = 3.0$, DVR further grows and still keeps axisymmetric characteristic. At this stage, there are no signals of the occurrence of vortex pinch-off. By $T_n = 4.0$, a closed boundary is composed by the r-LCS and a-LCS and the flux window is also closed. In fact, the r-LCS and a-LCS act as material barriers to prevent fluids across the LCSs entering the DVR. According to the analysis of Lawson and Dawson [25], the appearance of a-LCSs indicates the formation of a TPM, behind which there exists an adverse pressure gradient inhibiting vorticity transport crossing a-LCSs. As shown in Fig. 4d, the TPM indicted by the a-LCSs appears between the DVR and disc, thereby suggesting the onset of DVR pinch-off. Comparison of the flow patterns at $T_n = 4.0$ and $T_n = 5.0$ shows the size of DVR

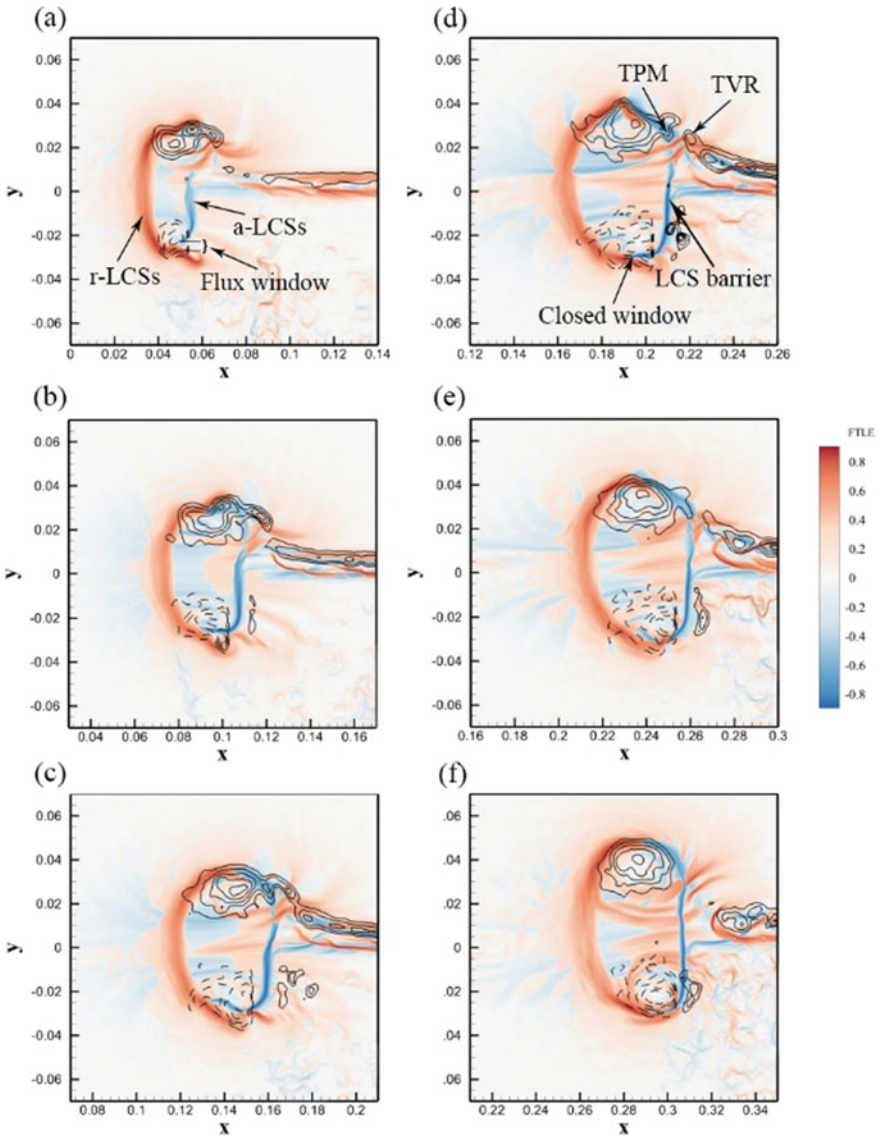

Fig. 4 (Colour online) Contours of the forward-time (white to red) and backward-time (white to blue) FTLE for DVRs at $T_n = 1.0$, 2.0, 3.0, 4.0, 5.0, and 6.0. **a**–**f** DVRs with $U = 0.1\sin(\pi/5.5\ t)$ m/s. Contours of vorticity are superimposed

determined by LCSs no longer grows and DVR becomes asymmetric, as shown in Fig. 4d–f. After DVR pinch off, the boundary of DVR still keep attachment with the disc without physical separation, as shown in Fig. 4d–f. For JVRs, they will physically separated from the trailing vortices after they pinch off. Thus, the pinch-off of DVR is one non-separated pinch-off but leads to the asymmetry of DVR.

By analysing kinematic genesis of vortex formation, David et al. [12] found that the hyperbolic LCSs defined by FTLE ridges actually define the advected bulk. In contrast, the elliptic LCSs have been shown to identify the closed boundary of the coherent Lagrangian vortex within which the fluid material remains as a coherent unit over a finite period of time [12, 20]. Thus, we tend to apply the concept of elliptic LCSs to analyse the kinematic genesis of DVR formation.

Based on the forward FTLE fields at $T_n = 5.0$, we detected the elliptic LCSs at this time, as shown in Fig. 5a. Then, the origin and evolution of the fluids enclosed by the elliptic LCS are investigated by backward advecting the fluids inside the elliptic LCS and forward advecting the material line of elliptic LCS. As shown in Fig. 5a, the advected elliptic LCSs at $T_n = 5.5$ and $T_n = 6.0$ still display robust Lagrangian coherence. The backward-advected positions of the material inside the elliptic LCS are shown in Fig. 5b–d. It is found that considerable fluids within the elliptic LCS come from the front of disc and are captured in the form of lobes.

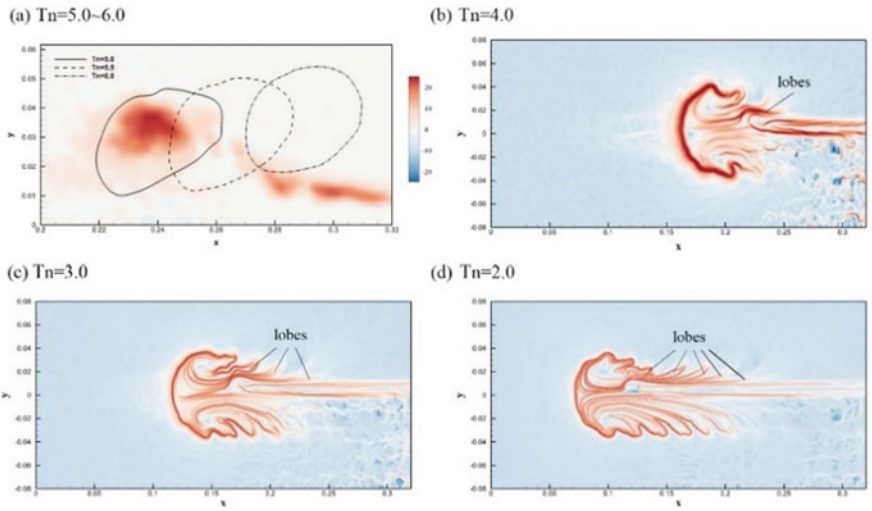

Fig. 5 (Colour online) **a** Elliptic LCS (solid line) extracted using the forward FTLE field at $T_n = 5.0$ shown in Fig. 4e. The background colour represents the instantaneous vorticity field at $T_n = 5.0$. The elliptic LCS at $T_n = 5.0$ is advected forward in time as material line to obtain the dashed and dash-dotted curves at $T_n = 5.5$ and $T_n = 6.0$, respectively. **b–d** Temporal tracer positions at $T_n = 4.0$, $T_n = 3.0$, and $T_n = 2.0$, by backward advection of the material inside the elliptic LCS at $T_n = 5.0$

4 Drag Generation Mechanism Owing to the Formation of DVR

As the fluid dynamic footprint of swimming and flying animals, the formation of vortex wake involves the unsteady aerodynamics of force generation. Thus, the instantaneous force associated with the balanced formation mode for DVRs is qualitatively investigated. According to the vorticity-moment theorem Wu [46], the force F generated by the ambient fluids on the immersed body in incompressible flow can be calculated by

$$F = -\frac{\rho}{2}\frac{d}{dt}\int_{V_\infty} \boldsymbol{x} \times \boldsymbol{\omega} \mathrm{dV} + \rho \frac{d}{dt}\int_{V_b} \boldsymbol{U} \mathrm{dV} \tag{4}$$

where V_b is the region occupied by the solid, V_∞ is the infinite unlimited space occupied jointly by the fluid and the solid, U is the velocity field, ω is the vorticity field, ρ is the density and x is the position vector. The first term on the right of equation indicates the force owing to the variation of fluid impulse, and the second term indicates the added-mass force generated by the variable motion of the body. This equation has a rigorous limitation that the control space V_∞ should be infinite unlimited. However, this equation demonstrates that the fluid forces are mostly contributed by the vortical region with compact vorticity. That *is*, in the presented study, the generation of fluid force is largely owing to the formation of DVR. As derived by Saffman [37], the impulse required to support the formation of DVR is given by

$$I = \frac{1}{2}\int_{V_{DVR}} \boldsymbol{x} \times \boldsymbol{\omega} \mathrm{dV} + \int_{S_{DVR}} \phi \boldsymbol{n} ds \tag{5}$$

where V_{DVR} is the region of DVR enclosed by the boundary S_{DVR} which is defined by the FTLE ridges, and ϕ is the velocity potential at the surface S_{DVR}. According to the Newton's third theorem, the axial fluid force generated by DVR formation is

$$F_{DVR} = \frac{dI}{dt} = \underbrace{\frac{1}{2}\frac{d}{dt}\int_{V_{DVR}} \boldsymbol{x} \times \boldsymbol{\omega} \mathrm{dV}}_{\text{Vortex impuls}} + \underbrace{\frac{d}{dt}\int_{S_{DVR}} \phi \boldsymbol{n} ds}_{\text{Vortex add}} \tag{6}$$

In fact, the two terms on the right of Eq. (6) indicate the contributions of vortex impulse and vortex added-mass, respectively (Fig. 6). In cylindrical coordinates, the first term can be rewritten by

$$\frac{1}{2}\frac{d}{dt}\int_{V_{DVR}} \boldsymbol{x} \times \boldsymbol{\omega} \mathrm{dV} \approx \frac{1}{2}\frac{d\Gamma}{dt} \times r + \frac{1}{2}\Gamma \times \frac{dr}{dt} \tag{7}$$

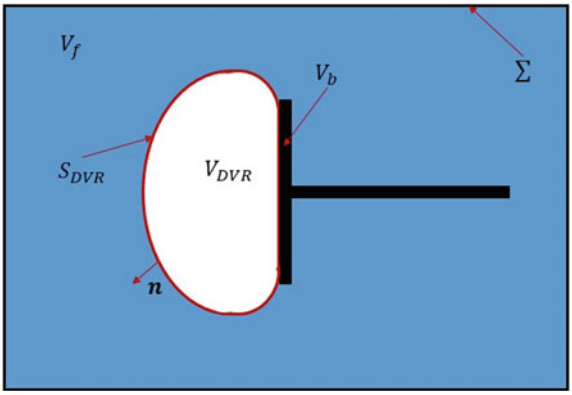

Fig. 6 (Colour online) Schematic of the definitions in the flow field

Based on the Lagrangian drift [7, 33], the axial coefficient of DVR added-mass (c_{DVR}) can be calculated by

$$c_{DVR} = \frac{1}{V_{DVR}U} \int_{S_{DVR}} \phi \boldsymbol{n} ds \tag{8}$$

Thus, the second term of Eq. (6) can be rewritten by

$$\frac{d}{dt} \int_{S_{DVR}} \phi \boldsymbol{n} ds = \frac{d}{dt} c_{DVR} \int_{V_{DVR}} u dV \tag{9}$$

Substituting Eqs. (7) and (9) into Eq. (6), one obtain

$$F_{DVR} = \underbrace{\frac{1}{2}\frac{d\Gamma}{dt} \times r}_{\text{circulation growth (F1)}} + \underbrace{\frac{1}{2}\Gamma \times \frac{d\mathrm{r}}{dt}}_{\text{vortex deformation (F2)}} + \underbrace{\frac{d}{dt} c_{DVR} \int_{V_{DVR}} u dV}_{\text{vortex added-mass (F3)}} \tag{10}$$

Equation (10) demonstrates that the generation of fluid force during DVR formation is attributed to three parts: the circulation growth rate (F1), the time-dependent deformation of vortex (F2), and the vortex added-mass effects (F3). Based on Eq. (10), one can well understand the drag generated by the starting motion of the disc, which was measured by Fernando and Rival [15, 16]. Owing to the accelerated growth of DVR circulation (F1) and the added-mass effect of the disc, the drag increases rapidly before it arrives the peak. Then, the drag decreases owing to the decelerated growth of DVR circulation (F1) until DVRs happen pinch-off. After DVRs pinch off, a slight increase of the drag is performed owing to the deformation of DVRs (F2) and the added-mass effects of DVRs (F3). These characteristics of drag evolution are dominated by the balanced formation mode of DVRs. Therefore, it is expected

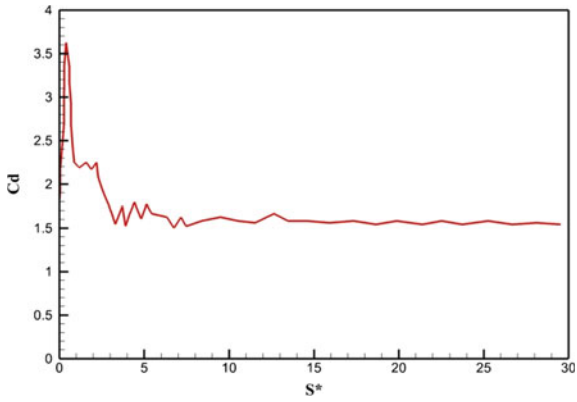

Fig. 7 Drag-coefficient histories for plates

that both the flapping-flight vortex loop and the aerodynamic forces evolution can be understood by the balanced formation mode of DVRs.

A model extracted from the experimental results of Fernando and Rival [16] shows the growth course of the drag coefficient for the plates in Fig. 7, which is a commonly tested model for discs. The drag of the disc quickly reaches a peak, then rapidly drops to a stable value and remains constant. Equation (10) can well explain this phenomenon. The accelerated growth of circulation growth rate (F1) and the vortex added-mass effects (F3) are the main causes of the peak at dimensionless distance $S^* = 0.4$. After that, as the growth of the DVR circulation (F1) slows, the drag decreases until the DVR pinches off at $S^* = 2.0$. After the DVRs are pinched off, the drag increases slightly due to the deformation of DVRs (F2) and the additional mass effect of the DVRs (F3), and then C_d decreases to 1.5 and become stable after $S^* = 5.0$.

5 Concluding Remarks and Discussion

In this paper, an experimental investigation on the formation of DVRs generated by the impulsive starting of a circular disc was performed. Experimental results demonstrated that the fluids roll up from the edge of disc to form a DVR. The DVR grows stably and symmetrically when $T_n < 4.0$. By $T_n > 4.0$, the DVR almost no longer grows and gradually becomes asymmetric. In addition, the growth rate of DVR circulation gradually decreases against the non-dimensional time T_n and the DVR circulation is found to satisfy the Logistic growth.

Lagrangian analysis of DVR formation were conducted by investigating the FTLE ridges and the elliptic LCSs. The evolution of FTLE ridges demonstrated that a closed boundary appears when $T_n{}^*$ exceeds approximately 4.0, thereby indicating the occurrence of vortex pinch-off. Beyond DVRs pinch off, the Lagrangian boundary still keeps attachment on the disc but the DVR becomes asymmetrical. In addition, fluid

entrainment is observed before DVR pinches off and fluid detrainment is observed after DVR pinches off by the form of dynamical lobes.

As two canonical vortex ring structures, JVRs and DVRs basically characterize the wake pattern of the biological propulsions. From the perspective of vortex ring family, DVRs and JVRs are both belong to the thin-core vortex rings and satisfy the classic dynamics of vortex rings. We explored that the generation of fluid force during DVR formation is attributed to three parts. In addition, and we would like to further investigate the force evolution during the impulsively starting disc based on Eq. (10).

Acknowledgements Financial support from the State Key Development Program of Basic Research of China (2014CB744802) is gratefully acknowledged. Besides, this work was also supported by NSFC Project (91441205).

References

1. Afanasyev YD (2006) Formation of vortex dipoles. Phys Fluids 18:037103
2. Akhmetov DG (2009) Vortex rings. Springer
3. Altshuler DL, Pan MPH, Lozano J (2009) Wake patterns of the wings and tail of hovering hummingbirds. Exp Fluids 46:835–846
4. Baik YS, Bernal LP, Granlund K, Ol MV (2012) Unsteady force generation an vortex dynamics of pitching and plunging aerofoils. J Fluid Mech 709:37–68
5. Benjamin T (1976) The alliance of practical and analytical insights into the non-linear problems of fluid mechanics. In: Applications of methods of functional analysis to problems in mechanics, vol 503, pp 8–28
6. Costello JH, Colin SP, Dabiri JO (2008) Medusan morphospace: phylogenetic constraints, biomechanical solutions, and ecological consequences. Invertebr Biol 127:265–290
7. Dabiri JO (2006) Note on the induced Lagrangian drift and added-mass of a vortex. J Fluid Mech 547:105–113
8. Dabiri JO (2009) Optimal vortex formation as a unifying principle in biological propulsion. Annu Rev Fluid Mech 41:17–33
9. Dabiri JO (2010) A wake-based correlate of swimming performance and foraging behaviour in seven co-occurring jellyfish species. J Exp Biol 213:1217–1225
10. Dabiri JO, Colin SP, Costello JH, Gharib M (2005) Flow patterns generated by oblate medusan jellyfish: field measurements and laboratory analyses. J Exp Biol 208:1257–1265
11. Dabiri JO, Gharib M (2005) Starting flow through nozzle with temporally variable exit diameter. J Fluid Mech 538:111–136
12. David MJ, Mathur M, Govardhan RN, Arakeri JH (2018) The kinematic genesis of vortex formation due to finite rotation of a plate in still fluid. J Fluid Mech 839:489–524
13. Dickinson MH (1996) Unsteady mechanism of force generation in aquatic and aerial locomotion. Am Zool 36:537–554
14. Didden N (1979) On the formation of vortex rings: rolling-up and production of circulation. J Appl Mech Phys 530:101–116
15. Fernando JN, Rival DE (2016a) On vortex evolution in the wake of axisymmetric and non-axisymmetric low-aspect-ratio accelerating plates. Phys Fluids 28:017102
16. Fernando JN, Rival DE (2016b) Reynolds-number scaling of vortex pinch-off on low aspect-ratio propulsors. J Fluid Mech 799R3:1–12
17. Gao L, Yu SCM (2010) A model for the pinch-off process of the leading vortex ring in a starting jet. J Fluid Mech 656:205–222

18. Gao L, Yu SCM (2012) Development of the trailing shear layer in a starting jet during pinch-off. J Fluid Mech 700:382–405
19. Gharib M, Rambod E, Shariff K (1998) A universal time scale for vortex ring formation. J Fluid Mech 360:121–140
20. Haller G, Beron-Vera FJ (2013) Coherent Lagrangian vortices: the black holes of turbulence. J Fluid Mech 731(R4):1–4
21. Jeon D, Gharib M (2004) On the relationship between the vortex formation process an cylinder wake vortex patterns. J Fluid Mech 519:161–181
22. Kelvin L (1880) Vortex statics. Phil Mag 10:97–109
23. Krueger PS (2005) An over-pressure correction to the slug model for vortex ring circulation. J Fluid Mech 545:427–443
24. Krueger PS, Gharib M (2003) The significance of vortex ring formation to the impulse and thrust of a starting jet. Phys Fluids 15:1271–1281
25. Lawson JM, Dawson JR (2013) The formation of turbulent vortex rings by synthetic jets. Phys Fluids 25:105113
26. Linden PF, Turner JS (2001) The formation of 'optimal' vortex rings, and the efficiency of propulsion device. J Fluid Mech 427:61–72
27. McPhaden CJ, Rival DE (2018) Unsteady force estimation using a Lagrangian drift-volume approach. Exp Fluids 59:64
28. Milano M, Gharib M (2005) Uncovering the physics of flat plates with artificial evolution. J Fluid Mech 534:403–409
29. Muijres FT, Johansson LC, Barfield R, Wolf M, Spedding GR, Heenstrom A (2008) Leading-edge vortex improves lift in slow-flying bats. Science 319:1250–1253
30. Onu K, Huhn F, Haller G (2015) LCS tool: a computational platform for Lagrangian coherent structures. Chaos 7:26–36
31. O'Farrell C, Dabiri JO (2010) A Lagrangian approach to identifying vortex pinch-off. Chaos 20:017513–017521
32. Pedrizzetti G (2010) Vortex formation out of two-dimensional orifices. J Fluid Mech 665:198–216
33. Peng JF, Dabiri JO (2008) An overview of a Lagrangian method for analysis of animal wake dynamics. J Exp Biol 211:280–287
34. Qin SY, Liu H, Xiang Y (2018) On the formation modes in vortex interaction for multiple co-axial co-rotating vortex rings. Phys Fluids 30:011901
35. Rayner JMV (1979) A vortex theory of animal flight. Part 1. The vortex wake of a hovering animal. J Fluid Mech 91:697–730
36. Rival D, Prangemeier T, Tropea C (2009) The influence of airfoil kinematics on the formation of leading-edge vortices in bio-inspired flight. Exp Fluid 46:823–833
37. Saffman PG (1992) Vortex dynamics. Cambridge University Press
38. Sallet DW (1975) Impulsive motion of a circular disk which causes a vortex ring. Phys Fluids 18:109–111
39. Shariff K (1992) Vortex rings. Annu Rev Fluid Mech 24:235–279
40. Shenoy AR, Kleinstreuer C (2008) Flow over a thin circular disk at low to moderate Reynolds numbers. J Fluid Mech 605:253–262
41. Shusser M, Gharib M (2000) Energy and velocity of a forming vortex ring. Phys Fluids 12:618–712
42. Shusser M, Rosenfeld M, Dabiri JO, Gharib M (2006) Effect of time-dependent piston velocity program on vortex ring formation in a piston/cylinder arrangement. Phys Fluids 18:033601–033611
43. Taylor GI (1953) Formation of a vortex ring by giving an impulse to a circular disc and then dissolving it away. J Appl Phys 24:104–105
44. Wang XX, Wu ZN (2010) Stroke-averaged lift forces due to vortex rings and their mutual interactions for a flapping flight model. J Fluid Mech 654:453–472
45. Wang XX, Wu ZN (2012) Lift force reduction due to body image of vortex for a hovering flight model. J Fluid Mech 709:648–658

46. Wu JC (1981) Theory for aerodynamic force and moment in viscous flows. AIAA J 19:432–441
47. Xiang Y, Lin HY, Zhang B, Liu H (2018a) Quantitative analysis of vortex added-mass and impulse generation during vortex ring formation based on elliptic Lagrangian coherent structures. Exp Therm Fluid Sci 94:295–303
48. Xiang Y, Qin SY, Liu H (2018b) Patterns for efficient propulsion during the energy evolution of vortex rings. Eur J Mech B Fluids 71:47–58
49. Yang AL, Jia LB, Yin XZ (2012) Formation process of the vortex ring generated by an impulsively starting circular disc. J Fluid Mech 713:65–85

A Review of Supersonic Turbines Based on Constant Volume Combustion Cycle

Liangjun Su and Fengbo Wen

Abstract In this paper, in response to the current demand for new aerospace power in the aerospace field, thermodynamic performance and thermal efficiency advantages of existing constant volume combustion cycles are reviewed. The main challenge in the practical implementation of Pressure Gain Combustion (PGC) into gas turbines and aero-engine is the lack of turbomachinery that can efficiently harvest work from the PGC exhaust gas. Therefore, this paper analyzes the supersonic inflow conditions with pressure, temperature and velocity pulsations at the outlet of the detonation combustion chamber, and puts forward the difficulties brought by the inflow conditions to the design of the turbine cascade. Secondly, this paper analyzes the aerodynamic characteristics of turbine cascade passage under supersonic inlet conditions, analyzes the influence of channel shock waves on aerodynamic losses, and expounds the importance of turbine under supersonic inlet conditions in detonation combustion cycle.

Keywords Constant volume combustion cycle · PGC · Detonation combustion inflow condition · Supersonic turbine

Nomenclature

List of Symbols

β_c Pressure ratio of compressor [–]
α Dimensionless heat absorption [–]
Q Heat [J]

L. Su · F. Wen (✉)
Harbin Institute of Technology, Harbin, China
e-mail: fengbo@hit.edu.cn

L. Su
e-mail: suliangjunhit@qq.com

Z. Jing and X. Zhan (eds.), *Proceedings of the International Conference on Aerospace System Science and Engineering 2020*, Lecture Notes in Electrical Engineering 680,
https://doi.org/10.1007/978-981-33-6060-0_12

ρ	Density [kg/m^3]
P	Pressure [Pa]
s	Entropy [J/(mol K)]
η_{th}	Thermal efficiency [–]
W	Output work [J]
H	Enthalpy [J/mol]
C_P	Specific heat capacity at constant pressure [J/(kg K)]
C_v	Specific heat capacity at constant volume [J/(kg K)]
T	Temperature [K]
γ	Ratio of specific heats [–]
M	Mach number [–]
u	Axial velocity [m/s]
a	Speed of sound [m/s]
β	Shock angle [°]
θ	Airflow angle [°]
R	Gas constant [J/(mol K)]
$L_{i,T}$	Flange work [J]
ζ	Correction coefficient

1 Introduction

Traditional aero-engines use Brayton cycle based on isobaric combustion. With the development of technology, its cycle efficiency has been greatly improved [1]. Although the technology and efficiency of aero-engine have been improved rapidly, a serious problem has been exposed. The efficiency of aero-engine is close to the limit of Brayton cycle, which means that the future development of aero-engine must make a breakthrough in thermal cycle. The quasi-constant volume combustion cycle based on detonation combustion [2] can not only improve the efficiency of aero-engine [3, 4], but also reduce the number of turbines and compressors because of the self-pressurization function of detonation combustor, So that the power plant is more compact and the manufacturing cost is significantly reduced [5], so as to increase the thrust-weight ratio [6]. As a result, the performance of aero-engine has been greatly improved, which meets the urgent demand of new air-to-space power with high thrust, large thrust-to-weight ratio and high speed in aviation field.

Engines based on detonation combustion cycles are mainly used in hypersonic aircraft, including rockets, missiles and drones, as well as new aerospace aircraft [7, 8]. Replacing the isobaric combustor of a traditional gas turbine engine with a detonation combustor is expected to significantly improve the engine performance [9]. This new type of propulsion device formed by the combined turbine of the detonation combustion chamber is called the detonation turbine engine. As a working mode of air-breathing detonation engine, detonation turbine engine can produce large thrust at low turbocharging ratio. As a result, the number of stages of compressors

and turbines can be reduced. This kind of combustion chamber is smaller in size, simpler in structure and can produce higher thrust-to-weight ratio. However, the flow conditions at the exit of the detonation combustor are very complex, and high temperature, supersonic and high frequency pressure, temperature and flow angle oscillations [10] are typical characteristics, which brings great difficulties for the turbine to achieve efficient power extraction. At present, the research on the design method of high-efficiency turbine after rotary detonation combustion is very few, and some studies have shown that if the existing conventional turbine design is adopted under this condition, the efficiency of turbine components will be less than 30% [11]. This will deplete the benefits of turbocharged combustion. Therefore, the development of high efficiency energy-power conversion turbine under the extreme conditions of high temperature, supersonic, high frequency pressure and temperature oscillation has become the key to the application of rotary detonation combustion in gas turbine power equipment.

The practical application of isovolumetric combustion cycle in aero-engine is to replace the traditional isobaric combustion chamber with self-pressurized combustion chamber (PGC). Because the propagation velocity of detonation wave is very fast (above 1000 m/s) [12], the product after combustion wave is too late to expand, and the detonation combustion process is close to isovolumetric combustion, so the detonation cycle process is similar to that of isovolumetric cycle [13]. The high thermal efficiency of the cycle based on detonation combustion is mainly due to the decrease of entropy in the combustion process, and another important reason is that the highest temperature of the cycle is higher than that of the Brayton cycle (that is, the average endothermic temperature is high). However, the main challenge facing the practical application of PGC in gas turbines and aero-engines is the lack of turbine machinery that can effectively obtain work from PGC exhaust [14].

Detonation turbine engine can be divided into two categories, namely rotary detonation turbine engine [10, 15, 16] and pulse detonation turbine engine [17–19]. The rotary detonation turbine engine uses the rotary detonation combustion chamber instead of the traditional isobaric combustion chamber, and the predetonation tube is often used to initiate the detonation wave after the fuel is premixed in advance or mixed in the combustion chamber; one or more detonation waves rotate and propagate along the circumferential direction at the head of the combustion chamber; the high temperature and high pressure products after combustion are rapidly ejected almost along the circular axis by expansion. In addition, the oblique shock wave and contact discontinuity are accompanied by the oblique detonation wave. In the process of detonation wave propagation, the combustible mixture is continuously charged into the combustion chamber from the head, and a triangular unburned propellant is formed in front of the detonation wave for detonation wave combustion. The pressure of the combustion product after the detonation wave decreases rapidly under the action of the sparse wave, the pressure in most areas behind the detonation wave is less than the injection pressure, and the premixed combustible gas begins to fill into the combustion chamber, which provides fresh fuel for the next cycle of detonation wave propagation [20–22]. Pulse detonation turbine engine replaces the traditional isobaric combustion chamber with pulse detonation combustion chamber [23].

Compared with rotary detonation combustion, it requires continuous pulse initiation and discontinuous fuel input, but it has high specific impulse and high efficiency. When the frequency is high enough, the thrust is also continuous. Its flying Mach number can reach 6 or more. After study [24] under the same design parameters, after the traditional turbojet engine uses the pulse detonation main combustion chamber, the engine unit thrust can be increased by 8.33%, and the fuel consumption can be reduced by 5.7%. Under non-design point conditions, compared with the traditional turbojet engine, the pulse detonation turbojet engine can increase the thrust by 2–6.5%, reduce the fuel consumption by 3.1–7.6%, and increase the unit thrust by 2.4–7.8% [25] (Fig. 1).

The exhaust flow of detonation combustor has high temperature, supersonic and high frequency pressure, temperature and flow angle oscillations characteristics [26]. This pressure, temperature, velocity fluctuation and supersonic outflow will have a great impact on the thermal-power conversion process of the turbine. Bring a lot of aerodynamic loss. When traditional turbine is directly combined with isovolumetric combustion chamber, its efficiency is low [27, 28]. In order to solve this problem, there are two ways. The first is to design a mixing chamber so that the incoming flow can be applied to traditional turbines. For example, Andrus et al. [29, 30] adopts a mixing chamber and an isolation section, and proposes to connect a mixing chamber at the exit of the detonation combustion chamber, so that the forward flow of the turbine is more uniform and the temperature is relatively low. The traditional turbine can adapt to this incoming flow condition, but this method will bring a lot of problems, first of all, it makes the structure of the whole engine more complex, and secondly, because the air flow in the mixer will decelerate and pressurize, it will increase the pressure in the mixing chamber and easily cause reflux. Another method is to focus on the special turbine design, so as to increase the flow rate and achieve the goal of obtaining more work efficiently [31]. Aiming at the second method, this paper puts forward the difficulties and key points in the design of supersonic turbine to adapt to the incoming flow conditions actively.

In order to design a high-efficiency supersonic turbine, we need to analyze the aerodynamic characteristics of the existing supersonic turbine cascade channel. For

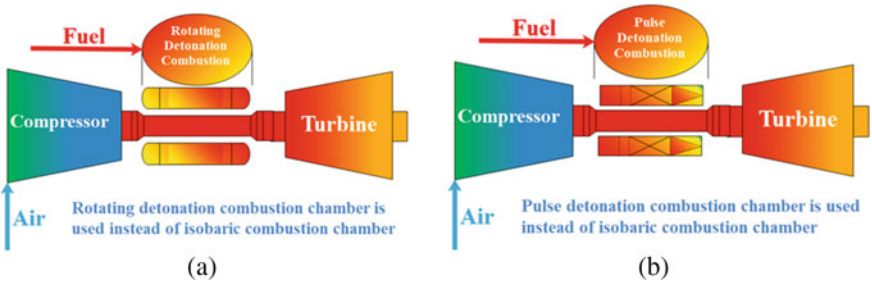

Fig. 1 Schematic diagram of rotary detonation turbine engine (**a**) and pulse detonation turbine engine (**b**)

supersonic flow, the interference of turbine blades is encountered. Shock waves will be generated at the entrance and channel of the turbine cascade, as well as at the trailing edge [32]. We need to analyze and evaluate the losses caused by the shock wave and the interaction between the shock wave and the boundary layer [33]. The method of minimum entropy increase is used to design supersonic turbine cascades so as to improve aerodynamic efficiency. We need turbine machinery that can effectively extract power from PGC outflows [26]. Under the condition of high efficiency supersonic flow, the downward turbine cascade can efficiently extract work and supply the compressor, in addition, it can also accelerate the expansion of the air flow, convert most of the internal energy into kinetic energy, and produce large thrust. To meet the needs of higher thrust and more efficient aerospace power plant.

2 Performance Advantage of Constant Volume Combustion Cycle

2.1 High Cycle Efficiency of Constant Volume Combustion

The Brayton cycle can be simplified into four reversible processes: adiabatic compression, constant pressure heating, adiabatic expansion and constant pressure exotherm (Fig. 2). With the development of technology, the efficiency and performance of gas turbine and aero-engine based on Brayton cycle have made great progress, but the efficiency of gas turbine needs to be improved. In the future, the development of gas turbine and aero-engine must make a breakthrough in the thermal cycle. In contrast, the application of isovolumetric combustion cycle in future power plants has great potential, while isovolumetric combustion cycle can be simplified into four processes: Isentropic compression, isovolumetric combustion, Isentropic expansion and isobaric heat release (Fig. 3). In ideal condition, its efficiency is higher

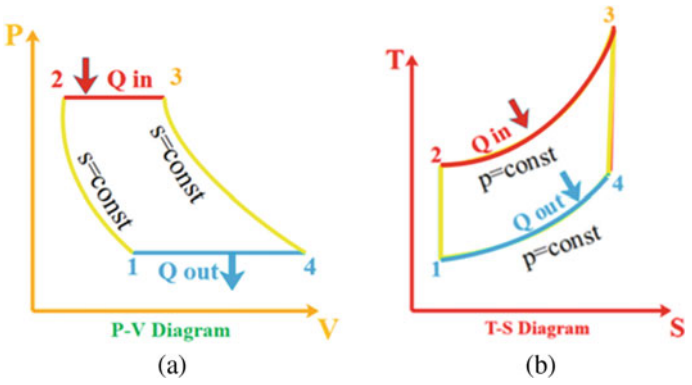

Fig. 2 P-V diagram (**a**) and T-S diagram (**b**) of Brayton cycle

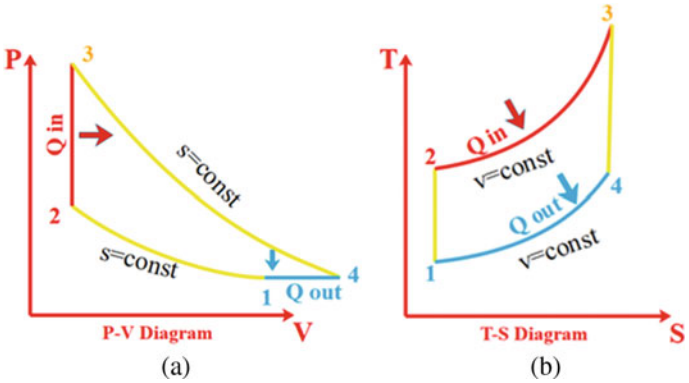

Fig. 3 P-V diagram (**a**) and T-S diagram (**b**) of constant volume combustion cycle

than that of Brayton cycle. Many scholars have carried on the thermodynamic analysis to the constant volume combustion cycle and put forward the advantage of the constant volume combustion cycle compared with other cycles. We have made a simple summary of it (Table 1).

It can be seen from Table 1 that in Ref. [34], under the condition of compressor pressure ratio 16 and the same heat absorption, the thermal efficiency of the engine

Table 1 Thermodynamic analysis of constant volume combustion cycle

Researcher	Conditions	Thermal efficiency	Specific fuel consumption	Specific power	Entropy production
Li et al. [34]	$\beta_c = 16$ Same heat absorption	+15.4% (compared with Brayton cycle)	−13.5% (compared with Brayton cycle)	+15.3% (compared with Brayton cycle)	
Braun et al. [35]	$\alpha = Q\rho_1/P_1 = 27.28$ (dimensionless heat absorption)	66.5% (Humphrey) 64.3% (FJ) 70% (ZND)		0.709 MJ/kg 0.834 MJ/kg 2.080 MJ/kg	3.08 kJ/(kg K) 3.12 kJ/(kg K) 3.12 kJ/(kg K)
Lu et al. [36]	Humphrey (7:1) Otto cycle (10:1) Brayton cycle (10)	55.0% (pressure ratio at the same thermal efficiency)	−28.02% (compared to conventional engine)	From 3.34 to 19.01 kW/h (pressure ratio 2–10)	
Sousa et al. [22]	Numerical simulation	+5% (higher than the deflagration engine)		20% performance improvement	

(continued)

Table 1 (continued)

Researcher	Conditions	Thermal efficiency	Specific fuel consumption	Specific power	Entropy production
Wu et al. [37]	Theoretical analysis	The Humphrey and Brayton cycles			
Andriani et al. [38]	Theoretical analysis	Produce a thermal efficiency as high as 40% ($\pi = 3$)	−15.65% (lower than the cycle)	Strong ability to do work	
Brophy [39] one approach to substantially improving gas turbine thermal efficiency is to replace the nearly constant pressure combustion process					

with constant volume combustion cycle is 15.4% higher than that of Brayton cycle, and the fuel consumption is reduced by 13.5%. The unit thrust increased by 15.3%. Braun et al. [35] analyzed the three isovolumetric combustion cycles of Humphrey, FJ and ZND. The thermal efficiency is more than 60% and the entropy increase is less than 3.2 kJ/(kg K). Lu et al. [36] analyzed the change of thermal efficiency with different pressure ratio and found that the pressure required by the Humphrey cycle with constant volume combustion is smaller than that of the Otto cycle and Brayton cycle when the same thermal efficiency is achieved. Through numerical simulation, Sousa et al. [22] found that the efficiency of rotary detonation turbine engine is improved by about 5%. The data in Table 1 show that the constant volume combustion cycle has some advantages over the traditional Brayton cycle in thermal efficiency. in order to analyze the reasons, we use the pressure diagram and temperature entropy diagram of the two cycles to explain this phenomenon.

According to the pressure volume diagram and temperature entropy diagram of the traditional Brayton cycle and isovolumetric combustion cycle, we can see that the two cycles do the same work. Ideally, the Isentropic expansion converts the internal energy into kinetic energy and mechanical energy. But the heating mode is different, the Brayton cycle uses isobaric heating, which has a larger entropy increase (which will be explained later), and the isovolumetric combustion cycle uses isovolumetric heating with low entropy and high thermal efficiency (Fig. 4).

Limiting the performance improvement of aero-engines and gas turbines is the turbine inlet temperature and pressure ratio, so we choose the two kinds of cycle turbine inlet temperature and pressure ratio conditions are the same, that is, the maximum temperature (heat absorption) of the two cycles is the same, and the compression ratio is the same. Finally, the isobaric expansion to the ambient temperature ends the whole cycle [40].

The thermal efficiency in a cycle is:

$$\eta_{th} = \frac{W_{out}}{Q_{in}} = \frac{Q_{out} - Q_{in}}{Q_{in}} \tag{1}$$

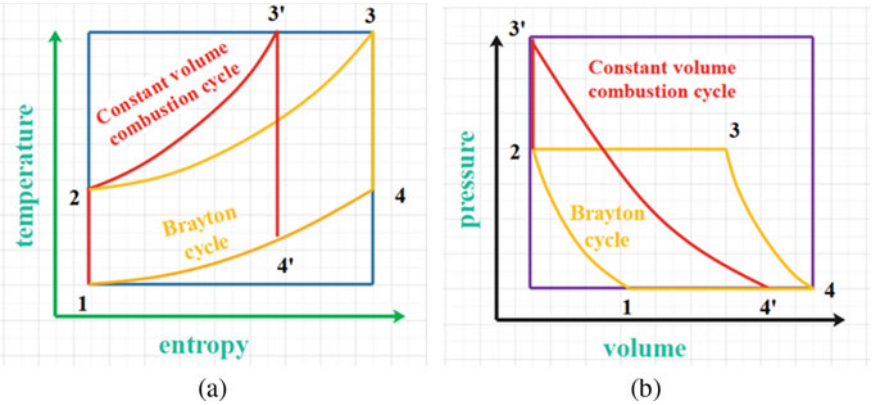

Fig. 4 Schematic diagram of isovolumetric combustion cycle (**a**) and Brayton cycle (**b**)

In a thermal cycle, output power equals the net heat flux through the engine, for constant volume combustion cycles:

Heat released (unity mass flow rate): $Q_{out} = H_{4'} - H_1 = C_p(T_{4'} - T_1)$

Heat introduced (unity mass flow rate): $Q_{in} = H_{3'} - H_2 = C_v(T_{3'} - T_2)$

$$\eta_{th} = \frac{W_{out}}{Q_{in}} = \frac{Q_{in} - Q_{out}}{Q_{in}} = \frac{C_v(T_{3'} - T_2) - C_p(T_{4'} - T_1)}{C_v(T_{3'} - T_2)} = 1 - \gamma\frac{(T_{4'} - T_1)}{(T_{3'} - T_2)} \tag{2}$$

where γ is the ratio of the specific heat respectively at constant pressure and constant volume. In an ideal cycle the compression and expansion respectively in the compressor and turbines are adiabatic and isentropic, so:

$$T_2 = T_1\left(\frac{P_2}{P_1}\right)^{\frac{\gamma-1}{\gamma}};\ T_{4'} = T_{3'}\left(\frac{P_{4'}}{P_{3'}}\right)^{\frac{\gamma-1}{\gamma}} \tag{3}$$

From the state equation of a perfect gas (PV = RT) and considering that the combustion occurs at constant volume it follows:

$$\frac{P_{3'}}{T_{3'}} = \frac{P_2}{T_2} \tag{4}$$

Indicating with β_c the pressure ratio p2/p1, from Eqs. (2) and (3) we have

$$P_{3'} = P_1\frac{T_{3'}}{T_1}\beta_c^{\frac{1}{\gamma}} \tag{5}$$

From Eqs. (2) and (4):

$$T_{4'} = T_{3'}\left[\frac{1}{(T_{3'}/T_1)\beta_c^{\frac{1}{\gamma}}}\right]^{\frac{\gamma-1}{\gamma}} \tag{6}$$

Substituting Eq. (5) into Eq. (1) and rearranging yields:

$$\eta = 1 - \frac{\gamma}{T_{3'}/T_1}\left\{\frac{T_{3'}/T_1\left(\left[\frac{1}{(T_{3'}/T_1)\beta_c^{\frac{1}{\gamma}}}\right]^{\frac{\gamma-1}{\gamma}}\right) - 1}{1 - \frac{\beta_c^{(\gamma-1)/\gamma}}{T_{3'}/T_1}}\right\} \tag{7}$$

And for the Brayton cycle, because 1–2 processes are Isentropic processes, 2–3 are isobaric heating processes, 3–4 are Isentropic expansion processes, and 4–1 are isobaric processes, so the relationship between Isentropic processes and isobaric processes can be obtained.

$$\frac{T_2}{T_1} = \left(\frac{P_2}{P_1}\right)^{\frac{\gamma-1}{\gamma}},\ \frac{T_3}{T_4} = \left(\frac{P_3}{P_4}\right)^{\frac{\gamma-1}{\gamma}} = \left(\frac{P_2}{P_1}\right)^{\frac{\gamma-1}{\gamma}} \tag{8}$$

By introducing the pressurization ratio, the thermal efficiency of the Brayton cycle is obtained.

$$\frac{P_2}{P_1} = \beta_c,\ \eta_{th} = 1 - \frac{1}{\beta_c^{\frac{\gamma-1}{\gamma}}} \tag{9}$$

It can be seen from this formula that the temperature difference between 4 point and 1 point is much larger than that between 4′ point and 1 point, so the difference between isobaric specific heat capacity and isovolumetric specific heat capacity can be ignored. Therefore, it is concluded that the efficiency of the isovolumetric cycle is greater than that of the Brayton cycle based on isobaric heating.

2.2 *Large Net Output Work of Constant Volume Cycle*

Ideally, we can analyze the relationship between the net output work of the two cycles, and we assume that the heat absorption is the same, as shown in Fig. 5.

Among them, the pink shadow part is the net output work of the isovolumetric combustion cycle, and the green shadow part is the net output work of the Brayton cycle. Our premise is that the heat absorption is the same, that is, the area enclosed by A–1–2–3–4–B is the same as that surrounded by A–1–2–3–4–C, as can be seen from Fig. 5. The heat release of isovolumetric combustion cycle is obviously smaller than that of Brayton cycle, so the area of pink shadow is larger than that of green shadow,

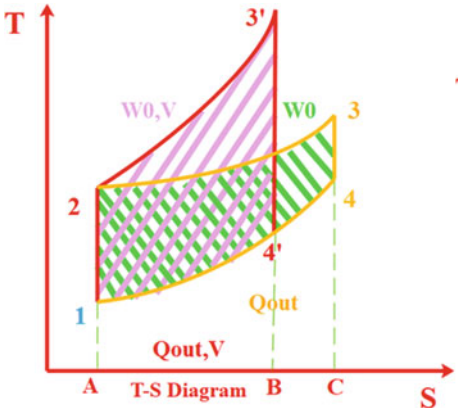

Fig. 5 Schematic diagram of net output power of isovolumetric combustion cycle and Brayton cycle

that is, the net output work of isovolumetric cycle is larger than that of traditional Brayton cycle. So in order to achieve the same turbine inlet conditions of the Joule cycle, the Humphrey cycle (constant volume combustion cycle) only needs to add less pressure to the compressor. As a result, the Humphrey cycle provides a potential surge in specific power and cycle efficiency. In order to obtain more power and economic benefits, the turbine efficiency should be higher than a certain threshold set by the increase of combustion chamber pressure and turbine entry temperature.

To sum up, the constant volume combustion cycle has obvious advantages in theory, with high thermal efficiency and large specific power [41]. And in the case of the same heat absorption, the net output power of the constant volume combustion cycle is large. To achieve the same turbine inlet conditions, only the compressor supercharging ratio is smaller. In other words, if we require the same work output, the Isentropic efficiency of the turbine can be further reduced. If we can further improve the Isentropic efficiency of the turbine cascade under this incoming flow condition, the work capacity and thrust-to-weight ratio of the aero-engine based on this isovolumetric cycle will be further improved.

3 Based on the Inlet Condition of Supersonic Flow Turbine in Detonation Combustion

Detonation combustion is a periodic intense combustion, and this combustion will make the exit of the detonation combustion chamber supersonic outflow, and its impact on the turbine is very strong [42]. In addition, the exit of the detonation combustion chamber has the fluctuation characteristics of high frequency pressure, temperature and velocity, and the air temperature at the exit is very high. Because of

Fig. 6 Based on the inlet condition of supersonic turbine under the condition of rotating detonation

the supersonic flow, in the case of blade disturbance, a shock wave will be generated in the turbine cascade channel, coupled with the interaction between the shock wave and the boundary layer [43], which further aggravates the turbine inlet conditions. This brings difficulties to the design of turbine cascades and blade profiles under supersonic flow conditions, in addition to the need to reduce the effect of shock waves, reduce aerodynamic losses and improve efficiency. The cooling and strength of the blade also need to be considered. The turbine inlet conditions can be briefly summarized in Fig. 6.

Here we analyze the difficulties in the design of supersonic turbine cascades caused by channel shock waves, pressure pulsations at high frequencies, and incoming flow conditions at high temperatures. The related models are established.

3.1 Leading Edge Bow Shock Model

Under the condition of supersonic flow, a bow shock wave will be formed in front of the arc leading edge of the supersonic turbine cascade, which is equivalent to two oblique shock waves [32] as shown in Fig. 7, the correction coefficient ζ is introduced here. The arc tangent of the leading edge of the turbine blade is passed through the midpoint of the bow shock wave, and the angle between the arc and the middle arc is θ, as the deflection angle of the incoming flow, and the oblique shock angle is β, making use of this simplified relationship. It also facilitates the calculation of the reflection and propagation of shock waves in the channel (see 4.1).

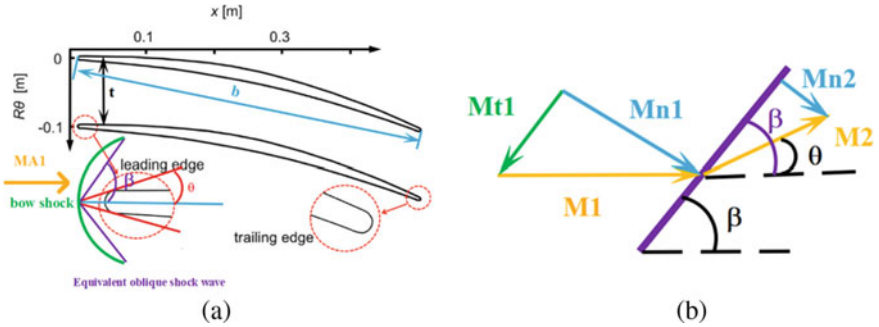

Fig. 7 Leading edge shock model (**a**) and diagrams of oblique shock calculation (**b**)

$$M_{n,1} = \frac{u_1}{a_1} = M_1 \sin\beta \tag{10}$$

$$M_{n,2} = \frac{u_2}{a_2} = M_2 \sin(\beta - \theta) \tag{11}$$

The bow shock wave is equivalent to an oblique shock wave, and the correction coefficient needs to be introduced.

$$M_{n,2}^2 = \zeta_1 \frac{1 + \left[(\gamma - 1)/2\right] M_{n,1}^2}{\gamma M_{n,1}^2 - (\gamma - 1)/2} \tag{12}$$

$$\frac{P_2}{P_1} = \zeta_2 \left(1 + \frac{2\gamma}{\gamma + 1}\left(M_{n,1}^2 - 1\right)\right) \tag{13}$$

Because this assumption will inevitably bring some errors, the correction coefficients ζ_1 and ζ_2 are introduced to obtain the Mach number loss and pressure change caused by bow shock wave. Here, ζ_1 is smaller than 1, and ζ_2 is larger than 1, because the attached oblique shock wave is generally a weak shock wave, while the bow shock wave is generally an detached shock wave, so the correction coefficient is greater than 1 when it is equivalent to an oblique shock wave.

3.2 High Frequency Pressure Fluctuation and Noise

As mentioned earlier, the study shows that the outlet of the constant volume combustion chamber has the pulsation of temperature, pressure and velocity, which will be greatly reduced in the first stage turbine, which makes the turbine work extraction more efficient and reasonable. The design of the first-stage turbine cascade is particularly important. The study shows that the pressure pulsation frequency at the exit of the constant volume combustion chamber is of the order of kilohertz [44], but the frequency range is different according to different studies. Table 2 is the conclusion

Table 2 Supersonic turbine inlet pressure pulsation

Researcher	Research methods/conditions	Peak pressure	Pressure pulsation frequency (KHz)
Sun et al. [45]	Numerical simulation Roe-FDS	5.05 MPa	7.766
Anand et al. [46]	Experimental	Pressure gain of 13–55 across the wave	Single wave: 3.7 Dual wave: 6.1
Roy et al. [47]	C_2H_4-O_2 mixture at normal condition	33.3 atm	Above 1 and very intense
Rasheed et al. [18]	Experimental	50 psig	Intense pressure pulsation
Jonathan et al. [48]	Experimental	Up to 17 atm	Intense pressure pulsation
Welsh et al. [21]	Experimental (Turbine T63)	Higher total inlet pressure (compared with Brayton cycle)	8.6
Liu et al. [49]	Numerical simulation	Higher total inlet pressure (compared with Brayton cycle)	Up to 10 kHz
Braun et al. [50]	Numerical simulation	7 MPa	2.600
Xue et al. [51]	Experimental	23 bar	7.732

drawn by some researchers. It can explain the high-frequency pressure pulsation pressure at the exit of the detonation combustor, that is, the inlet of the supersonic turbine.

We can see from Table 2 that the pressure at the exit of the detonation combustor obtained by either numerical simulation or experiment is very high, and there is a high frequency pressure fluctuation and Oscillating flow sweep of the order of magnitude of kHz, which is a great test for the supersonic turbine. According to the frequency spectrum analysis of pressure, we can know that the frequency of pressure pulsation is high, and this high-frequency pulsation will bring noise problems. At the same time, this high-frequency pressure pulsation will cause fatigue of metal materials. Coupled with the thin leading edge and trailing edge of supersonic turbine, it is easy to cause fatigue fracture, which puts forward a more severe test for the design of turbine. At present, there are two solutions. The first is to set up a mixing chamber in front of the turbine, which aims to reduce the pressure and the pulsation of speed and temperature, so as to achieve the conditions that the turbine can bear. The second method is to further improve the design level of the turbine to adapt to this incoming flow condition. According to the method of minimizing entropy increase of supersonic turbine cascades proposed in Sect. 4.1 below, it is necessary to reduce the thickness of the leading edge of the blade, and the pulsation of flow pressure proposed by this section will cause metal fatigue, and it is necessary to improve the strength of the blade, that is, the leading edge of the blade should not be too thin. Therefore, it is necessary to balance the contradiction between the two.

3.3 High Temperature Inflow Condition

At present, we not only know that the exit of detonation combustion chamber (isovolumetric combustion chamber) has the fluctuation of pressure, velocity and temperature, but also because this kind of detonation combustion chamber uses the self-pressurization function of detonation wave, which will bring a great increase in temperature. According to the current research, the temperature at the exit of the detonation combustor, that is, the supersonic turbine inlet, can reach 2000 K and above (Table 3).

Assuming that the detonation combustion chamber model is as follows, and assuming that its pressurization function is realized by pure isovolumetric combustion, then according to the relationship between pressure and temperature in the isovolumetric process (Fig. 8).

According to the relationship of isovolumetric combustion process and Clapeyron equation PV = RT, there are:

$$\frac{T_B}{T_A} = \frac{P_B}{P_A} \tag{14}$$

Then, according to the temperature and pressure at the inlet of the combustion chamber, as well as the maximum pressure of the combustion chamber, we can know the temperature at the exit of the combustion chamber. According to the study, it is found that the outlet temperature can reach 2000 K and above. At the present

Table 3 Incoming flow temperature conditions

Researcher	Research methods/conditions	Peak temperature (K)
Sun et al. [45]	Numerical simulation Roe-FDS	3480
Roy et al. [47]	C_2H_4-O_2 mixture at normal condition	3937
Jonathan et al. [48]	Experimental	3000
Welsh et al. [21]	Experimental (Turbine T63)	2350
Vinha et al. [52]	Numerical simulation	2500
Braun et al. [50]	Numerical simulation	3600
Braun et al. [35]	The theoretical analysis	2550
Eric et al. [53]	The theoretical analysis	Above 2000
Nordeen et al. [54]	The theoretical analysis	Above 2000

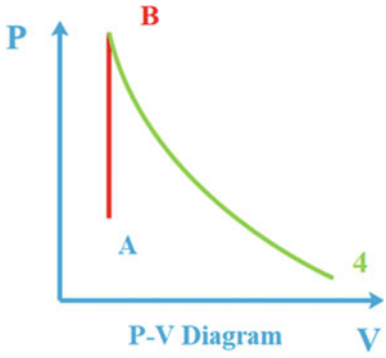

Fig. 8 Constant volume combustion chamber model

stage, the highest temperature that our superalloy can bear is about 1400 K, so the high temperature at the outlet of the isovolumetric combustion chamber brings some difficulties to the design and cooling of turbine cascades. In addition, in order to improve the aerodynamic performance, the thinner the turbine leading edge is, the more likely it is to be ablated, so the cooling of supersonic turbine blades [55] is also a key problem to be studied.

4 Aerodynamic Characteristics of Turbine Cascade Passage Under Supersonic Flow

We know that the biggest problem of isovolumetric combustion cycle at this stage is the lack of corresponding efficient turbines to extract work, so it is necessary for us to study the flow characteristics of turbine cascades under the condition of supersonic flow at present. To provide some reference for the design of more efficient turbines.

4.1 Channel Shock Model

When the supersonic flow encounters the interference of the turbine blade, the shock wave will be generated at the entrance of the cascade passage. Of course, the type and position of the inlet shock wave are different for different shapes of turbine blades. At present, the blade profiles of turbine cascades under supersonic flow can be divided into the following two categories, one is impulse supersonic flow condition [56], and the other is precompressed blade profile under supersonic flow condition [54]. The common characteristics of the two types of blades are that the leading edge and trailing edge are thin, and the cascade channel converges at first and then expands. The purpose is to obtain work that meets certain conditions while minimizing the interference to the air flow, reducing the flow loss and improving the aerodynamic

Table 4 Passage shock wave

Researcher	Research methods	Passage shock wave	Loss
Sousa et al. [31]	The method of characteristics The numerical simulation	Leading edge shock Reflected shock Trailing edge shock	Entropy generated by the supersonic passage was reduced by 15% (the optimized)
Liu et al. [57]	The numerical simulation	Leading edge shock waves	Total pressure loss is 11.7%
Paniagua et al. [58]	Conventional subsonic turbines Inlet Mach number of 3.5	Leading edge shock Reflected shock Trailing edge shock	Up to 80% total pressure loss (with typical pressure losses from inlet to outlet of about 5% in Brayton)
Sousa et al. [59]	The numerical simulation		Up to 14.8% total pressure loss

efficiency. The difference is that the impulse blade profile is mostly symmetrical blade profile, which is designed by multi-arc design method, while for the pre-compressed blade profile, it borrows the wedge shape of the inlet, mostly the wedge shape or the front stage cascade shape of the compressor. The channel shock wave will bring a large total pressure loss, and the shock wave will lead to the deceleration of the air flow. Many scholars use the method of numerical simulation to study the channel shock wave and its related loss (Table 4).

It can be seen from Table 4 that if the subsonic turbine cascade is used, the loss can reach more than 80%, so it is necessary to design a supersonic cascade suitable for incoming flow, but the shock wave problem will also bring more than 11.7% of the total pressure loss.

The passage shock wave will bring a lot of problems, the airflow through the shock wave will produce a large total pressure loss, and its airflow velocity will decrease, resulting in momentum loss and energy loss, resulting in the decrease of engine thrust and the work capacity of the airflow. Coupled with the interaction between the shock wave and the boundary layer, the separation of the boundary layer will be accelerated. The turbulence is enhanced, in addition, the shock wave will also lead to viscous heating, resulting in an increase in the wall temperature of the turbine blade.

Due to the action of the blunt body at the leading edge of the turbine blade, most of the shock waves produced at the entrance of the turbine cascade channel are bow shock waves, which will extend into the turbine cascade channel, so from a common sense point of view, in order to reduce the loss, although we want to reduce the number of shock waves in the channel, the less the number of shock waves reflected in the channel, the better, so we come to the conclusion that the smaller the angle of the bow shock wave, the better. Therefore, under the condition of supersonic flow, the thinner the leading edge of the cascade is, the better.

But the design difficulties caused by this are also obvious. On the one hand, because the leading edge of the blade contacts the high temperature gas at the exit

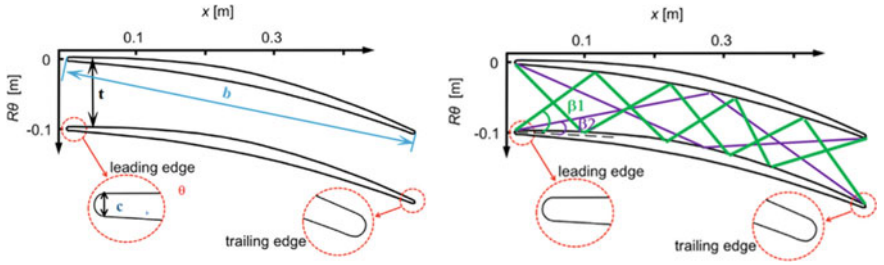

Fig. 9 Schematic diagram of supersonic turbine blade and different shock angles

of the combustion chamber, the leading edge of the turbine blade is easy to cause ablation, so it is necessary to take necessary active cooling measures, on the other hand, the strength of the leading edge of the blade has also been greatly tested. According to the study, it is found that the pulsation of temperature, pressure and velocity at the exit of the constant volume combustion chamber decreases especially in the first stage turbine, so the test of the first stage turbine will be very great.

With the continuation of the front bow shock model, if the equivalent oblique shock angle is smaller, the shock intensity of the oblique shock wave will be weaker, so in the design of supersonic turbine cascades, the deflection angle should be reduced as much as possible, so that the disturbance is smaller and the shock wave intensity is weaker. As shown in Fig. 9, the grid distance is t, the chord length is b, and the leading edge thickness is c.

As mentioned earlier, the smaller the oblique shock angle is, the weaker the shock wave intensity is, and the advantage is that the smaller the angle is, the less the reflection times of the turbine cascade with a certain chord length b is, the less the total shock number of the shock series is, and the smaller the entropy production is [31]. In other words, the aerodynamic efficiency of the turbine cascade channel is higher.

In the image above, the equivalent oblique shock waves produced by cascades with leading edge thicknesses of C_1 and C_2 ($C_1 > C_2$) are β_1 and β_2, respectively. Of course, this is only a simplified model, but it can show how to achieve the design of supersonic turbine cascades with minimal entropy increase. Of course, the smaller the leading edge thickness, the better, but this contradicts the strength requirements of the leading edge of the turbine blade. In addition, the thickness is too small, the leading edge of the turbine blade is easy to be ablated, and the cooling of the turbine blade is also difficult to achieve.

For the turbine cascade under the condition of supersonic flow, due to the interference of the blade, the shock wave will inevitably be generated, and the shock wave will reflect and propagate in the cascade channel. In order to study the shock wave in the channel, we need to classify the shock wave according to its characteristics. Under the condition of supersonic flow, there are four types of shock waves in turbine cascades [19]: (1) detached bow shock wave and the shock wave extending in front of the cascade; (2) pre-compression shock wave; (3) front channel shock wave; (4)

rear channel shock wave; the cause and intensity of these shock waves are different. The supersonic flow at the entrance of the cascade encounters a blade leading edge with a certain thickness to form a detached bow shock. The upper half of the bow wave extends to the far front of the cascade, and the lower half of the bow wave enters the blade channel and intersects with the suction surface of the next blade to form a front channel shock wave. The shock wave in the rear channel is a normal shock wave, and its strength and position are determined by the back pressure.

4.2 Flow Characteristics of Supersonic Turbine Cascades

The second is its flow characteristics, or its expansion work characteristics, we know that for supersonic flow, it will expand and accelerate in the expansion channel and compress and decelerate in the convergence channel. Most of the existing supersonic turbine cascade channels are convergence-expansion channels. Here, we might as well boldly assume that the full expansion channel is used and compare the performance of the two kinds of turbine cascade channels. We assume that the chord length b, expansion ratio and pitch t of the two cascade channels are the same. As shown in Fig. 10.

Assuming that the incoming flow temperature T3, incoming flow pressure P3, incoming flow velocity v and total flow m are the same, the relationship is as follows (the influence of channel shock wave is not considered here): The Isentropic expansion work is used to describe the flow expansion work characteristics of two kinds of turbine cascades.

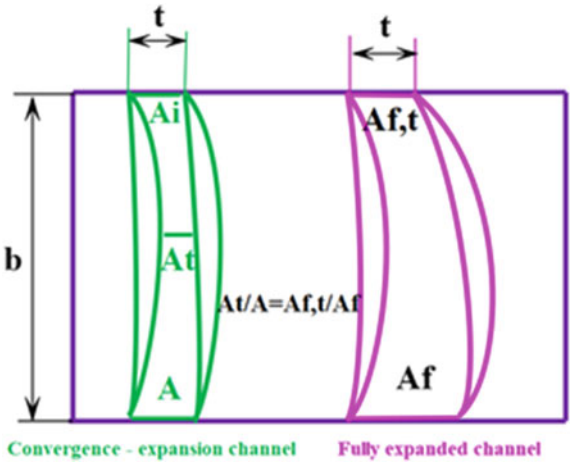

Fig. 10 Supersonic turbine cascade contraction–expansion channel and full expansion channel

$$L_{i,T} = \frac{\gamma}{\gamma - 1} RT_3 \left(1 - \frac{1}{\left(\frac{P_3}{P_{3,1}} \right)^{\frac{\gamma - 1}{\gamma}}} \right) \tag{15}$$

According to the characteristics of the Isentropic expansion work, we only need to know that the Isentropic expansion work can be judged by the drop-pressure ratio. According to the calculation method of the drop-pressure ratio, for the fully expanded supersonic turbine cascade channel, when the incoming pressure condition and surface-throat ratio are the same, the drop-pressure ratio is larger than that of the convergence-expansion channel, so the Isentropic expansion work of the convergence-expansion channel is smaller than that of the convergence-expansion channel. But from another point of view, because the combustion chamber of the constant volume combustion cycle has the function of self-pressurization, if the work to be extracted by the turbine does not need to be too large to meet the turbocharging requirements of the compressor, then more thermal energy will be converted into kinetic energy. The generation of greater thrust will greatly increase the thrust-to-weight ratio of the aero-engine, while the full expansion channel can not only bring a greater drop-to-pressure ratio, but also bring faster acceleration expansion of the air flow. Just enough to meet this demand, if a multi-stage turbine is needed, the next stage uses impulse supersonic turbine cascades to obtain more work.

5 Significance of Supersonic Turbine

According to the research, isovolumetric combustion cycles usually produce higher specific work, and it is also mentioned earlier that supersonic turbines are lack of efficient power extraction at this stage, which is one of the important significance of supersonic turbine research. From another point of view, supersonic turbines solve the problem that pulse detonation turbine engines and rotary detonation turbine engines cannot start themselves at the present stage, and at the same time, it has a large thrust-to-weight ratio. The development of high-efficiency engines provides the direction. Specifically, we explained previously that the thermal efficiency of the engine based on constant volume combustion cycle is high, but in practical application, there is a lack of turbine machinery that can effectively extract work, if it can effectively improve the Isentropic efficiency of the turbine, it can greatly improve the amount of effective work extraction and obtain more flange work, which can be used as output power generation and can also be used in aero-engines to supply compressors. We know that the detonation engine uses the detonation wave in the combustion chamber to realize the self-boosting function, but the generation and self-sustaining and stable propagation of the detonation wave still need to be solved. If the incoming pressure can be increased, the air pressure entering the detonation combustion chamber increases, the detonation wave will be generated relatively easily, and to realize the compressor's increase in the pressure of the incoming gas, it is necessary to rely on the turbine behind. This is also one of the meanings of supersonic turbines.

6 Conclusions

1. Compared with the Brayton cycle, the constant volume combustion cycle has obvious advantages in theory, with high thermal efficiency and large specific power. And in the case of the same heat absorption, the net output power of the constant volume combustion cycle is large. To achieve the same turbine inlet conditions, only the compressor supercharging ratio is smaller. In other words, if we require the same work output, the Isentropic efficiency of the turbine can be further reduced. If we can further improve the Isentropic efficiency of the turbine cascade under this incoming flow condition, the work capacity and thrust-to-weight ratio of the aero-engine based on this isovolumetric cycle will be further improved.
2. Based on the detonation isovolumetric combustion cycle, the incoming flow of supersonic turbine has velocity, temperature and pressure pulsation. At the same time, because of the supersonic flow, a bow shock wave will be generated at the leading edge of the supersonic turbine, which is equivalent to an oblique shock wave, which shows that under the condition of supersonic flow, the thinner the turbine leading edge is, the better, but at the same time, it contradicts the turbine strength and the leading edge is easy to be ablated, and needs to be balanced with each other.
3. The supersonic turbine channel needs to be designed by the minimum entropy increase method. The smaller the number of shock wave reflection in the channel, the smaller the entropy increase, the higher the Isentropic efficiency and the greater the Isentropic expansion work.
4. Under the condition of supersonic flow, the turbine cascade can take the form of convergence-expansion or full expansion in order to achieve the purpose of expansion acceleration. If the full expansion channel is adopted, its Isentropic expansion work is less than that of the convergence-expansion channel. However, its drop-pressure ratio is larger and converted into more kinetic energy, which is more beneficial for generating large thrust. In specific applications, the use of convergence-expansion channel or full-expansion channel also needs to be weighed.
5. If the Isentropic efficiency of the turbine can be effectively improved, the amount of effective work extracted can be greatly increased and more flange work can be obtained. This part of flange work can not only be used as output power generation, but also can be used in aero-engine to supply compressor. The detonation engine uses the detonation wave in the combustion chamber to realize the self-pressurization function, but the generation and self-sustaining stable propagation of the detonation wave still need to be solved. If the incoming pressure can be increased, the air pressure entering the detonation combustor increases. The generation of detonation waves will be relatively easy. That's why supersonic turbines exist.

References

1. 张恩慧 (2018) 定容燃烧在未来燃气轮机热力循环中的应用前景. Prospect of constant volume combustion in future gas turbine cycle. 科技视界 (032):42–43, 28
2. 计自飞, 张会强, 谢峤峰 et al (2018) 连续旋转爆震涡轮发动机热力过程与性能分析. Thermodynamic process and performance analysis of the continuous rotating detonation turbine engine. 清华大学学报 (自然科学版) 058(010):899–905
3. Kailasanath K (2000) Review of propulsion applications of detonation waves, AIAA J 1–81
4. Schawer D, Kailasanath K (2011) Numerical investigation of the physics of rotating detonation engines. In: Proceedings of the combustion institute
5. Zhou R, Wu D, Wang JP (2016) Progress of continuously rotating detonation engines. Chin J Aeronaut 29(1):15–29
6. 邓君香, 严传俊, 郑龙席 et al (2008) 装有脉冲爆震主燃烧室的燃气涡轮发动机热力性能计算. Calculating performance of gas turbine engine with embedded PDC (pulse detonation combustor). 西北工业大学学报 026(003):362–367
7. 王宇辉, 何修杰 (2017) 旋转爆轰发动机的研究进展. Advances in rotating detonation engine research. 南京航空航天大学学报 049(003):325–339
8. 卢杰. 脉冲爆震涡轮发动机关键技术研究
9. Nordeen C, Schwer D, Schauer F, Hoke J, Cetegen B, Barber T (2011) Thermodynamic modeling of a rotating detonation engine. In: 49th AIAA aerospace sciences meeting
10. Frolov SM, Dubrovskii AV, Ivanov VS (2016) Three-dimensional numerical simulation of a continuously rotating detonation in the annular combustion chamber with a wide gap and separate delivery of fuel and oxidizer. In: Progress in propulsion physics. EUCASS proceedings series
11. Van ZD, Envia E, Turner MG (2007) The attenuation of a shock wave by an aircraft engine axial turbine stage. In: Proceedings of the international symposium on airbreathing engines. Paper 2007–1260, Beijing
12. Fang W, Chunsheng W, Baoxing LI et al (2018) 连续旋转爆轰波传播过程试验研究. Experimental investigation on the propagation process of continuous rotating detonation wave. 固体火箭技术 041(006):688–693
13. Gray J, Vinkeloe J, Moeck J et al (2016) Thermodynamic evaluation of pulse detonation combustion for gas turbine power cycles. In: ASME turbo expo 2016
14. Heiser W, Pratt D (2002) Thermodynamic cycle analysis of pulse detonation engines. J Propul Power 18:68–76
15. Rankin BA, Fotia ML, Naples AG et al (2016) Overview of performance, application, and analysis of rotating detonation engine technologies. J Propul Power 1–13
16. Ishiyama C, Miyazaki K, Nakagami S et al (2016) Experimental study of research of centrifugal-compressor-radial-turbine type rotating detonation engine. In: Proceedings of the 52nd AIAA/SAE/ASEE joint propulsion conference, Salt Lake City. AIAA
17. Endo T, Masuda K, Watanabe W et al (2016) Reduction of air flow rate for pulse-detonation-turbine-engine operation by water-droplet injection. J Therm Sci Technol 11(2):JTST0022
18. Rasheed A, Tangirala VE, Vadervort CL et al (2013) Interactions of a pulsed detonation engine with a 2D blade cascade. AIAA J
19. Huang X, Guo Z, Liu K et al (2016) Experimental investigation on noise radiation characteristics of pulse detonation turbine engine. Proc Inst Mech Eng Part G J Aerosp Eng 0954410016636160
20. Wolański P (2015) Application of the continuous rotating detonation to gas turbine. Appl Mech Mater 782:3–12
21. Welsh DJ, King PI, DeBarmore ND et al (2014) RDE integration with T63 turboshaft engine components. In: Proceedings of the 52nd aerospace sciences meeting, National Harbor Maryland: AIAA, 2014
22. Sousa J, Paniagua G, Collado ME (2017) Thermodynamic analysis of a gas turbine engine with a rotating detonation combustor. Appl Energy 195:247–256
23. 何龙, 郑龙席, 邱华 et al (2012) Calculating performance of pulse detonation turbo engine. 脉冲爆震涡轮发动机性能计算. 推进技术 033(005):665–670

24. Tellefsen J, King P, Schauer F et al (2012) Analysis of an RDE with convergent nozzle in preparation for turbine integration. In: 50th AIAA aerospace sciences meeting including the new horizons forum and aerospace exposition
25. Griffin L, Dorney D (2000) Simulations of unsteady flow through the fastrac supersonic turbine. ASME J Turbomach 122(2):225–233
26. Müller Breslau Str. 8 (2018) Comprehensive thermodynamic analysis of the Humphrey cycle for gas turbines with pressure gain combustion. J Energies 12, 18
27. Ma F, Choi JY, Yang V (2005) Thrust chamber dynamics and propulsive performance of multiple pulse detonation engines. J Propul Power 21:512–526
28. Bach E, Bohon M, Paschereit CO, Stathopoulos P (2018) Development of an instrumented guide vane set for RDC exhaust flow characterization. In: 2018 joint propulsion conference. American Institute of Aeronautics and Astronautics, Reston, VA
29. Andrus IQ, King PI (2007) Evaluation of a high bypass turbofan hybrid utilizing a pulsed detonation combustor. In: 43rd AIAA/ASME/SAE/ASEE joint propulsion conference & exhibit, AIAA 2007-5074
30. Andrus IQ (2007) Comparative analysis of a high bypass turbofan using a pulsed detonation combustor. Air Force Institute of Technology
31. Jorge S, Guillermo P (2015) Entropy minimization design approach of supersonic internal passages. Entropy 17(12):5593–5610
32. Paniagua G, Iorio MC, Vinha N, Sousa J (2014) Design and analysis of pioneering high supersonic axial turbines. Int J Mech Sci
33. Sousa J, Paniagua G, Collado-Morata E (2017) Analysis of the aerodynamic losses in a supersonic turbine. In: Proceedings of the ASME 2017 power conference joint with ICOPE-17, Charlotte, 26–30 June 2017. POWER-ICOPE2017-3624. https://doi.org/10.1115/POWER-ICOPE2017-3624
34. 李晓丰, 肖俊峰, 王玮 et al (2016) Ideal thermodynamic cycle analysis of gas turbine based on detonation combustion. 基于爆震燃烧的燃气轮机理想热力循环分析. 西北工业大学学报 (001):112–117
35. Vutthivithayarak R, Braun EM, Lu FK (2012) On thermodynamic cycles for detonation engines. In: 28th international symposium on shock waves. Springer, Berlin Heidelberg
36. Lu Y, Roskilly AP, Yu X et al (2018) Technical feasibility study of scroll-type rotary gasoline engine: a compact and efficient small-scale Humphrey cycle engine. Appl Energy 221:67–74
37. Wu YH, Ma FH, Yang V (2002) System performance and thermodynamic cycle analysis of air-breathing pulse detonation engines. 中國航空太空學會學刊 34(1):1–11
38. Andriani R, Ghezzi U, Pasini S (2010) Thermodynamic study of gas turbine engine with constant volume combustion. In: 46th AIAA/ASME/SAE/ASEE joint propulsion conference & exhibit
39. Brophy C (2009) Benefits and challenges of pressure-gain combustion systems for gas turbines. Mech Eng 131(03)
40. Ghezzi U (1990) Motori per Aeromobili. CLUP, Milano
41. Travis JT (2014) A computational investigation of a constant volume combustion jet engine. Dissertations & Theses Gradworks
42. Kumazawa Y, Fujii J, Matsuo A et al (2016) Numerical study for rotating detonation propagation in a two-parallel-plane combustor. In: 52nd AIAA/SAE/ASEE joint propulsion conference
43. 曾荣鹏 (2005) 超音速叶栅内的激波系及其与附面层相互作用的数值研究. 华北电力大学 (北京)
44. Fujii J, Kumazawa Y, Matsuo A et al (2016) Numerical investigation on detonation velocity in rotating detonation engine chamber. Proc Combust Inst S1540748916302139
45. Sun J et al (2018) Plume flowfield and propulsive performance analysis of a rotating detonation engine. Aerosp Sci Technol. https://doi.org/10.1016/j.ast.2018.08.024
46. Anand V, George AS, Gutmark E (2015) Hollow rotating detonation combustor
47. Roy GD et al (2004) Pulse detonation propulsion: challenges, current status, and future perspective. Progr Energy Combust Sci

48. Tellefsen JR et al (2012) Build up and operation of an axial turbine driven by a rotary detonation engine. USA
49. Liu Z, Braun J, Paniagua G (2017) Performance of axial turbines exposed to large fluctuations. In: Proceedings of the 53rd AIAA/SAE/ASEE joint propulsion conference, Atlanta, 10–12 July 2017. AIAA 2017-4817. https://doi.org/10.2514/6.2017-4817
50. Braun J, Saracoglu BH, Paniagua G (2016) Unsteady performance of rotating detonation engines with different exhaust nozzles. J Propul Power 1–10
51. Xue S, Liu H, Zhou L et al (2018) Experimental research on rotating detonation with liquid hypergolic propellants. Chin J Aeronaut 31(12):18–24
52. Vinha N, Paniagua G, Sousa J et al (2016) Axial bladeless turbine suitable for high supersonic flows. J Propul Power 32(4):V02CT38A061
53. Eric W et al (2006) Stagnation Hugoniot analysis for steady combustion waves in propulsion systems. J Propul Power
54. Nordeen C, Schwer D, Schauer F et al (2011) Thermodynamic modeling of a rotating detonation engine. In: 49th AIAA aerospace sciences meeting including the new horizons forum and aerospace exposition. Pleiades Publishing
55. 费微微, 单勇, 王敏敏 et al (2016) Numerical study of supersonic film cooling in supersonic turbine cascade. 超声速涡轮叶栅超声速气膜冷却数值研究. 推进技术 037(005):916–921
56. Goldman LJ (1972) Supersonic turbine design and performance, 26–30 Mar 1972
57. Liu Z, Braun J, Paniagua G (2018) Characterization of a supersonic turbine downstream of a rotating detonation combustor. J Eng Gas Turb Power. https://doi.org/10.1115/1.4040815
58. Paniagua G, Lorio MC, Vinha N, Sousa J (2014) Design and analysis of pioneering high supersonic axial turbines. Int J Mech Sci 89:65–77. https://doi.org/10.1016/j.ijmecsci.2014.08.014
59. Sousa J, Paniagua G, Saavedra J (2017) Aerodynamic response of internal passages to pulsating inlet supersonic conditions. Comput Fluids 149:31–40. https://doi.org/10.1016/j.compßuid.2017.03.005

An Application of QFD in Aircraft Conceptual Design

Shiyu Wang, Zhouwei Fan, and Xiongqing Yu

Abstract Aircraft conceptual design is the very beginning of aircraft design process in which one or several aircraft configurations are created to meet the top-level requirements of aircraft. The aim of this paper is to build a more traceable, structured and systematic process of aircraft conceptual design by use of Quality Function Deployment (QFD) method. The conceptual design of a narrow body commercial aircraft is used as an example to illustrate application of the QFD. The top-level requirements of the commercial aircraft are defined. The conceptual design activities such as initial sizing of aircraft, wing configuration design, fuselage configuration design, and empennage configuration design are accomplished using House of Quality (HOQ). During initial sizing of aircraft, the top-level requirements of aircraft are converted into the requirements for aerodynamics, propulsion and weight with the aid of HOQ and constraint analysis. During configuration designs of the wing, fuselage and empennage, their requirements are identified based on the top-level requirements and output of the initial sizing, and consist of requirements of aerodynamics, structure, control, safety, operation, cost and etc. Several HOQs representing the relationships between the requirements and the configuration design parameters are created. After that, the configuration design parameters are selected with the aid of the HOQ and relevant design knowledges. By use of the QFD, aircraft conceptual design activities are represented by a number of the HOQ and the design process of configuration parameters is traceable through the HOQ. It is concluded that the QFD-based aircraft conceptual design is more traceable, structured and systematic than the traditional method.

S. Wang (✉) · Z. Fan · X. Yu
College of Aerospace Engineering, Nanjing University of Aeronautics and Astronautics, Nanjing, China
e-mail: wsy@nuaa.edu.cn

Z. Fan
e-mail: fanzhouwei@nuaa.edu.cn

X. Yu
e-mail: yxq@nuaa.edu.cn

Z. Jing and X. Zhan (eds.), *Proceedings of the International Conference on Aerospace System Science and Engineering 2020*, Lecture Notes in Electrical Engineering 680,
https://doi.org/10.1007/978-981-33-6060-0_13

Keywords Aircraft conceptual design · Systems engineering · Quality function deployment · House of quality · Commercial aircraft

1 Introduction

Aircraft design can be divided into three interrelated and interdependent stages: conceptual design, preliminary design and detail design. Although conceptual designers account for only 1% of the total design staff, the impact of the conceptual design stage on the life cycle cost of the aircraft is as high as 65% [1]. Therefore, the conceptual design stage is crucial for aircraft design. Generally, aircraft design begins with customer requirements. In the conceptual design stage, designers need to convert these requirements into aircraft engineering characteristics. Quality Function Deployment (QFD) is a systematic, structured and traceable analysis method, which can effectively transform customer requirements into product engineering characteristics.

There have been some QFD applications in the field of aircraft design. Tan [2] applied QFD to the conceptual configuration design phase of low speed High Altitude Long Endurance (HALE) UAVs, using a four-level QFD model to compete customer requirement to performance parameters, performance parameters to parts characteristics, parts characteristics to manufacturing processes, manufacturing processes to manufacturing controls conversion. Through this process, the important design variables at all stages of HALE UAVs design to manufacturing were identified. Lin and Wang [3] adopted a two-level QFD model to identify the important design features of a HALE UAV. Kamal and Ramirez-Serrano [4, 5] used a two-level QFD model combined with multiple analysis and decision-making methods to select the best baseline configuration for hybrid UAVs among several aircraft conceptual configurations. Ashtiany and Alipour [6] completed the redesign of the Beech Barbon58 tail using the Axiomatic Design (AD) method integrated with QFD in the conceptual design of the aircraft tail. Currently, the applications of QFD in the conceptual design phase of aircraft mainly focus on identifying key technologies.

The purpose of this paper is to build a more traceable, structured and systematic aircraft conceptual design process by use of QFD. Several HOQs are created to convert customer requirements into engineering characteristics. Based on these HOQ and the relevant aircraft design knowledge, the aircraft design parameters, including the top-level and component-level design parameters are determined.

The following sections will describe QFD method, detailed procedures for QFD-based aircraft conceptual design, and an application of the QFD to configuration design of a narrow body commercial aircraft.

2 Methodology

2.1 Quality Function Deployment

QFD is a product design and quality assurance method driven by customer requirements, which can capture customer requirements and systematically convert them into engineering characteristics, and convert qualitative requirements into relevant quantitative design parameters [7]. This method was first proposed by Dr. Yoji Akao in the 1960s to solute the problem that product quality was difficult to be guaranteed. After continuous development, American Supplier Institute (ASI) launched the four-level QFD model, which corresponds to product planning, product design, process planning and production planning of the entire product development process. Through these four steps, customer requirements are gradually converted into performance parameters, parts characteristics, manufacturing processes and controls [2]. The four-level QFD model is shown in Fig. 1.

The House of Quality (HOQ) is the core tool of QFD. The general HOQ template is shown in Fig. 2, and consists of the following elements [8]:

(1) Section A is about Whats matrix containing customer requirements and their importance, which indicates what needs to be done.
(2) Section B is about Hows matrix containing engineering characteristics, which indicates how to do it according to the requirements.
(3) Section C is about the correlation between engineering characteristics, which can be a positive, negative or no correlation.
(4) Section D is about the relationship between customer requirements and engineering characteristics, which can be a strong, medium, weak or no correlation.

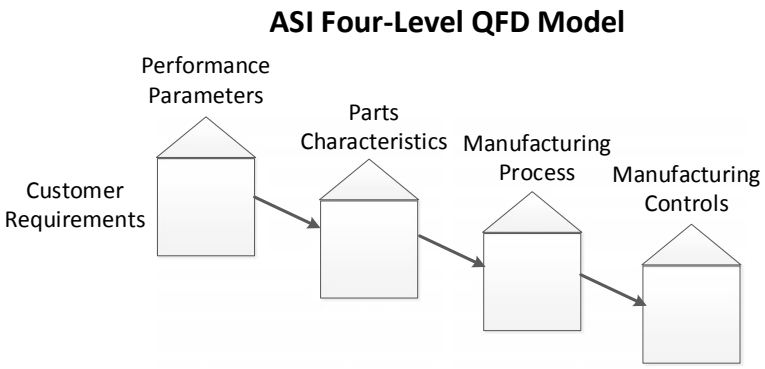

Fig. 1 Four-level QFD model

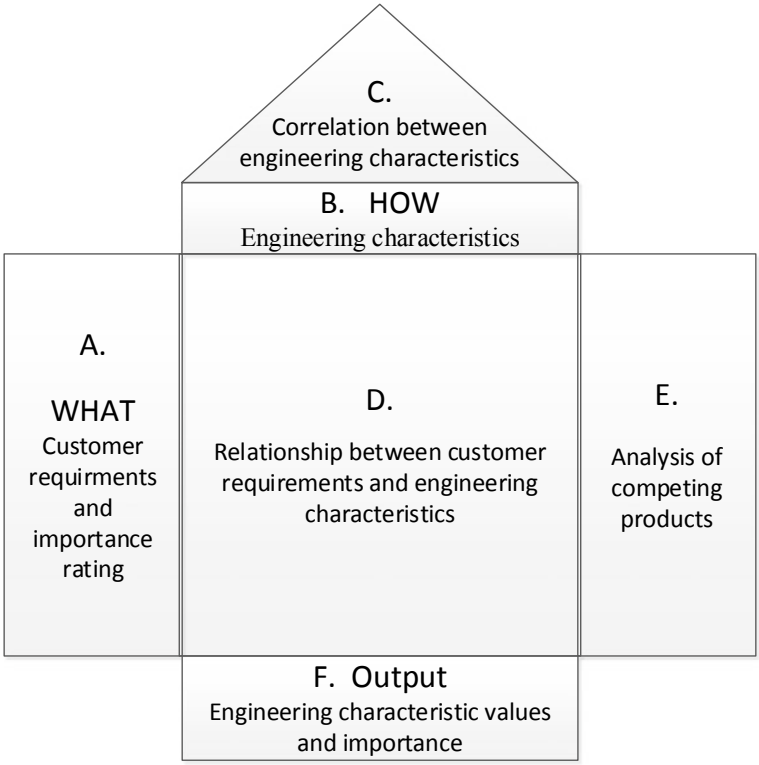

Fig. 2 House of quality

(5) Section E is about the evaluation matrix, which is an analysis of similar competitive products.
(6) Section F is the output of Hows matrix including the value and importance of engineering characteristics.

2.2 Systematic Process

In this paper, a traceable, structured and systematic process of aircraft conceptual design was developed by applying the QFD method. The whole process, as shown in Fig. 3, is divided into four steps: (1) identifying the customer requirements, (2) identifying the engineering characteristics; (3) building the top-level HOQ and constraint analysis; (4) building the component-level HOQ and the components configuration design.

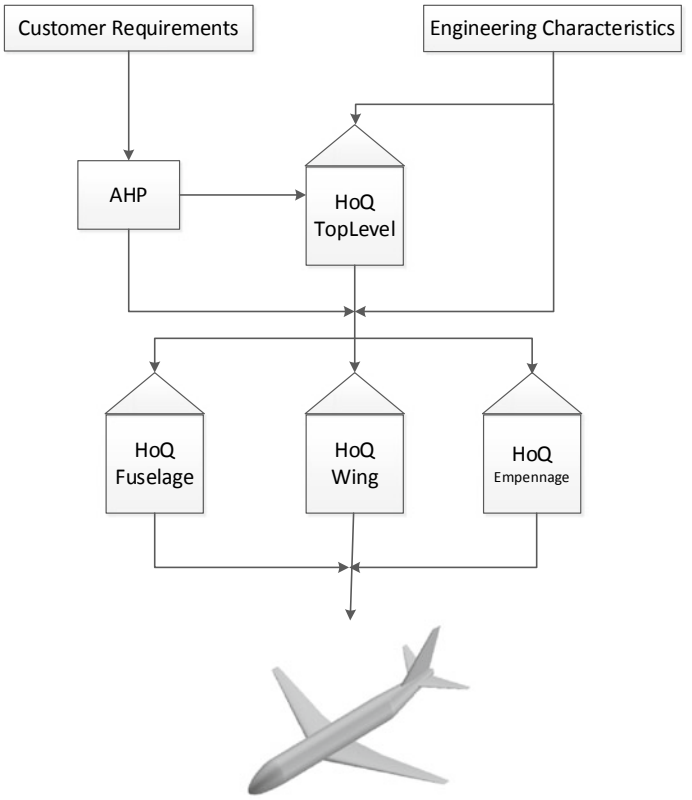

Fig. 3 Systematic process

Aircraft top-level and component-level requirements. The purpose of this step is to identify customer requirements. It is the most critical step in the QFD process to define requirements accurately, as the requirements are the initial driver of the entire process [9]. Although, aircraft requirements are gathered from many sources including aircraft manufacturers, airliners, passengers, freight operators, regulatory agencies, and suppliers and partners, etc. However, the primary requirements come from the operation of the air transport system, regulatory agencies and aircraft customers. A database is created during gathering the requirements and then the affinity diagram is used to classify the customer requirements. The affinity diagram (or KJ method) was designed by Jiro Kawakita in the 1960s and has been used as a tool to classify and organize a large amount of messy and unstructured information into logically connected groups [10]. In the conceptual design phase, aircraft customer requirements can be divided into aerodynamics, structure, control, safety, operation, cost, etc. in term of category, and can be divided into top-level and component-level requirements in term of level. According to the current survey, aircraft top-level

	Leve1	Level2
Top-level requirements	Performance	Range
		Cruise Mach
		Take-off distance
		Landing distance
		Climb gradient at the second segment
		Climb gradient at the missed approach
	Marketability	Payload
	Airworthiness	Approach speed
		Cruise altitude
		Climb gradient at the cruise altitude

Fig. 4 Aircraft top-level requirements

requirements are shown in Fig. 4 and the component-level requirements are shown in Sect. 3.

Aircraft engineering characteristics. The purpose of this step is to identify engineering characteristics. Generally [9], each engineering characteristic should be related to at least one customer requirement and describe the aircraft features in a quantifiable form from a certain aspect, such as geometry, aerodynamics, weight or propulsion parameters, etc. This step is extremely essential in the QFD process since the incorrect identification of the engineering characteristics will lead to unsatisfying customer requirements. The aircraft engineering characteristics can be divided into top-level and component-level characteristics. The affinity diagram is applied to classify the engineering characteristics, aircraft top-level engineering characteristics are shown in Fig. 5, and the component-level characteristics are shown in Sect. 3.

Top-level HOQ and initial sizing. The purpose of this step is to determine the main parameters in the conceptual design of the aircraft. Firstly, build the top-level HOQ based on top-level customer requirements and engineering characteristics, then

	Level1	Level2
Top-level engineering characteristics	Aerodynamics	Takeoff maximum lift coefficient
		Landing maximun lift coefficient
		Lift coefficient at cruise
		Lift-to-drag ratio at cruise
		Lift-to-drag ratio at climb
		Lift-to-drag ratio at missed approach
	Propulsion	Thrust-to-weight ratio
		Bypass ratio
		Specific fuel consumption during cruise
	Weight	Maximum takeoff weight
		Wing loading
		Landing-to-takeoff weight ratio

Fig. 5 Aircraft top-level engineering characteristics

complete constraint analysis to determine the main parameters of the aircraft. The steps of construction of the top-level HOQ are as follows:

(1) Based on the top-level requirements, complete the Whats matrix.
(2) Based on the top-level engineering characteristics, complete the Hows matrix.
(3) Based on the correlation analysis between engineering characteristics and qualitative analysis by experts, determine the correlation matrix. In this paper, "+" indicates a positive correlation, "−" indicates a negative correlation, and null indicates no correlation.
(4) Based on the correlation analysis of the requirements and engineering characteristics and qualitative analysis by experts, determine the relationship matrix. In this paper, "9" indicates a strong correlation, "3" indicates a medium correlation, "1" indicates a weak correlation, and null indicates no correlation.
(5) Based on the analysis of similar competitive products, determine the market competitive evaluation matrix.
(6) Calculate the importance of engineering characteristics based on Eq. (1).

$$IEC_j = \sum_{i=1}^{n} ICR_i \times R_{ij}, \quad j = 1, 2, 3 \tag{1}$$

where IEC_j is the importance of the jth engineering characteristic

ICR_i is the importance of the ith customer requirement

R_{ij} is the relationship between the ith requirement and jth characteristic.

Component-level HOQ and parts configuration design. The purpose of this step is to complete the component configuration design including the fuselage, wing and empennage. Firstly, we build component-level HOQ using the method similar to Sect. 2.2.3 and then complete the component configuration design. During building HOQ of the fuselage, wing and empennage, their requirements are identified based on the top-level requirements and output of the initial sizing, and consist of requirements of aerodynamics, structure, control, safety, operation, cost and etc. Finally, the configuration design parameters are selected with the aid of the HOQ and relevant design knowledges.

3 Application Example

This paper applies the systematic process to the conceptual design process of the narrow body commercial aircraft. In the next subsections, the detailed procedure and results of each step are presented.

3.1 Initial Sizing

Firstly, the top-level HOQ of aircraft is built. The main function of the top-level HOQ is to convert the customer top-level requirements into top-level engineering characteristics and analyze the relationship between them. After that, with the aid of the HOQ and constraint analysis, the thrust-to-weight ratio and wing loading are determined. The top-level HOQ is built using the method in Sect. 2.2.3:

(1) Identify the customer requirements, and then apply analytic hierarchy process (AHP) to determine the importance of the requirements shown in Fig. 6. The AHP is a multi-criteria decision-making method for complex problem, which transforms individual qualitative judgment into quantitative importance [11].
(2) Identify the engineering characteristics, which mainly consist of aerodynamics, weight and propulsion parameters. For subsequent constraint analysis, based on empirical data and mission profile analysis, estimate the value of some engineering characteristics, as shown in Table 1.

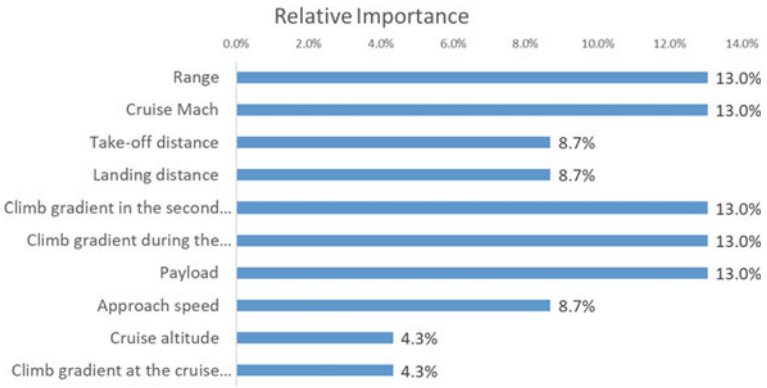

Fig. 6 The relative importance of the top-level customer requirements

Table 1 Estimated data of some engineering characteristics

Engineering characteristics	Value
Takeoff maximum lift coefficient	2.4
Landing maximum lift coefficient	3.0
Lift coefficient at cruise	0.4
Lift-to-drag ratio at cruise	18
Lift-to-drag ratio at climb	9
Lift-to-drag ratio at missed approach	8
Bypass ratio	6
Specific fuel consumption at cruise (kg/(daN*h))	0.62
Maximum takeoff weight (kg)	79,201
Landing-to-takeoff weight ratio	0.878

(3) Complete the correlation matrix between engineering characteristics based on qualitative analysis by experts. For examples, given the same mission range, with higher specific fuel consumption, the more fuel is required. The more fuel leads to an increase of aircraft take-off weight. Therefore, the specific fuel consumption is related positively to the take-off weight. In general, with the increase of the bypass ratio of the engine, the fuel consumption decreases. Therefore, the fuel consumption is correlated negatively with the bypass ratio of the engine.

(4) Complete the relationship matrix based on qualitative analysis by experts and quantitative analysis of the relationship between the requirements and characteristics. For examples, for jet aircraft, from Eq. (2) [12] for estimating the range, it can be seen that the range is directly related to some engineering characteristics such as specific fuel consumption rate, lift-to-drag ratio, and aircraft weight at the start and end of cruise. From Eq. (3) [13] for estimating the takeoff ground run distance, it can be seen that the takeoff ground run distance is directly related to some engineering characteristics such as lift coefficient, wing loading, and thrust-to-weight ratio. Therefore, according to the functional relationship between requirements and characteristics, an impact analysis (Rough-Order-of-Magnitude Analysis [2]) can quantitatively analyze the relationship between them.

(5) Complete the competitive evaluation matrix based on the data of the same type of narrow body commercial aircraft on the market and then determine the value of top-level requirements, as shown in Fig. 7.

(6) Calculate the importance of engineering characteristics based on Eq. (1) in Sect. 2.2.3, the result is shown in Fig. 8.

The top-level HOQ is shown in Fig. 9. With the aid of the HOQ and relevant design knowledges, a constraint analysis is performed [13]. In the constraint diagram as shown in Fig. 10, select the thrust-to-weight ratio (0.32) and wing loading (535 kg/m^2) that meet the requirements.

$$Range = \frac{V}{C}\frac{L}{D}\ln\frac{W_i}{W_f} \tag{2}$$

Requirements	Goal	A319	A320	B737
Range(km)	5300	3518.8	5000.4	5248.2
Cruise Mach	0.8	0.78	0.78	0.75
Take-off distance(m)	1750	1750	2180	1939
Landing distance(m)	1350	1350	1440	1396
Climb gradient at the second segment	2.4%	-	-	-
Climb gradient at the missed approach	2.1%	-	-	-
Payload(kg)	14250	11780	14250	12160
Approach speed(m/s)	67	67.3	68.9	68.4
Cruise altitude(m)	11000	11277.6	11277.6	10668
Climb gradient at the cruise altitude	0.21%	-	-	-

Fig. 7 Competitive evaluation matrix

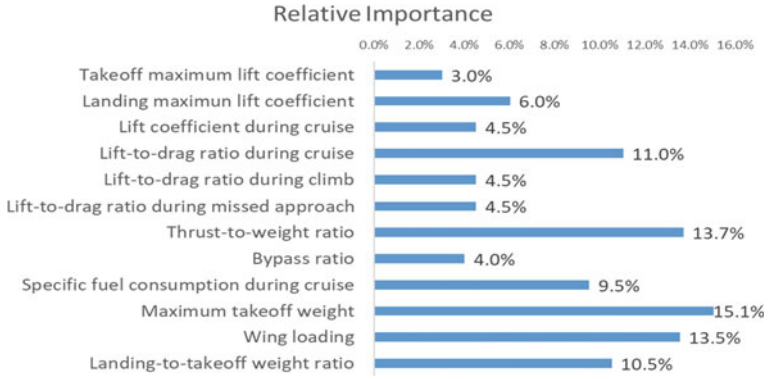

Fig. 8 The relative importance of the top-level engineering characteristics

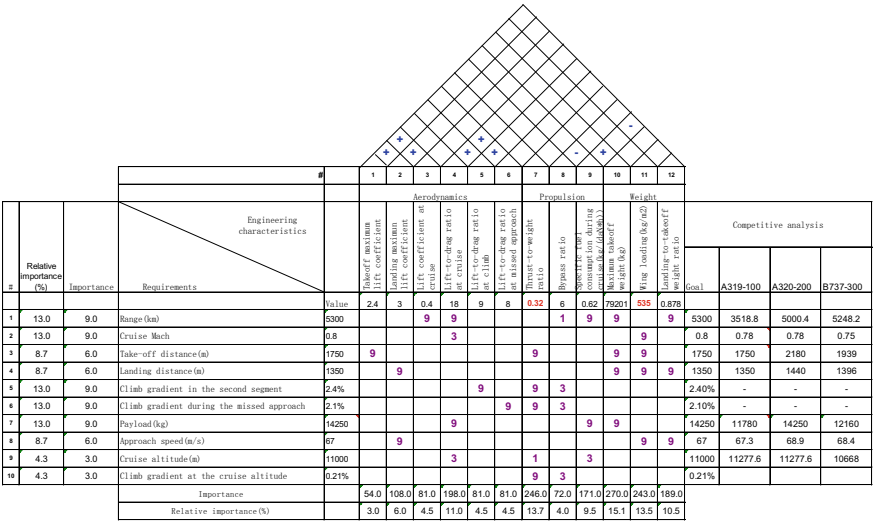

#	Relative importance (%)	Importance	Requirements / Engineering characteristics		1 Takeoff maximum lift coefficient	2 Landing maximun lift coefficient	3 Lift coefficient at cruise	4 Lift-to-drag ratio at cruise	5 Lift-to-drag ratio at climb	6 Lift-to-drag ratio at missed approach	7 Thrust-to-weight ratio	8 Bypass ratio	9 Specific fuel consumption during cruise (kg/(kN·h))	10 Maximum takeoff weight (kg)	11 Wing loading (kg/m2)	12 Landing-to-takeoff weight ratio	Competitive analysis: Goal	A319-100	A320-200	B737-300
				Value	2.4	3	0.4	18	9	8	0.32	6	0.62	79201	535	0.878				
1	13.0	9.0	Range(km)	5300			9	9				1	9	9		9	5300	3518.8	5000.4	5248.2
2	13.0	9.0	Cruise Mach	0.8				3							9		0.8	0.78	0.78	0.75
3	8.7	6.0	Take-off distance(m)	1750	9						9			9	9		1750	1750	2180	1939
4	8.7	6.0	Landing distance(m)	1350		9								9	9	9	1350	1350	1440	1396
5	13.0	9.0	Climb gradient in the second segment	2.4%					9		9	3					2.40%	-	-	-
6	13.0	9.0	Climb gradient during the missed approach	2.1%						9	9	3					2.10%	-	-	-
7	13.0	9.0	Payload(kg)	14250			9						9	9			14250	11780	14250	12160
8	8.7	6.0	Approach speed(m/s)	67		9									9	9	67	67.3	68.9	68.4
9	4.3	3.0	Cruise altitude(m)	11000			3				1		3				11000	11277.6	11277.6	10668
10	4.3	3.0	Climb gradient at the cruise altitude	0.21%							9	3					0.21%			
			Importance		54.0	108.0	81.0	198.0	81.0	81.0	246.0	72.0	171.0	270.0	243.0	189.0				
			Relative importance(%)		3.0	6.0	4.5	11.0	4.5	4.5	13.7	4.0	9.5	15.1	13.5	10.5				

Fig. 9 The top-level HOQ

where V is the true cruise speed

C is the engine specific fuel consumption at cruise conditions

L/D is the aircraft lift-to-drag ratio at cruise conditions

W_i is the aircraft weight at the start of cruise

W_f is the aircraft weight at the end of cruise.

$$S_{TOG} = \frac{g}{\rho \cdot C_{L,LOF}} \cdot \frac{m_{MTO}/S_w}{T_{TO}/(m_{MTO} \cdot g)} \tag{3}$$

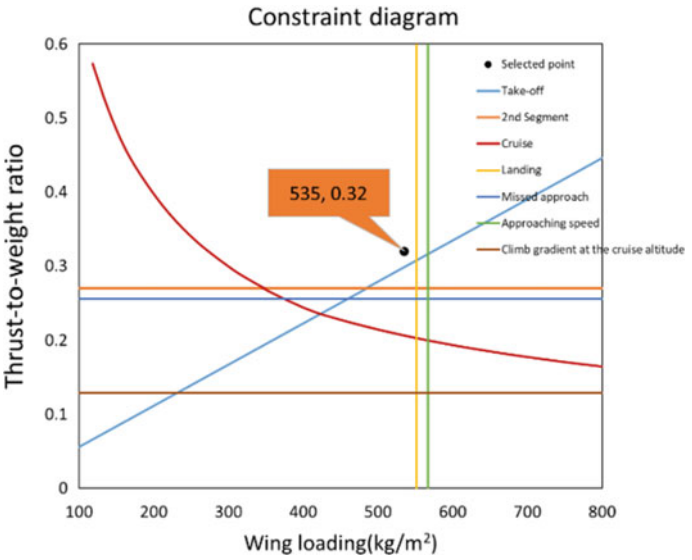

Fig. 10 Constraint diagram

where S_{TOG} is the takeoff ground run distance

$C_{L,LOF}$ is the lift coefficient when the aircraft lifts off the ground

m_{MTO}/S_w is the wing loading

$T_{TO}/(m_{MTO} \cdot g)$ is the thrust-to-weight ratio.

3.2 Fuselage Configuration Design

Firstly, build the fuselage HOQ, and then complete the fuselage configuration design. The first step in building a fuselage HOQ is to identify the fuselage design requirements. For commercial aircraft, the main function of the fuselage is to accommodate passengers, cargo, and various system facilities. For airlines, the lowest cost per seat is one of the important requirements; for passengers, comfortable seats and low cabin noise may be their concerned requirements. For regulatory agencies, safety is their mostly concerned requirement. The fuselage HOQ is to comprehensively consider the requirements of multiple parties, to convert them into the fuselage engineering characteristics, and to analyze the relationship between the requirements and characteristics. Build the fuselage HOQ using the method in Sect. 2.2.3:

(1) Identify the fuselage requirements, which consist of accommodation, aerodynamics, structure, airworthiness and etc. And then apply AHP to determine the importance of the requirements shown in Fig. 11.

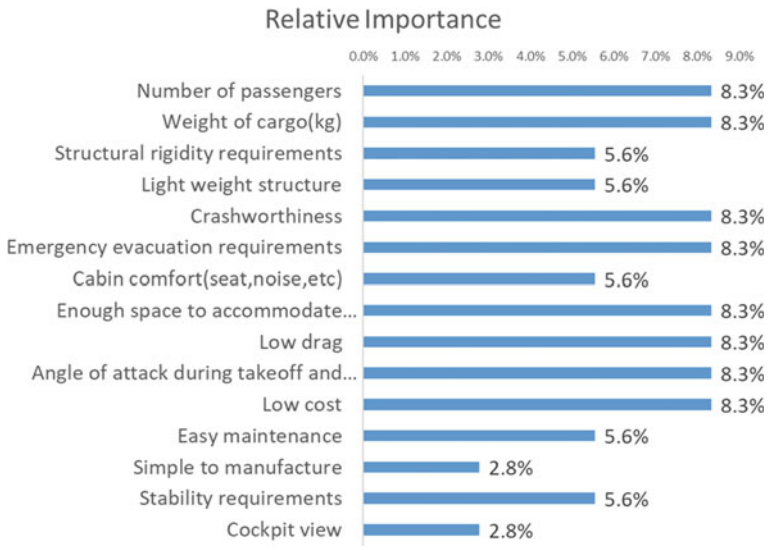

Fig. 11 The relative importance of the fuselage requirements

(2) Identify the fuselage engineering characteristics, as shown in Fig. 12.
(3) Complete the correlation matrix between engineering characteristics based on qualitative analysis by experts. For examples, given the number of passengers, the cabin width is positively related to the seat sizes and the aisle width. In addition, the middle fuselage length is positively related to the seat pitch.

	level1	level2
Fuselage	Airworthiness	Crash worthiness
		Emergency evacuation requirements
	Accommodation	Number of passengers
		Cargo weight
	Aerodynamics	Low drag
	Structure	Structural rigidity requirements
		Light weight structure
	Stability	Stability requirements
	Comfort	Low noise
		Comfortable seat
	Interior layout	Enough space
	Marketability	Low cost
	Manufacturability	Simple to manufacture
	Maintainability	Easy maintenance

Fig. 12 Fuselage design requirements

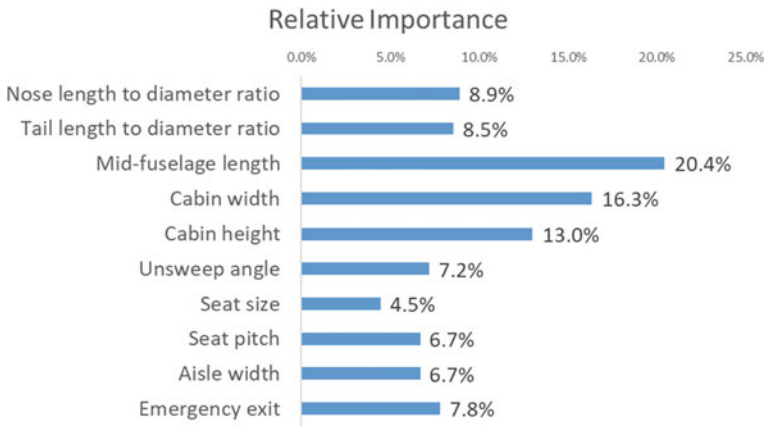

Fig. 13 The relative importance of the fuselage engineering characteristics

(4) Complete the relationship matrix based on qualitative analysis by experts and quantitative analysis of the relationship between the requirements and characteristics. For examples, it can be clearly seen that the number of passengers is directly related to some engineering characteristics such as the middle fuselage length, cabin width, seat size, seat pitch, aisle width, and emergency exit. In addition, seat comfort is directly related to some engineering characteristics such as the cabin width, cabin height, seat size and seat pitch.
(5) Calculate the importance of engineering characteristics based on Eq. (1) in Sect. 2.2.3, the result is shown in Fig. 13.

The fuselage HOQ is shown in Fig. 14. In the conceptual design phase, the fuselage configuration design mainly involves the fuselage geometry shape and cabin layout. With the aid of the fuselage HOQ and relevant design knowledges, determine the value of the fuselage engineering characteristics as shown in Table 2. The fuselage geometry shape and cabin layout are shown in Fig. 15.

3.3 Wing Configuration Design

The main function of the wing is to provide sufficient lift and space to accommodate the fuel required for the flight mission and other devices. The wing HOQ is to consider the comprehensive requirements of multiple parties, to convert them into the wing engineering characteristics, and to analyze the relationship between the requirements and characteristics. Build the wing HOQ using the method in Sect. 2.2.3:

(1) Identify the wing requirements, which consist of aerodynamics, structure, interior space and etc. And then apply AHP to determine the importance of the requirements shown in Fig. 16.

#	Relative importance(%)	Importance		Requirements \ Engineering characteristics		1 Nose length to diameter ratio	2 Tail length to diameter ratio	3 Mid-fuselage length(m)	4 Cabin width(m)	5 Cabin height(m)	6 Unsweep angle(°)	7 Seat size	8 Seat pitch	9 Aisle width(m)	10 Emergency exit
					Value	1.7	2.4	19.28	4.12	4.01	8			0.51	
1	8.3	9.0	Accommodation requirments	Number of passengers	150			9	9			3	9	9	9
2	8.3	9.0		Weight of cargo(kg)	0			9	9	9					
3	5.6	6.0	Structural requirments	Structural rigidity requirements		3	3	9	9	9	3				
4	5.6	6.0		Light weight structure		3	3	9	3	3	3				
5	8.3	9.0	Airworthiness regulations and requirements	Crashworthiness				3							
6	8.3	9.0		Emergency evacuation requirements				9							9
7	5.6	6.0	Comfort	Cabin comfort(seat,noise,etc)					9	9		9	9	9	
8	8.3	9.0	Interior layout	Enough space to accommodate payload, fuel and other equipments		9	9	9	9	9	1				
9	8.3	9.0	Aerodynamics	Low drag		9	9	1	3	3	3				
10	8.3	9.0		Angle of attack during takeoff and landing							9				
11	8.3	9.0	Marketability	Low cost								3	3	3	
12	5.6	6.0	Maintainability	Easy maintenance											3
13	2.8	3.0	Manufacturability	Simple to manufacture		3	3	3			1				3
14	5.6	6.0	Stability	Stability requirements				3			3				
15	2.8	3.0	View	Cockpit view		3									
				Importance		216.0	207.0	495.0	396.0	315.0	174.0	108.0	162.0	162.0	189.0
				Relative importance(%)		8.9	8.5	20.4	16.3	13.0	7.2	4.5	6.7	6.7	7.8

Fig. 14 The fuselage HOQ

Table 2 The value of the fuselage engineering characteristics

Engineering characteristics	Value
Nose length to diameter ratio	1.7
Tail length to diameter ratio	2.4
Mid-fuselage length (m)	19.28
Cabin width (m) Cabin height (m) Unsweep angle (°) Seat pitch (in.) Aisle width (m)	4.12 4.01 8 36 (first class)/32 (economy class) 0.51

(2) Identify the wing engineering characteristics, as shown in Fig. 17.
(3) Complete the correlation matrix between engineering characteristics based on qualitative analysis by experts. For examples, due to the phenomenon of pitch up, with increase of the sweep angle of the wing, the upper limit of the aspect ratio decreases. As a result, the relationship between the sweep angle and the aspect ratio is a negative correlation [12]. According to the influence of the

Fig. 15 The top and side views of the fuselage

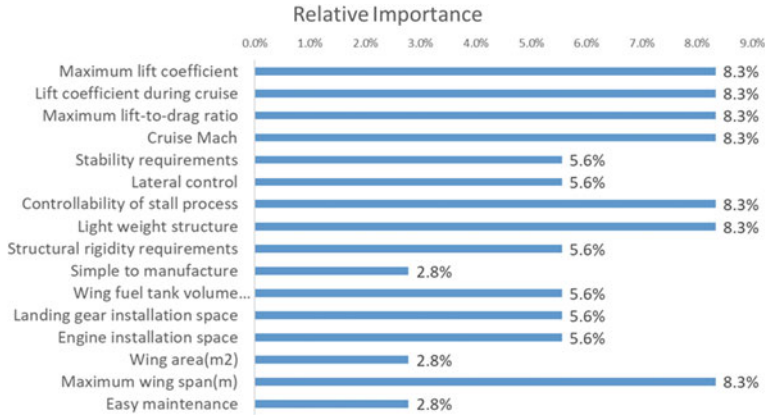

Fig. 16 The relative importance of the wing requirements

	level1	level2
Wing	Aerodynamics	Wing maximum lift coefficient with HLD
		Wing lift coefficient at cruise
		Wing maximum lift-to-drag ratio
	Performance	Cruise Mach
	Stability	Stability requirements
	Control	Lateral control
		Controllability of stall process
	Structure	Structural rigidity requirements
		Light weight structure
	Interior space	Wing fuel tank volume requirements
		Landing gear installation space
		Engine installation space
	Manufacturability	Simple to manufacture
	Size constraint	Wing area
		Maximum wing span
	Maintainability	Easy maintenance

Fig. 17 Wing design requirements

sweep angle on the taper ratio [12], with increase of the sweep angle of the wing, the taper ratio should be smaller. Therefore, the sweep angle and the trapezoid ratio are negatively correlated. According to statistical data [13], with increase of the sweep angle of the wing, the thickness ratio of the wing could be larger. Therefore, the sweep angle is positively correlated with the thickness ratio. In addition, roughly speaking, 10° of sweep provides about 1° of effective dihedral, so the sweep angle is negatively correlated with the dihedral angle [12].

(4) Complete the relationship matrix based on qualitative analysis by experts and quantitative analysis of the relationship between the requirements and characteristics. For examples, for most subsonic moderate sweep aircraft, Eq. (4) [12] can be used to calculate the maximum lift coefficient of the clean wing. The maximum lift coefficient must also consider the effect of the high lift devices (HLD), Eq. (5) [12] provides a method to estimate the increased effect of different HLD. According to Eqs. (4) and (5), it can be seen that the maximum lift coefficient is related to the airfoil maximum lift coefficient, the sweep angle and the type of HLD.

(5) Calculate the importance of engineering characteristics based on Eq. (1) in Sect. 2.2.3, the result is shown in Fig. 18.

The wing HOQ is shown in Fig. 19. In the conceptual design phase, the wing configuration design mainly involves the wing geometry shape and the layout of the control surface. With the aid of the wing HOQ and relevant design knowledges, determine the value of the wing engineering characteristics as shown in Table 3. The wing geometry shape is shown in Fig. 20.

$$C_{L_{max}}(clean) = 0.9C_{l_{max}} \cos \Lambda_{0.25c} \tag{4}$$

where $C_{L_{max}}(clean)$ is the maximum lift coefficient of the "clean" wing

$C_{l_{max}}$ is the airfoil maximum lift coefficient

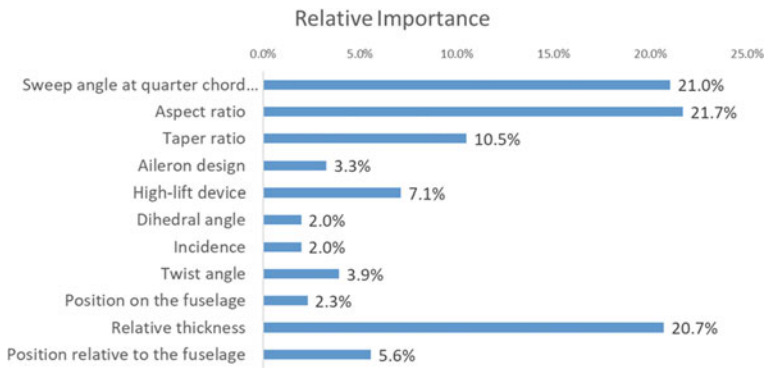

Fig. 18 The relative importance of the wing engineering characteristics

#	Relative importance (%)	Importance		Requirements \ Engineering characteristics		1 Sweep angle at quarter chord line	2 Aspect ratio	3 Taper ratio	4 Aileron design	5 High-lift device	6 Dihedral angle(°)	7 Incidence(°)	8 Twist angle(°)	9 Position on the fuselage	10 Relative thickness (%)	11 Position relative to the fuselage
					A320-200	25	9.39	0.240								
					B717-200	24.5	8.68	0.196							11.6	
					B737-300	25	9.17	0.240							12.89	
					Value	24	9.8	0.19			4.2	1	-3		12.00	Low wing
1	8.3	9.0	Aerodynamics	Wing maximum lift coefficient	3.16	9	9	1		9					9	
2	8.3	9.0		Wing lift coefficient at cruise	0.44	9	9	1				3			9	
3	8.3	9.0		Wing maximum lift-to-drag ratio	23.09	9	9	3				3	3		9	
4	8.3	9.0	Performance	Cruise Mach	0.8	9									3	
5	5.6	6.0	Stability	Stability requirements		3				1	9			9		3
6	5.6	6.0	Control	Lateral control					9	3						
7	8.3	9.0		Controllability of stall process		9	9	9		3			9	1	9	
8	8.3	9.0	Structure	Light weight structure		9	9	9	3	3					9	
9	5.6	6.0		Structural rigidity requirements		9	9	9							9	
10	2.8	3.0	Manufacturability	Simple to manufacture			3	3	3	3					3	
11	5.6	6.0	Interior space	Wing fuel tank volume requirements		3	3	3							9	
12	5.6	6.0		Landing gear installation space											3	9
13	5.6	6.0		Engine installation space												9
14	2.8	3.0	Size constraint	Wing area(m^2)	148.04		9									
15	8.3	9.0		Maximum wing span(m)			9									
16	2.8	3.0	Maintainability	Easy maintenance						9						9
				Importance		576.0	594.0	288.0	90.0	195.0	54.0	54.0	108.0	63.0	567.0	153.0
				Relative importance(%)		21.0	21.7	10.5	3.3	7.1	2.0	2.0	3.9	2.3	20.7	5.6

Fig. 19 The wing HOQ

Table 3 The value of the wing engineering characteristics

Engineering characteristics	Value
Sweep angle (°)	24
Aspect ratio	9.8
Taper ratio	0.24
Dihedral angle (°)	4.2
Incidence (°)	1.0
Twist angle (°)	−3.0
Thickness ratio (%)	12
Position relative to the fuselage	Low wing

$\Lambda_{0.25c}$ is the sweep angle at 1/4 chord of the wing

$$\Delta C_{L_{max}} = 0.9 \Delta C_{l_{max}} \left(\frac{S_{flapped}}{S_{ref}} \right) \cos \Lambda_{H.L.} \tag{5}$$

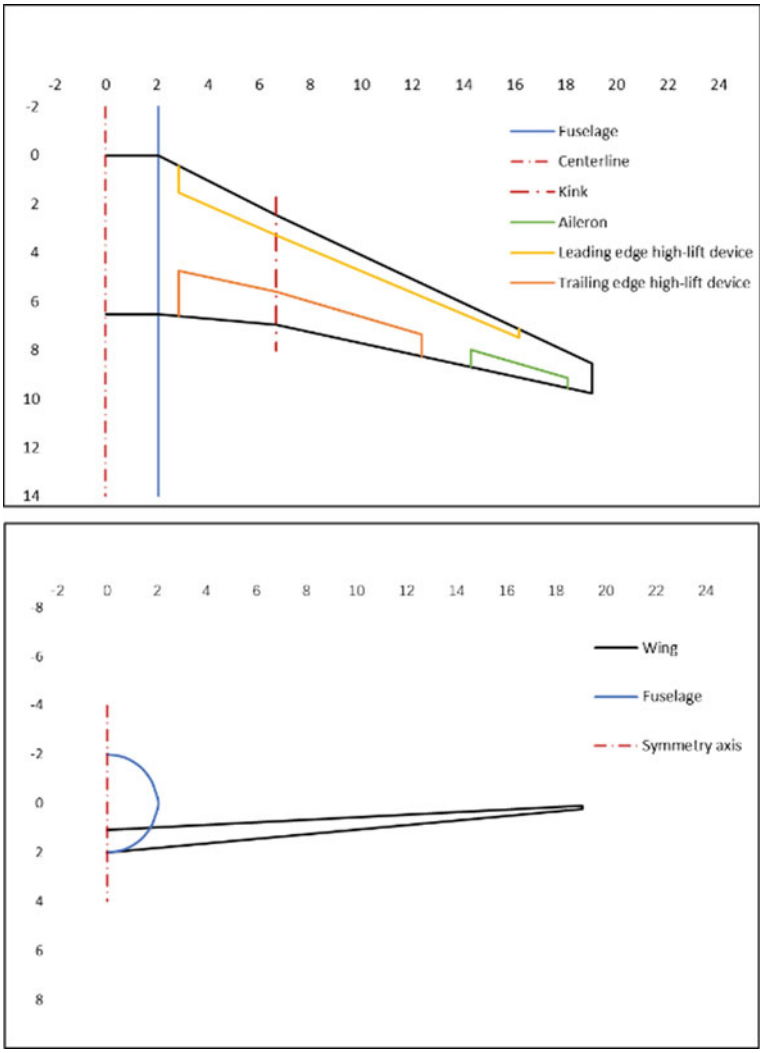

Fig. 20 The top and side views of the wing

where $\Delta C_{L_{max}}$ is the increase in maximum lift coefficient

$\Delta C_{l_{max}}$ is the increase of the two-dimensional section of the HLD

$S_{flapped}$ is the area of the wing covered by the flow through HLD

S_{ref} is the reference area of wing

$\Lambda_{H.L.}$ is the sweep angle at the hinge line of the HLD.

3.4 Empennage Configuration Design

For conventional aircraft, the main function of the empennage is to ensure aircraft stability and control. The empennage HOQ is to comprehensively consider the requirements of multiple parties, to transform them into the engineering characteristics, and to analyze the relationship between the requirements and the characteristics. Build the empennage HOQ using the method in Sect. 2.2.3:

(1) Identify the empennage requirements, which mainly consist of the requirements of stability, control, airworthiness and etc. And then apply AHP to determine the importance of the requirements shown in Fig. 21.
(2) Identify the empennage engineering characteristics, as shown in Fig. 22.
(3) Complete the correlation matrix between engineering characteristics based on qualitative analysis by experts. The correlation analysis of the empennage is similar to that of the wing.
(4) Complete the relationship matrix based on qualitative analysis by experts and quantitative analysis of the relationship between the requirements and characteristics. The relationship analysis of the empennage is similar to that of the wing.
(5) Calculate the importance of engineering characteristics based on Eq. (1) in Sect. 2.2.3, the result is shown in Fig. 23.

The empennage HOQ is shown in Fig. 24. In the conceptual design phase, the empennage configuration design mainly involves the empennage geometry shape and the layout of the control surface. With the aid of the empennage HOQ and

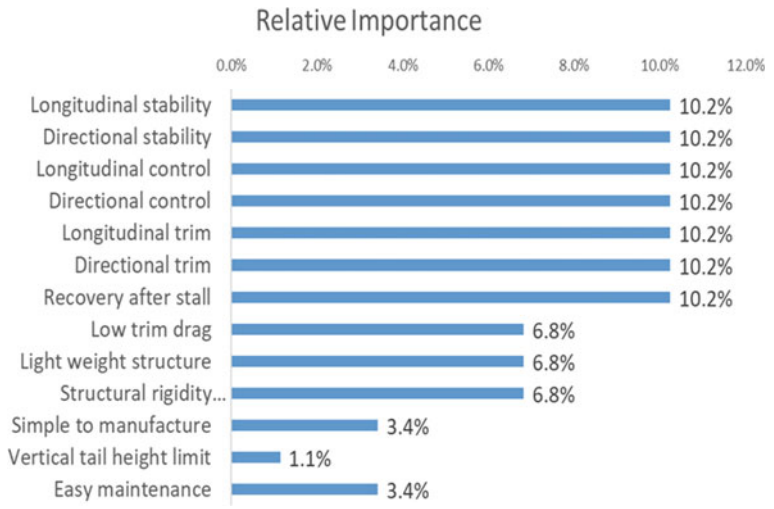

Fig. 21 The relative importance of the empennage requirements

	level1	level2
Empennage	Trim	Longitudinal trim
		Directional trim
	Stability	Longitudinal stability
		Directional stability
	Control	Longitudinal control
		Directional control
	Manufacturability	Simple to manufacture
	Structure	Structural rigidity requirements
		Light weight structure
	Aerodynamics	Low trim drag
	Size constraint	Vertical tail height limit
	Airworthiness	Recovery after stall
	Maintainability	Easy maintenance

Fig. 22 Empennage design requirements

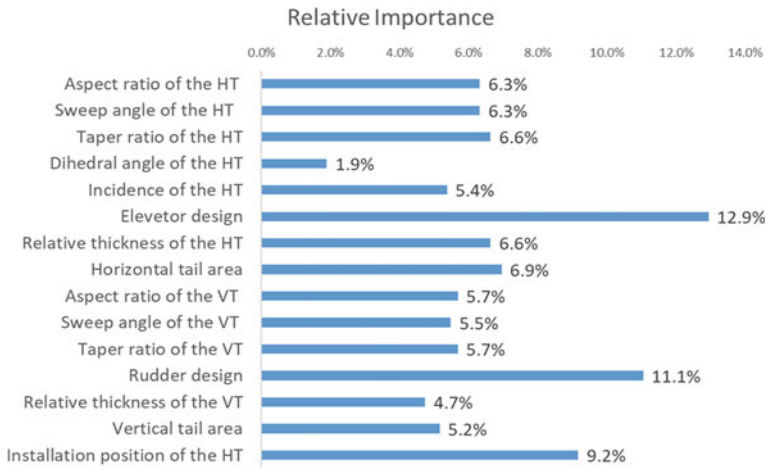

Fig. 23 The relative importance of the empennage engineering characteristics

relevant design knowledges, determine the value of the empennage engineering characteristics, as shown in Table 4. The empennage geometry shape is shown in Fig. 25.

3.5 Fuselage-Wing-Empennage Configuration

The previous sections have completed the configuration design of the fuselage, wing and empennage. Based on the knowledge of the conceptual design of the aircraft, the relative positional relationship of the three major components is determined. The final body-wing-empennage conceptual configuration is modeled by OpenVSP [14] as shown in Fig. 26.

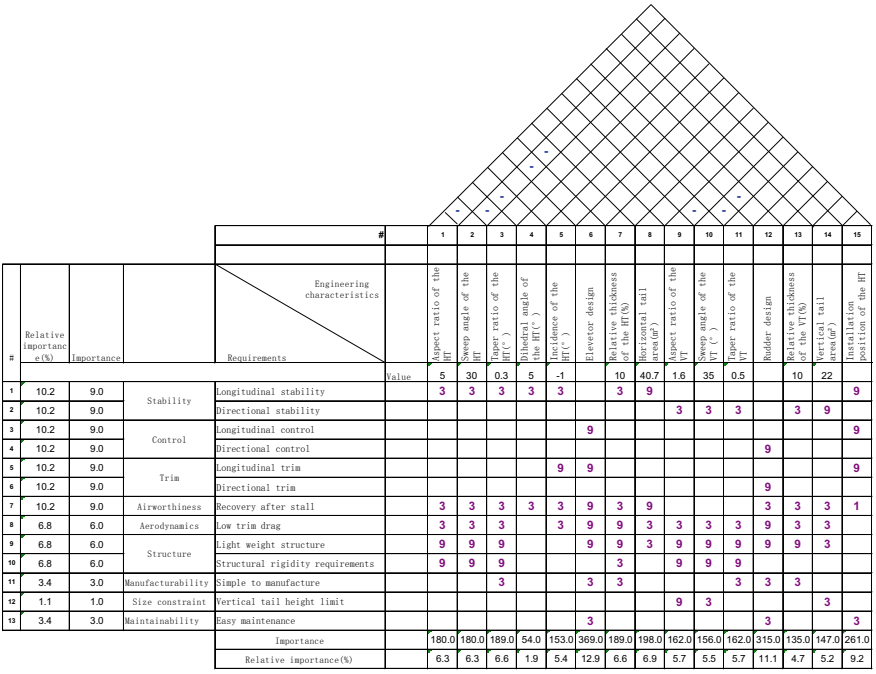

#	Relative importance(%)	Importance		Engineering characteristics / Requirements	Value	1 Aspect ratio of the HT	2 Sweep angle of the HT	3 Taper ratio of the HT(°)	4 Dihedral angle of the HT(°)	5 Incidence of the HT(°)	6 Elevator design	7 Relative thickness of the HT(%)	8 Horizontal tail area(m²)	9 Aspect ratio of the VT	10 Sweep angle of the VT (°)	11 Taper ratio of the VT	12 Rudder design	13 Relative thickness of the VT(%)	14 Vertical tail area(m²)	15 Installation position of the HT
				Value		5	30	0.3	5	-1		10	40.7	1.6	35	0.5		10	22	
1	10.2	9.0	Stability	Longitudinal stability		3	3	3	3	3		3	9							9
2	10.2	9.0		Directional stability										3	3	3		3	9	
3	10.2	9.0	Control	Longitudinal control							9									9
4	10.2	9.0		Directional control													9			
5	10.2	9.0	Trim	Longitudinal trim						9	9									9
6	10.2	9.0		Directional trim													9			
7	10.2	9.0	Airworthiness	Recovery after stall		3	3	3	3	3	9	3	9				3	3	3	1
8	6.8	6.0	Aerodynamics	Low trim drag		3	3	3		3	9	9	3	3	3	3	9	3	3	
9	6.8	6.0	Structure	Light weight structure		9	9	9			9	9	3	9	9	9	9	9	3	
10	6.8	6.0		Structural rigidity requirements		9	9	9				3		9	9	9				
11	3.4	3.0	Manufacturability	Simple to manufacture				3			3	3				3	3	3		
12	1.1	1.0	Size constraint	Vertical tail height limit										9	3				3	
13	3.4	3.0	Maintainability	Easy maintenance							3						3			3
				Importance		180.0	180.0	189.0	54.0	153.0	369.0	189.0	198.0	162.0	156.0	162.0	315.0	135.0	147.0	261.0
				Relative importance(%)		6.3	6.3	6.6	1.9	5.4	12.9	6.6	6.9	5.7	5.5	5.7	11.1	4.7	5.2	9.2

Fig. 24 The empennage HOQ

Table 4 The value of the empennage engineering characteristics

Engineering characteristics	Value
Aspect ratio of the horizontal tail	5
Sweep angle of the horizontal tail (°)	30
Taper ratio of the horizontal tail	0.3
Dihedral angle of the horizontal tail (°)	5
Incidence of the horizontal tail (°)	−1
Thickness ratio of the horizontal tail (%)	10
Horizontal tail area (m^2)	40.7
Aspect ratio of the vertical tail	1.6
Sweep angle of the vertical tail (°)	35
Taper ratio of the vertical tail	0.5
Thickness ratio of the vertical tail (%)	10
Vertical tail area (m^2)	22

4 Conclusion

In this paper, a traceable, structured and systematic aircraft conceptual design process was built by applying the QFD, and a fuselage-wing-empennage configuration for the commercial aircraft conceptual design is used as an example to illustrate application of the QFD in aircraft conceptual design.

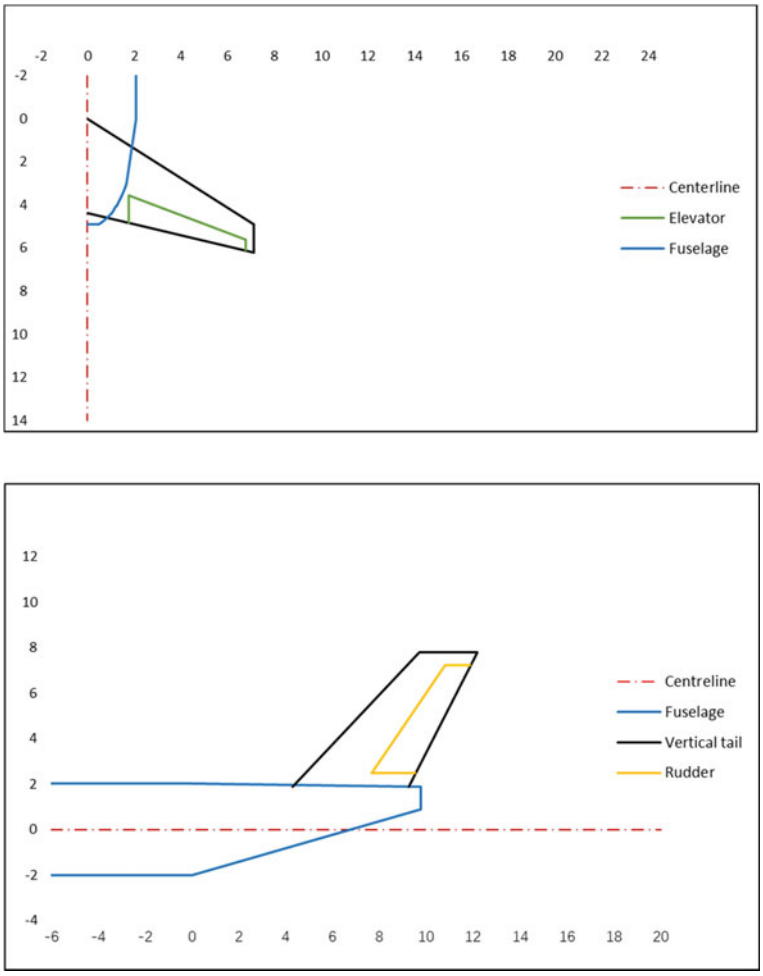

Fig. 25 The top and side views of the empennage

This method takes customer requirements as the initial design driver, which converts requirements into engineering characteristics through several HOQs. If the top-level or component-level requirements change, the HOQ can help one directly trace to the corresponding engineering characteristics. Compared with traditional methods, the process built is more traceable and systematic. In addition, each HOQ can also identify the importance of the engineering characteristics, which can help designers identify the critical technology, hold the design focus, rationally allocate limited design resources, and develop the aircraft configuration that better meets customer requirements.

This work is an initial attempt in QFD application for aircraft conceptual design. Only the fuselage, wing, empennage configuration designs are used an example

Fig. 26 Body-wing-empennage model

to illustrate the QFD application. The follow-up work will carry on application of QFD to propulsion system selection and the initial design of landing gear and other components.

Acknowledgements This work is partially supported by Commercial Aircraft Corporation of China Ltd (COMAC).

References

1. Sadraey MH (2012) Aircraft design—a systems engineering approach. Wiley
2. Tan RKW (2000) Quality functional deployment as a conceptual aircraft design tool. Dissertation, Naval Postgraduate School
3. Lin Y, Wang HP (2008) A method for identifying important design features in aircraft conceptual design phase. Comput Simul 25(8):47–50 (Chinese)
4. Kamal AM, Ramirez-Serrano A (2019) Systematic approach to conceptual design selection for hybrid UAVs using structured design methods. In: AIAA, pp 2019–2097. https://doi.org/10.2514/6
5. Kamal AM, Ramirez-Serrano A (2020) Systematic methodology for aircraft concept development with application to transitional aircraft. J Aircr. https://doi.org/10.2514/1.C035437
6. Ashtiany MS, Alipour A (2016) Integration axiomatic design with quality function deployment and sustainable design for the satisfaction of an airplane tail stakeholders. Procedia CIRP 53:142–150
7. Dasuki NK, Romli FI (2018) Quality function deployment for new standing cabin concept of commercial transport aircraft. J Mech Eng 5(2):247–257
8. Hauser RJ, Clausing D (1998) The house of quality. Harv Bus Rev. https://hbr.org/1988/05/the-house-of-quality Accessed 20 Apr 2020
9. Bae BY, Kim S, Lee JW (2017) Process of establishing design requirements and selecting alternative configurations for conceptual design of a VLA. Chin J Aeronaut 30(02):738–751
10. Awasthi A, Chauhan SS (2011) A hybrid approach integrating affinity diagram, AHP and fuzzy TOPSIS for sustainable city logistics planning. Appl Math Model 36(2):573–584

11. Deng X, Li JM, Zeng HJ (2012) Research on computation methods of AHP weight vector and its applications. Math Pract Theory 42(07):93–100 (Chinese)
12. Raymer D (2018) Aircraft design: a conceptual approach. In: AIAA, 6rd edn. Reston
13. Scholz D. Exams and solutions for the lecture aircraft design. Haw Hamburg. https://www.fzt.haw-hamburg.de/pers/Scholz/KlausurFE.html. Accessed 20 Apr 2020
14. McDonald RA (2016) Advanced modeling in OpenVSP. In: AIAA. https://doi.org/10.2514/6.2016-3282

Parametric Optimization of the PCM Caisson Structural Strength Elements

Aleksandr Bolshikh and Valentin Eremin

Abstract In modern passenger aircraft, polymeric composite materials (PCM) are used to ensure the mass excellence of both lightly loaded elements and aggregates, including wings and feathers caissons. The use of such materials instead of metal alloys makes it possible to reduce the weight of structures, increase the service life, and reduce the complexity of manufacturing and material consumption. Based on the finite element method, a caisson model was created using shell finite elements (FE), considering the anisotropic properties of PCM. To solve the problems of buckling of the elements of the caisson from the PCM, a method of analytical optimization of the stringers pitch and web plates has been developed. Analytical calculation of the local model based on the loads obtained from the global shell finite element model (FEM). The developed methodology allows obtaining a design of a caisson with a minimum mass while maintaining the necessary stiffness and strength characteristics.

Keywords Parametric optimization · Composite materials · Aircraft engineering · Vertical plumage · Strength PCM

1 Introduction

One of the main characteristics that significantly affect the flight performance and economic performance of an aircraft is the mass of its structure. Due to the anisotropic properties of PCMs, determining the required geometric characteristics when designing structural elements is a laborious technical task. In this part of the paper, we consider the urgent problem of determining and optimizing the structural parameters of the main power elements of a carbon fiber caisson, considering rational reinforcement schemes.

Composite materials have a substantially lower specific weight compared with conventional materials such as aluminum alloys, titanium alloys, steel, etc. Currently, composite materials have several disadvantages that reduce the effect of their use. The

A. Bolshikh (✉) · V. Eremin
Moscow Aviation Institute (National Research University), Moscow 125993, Russia
e-mail: bolshikhaa@mai.ru

Z. Jing and X. Zhan (eds.), *Proceedings of the International Conference on Aerospace System Science and Engineering 2020*, Lecture Notes in Electrical Engineering 680,
https://doi.org/10.1007/978-981-33-6060-0_14

disadvantages include significant fragility, poor operational survivability (impact) and the influence of climatic factors on the decrease in the properties of composite materials. Due to the anisotropic properties of the layered polymer composite material (laminate), the process of modeling composite materials using finite element calculations is complicated [1–3]. The developed technique takes into account the anisotropic properties of the laminate during parametric optimization of the thickness of such elements of the caisson as spars, ribs, and casing, with restrictions on strength indicators, as well as analytical optimization of the stringer pitch and web plates with restrictions on stability loss [4, 5]. The technique is considered on the example of the vertical plumage (VP) caisson.

The essence of the methodology is to select the geometric parameters of the structural elements of the caisson by phased optimization. The first pitch determines the thickness of the spars, ribs and effective thicknesses of the shell elements, including the cross-sectional area of the stringers. As the aim of objective function, the mass is chosen. The limitations for the design elements made of metal alloys are permissible stresses. For parts made from PCM, the maximum principal tensile and compression strains are selected as constraints. Further, the stringers pitch and web plates with buckling are optimized.

The developed methodology allows obtaining a design of a caisson with a minimum mass while maintaining the necessary stiffness and strength characteristics.

Figure 1 shows three-dimensional shell models of the studied object—the VP box with the shown mechanization elements (Fig. 1a) and the caisson model without mechanization elements, root ribs and brackets for attaching to the fuselage (Fig. 1b).

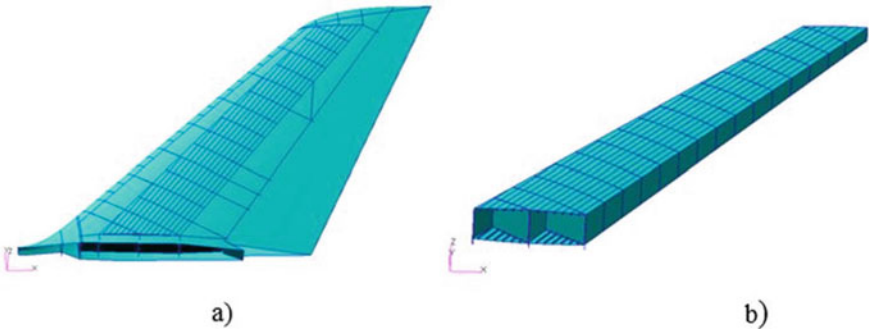

Fig. 1 3D model of the vertical tail caisson: **a** 3D surface model of the VP caisson; **b** a surface model of the VP caisson (root rib, fuselage mounting brackets and mechanization are not shown)

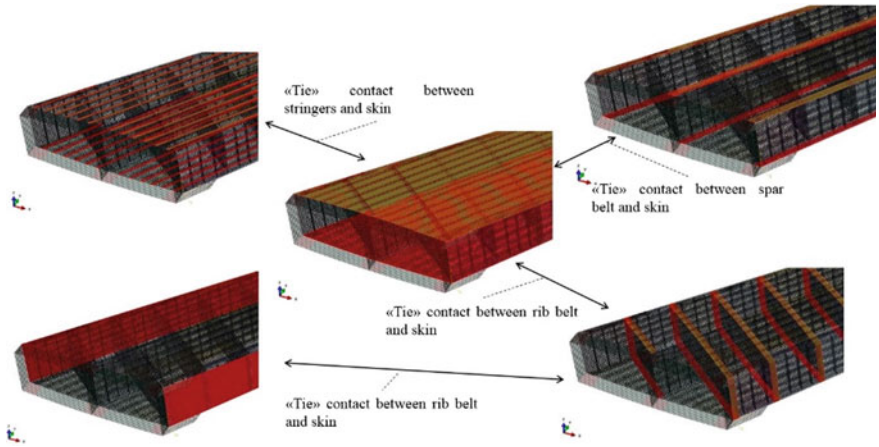

Fig. 2 Designations of "tie" contacts in the FEM of the VP caisson

2 Description of the VP Caisson's Mathematical Model

Based on the geometric model, a finite element model is developed, consisting of:

– trio and quad shell elements;
– RBE3 elements for load application.

Sheathing, spars, and ribs are modeled by shell finite elements.

The finite element model (FEM) includes 156,845 finite elements and 153,369 nodes (Fig. 3a, b).

The bends of the spars and ribs are modeled by shell elements, Fig. 2 shows the locations of the "tie" contacts of the spars' bends and rib belts with sheathing, the rib belts with spars. A "tie" contact is used to connect the finite elements with each other by creating absolutely rigid bonds between the nodes on the dependent and independent contact surfaces [6, 7].

3 Parameters of Materials

For wing panels, a laminate with laying 50/40/10 is used (50% of fibers directed at an angle of 0°, 40% of fibers directed at an angle plus-minus 45° and 10% of fibers directed at an angle of 90°). For wing spars, a laminate with 10/80/10 laying is used [8–10].

For metal parts, the characteristics of 1163T material in the form of semi-finished products in the form of plates were used.

All strength criteria for composite materials are indicated for packages [11].

4 Loads Modes

The stress–strain state is considered for the determining case of loading.

To load the model, ten concentrated forces are used, uniformly distributed over the span of the casing. The forces act on the keel through RBE3 elements applied to the nodes of the caisson panel, the independent nodes of which are located on the axis of stiffness.

The axis of stiffness of the caisson is divided into equal intervals in span. Loads are applied to independent nodes and are determined from the shear force and torque diagrams.

5 Optimization Method

As a tool for selecting thicknesses, parametric FEM optimization (gauge optimization) was used. This method involves the strain (i.e., the movement of mesh elements without violating its topology) of the originally constructed mesh by the given law of its movement. This law, which is a solution of the equations of the deformable grid, when the boundary conditions for these equations are given by some relations, which include parameters that characterize the permissible changes in the geometry of the structure. Thus, according to this method, modification of the geometry takes place in an iterative process with the deformable mesh without destroying its topology [12–14].

6 Optimization Parameters

As the target of objective function, the mass is chosen.

Optimization constrains:

- Buckling of all types in all types of PCM parts is not allowed;
- The values of the main tensile strains in the plane should not exceed 0.45% for all PCM parts;
- The values of the main compressive strains in the plane should not exceed 0.35% for all PCM parts;
- The ratio of the area of the stringer cross section and the attached skin is ~50–50%;
- Total buckling for metal parts is not allowed;
- The values of the stresses of the ribs should not rich 300 MPa;
- The minimum skin thickness is at least 6 mm.

Permissible strains are determined by the characteristics of the material used.

The optimization task is to minimize the objective function.

After optimization of the effective thickness of the skin, the thickness of the spars and ribs, parametric optimization of the stringers pitch and ribs of the web plates is carried out with a restriction on the buckling of the skin, respectively, to optimize the stringers pitch and spars to optimize the pitch of the web plates.

At the end, a verification calculation of the caisson model is carried out considering the parameters obtained after optimization.

7 Stringers Pitch Optimization

To determine the stringers pitch, a technique has been developed that allows you to choose the optimal pitch, considering restrictions on the buckling.

Stringer thicknesses are selected based on effective skin thicknesses and optimized stringers pitch.

The skin is divided into many parts, it is proposed to take the median planes of the ribs as dividing lines, then the compressive force on the resulting part is determined, and the buckling of this part is calculated, in case of buckling, the part is divided into even smaller parts, up to of the moment until it ceases to lose stability, the minimum part size and is the obtained optimal stringers pitch [15, 16].

Equations for determining the compressive forces at which the panel begins to be buckling depending on the boundary conditions and sizes [17].

8 Optimization of the Web Plates Pitch

To determine the pitch of the web plates, a technique has been developed that allows you to choose the optimal pitch, considering restrictions on the buckling of the spars.

The web plate optimization algorithm is identical to stringers pitch calculation algorithm.

Equations for determining shear forces at which the spar begins to be buckling are presented below [17].

9 Verification Calculation

Figure 3 shows the FEM of the VP caisson for verification calculation. The boundary conditions of the verification calculation coincide with the boundary conditions used in the optimization. “Tie” contacts are modeled in the same way as for parametric optimization of the thickness of the structural elements of the caisson. Since effective thicknesses were used in the optimization of the sheathing thickness (the sheathing area includes the area of the stringers), and in the verification calculation the stringers are modeled separately, contacts between the stringer shelves and the sheathing are

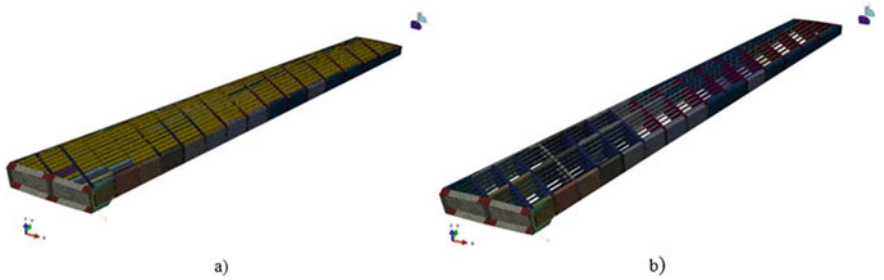

Fig. 3 VP caisson FEM for verification calculation: **a** a general view of the finite element model of the VP caisson for verification calculation; **b** a general view of the finite element model of the VP caisson for verification calculation (sheathing is not conventionally shown)

added. Figure 4 presents the results of the verification calculation of the caisson. Figure 4a shows the displacements of the VP caisson in a scale of 10–1; the maximum displacements are 299.5 mm.

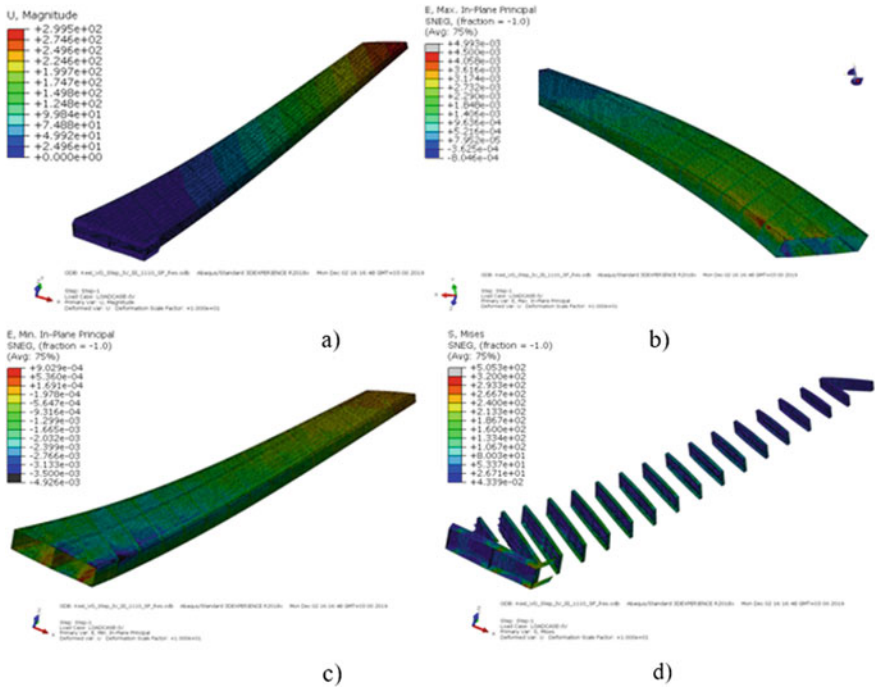

Fig. 4 Verification calculation results: **a** displacement, mm (scale of the deformed structure 10:1); **b** the maximum main strains of the VP in the plane, mm/mm; **c** the minimum main strains of the VP in the plane, mm/mm; **d** VP equivalent Von Mises stress, MPa

The maximum main strains in the spar web, excluding the zones of strain bursts at the root of the caisson, $\varepsilon = 0.0039$ (Fig. 4b). The strength margin of the spar web of the caisson VP:

$$\eta = [\varepsilon]/\varepsilon = 0.004/0.0039 = 1.02.$$

The maximum main strains in the spar web, excluding the zones of strain bursts in caisson root, $\varepsilon = 0.0039$ (Fig. 4b). The strength margin of the spar web of the caisson VP:

$$\eta = [\varepsilon]/\varepsilon = 0.004/0.0039 = 1.02.$$

Minimum main strains in the spar web, excluding the zones of strain bursts at the root of the caisson, $\varepsilon = 0.004$ (Fig. 4c). The strength margin of the spar web of the caisson VP:

$$\eta = [\varepsilon]/\varepsilon = 0.004/0.004 = 1.00.$$

Minimum main strains in the spar web, excluding the zones of strain bursts in the caisson root, $\varepsilon = 0.004$ (Fig. 4c). The strength margin of the spar web of the caisson VP:

$$\eta = [\varepsilon]/\varepsilon = 0.004/0.004 = 1.00.$$

The maximum acting stresses in the rib's web and rib's ribs $\sigma = 170\,MPa$ (Fig. 4d). The strength margin of the rib webs of the caisson VP:

$$\eta = [\sigma]\big/\sigma = 300\,MPa\big/220\,MPa = 1.36.$$

The buckling for the spar elements, the safety factor equals 1.03, the buckling for the rib elements, the safety factor is 1.04.

10 Conclusions

As a result, the proposed method allows to achieve the following results:

- The minimum thickness of the VP caisson for the defining case of loading, satisfying the strength limitations, were calculated.
- The results of calculating the distribution of tensile and compressive strains in the skin elements and side members, as well as the stresses in the rib structures are presented.
- The optimal stringers pitch and web plate are determined.

– In both cases of loading, there is no buckling of the lining elements, the spar web, and ribs. The strength of metal ribs is provided, for which the stresses do not archive the yield strength.
– The weight of the caisson design is reduced by 8–15% while maintaining strength and stiffness characteristics.

References

1. Kassapoglou C (2010) Design and analysis of composite structures with applications to aerospace structures. Delft University of Technology, The Netherlands
2. Andrienko VM, Belous VA (2001) Optimal design of composite panels of the wing caisson according to the conditions of strength and stability. Works TsAGI 2642:151–158
3. Christensen RM (1982) Mechanics of composite materials. Lawrence Livermore Laboratory, University of Californian Livermore
4. Vasiliev VV, Razin AF (2006) Anisogrid composite lattice structures for spacecraft and aircraft applications. Compos Struct 76:182–189
5. Gavva LM (2019) Buckling problems of structurally–anisotropic composite panels of aircraft with influence of production technology. Mater Sci Forum 971
6. Abaqus analysis user's manual, part VIII: constraints
7. Goncharov PS, Artamonov IA, Khalitov TF, Dinisikhin SV, Sotnik DE (2012) NX advanced simulation. Engineering analysis. DMK Press, Moscow
8. Kaw AK (2006) Mechanics of composite materials. Boca Raton, Taylor & Francis Group, p 457
9. Kasumov EV (2015) The search technique for rational design parameters using the finite element method. Sci Notes TsAGI 46(2):63–79
10. Mitrofanov OV (2017) On the issue of optimal reinforcement of reinforced panels of thin-walled structures made of composite materials. Actual Probl Mod Sci 5(96):49–53
11. Estimated characteristics of aviation metallic structural materials guide. Issue 1. JSC UAC, Moscow, 2009
12. COMSOL Multiphysics. Optimization module user's guide
13. Vasiliev VV (1988) Mechanics of constructions from composite materials. Mechanical Engineering, Moscow, 272 p
14. Li D, Xiang J (2013) Optimization of composite wing structure for a flying wing aircraft subject to multi constraints. In: 54th AIAA/ASME/ASCE/AHS/ASC structures, structural dynamics, and materials conference, Boston. AIAA Paper No. 2013-1934, pp 1–11
15. Huang L, Sheikh AH, Ng C-T, Griffith MC (2015) An efficient finite element model for buckling analysis of grid stiffened laminated composite plates. Comps Struct 122:41–45
16. Walker M (2002) The effect of stiffeners on the optimal ply orientational and buckling load of rectangular laminated plates. Comput Struct 4:30–44, 125
17. Laszlo P, Kollar G, Springer S (2003) Mechanics of composite structures. Cambridge University Press, Cambridge, p 469

Influence and Correction of Satellite Phase Center Offsets for RNSS Performance of BDS-3

Cheng Liu, Weiguang Gao, Chengpan Tang, and Wei Wang

Abstract BDS-3 provides three kinds of Radio Navigation Satellite Services (RNSS), including primary Positioning Navigation and Timing (PNT), Satellite Based Augmentation System (SBAS) and Precise Point Positioning (PPP). Satellite phase center offsets are important error sources for service performance. Misalignments of frequency-dependent phase centers decrease the service performance further. Therefore, approaches accounting for satellite phase center offsets and the misalignments are prerequisite for satisfactory service performance. Phase center offsets induced errors on ranging and positioning accuracy are analyzed. Different feasible approaches accounting for phase center offsets are presented with reached accuracy. Finally, optimal approaches accounting for the phase center offsets are concluded for all the kinds of RNSS services with real measurements.

Keywords BDS · Satellite phase center offsets · Satellite based augmentation system · Precise point positioning · Total group delay

1 Introduction

On December 27, 2018, the third phase of the BeiDou navigation satellite system (BDS) started providing basic global navigation services, marking the completion of its preliminary system, which consisted of 18 medium Earth orbit (MEO) satellites. BDS-3 is expected to complete the final system—which will consist of three geostationary Earth orbit (GEO) satellites, three inclined geosynchronous orbit (IGSO) satellites, and 24 MEO satellites—and officially provide comprehensive global services by the end of 2020 [1].

C. Liu · W. Gao · W. Wang
Beijing Institute of Tracking and Telecommunication Technology, Beijing, China

C. Tang (✉)
Shanghai Astronomical Observatory, Shanghai, China
e-mail: cptang@shao.ac.cn

Z. Jing and X. Zhan (eds.), *Proceedings of the International Conference on Aerospace System Science and Engineering 2020*, Lecture Notes in Electrical Engineering 680,
https://doi.org/10.1007/978-981-33-6060-0_15

Table 1 Planned open RNSSs to be provided by BDS-3

Service type	Broadcast signals	Broadcasting satellites	Service area	Precision of service (95%)
PNT	B1I, B3I	GEO, IGSO, MEO	Global	Horizontal: 5 m; elevation: 5 m
	B1C, B2a, B2b	GSO, MEO		
SBAS	B1C, B2a	GEO	China and surrounding areas	Meter-level; better than that for basic navigation
PPP	B2b	GEO	China and surrounding areas	Decimeter and centimeter-level for dynamic and static navigation, respectively

The plan is for BDS-3 to provide three types of radio navigation satellite services (RNSSs), namely, basic positioning, navigation, and timing (PNT); satellite-based augmentation system (SBAS) services; and precise point positioning (PPP), as shown in Table 1 [2]. The PNT and SBAS services involve mainly single- or dual-frequency pseudorange measurements [3, 4], whereas the PPP services involve mainly dual-frequency carrier-phase measurements [5–7].

Generally, the satellite antenna phase center (SAPC) and center of mass (CoM) of a navigation satellite do not coincide. Offsets of the SAPC relative to the CoM is referred to as the SAPC offsets [8]. It has been noted that the SAPC offsets of navigation satellites, which can be as large as 2 m, are a major source of navigation and positioning errors and thus must be corrected [8, 9]. To this end, various satellite navigation systems or service organizations have adopted the corresponding countermeasures. Specifically, the Global Positioning System (GPS) of the US and the Quasi-Zenith Satellite System (QZSS) of Japan perform an integrated computation of the satellite orbit and clock error through an ionosphere-free linear combination of the pseudorange and carrier-phase observations at the L1 and L2 frequencies. In other words, the L1/L2 dual-frequency ionosphere-free combination is adopted to compute the virtual SAPC. For the GPS and QZSS, the SAPC serves as the temporal and spatial reference point to define satellite clock errors and generate the satellite broadcast ephemerides, respectively. Furthermore, for the centimeter-level augmentation services of the QZSS, the SAPC serves as the temporal and spatial reference point to define the satellite clock errors and enable precise orbit determination correction, respectively. Thus, the GPS and QZSS require no additional SAPC correction on the user side, making the services easy to use [10]. Similar to the GPS, the Galileo uses a virtual phase center offset (PCO) based on the E1/E5a dual-frequency ionosphere-free combination to generate the freely accessible navigation message (F/NAV). To facilitate interoperability among the global navigation satellite systems (GNSSs), the International GNSS Service (IGS) provides precise ephemerides based on the satellite CoM and the SAPC correction files. To obtain the precision products

of the IGS, the user must convert the ephemerides based on the satellite CoM to those based on the SAPC by considering the correction specified in the files [11, 12].

Compared with the GPS, QZSS, and Galileo, the BDS involves a more complex SAPC correction problem that must be resolved [10]. Specifically, the BDS broadcasts the downlink navigation signals at three different frequencies, namely, B1, B2, and B3; however, the SAPC varies with the frequency, leading to different SAPC variations at the three frequencies. In addition, the RNSSs (PNT, SBAS, PPP) provided by the BDS require different levels of precision, and thus, a suitable SAPC correction must be applied for each service by using different methods.

In this work, the influence of the SAPC offsets on the user ranging error and positioning precision of the BDS was theoretically analyzed. Considering the findings, different methods to correct the SAPC variations of the BDS were summarized and described by performing a comparative analysis of the applicability and performance of each approach. Finally, the methods were validated and evaluated using in-orbit observations, and recommendations were made to improve the SAPC correction for the different RNSSs of the BDS.

2 Effect of SAPC Offsets on User Ranging

SAPC variations are fixed with reference to the satellite body, and thus, they can be described using the satellite-fixed coordinate system. The origin (O) of the satellite-fixed coordinate system is the satellite CoM; the Z-axis points to the center of the Earth; the plane XOY is perpendicular to the Z-axis and tangential to the satellite motion trajectory. For the MEO and IGSO satellites of the BDS, the Y-axis is the cross product of the Z-axis and the direction pointing from the satellite to the sun; the X-, Y-, and Z-axes constitute a right-handed coordinate system. For the GEO satellites of the BDS, the Y-axis is the cross product of the Z-axis and the direction of the satellite velocity; in addition, the X-, Y-, and Z-axes constitute a right-handed coordinate system. Generally, the SAPC variation, which is a major source of the user ranging error, is related to the angle between the direction pointing from the satellite to the user and the Z-axis of the satellite-fixed coordinate system, θ, as shown in Fig. 1.

If the SAPC is projected onto the satellite-fixed coordinate system, and the components of the projection on the Z-axis and plane XOY are designated as dz and dxoy, respectively, the component of the projection in the user ranging direction, dr, can be expressed as follows:

$$dr = \cos\theta \cdot dz + \sin\theta \cdot dxoy \tag{1}$$

For the BDS MEO satellites, given the distance between the satellite and the center of the Earth, L ≈ 27,900 km, and the Earth radius R ≈ 6400 km, the maximum and minimum values of θ can be computed as $\theta_{\max} = \arctan\left(\frac{R}{L}\right) = 12.91°$ and $\theta_{min} = 0°$, respectively. Given the range of values of θ, the following equation can be derived:

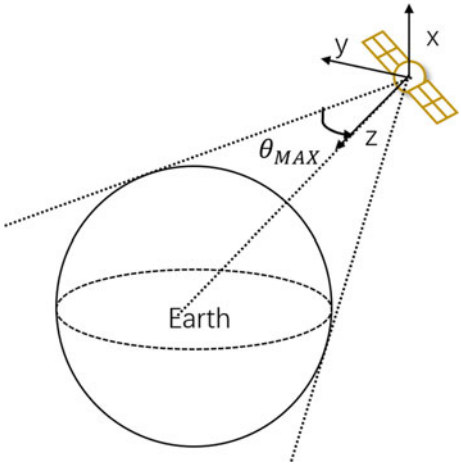

Fig. 1 Schematic of the angle between the direction pointing from the satellite to the center of the Earth and the satellite radial direction [1]

$$dr = (1 \sim 0.975) \cdot dz + (0 \sim 0.223) \cdot dxoy \tag{2}$$

For the GEO and IGSO satellites of the BDS, given the distance between the satellite and the center of the Earth, L $\approx$ 42,000 km, the maximum and minimum values of θ can be obtained as $\theta_{max} = 12.91°$ and $\theta_{min} = 8.7°$, respectively. Given the range of values of θ, the following equation can be derived:

$$dr = (1 \sim 0.989) \cdot dz + (0 \sim 0.151) \cdot dxoy \tag{3}$$

Equations (2) and (3) show that the component of the projection of the SAPC on the Z-axis, *dz*, is the major source of the user equivalent range error (UERE). Thus, when the direction of the vector of the SAPC offsets approximate that of the Z-axis of the satellite-fixed coordinate system, the SAPC offset considerably influences the UERE, with the maximum influence equal to the absolute value of the SAPC offset (up to 2 m, as mentioned previously). In addition, if the multiple-frequency signals of the BDS are combined to realize navigation and positioning, the presence of frequency-specific SAPC variations is expected to further increase the UERE.

In summary, the impact of the SAPC variations cannot be neglected even for the PNT services with meter-level precision, because the presence of SAPC variations can lead to a maximum UERE of several meters. For the SBAS, PPP, and other augmentation services, it is critical to reasonably and effectively correct the SAPC variations.

3 Methods to Correct the BDS SAPC Variations and Comparative Analysis

3.1 SAPC Orbit Broadcast-Based Correction Methods

Full correction model. The SAPC variations can be corrected based on the SAPC orbital parameters. In this method, the ground operation control system (GOCS) computes the SAPC-referenced orbital parameters and uploads them onto the satellite to broadcast the ephemeris.

Specifically, first, the GOCS performs dynamic and static orbit determination based on observations, thereby obtaining the CoM-referenced numerical orbit of the navigation satellite [13]. Subsequently, the SAPC offsets vector in the satellite-fixed coordinate system, $[dx_{\text{phs}} \quad dy_{\text{phs}} \quad dz_{\text{phs}}]^{\text{T}}$, is transformed into a vector in the Earth-centered Earth-fixed coordinate system (ECEF) by using the following equation [13]:

$$\begin{bmatrix} dx_{\text{ECEF}} \\ dy_{\text{ECEF}} \\ dz_{\text{ECEF}} \end{bmatrix} = \boldsymbol{R}_{\text{ciscts}} \cdot [\boldsymbol{e}_x \quad \boldsymbol{e}_y \quad \boldsymbol{e}_z] \cdot \begin{bmatrix} dx_{\text{phs}} \\ dy_{\text{phs}} \\ dz_{\text{phs}} \end{bmatrix} \tag{4}$$

where $[dx_{\text{ECEF}} \quad dy_{\text{ECEF}} \quad dz_{\text{ECEF}}]^{\text{T}}$ is the SAPC offsets vector in the ECEF; $\boldsymbol{R}_{\text{ciscts}}$ is the rotation matrix for the transformation between the satellite-fixed inertial coordinate system and the ECEF; and $[\boldsymbol{e}_x \quad \boldsymbol{e}_y \quad \boldsymbol{e}_z]$ is the vector of the satellite-fixed coordinate system, which is related to the satellite attitude.

The satellite orbits in reference to the SAPC at different frequencies can be obtained by superimposing the SAPC offsets vector in the ECEF, $[dx_{\text{ECEF}} \quad dy_{\text{ECEF}} \quad dz_{\text{ECEF}}]^{\text{T}}$, onto the satellite CoM numerical orbit. The GOCS generates the ephemerides to be broadcast by using the SAPC-referenced orbits [14] and uploads the ephemerides onto the satellite to be broadcasted.

The GPS and QZSS have already adopted this method, and this approach is applicable to the BDS, albeit with certain minor modifications. First, the numerical orbits in reference to the SAPC at different frequencies (B1, B2, and B3) need to be converted into separate broadcast ephemerides, which are later uploaded onto the satellite, to be broadcasted.

In addition, for the BDS, the vector of the satellite-fixed coordinate system, $[\boldsymbol{e}_x \quad \boldsymbol{e}_y \quad \boldsymbol{e}_z]$, needs to be computed using different methods for satellites having different types of orbits. In particular, for the MEO and IGSO satellites, the reference coordinate system under the yaw-steering mode can be expressed as follows:

$$\begin{cases} \boldsymbol{e}_z = -\dfrac{\boldsymbol{r}}{|\boldsymbol{r}|} \\ \boldsymbol{e}_y = \boldsymbol{e}_z \times \dfrac{\boldsymbol{r}_{\text{sun}} - \boldsymbol{r}}{|\boldsymbol{r}_{\text{sun}} - \boldsymbol{r}|} \\ \boldsymbol{e}_x = \boldsymbol{e}_y \times \boldsymbol{e}_z \end{cases} \tag{5}$$

where r and r_{sun} denote the position vectors of the satellite and the sun in the inertial coordinate system, respectively. For the GEO satellites, the reference coordinate system under the orbit-normal mode can be expressed as follows:

$$\begin{cases} \boldsymbol{e}_z = -\dfrac{\boldsymbol{r}}{|\boldsymbol{r}|} \\ \boldsymbol{e}_y = \boldsymbol{e}_z \times \dfrac{\boldsymbol{v}}{|\boldsymbol{v}|} \\ \boldsymbol{e}_x = \boldsymbol{e}_y \times \boldsymbol{e}_z \end{cases} \tag{6}$$

where v is the satellite velocity vector in the satellite-fixed inertial coordinate system.

In this method, the SAPC serves as both the spatial and temporal reference points for the navigation satellite broadcast ephemeris and satellite clock error, respectively. The advantages of this method are that the SAPC variations in the broadcast ephemerides exhibit nearly no precision loss, and no additional corrections are required on the user side. However, broadcasting the ephemerides in reference to the SAPC at different frequencies requires a simultaneous upload of several sets of navigation messages from the GOCS to the satellite, thereby significantly increasing the message transmission load on the GOCS, which is the most notable limitation in the application of this approach to the BDS.

Group delay-based correction model. To reduce the computation and message transmission load on the GOCS in the full correction model, the BDS can broadcast the satellite navigation messages for the reference frequency and use the group delay to correct the SAPC offsets at the other frequencies relative to that at the reference frequency.

Equations (1) to (3) show that the component of the projection of the SAPC offsets on the Z-axis, *dz*, is the major source of the ranging error, whereas the component of the projection on the plane *XOY*, *dxoy*, exerts only a relatively small impact on the ranging error. Thus, to reduce the computation and processing load on the system and user receivers, a straightforward implementation of the aforementioned full correction model involves broadcasting the component of the SAPC projection on only the Z-axis.

Specifically, only the broadcast ephemeris in reference to the SAPC at a single frequency (the reference frequency) is uploaded onto the satellite for broadcasting. The component of the projection of the SAPC offsets at the other frequencies relative to that at the reference frequency on the Z-axis (the direction pointing from the satellite to the center of the Earth) is approximated and corrected using the group delay, as shown in Fig. 2 (where c is the speed of light).

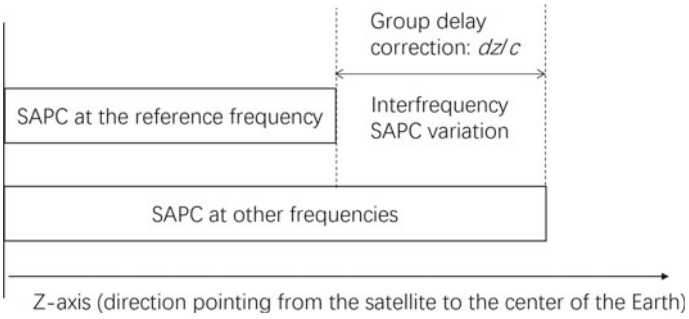

Fig. 2 Schematic of group delay-based SAPC correction model [2]

Consequently, the broadcast ephemerides for the signals at the different frequencies have the same satellite orbit and clock error, and the only difference is in terms of the parametric values for the signal group delay, thereby considerably reducing the uplink data transmission load on the GOCS.

3.2 Satellite CoM Orbit Broadcast-Based Correction Methods

Correction model based on the conversion of the satellite CoM to the SAPC. The SAPC can be corrected by converting the satellite CoM to the SAPC. In particular, the GOCS uploads the CoM-based broadcast ephemerides. The three-axial variations of the SAPC relative to the satellite CoM are provided to the user through a separate means of communication (for example, the internet). Subsequently, the corresponding vector corrections to the CoM are implemented using the method described in Sect. 3.1, thereby correcting the SAPC. This method reduces the computation and communication load on the GOCS; however, it increases the computation and communication load on the user side.

Satellite clock error and group delay-based correction model. The correction model based on the conversion of the satellite CoM to the SAPC can offset the impact of the SAPC offsets with almost no precision loss. However, the parametric settings to convert the satellite CoM to the SAPC for each satellite must be provided to the user through a separate means of communication (for example, the internet), thereby reducing the ease of use of the approach. To simplify the system broadcast and process flow, on the premise of broadcasting the satellite CoM-based orbital parameters, the SAPC can be corrected using the satellite clock error and group delay.

Specifically, first, the SAPC offsets at the reference frequency is approximated and expressed in terms of the satellite clock error a_0. Next, the SAPC offsets at the other frequencies relative to that at the reference frequency is approximated and expressed using the group delay.

Subsequently, the SAPC correction for the reference frequency in the direction from the satellite to a given ground observation station P (with known coordinates) in the service area, $d\rho_{phs}$, can be computed using the following equation, based on observations at a predefined sampling interval:

$$\mathrm{d}\rho_{phs} = \begin{pmatrix} \Delta X \\ \Delta Y \\ \Delta Z \end{pmatrix}^{T} \cdot \frac{\boldsymbol{r}_{sta} - \boldsymbol{r}}{|\boldsymbol{r}_{sta} - \boldsymbol{r}|} \tag{7}$$

where r_{sta} and r are the position vectors of the ground observation station P and the satellite in the ECEF, respectively. Considering the multiple samples collected at a predefined sampling interval for a given period and the $d\rho_{phs}$ value computed for each sample, the statistical mean of the $d\rho_{phs}$ values, Δa_0, can be used as the SAPC correction:

$$\Delta a_0 = \frac{\sum_{i=1}^{n} d\rho_{phs}}{c * n} \tag{8}$$

where c is the speed of light ($c = 3 \times 10^8$ m/s); and n is the number of observation samples collected in the observation period for the SAPC correction. The SAPC correction for the service area can be realized by correcting the satellite clock error (a_0) by using the resulting Δ_{a0} value.

This method uses the satellite clock error to approximate the SAPC offsets at the reference frequency; however, the projection of this offsets in the direction of the Earth may change. Therefore, the precision of this method depends on the anisotropy of the projection of the SAPC offsets at the reference frequency. In addition, because the SAPC offsets at the other frequencies relative to that at the reference frequency is approximated using the group delay, the precision of this method depends on the anisotropy of the projection of the frequency-specific SAPC variation.

3.3 Comparative Analysis of the Methods

Precision of correction. The difference in the precision values of the aforementioned SAPC correction methods can be attributed to the fact that the approaches neglect the anisotropy of the SAPC to different extents. Specifically, although the full correction model realizes a full correction of the SAPC, the satellite CoM-SAPC conversion-based correction model provides the user with the relationship to convert the satellite CoM orbit to the SAPC orbits at different frequencies. However, both the methods consider the anisotropy of the SAPC and can thus correct the SAPC offsets with almost no precision loss.

In contrast, the group delay-based correction model considers the anisotropy of the SAPC offsets at the reference frequency (B3) but neglects the anisotropy of the frequency-specific SAPC variations. The maximum projection of the frequency-specific SAPC variations in the pseudorange direction can be expressed as follows:

$$\max\_\text{diff}\, dr = |\cos\theta_{\max} - \cos\theta_{\min}| \cdot dz + |\sin\theta_{\max} - \sin\theta_{\min}| \cdot dxoy \quad (9)$$

For the MEO satellites, Eq. (9) can be rewritten as follows:

$$\max\_\text{diff}\, dr = 0.025 \cdot dz + 0.223 \cdot dxoy \quad (10)$$

For the GEO and IGSO satellites, Eq. (9) can be rewritten as follows:

$$\max\_\text{diff}\, dr = 0.011 \cdot dz + 0.151 \cdot dxoy \quad (11)$$

For the BDS, if the Z-axis component of the frequency-specific SAPC offset is 0.3 m, and the component in the plane *XOY* is 0.02 m, the anisotropy of the projection of the frequency-specific SAPC offsets is 0.006 m for the GEO and IGSO satellites and 0.012 m for the MEO satellites.

The satellite clock error and group delay-based correction model is based on the group delay-based correction model; however, the satellite clock error is used instead of the broadcast ephemeris to approximate and express the SAPC offsets at the reference frequency. Therefore, the precision of this method depends on the anisotropy of the projection of the SAPC offsets at the reference frequency as well as that of the frequency-specific SAPC variation. Consequently, this approach involves the largest precision loss. Equation (1) shows that the direction of projection of a satellite varies with the location of the ground users; thus, the user ranging error caused by the SAPC offsets also varies.

Generally, the components of the projection of the SAPC offsets on the Z-axis, *dz*, and that in the plane *XOY*, *dxoy*, have a maximum value of approximately 1 m and several decimeters, respectively. If $dz = 1.0$ m, and $dxoy = 0.6$ m, the offsets in the ranging error caused by the SAPC offsets at the reference frequency for different ground users can reach 0.15 m for the MEO satellites of the BDS and 0.11 m for the GEO and IGSO satellites.

Table 2 lists the estimated precision losses of the different correction models.

Uplink load and user friendliness. Among the four methods of correction, the full correction model exerts the largest uplink load on the GOCS. In particular, for the BDS, this method requires the generation and upload of the navigation messages for the SAPC variations at all the three frequencies (B1, B2, and B3). The group delay-based correction model and the satellite clock error and group delay-based correction model exert the smallest uplink loads, because the navigation messages for the different frequencies are different only in terms of the satellite clock error and group delay. The correction model based on the conversion of the satellite CoM to the SAPC requires the uploading of only one set of navigation messages; however,

Table 2 Estimated precision losses of different correction models (unit: m)

Source of precision loss	Correction based on SAPC orbit broadcast		Correction based on satellite CoM orbit broadcast	
	Full correction model	Group delay-based correction model	Correction model based on the conversion of the satellite CoM to the SAPC	Satellite clock error and group delay-based correction model
Anisotropy of the projection of the SAPC offsets at the reference frequency	0	0	0	0.11–0.15
Anisotropy of the frequency-specific SAPC variation	0	0.006–0.012	0	0.006–0.012

the relationship to convert the satellite CoM to the SAPC must be provided to the user through a separate means of communication, thereby increasing the load on the GOCS.

In terms of user experience, the full correction model, group delay-based correction model, and satellite clock error and group delay-based correction model provide SAPC corrections that are not provided to the user, requiring no additional corrections on the user side. In comparison, the correction model based on the conversion of the satellite CoM to the SAPC requires the user to receive parameters or files to convert the satellite CoM to the SAPC and is thus more complex to use.

Lateral comparison. Table 3 summarizes the comparative analysis results of the correction models in terms of their precision, uplink load on the ground system, and user friendliness.

4 Test and Validation

4.1 Anisotropy of the Ranging Error Induced by the SAPC Offsets at the Reference Frequency

The anisotropy of the ranging error induced by the SAPC offsets at the reference frequency impacts the precision of the satellite clock error and group delay-based correction model.

This anisotropy for a BDS MEO satellite was computed using the ranging errors for five observation stations located in North, Northeast, Northwest, Southwest, and South China, with the results shown in Fig. 3. The maximum offsets in the anisotropy

Table 3 Comparison of the performance of the correction models

Performance parameter	Correction based on SAPC orbit broadcast		Correction based on satellite CoM orbit broadcast	
	Full correction model	Group delay-based correction model	Correction model based on the conversion of the satellite CoM to the SAPC	Satellite clock error and group delay-based correction model
Precision of correction	High	Average	High	Low
Uplink load on the ground system	High	Low	Average	Low
User friendliness	High	High	Low	High

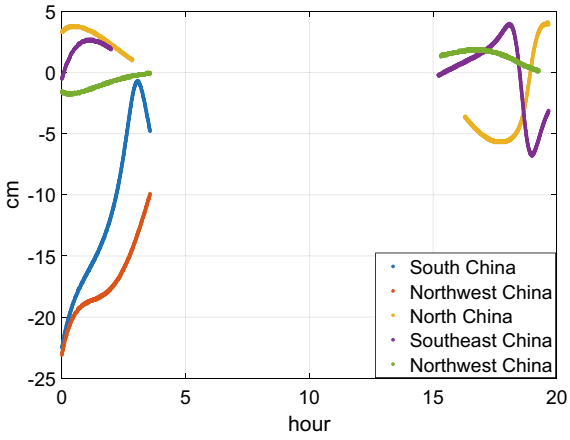

Fig. 3 Anisotropy of the projection of the SAPC offsets at the reference frequency of a BDS MEO satellite [3]

of the ranging error was 25 cm, which is consistent with the theoretical estimation presented in previous sections.

4.2 Anisotropy of the Projection of the Frequency-Specific SAPC Variation

The anisotropy of the projection of the frequency-specific SAPC offsets impacts the precision of the group delay-based correction model and the satellite clock error and group-delay-based correction model.

Figures 4, 5, and 6 show the anisotropies of the projection of the B1/B3

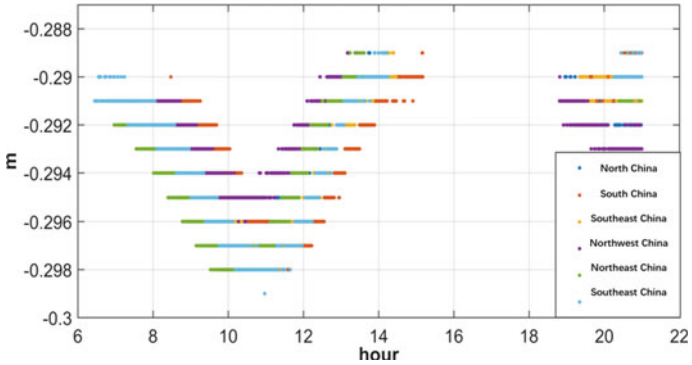

Fig. 4 Anisotropy of the projection of the B1/B3 frequency-specific SAPC offsets differences of a BDS MEO satellite [4]

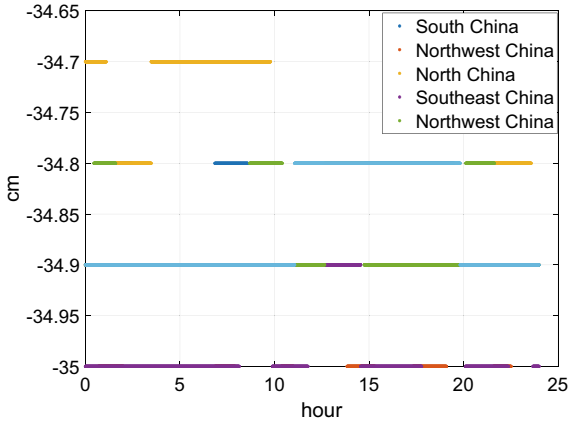

Fig. 5 Anisotropy of the projection of the B1/B3 frequency-specific SAPC offsets differences of a BDS GEO satellite [5]

frequency-specific SAPC offsets of the MEO, GEO, and IGSO satellites of the BDS, respectively.

The maximum offsets in the anisotropy of the projection of the frequency-specific SAPC offsets was 1 cm for the MEO and IGSO satellites, which is of the same order of magnitude as the theoretical estimation presented in Sect. 3.3. An error of this order of magnitude cannot be neglected for the PPP and PPP/RTK services.

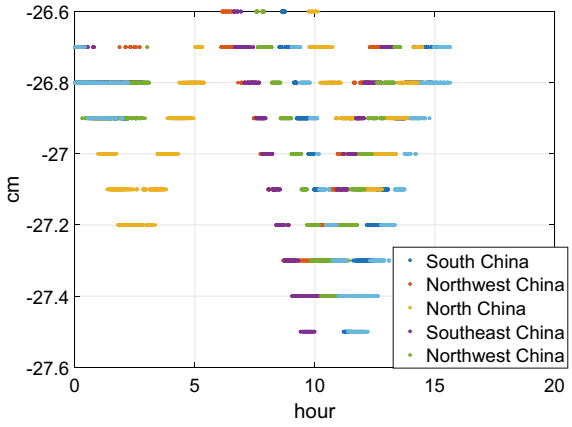

Fig. 6 Anisotropy of the projection of the B1/B3 frequency-specific SAPC offsets differences of a BDS IGSO satellite [6]

4.3 Impact of the Different SAPC Correction Methods on the Positioning Precision of the BDS

Impact on the PNT services. The observations obtained from five ground observation stations located in China during the period of November 1–10, 2019 were used to evaluate the BI/B3I dual-frequency PNT in the context of different SAPC correction methods. The results are summarized in Table 4.

Table 4 Errors in the BDS PNT generated when using different SAPC correction models (95%; unit: m)

Observation station	No SAPC correction	Correction based on SAPC orbit broadcast		Correction based on satellite CoM orbit broadcast	
		Full correction model	Group delay-based correction model	Correction model based on the conversion of the satellite CoM to the SAPC	Satellite clock error and group delay-based correction model
bjf1	3.89	3.10	3.12	3.10	3.39
chu1	4.12	3.46	3.47	3.46	3.71
gua1	3.11	2.00	1.99	2.00	2.13
kun1	2.96	1.67	1.68	1.67	2.17
xia1	3.67	2.79	2.76	2.79	2.84
Mean	3.55	2.60	2.60	2.60	2.85

The error in the BDS PNT caused by the SAPC offsets was approximately 1 m for the five ground observation stations. Thus, correcting the SAPC is necessary for the meter-level-precision PNT services. Although the four correction methods have different levels of precision performance, the values are acceptable for the PNT services. The full correction model and the correction model based on the conversion of the satellite CoM to the SAPC exhibited the highest precision, followed by those of the group delay-based model and the satellite clock error and group delay-based model.

Impact on the SBAS services. The observations obtained from five ground observation stations located in China during the period of November 1–10, 2019 were used to evaluate BI/B3I dual-frequency augmented positioning when using the different SAPC correction methods. The results are summarized in Table 5.

The errors in the BDS SBAS positioning generated owing to the SAPC variations are more than 1 m for the five ground observation stations. Thus, correcting the SAPC is necessary for the meter-level-precision SBAS positioning services. As in the case of the PNT services, although the four correction methods exhibit different levels of precision performance, the values are acceptable for the SBAS positioning services. Specifically, the full correction model and the correction model based on the conversion of the satellite CoM to the SAPC exhibit the highest precision, followed by those of the group delay-based model and the satellite clock error and group delay-based model.

Impact on the PPP services. The observations obtained from five ground monitoring stations located in China during the period of November 1–10, 2019 were used to evaluate the BI/B3I dual-frequency PPP services when using the different SAPC correction methods, and the results are summarized in Table 6. In the computation,

Table 5 Errors in BDS SBAS positioning when using different SAPC correction methods (95%; unit: m)

Observation station	No SAPC correction	Correction based on SAPC orbit broadcast		Correction based on satellite CoM orbit broadcast	
		Full correction model	Group delay-based correction model	Correction model based on the conversion of the satellite CoM to the SAPC	Satellite clock error and group delay-based correction model
bjf1	3.24	2.10	2.13	2.10	2.22
chu1	3.42	2.74	2.77	2.74	2.81
gua1	2.76	1.84	1.88	1.84	1.96
kun1	2.12	1.55	1.60	1.55	1.70
xia1	3.01	2.41	2.43	2.41	2.55
Mean	2.91	2.13	2.16	2.13	2.25

Table 6 Errors in BDS PPP positioning when using different SAPC correction models (95%; unit: m)

Observation station	No SAPC correction	Correction based on SAPC orbit broadcast		Correction based on satellite CoM orbit broadcast	
		Full correction model	Group delay-based correction model	Correction model based on the conversion of the satellite CoM to the SAPC	Satellite clock error and group delay-based correction model
bjf1	10.3	1.0	2.0	1.0	4.0
chu1	9.5	1.4	1.9	1.4	5.1
gua1	11.4	1.6	2.4	1.6	3.9
kun1	8.5	0.9	3.0	0.9	4.5
xia1	6.9	1.2	2.3	1.2	5.2
Mean	9.3	1.2	2.3	1.2	4.5

the satellite precision ephemeris and clock error were based on the satellite station and intersatellite combined orbit determination, respectively.

The maximum errors in the BDS PPP positioning generated owing to the SAPC variations for the five ground observation stations are approximately 10 cm. Thus, SAPC correction is necessary. The full correction model and the correction model based on the conversion of the satellite CoM to the SAPC exhibit the highest precision. The group delay-based correction model involved an additional precision loss of approximately 1–2 cm, and the satellite clock error and group-delay-based correction model had a further precision loss of approximately 2–3 cm. Thus, for the PPP and PPP-RTK services with centimeter-level precision, the SAPC should be corrected with discretion.

5 Conclusion

The plan for the BDS-3 is to provide three types of open RNSSs (PNT, SBAS, and PPP). However, the offsets in the SAPC is a major source of error of the BDS RNSSs and thus must be corrected. The SAPC of the BDS navigation satellites varies with the frequency. Thus, both the SAPC offsets at the reference frequency and the frequency-specific SAPC offsets must be corrected when applying the BDS RNSSs, which is a unique challenge that does not occur in the case of the GPS and QZSS.

In this study, the impact of the SAPC offsets on the user ranging and positioning precision of the BDS was theoretically analyzed. Considering the findings, methods to correct the SAPC offsets of the BDS, including the method currently used by the BDS system, that is, the group delay-based method, were summarized and described. Subsequently, the methods were comprehensively compared in terms of the precision

of correction, uplink load on the ground system, and user friendliness. Finally, the performance of the methods was evaluated by using BDS observations, thereby validating the effectiveness of the methods and confirming the results of the theoretical analysis.

Overall, the SAPC correction currently used by the BDS, that is, the group delay-based correction, is acceptable for the PNT and SBAS services, as it does not involve a significant precision loss. However, for the BDS PPP services, which require a centimeter-level precision, the currently used SAPC correction must be improved and upgraded. The satellite CoM expression-based SAPC correction results in a precision loss for the BDS PNT and SBAS services, and thus, the navigation message generation strategy currently used by the BDS GOCS must be modified. Thus, we propose the SAPC correction to be upgraded based on the SAPC expression. Specifically, we recommend that the uplink processing capacity of the GOCS is increased to realize the upload of multiple-frequency navigation messages, thereby allowing the adoption of the full correction model. If the currently used group delay-based correction must be retained, we recommend the additional correction of the frequency-specific SAPC offsets for the PPP services and the provision of the corrections to the users through navigation message broadcasting or the internet.

Acknowledgements The project is supported by National Natural Science Foundation of China (Grant Nos. 42074044, 41874039, and 41804030).

References

1. Development of the BeiDou navigation satellite system (Version 4.0). China Satellite Navigation Office, Dec 2019
2. BeiDou navigation satellite system open service performance standard (Version 2.0). China Satellite Navigation Office, Dec 2018
3. SBAS IWG (2016) Satellite-based augmentation system dual-frequency multi-constellation definition document. SBAS IWG 31, Senegal, 29 Nov–1 Dec 2016
4. SBAS IWG (2016) SBAS L5 DFMC interface control. In: SBAS IWG 31, Senegal, 29 Nov–1 Dec 2016
5. Yang Y, Xu Y, Li J et al (2018) Progress and expected performance of the BeiDou-3 system: analysis of test validation data. Sci Sin (Terrae) 48(5):584–594 (in Chinese)
6. Guo S, Cai H, Meng Y et al (2019) BDS-3 RNSS technical characteristics and service performance. Acta Geod Cartograph Sin 48(7):810–821 (in Chinese with English abstract)
7. Yang Y, Gao W, Guo S et al (2019) Introduction to BeiDou-3 navigation satellite system. Navigation 66(1):7–18
8. Montenbruck O, Schmid R, Mercier F et al (2015) GNSS satellite geometry and attitude models. Adv Space Res 56(6):1015–1029
9. Dilssner F, Springer T, Schönemann E et al (2014) Estimation of satellite antenna phase center corrections for BeiDou. In: IGS workshop, pp 23–27. MLA
10. Bertiger W, Bar-Sever Y, Harvey NK et al (2010) Next generation GPS ground control segment (OCX) navigation design. In: Institute of navigation GNSS meeting, Portland, OR, Sept 2010
11. Dow JM, Neilan RE, Rizos C (2009) The international GNSS service: in a changing landscape of global navigation satellite systems. J Geod 83:191–198

12. Kouba J, Héroux P (2001) Precise point positioning using IGS orbit and clock products. GPS Solut 5(2):12–28
13. Schutz B, Tapley B, Born GH (2004) Statistical orbit determination. Elsevier
14. Cui X, Jiao W, Jia X et al (2004) The fitting algorithm of GPS broadcast ephemeris parameters. J Inst Surv Map (J Geomatics Sci Technol) 21(4):244–246 (in Chinese with English abstract)

Effects of Tube Wall Thickness on Combustion and Growth Rate of Supersonic Reacting Mixing Layer

Di Lu and Fang Chen

Abstract The study of supersonic reacting shear layer has been paid great attention to further understand flow characteristics and mechanism of the engine combustion process. However, most past studies remain narrow in focus dealing only with infinitely small tube thickness or fixed ones which neglects the complex flow structures reflecting some general features of scramjet engine mixing and combustion process. In the present study, supersonic reacting mixing layer has been studied under different tube thickness. Numerical simulations have been carried out with CFD++ 14.1 to solve the Reynolds averaged equation on the Evan's configuration which is closed by Menter's Shear Stress Transport turbulence model and finite reaction rate chemical kinetic model. The flow field evolution, mixing layer growth and combustion ignition are the major focus of current study. The obtained results show that the existence of finite tube thickness brings unique flow field characteristic such as expansion fans and shock systems which is not included in the tradition simplified analysis of reacting shear with infinitesimal tube thickness. The tube thickness has a positive effect on growth of mixing layer and ignition delay that 50% of decrease in ignition delay has achieved by enough tube wall thickness.

Keywords Supersonic reacting shear layer · Non-premixed turbulent combustion · Tube thickness effect

1 Introduction

In recent years, researchers have shown an increased interest in ramjet engine as propulsion system for hypersonic vehicles and orbit missions [1] for its low payload costs and high specific impulse [2]. However, effective operation of ramjet

D. Lu · F. Chen (✉)
Shanghai Jiao Tong University, Shanghai, China
e-mail: fangchen@sjtu.edu.cn

D. Lu
e-mail: ludi96@sjtu.edu.cn

Z. Jing and X. Zhan (eds.), *Proceedings of the International Conference on Aerospace System Science and Engineering 2020*, Lecture Notes in Electrical Engineering 680,
https://doi.org/10.1007/978-981-33-6060-0_16

engine over wide speed range is still tricky in the design of hypersonic vehicles [3]. One of the main obstacles is ignition and combustion stability in high speed flow [4] which requires fundamental study in supersonic combustion process. For this reason, the study of supersonic reacting shear layer aims to further understand flow characteristics and mechanism of the engine combustion process.

Since Zeldovich number [5] was proposed to describe the influence of free shear and flow Mach number on ignition, many researches have been conducted on ignition and flameout. It was found that shock wave impingement [6], vortex shedding [7], inflow fluctuation [8] and additive effects [9] acted a prominent role in ignition characteristic, whereas low temperature of mixture dominates rich combustion flameout [7]. In addition to combustion characteristics, compressibility has a negative effect on the growth rate of reacting shear layer [10], while heat release effect is closely related to the convective Mach number [11, 12]. The further reason of heat release and compressibility effect has been attributed to reduced production of Reynolds stress [13].

However, most previous studies are limited to the infinitesimal or fixed wall thickness, and only a few works consider the influence of the tube wall thickness [14, 15]. The effect of tube wall thickness on evolution of mixing layer and flow structure in supersonic reacting layer has not be systematically explored.

The aim of this investigation has been to establish relationship between tube wall thickness on flow filed characteristic of co-axial hydrogen and air jet flame. The paper is divided into 4 sections. The first section includes a review of the past studies on reacting mixing layer. The second section briefly introduces the numerical methods of the study and gives out model validation. The third section presents the simulation results under different tube thickness. The final section gives out the conclusion.

2 Numerical Methodology

2.1 Computational Fluid Dynamic

The Reynolds Average conservation equations of mass, momentum, species and energy for multicomponent compressible reacting system are solved by CFD++ 14.1 based on finite volume method. Multi-component diffusion model described by Fick's law has been applied for species transport property. The turbulence closure has been achieved by Menter's Shear Stress Transport (SST) model.

A nine-species, eighteen-step mechanism [16] is employed for the chemical kinetics of hydrogen and air. This model was validated in the CFD++ 11.1 official tutorial of Burrow combustor against experiment data. Nitrogen is defined as an inert gas which is evaluated automatically after other species are given.

The governing equations are solved by the finite-volume method approach. Second order differential scheme has been applied for inviscid term. Multi-dimensional total

variation diminishing (TVD) polynomial interpolation has been used for reconstructions over nodes. To accelerate the computation, a spatial discretization blending between first and second order has also been applied.

2.2 Model Validation

The baseline model used in this study is a confined coaxial hydrogen jet flame with a design Mach number of 2.0 [17] whose salient features are shown in Fig. 1. The radius of the internal hydrogen jet nozzle r_j is 3.2625 mm with a tube thickness δ_w of 1.5 mm, and the radius of the whole tube R is 32.65 mm. Since little knowledge of the nozzle lip structure was given, a straight wall is assumed to consider the boundary layer effect of the injector.

The inflow condition of the hydrogen jet is characterized by 251 K, 0.1 atm and 2.0 Ma with pure hydrogen. The inflow condition of the vitiated air is characterized by 1495 K, 0.1 atm and 1.9 Ma with species composed of 0.241 oxygen, 0.281 water, and 0.478 nitrogen. X-axial symmetry has been applied on the centerline of the tube to utilize the symmetry feature of the problem. No-slip adiabatic condition has been specified for the solid wall.

To establish the fidelity of the numerical simulation, grid convergence study has been conducted on the baseline geometry with three sets of computational meshes. These three sets of meshes are namely Mesh A, Mesh B and Mesh C containing 150, 250 and 490 K grid points respectively. The species distributions at different cross sections of the duct are in comparison with the experiment [17]. Figure 2 has given out the radial distribution of OH, H2O, N2, H2 at x/dj = 8.26, 15.5, 21.7 and 27.9. It is shown that the results for the Mesh B and Mesh C collapse almost perfectly, thus the further analysis is based on Mesh B. Some deviations have behaved between simulated results and experimental results for ignition delay. This is mainly caused by uncertainties in inflow turbulence boundary layer of the experiment configuration and deficiency of inconsideration of turbulence chemistry interaction in combustion process.

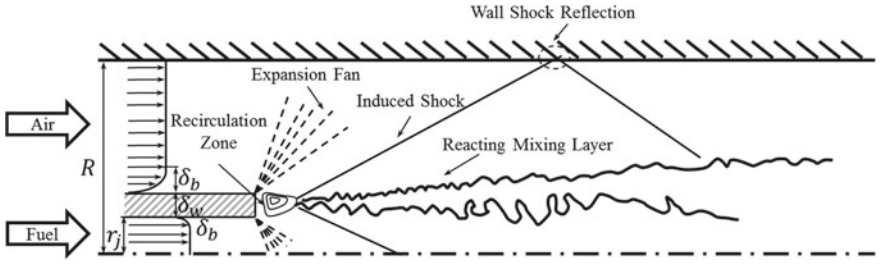

Fig. 1 Baseline configuration

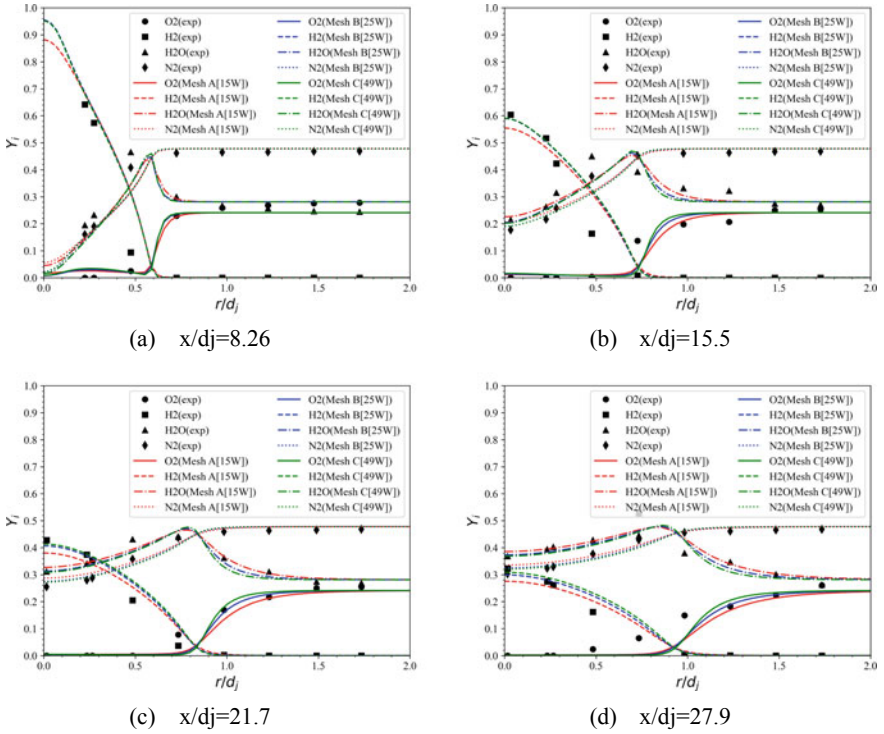

(a) x/dj=8.26 (b) x/dj=15.5

(c) x/dj=21.7 (d) x/dj=27.9

Fig. 2 Comparison of species radial distribution at different cross section for x/dj = 8.26, 15.5, 21.7, 27.9

3 Result and Discussion

3.1 Flow Field Characteristic

In this section the general flow field characteristic has been analyzed under finite tube wall thickness and infinitesimal tube wall thickness. For the finite tube wall thickness case, a tube wall thickness of 1.5 mm has been applied just as the baseline model which has been discussed in Sect. 2.2. For the infinitesimal tube wall thickness condition, an inlet velocity profile has been applied characterized by the formula (1) below:

$$U = \frac{u_{up}+u_{down}}{2} + \frac{u_{up}-u_{down}}{2}\tanh\left(\frac{y-y_c}{2\delta_0}\right) \tag{1}$$

In which u_{up} and u_{down} are the velocity of air and fuel, y_c is the separation location of two fluid, δ_0 is considered as the initial mixing thickness.

From Fig. 3, a major difference of the flow fields between reacting mixing layer with and without tube wall thickness can be summarized to the existence of expansion

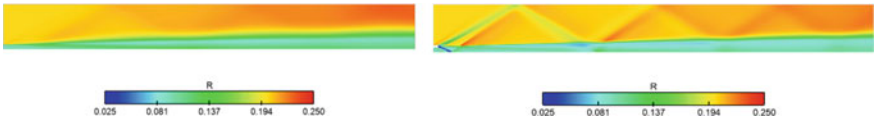

(a) Density contour (Infinitesimal thickness) (b) Density contour (Finite thickness)

Fig. 3 Density contour with and without finite tube wall thickness

waves, recirculation zone and reattached shocks which brings great complexity to the evolution of the flow field.

To better visualize the flow field with finite tube wall thickness, a contour graph of density gradient norm in global view is given in Fig. 4 to discriminate the shock structure combined with local streamlines. In Fig. 4a's global view, the flow field of supersonic reacting mixing layer with finite tube wall thickness is characterized by near-field expansion fan, shock wave, and recirculation zone combined with far-field shock reflection, shock-reacting layer interaction. From Fig. 4b, oxidant and fuel separated by finite tube thickness induces a recirculation zone downstream of the tube tip in the near-field. The inward wall causes two expansion fans surrounding the tube tip making the stream merge together. After the merge of the two streams, reattach shocks are formed reflecting outward leading to complex shock system in the tube. In the far-field, reattach shocks induced by merge of the stream turning outward strikes the outer tube wall and reflects inward impinging on the reacting mixing layer which leads to a strong local interaction with the reacting mixing layer. On the other hand, reattach shocks turning inward interacts with the one caused by the symmetry part, reflects outward and finally merges the reattach shocks turning outward after interaction with mixing layer.

Combustion process is another important flow field characteristic in reacting mixing layer which is given in Fig. 5. From Fig. 5a, the combustion process is started by ignition in mixing layer which characterized by premix combustion, then the flame extends to the core flow. The combustion mode in the core flow undergoes transition from non-premix to partially premix. From Fig. 5b, a clearer view of the

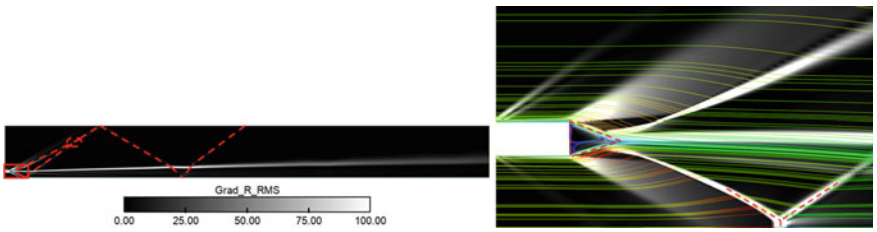

(a) Contour of density gradient norm (Global view) (b) Contour of density gradient norm (Local enlarged view)

Fig. 4 Contour of density gradient norm under finite tube wall thickness ($\delta_w = 1.5$ mm)

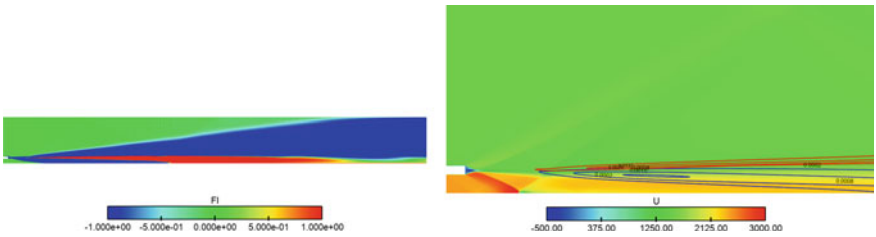

(a) Contour of flame index (FI)

(b) Velocity contour with OH and HO2 concentration contour lines

Fig. 5 Contour of flame index and velocity under finite tube wall thickness ($\delta_w = 1.5$ mm)

combustion process can be visualized by the OH (colored by red) and HO_2 (colored by blue) contour. On the outside edge of mixing layer, the OH species is majorly produced due to the fully mixing of fuel and oxygen. In the centerline region, high fuel concentration is exhibited which causes weak reaction leading to a region of fuel-rich combustion. As a result, the HO2 is majorly produced in the centerline region.

3.2 Effects of Tube Wall Thickness on Flow and Combustion

To study the effects of tube wall thicknesses, tube wall thicknesses of 0.5 mm, 0.8 mm, 1.0 mm, 1.5 mm, 2.5 mm have been applied other than the baseline case of 1.5 mm. The inflow mass flow rate is maintained during the variation of tube wall thickness.

First, flow field evolution under different tube wall thickness has been compared in Fig. 6. It shows that with the increase of the tube thickness a larger recirculation zone is formed which causes an enlarged initial expansion fan and weaker initial shock wave characterized by smaller shock angle. On the other hand, the bigger tube thickness leads to stronger overexpansion in the inner fuel inject and thus finally

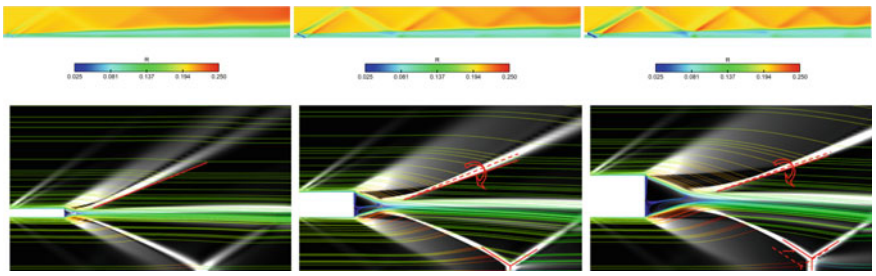

(a) Tube thickness 0.5mm (b) Tube thickness 1.5mm (c) Tube thickness 2.5mm

Fig. 6 Comparison of flow structure at different tube thickness for t = 0.5 mm, 1.5 mm, 2.5 mm

results in Mach disk in the center of the jet flow. The location of Mach disk can be estimated by an empirical expression as proportional to square root of ratio between nozzle total pressure and back pressure (Ashkenas and Sherman 1966) as formula (2) which agrees well with the simulation results. With the increase of tube wall thickness from 0.5 mm to 2.5 mm, the Mach disk position has been postponed by 16%.

$$\frac{x_M}{d} \propto \sqrt{\frac{P_{tot}}{P_b}} \tag{2}$$

Figure 7 gives out the growth of the reacting layer characterized by the vorticity thickness which is defined in formula (3):

$$\theta_w = \frac{\Delta U}{\left(\frac{\partial U}{\partial y}\right)_{max}} = \frac{u_{up} - u_{down}}{\left(\frac{\partial U}{\partial y}\right)_{max}} \tag{3}$$

Figure 7 indicates a general trend that increase of the tube wall thickness leads to larger reacting mixing layer growth, which can be also seen clearly from the vorticity contour from Fig. 8. The major reason attributes to a more vortex generation due to the larger tube wall thickness. On the other hand, sudden drops can be visualized in the stream wise distribution of vorticity thickness which is always co-occurrence of shock impinge indicated by stream wise Mach number monitor. Such a fact indicates that the shock wave impinge has a strong depression effect on the growth rate of mixing reacting layer which is attributed to the great compression effect brought by the shock wave. Downstream of the shock, the growth rate of the mixing reacting

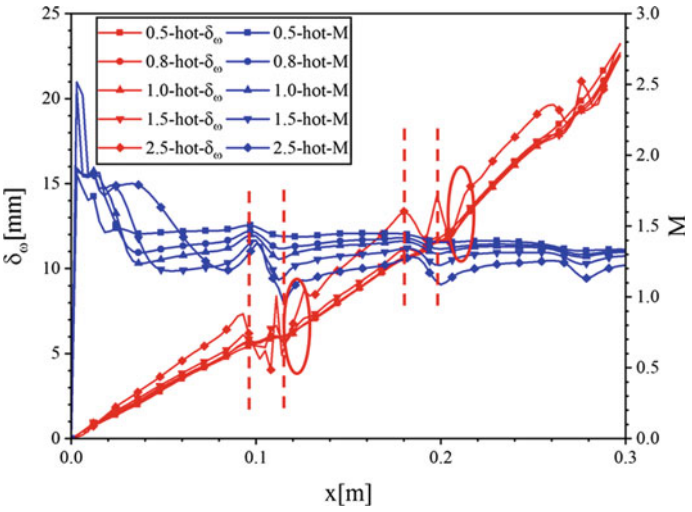

Fig. 7 Streamwise vorticity thickness distribution and Mach number distribution at different tube thickness for t = 0.5 mm, 0.8 mm, 1.0 mm, 1.5 mm, 2.5 mm

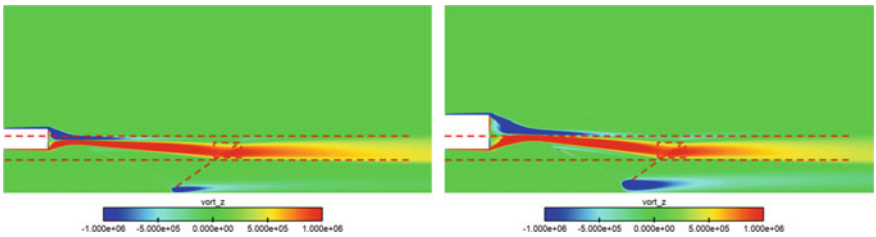

(a) Contour of vorticity ω_z ($\delta_w = 1.5mm$)

(b) Contour of vorticity ω_z ($\delta_w = 2.5mm$)

Fig. 8 Vorticity contour under tube wall thickness of 1.5 mm, 2.5 mm

layer faces a rapid increase due to the increase of the vorticity magnitude which can be observed from Fig. 8.

To express the effect of wall thickness on combustion process, species indicator combined with the combustion efficiency have been used to represent the microscopic and macroscopic view point of combustion. The species indicator is defined as the maximum concentration in a section, while consumption of the fuel is utilized to evaluate the combustion efficiency.

From Fig. 9a, with the increase of tube thickness, combustion happens with less ignition delay. In detail, at a smaller tube thickness of 0.5 mm and 0.8 mm, the ignition happens almost the same position for not enough large recirculation zone to support early mixing. With an enough large recirculation zone formed by large tube thickness, the ignition delay is decreased by 50% relative to the low tube wall thickness. However, even larger tube thickness makes no contribution to less ignition delay. In current case, the threshold value of tube thickness is 1.5 mm. One more interesting founding can be observed from Fig. 9b that though increase of tube thickness leads to early combustion it does not necessarily increase the total combustion efficiency.

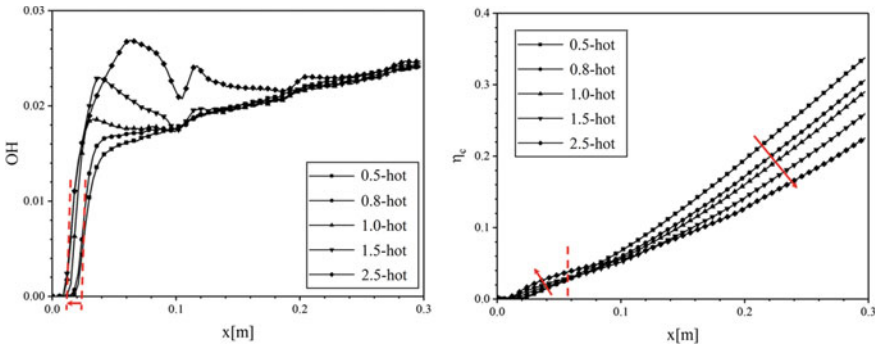

(a) OH indicator

(b) Combustion efficiency

Fig. 9 Comparison of combustion process at different tube thickness

4 Conclusion

The effects of tube thickness on supersonic reacting mixing layer growth and combustion process have been investigated in this paper, the conclusions are as follow:

(1) Tube thickness has significant impact on the growth of reacting mixing layer and combustion process for the introduction of complex shock systems.
(2) The increase of tube thickness increases the mixing layer thickness growth which promotes more thorough mixing. On the other hand, the ignition delay is 50% less than that of the infinite tube when the tube wall thickness is 1.5 mm. However, there is a thickness threshold for the above effects that the increase of thickness above the threshold will not further reduce the ignition delay. Under the current situation, the threshold value of tube thickness is 1.5 mm.

Acknowledgements The support of National Natural Science Foundation of China (No. 11672183) is gratefully acknowledged.

References

1. Fry RS (2004) A century of ramjet propulsion technology evolution. J Propul Power 20:27–58. https://doi.org/10.2514/1.9178
2. Huang W, Yan Li, Tan J-G (2014) Survey on the mode transition technique in combined cycle propulsion systems. Aerosp Sci Technol 39:685–691. https://doi.org/10.1016/j.ast.2014.07.006
3. Firsov A, Savelkin KV, Yarantsev DA (2015) Plasma-enhanced mixing and flameholding in supersonic flow. Phil Trans Royal Soc A: Math, Phys Eng Sci 373(2048):20140337. https://doi.org/10.1098/rsta.2014.0337
4. Capecelatro J, Bodony DJ, Freund JB (2019) Adjoint-based sensitivity and ignition threshold mapping in a turbulent mixing layer. Combust Theor Model 23(1):147–179. https://doi.org/10.1080/13647830.2018.1495342
5. Jackson TL, Hussaini MY (1988) An asymptotic analysis of supersonic reacting mixing layers. Combust Sci Technol 57(4–6):129–140
6. Huete C, Sánchez AL, Williams FA (2017) Diffusion-flame ignition by shock-wave impingement on a hydrogen–air supersonic mixing layer. J Propul Power. 256-263. https://doi.org/10.2514/1.B36236
7. Zhang YL, Wang B, Zhang HQ (2014) Ignition, flame propagation and extinction in the supersonic mixing layer flow. Sci China Technol Sci 57(11):2256–2264. https://doi.org/10.1007/s11431-014-5655-5
8. Tahsini AM (2013) Turbulence and additive effects on ignition delay in supersonic combustion. Proc Inst Mech Eng, Part G: J Aerosp Eng 227(1):93–99. https://doi.org/10.1177/0954410011428981
9. Tien JH, Stalker RJ (2002) Release of chemical energy by combustion in a supersonic mixing layer of hydrogen and air. Combust Flame 131(3):329–348. https://doi.org/10.1016/s0010-2180(02)00371-1
10. Givi P, Madnia CK, Steinberger CJ et al (1991) Effects of compressibility and heat release in a high speed reacting mixing layer. Combust Sci Technol 78(1–3):33–67. https://doi.org/10.1080/00102209108951740

11. Calhoon W (2003) Heat release and compressibility effects on planar shear layer development. 41st Aerospace sciences meeting and exhibit. 1273. https://doi.org/10.2514/6.2003-1273
12. Yao X, Tan J, Zhang D (2019) Combustion of H2/air supersonic mixing layers with splitter plate: Growth rates and transport characteristic. Acta Astronaut 165:401–413. https://doi.org/10.1016/j.actaastro.2019.09.036
13. Liu H, Gao Z, Jiang C et al (2019) Numerical study of combustion effects on the development of supersonic turbulent mixing layer flows with WENO schemes. Comput Fluids 189:82–93. https://doi.org/10.1016/j.compfluid.2019.05.019
14. Otakeyama Y, Takeshi Yokomori T, Mizomoto M (2009) Stability of CH4—N2/Air jet diffusion fame for various burner rim thicknesses. Proc Combust Inst 32:1091–1097. https://doi.org/10.1016/j.proci.2008.05.002
15. Zhang L, Choi JY, Yang V (2015) Supersonic combustion and flame stabilization of coflow ethylene and air with splitter plate. J Propul Power 2015:1–14. https://doi.org/10.2514/1.B35740
16. Drummond JP, Rogers RC, Hussaini MY (1987) A numerical model for supersonic reacting mixing layers. Comput Methods Appl Mech Eng 64:39–60. https://doi.org/10.1016/0045-7825(87)90032-6
17. Evans JS, Schexnayder Jr CJ, Beach Jr HL (1978) Application of a two-dimensional parabolic computer program to prediction of turbulent reacting flows. https://ntrs.nasa.gov/archive/nasa/casi.ntrs.nasa.gov/19780012520.pdf

An Investigation for Effective Thermal Properties of Titanium Alloy Lattice Sandwich Panels

Junpeng Li and Zhibin Yang

Abstract Multifunctional sandwich panel presents a unique Integrated Thermal Protection System (ITPS) for hypersonic vehicles. In this paper, a novel method to evaluate the effective thermal properties of metal alloy lattice core sandwich panels is presented. The thermal transfer process between lattice core and face sheet was analyzed, and the behavior schemes were detached in three categories according to the existence of insulation material filling and active convection. For each category, equations were presented to calculate the effective density, specific heat and thermal conductivity for pyramid lattice core and tetrahedral lattice core using Representative Volume Element (RVE). Two sandwich panels were constructed separately with the two lattice cores made by the material of titanium alloy. Numerical Simulation based on Finite Element Method (FEM) was employed to verify the effective techniques. Two kinds of FEM models were built with detailed solid element level and simplified effective solid element level. The heat transfer process from top sheet to bottom sheet across lattice core were simulated, consistency of temperature responses could be observed obviously between the different level FEM simulations. It could be concluded that the effective properties deduced with the method in this paper are accurate to predict the thermal performance of titanium alloy lattice core sandwich panels, and are very promising for potential application in the analysis and design of TPS for hypersonic vehicles.

Keywords Effective thermal properties · Lattice core panels · Thermal protection system

J. Li (✉) · Z. Yang
Aircraft Strength Research Institute of China, Xi'an, Shaanxi, China
e-mail: skyeaglecn@qq.com

Z. Yang
e-mail: hk623yzb@163.com

Z. Jing and X. Zhan (eds.), *Proceedings of the International Conference on Aerospace System Science and Engineering 2020*, Lecture Notes in Electrical Engineering 680,
https://doi.org/10.1007/978-981-33-6060-0_17

1 Introduction

Reusable Launch Vehicle (RLV) and hypersonic vehicles have attracted more and more attention both in military and civil sphere. It has been revealed that the key challenge to successfully develop RLVs is to conquer the rigor thermal load [1, 2]. Because of the com-pression due to excessive flight speed, structures should survive in service under extremely server aerodynamic heating and pressure load. Thermal Protection System (TPS) plays the core role to keep the interior structures from overheating and also helps to maintain reasonable strength and stiffness thus could retain an idea aero-dynamic shape [3]. Great efforts have been invested in the research and design of TPS, and varied TPS types have been promoted, such as blanket insulation, ceramic matrix composite TPS and metallic TPS (MTPS) [4] (Glass). Recently, a novel Integrated TPS (IPTS) which could structurally withstand both thermal and mechanical load was widely advocated due to its high efficiency and low maintenance [5–7]. Advantages of ITPS with cellular sandwich panels include robust load bearing and beneficiary insulation filling. The design ability of ITPS has been demonstrated to possess potential applications in wide range [8–10].

There are two kinds of ITPS, the corrugated core configuration and the lattice core configuration. Compare to the corrugated configuration, the lattice configuration has higher porosity and more optimal mesostructures. Lattice core ITPS incorporates relative low density into designable multifunction features. Therefore, the mechanical, thermal and other performance could be adjusted and optimized for specific purpose and lattice core sandwich panels are expected to be the most promising candidate for ITPS.

To design an ITPS with lattice core sandwich panels, it is premised to intensively investigate the mechanical and thermal properties. The thermal transfer process is far more complicated than the mechanical load bearing character. Lattice core sandwich panels manufactured with metal such as aluminum, titanium, nichrome, stainless steel and copper are widely procurable. Titanium alloy is especially attractive due to its high performance in both thermal and mechanical load bearing. Through 3D printing and Super Plastic Forming (SPF) technique, Titanium alloy could be fabricated into lattice core sandwich panels. It's very promising to be applied in the hypersonic vehicle structures.

The objective of this paper is to disclose the heat transfer behavior character of lattice core sandwich panels, and present a scheme to quantify the effective thermal properties such as effective density, effective specific heat and effective thermal conductivity using Representative Volume Element (RVE) method.

2 Heat Transfer Behaviour of Titanium Alloy Lattice Core Sandwich Panels

Typically there are two types of lattice core sandwich panels, the pyramid and the tetrahedral, as show in Fig. 1.

Because of its high porosity, the heat transfer behaviour in lattice core sandwich panels from hot face sheet to cold face sheet could be tuned through insulation material filling and active forced convection in the pore space. Accompany with the existence of radiation among face sheets and lattice core, the heat transfer performance could be further adjusted through the surface emissivity rectification while the surface emissivity could be tuned through the surface roughness.

Thus the heat transfer behaviour of lattice core sandwich panels could be detached to three categories.

2.1 Case 1: Heat Transfer with Insulation Filling

In this case, the pore space in lattice core was filled with insulation material, and the heat transfer behavior was only thermal conduct.

2.2 Case 2: Heat Transfer Without Insulation Filling

In this case, the pore space in lattice core was empty, and the heat transfer behaviour includes thermal conduct, thermal radiation.

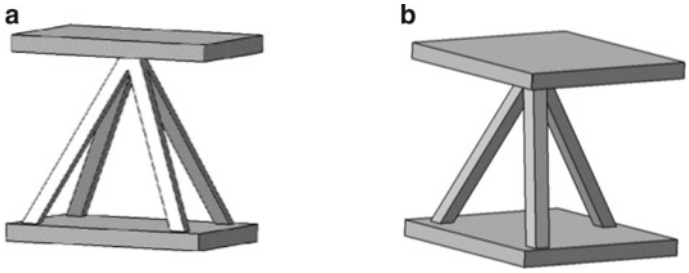

Fig. 1 **a** Pyramid lattice **b** Tetrahedral lattice

2.3 Case 3: Heat Transfer with Active Convection

In this case, the pore space in lattice core is filled with flowing compressed air or some other fluid cooling medium. Because of the fluid flowing, forced convection occurred on the surface of face sheets and lattice core. In the case of transparent cooling medium, the heat transfer behaviour includes thermal conduct, radiation, and convection. If the medium is non-transparent, there is no radiation.

3 Effective Thermal Properties of Titanium Alloy Lattice Core Sandwich Panels

During the thermal performance analysis of lattice core sandwich panels, effective properties such as effective density, effective specific heat, and effective thermal conductivity of the lattice core are essential. They should be advanced for different cases.

The RVE definition parameters of pyramid lattice core and tetrahedral lattice core are shown in Fig. 2.

3.1 Effective Density

(a) Pyramid lattice core

Case 1:

$$\rho_e = V_v\rho_s + (1 - V_v)\rho_f = \frac{2dt}{ah\left(1 - \frac{h^2}{a^2}\right)}\rho_s + (1 - \frac{2dt}{ah\left(1 - \frac{h^2}{a^2}\right)})\rho_f \quad (1)$$

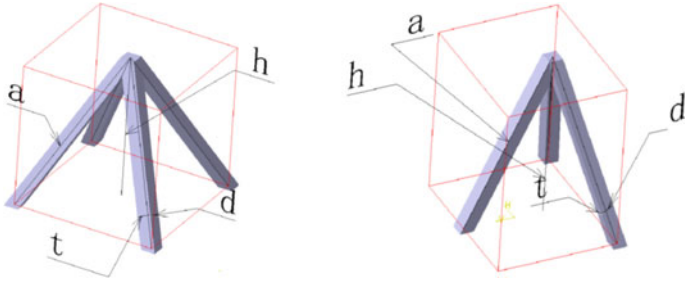

(a) Pyramid (b) Tetrahedral

Fig. 2 RVE definition parameters of lattice core

Case 2 and case 3:

$$\rho_e = V_v \rho_s = \frac{2dt}{ah(1 - \frac{h^2}{a^2})} \rho_s \tag{2}$$

where ρ_s and ρ_f are the density of core material and insulation filling material.

(b) Tetrahedral lattice cores

Case 1:

$$\rho_e = V_v \rho_s + (1 - V_v)\rho_f = \frac{2dt}{\sqrt{3}ah\left(1 - \frac{h^2}{a^2}\right)} \rho_s + \left(1 - \frac{2dt}{\sqrt{3}ah\left(1 - \frac{h^2}{a^2}\right)}\right) \rho_f \tag{3}$$

Case 2 and case 3

$$\rho_e = V_v \rho_s = \frac{2dt}{\sqrt{3}ah(1 - \frac{h^2}{a^2})} \rho_s \tag{4}$$

where ρ_s and ρ_f are the density of core material and insulation filling material.

3.2 Effective Specific Heat

(a) Pyramid lattice core

Case 1:

$$c_e = \frac{\rho_s \frac{2dt}{ah\left(1 - \frac{h^2}{a^2}\right)} c_s + \rho_f (1 - \frac{2dt}{ah\left(1 - \frac{h^2}{a^2}\right)}) c_f}{\rho_s \frac{2dt}{ah\left(1 - \frac{h^2}{a^2}\right)} + \rho_f (1 - \frac{2dt}{ah\left(1 - \frac{h^2}{a^2}\right)})} \tag{5}$$

Case 2 and case 3:

$$c_e = \frac{2dt}{ah\left(1 - \frac{h^2}{a^2}\right)} c_s \tag{6}$$

where c_s and c_f are the density of core material and insulation filling material.

(b) Tetrahedral lattice core

Case 1:

$$c_e = \frac{2dt}{\sqrt{3}ah\left(1-\frac{h^2}{a^2}\right)}c_s \tag{7}$$

Case 2 and case 3:

$$c_e = \frac{\rho_s \frac{2dt}{\sqrt{3}ah\left(1-\frac{h^2}{a^2}\right)}c_s + \rho_f\left(1-\frac{2dt}{\sqrt{3}ah\left(1-\frac{h^2}{a^2}\right)}\right)c_f}{\frac{2dt}{\sqrt{3}ah\left(1-\frac{h^2}{a^2}\right)}\rho_s + \left(1-\frac{2dt}{\sqrt{3}ah\left(1-\frac{h^2}{a^2}\right)}\right)\rho_f} \tag{8}$$

where ρ_s and ρ_f are the density of core material and insulation filling material.

3.3 Effective Thermal Conductivity

For all the cases of pyramid and tetrahedral lattice core sandwich panels, the thermal conducted through lattice core could be expressed:

$$q_{total} = q_{coduct} + q_{radiate} + q_{convect} = k_e A\frac{T_1 - T_2}{h} \tag{9}$$

where $q_{\_coduct}$ is the thermal conducted through core and filling materials, $q_{\_radiate}$ is the thermal radiated, and $q_{\_convect}$ is the convection thermal because of the flow of cooling medium, k_e is the effective thermal conductivity, A is cross-section area of the RVE, T_1 is the hot surface temperature and T_2 is the cold surface temperature. Effective thermal conductivity could be deduced by the analysis and quantify of all the three sources.

(a) Pyramid lattice core

Case 1:

$$k_e = \frac{2dth}{a^3\left(1-\frac{h^2}{a^2}\right)}k_s + \left(1-\frac{2dth}{a^3\left(1-\frac{h^2}{a^2}\right)}\right)k_f \tag{10}$$

Case 2:

$$k_e = \frac{2dth}{a^3\left(1-\frac{h^2}{a^2}\right)}k_s + \left(1-\frac{2dth}{a^3\left(1-\frac{h^2}{a^2}\right)}\right)k_{gas} + 4B\varepsilon h\sigma T_{avg}^3 \tag{11}$$

Case 3 for transparent cooling medium:

$$k_e = \frac{2dth}{a^3\left(1-\frac{h^2}{a^2}\right)}k_s + (1 - \frac{2dth}{a^3\left(1-\frac{h^2}{a^2}\right)})k_{gas} + 4B\varepsilon h\sigma T_{avg}^3 + R_c h \quad (12)$$

Case 3 for non-transparent cooling medium:

$$k_e = \frac{2dth}{a^3\left(1-\frac{h^2}{a^2}\right)}k_s + \left(1 - \frac{2dth}{a^3\left(1-\frac{h^2}{a^2}\right)}\right)k_{gas} + R_c h \quad (13)$$

where k_s is the thermal conductivity of core material, k_f is the thermal conductivity of insulation filling material, k_{gas} is the thermal conductivity of air or cooling medium, T_{avg} is the temperature of lattice core, R_c is the convective heat transfer coefficient, B is the correction factor because of lattice shadow effect, σ is the surface emissivity, εis the Stefan-Boltzmann constant.

(b) Tetrahedral lattice core

Case 1:

$$k_e = \frac{2dth}{\sqrt{3}a^3\left(1-\frac{h^2}{a^2}\right)}k_s + (1 - \frac{2dth}{\sqrt{3}a^3\left(1-\frac{h^2}{a^2}\right)})k_f \quad (14)$$

Case 2:

$$k_e = \frac{2dth}{\sqrt{3}a^3\left(1-\frac{h^2}{a^2}\right)}k_s + (1 - \frac{2dth}{\sqrt{3}a^3\left(1-\frac{h^2}{a^2}\right)})k_{gas} + 4B\varepsilon h\sigma T_{avg}^3 \quad (15)$$

Case 3 for transparent cooling medium

$$k_e = \frac{2dth}{\sqrt{3}a^3\left(1-\frac{h^2}{a^2}\right)}k_s + (1 - \frac{2dth}{\sqrt{3}a^3\left(1-\frac{h^2}{a^2}\right)})k_{gas} + 4B\varepsilon h\sigma T_{avg}^3 + R_c h \quad (16)$$

Case 3 for non-transparent cooling medium

$$k_e = \frac{2dth}{\sqrt{3}a^3\left(1-\frac{h^2}{a^2}\right)}k_s + (1 - \frac{2dth}{\sqrt{3}a^3\left(1-\frac{h^2}{a^2}\right)})k_{gas} + R_c h \quad (17)$$

where k_s, k_f, k_{gas}, T_{avg}, R_c, B, σ, andεare the same as before.

4 Verification of Effective Thermal Properties Through FEM Simulation

A Pyramid lattice core sandwich panel and a tetrahedral lattice core sandwich panel were built with the titanium alloy TC4, as shown in Fig. 3.

In case 3, the cooling medium is set to be compressed air about 0.8 MPa.

The verification is processed through Finite Element Method (FEM) simulation. The heat transfer behaviours of pyramid and tetrahedral lattice core sandwich panels are simulated through different thermal boundary conditions, and the heat transfer process from top sheet to bottom sheet across lattice core were investi-gated by numeric computation. A detailed solid element model with insulation fill-ing material and core material was constructed accompany with a simplified solid element model. Heat transfer processes were comparatively studied.

4.1 Pyramid Lattice Core Sandwich Panel

Detailed FEM model and Simplified FEM model were shown in Fig. 4.

In Fig. 4, (a) is the detailed FEM model without insulation filling, (b) is the de-tailed FEM model with insulation filling, and (c) is the simplified FEM model.

The verification results are shown in Fig. 5.

From Fig. 5, it could be concluded that there are significant consistencies of temperature response between effective model and detailed model.

4.2 Tetrahedral Lattice Core Sandwich Panel

Detailed FEM model and Simplified FEM model were shown in Fig. 6.

The verification results are shown in Fig. 7.

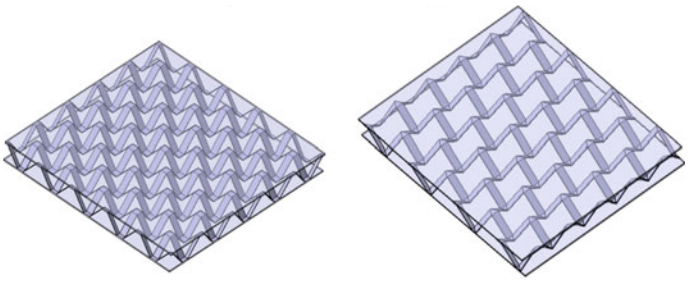

(a) Pyramid (b) Tetrahedral

Fig. 3 Geometry of lattice core sandwich panels

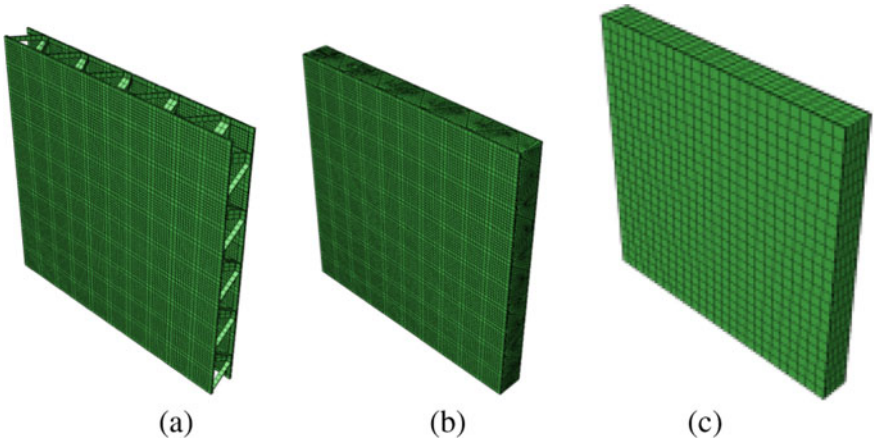

Fig. 4 FEM Models of pyramid lattice core sandwich panels

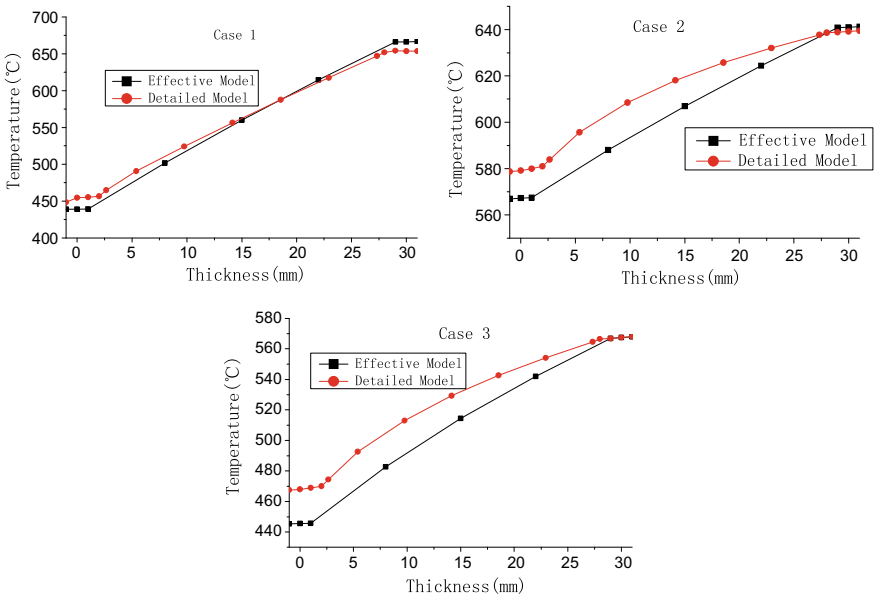

Fig. 5 Verification results of pyramid lattice core sandwich panel

In Fig. 7, the temperature response of effective FEM model and detailed FEM model shows very little difference.

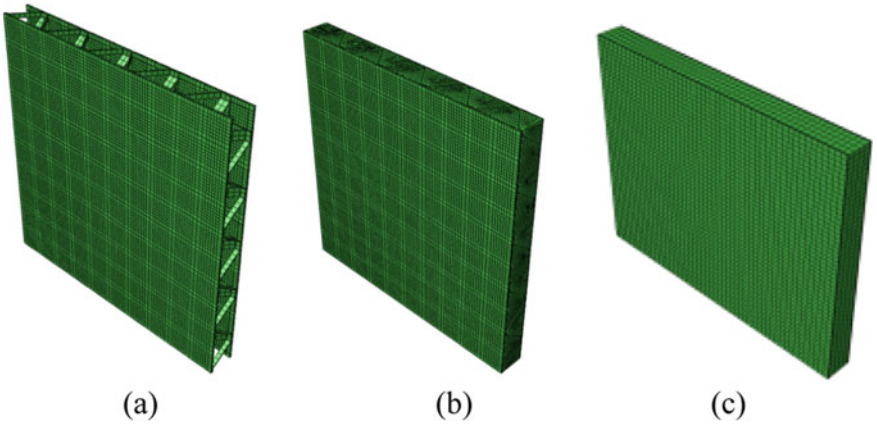

Fig. 6 FEM Models of tetrahedral lattice core sand-wich panels

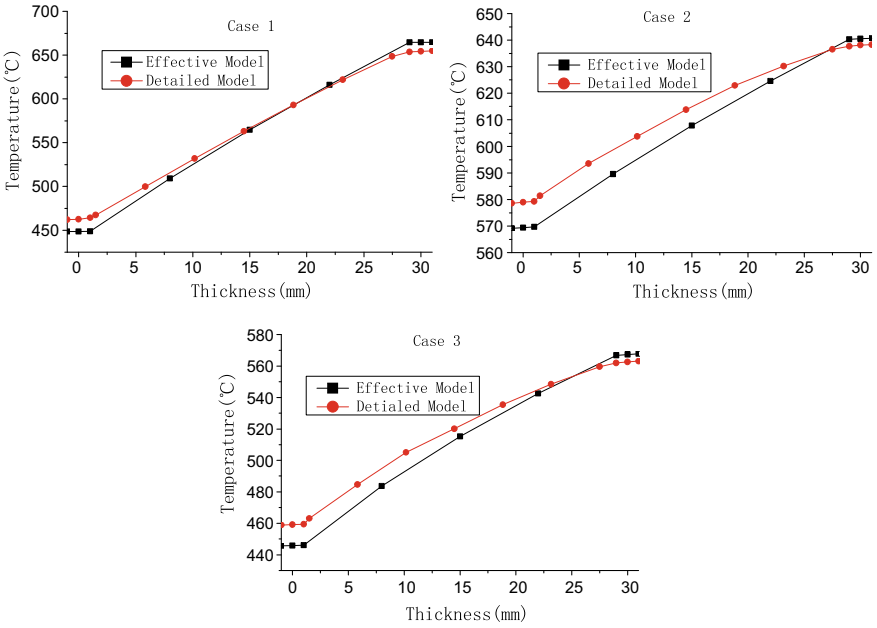

Fig. 7 Verification results of tetrahedral lattice core sandwich panel

5 Conclusion

In this paper, a method to evaluate the effective thermal properties of lattice core sandwich panels was advanced based on the analysis of heat transfer behaviour, and through the method, the lattice core could be simplified as a unified material,

thus the thermal performance of lattice core sandwich panels could be predicted in a convenient way. The method was verified with a pyramid lattice core sandwich panel and a tetrahedral lattice core sandwich panel fabricated by titanium alloy through FEM simulation. Consistence of temperature response from the effective FEM model and detailed FEM model could be observed. The results proved that the method in this paper is applicable in the design of lattice core sandwich panels.

References

1. Wei K, Cheng X, Zhang R, Pei Y, Fang D (2014) Fabrication and mechanical properties of lightweight ZrO2 ceramic corrugated core sandwich panels. Mater Des 64. https://doi.org/10.1016/j.matdes.2014.07.038
2. Wei K, He R, Cheng X, Zhang R, Pei Y, Fang D (2015) A lightweight, high compression strength ultra high temperature ceramic corrugated panel with potential for thermal protection system applications. Mater Des 66:552–556. https://doi.org/10.1016/j.matdes.2014.06.024
3. Biamino S et al (2010) Multilayer SiC for thermal protection system of space vehicles with decreased thermal conductivity through the thickness. J Eur Ceram Soc 30(8):1833–1840. https://doi.org/10.1016/j.jeurceramsoc.2010.01.040
4. Glass D Ceramic matrix composite (CMC) Thermal protection systems (TPS) and Hot structures for hypersonic vehicles. In: 15th AIAA international space planes and hypersonic systems and technologies conference
5. Wei K, Cheng X, Mo F, Wen W, Fang D (2016) Design and analysis of integrated thermal protection system based on lightweight C/SiC pyramidal lattice core sandwich panel. Mater Des 111:435–444. https://doi.org/10.1016/j.matdes.2016.09.021
6. Gogu C, Bapanapalli SK, Haftka RT, Sankar BV (2009) Comparison of materials for an integrated thermal protection system for spacecraft reentry. J Spacecraft Rockets 46(3):501–513. https://doi.org/10.2514/1.35669
7. Martinez O, Sankar B, Haftka R, Blosser ML (2012) Two-dimensional orthotropic plate analysis for an integral thermal protection system. AIAA J 50(2):387–398. https://doi.org/10.2514/1.J051172
8. Martinez OA, Sankar BV, Haftka RT, Bapanapalli SK, Blosser ML (2007) Micromechanical analysis of composite corrugated-core sandwich panels for integral thermal protection systems. AIAA J 45(9):2323–2336. https://doi.org/10.2514/1.26779
9. Martinez OA, Sharma A, Sankar BV, Haftka RT, Blosser ML (2010) Thermal force and moment determination of an integrated thermal protection system. AIAA J 48(1):119–128. https://doi.org/10.2514/1.40678
10. Bapanapalli S, Martinez O, Gogu C, Sankar B, Haftka R, Blosser M (Student Paper) analysis and design of corrugated-core sandwich panels for thermal protection systems of space vehicles. In: 47th AIAA/ASME/ASCE/AHS/ASC Structures, structural dynamics, and materials conference

Modeling and Analysis of Gate to Gate Flight Process Based on SysML in Commercial Aircraft

Hongyu Li, Miao Wang, Gang Xiao, Guoqing Wang, Bei Tian, and Zihang Chen

Abstract The design and development of commercial aircraft is a complex system engineering. At present, operational scenario analysis is gradually used for aircraft function identification and requirement capture. In the analysis process, the time dimension factors of the aircraft in civil aviation operations must be considered, that is, the complete process of aircraft operation must be defined. Guided by the idea of system modeling, this paper presents research on the modeling method of Gate to Gate flight process. The basic elements and hierarchical division of flight process models are constructed. Finally, the paper proposes the method and procedure of establishing Gate to Gate model based on SysML. Based on the previously proposed method and a complete description of commercial aircraft operation process, this paper establishes a summary behaviour model of aircraft's Gate to Gate flight process, covering the preparation before takeoff, push back, taxi out, taxi before takeoff, takeoff roll, takeoff, climb, ocean-based cruise, land-based cruise, descent, approach, final approach, landing, taxi after landing, and taxi to aircraft stand. SysML is used to model the flight process, which includes aircraft itself, ATC, AOC, airport tower and other models. The model is drawn to form Use Case diagrams, Activity diagrams, State Machine diagrams, and Sequence diagrams under each flight phase. The model mainly focuses on the collaborative process between aircraft and various

H. Li · M. Wang (✉) · G. Xiao · G. Wang · B. Tian · Z. Chen
Shanghai Jiao Tong University, Shanghai, China
e-mail: miaowang@sjtu.edu.cn

H. Li
e-mail: lihongyu39@sjtu.edu.cn

G. Xiao
e-mail: xiaogang@sjtu.edu.cn

G. Wang
e-mail: wang_guoqing@careri.com

B. Tian
e-mail: tianbei@sjtu.edu.cn

Z. Chen
e-mail: chenzihang_jy@sjtu.edu.cn

Z. Jing and X. Zhan (eds.), *Proceedings of the International Conference on Aerospace System Science and Engineering 2020*, Lecture Notes in Electrical Engineering 680,
https://doi.org/10.1007/978-981-33-6060-0_18

stakeholders, such as the collaborative interaction process between aircraft and ATC, AOC, as well as the collaborative interaction process between aircraft and airport tower during the takeoff and landing phase. This paper provides a method to describe the flight process systematically and graphically. It can also be used as an exploration of function identification and requirements capture methods.

Keywords Flight process · SysML · Behaviour diagram · Commercial aircraft

1 Introduction

Modern civil aircraft development is a highly complex multi-system integration project, which is characterized by numerous subsystems, complicated cross-linking between systems, technology intensive, and cross-disciplinary. How to systematically analyze the functional requirements of civil aircraft has always been an important task of civil aircraft design and development. Analysis methods based on document management are a thing of the past. Today, model-based systems engineering (MBSE) ideas are widely used in civil aircraft design to support activities such as capturing, analyzing, and verifying system requirements.

The design process of civil aircraft is a top-down, layer-by-layer decomposition based on user needs. Therefore, the premise of accurately grasping the functional requirements is to be able to obtain accurate and complete top-level use cases, and gradually expand into sub-use cases, which ultimately correspond to the needs and functions of civil aircraft. The MBSE method is now widely used in the field of aircraft design, and there are many researches using SysML for functional analysis and logic design [1]. Research literature [2] has carried out the functional design and logic verification of flight control system according to the demand-function-logic-physics system engineering method. Paper [3] proposed a MBSE method to analyze and design critical safety systems for aircraft. The MBSE method has been successfully applied in the practice of several projects of Boeing and Airbus [4].

In the above-mentioned related research, the top-level use cases on which requirements analysis relies are generally from a single running scenario, and system-level functional requirements are analyzed from the scenarios [5]. The top-level use cases from this source are likely to cause imperfect requirements capture. Therefore, it is necessary to consider the complete flight process of the aircraft and build a multi-dimensional flight environment and scene. In recent years, scene analysis has gradually been used to identify aircraft functions and capture requirements. The analysis process must consider the time dimension of the aircraft being put into civil aviation operation, that is, the complete process of aircraft operation must be defined. In the initial stage of civil aircraft design, the aircraft is considered under the civil aviation operation and management system. Taking the complete operation process of the aircraft as a scenario, it can ensure the close integration of requirements and functional design in the development life cycle.

In the first section of this paper, based on the complete description of civil aircraft flight process, the basic elements of constructing a summary model of aircraft Gate to Gate process are proposed, covering the entire operation process under the current civil aviation management system. In the second section, based on SysML, a summary model of the Gate to Gate process covering the basic elements is established, the Use Case, Activity, State Machine, and Sequence diagram in each operation phase are formed and further analyzed.

2 Gate to Gate Flight Process

The basic requirement for establishing a Gate to Gate flight process summary model is to cover the basic operation process and scenarios of aircraft under cur-rent civil aviation management system. Guided by the regulations of civil aviation management, according to the different flight missions under time dimension of civil aviation operation, the whole flight process of aircraft is subdivided into several phase.

Since this article builds a summary model, the basic elements contained in the model are required to be complete, but at the same time it should be concise and clear. Each flight process contains a large amount of information transmission, collaborative decision-making, and operation interaction. Therefore, when using SysML behaviour diagrams to describe, we should select the parts that help complete the requirements capture.

The Gate to Gate flight process model established in this paper focuses on collaborative decision-making with various participants and the state changes of key aircraft systems. The following is a detailed analysis from the three aspects of participants, system composition and flight process.

2.1 Participants

When modelling the Gate to Gate flight process, the first thing to determine is the members who are mainly involved in the flight scenario. According to the current civil aviation operation and management system, and the general procedures for aircraft operation, as well as airline operation and control regulations, the entire flight process is sorted out. Participants of Gate to Gate flight process model refer to all members participating in the flight scenario, including the aircraft, airlines, airports, air traffic control, etc.

Aircraft. The aircraft includes the aircraft's own equipment and systems, and the flight crew which is responsible for completing the aircraft's driving and manoeuvring. According to the current civil aviation regulations, usually the flight crew consists of two or more pilots. Specific to the distribution of responsibilities, it is divided into captain and co-pilot. When considering the division of labour in flying

an aircraft, it is generally divided into PF and PM, that is, pilot-flying and pilot-monitoring. The PF is mainly responsible for driving and manoeuvring the flight, and the PM is mainly responsible for the status monitoring of the flight. Specific to each flight phase, according to the requirements of different airlines and different types of aircraft, the cockpit areas of the two are different [6].

Airlines. The airline part involved in Gate to Gate flight process model mainly refers to the airline's operation control centre (AOC). The AOC can realize the integration of airline resources, complete the tasks including flight dispatch, maintenance, ground support, crew deployment, etc., is the core of the airline's command. Specific to the Gate to Gate flight process model, the AOC mainly involved in this article includes flight dispatch and ground support. The airline is responsible for organizing the initial flight plan of the aircraft flight and participating in the modification and adjustment of the real-time flight plan during the flight. At the same time, when the aircraft is in the pre-flight preparation phase on the ground, the airline's ground crew need to assist the flight crew to complete the pre-flight inspection and pushing back.

Airports. The airports part of Gate to Gate flight process model mainly includes deliver control center (DEL), ground control center (GND) and tower control center (TWR) in airport control. Among them, the DEL needs to make a comprehensive judgment based on the flight plan, airport flow and route weather, destination airport status and other information, issue a release permit to the aircraft, and allow the aircraft to complete the flight plan. GND is responsible for scheduling management and permit issuance of aircraft in surface operation, according to the traffic conditions of the airport surface and the sorting queues for entry and exit, the aircraft is issued with permission to launch and start the engine, and directs the aircraft to complete the surface taxi according to the route. The TWR is mainly responsible for the command and dispatch of aircraft entering and leaving the port, including directing the departing aircraft to enter the runway, issuing the take-off permission, and issuing the landing permission to the incoming aircraft.

Air traffic control. The air traffic control part of the model is mainly composed of area control center (ACC) and approach control center (APP), and is responsible for providing air traffic control services, flight information and warning services in specific flight areas. Area control areas generally refer to high-altitude control areas, and approach control areas are the connection between the tower control area and the area control area. APP is responsible for sequencing landing aircraft and adding routes to departing aircraft.

2.2 System Composition

The purpose of establishing a Gate to Gate flight process summary model is to perform aircraft function identification and requirements capture, so it is not perfect to obtain only the aircraft-level requirements. In the summary model, the participating

aircraft will be further decomposed to analyze the functional requirements of the key systems.

In addition to distinguishing the concept of human–machine and dividing the model into pilot and aircraft, the aircraft model established in this paper also subdivides the typical systems and equipment to form the system components of the model. The system composition includes the system involved in the whole flight process, which is obtained by subdividing the participating subjects layer by layer.

2.3 Division Method

For civilian aircraft, the fundamental mission of the aircraft is to fulfill the transportation needs, which is reflected in the ability, performance and effective-ness of flight. The flight process of aircraft is the application of capability, performance and effectiveness.

Taking current civil aviation operation and management system as a reference, the entire flight process is divided into: preparation before takeoff, push back, taxi out, taxi before departure, takeoff roll, takeoff, climb, ocean-based cruise, land-based cruise, descent, approach, final approach, landing, taxi after landing, sliding into the parking space. There are obvious flight tasks or status transition signs between each phase, and they are closely connected with the front and back phases, forming the whole process from flight preparation to flight completion. The definition and division of each phase are introduced as follows.

Preparation before takeoff. The preparation before take-off starts with the flight plan, and also includes the direct preparation work after the crew arrives at the aircraft stand. The main mission of the participants in this phase is to negotiate to formulate a flight plan. At the same time, the crew needs to complete the safety check, ground preparation and information acquisition, and finally apply for clearance to DEL.

Push back. After obtaining the clearance, the crew can begin preparations for push back. After applying for GND permission, the crew can complete push back of the aircraft and start engine with the help of ground crew. The phase ends with the aircraft reaching the stop line and engine keeping the idle stable.

Taxi out. The taxi-out phase refers to the phase in which the aircraft moves from the stop line to before the taxi area. During the phase, the crew needs to complete the preparations for taxiing, and apply to GND for taxiing instructions.

Taxi before takeoff. The phase refers to the process of the plane taxiing in the taxi area of airport surface. Depending on the situation, the crew may need to taxi to a specific area for de-icing operations. Or the crew needs to follow the GND commands to cross the runway. After taxiing, the aircraft should wait outside the runway for instructions.

Takeoff roll. The takeoff roll phase is defined as the time when the aircraft enters the flight runway until the aircraft completes the acceleration roll and retracts the landing gear in the air. The division is based on the relevance of the series of actions of crew after take-off. At the same time, the participants in the stage also have TWR,

which is responsible for issuing take-off instructions to the aircraft at the beginning of the phase.

Takeoff. To ensure the continuity of previous phase, the aircraft had retracted its landing gear at the beginning of take-off phase. Therefore, the main content of take-off phase is that the crew applies to APP for departure instructions, and at the same time completes the post-takeoff inspection. This phase can be regarded as the transitional phase between takeoff roll and climb.

Climb. The climb phase refers to the process until the aircraft rises to the cruising altitude. Generally, after take-off, the operation of aircraft is handed over to the autopilot system, so the subsequent few phases of crew operation activities are less, and the proportion of collaborative decision-making with ATC will increase. The control unit of the aircraft during the climb phase was transferred from APP to ACC.

Ocean-based cruise. The cruise phase will be divided into ocean-based and land-based depending on where the aircraft is located. Among them, ocean-based cruise refers to the cruise flight process of an aircraft crossing the ocean. The characteristic of this phase is that there are basically no navigation facilities in the ocean area. Therefore, when the aircraft is flying in the ocean area, its navigation and communication methods have changed greatly. To put it simply, during the cruise in the ocean area, aircraft rely more on HF or satellite communication, and the control mode is switched from radar control to procedure control.

Land-based cruise. The flight environment of aircraft during the land-based cruise phase has not changed much, because the radar stations and communication stations below the route are relatively dense. The aircraft will still fly under radar control. The collaborative decision-making between aircraft and ACC during the cruise phase usually includes application to change altitude, application to change routes, and ACC control handover.

Descent. Generally speaking, when flying to 80 nautical miles before the descent apex, the aircraft must begin preparations for descent. In addition to the necessary adjustment of flight status, it is also necessary to obtain the landing conditions of the destination airport. The descent phase ends after the control of aircraft is transferred from ACC to APP.

Approach. The whole landing process is divided into several small phase. Among them, the approach phase refers to the flight activities in the area controlled by APP. At this phase, the aircraft needs to complete preparations and inspections before approaching. The APP needs to sequence the arrival of aircraft in the area, and issue an approach command to each aircraft.

Final approach. In the final approach phase, control of the aircraft will be transferred to the airport's TWR. This is also the last phase of aircraft in the air during the entire flight. In addition to completing the pre-landing inspection at this stage, the crew needs to decide whether to go around based on the airport environment. TWR needs to grant landing permission to the aircraft based on the air traffic above the airport and surface.

Landing. For aircraft that require manual approach, more operations need to be completed by crew during the landing phase. The main content of this phase is to slow down the aircraft. At the same time, there is a control handover process. When

the aircraft decelerates and leaves the runway, it needs to be transferred from TWR to GND.

Taxi after landing. Before leaving the runway, the crew needs to apply to GND for taxi instructions. In addition to the necessary system control required by the flight manual during the taxi phase after landing, the rest of the content is basically the same as the flow during the taxi phase before take-off.

Taxi to aircraft stand. After leaving the taxi area of airport, the aircraft will enter the aircraft stand. According to the airport situation, the ground crew can choose to assist in entering stand. After completing the shutdown of the system, the entire flight process has also been completed, and the fifteen phases will constitute the Gate to Gate flight process.

Each phase model should include multiple participants such as aircraft, ATC, AOC, etc., and should cover air-ground collaborative interaction, aircraft-ATC-AOC, etc. Take the approach phase as an example, that is, when the aircraft descends to an excessive level until the landing checklist is completed before the aircraft is landed, the process should include the operation of the aircraft's local pilot under normal procedures, pilot and APP and TWR. Collaboration and interaction, as well as the handling and release of route conflicts under abnormal conditions, decision-making for approach and go-around, etc.

3 Modeling Based on SysML

Based on the above analysis of summary model, the basic elements required by it have been determined, and the start or end signs of each phase have been divided. The next step is to complete the summary model based on SysML behaviour diagram. Use Enterprise Architect software to complete the MBSE-based system model building and integration, establish a unified standard Gate to Gate model, build the model of basic participants and system components, with Activity, Use Case, Sequence and State Machine diagram [7], [8].

The characteristics and modelling methods of four behaviour models are introduced below, taking the take-off phase as an example. In order to better show the details, we reconstructed some models with Visio.

Activity diagram. Activity diagram can clarify the specific flow of a use case, such as the flow of take-off phase. In the take-off phase, the work of aircraft and ATC consists of a series of activities. In the activity diagram, two partition are drawn respectively, corresponding to the workflow of aircraft and APP. The model usually includes a basic branch and one or more alternative branch. The switching of branch needs to use a control node [9], 10, 11 (Fig. 1).

An activity diagram is a dynamic view that illustrates the sequence of actions and events that occur over time. Activity diagrams can express the flow of information and instructions through behaviours, and pay attention to how objects are accessed and modified during the execution of behaviours, and can express more complex control logic. Taking the take-off phase activity diagram as an example, the figure

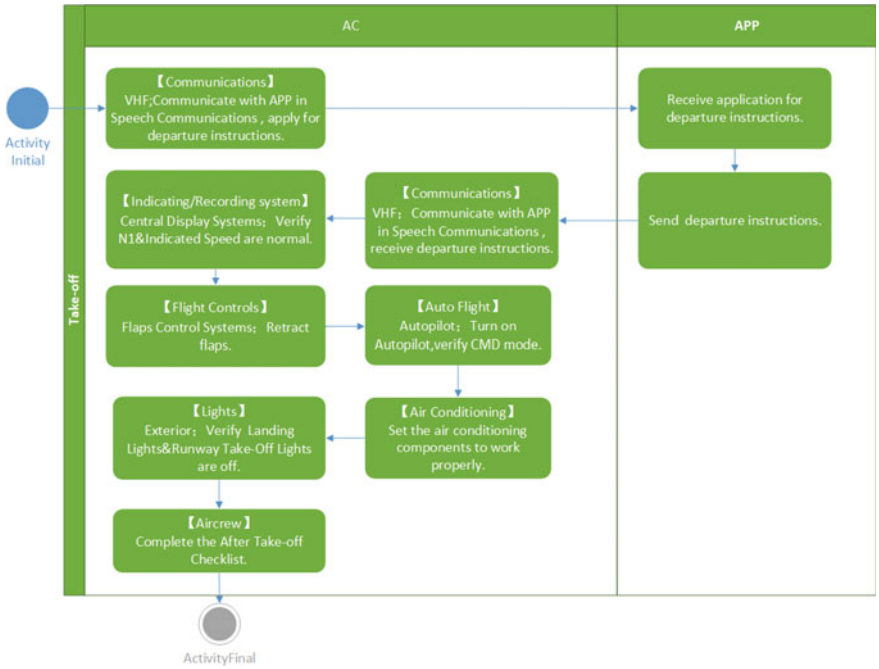

Fig. 1 Activity diagram during take-off phase

can clearly show the collaborative decision-making and information transmission process between aircraft and APP, and also describes the operations that flight crew within the aircraft needs to complete or the status changes in the key systems after take-off.

Sequence diagram. Sequence diagram is the same as activity diagram, expressing the dynamic view of system. Each participant can interact with each other through operation calls and asynchronous signals. Compared to activity diagrams, sequence diagrams focus more on expressing three types of information: the order in which actions are performed, which participants will perform which actions, and which structures trigger which actions (Fig. 2).

Sequence diagram uses lifelines to model the aircraft and APP, and uses messages between the lifelines to model the interaction between participants, which is convenient for describing various interactive behaviours and interactive executions. As shown in the figure, the left side is the time sequence of aircraft's behaviour during the take-off phase, and the right side is APP. The sequence diagram is more intuitive in expressing the execution order of behaviour and activities.

State Machine diagram. State Machine diagram also describes the dynamic behaviour information of system. The difference is that State Machine focuses on how the structure in system changes state according to events that occur over time. The concept of state is difficult to formally define. In summary model, the state will

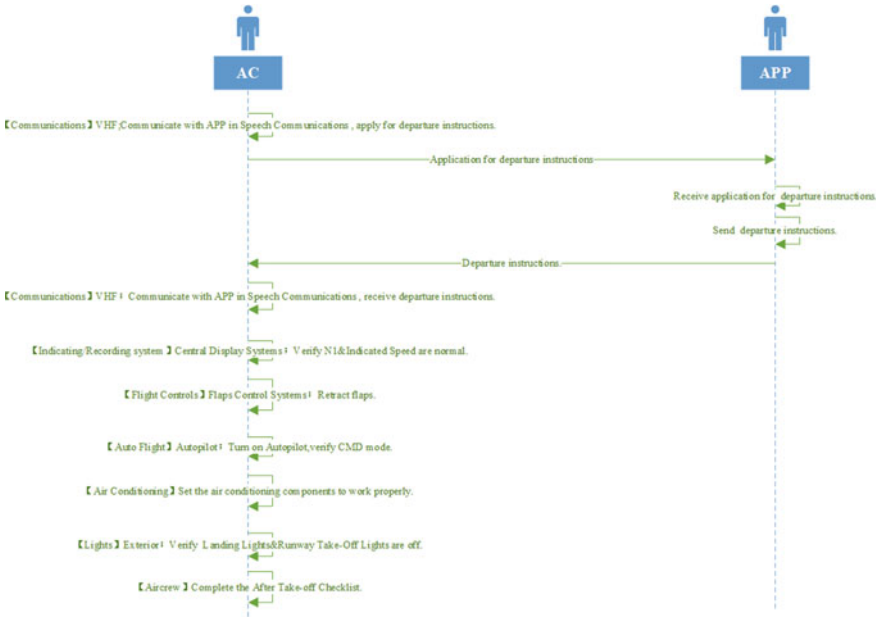

Fig. 2 Sequence diagram during take-off phase

be specifically defined according to different flight phases and environments, and the situation of system (Fig. 3).

State Machine is slightly different from activity diagram and sequence diagram, showing the state change process. There is no state transition in the take-off phase, so there is only one block diagram in the figure. In other phases, the State Machine has different complexity according to the activities, and there are judgment conditions between each state. The current summary model only takes the aircraft as main

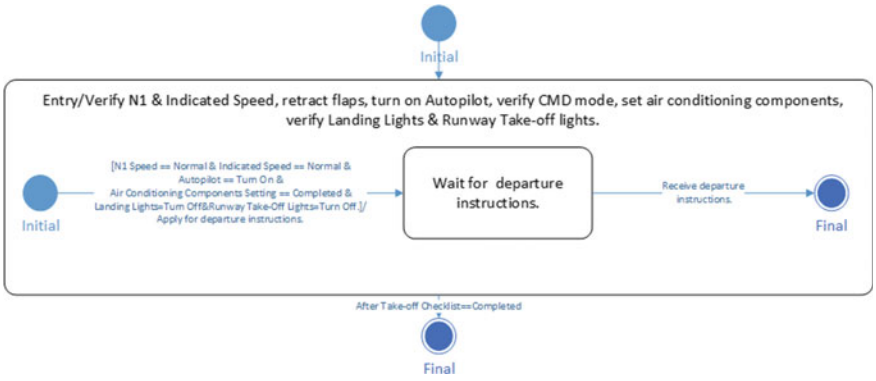

Fig. 3 State Machine diagram during take-off phase

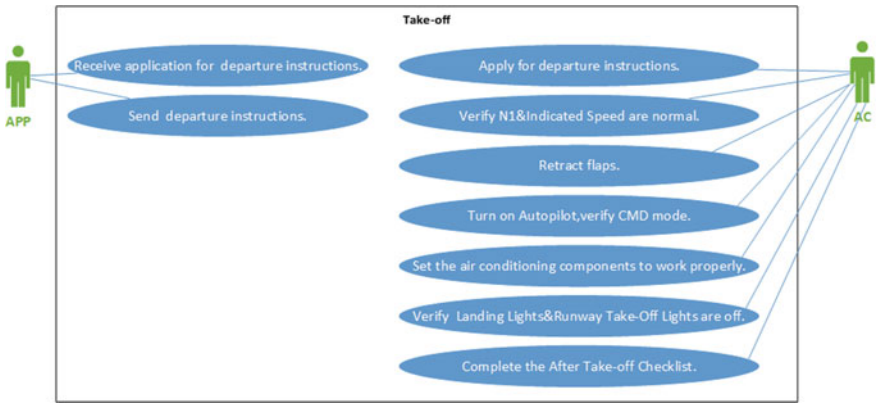

Fig. 4 Use Case diagram during take-off phase

body, and in a more detailed model, the key system of aircraft will have its own State Machine diagram to show the state of key system, in order to analyze the function and requirements of system.

Use Case diagram. Use Case diagram is different from the above three diagrams and is a situation diagram of system. Specifically, Use Case diagram can explain the service information provided by system, that is, all externally visible services. Each Use Case diagram contains several use cases, and each use case is associated with the executor who triggered and participated in the use case (Fig. 4).

The figure shows all use cases involving the aircraft and APP during the take-off phase. At some phases, there are multiple executions or participants in a single use case. The Use Case diagram also supports the rapid screening of use cases where the current participant participates in all stages. The existence of Use Case diagram can clearly show the relationship between behaviour and participants.

Model of flight phase. Taking the take-off phase as an example, the above content introduces the characteristics and modelling methods of four behaviour diagrams in detail. Due to space limitations, the remaining 14 phases will not be introduced one by one. Only some special behaviour diagrams are introduced below Fig. 5.

The first is the sequence diagram at push back phase. As mentioned above, during the push back phase, the crew needs to apply to GND for a start clearance. The GND needs to make judgments based on the flight plan and traffic conditions. If the situation permits, the aircraft can be pushed back directly. If the situation is not allowed, the aircraft needs to wait on the bridge until the GND grants permission. The logic of this part is a little more complicated, and the loop judgment structure in the behaviour diagram needs to be used. As shown in the figure below, the middle part shows the negotiation process between the crew and the GND.

The following figure is a Use Case diagram of taxi out phase. There are many behaviours and activities included in this phase, so we divide this into several processes. As shown in the figure, all use cases are listed and included in the process.

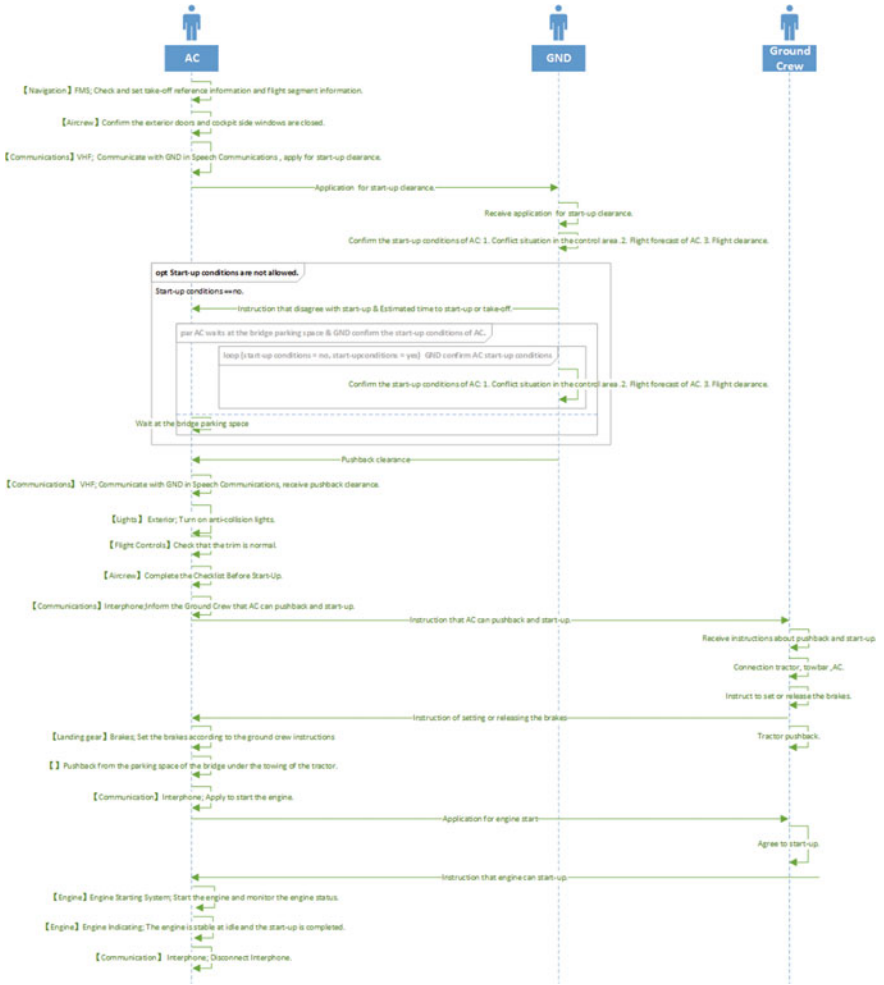

Fig. 5 Sequence diagram during push back

This is also known as the inclusion relationship between use cases. Sub-use cases eventually point to the executor through upper-level use cases (Fig. 6).

The following figure is a Sequence diagram of taxi phase before take-off. Considering that there may be situations where it is necessary to cross the runway during the operation of airport surface, the model adds a judgment step. When the aircraft needs to cross the runway, it will trigger the behaviour in the opt. The crew needs to change the lights and navigation settings and observe the runway. This is reflected in the sequence diagram as shown below (Fig. 7).

During the cruise phase, when flying across two ATC control areas, or across different sectors in the same control area, control handover is required. That is, the aircraft disconnects the radio connection from the original control center and

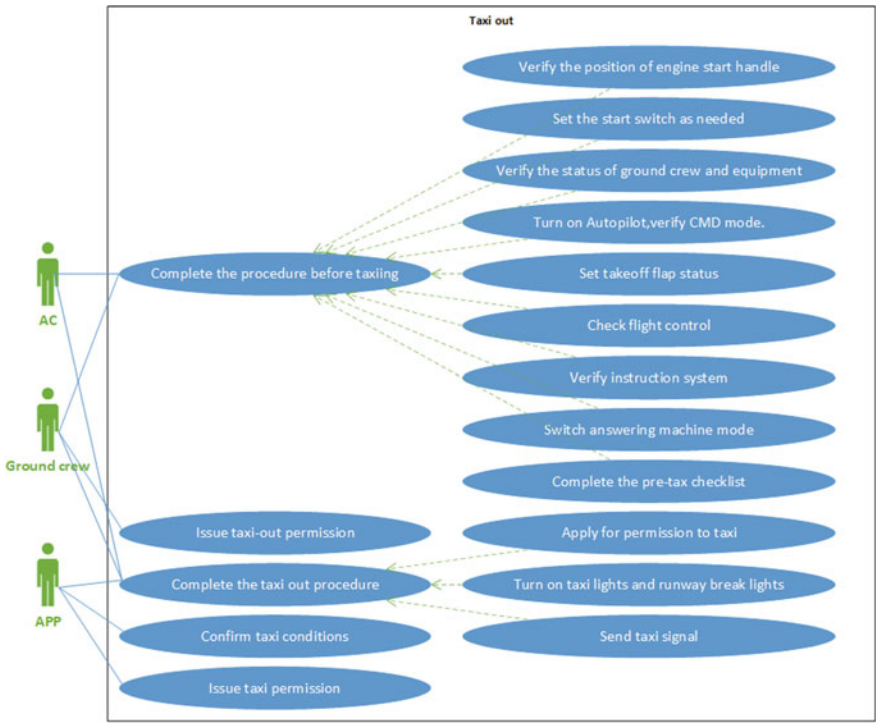

Fig. 6 Use Case diagram during taxi out phase

adjusts the radio to the new frequency. At the same time, if the pilot has a need to adjust the aircraft's altitude or speed, they also need to apply and negotiate with ACC. The above process is reflected in the activity diagram, that is, it has become an interactive activity across multiple partition. The transmission of information is shown in the interactive behaviour, representing the negotiation between the crew and ACC (Fig. 8).

The Activity diagram in the approach phase mainly shows the collaborative decision-making process between aircraft and ATC. Aircrew need to obtain permission from ACC when descending. And obtain permission from APP when approaching. This process is mainly achieved through VHF voice communication (Fig. 9).

The following figure is State Machine diagram of taxi to aircraft stand phase. At this phase, several states are divided, so the structure of State Machine diagram is slightly complicated. During taxiing, there is a possibility that the aircraft needs to cross the runway. Therefore, in the State Machine, there are judgment modules and sub-states. Generally, the input, execution, and output of states need to be described, and transition conditions need to be set between different states (Fig. 10).

Based on the SysML behaviour diagram, the 15 phases of Gate to Gate flight process are modeled. Analyzing the above models, we can find that the Use Case

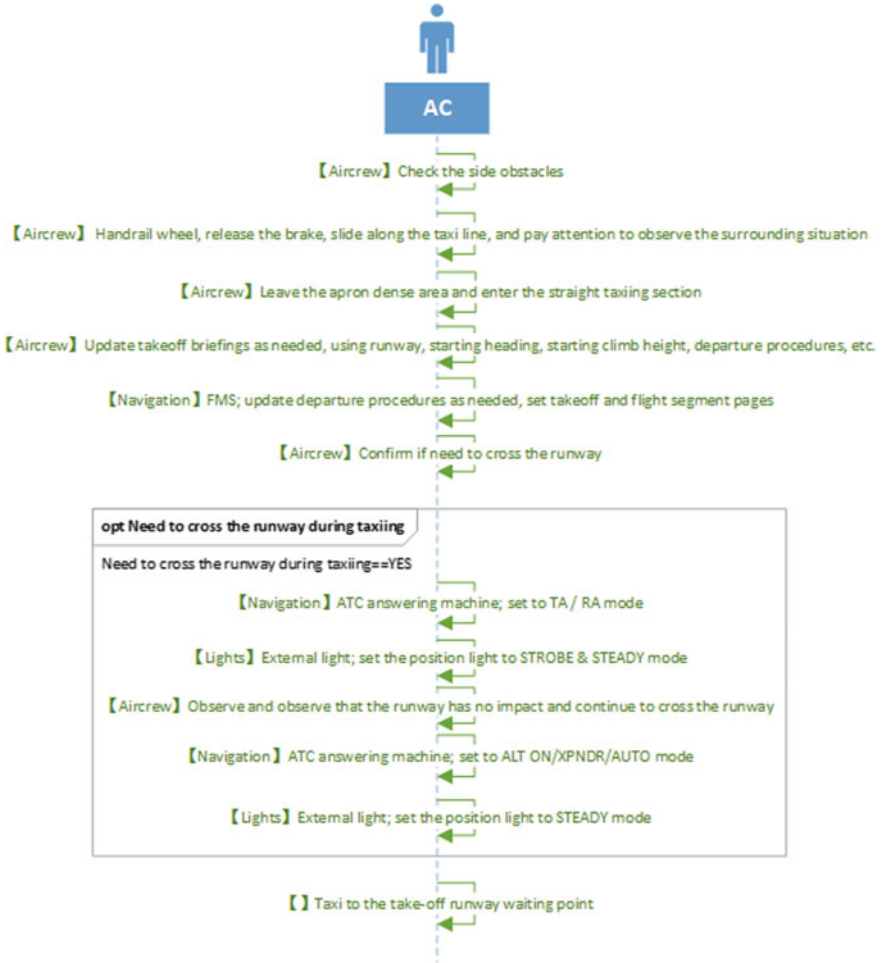

Fig. 7 Sequence diagram during taxi phase

diagram can obtain the behaviour activities that the participants need to participate in or perform during the full operation process. It can provide the sequence of actions required by each participant in a specific stage, and the State Machine can show the status changes and conditions of the aircraft or critical system. Therefore, the SysML behaviour diagram can meet the requirements of establishing a summary model of Gate to Gate flight process, and supports the analysis of functions and requirements of aircraft and key systems.

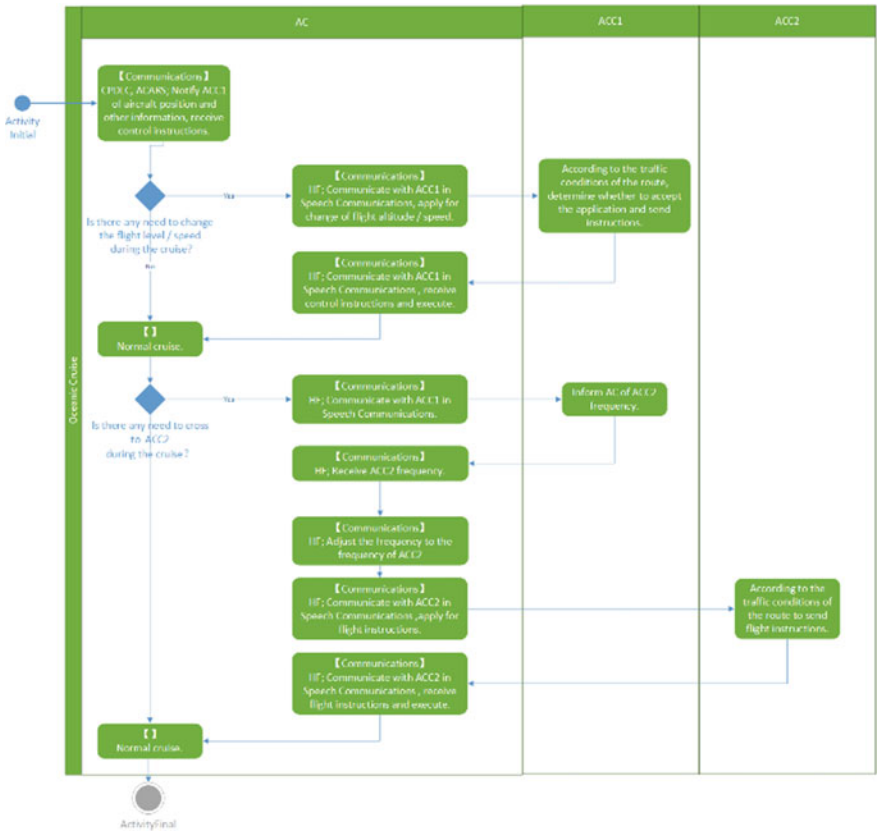

Fig. 8 Activity diagram during ocean-based cruise

4 Conclusion

In this article, we first analyze the basic elements required for the summary model, clarify and subdivide the parties including aircraft, air traffic control, airlines, etc., and divide the key components and systems of aircraft. At the end of the first section, the Gate to Gate flight process is defined. Then, based on the idea of system modeling, the model is established at the system level of aircraft, and the SysML behaviour model is built around the key systems involved in the flight process of aircraft. It can be obtained by analyzing the model that the behaviour diagram can provide a method for describing the flight process systematically and graphically, and can also be used as an exploration of function identification and requirement capture method in aircraft design process.

The work involved in this article is still insufficient. The first is that key systems are not the basis of behaviour model. To focus on the key system, it will take a large amount of work and require that relevant standards can be formulated in advance.

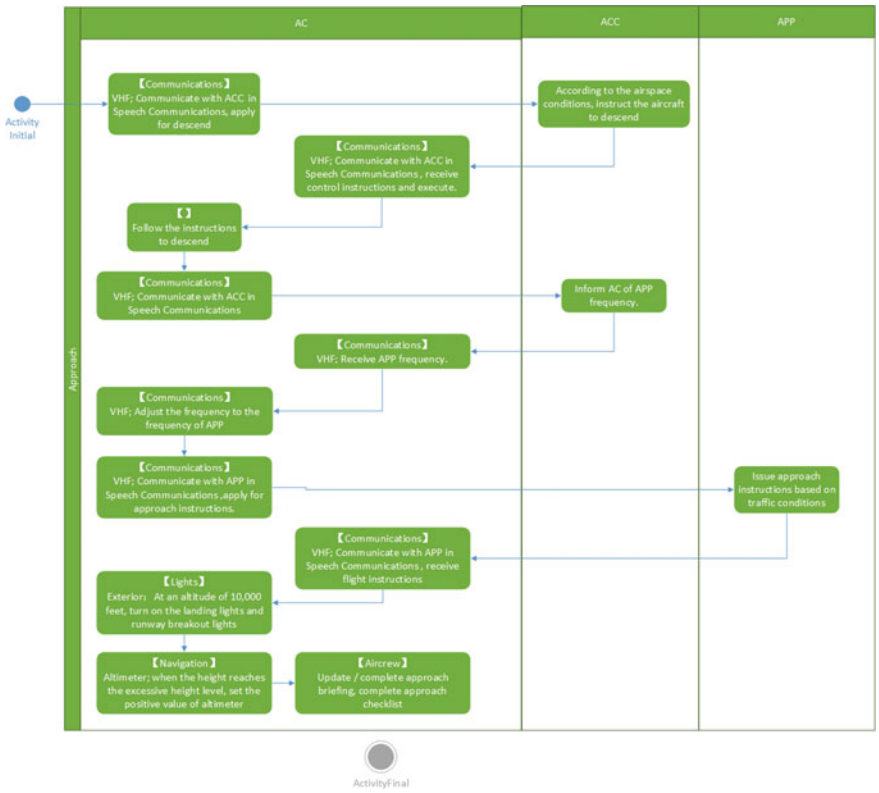

Fig. 9 Activity diagram during approach phase

This part of work still needs to be deepened and improved in the future. The second is that although the behaviour model supports simulation, as the details of current model are not perfect, the simulation process needs to be injected with conditions, so the result is of low significance. In the next stage of work, we need to further consider model simulation issues, and give full play to the role of summary model in simulating the flight process of aircraft and completing the requirements analysis.

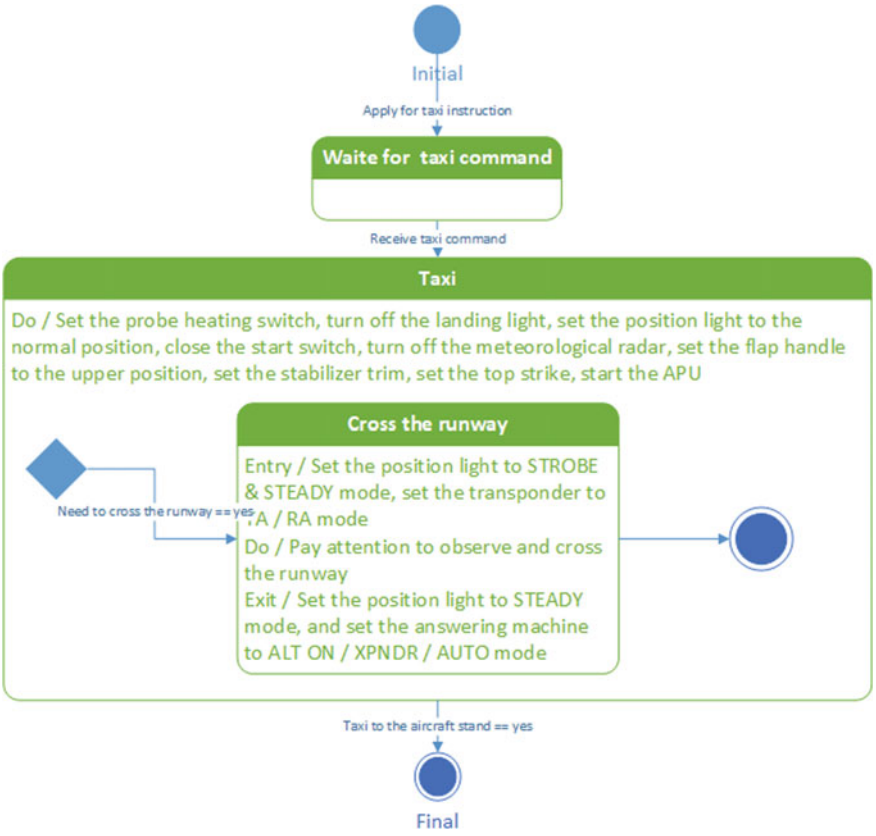

Fig. 10 State Machine diagram during taxi to aircraft stand phase

Acknowledgements The project is supported by National Program on Key Basic Research Project (2014CB744903), National Natural Science Foundation of China (61673270), New Young Teachers Launch Program of Shanghai Jiaotong University (20X100040036), Shanghai Pujiang Program (16PJD028), Shanghai Industrial Strengthening Project (GYQJ-2017-5-08), Shanghai Science and Technology Committee Research Project (17DZ1204304) and Shanghai Engineering Research Center of Civil Aircraft Flight Testing.

References

1. Qiao WF, Li ZQ, Huang S, Yao ZC (2015) Research on model-based integrated design of civil aircraft. Aviat Manufact Technol 2015(04):72–77
2. Xu YZ (2018) Application of model-based requirements-function-logic-physical system engineering method in aeronautical system design. Chinese Aeronaut Soc. Proceedings of the 8th China aeronautical society youth science and technology forum 2018: 1386–1391

3. Zhang SJ, Li ZQ, Hai XH et al (2018) Design of safety critical system for civil aircraft based on MBSE. Chin Sci: Tech Sci 2018(3):299–311
4. Mei Q, Huang D, Lu Y (2018) Design method of civil aircraft functional architecture based on MBSE. J Beijing Univer Aeronaut Astronaut 2019 45(05): 1042–1051
5. Ren BX, Lu Y, Fu S, Huang D (2019) Identification and confirmation of civil aircraft functional requirements based on MBSE. Syst Eng Elect Technol 41(09): 2016–2024
6. Zhu HY (2019) Research on the evaluation method of the minimum crew workload of civil aircraft. Int Combust Engine Parts 2019(08):185–187
7. Lenny D (2014) SysML distilled: A brief guide to the systems modelling language, 1st edn. Addison-Wesley Professional
8. Graves H, Bijan Y (2011) Using formal methods with SysML in aerospace design and engineering. Ann Math Artif Intell 2011(63):53–102
9. Friedenthal S (2015) A practical guide to SysML: the systems modeling language, 2nd edn. Morgan Kaufmann
10. Weilkiens T (2008) Systems engineering with SysML/UML. Burlington: Morgan Kanfmann SMG Press, pp 18–22
11. Holt J, Perry S (2008) SysML for systems engineering, 2nd edn: A model-based approach[M]. London: The Institution of Engineering and Technology, pp 121–222

Research of Commercial Aircraft's Battery Layout Design Method Based on Ditching Situation

Li Wen Wu

Abstract From Airworthiness regulation, the electronic power supply system must meet the requirement of power demanding devices which are used to support emergency evacuation of passengers, during emergency landing, including ditching situation. In this situation, the main power supply is often failure, and battery will supply power instead. However, after ditching, the fuselage structure is often damaged, water will flow over into fuselage, if battery, charge or wires are under water and short circuit, then all the devices which are used to support emergency evacuation will failure to work, and passenger evacuation will be very dangerous. For this problem, this paper researches the ditching floating characteristics of commercial aircraft, especially the leakage time of compartment, time-variation of water level, etc. At the same time, this paper analyzes the time of passenger evacuation. Based on those impact facts, this paper researches the battery layout design method of commercial aircraft.

Keywords Commercial aircraft · Battery layout · Ditching

1 Background

Commercial aircraft's ditching situation is a special case of emergency landing, and its risk level is very high. The operation procedure of pilot during ditching is different from ground landing, and usually the bottom of rear fuselage will strike water surface firstly with high striking load in this situation, structure or system of aircraft, especially portion of the skin, beam, stringer or doors of rear fuselage and part of system devices may be damaged due to striking load. Furthermore, emergency evacuation procedure of ditching is also different from ground landing, for example, Life rafts' removal, releasing and launching must be added into evacuation procedure of ditching, so the evacuation time is usually longer than ground landing. After landing, the aircraft will continuously fall down below water surface due to water

L. W. Wu (✉)
Shanghai Aircraft Design & Research Institute, Shanghai, China
e-mail: usweapon@21cn.com

Z. Jing and X. Zhan (eds.), *Proceedings of the International Conference on Aerospace System Science and Engineering 2020*, Lecture Notes in Electrical Engineering 680,
https://doi.org/10.1007/978-981-33-6060-0_19

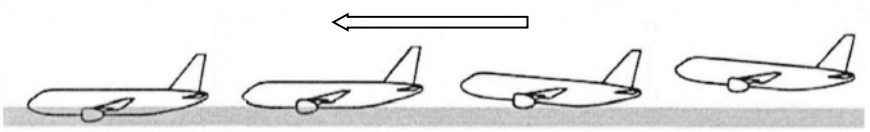

Fig. 1 Ditching process of commercial aircraft

flowing into fuselage, and the aircraft can't remain floating for a long time. In this situation, evacuation of all the crew and passenger during ditching will be more dangerous and difficult than ground landing. Figure 1 shows typical ditching process.

2 Analysis Procedure

The commercial aircraft which requests for certification with ditching must meet the ditching requirements of China Civil Aviation Regulations (CCAR part 25) in China, and the requirements are the same as Federal Aviation Administration's or European Aviation Safety Agency's.

The regulations related to ditching directly are CCAR25.801(a) ~ (e), 25.807(i), 25.1411, 25.1415(a), meantime, because ditching case is one of emergency landing cases, so it must also meet the regulations about emergency landing below:

(1) CCAR25.561(b)
(2) CCAR25.561(c)
(3) CCAR 25.787
(4) CCAR25.1362

Based on regulations of CCAR25.801(b) ~ (e), floating characteristic and floating time of aircraft must be calculated, and based on CCAR25.1362, layout of battery and its wires must be isolated and avoided from impact of structure damage or the water that flowing into the compartment, in order to provide electric power to devices that supporting emergency evacuation. The analysis procedure of this problem is showed as Fig. 2.

3 Analysis of Structure Damage and Leakage Sources

3.1 Structure Damage During Ditching

The weight of commercial aircraft during ditching is usually maximum landing weight, and bottom of rear fuselage contact to water firstly, with water impact load which reaches to very high level, after contacting, the skin, frame, beam of rear fuselage's bottom structure may be damaged due to excessive stress, open section of

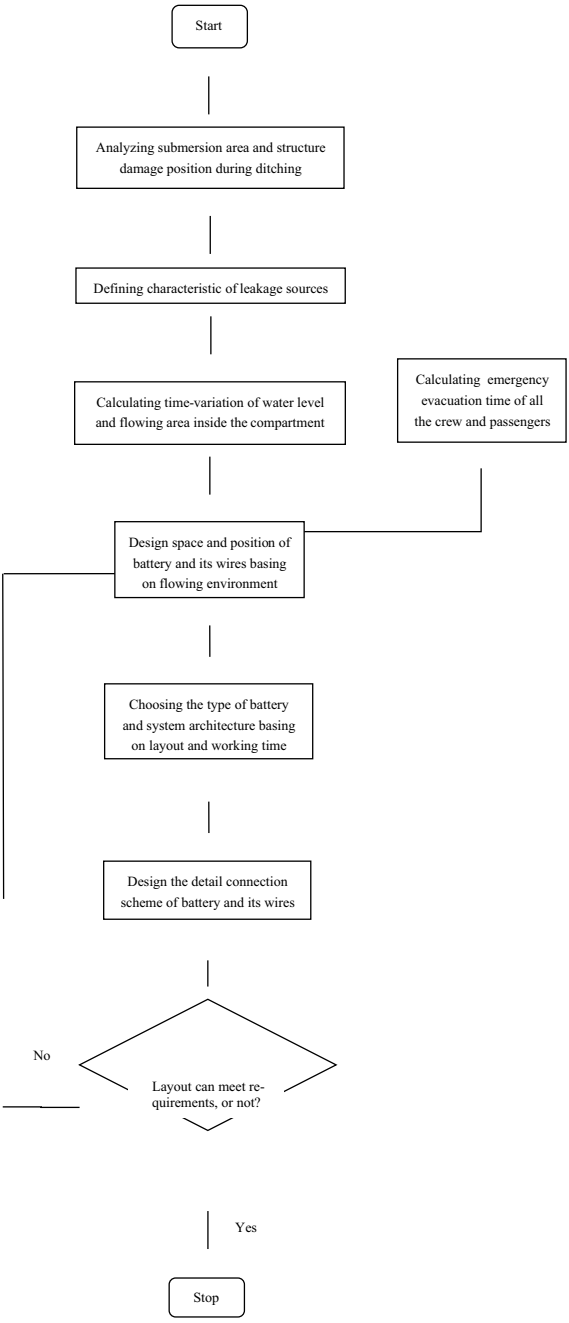

Fig. 2 Analysis procedure of battery layout design for ditching case

fuselage structure may be torn due to local stress concentration, and the dimension of clearance between compartment's door and skin will be too big due to deformation of fuselage structure, all these damage structure will cause water flowing into compartment. In the same time, structure broken and deformation will also damage the system devices near the structure. The characteristic and dimension of the structure broken can be calculated or tested by stress analysis method.

3.2 Leakage Sources During Ditching

Leakage sources means the non-sealing section of structure which is belonged to aircraft skin itself. When the aircraft floats on the water, the water can flow into compartment through those non-sealing section such as:

Drainage holes of fuselage skin under water level, ventilation holes of environment control system on the skin, normal structure clearance, and other structure without sealing.

Base on ditching operation procedure, pilot will shut off the ventilation holes of environment control system and other similar systems' holes before ditching, only the drainage holes of fuselage skin, normal structure clearance, and other structure without sealing which are under water level should be defined as leakage sources. Calculation of the position, shape, dimension, and structure's material of these sources are essential for analysis of water level time-variation and flowing impact zone inside the compartment.

4 Calculation of Flooding Process in Time-Domain

Based on the analysis results of structure damage and leakage sources, build mathematical model of flooding during aircraft's ditching, using Bernoulli equation, considering of steady flowing and ignoring energy losing.

In the structure broken or the leakage sources, the flowing speed equation is showed below:

$$v = \sqrt{2g(h_1 - h_2)} \tag{1}$$

In Eq. (1), g is gravitational acceleration, h_1, h_2 mean the vertical distance between inside, outside water level and the center of structure broken or leakage sources, when the water level inside the compartment is under structure broken or leakage sources, $h_2 = 0$, when $h_1 = h_2$, flow procedure stops, the sketch is showed as Fig. 3.

For the floating status is changed with time-variation, and is a dynamic procedure of aircraft's motion, water flowing into the compartment cause the aircraft's weight and core of gravity position changing, the water level will rise, the pitch angle and roll angle will be changed.

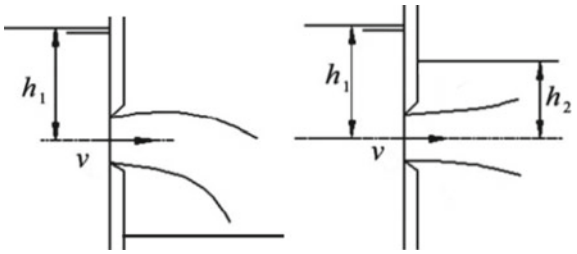

Fig. 3 Sketch of cabin flooding

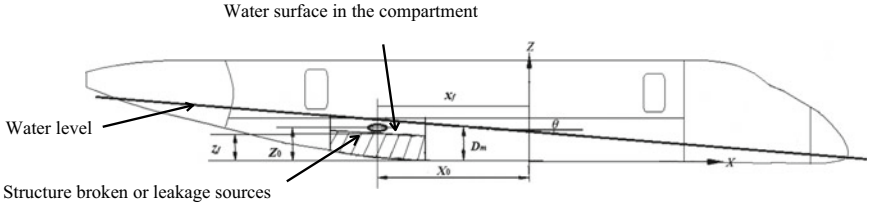

Fig. 4 Floating characteristic model

Changing of those data will change value of h_1, h_2, v, conversely.

Based on those variable data, build floating characteristic model of aircraft's ditching, this is showed as Fig. 4.

In Fig. 4, the reference coordinate system is rectangular coordinate system including z axis which goes through the meta-center of aircraft(the meta-center is refer to terminology definition of shipping), and x axis which goes through the mid-surface of fuselage and the two part which are divided by this mid-surface are symmetrical. For the roll angle which is caused by water flowing is very small, and the floating force of left and right wing can offset part of roll moment, this paper considers that the roll angle can be ignored, and only the aircraft's pitch angle changed during flowing on the water.

Due to changing of water level position outside aircraft and pitch angle, the vertical distance h_1 between water surface outside aircraft and structure broken is showed as Eq. (2), the vertical distance h_2 between water surface inside the aircraft and leakage sources is showed as Eq. (3):

$$h_1 = D_m - Z_0 + X_0 \tan\theta \tag{2}$$

$$h_2 = \left(z_f - Z_0\right)\cos\theta + X_0 \tan\theta \tag{3}$$

In Eqs. (2) and (3), D_m(m) is the average distance between water level and bottom of aircraft at a certain instant, $\theta(^\circ)$ is the pitch angle of aircraft at a certain instant,X_0(m) is the distance between structure broken or leakage sources and z axis,

Z_0(m) is the distance between structure broken or leakage sources and x axis, X_f(m) is the distance between water surface inside aircraft and z axis, Z_f(m) is the distance between water surface inside aircraft and x axis.

Volume of flowing water at a certain instant is calculated as below:

$$\begin{aligned} dV &= \int_0^t Q dt = \int_0^t C_d v A dt \\ &= \int_0^t C_d \sqrt{2g(h_1 - h_2)} A dt \end{aligned} \tag{4}$$

In Eq. (4), Q is the rate of flow (m^3/s) at a certain instant, C_d is correction coefficient that considering factors such as the sharp of structure broken or leakage sources, the liquid viscosity, etc.

Volume of flowing water at a certain instant can also be calculated as below:

$$dV = \int_{z_{f1}}^{z_{f2}} A_{h1} dz_f \tag{5}$$

In Eqs. (5), $A_{h1}(m^2)$ is the projection area in the fuselage's cross-section of compartment flowing water, z_f(m) is the distance between water surface inside aircraft and x axis.

Based on Eqs. (4) and (5), the function between z_f and t can be calculated.

Core of gravity position during water flowing in the compartment is showed as below:

$$x_G^{'} = \frac{m \cdot x_G + dm \cdot dx_g}{m + dm} \tag{6}$$

$$z_G^{'} = \frac{m \cdot z_G + dm \cdot dz_g}{m + dm} \tag{7}$$

For the z axis of reference coordinate goes through the meta-center of aircraft, changing about the position core of gravity can be corresponded to the changing of aircraft's pitch angle, and can be calculated as follows:

$$\tan\theta = \left| z_G^{'} - z_G \right| / \left| x_G^{'} \right| \tag{8}$$

Based on Eqs. (2)-(8), calculates parameters of floating characteristic and water flowing process of compartment in time-domain by means of weight added method which is compiled into computer program.

A calculation example is showed as Figs. 5 and 6. In this example, the original average distance between water level and bottom of aircraft is $D_m = 1.0$ m, original weight of aircraft is $m = 50000$Kg, original core of gravity coordinate is $x_G = 3.0$ m, $z_G = 1.2$ m, original equivalent position of structure broken and leakage sources

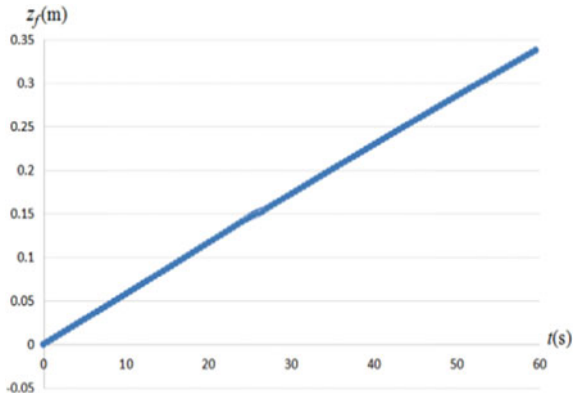

Fig. 5 Relationship curve of z_f (z coordinate value of water surface inside the compartment) and t (time)

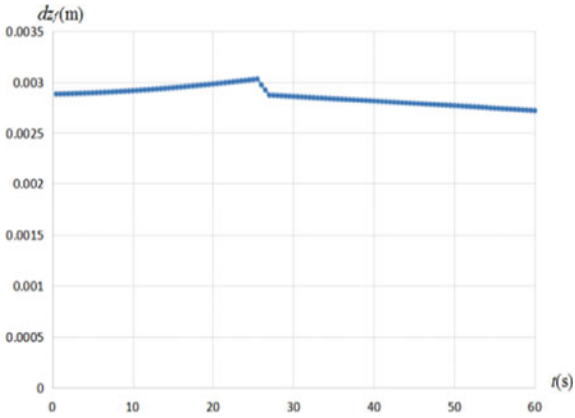

Fig. 6 Relationship curve of dz_f (incremental z coordinate value of water surface inside the compartment) and t (time)

is $X_0 = 5.0$ m, $Z_0 = 0.15$ m, the equivalent area of structure broken and leakage sources is $A = 0.0017\text{m}^2$, correction coefficient is $C_d = 0.60$.

From Fig. 5, z coordinate value of water surface inside the compartment z_f increases from 0 m to 0.35 m in 60 s, and the relationship curve is approximately straight line (ignore the curvature).

From Fig. 6, incremental z coordinate value of water surface inside the compartment increases with time until the position of water surface inside compartment is higher than the equivalent position of structure broken and leakage sources, then the incremental value decreases continuously.

Based on this calculation, the emergency evacuation time, the position of water surface inside compartment and impact zone of flowing in time-domain can be analyzed, and this information can be used for layout design of emergency battery and its wires.

5 Battery Layout Design Method for Ditching

For the battery and its wires are often connected to the fuselage structure by bracket, so the layout of battery and its wires must be designed to avoid from the impact area of damage structure which will damage battery and its wires due to distorted and sharp edge.

Normally, the rear fuselage will strike water surface first during ditching, damage structure and water flowing location are in the bottom of rear fuselage, so it is not a ideal position for installation of battery and its wires, this position usually includes the bottom zone and triangle zone of after cargo.

Based on the types of water-resistant test for airborne devices from RTCA (Radio Technical Commission for Aeronautics) DO-160G, the types of battery are:

(1) Type Y devices which achieve test of resisting condensation
(2) Type W devices which achieve test of resisting water drop
(3) Type R devices which achieve test of resisting water spray
(4) Type S devices which achieve test of resisting continuous water splash.

The priority type of battery and its wires for ditching and emergency evacuation is type R or type S devices which have achieve high level water-resistant test. However, the battery and its wires do not only suffer damage from water flowing of structure broken or leakage sources, but also suffer damage from submerging due to water surface rising inside the compartment, and the damage from distorted and sharp structure, so type R or type S devices may not work normally during this situation, meanwhile, the selection considering factor of battery type and its wires also includes price, volume, capacity of electricity, compatibility with other systems, maintenance performance, etc., ditching situation is only one of all those factors, so this ditching impact problem can't be solved only by the way of selecting battery and its wires type. Best method to solve this problem is appropriate layout design.

For emergency landing on the ground, FAA (Federal Aviation Administration), CAAC (Civil Aviation Administration of China) require that the total time of evacuation must be less than 90 s [1, 2] (be called as golden 90 s), and this time must be designed, test and verified by commercial aircraft's manufacturer. However, the evacuation time is more than 90 s in ditching, because of more evacuation procedure and more difficulty. So the water flowing into compartment and aircraft falling down to the water will continue for a long time before all the crew and passengers have evacuated, thus, battery and its wires' layout design must be ensure that these devices are not fail to work during the time, and based on the method from Chap. "Analysis of Supersonic Axisymmetric Air Intake in Off-Design Mode" of this paper, select and design position to avoid impact zone of water surface and water flowing which are changing in time inside compartment. In Fig. 7, the shadow part in the cross-section of fuselage is the impact zone.

From Chap. "Analysis of Supersonic Axisymmetric Air Intake in Off-Design Mode" of this paper, water flowing speed is very fast, and water surface rises quickly inside the compartment, though the area of structure broken and leakage sources is

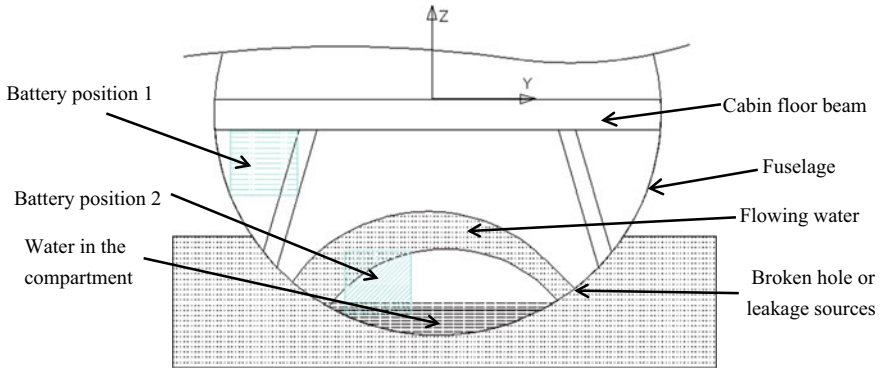

Fig. 7 Impact zone of water surface and water flowing inside compartment

small, considering the typical aircraft's parameters during ditching situation. So the best layout of battery and its wires should be that the devices are all installed in the forward fuselage zone which is up to the cabin floor, the distance from battery and its wires to water flowing zone is farther than other layout types, and this layout provides more time to avoid from impact of water flowing, at the same time, other devices which require electric power of battery should be installed far from water flowing zone, too. Best layout zone is the yellow and purple zone which is showed as Fig. 8.

If the battery and its wires can't be installed up to the cabin floor of forward fuselage, another zone of forward fuselage should be the zone between cabin floor and cargo ceiling, or triangle zone of cargo.

If these devices can't be installed in the forward fuselage, then install them in the zone between cabin floor and cargo ceiling, or triangle zone of cargo, or the cabin of rear fuselage, considering the impact zone of water flowing and the rising altitude of water surface inside compartment during evacuation exactly.

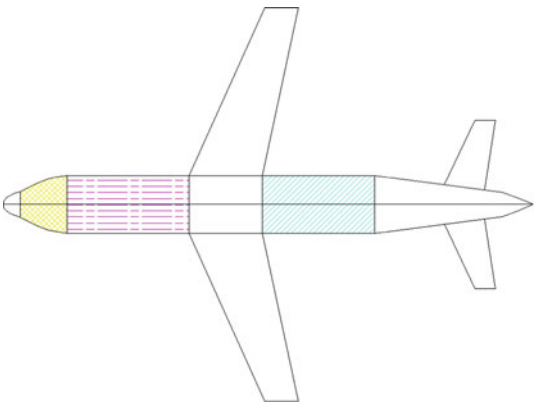

Fig. 8 Probable installation zone of battery and its wires

6 Conclusion

This paper provides method of calculating leakage time and time-variation of water level during ditching. Based on these calculating, this paper introduces commercial aircraft's battery layout design method for ditching case.

The layout design of battery and its wires must consider a lot of factors [3], for example, the lithium-ion battery must be far from fire zone of aircraft, because electrolyte of this battery is inflammable, and should be installed in the bottom of compartment in order to avoid electrolyte leaking and impacting other devices unexpectedly, furthermore, the leakage electrolyte can be drained out of aircraft easily. However, this layout contradicts to the layout design requirement for ditching, so all the factors should be considered systematically in layout design.

Reference

1. Snow CC, Carroll JJ, Allgood MA (1970) Survival in emergency escape from passenger aircraft. DOT/FAA/AM/70–16, Department of transport, federal aviation administration
2. Hasbrook AH, Garher JD, Snow CC. (1962) Evacuation pattern analysis of a survivable commercial aircraft crash. AD No.282 893
3. Qian L (2018) Study on the selection of battery for civil aircraft. Sci Technol Vis. https://doi.org/10.19694/j.cnki.issn2095-2457.2018.19.094

Model-Based Surface Trajectory-Based Operations Analysis in Airport Surface Management

Wenhao Zhao, Miao Wang, Gang Xiao, and Guoqing Wang

Abstract The efficiency and safety of airport surface operations have long been a hot topic in air traffic management domain. The current mode of surface operation management in civil airports is mostly based on the constraint point concept, which does ensure the safety of surface operations but, in quite a lot causes, leads to a waste of time and causes delay in civil airlines. The related researches focus mainly on the improvements of navigation accuracy and the development of surveillance technology, yet they would not escape from the inherent ceiling of the constraint point mode itself. The research of this paper is inspired by Surface Trajectory-Based Operations (STBO) concept. The STBO concept suggests that the new mode of airport surface operation management will allow the strategic automation to develop routes that deliver aircraft to runways and taxiway intersections in a conflict-free manner with the help of 4D trajectory. In the research, the models of some typical surface scenarios are built according to the joint operations in between aircraft, airline and air traffic control with system modeling language, which meet the requirements of specifications and instructions of surface operations. The modeling is carried out in control experiments where one is under constraint points theory and the other is under STBO concept in the same surface scenario. The results are show that the latter one provides adequate safety and better efficiency than the former one in studied scenarios. It is just a start in the exploration of new mode in airport surface management, and the further implement and improvements of STBO concept is looking forward to lead the air traffic management to a new era.

W. Zhao · M. Wang (✉) · G. Xiao · G. Wang
Shanghai Jiao Tong University, Shanghai, China
e-mail: miaowang@sjtu.edu.cn

W. Zhao
e-mail: ericchiu@sjtu.edu.cn

G. Xiao
e-mail: xiaogang@sjtu.edu.cn

G. Wang
e-mail: wang_guoqing@careri.com

Z. Jing and X. Zhan (eds.), *Proceedings of the International Conference on Aerospace System Science and Engineering 2020*, Lecture Notes in Electrical Engineering 680,
https://doi.org/10.1007/978-981-33-6060-0_20

Keywords STBO · Air traffic management · 4D trajectory · sysML

1 Introduction

With the rapid development of civil aviation, the terminal air density has also increased, the most direct outcome of which is that the airport surface has become unprecedentedly crowded and busy. The airport surface is simultaneously carrying out the operation of aircraft and other ground equipment. It involves multiple participants such as aircraft, air traffic control, airlines, and ground equipment, making it undoubtedly a complex system. Therefore, the management of the airport surface has been a hot topic in the field of air traffic management. Since the last century, the most common mode of surface operation management in civil airports is based on the constraint point (CP) concept, which does ensure the safety of surface operations but, in quite a lot causes, leads to a waste of time and causes delays in civil airlines. However, the skyrocketing traffic flow has gradually approached the bottleneck of surface management under the old model. Therefore, research on airport surface management under a new model has attracted widespread attention.

A new concept of operations for surface trajectory-based operations (STBO) directly points out the current issues in airport surface management [1], including inefficient departures with long queues and frequent aircraft stops and starts with high temporal uncertainty. In contrast with the constraint point concept, the STBO concept suggests a new mode of airport surface management in which it allows the strategic automation to develop routes that deliver aircraft to runways and taxiway intersections in a conflict-free manner with the help of 4D trajectory.

In this paper, we study the airport surface management mode based on the STBO concept according to the surface management objectives of the airport surface operation process. By analyzing the main participants and their activities in airport surface operations, and constructing various models of the typical operation process of the airport surface, we aim to implement a new model of airport surface management based on the STBO concept. Taking the departure process in the airport surface operations as an example, we conducted an analysis and modeling, and concluded that the STBO mode can reduce the accidental start and stop, and improve the efficiency of airport surface operations on the premise of ensuring basic safety.

2 Constraint Point Concept

In constraint point concept, strategic aircraft sequencing is accomplished by setting constraint points along the taxi route as shown in Fig. 1. The constraint points divide the taxi route into few segments, and each is assigned with a RTA, requiring the pilot to meet. DataComm is the primary mode of communication between pilots and ATC for clearances transmission, and voice will be used for tactical and time-critical

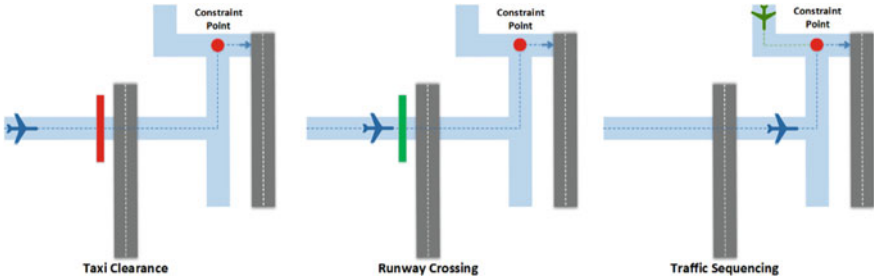

Fig. 1 Sketch of constraint point theory

communications when taxi onto, or across active runways. Traffic sequencing is basically accomplished by assigning non-overlapping RTAs at common constraint points.

The clearance is transmitted to the flight deck in 2D form, divided into segments by constraint points with an RTA window each. The constraint points can be assigned anywhere along the taxi route. When multiple aircrafts converge on the same constraint point, assigned RTA windows are supposed to be non-overlapping with safety margins. Pilots are free to taxi at safe speed, while ensuring on-time arrival at given constraint points. Aircraft are enforced to hold at the constraint point unless cleared to proceed prior to arriving at the point.

Based on this, previous work has focused on optimizing the scheduling delay on the surface between runway scheduling and surface management [2], introducing a "spot release planner" which provides sequence and timing advisories to the controllers to maximize the runway usage [3], optimizing the sequencing of taxi management by genetic algorithms [4], improving the utilization of surface area involving the coordination of humans and machines [5]. Nevertheless, the bottleneck of the theory itself stands still there.

3 STBO Concept

3.1 Theory

STBO concept assumes adoption of advanced flight deck equipage enabling higher temporal precision sufficient to support aircraft conformance to 4D trajectories, with an x–y location for all times t [1]. In this concept, sequencing is basically accomplished by generating non-conflicted 4D trajectories as shown in Fig. 2. Besides, researchers identify and describe the necessary functions of the trajectory based surface taxi operations concept and explains the relationships among them [6]. This allows more precision and less temporal uncertainty at all times along the route.

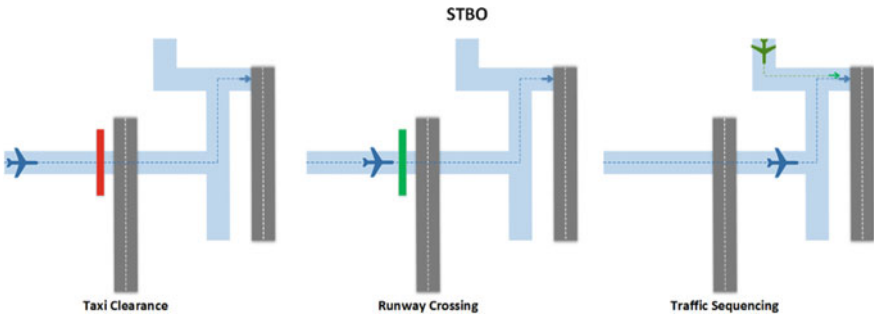

Fig. 2 Sketch of STBO theory

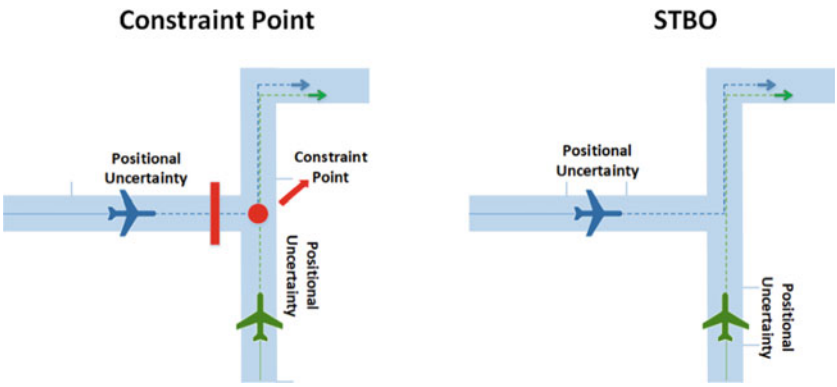

Fig. 3 Comparison between constraint point and STBO theory

A simple comparison can explain the major difference between the two concepts. For example, as shown in the left of Fig. 3, aircrafts are issued RTAs to a common constraint point to ensure that AC I arrives at the departure queue before AC II. If AC II arrives at the constraint point ahead of schedule, and before AC I accidentally, AC II will not be released and the pilot should hold at the constraint point. AC II can be released from the point to continue to the queue after surveillance detects that AC I has crossed the constraint point. As shown in the right of Fig. 3, according to the schedule, both aircraft will maintain their position within the acceptable bounds in normal situation, AC I will pass through the intersection before AC II, and will be sequenced for take-off at the departure queue. Conformance monitoring is simplified in STBO compared to constraint point, because there is a known x–y location for each aircraft at all times. This also improves earlier detection of non-conformance, rather than monitoring conformance only at constraint points. When an aircraft is beyond the pre-determined distance from their required location, a re-planning of taxi route will be triggered.

3.2 Scenarios

The most common scenarios in airport surface management are departure and arrival operations. And put aside the operations away from the ground, there are more than a lot in common. Thus the departure scenario is selected for modelling. The departure scenario basically refers to the procedure that the aircraft is pushed from the gate to the lift of front wheel of the plane. More specifically, the departure scenario can be divided into nominal and off-nominal situations. The nominal situation is the normal state of departure procedure with no unexpected events, which normally includes push out, taxiing, crossing and take off. By contrary, the off-nominal situation is the one with unexpected events, which mainly consist of in trial conflict, priority conflict, runway contingency hold and pilot schedule non-conformance.

Nominal Departure. The nominal situation is the normal state of departure procedure with no unexpected events, which normally includes push out, taxiing, crossing and take off.

In Trail Conflict. In trail conflict describes a situation where another plane suddenly turned and taxied ahead of the current taxiing runway, In order to maintain a safe distance from the preceding aircraft, the aircraft slowed down and waited for the aircraft ahead to leave. The pilot increases the speed to reach the next constraint point within the required time.

Priority Conflict. Priority conflict happens when aircrafts with accidental event appears. The system will consider many factors when determining the order of the aircraft. Due to medical treatment, take-off and landing failures or other unexpected situations, when one aircraft is determined to be a priority aircraft, it can use the runway according to the original or the updated plan.

Runway Contingency Hold. Due to the impact of emergency, the pilot may receive a mandatory runway contingency hold [7] request before entering the runway entrance. The system will collect this information and recalculate the new RTA and the last RTA until it confirms that the runway if free, then the runway contingency hold is cleared. Otherwise, the runway contingency hold is enforced.

Pilot Schedule Non-Conformance. Due to unexpected events, the pilot slows down the aircraft so that the aircraft cannot taxi according to the time schedule. The system detects that the current position of the aircraft is inconsistent with the expected position and reports it to ATC. The pilot returns to the apron or applies for a new RTA. If a new RTA is applied, the system will remind the aircraft to speed up to reach next constraint point with new RTA.

4 Modelling and Analysis

Systems modelling language (SysML) is suitable for describing the operations and events in this case. Among all that much diagrams of SysML, the behaviour diagram meets the requirement the most, with which the flight events are described, including

activity diagrams, use case diagrams, timing diagrams, and state diagrams, thus reflecting the cross-linking relationship and dynamic process of the system.

According to the previous descriptions and Yang's work [8], the model architecture of departure scenario is divided into two root phases, in which it contains different behaviour diagrams. Referring to multiple flight handbooks [9, 10] and instructions [11–13] from the industry, these models are built with sysML in enterprise architecture and are shown as follows.

4.1 Constraint Point Case

A full diagram consists of too many blocks so that it is quite confusing to identify the information inside. Therefore, taking priority conflict in off-nominal situation as an example, the behaviour diagrams can be clearly understood and they are as follows (Fig. 4).

The use case diagram shows the cases that the major participants, the pilot and the ATC control, triggers. The pilot can detect potential conflict, report potential conflict and accept priority request, while ATCo can detect runway conflict, accept conflict report, determine priority and publish priority (Fig. 5).

The activity diagram presents how the current aircraft (AC), air traffic control (ATC) and target aircraft (target AC) collaborate and interact with each other in

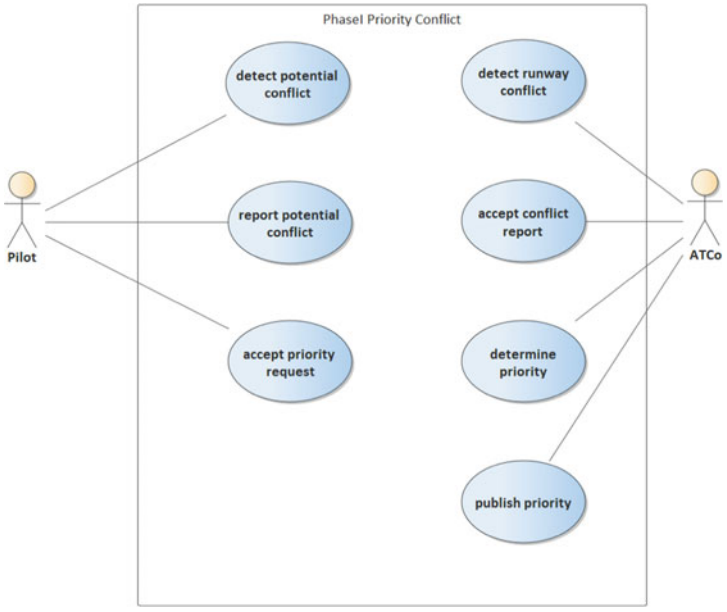

Fig. 4 CP priority conflict use case diagram

Fig. 5 CP priority conflict activity diagram

certain situation. As is shown in the figure, pilots of AC and target AC both detects potential runway conflict with the help of CDTI warning when lining in the queue, and the ATCo of ground control also detects it by system report. Then, the pilots report the conflict to ATCo and ATCo receives it after which ATCo determines priority in this conflict according to flight state, publishes to related ACs and ask to keep priority. Both pilots then receive and accept priority request and in this case, AC is determined as high priority and target AC is determined as low priority. Thus AC keep the speed and pass while target AC stop and wait until AC passes. The conflict is resolved (Fig. 6).

In the sequence diagram, the sequence in perspective of time can be illustrated clearly. In the same case of the two figures above, this sequence diagram gives a better view that the report is after two detections and operations are after the determination of priority (Fig. 7).

The state machine diagram focus mainly on the change of state. Since AC is the object to be considered, this figure shows the two major state in the priority conflict situation, that is waiting for command from ATC after reporting potential conflict and keeping speed and pass after receiving command.

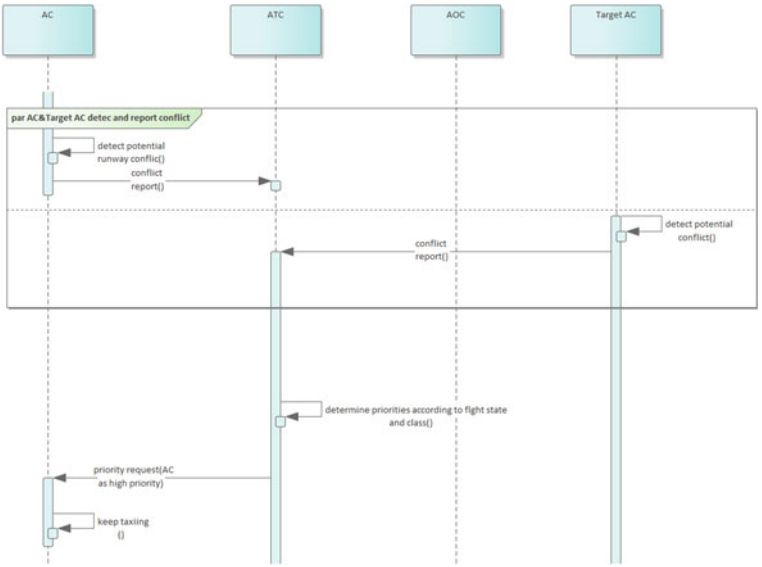

Fig. 6 CP priority conflict sequence diagram

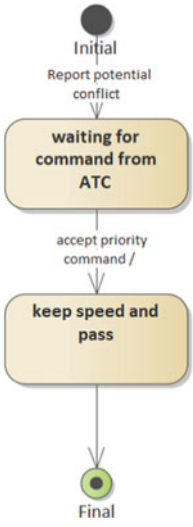

Fig. 7 CP priority conflict state machine diagram

4.2 STBO Case

In STBO case, taking the same situation as an example, the behavior diagrams are as follows (Fig. 8).

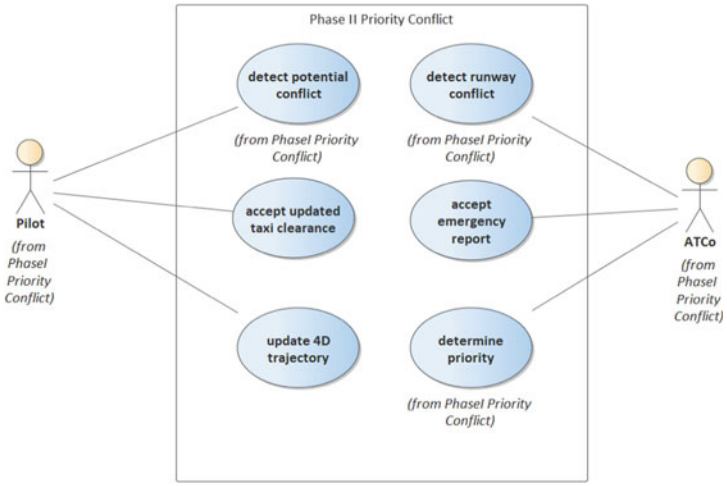

Fig. 8 STBO priority use case diagram

The participants are the same as those in CP. However, the triggers related to these participants are not all the same. Not like it in CP that the pilots of ACs need to receive and accept priority report, these operations are carried out by automation systems. A new trigger in STBO is updating 4D trajectory after the priority trigger. Besides, since the regular report trigger is also carried out by automation system, the pilots and ATCo are extricated from normal conditions and will only be involved when emergency report occurs (Fig. 9).

The activity diagram in STBO shares a lot with that in CP in the beginning of this priority conflict situation. They both involves conflict detecting and reporting, receiving and processing. Nevertheless, there is a huge different between the two phases, that is when the an emergency occurs and the priority is determined by ATC. This leads to suspension of all related ACs, runways and other ground facilities in CP while in STBO, the system would re-plan the routes and publish new clearances which results in fewer influence on other on-surface objects. In this figure, when the target AC is determined as high priority, the current AC does not need to stop right away to resolve the conflict. Sticking to the new clearance and updating the 4D trajectory would have already resolve it, which does not require a pause (Fig. 10).

In a case similar to that in CP, this sequence diagram gives a better view of how operation triggers and how state changes in a matter of time. After the determination of priorities, the system triggers a re-planning operation, which results in the non-stop resolution of the two aircrafts in this conflict (Fig. 11).

The state machine diagram in STBO has no much difference from that in CP. The only difference is that the current AC is determined as high priority in CP so that it could keep speed and pass, while the current AC could still update 4D trajectory and taxi according to the new clearance even it is determined as low priority in STBO.

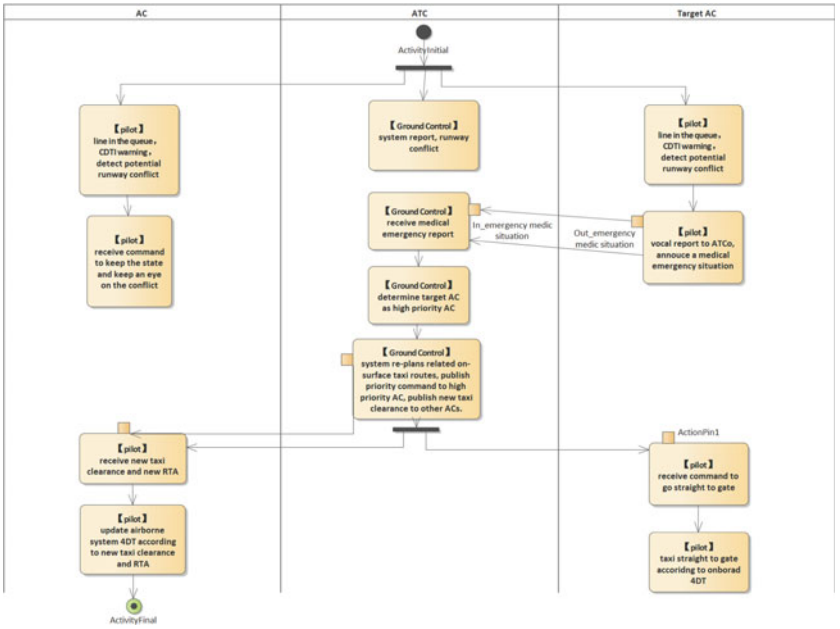

Fig. 9 STBO priority conflict activity diagram

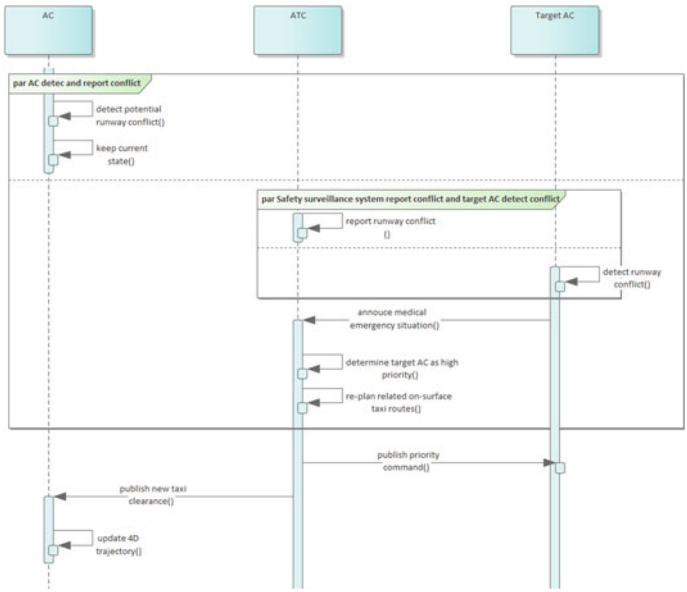

Fig. 10 STBO priority conflict sequence diagram

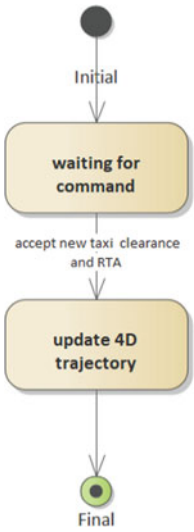

Fig. 11 STBO priority conflict state machine diagram

Compare the models and diagrams of the two phases in the previous chapter and other nominal and off-nominal situations mentioned above, STBO and CP can both offer adequate safety under the operating framework respectively. In the example situation, it shows that STBO concept reduces most meaningless stops in priority conflict, a re-planning would resolve the conflict. In other unlisted situations, a similar performance and conclusion can be found. As for in trail conflict, the pilots can maintain a moderate speed to resolve the conflict according to the 4D trajectory navigation in STBO while the pilots need to slow down or stop the aircraft at first and speed up when clear in CP. In schedule non-conformance situation, STBO case can provide an active online clearance update when the aircraft is deviated from the regular plan while in CP, the pilots need to apply for a new clearance which may probably cause taxi pauses. The STBO concept provides a better performance than constraint point concept, especially when off-nominal situation occurs.

5 Conclusion

This paper introduces the two modes (Constraint Point concept and STBO concept) of airport surface management. In addition, we study the typical scenarios including nominal ones and off-nominal ones on surface operations under the new STBO mode. Then, in selected scenarios, we build a series of models and analyze the performance and finally reached a conclusion that the STBO concept could reduce accidental starts and stops in surface operations, and improve the efficiency of airport surface management when ensuring basic safety.

Acknowledgements This paper is Sponsored by National Program on Key Basic Research Project (2014CB744903), National Natural Science Foundation of China (61673270), New Young Teachers Launch Program of Shanghai Jiao Tong University (20X100040036), Shanghai Pujiang Program (16PJD028), Shanghai Industrial Strengthening Project (GYQJ-2017-5-08), Shanghai Science and Technology Committee Research Project (17DZ1204304) and Shanghai Engineering Research Center of Civil Aircraft Flight Testing. The authors would like to acknowledge Bei Tian, Donglei Xu, Hongyu Li, Zihang Chen and Min Li for their work and assistance.

References

1. Hooey BL, Cheng VHL, David CF (2014) A concept of operations for far-term surface trajectory-based operations (STBO)
2. Deau R, Gotteland J-B, Durand N (2009) Airport surface manage-ment and runways scheduling
3. Yoon J et al (2010) A concept and implementation of optimized operations of airport surface traffic.10th AIAA aviation technology, integration, and operations (ATIO) conference
4. Lucas RP et al (2013) Genetic algorithms for management of taxi scheduling.Proceedings on the international conference on artificial intelligence (ICAI). The steering committee of the world congress in computer science, computer engineering and applied computing (WorldComp)
5. Robert M et al (2016) Planning, scheduling and monitoring for airport surface operations.workshops at the thirtieth AAAI conference on artificial intelligence
6. Jan Nikolai O et al (2016) A concept of operations for trajectory-based taxi operations.16th AIAA aviation technology, integration, and operations conference
7. Deborah BL et al (2013) NextGen surface trajectory-based operations: contingency-hold clearances.2013 IEEE/AIAA 32nd digital avionics systems conference (DASC). IEEE
8. Lei Y et al (2017) Fundamental diagrams of airport surface traffic: models and applications.Transp Res Part B: Methodological 106: 29–51
9. United States Department of Transportation (2016) Federal aviation administration, airman testing standards branch. “Airplane flying handbook FAA-H-8083–3B.”
10. Federal Aviation Administration, and United States (2009) Federal aviation administration. Pi-lot’s handbook of aeronautical knowledge. Skyhorse Publishing Inc
11. International Civil Aviation Organization (2005) Global air traffic management operational concept
12. International Civil Aviation Organization (2006) “Aircraft operations volume I flight procedure.” https://www.aviationchief.com/uploads/9/2/0/9/92098238/icao_doc_8168_vol_1.pdf
13. International Civil Aviation Organization (2006) “Aircraft operations volume II flight procedure.” https://code7700.com/pdfs/icao/icao_doc_8168_vol2.pdf

Development and Application of a Functional Analysis Method for Aero Engine Requirement Management

Yan Ji, Zhenyu Sun, and Zhimin Li

Abstract Civil aero engine is a typical complex product, the development of complex product and system is characterized by high comprehensive integration, high functional coupling. With the development of technology, the design of civil aero engine has become more comprehensive and not only requires the high performance, high reliability, long-life, but also need effective approaches to create successful products. Systems engineering is a methodical, recommend approach for the development of complex product, and functional analysis plays an important role in systems engineering of requirement management process, by using a functional analysis method capture and analysis the function of civil aero engine improve the completeness of requirements, and provide a common understanding of the product. In this work, a functional analysis method is illustrated based on operating modes and using context diagram to identify functions of system. The proposed approach is studied and applied to propulsion system to prove that the method is effective. The typical operating modes of propulsion system are outlined, and the functions of propulsion system promote the definition of requirement document. Furthermore, the functional analysis method can also be widely used in aero engine systems and sub-systems and component levels.

Keywords Functional analysis · Systems engineering · Aero engine · Propulsion system

Y. Ji (✉) · Z. Sun · Z. Li
AECC Commercial Aircraft Engine Co., Shanghai, China
e-mail: ad_future_jy@163.com

Z. Sun
e-mail: sunzhenyu@acae.com.cn

Z. Li
e-mail: ZhiminLi@acae.com.cn

Z. Jing and X. Zhan (eds.), *Proceedings of the International Conference on Aerospace System Science and Engineering 2020*, Lecture Notes in Electrical Engineering 680,
https://doi.org/10.1007/978-981-33-6060-0_21

1 Introduction

Civil Aero engine product development must meet safety requirements, and airworthiness regulation is a civil aviation minimum safety standard, SAE ARP 4754A [1] provide guidelines to apply system engineering method for aircraft and its system development process and propose that shall follow functional development assurance. A particular challenge is the high complexity and comprehensive degree of integration, aero engine product systems interact with each other in a functional higher-level environment. A function is a characteristic action to be accomplished by one of the system elements, function as the basis of safety assessment, the integrity and correctness of engine function directly affect the process of safety analysis. It should be noted that each system exists to serve at least one or more functions required for the product to meet its requirements. It is also important to understand and keep track of functions of each system, because a design team involved in designing each system must make sure that the system performs its functions and encourages exploring different solutions to achieve the same functions. The purpose of the functional analysis is to determine functions of systems, functions introduce performance requirements and performance requirements telling how well the system or product performing and are applying to satisfy the needed functionality. Functional requirements describe system functionality and what functions need to be performed to accomplish the product objectives (i.e., its operation or use). Functional requirements [2] are minimum set of independent requirements that completely characterize the operations (or tasks) that the product should perform and are the most important part of the requirements set. The functional breakdown creates a clear purpose and responsibility of a design team. Identify and analyze system functions and sub-functions can improve the completeness of requirements. The systems engineer must progressively identify and analyze system functions and sub-functions in order to identify alternatives to meet the system specified performance requirements. Functional requirements analysis is the identification of functions that must be performed to satisfy product overall goals. Functional requirements analysis methodology is function decomposition which starts at a high level function and continues to lower levels until a specific end item. The function identification task is performed in conjunction with function allocation and design synthesis.

In aircraft industrial, like Boeing company implemented system engineering on the Boeing777 aircraft from the early 1980s. In China, COMAC (Commercial Aircraft Corporation of China) also applies requirements management on the Aircraft program a few years ago [3]. It has been widely applied in aircraft and aero engine in European countries. Due to the complexity of aero engine and more and more attention of system engineering, the application of functional analysis in China civil aero engine is essential. This paper proposes a functional analysis method standardized indicate the functions that must be accomplished by the system, and an example of propulsion system is used as the application of this method. The functional analysis method can also be used in aero engine systems and sub-systems and other levels.

2 Functional Analysis Approach Introduction

The Functional Analysis approach is shown in Fig. 1. The concept is based on systems engineering and introduce Context Diagram to discover the functions of a system. Before writing product requirements, the functions analysis work should finished as early as possible. Compare to model-based system engineering (MBSE), using context diagrams is an easy way to indicate hardware and software intensive systems. Context Diagram [4] is a component of functional modeling that stands on its own as a valuable tool, it allows a team or an individual to produce a high-level model of an existing or planned system that defines the boundary of the system of interest and its interactions with the critical elements in its environment. MBSE usually used tools to generate Systems Modeling Language (SysML), such as Rhapsody, and is recommend used in software system, it is complicated and limited to develop hardware function, so this paper outlines traditional functional flow diagram. In functional analysis process, identifies and links system functions, interface characteristics, and rationales to requirements. It is usually based on the ConOps (concept of operations) for the system. The standard approach to develop system functions as follow.

First step is to define stakeholders and capture stakeholders' needs. The stakeholders can be a top level system or other system that interacting with the selected system and translate top-level stakeholder's requirements into functions that must be performed to accomplish the requirements. Second step is to define system boundary, describe system boundary/interface. The system boundaries must be described as detailed as possible. Third, specify all the system operating modes, including normal, internal failure, external failure modes. Functional analysis based on the system operating target, functional requirements are different for each operating condition of the engine. The purpose of define different operating modes is to obtain as much

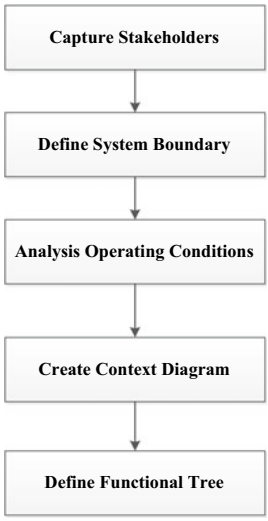

Fig. 1 Functional analysis process of aero engine

functions as possible in the early stage. The engine operating conditions are based on the aircraft operating condition. New operating conditions can appear when the engine design becomes more mature, such as particular internal failure cases. Third step is to create context diagram, which displays the flow of information between the selected system and the stakeholders, including inputs and outputs, and then grouping them into functions that convert an input into an output. The starting point can be the stakeholder needs. A context diagram is a useful tool in understanding how various systems, subsystems, and components are interfaced with each other [5]. The diagram can be created at any level. Through context diagram can effectively identify the key functions and requirements of system and together with system interfaces. The last step is to generate functional tree, decompose and allocate the functions to lower levels of the product breakdown structure, function flow down from top level to sub-functions in categories. These functions will be the basic structure in the requirements document. The function decomposition usually starts at high-level functions where a very general picture of major functions is described and continuing to lower levels.

3 Propulsion System Case Study

3.1 Propulsion System Stakeholders

The main function of propulsion system is to deliver thrust, which is stored in the aircraft. The propulsion system consists of turbofan engine to generate pressurized exhaust air and the nacelle, which guides and expands pressurized exhaust air to generate thrust. As by-products, the typical stakeholders are airframe, airworthiness authority, and airline. These stakeholders will give top level requirements to propulsion system.

The identification of functions for the propulsion system is obtained first by defining general or fundamental objective of the propulsion system operation. Then by breaking down the top-level functions, allowing those objectives to be fulfilled into hierarchy of functions called sub-functions. The breaking down methodology is function decomposition, a common function analysis tool.

3.2 Propulsion System Boundary

The propulsion system boundary is created by the outer skin of the nacelle, as illustrated in Fig. 2.

Top level interfaces with the aircraft are:

(a) The aircraft get hydraulic pressure and electrical power supplied by the propulsion system. The propulsion system provides a mounting pad and shaft power

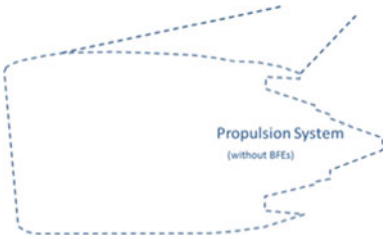

Fig. 2 Propulsion system boundary

to install and drive an electrical generator and hydraulic pump delivered by the aircraft manufacturer. The engine also accommodates the piping and hardness from the pump and generator to the aircraft.

(b) For the cabin environmental control system and cabin pressure system, pressurized air from the propulsion system is used. Bleed ports on the high pressure compressor are connected to aircraft environmental system. The bleed air valves and piping on the engine which regulate the bleed flow are part of the aircraft.

(c) Another pneumatic connection is the pressurized air pipe connected to the air turbine starter for engine starting with APU air, air from second engine or ground cart.

(d) The engine is attached to the pylon through the forward and aft mounts as well as the thrust links.

(e) The engine also interface with the aircraft through: Fuel feed from the air-craft fuel tanks to the fuel pump; connectors for electronic data exchange, including throttle lever angle, engine status data and maintenance data.

3.3 Propulsion System Operating Modes

The engine operating conditions are mainly based on the aircraft operating condition. Figure 3 shows a typical operating profile of civil aircraft. In different operating modes, normally require different functions or requirements. For example, during engine starting mode, engine receive pressurized air from the aircraft or ground cart,

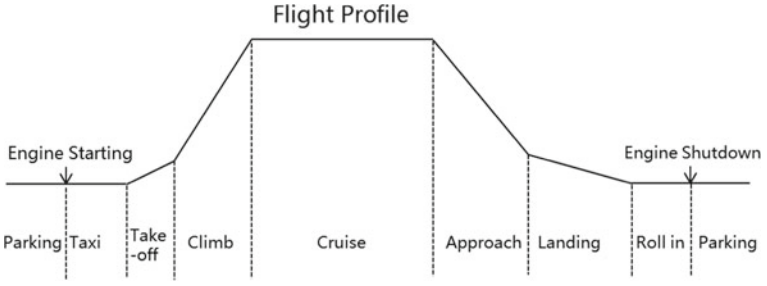

Fig. 3 Civil aircraft flight profile

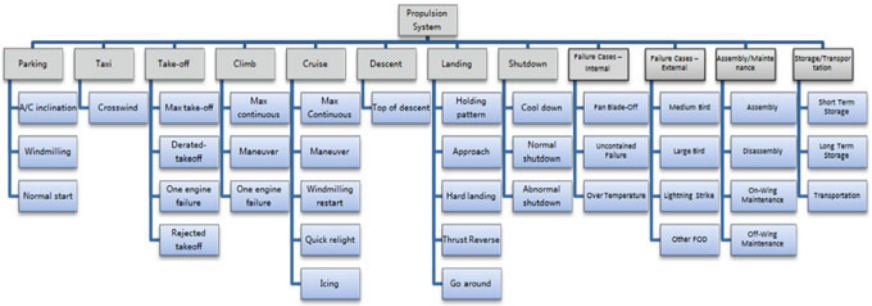

Fig. 4 Propulsion system operating modes

the engine shall provide the function "To receive pressurized air from the aircraft for starting"; during normal operating mode, the engine provide clean, heat and pressurized air for aircraft services, the function is "To provide clean, heat and pressurized air for aircraft services". Sometimes during different operating modes, the function is the same, but the requirements are different, for example in take-off, climb and cruise condition, the engine achieve the same function "To provide forward thrust", but in different conditions the engine shall meet different thrust level requirements required by aircraft. In order to obtain a full functions set, the operating conditions should be analyzed adequately with all the typical conditions and scenarios included. Figure 4 shows the propulsion system typical operating modes, consists of normal operating modes, internal failure modes and external failure modes. Noted that new operating conditions can appear when the engine design becomes more mature, such as particular internal failure cases.

As can be seen in Fig. 4, the key operating condition is managed together as operating flight or manufacture phase, in total 12 typical operating categories is defined, each category has several detailed operating modes.

Operating mode 1: Parking, the Aircraft on the ground, due to ground curvature in the parking spot, the inclination might influence the performance of engine oil inspection. And before the flight, engine starts with the use of APU systems or external air source.

Operating mode 2: Taxi, the aircraft rolls from the parking spot to the runway with the engines on the ground idle mode. The engine operates with crosswind, which produces a negative effect.

Operating mode 3: Take-off, Engines provide maximum take-off thrust, reduced take-off level thrust and including Rejected Take-Off condition, while the take-off process is interrupted for a reason and the engines are set to the ground idle mode or reverse thrust and aircraft starts to slow down.

Operating mode 4: Climb, engines work at the maximum climb thrust can continuously keep to rapidly climbing to the expected altitude. For a twin engine air-craft, the maximum continuous thrust of two engines must enable the aircraft to climb to the design ceiling and when one of the engines fails the other engine must be able to keep the aircraft at a given rate of climb.

Operating mode 5: Cruise, engines provide cruise thrust to enable the aircraft cruise at the expected altitude and speed. In cruise condition, the engine fuel consumption shall keep a low level to ensure competitive. Windmilling Restart or quick relight might occur in flight status due to abnormal event.

Operating mode 6: Descent, an aircraft descend with the engines on flight idle mode.

Operating mode 7: Landing, The power of the approach idling engines must be low enough to enable the aircraft to descent at the given angle, and meanwhile the engine shall be able to raise its power to go around if landing requirement is not allowed. Normally, a landed aircraft decelerates with the assistance of the engine thrust reverser. If landing of aircrafts might be aborted in final approach for various reason and aircrafts need to climb to an appropriate attitude. This operation requires the capability to quickly accelerate to full power.

Operating mode 8: Shut down, A cool down time should be allowed before shut down, during which engines is recommended to operate on the ground idle mode. An engine on ground idle shall be able to operating with normally shut down and abnormal shut down.

Operating mode 9: Internal failure conditions, typical internal failure conditions including fan blade off, uncontained fire and over temperature, these failure modes that affect the aircraft safety shall be identified.

Operating mode 10: External failure conditions, such as bird ingestion, lightning strike and ice ingestion, the engine shall at least meet these FOD conditions required by airworthiness regulations.

Operating mode 11: Assembly and Maintenance, the engine shall consider airlines and customer service and provide maintenance tasks, such as oil sample analysis, LRU replace to include maintainability in the design.

Operating mode 12: Storage and Transportation, The engine shall be designed for long term storage. And specify the storage and transportation scenarios to enable transportation.

3.4 Propulsion System Context Diagram

The Context Diagram is a Functional Modeling that stands on its own defines the boundary of the system and its interactions with the environment and is a single picture that has the system of interest at the center, with no details of its interior structure or function, surrounded by those elements in its environment with which it interacts [4]. The context diagram considers the whole system as one black box and used to analysis the system and shows the whole system functionality, the notational elements are shown in Fig. 5, the operating requirement is the mission statement or key purpose of the selected system. In this approach, through the context diagram identify all kinds of flows (information, control, material or energy) between the background context and the system. And then group flows into functions. Context diagram

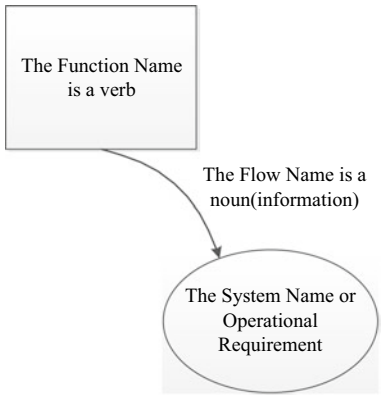

Fig. 5 Context diagram notations

also can be used to help to define the functional interfaces which are the movement and transfer of data and information between the system and its environment.

The normal operating mode is chosen as an example to show the context diagram of propulsion system. For different operating conditions, repeat steps can get a complete functions list.

The Propulsion system as a whole is a functional system, and main purpose is "To provide controlled thrust in the direction demanded by the pilot". It takes in fuel, air, and signal from aircraft and outputs is thrust. Based on the above operating modes and stakeholders' requirements, all flows going through the system boundary are identified in the context and top level functional flow diagrams shown in Fig. 6.

3.5 Propulsion System Functions and Functional Tree

The top level functions of propulsion system in normal operating condition summarized in Table 1.

A top level function can be decomposed into sub-functions which are required to achieve the top level functions. Due to the complexity of propulsion system, the top level functions can be further breakdown to lower level, the logical decomposition is repeated from the top down [6], a functional breakdown structure also calls Functional Tree is formed. Figure 7 shows a simplified functional tree of propulsion system.

4 Requirements Document Structure Based on Functions

Requirements are limitations to a function and determine how well these functions should be performed. Each function 'carries' a list of requirements. The Requirements document consists of three sections: Operational Requirement, Functional

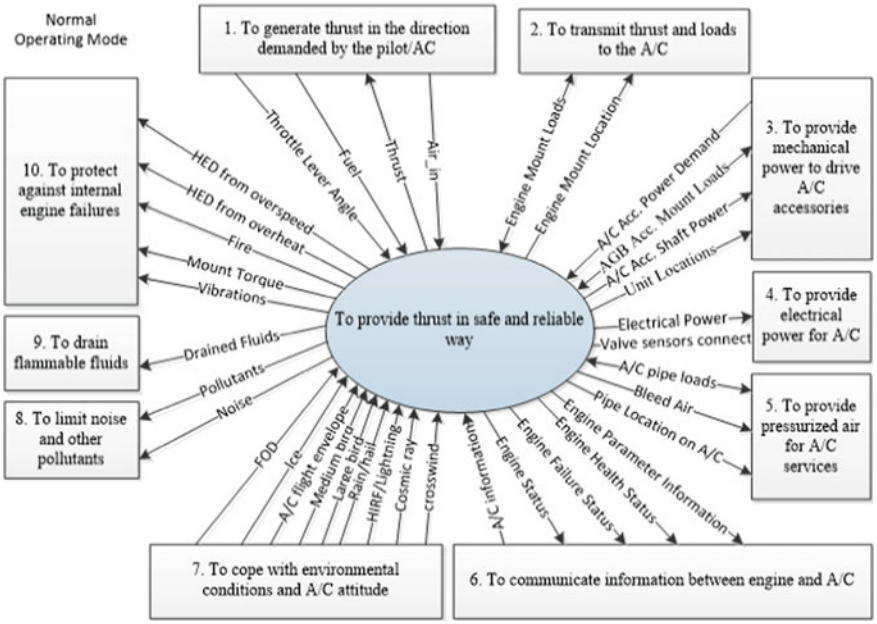

Fig. 6 Normal operating modes of propulsion system (in flight)

Requirements and Non-functional Requirements. The functional requirements are organized based on operating condition and function. Table 2 lists the basic concept of the requirements document structure.

5 Conclusions

Functional analysis is the primary method used in system architecture development and functional requirement decomposition. In this paper, a method to analysis functions of propulsion system is described, using this method the functions can be easily obtained, and based on the functions, the requirement document can organized by functional and non-functional. The functional analysis process has a close relationship to other areas, such as safety assessment, interface Management and requirements definition and configuration management. The functional analysis process also defines the functional interfaces, especially the external interface, it is a helpful method to define requirement. The current study is focus on normal flight condition, failure mode and maintenance mode is incomplete, in future it needs to continue to finish the functional analysis of propulsion system. In future, this method will be extended to sub-system level and components.

Table 1 Top level functions of propulsion system (In flight)

No	Stakeholder	Basic elements	Function name
1	Aircraft	Air_in, fuel, throttle lever angle (TLA)	To provide controlled thrust in the direction demanded by the pilot
2	Aircraft	Mount loads, mount location	To transmit thrust and loads to the A/C
3	Aircraft	Accessories mount loads, power demand from aircraft accessories, accessory locations	To provide mechanical power to drive A/C accessories
4	Aircraft	Electrical power	To provide electrical power for A/C FCS
5	Aircraft	Bleed air, wing anti ice air	To provide pressurized air for A/C services
6	Aircraft	Aircraft information, engine parameter information, engine status, engine health status, engine failure status	To communicate information between engine and A/C
7	Aircraft Airworthiness	Crosswind, cosmic ray, HIRF/Lightning/EMI, rain/hail, large bird, medium bird, ice, etc	To cope with environmental conditions and A/C attitudes
8	Aircraft Airworthiness	Noise, pollutants	To limit noise and pollutants
9	Aircraft Airworthiness	Leaked fuel, leaked oil, leaked hydraulic Oil	To drain flammable liquids
10	Aircraft Airworthiness	High energy debris (HED) from overspeed, HED from overheat, fire, mount torque, vibrations	To protect aircraft against internal engine failures

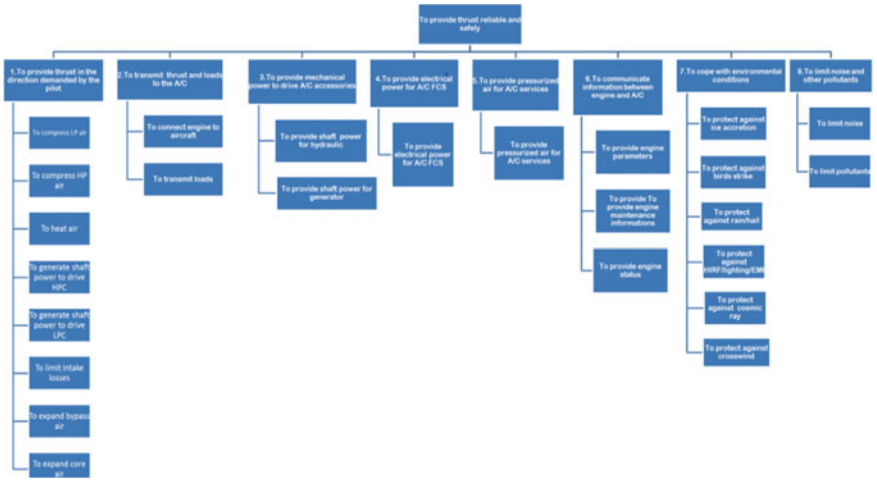

Fig. 7 Simplified functional tree of propulsion system

Table 2 Basic concept of the requirements document structure

No	Items	Basic elements
1	Operational requirement	Major purpose of a system
2	Non-functional requirements	Major purpose of a system Key Attributes i.e.: Style, Size, Weight, Cost, Higher Level Design Decisions, Material Limits, Installation Constraints Reliability, Maintainability, Safety
3	Functional requirements	Operating condition 1 3.1.1 Function 1 Performance requirements 3.1.2 Function 2 Performance requirements operating condition 2 ……

References

1. SAE ARP 4754A (2010) Guidelines for development of civil aircraft and systems (2010), society of automotive engineers. pp 22–28
2. Bhise VD (2014) Designing complex products with systems engineering process. CRC Press. pp 25–29
3. Haomin Li et al (2019) A functional requirements development and management approach applied to a civil aircraft program, The proceedings of the 2018 Asia-Pacific international symposium on aerospace technology (APISAT 2018). Lecture notes in electrical engineering. https://doi.org/10.1007/978-981-13-3305-7
4. Burge S, The systems engineering tool box. Context Diagram (CD). https://www.burgehughes walsh.co.uk/Documents/Context-Diagram-Tool-Draft-2.pdf
5. Grady JO (2014) System requirements analysis 2nd edn. pp 185–200
6. National Aeronautics and Space Administration (2016) Expanded guidance for NASA systems engineering, vol 1: systems engineering practices, Washington, D.C. 20546, 111:112

Research on Civil Aero Engine Requirements Development and Management

Zhenyu Sun, Yan Ji, and Zhimin Li

Abstract Aero engine not only need to meet aircraft requirements and also airworthiness and other stakeholder's requirements. Due to the increasing complexity of requirements, the development of civil aero engine within the required time and cost present a considerable challenge. In this work, a requirements development and management approach is introduced in civil aero engine development process, the aim is to bring forward new experiences on aero engine requirements management in practice. The requirements and design definition is presented in a requirement V model and the aero engine design is decomposed from the whole system to sub-systems and then to the components, a typical civil aero engine requirements architecture is defined. Based on the requirement development model, the requirements related files of aero engine are illustrated. The requirements flow down case shows how requirements allocate and interacting between systems. By managing the status of requirements throughout the whole engine development, the traceability between requirements and design and verification data are established to ensure the consistency of requirements.

Keywords Requirements development · System engineering · Aero engine · Requirements management

Z. Sun (✉) · Y. Ji · Z. Li
AECC Commercial Aircraft Engine Co., Shanghai, China
e-mail: sunzhenyu@acae.com.cn

Y. Ji
e-mail: jiyan@acae.com.cn

Z. Li
e-mail: ZhiminLi@acae.com.cn

Z. Jing and X. Zhan (eds.), *Proceedings of the International Conference on Aerospace System Science and Engineering 2020*, Lecture Notes in Electrical Engineering 680,
https://doi.org/10.1007/978-981-33-6060-0_22

1 Introduction

Civil aero engine as part of aircraft is a typical complex system. According to INCOSE [1], Systems Engineering (SE) has emerged as key discipline to help manage the complex processes throughout the life cycle of the product. The SE considers "top-down" approach that views the product (or the entire system) as a whole and then sequentially breaks down (or decomposes) the product into its lower levels such as systems, subsystems, and components. In the complex development environment, a strong focus on requirements is essential for the creation of good products as the requirements are the source of product development. The correctness and completeness directly affect the success of product, so requirements management is critical to product development. Civil aero engine has many stakeholders and long life cycle, therefore requirements in practice are often changeable and incomplete or missing, which will cause costs or a failure of product. For requirements management, the management method is not difficult to study, but due to civil aero engine development is very complex, in practice how to generate good quality requirements and meet different customers' requirements in civil aero engine is core issue.

In SAE ARP4754A [2], a general civil aircraft and systems requirements development and management guidelines are introduced, aero engine as one of the most important systems of aircraft, should consider its own operating characteristics and transfer the guidelines into engineering applicable process. In this study, a standardized aero engine requirements management process is outlined, including requirements architecture, requirements analysis, design definition, requirements allocation, and verification activities are introduced to ensure that requirements are identified and correctly defined and achieved in the civil aero engine development life cycle.

2 Requirements Development Approach

2.1 Requirements Flow Down Model

The purpose of Systems Engineering in requirements management is to provide a structured approach to requirements generation, requirements management, design and verification. Systems engineering ensures that the system is developed and optimized as a whole instead of a collection of optimized individual components. Requirements development and management approach describes how requirements are captured and managed and how to apply the systems engineering tools for the benefit of creating proper requirements. The major deliverable from the requirements definition process is a set of approved and documented requirements that will drive the system design. The requirements development process [3] is a top down approach and wherein high-level requirements lead to major design decisions which in turn lead to progressively lower level requirements and designs.

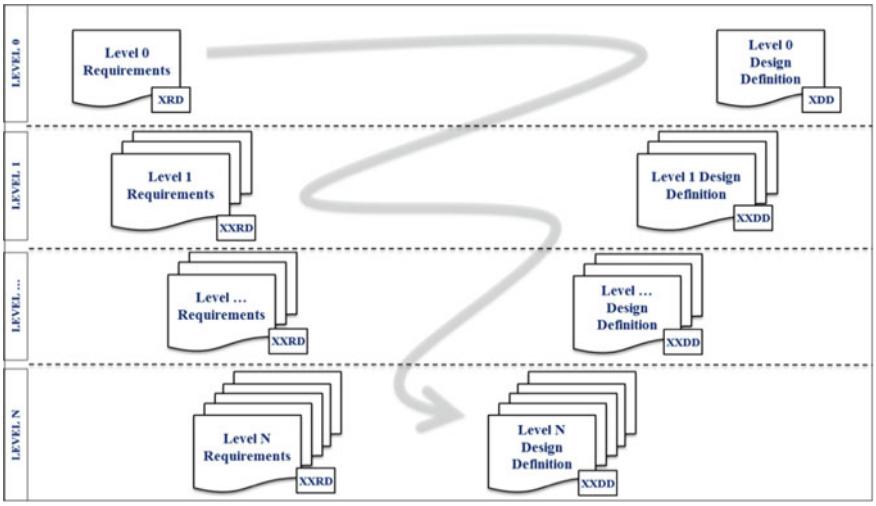

Fig. 1 Requirements V model

Requirements management approach is to define standards and procedures for creating requirements and organizing requirements. In order to show the relation between requirements and design process, the aero engine requirements flow down structure is introduced in Fig. 1, is similar to typical system engineering V model associated with the development of a product, but it is used to show how the requirement is decomposed and flow down to lower level. Every level system prepares two documents: requirements document and design definition document. Requirements document (RD) considers the system as a black box, with a top level function; RD explains what the system must achieve and collects requirements from the stakeholders. Design definition document (DD) opens the box and describes the sub-functions and requirements to achieve the top level function, DD also explains how the requirements are achieved and describes the solution to meet the requirements. New requirements, derived or decomposed requirements can be created in DD and allocated to new stakeholders. The requirements whether in RD or DD should be documented, actionable, measurable, testable, and traceable.

Requirements architecture is the basis of requirement management. The hierarchical breakdown of the requirements is a logical decomposition [4], design of the product architecture occurs simultaneously with the allocation of requirements and analysis of the product and system functions. An example aero engine requirement hierarchy contains four levels, the requirements flow down structure shown in Fig. 2. The first level is engine level, the second is product system level, and the third is Sub-System level, the lowest level is components level.

In the requirements architecture, engine level consider the engine as a whole product, mainly capture top level stakeholder's requirements and integrate into a project's technical requirements. Product system level consists of different functional system and don't directly own hardware, but provide requirements and de-sign

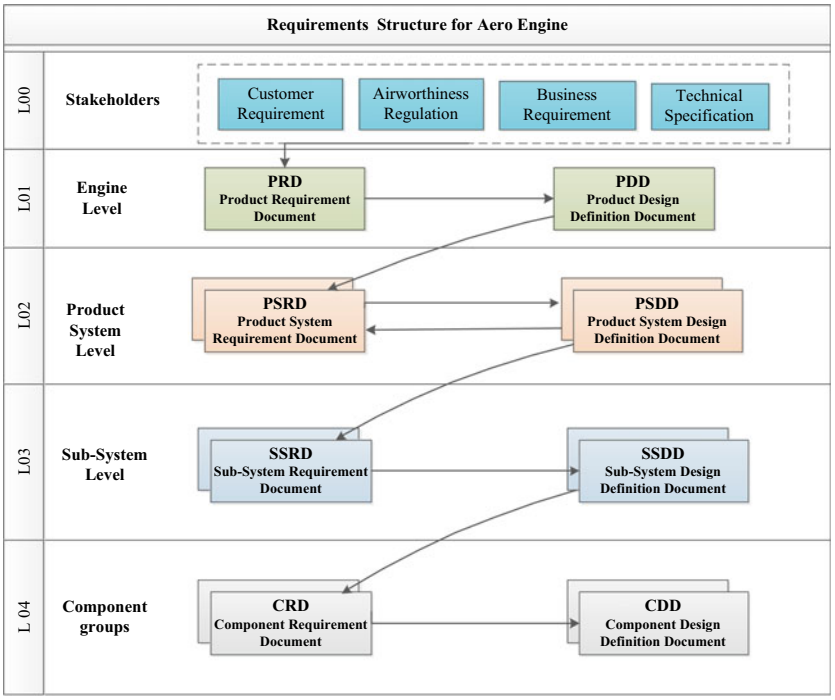

Fig. 2 Requirements documents model of civil aero engine

constraints onto lower level sub-system. A product system is an integrator on engine level. Sub-System level represents integrated engine modules/hardware. The structure is defined based on functional analysis and considering basic engine structure. If all requirements are created and linked in this structure and updated in the design iteration process, the benefits are possibility to perform structured verification. The verification work is a flow up from component level, to Sub-System to engine level, so the engine non-compliance status becomes clear and provides possibility to perform structured risk management.

As shown in Fig. 2, in aero engine top level, the main stakeholders are: aircraft manufacturer, airworthiness authority, marketing service, and the engine company itself. The PRD collects requirements are defined as follow:

(a) Customer requirements document: technical requirements from aircraft manufacturer, these requirements for the aero engine are agreed with the customer and Engine Company.
(b) Business Requirements: including marketing requirements, cost requirements, sales plan and service requirements for the entire project.
(c) Airworthiness Requirements: CCAR, FAA, EASA regulations, the aero engine design not only should satisfy CCAR33, which is similar to FAR 33, also

need to consider the applicable CCAR25 regulations for supporting aircraft certification.

(d) Technical Specifications: in Aerospace there are a lot of industry standards and company internal standards, each design department create departmental or enterprise standards for design activity [5]. Technical Specifications is a location to define all the product design standards, and record specific centralized design requirements from Chief Engineer.

A clear definition of the requirements for the product allows avoiding the problems at the stages of its design, development, manufacturing, operation and maintenance. The PRD address the whole engine functionality, performance, availability, safety, and operation and maintenance requirements, allocated to product systems which responsible for engine functional design.

2.2 *Requirements Allocation and Breakdown*

For product system level, a product system can provide requirements to other product systems and will be designed and optimized first, before transferring requirements to sub-systems. At Product System level, the PSRD collects allocated requirements from the PDD and PSDDs. At Sub System level, the SSRD collects allocated requirements from the PSDD. It is not allowed to exchange requirements between sub-systems, if this is required an interface document should be introduced to provide requirements or definition, as shown in Fig. 3. At Component level, the CRD collects requirements from the SSDD, to which they belong. The designer would be able to find all requirements by filtering the requirements in the SSDD. Requirements in the design definition cannot be allocated to a higher level, also can use interface document to transfer these information.

Basic requirements decomposition rules in the design definition are the requirements from the RD are decomposed in the DD and allocated to the systems or sub-systems. A classic example is weight target, which is decomposed to sub-systems in the whole engine structure PSDD. In the Sub-System DD, the weight target is decomposed to component targets.

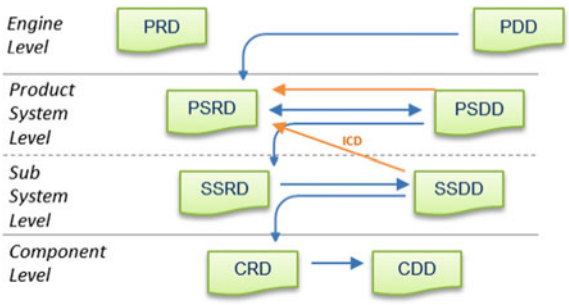

Fig. 3 Requirements allocation

Airworthiness Requirements are one of most critical requirements in civil aero engine. In the requirements allocation and breakdown structure, airworthiness requirements allocated to product systems by engine level, follow the requirements rule Product Systems are responsible for translating the original Airworthiness regulation into solutions and requirements for sub-systems. On product system level, airworthiness requirements are translated into hardware specific requirement. Ideally, all airworthiness requirements are covered by a product system. If all product systems requirements are met, the engine also satisfies the airworthiness requirements.

3 Requirements Management Tool and Method

Requirements management is a technical management process, the purpose is to management all stakeholders and their requirements for the product throughout its lifecycle, to ensure completeness, correctness and effectiveness of requirements at each level and between levels of the solution and also define a basis for the verification tasks, track the requirements flow-down and provide requirements baseline to configuration management.

Commercial requirements management tools usually offer multiple functions to management requirements efficiently, in civil aero engine development the IBM Rational DOORS (Dynamic Object-oriented Requirements System) is chose as the referred requirements management tool. In DOORS, requirements are organized by line item and contain additional information stored in different attributes these attributes can be defined according to the user need. Links are generated between design definition and requirements document to show the traceability.

On a weekly basis, the status of the DOORS document must be checked. Each document is checked and reported for not-finished requirements, unlinked requirements, and discrepancies with source, open questions and comments. This is performed for all documents, at all levels and reported to the authors.

3.1 Requirements Validation

The major deliverable from the requirements definition process is a set of approved and documented requirements that will drive the system design. The major emphasis of Requirements Validation is to ensure completeness and correctness of the requirement within the requirements set and the requirements set itself [6]. Requirements reviews are probably the most traditional and commonly used technique. During the review, the requirements will be inspected and analysed from a group of stakeholders and design teamers to report different viewpoints to identify missing, conflicting or incorrect requirements. Reviews are conducted by acknowledged experts and at specified stages of the lifecycle to ensure that all the functional requirements fully comply with their design.

Fig. 4 Requirements allocation matrix

PSDD	PS 1	PS 2	PS…	PS N	SS 1	SS 2	SS …	SS N
PS 1		1	6	4	30	55	0	12
PS 2	0		0	0	23	0	0	0
PS …	0	3	1	0	0	0	17	0
PS N	0	2	0		0	3	0	13

In DOORS, a "Requirements Review Comments" attribute is applied, this is based on the requirements review meeting, and typical options include ambiguity in statements, inconsistent writing, conflicting requirements, and incomplete requirements. These issues will be collected and become the input for next design iteration to refine the requirements and design definitions.

3.2 Requirements Allocation

The allocation process was to assign each requirement to one or more product or sub-system. Here, the product system to other product systems and Sub-systems Matrix are created to provide the overall view of the product systems requirements allocation, shown in Fig. 4. In DOORS, if the requirement is acceptable, a link will be created to ensure the traceability. Through the allocation and traceability enables the quality of flow down.

3.3 Requirements Verification

The verification purpose is to confirm product design, has the system been designed right? Verification process provides evidence that a solution meets requirement(s). It may be a calculation, computer model, scenario plan or test etc. The verification evidence shall be documented. The verification matrix describes how the methods of verification (test, inspection, analysis, demonstration) are to be applied and specifies the level in the hierarchy at which the requirements will be verified, as specified in Fig. 5. Through verification matrix will establish the link between requirements and experiments, it needs to be determined during the design phases as the requirements are developed.

4 Requirements Development and Management Case Study

Base on the functional analysis, an example Product System and Sub-systems are presented in this section, to provide an appreciation of how the approach works out in practice. The engine product system contains 12 product systems and 10 sub-systems,

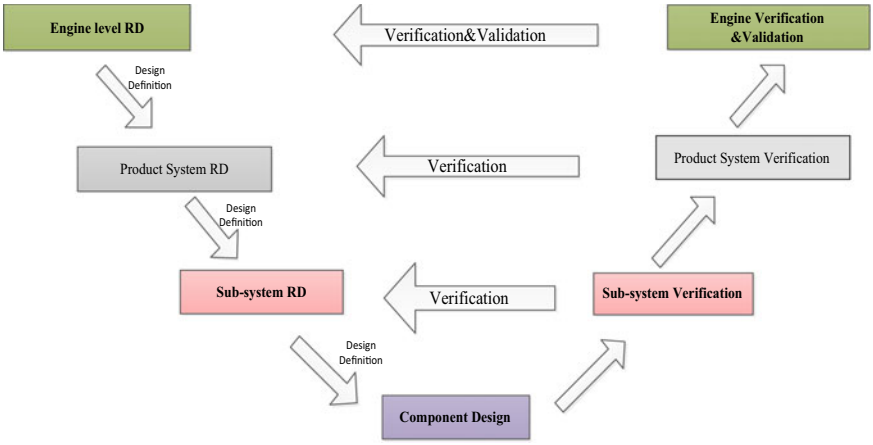

Fig. 5 Typical aero engine development V model

is shown in Fig. 6. Each product system have a system boundary and certain functions and requirements, Table 1 shows some examples. The product system represent 'whole engine' level, coordinating the relationships of the various subsystems and trading them to optimize the overall engine design. There are various ways of dividing the system architecture, and the principle is product system combined should cover engine level functions.

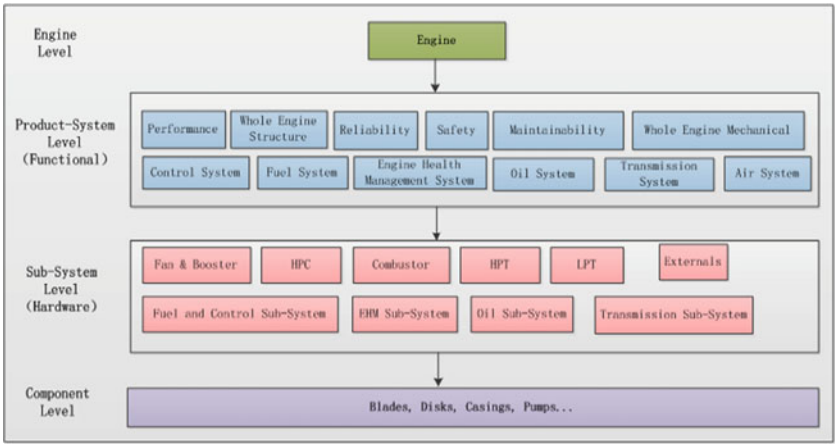

Fig. 6 Typical aero engine requirements architecture

Table 1 Product system operational requirement

Product system	Operational requirement
Performance	The purpose of performance is to generate thrust and take care of fuel consumption
Whole engine mechanics	To limit mount loads and vibrations loads during normal operation and in the event of failures such as birds ingestion event
Air system	Distributing air for internal cooling, sealing, anti-ice, etc
Transmission system	Looking after the torque path transfer to accessories
Oil system	Looking after oil through engine, to lubricate, cool and collect particles from bearing
Fuel system	Looking after fuel through engine, to regulate fuel for engine burning and to displace actuators
Control system	Receiving electrical signals from aircraft to control thrust and detect sensors failure conditions

5 Requirements Management Tool and Method

Figure 7 illustrates the documents discussed in above chapter, each level generates four categories of documents: requirements documents, interface documents, design definition documents, and verification documents. For the design point of view, requirements documents, interface documents, design definition documents, these three types of files belong to the design work, they are on the left side of system engineering V model, the verification documents are on the right side.

In this section, we briefly outline the core technical details of each type document.

(a) Requirements Document
The requirements document is a container and collects all higher level allocated requirements in the requirement management system. New requirement from outside the system can be introduced if the source, such as a report or

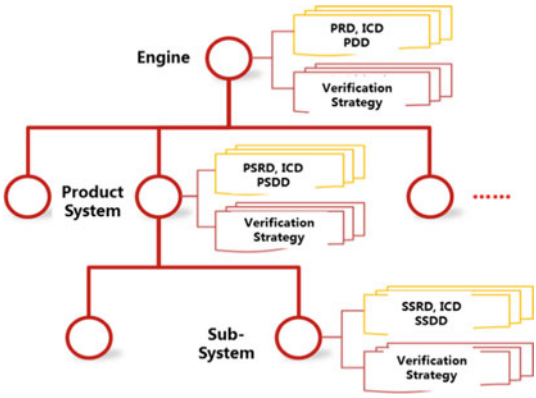

Fig. 7 Typical aero engine configuration files

lessons learned, is clearly defined. The document consists of functional and non-functional requirements. Technical requirements for product/system/sub-system or component, including functional requirements, performance requirements and non-functional requirements (weight, life, cost, reliability, maintainability, safety).

(b) Design Definition
Describe the design solution/scheme of the product/system and its component, and decompose functional and non-functional requirements through the design. In addition, it decomposes requirements for the next level down, if they are not covered by the design definition. New requirements can only be introduced in design definitions. Each design definition is written as a requirement (contains the word 'shall', 'should', 'must', 'will') and is allocated to a sub-system or product system. The document consists of concept description [7], decomposed functional and decomposed non-functional requirements.

(c) Interface Control Document
In an interface document records an agreement between two design teams and database owner. There are two fundamental types of interfaces, Geometrical Interface and Functional Interface. Exchange of information between different product-system sub-functions are always functional interfaces. Geometrical interface describe an agreement on a geometrical feature which connect two sub-systems or component groups. A functional interface control document contains functional requirement agreed between two design teams, including functional, aerodynamic, thermal, load, electrical, mechanical and other interface in-formation.

(d) Verification Document
Based on the requirements documents, the key verification document is verification strategy created to outline how each level requirement will be verified. Normally, verification documents including verification methods/strategy, engine test plan, and test data report.

6 Conclusions

A civil aero engine requirements management approach has been introduced. The requirements architecture and requirements flow down model are presented in this paper. An example of civil aero engine requirements management process validated the approach. Some guidance is provided for aero engine to conduct requirements management, and the conclusions are as follow:

(a) Requirements architecture is the basis of requirements development and need to be defined at the beginning of design.

(b) Design solutions are developed according to the requirements documents and the resulting from the design that are requirements give to lower level.

(c) Requirements development process is iterative and contains several development loops. The cascading of requirements starts with a rough idea in the first loop and becomes more and more detailed after several iterations.

The further research requires more detailed study of requirements compliance and risk assessment, in particular, further thought is to focus on the non-compliances and risks.

Acknowledgements This paper is a result of teamwork. The contributions of many colleagues with whom the authors have discussed the concepts described here are hereby gratefully acknowledged. The authors would like to acknowledge the application of Systems Engineering approach at AECC CAE.

References

1. INCOSE (2007) Systems engineering handbook. A guide for system life cycle processes and activities, version 3.1
2. SAE ARP 4754A (2010) guidelines for development of civil aircraft and systems (Rev A, 2010), society of automotive engineers
3. NASA/SP-2007–6105NASA (2007) Systems engineering handbook. National aeronautics and space administration, NASA headquarters, Washington, D.C
4. Akhmatova M-S, Brotsman Y (2018) The system design of the civil aircraft based on NASA systems engineering approach, aerospace systems
5. Wang Y, Gao D (2019) The research on modern civil Jets top level design requirements based on systems engineering method, 2019 IEEE 10th international conference on mechanical and aerospace engineering
6. Henning Buus et al (April 1997) 777 Flight controls validation, process, IEEE transactions on aerospace and electronic systems 33(2): 656–666
7. Royet R et al (2004) Documenting technical specifications during conceptualization stages of aeroengine product development, international design conference design

Investigations on the Acoustic Resonance in Aeroengine Multi-Stage Compressor

Zihao Wu and Xiaohua Liu

Abstract Acoustic resonance, which is caused by the coupling and interaction of flow and acoustic field in aeroengine, can not only produce noise with very high amplitude in compressor, but can also lead to the fatigue of the materials and endanger the structural integrity of aeroengine. Unlike the unsteady flow phenomenon such as surge, rotating stall, and rotation instability, researchers still cannot fully explain and understand acoustic resonance well, because there are only few investigations about acoustic resonance and the coupling between acoustic and flow field is quite complicated in the aeroengine. Thus, this study firstly summarizes the phenomenon of acoustic resonance, and systematically describes its characteristics. After that, some theoretical models and methods used for the prediction of the acoustic resonance is introduced. Finally, proper orthogonal decomposition method is firstly proposed and applied for the study of acoustic resonance. A full passage unsteady numerical simulation is demonstrated with this method.

Keywords Aeroengine compressor · Acoustic resonance · Unsteady flow

1 Introduction

To maintain the stability of an aero engine under off-design condition, the design of the compressor becomes a key stage. Two main factors will limit the development of modern compressors. The first one is flow stability, while the other one is the structure. For flow stability, researchers have dedicated to study on the phenomenon

Z. Wu · X. Liu (✉)
Shanghai Jiao Tong University, Shanghai, China
e-mail: xiaohua-liu@sjtu.edu.cn

Z. Wu
e-mail: steven-wu@sjtu.edu.cn

X. Liu
Key Laboratory (Fluid Machinery and Engineering Research Base) of Sichuan Province, Chengdu, China

Z. Jing and X. Zhan (eds.), *Proceedings of the International Conference on Aerospace System Science and Engineering 2020*, Lecture Notes in Electrical Engineering 680,
https://doi.org/10.1007/978-981-33-6060-0_23

like rotation instability and stall for decades. Generally, the rotating stall is a kind of blockage in the passage caused by flow separation, which will propagate circumferentially. Such condition may further develop into surge, and it usually happens far from the design point [1]. While the flow instability can occur under stable operation condition, it is also due to the flow separation but without blockage. On the pressure spectra, it appears as a broad band peak located below the blade passing frequency [2]. For structure, researchers found that the structural fracture and failure due to vibration sometimes could cause even more severe consequence then flow instability. Even though the study on mechanical vibration has last for centuries, some structure-damaged cases under stable operation condition are still found, it finally turned out that it is caused by acoustic resonance, which is the coupling and interaction between acoustic and flow field. Generally, the main sound source of an aero engine comes from the compressor and nozzle, while the sound contributed by nozzles now have been perfectly suppressed. The sound comes from the compressors remains a trouble not only for its loud noise but also for the threaten to the structural integrity. Some researchers used two speakers laid 5 mm away from the rotors of a compressor to simulate the noise source and found when the sound pressure level will exceed 150db. When the acoustic resonance occurs, it will exceed the 12% of the fatigue limitation of the material [3]. They also verified when the distance between the rotors and acoustic source increases, the pressure amplitude on the maximal stress point of the rotor will rapidly decrease, which means other noise source like nozzles could hardly contribute to the fatigue of rotor blade.

Until now, researchers have studied on the acoustic resonance for more than half century, but the process is much about the observation and comparison in order to find the regularity in this phenomenon. However, the understanding on the mechanism, the description for the acoustic field and prediction model of acoustic resonance for both the frequency and amplitude are still in the initial stage. In the last century, researchers usually study this by experiment due to the limitation of computational resources. These years, with the breakthrough of computer science, the simulation with some commercial software becomes possible, which may lead to a rapid development on this phenomenon. Thus, the main purpose of this paper is to summarize the current result and research methods on acoustic resonance in the aeroengine and propose a new possible research method.

2 Phenomenon and Characteristics of Acoustic Resonance in Aeroengine

2.1 Some Phenomenon of Acoustic Resonance

Since the middle of the last century, more and more phenomenon of acoustic resonance has been discovered by researchers. In 1968, Parker first demonstrated the acoustic resonance in a single stage low-speed axial compressor and implied that

acoustic resonance is another factor may lead to the failure of blades and become a threat to the stability and life of an aeroengine [4]. When investigating the clearance noise in an axial fan, in addition to some broad-band noise which may related to the rotation instability, some narrow-band peak just below the blade passing frequency, which fits the characteristics of acoustic resonance. He also found out such narrow-band noise component not only related to the width of tip clearance but also related to the mass flow rate, which could be caused by the interaction of flow separation and tip clearance vortex [5]. Since that, researchers began to put emphasis on the excitation and mechanisms of the acoustic resonance so that they can take it into consideration during the design stage. Legerton et al. also found a similar acoustic phenomenon induced by flow in an annular cascade, which may be generated by vortex shedding [6]. Camp did an experimental investigation on C106, a low speed 3.5 stage axial compressor. Through spectrum analysis, he found six dominant peaks of pressure amplitude, four of them are cut-off mode, and two remaining modes have very similar characteristic with the phenomenon of acoustic resonance [7]. Hellmich and Seume also found the acoustic resonance in a high-speed multi-stage axial compressor near stall condition [8].

2.2 *Characteristics of the Acoustic Resonance in Axial Compresso*

Many of the pioneering and preliminary research and investments have already been done by the flat plates in the wind tunnel. Such simulation is quite meaningful for the research in the turbomachine because many similarities can be found in the result. The research on the turbomachine is much more complex, mainly for three reasons: (a) the flow field in the annular duct is nonuniform and there exist many swirl (b) under high rotation speed, the load on the blade is extremely high (c) the cross section of the duct is not a constant. As shown in the Fig. 1, the acoustic resonance usually occurs in two places of the axial compressor, the first one is the passage between blades, while the other one is the inter-row section. The former one is generally caused by vortex shed major from the trailing edge of the blade of the previous stage, while the later one is usually formed by the vortex leak from the tip clearance.

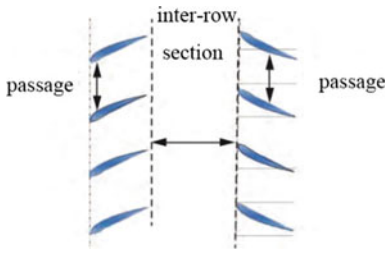

Fig. 1 Demonstration of an elementary stage in the axial compressor

Generally, acoustic resonance relates to the reaction of acoustic field, thus acoustic approach is needed for the investigation. Many investigations and researches decided to measure the static pressure on the casing wall to reflect the sound pressure so that they can capture some regularity of this phenomenon. Hellmich and Seume put some transducers between the inlet guide vane (IGV) and the first row of the rotors and continuously decrease the mass flow rate. They found when the compressor approaches its stall limit, a sharp peak frequency of acoustic resonance was detected, and its pressure amplitude even higher than the dominated blade passing frequency (BPF). Such phenomenon was detected at different axial and circumferential positions of the compressor. Furthermore, acoustic resonance signal presents several sharp peaks, unlike the signal of rotation instability, which is usually a broad band peak. In addition, they also found some modulation between the BPF and the characteristic frequency, there exist peaks whose frequency equal to the combination of the characteristic frequency and BPF, such as BPF-AR and BPF+AR [8]. Normally, the amplitude of these modulation frequencies is lower than the amplitude of BPF and the reason beyond this maybe caused by the phase difference of waves of different frequencies, which remains to be further explored [9].

A very famous and important phenomenon of acoustic resonance is "lock on" effect. Such idea was first proposed by Cumpsty and Whitehead. They also conducted the experiment in the wind tunnel and use flat plates to simulate the blade. When the frequency of the vortex shedding approaches to the frequency of the duct, the "lock on" effect will exist, which means the frequency of vortex shedding will continuously approach and finally become exactly the frequency of the duct and maintain this frequency for a certain range of flow speed. When this value happens to equal one of the natural frequencies of blade, the acoustic resonance occurs [10]. At the first glance, such coincidence is hard to realize. However, a typical compressor will usually contain more than 30 blades, each of which will shed vortices with different frequencies [11], and for each blade it will also has different modes of nature frequencies. In addition, with the help of "lock on" phenomenon, it is not so hard to begin acoustic resonance. In addition to the unchanged resonant frequency, it was found that in a certain range, the change of mass flow rate will not change the characteristic frequency, but with the decrease of mass flow, the amplitude of characteristic frequency will increase. Although the amplitude of BPF will decrease, but the total acoustic energy will almost remain the same [12]. Even if the degree of the IGV has been changed, it was found no matter increase or decrease the degree, the amplitude of AR will decrease, but the amplitude of BPF will increase, i.e., the total acoustic energy almost remains the same.

The location of the most dominant pressure along the axial is another most concerned topic when the acoustic resonance occurs. Hellmich and Seume found this position located near third row of the rotors in their experiment, and the amplitude of the acoustic pressure could even reach to 180db as shown in the Fig. 2 [8]. Courtiade and Ottavy later in their experiment on a 3.5 stage high-speed axial compressor further defined that the location of the highest amplitude always tend to appear at the rear part of the compressor, to be more specific, just downstream of the second stator [13]. Camp put 8 transducers in different axial positions of

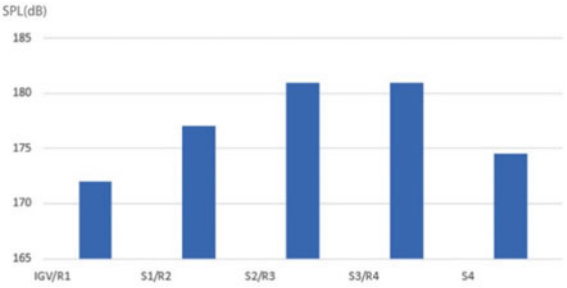

Fig. 2 Acoustic pressure level close to stability limit [8]

the compressors, and found amplitude reached maximum near the fourth stator exit plane. He continued to measure the pressure distribution at this plane, the contour plot is shown in the picture [7]. It confirmed that the pressure will have a pitch wise change, which will decrease from the suction side to the pressure side of the blade. However, along the spanwise direction, it almost remains unchanged, which is a little bit different from the result of yang et al. They measured the surface pressure of the first stage blade radially, with the largest amplitude near the tip, followed by the root, while the remaining position is relatively small [9].

3 Prediction of the Acoustic Resonance in the Aeroengine

After much investigation and research on the mechanism behind the acoustic resonance, researchers always hope to predict the onset of the acoustic resonance so that we can avoid it at the very beginning stage. According to our basic understanding on the mechanism behind this phenomenon, the prediction can be divided into frequency part and amplitude part respectively. Turning points of acoustic modes are very essential to the beginning of the acoustic resonance, which could be caused by the variation of cross section of duct. However, the investigation on this cause may not represents all the condition for different compressors. Another cause for the formation of turning points is the switch from cut-on to cut-off condition due to the swirl [14]. Therefore, how to calculate the cut-off frequency becomes a key step. While due to the complexity of the flow field in the compressor, a simplified approach is established, which is based on the result that mode scattering and trapping can be neglected if the number of lobes is relatively small to the number of blades, i.e., the pitch distance is relatively big [8]. Meanwhile, the swirl can also be overlooked because of the high resonant frequency compared with rotating frequency which has been shown by Kerrebrock [15]. Then the pressure distribution can be derived from Eq. (1). If the mean flow is regarded as a rigid body, then the axial wave number k_x is derived with Eq. (2). The cut-off frequency for different radial and circumferential mode can be derived from Eq. (3).

$$p_{m,n}(r,\varphi,z,t) = f\left(k_{r,m,n}r\right)\left[B_1\exp(im\varphi) + B_2\exp(im\varphi)\right]\exp\left[i\left(k_z - \omega t\right)\right] \quad (1)$$

$$k_{\pm x\pm\theta} = \frac{\mp M_x\left(k\pm M_\theta k_{r,m,n}\right)+\sqrt{\left(k\pm M_\theta k_{r,m,n}\right)^2-\left(1-M_x^2\right)k_{r,m,n}^2}}{1-M_z^2} \tag{2}$$

$$f_{m,n}^{cut} = \frac{ak_{r,m,n}}{2\pi}\left(\sqrt{1-Ma_z^2}\mp Ma_\varphi\right) \tag{3}$$

Most of the prediction on the frequency part now is based on this model. Another step-forward model also successfully calculated the cut-off frequency of the compressor under different off-design operation points and explained the reasons more precisely [13]. It can be basically summarized as follows: (1) If the k_x is a complex number, the pressure along the axial will decay exponentially, which is defined as cut-off condition. If k_x is a real number, the energy will propagate downstream. The real part of k_x is defined in Eq. (2). To get the cut-off frequency, the Eq. (2) should be zero, and so that we can get the Eq. (3). For the situation there is no mean flow in the duct, k_x will become zero and energy cannot be dissipated so that the resonance will occur. Later, Liu et al. first built a simplified model to calculate and predict the onset frequency of acoustic resonance in a multi-stage axial compressor based on his earlier model [16], which is used to calculate the flow instability inception in the axial compressor. However, this model is not good at dealing with problems of multi-stage compressor. This new model is based on the unsteady, three-dimensional, compressible Euler equation with a novel body force approach so that the three -dimensional flow field is reconstructed in a relatively real situation [17]. After global stability analysis, eliminating the mean flow data and linearizing, the origin Euler equation now becomes the Eq. (4). While the column vector X contains all the perturbation terms in the flow field. Obviously, it is a linear equation, and the condition number of matrix A will reflect the influence of any perturbation from the vector X, i.e., the susceptible onset of acoustic resonance will make the condition number of matrix A extremely large. The model was verified by the result of the numerical simulation of a multistage axial compressor at the University of Hannover. However, due to the computational limitation, the resolution of the frequency spectra is relatively low, this model still needs a further validation. Nevertheless, this proposed model is different from the tradition streamline method for it also considers three-dimensional vortex and turbulent flow in the field. Therefore, it indeed gives researchers some novel guide for future turbomachine design.

$$A(\omega)X = 0 \tag{4}$$

Pressure amplitude distribution of acoustic resonance along the axial direction was first predicted by Courtiade and Ottavy with a propagation method [13]. On a 3.5 high-speed multistage axial compressor, they normalized the maximum amplitude where happens at the inter-row section of stator 2 and rotor 3 and get the relative amplitude at other axial position by Eq. (1). D(x) damping factor calculated by decay situation of the pressure signal. With some modification and adjustment to this model, the prediction finally got a good agreement with the experiment results. However, in

the inter-row section of rotor and stator, such as position 26A and 27A, this model cannot predict well without the adjustment.

4 Proper Orthogonal Decomposition (POD) Method for Acoustic Resonance Study

4.1 Introduction of POD Method

As mentioned before, due to high computational resources cost in the past, researchers usually conduct experiments on the aeroengine for their research. However, different from the numerical simulation, the number of probes and sensors will be restricted by its size in the reality, which means it is impossible to collect a large amount of data at one specific moment. Except for some regular analysis method such as Fourier transformation and Spatial mode decomposition, some mode analysis method indeed requires lots of data information. Nowadays, with the development of computer science, numerical simulation becomes more popular, thus some mode analysis methods become possible, which are very useful in analyzing the acoustic field.

Proper orthogonal decomposition (POD) method origins from the machine learning, which aims to decrease the dimension order of the high-dimension data. For the aeroengine research, it also becomes helpful on decomposing the high-dimension flow field data. Many researchers have already applied this method successfully in recent years. Kou et al. use POD method reconstruct the unsteady transonic flow field over the airfoil surface and accurately extract the mode of their target phenomenon [18]. Luo et al. also use POD method to analyze and predict the flow field around an airfoil [19]. POD method can optimally extract and separate the modes by energy proportion. Each mode is the multiplication of basis and coefficient function. The basis of different modes is orthogonal to each other, which represents the spatial distribution in the flow field, while the coefficient vector is actually a time fluctuation function. Thus, the combination of the spatial basis and time coefficient could represent a specific flow structure.

The classical POD method will be briefly introduced here, the target data should be arranged in a specific order like the Eq. (5):

$$P = \begin{pmatrix} p_1^1 & p_1^2 & \cdots & p_1^n \\ p_2^1 & p_2^2 & \cdots & p_2^n \\ \vdots & \vdots & \ddots & \vdots \\ p_m^1 & p_m^2 & \cdots & p_m^n \end{pmatrix} \tag{5}$$

The row vector represents a specific point's parameter varying with the time, while the column vector represents all the points in the target region at a specific

moment. For the arrange of vector data, there is a detail introduction and example in the research of Liu and Chen [20]. A time dependent parameter consists two parts like the Eq. (6). On the right-hand side, the first one is mean value term, the second one is perturbation term. ξ represents the location, while t represents the moment. Due to our focus is on the perturbation caused by the acoustic resonance, thus the mean value term should be eliminated.

$$p(\xi, t) = \overline{p}(\xi) + p^{'}(\xi, t) \tag{6}$$

After that, the singular value decomposition (SVD) should be applied on the perturbation term like the Eq. (7), then the mode basis can be found in Eq. (8).

$$p^{'}(\xi, t) = U \Sigma V^{T} \tag{7}$$

$$p^{'}(\xi, t)(v_1, v_2, \ldots, v_n) = (\varphi_1, \varphi_2, \ldots, \varphi_n) \begin{pmatrix} \sigma_1 & 0 & \cdots & 0 \\ 0 & \sigma_2 & & \vdots \\ \vdots & \ddots & \ddots & \vdots \\ \vdots & & \ddots & \sigma_n \\ 0 & \cdots & \cdots & 0 \end{pmatrix} \tag{8}$$

The eigenvalue is just the square of the singular value, which represents the energy levels, thus Eq. (9) is to decide number of modes we need to represent the fluctuation of the flow field.

$$E = \frac{\sum_{i=1}^{r} \sigma_i^2}{\sum_{i=1}^{n} \sigma_i^2} \tag{9}$$

Once the first r mode has been decided, the coefficient matrix can be determined by Eq. (10). The origin flow field thus can be represented with the first r mode and its coefficient function as Eq. (11).

$$C_{r \times n} = U_{r \times m}^{T} \times p_{m \times n}^{'} \tag{10}$$

$$p'(\xi, t) = \sum_{i=1}^{r} U_{mode(i)}(\xi) \times C_{mode(i)}(t) \tag{11}$$

In addition to the classical POD method, there is a snapshot POD method, which will save a lot of computational resources by using eigenvalue decomposition (EVD) rather than the SVD. Mode basis can now be derived as Eq. (12), where λ_j and ψ_j is the eigenvalue and eigenvector of covariance matrix of P'. Such method is usually preferred for processing high dimensional data.

$$\varphi_j = \frac{1}{\sqrt{\lambda_j}} P' \Psi_j \tag{12}$$

After having extracted the major modes, to identify the characteristic mode that could most likely represents the perturbation caused by the acoustic resonance, the Fast Fourier Transformation (FFT) should be applied to the coefficient of different modes. If one of the mode's frequency spectra is dominated by the frequency of acoustic resonance, then this mode can be regarded as the characteristic mode, which major represents phenomenon of acoustic resonance. What should be noticed here is that the mode is separated by the spatial distribution, thus one mode could contain more than one phenomenon instead of only representing the target phenomenon, i.e., the target phenomenon could be slightly influenced by some other phenomenon [21]. Nevertheless, this method still helps to remove as much interference as possible and let the researchers to focus on the target phenomenon only, which will bring us a lot of benefits. For example, through plotting the contour of specific mode, it can recognize the pattern of acoustic resonance and also its variation across the time.

After all, this mode analysis method is very helpful for the research on acoustic resonance in aeroengine. However, to the best of author's knowledge, no one has tried this so far.

4.2 Application of POD Method on Acoustic Resonance in a Multi-Stage Axial Compressor

In order to see the effect of POD method on the study of acoustic resonance, the author have tried this on the data of numerical simulation result conducted in the workstation of Shanghai Jiao Tong University. The simulation target is a four-stage high-speed compressor. For unsteady flow, full passage simulation is necessary. However, for each passage there are more than one million discrete grids. In order to save the computational resources and time, only 1.5 stage is simulated. Due to the suspicious location of acoustic resonance is around rotor 3. Therefore, only stator 2 (S2), rotor 3(R3) and stator 3(S3) are simulated as demonstrated in the Fig. 3. Some basic parameter of this compressor has been introduced in table one. Due to the target of this chapter is the application of POD method on the study of acoustic resonance, thus

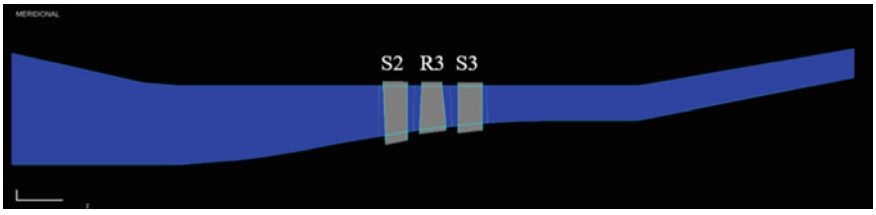

Fig. 3 Meridional demonstration of 1.5 stage simulation

Table 1 Basic parameter of simulated the compressor

Parameters	Value
Rotation frequency (RF)	285 Hz
Rotation speed	17100 rpm
Number of blades	29
Blade passing frequency	29RF

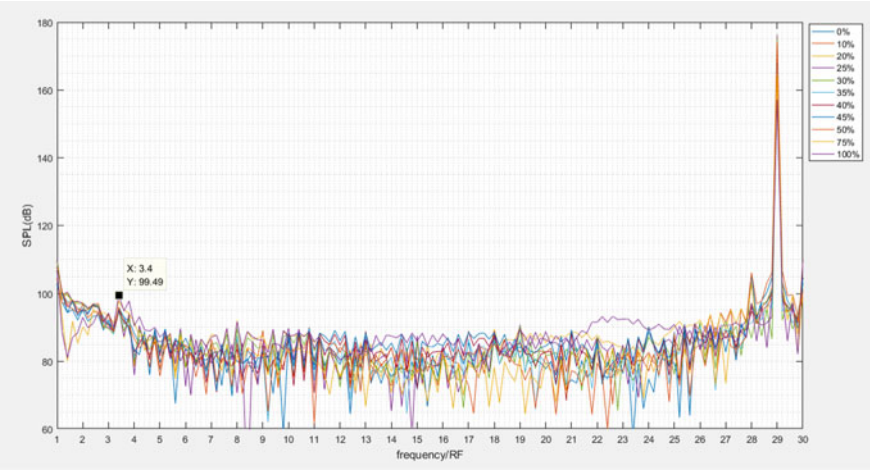

Fig. 4 A 99.2% spanwise frequency spectra

the process and validation of simulation will not be introduced here. More details have been introduced in [17]. In addition, the simulation has been conducted for five rounds so far, thus the resolution of the frequency is 1/5 RF (Table 1).

As shown in the Fig. 4, FFT has been conducted on the pressure data around blade tip under stationary coordinate, which is 99.2% spanwise direction, slightly below the blade tip. The abscissa has been normalized by rotation frequency (RF). Same as the result of Xiaohua Liu [17], we have found the suspicious characteristic frequency between 3 and 4RF.

Through classical POD method, we can decompose the pressure field into 19 modes, which accounts for 99.9999% of the origin field as shown in the Fig. 5. As mentioned before, in order to define the mode that could most represents the phenomenon of acoustic resonance, the FFT has been applied on the coefficient of each mode to see which mode is dominated by the suspicious characteristic frequency.

As shown in the Fig. 6, mode one to mode seven is dominated by the blade passing frequency or rotation frequency, it can also be verified that their time domain plots are periodical as shown in the Fig. 7.

However, we can see from Fig. 8 that mode eight is dominated by the nonsynchronous sharp peak around 3.4RF, and since mode nine many modes have a sharp peak at 3.4RF, and the peak at the blade passing frequency is not obvious anymore.

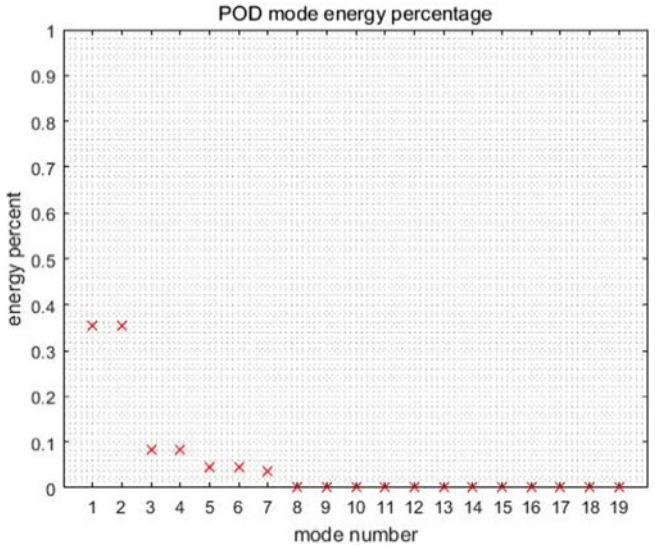

Fig. 5 POD mode energy percentage

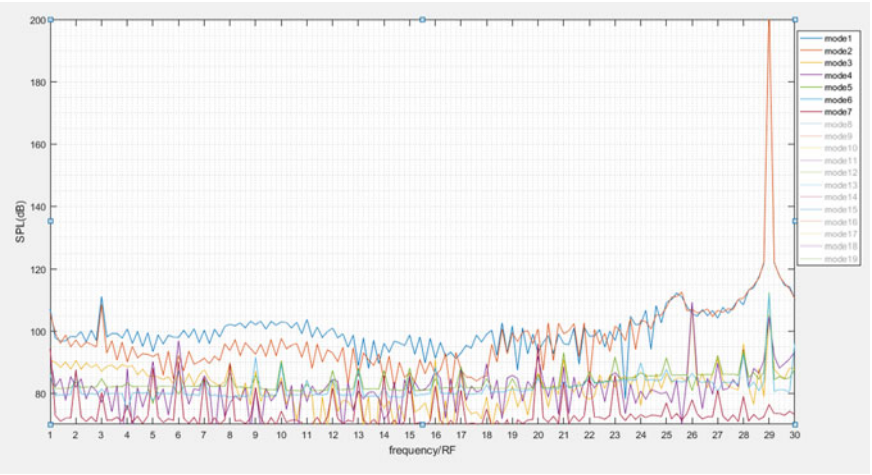

Fig. 6 POD frequency spectra of mode 1 to 7

In addition, we can see from Fig. 9 that the time domain plot of mode eight is not periodical anymore.

The contour plot of the first moment of mode eight has also been plotted as shown in the Fig. 10, and it is glad to see that the flow structure is clearly demonstrated. It becomes more easier to analyze the development and distribution of the acoustic resonance. Thus, it is reasonable to do some further research on acoustic resonance by POD method.

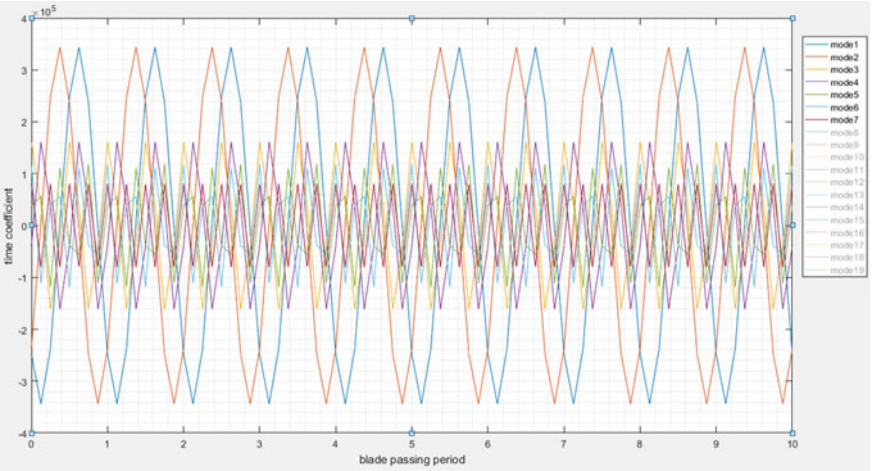

Fig. 7 POD time domain plot of mode 1 to 7

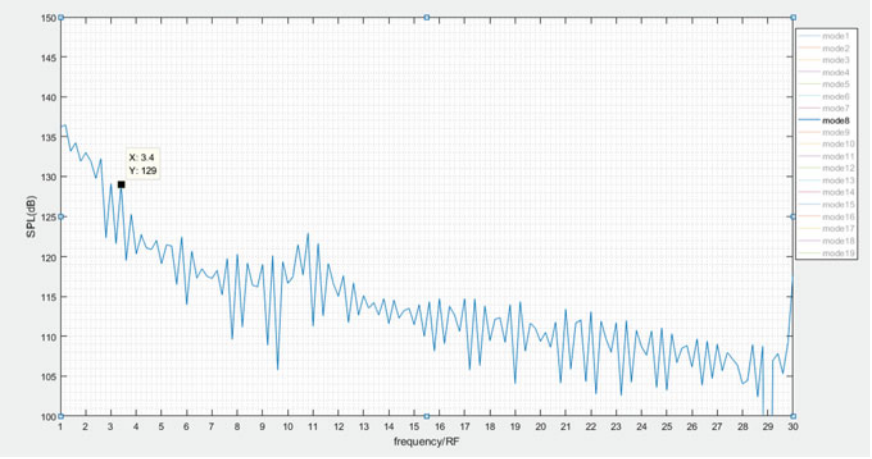

Fig. 8 POD frequency spectra of mode 8

5 Conclusion

The development of aeroengine has lasted over a century, people's expectation and demand on it become higher, which gives researchers and engineers some new challenges in the design stage. The phenomenon of acoustic resonance is just one of them. Lots of valuable discovers upon this phenomenon have been discovered by some pioneering researchers, which has been summarized by this paper. In general, the

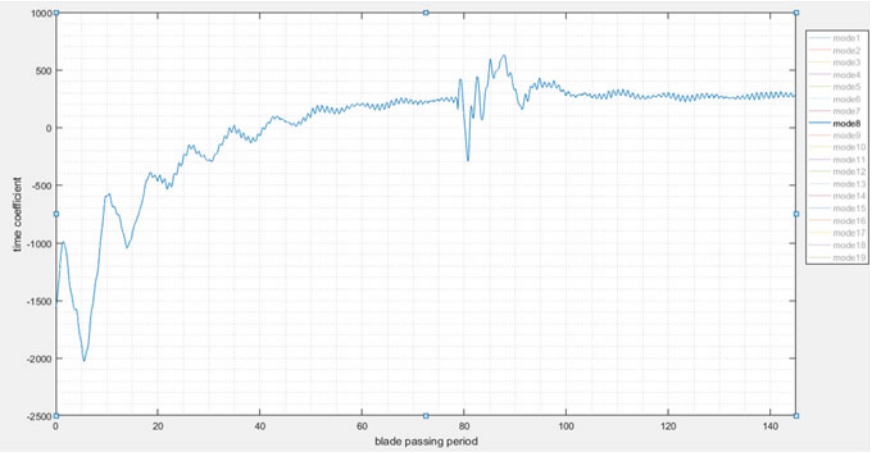

Fig. 9 POD time domain plot of mode 8

Fig. 10 Full-passage pressure contour plot of first moment of mode eight

research on this phenomenon can be divided into five parts: discovering, observing, exploring, predicting and controlling.

The discovering of acoustic resonance in compressors has never stopped. Some real cases of the consequences of the acoustic resonance in the aeroengine has been mentioned in the second chapter. In short, it can not only produce a high-level noise but also may exceed the fatigue limit of the material, thus it will influence the comfortability as well as endangering the flight safety. However, compared with some other factors that may endanger the reliability of an aeroengine, such as stall, surge, and some machinal vibration, acoustic resonance is not that much danger.

Almost all the discovered characteristics of acoustic resonance has been introduced, which can be summarized as follows: (1) For an axial multi-stage compressor, it usually occurs either in the inter-row section or in the cascade. (2) It is a nonsynchronous vibration and appears as a sharp peak in the frequency spectra. (3) The characteristic frequency will have a step change when increasing the flow speed gradually, which is also called “lock on” effect. (4) The phenomenon of acoustic resonance will decrease from the suction side to the adjacent pressure side, but almost remain the same spanwise in the blade tip region.

After decades of exploring, the mechanism beyond this phenomenon remain to be further revealed due to the complexity of the coupling between acoustic field and flow field. Nevertheless, the vortex shedding has been regarded as the factor of this phenomenon, which will usually occur at the tip clearance and edge of the blade.

Meanwhile, the propagation of acoustic resonance is also found as a helical mode, which means it will propagate both in circumferential and axial direction.

Prediction of the acoustic resonance is a vital preliminary work for the controlling part. The prediction work can be separated into two parts: frequency and amplitude. For the former one, many theoretical models have been proposed and have a good agreement with the experiment results, but all of these models are based on global liner theory. Meanwhile the precision of the prediction remains to be enhanced. For the amplitude prediction, the amplitude in the inter-row section is still hard to predict. Actually, predicting through numerical simulation may become a good way in the future, but it still costs unacceptable computational resources up to now.

After summarizing all the current results, research methods and research progress on the acoustic resonance in an aeroengine. The author also introduces the POD method, which has been widely used in data processing, and has recently been successfully used in flow field analysis. This method is good at extracting and demonstrating the target flow structure, some basic POD analysis has also been applied on the study of acoustic resonance and seems to have a good effect, but the result remains to be further explored, the author believes that it will become a useful and powerful tool in the future research of acoustic resonance.

Acknowledgements This work is partially supported by National Natural Science Foundation of China (Grant No. 51976116), Natural Science Fund of Shanghai (grant No. 19ZR1425900), and the Open Research Subject of Key Laboratory (Fluid Machinery and Engineering Research Base) of Sichuan Province (grant No. szjj2019-022).

References

1. Greitzer EM (1976) Surge and rotating stall in axial flow compressors—part II: experimental results and comparison with theory. J Eng Gas Turbines Power 98(2): 199
2. Beselt C et al (2012) Experimental and numerical investigations of rotating instability phenomenon in an axial compressor stator. In: Proceedings of 42nd AIAA fluid dynamics conference and exhibit
3. Lin Z, Li K, Yang S (2010) Experimental research on sound waves excitation to aero-engine compressor rotor blade. J Dyn Control 008(1):12–18
4. Parker R (1968) An investigation of acoustic resonance effects in an axial flow compressor stage. J Sound Vib 8(2):281–297
5. Kameier F, Nawrot T, Neise W (1992) Experimental investigation of tip clearance noise in axial flow machines. in DGLR—AIAA 14th Aeroacoustics Conference
6. Legerton M, Stoneman S, Parker R (1991) An experimental investigation into flow induced acoustic resonances in an annular cascade
7. Camp TR (1999) A study of acoustic resonance in a low-speed multistage compressor. J Turbomach 121(1):36–43
8. Hellmich B, Seume JR (2008) Causes of acoustic resonance in a high-speed axial compressor. J Turbomach 130(3)
9. Yang M et al (2012) Study of acoustic resonance for aeroengine compressors. Aeroengine 38(5):36–42
10. Cumpsty NA, Whitehead DS (1971) The excitation of acoustic resonances by vortex shedding. J Sound Vib 18(3):353–369

11. Welsh MC, Gibson DC (1979) Interaction of induced sound with flow past a square leading edged plate in a duct. J Sound Vib 67(4):501–511
12. Luan X et al (2014) Investigation into noise characteristics corresponding to acoustic resonance in a multi-stage axial compressor. J Shenyang Aerosp Ace Univ 31(02):9–13
13. Courtiade N, Ottavy X (2013) Study of the acoustic resonance occurring in a multistage high-speed axial compressor. Proc Inst Mech Eng, Part A: J Power Energ 227(6):654–664
14. Cooper AJ, Peake N (2000) Trapped acoustic modes in aeroengine intakes with swirling flow. J Fluid Mech 419:151–175
15. Kerrebrock JL (1977) Small disturbances in turbomachine annuli with swirl. Aiaa Journal 15(6):794–803
16. Liu X et al (2015) Calculation of flow instability inception in high speed axial compressors based on an eigenvalue theory. J Turbomach
17. Liu X et al (2018) A theory on the onset of acoustic resonance in a multistage compressor. J Turbomach 140(8)
18. Kou J, Zhang W, Gao C (2016) Modal analysis of transonic buffet based on POD and DMD method. Acta Aeronautica Et Astronautica Sinica 37(9):2679–2689
19. Luo J, Duan Y, Cai P (2014) A quick method of flow field prediction based on proper orthogonal decomposition. Advan Aeronaut Sci Eng 5(3):350–357
20. Liu G, Chen B (2017) Fluctuation characteristic analysis of unsteady flow field based on proper orthogonal decomposition. Chinese J Sci Instrum 38(3):703–710
21. Taira K et al (2017) Modal analysis of fluid flows: an overview. AIAA J 55:1–29

Computational Method in the Throughflow Simulation of Aeroengine Compressor

Qitian Tao, Hailiang Jin, and Xiaohua Liu

Abstract The computational method in throughflow simulation is investigated in this paper. The present investigation reported the current research status and compared the advantages and disadvantages between different computational models including streamline curvature method, matrix method and throughflow calculation based on time marching. For the most commonly used time marching method, we discussed one key issue in application in engineering reality which is called as the simulation of blade force, which was divided into two categories according to whether to solve the circumferentially momentum equation as master equation or not. In conclusion, compared with other methods, time marching method has more advantages in transonic flow adaptability, shock capture ability and calculating accuracy, so that it has more potentials and prospects in the future research. The blade force model, as a key link in the time marching method, has developed rapidly. However, there is still no unified highprecision model and the modeling of blade force needs more study. With further development, this method is expected to become a standard tool during the aeroengine compressor design stage.

Keywords Aeroengine compressor · Throughflow · Time marching method · Blade force

Q. Tao · X. Liu (✉)
Shanghai Jiao Tong University, Shanghai, China
e-mail: xiaohua-liu@sjtu.edu.cn

Q. Tao
e-mail: sjtu-tqt@sjtu.edu.cn

H. Jin
AECC Hunan Aviation Powerplant Research Institute, Beijing, China

X. Liu
Key Laboratory (Fluid Machinery and Engineering Research Base) of Sichuan Province, Chengdu, China

Z. Jing and X. Zhan (eds.), *Proceedings of the International Conference on Aerospace System Science and Engineering 2020*, Lecture Notes in Electrical Engineering 680,
https://doi.org/10.1007/978-981-33-6060-0_24

1 Introduction

Because of the mismatch between the complexity of the flow in fan/compressor and the computational power and design methods, people try to find all the ways to simplify flow field. There are two kinds of main ideas to simplify it, and one is trying to ignore some details about the flow field and the other is to reduce dimension. In general, less simplification means more realism and reliability.

Wu [1] provide a general theory of three-dimensional flow and through his theory we can decompose three-dimensional flow inside the turbomachinery into two kinds of two-dimensional relative stream surface. This method based on steady flow and suppose S1 plane (section of blade) is one whose intersection with a z plane either upstream of the blade row or midway in the blade row forms a circular arc. S2 plane (meridian plane) is one whose intersection with a z plane either upstream of the blade row or somewhere inside the blade row forms a radial line. This theory can estimate a steady three-dimensional flow by iterative calculation the two kinds of relative stream surface. Wu divided the governing equation in different surfaces and different directions and the design methods we used nowadays are all developed around his theory.

In the early research on the inner flow of turbomachinery, due to the limit of computation power we did axisymmetric hypothesis and ignoring the circumferential differences we can pay more attention to S2 stream surface. Studying the two-dimensional flow on S2 stream surface can grasp the essence and key of the problem so that throughflow calculation on S2 be widely used in fan/compressor design progress. Although with the quick development of CFD we can do full three dimensional at some local area of turbomachinery nowadays, throughflow calculation still very necessary. On the one hand it can save several orders of magnitude of computation time in the initial design stage, on the other hand the results form throughflow calculation can check the physical models and the answers from full three-dimensional calculation.

2 Throughflow Methods

At present, there are three popular methods for throughflow calculation: streamline curvature computing procedures, matrix method computing procedures and throughflow calculations based on time marching.

2.1 Streamline Curvature Approach

Based on the developed motion equation, continuity equation and the equation defined the fluid, Novak [2] got the solution of fluidflow by streamline curvature approach. Novak did a consistent and non-axisymmetric treatment to the flow field

and restricted itself in cylindrical coordinate system. During the calculation, firstly assumed the position of the initial streamline, then added the curvature of the streamline to the main equations and got a new streamline. keeping iterating, adjusting the position of streamline until the streamline basically coincides. By this way, Novak got the velocity distribution at different place of a turbomachine with the assumption of constant stagnation enthalpy.

This approach is easy to understand and the used equations are concise so be widely used in the engineering practice. Frost [3] used this way to code a computer program for calculation compressor airfoils. But when it comes to transonic calculation, because of the Mach number at the rotor is larger than 1, channel may be blocked partial or complete. In the case of blockage, maximum flow rate G max is only decided by $p0 * T0*$ and A. So even there is a small difference between G max and the flow rate gives may cause divergent calculation especially in direct problem.

2.2 Matrix Method

Matrix method was firstly put proposed by Wu, but was firstly realized by Marsh [4]. Matrix method changes differential equation of the stream function into a difference equation and solve it numerically. Marsh's program forms the distorted grid, the finite difference approximation, the band matrix [M] and the band uptriangular factors [U] and lowtriangular factors [L]. Though solving the tridiagonal matrix equation can get the stream function at every position, then use the stream function to calculate velocity.

With the help of chasing method, we can solve the matrix equation quickly compared with iterative process. But the obvious disadvantage of matrix method is it takes up a lot of memory. Marsh also said his method only applicable to subsonic flow from the same reason with streamline curvature approach. Yuan [5] has concluded that in addition to what has been mentioned above, the matrix method has its own equation defects when it comes to supersonic flow field. First of all, the correct velocity value cannot be uniquely derived from the partial derivative of the stream function in the transonic region. This means that for direct problem as long as the velocity on S2 stream surface is supersonic, there will be a two value problem of velocity. We can only solve for the velocity by integrating. What is more, the main equation of stream function method belongs to mixed partial differential equation, and different cases may have different forms of partial differential equations. This will bring many difficulties to boundary conditions and numerical solutions.

In a word, both streamline curvature approach and matrix method have great defects in predicting blockage conditions, capturing shock waves, transonic calculation and unsteady case. With the rapid development of computer and CFD, throughflow calculations based on time marching emerges.

2.3 Throughflow Calculations Based on Time Marching

In the past few decades, finite volume and finite difference methods commonly used in three-dimensional numerical calculation have been gradually applied to quasi-3d calculation. Time marching based method to solve the main equation is more and more popular. According to different main equation, this method can be divided into two classes. One kind is to solve Euler equation and the other is to solve Navier-Stokes equation. It should be noted that solving Euler equation by time marching on a coarse grid does not mean that the effect of viscosity is ignored, and the effect of viscosity will be considered by introducing loss model.

Time Marching Based on Euler Model Spurr [6] was the first to get the numerical simulation by combining time marching circumferentially averaging with S1 flow field calculation program. Spurr iteratively solved the blade forces and compared with the three-dimensional Euler results. Because the time marching throughflow analysis program and the three-dimensional CFD method use similar solvers, many time marching throughflow programs are changed from three dimensional CFD programs. Dawes [7] attempted to combine Euler throughflow calculation with three-dimensional viscous numerical simulation, and in this case, only one row of blades needs to be numerically calculated in three dimensions, and Euler throughflow can be used for the remaining rows of blade. The blade forces and loss for throughflow calculation can be correlated or processed from previous three-dimensional solution. Dawes presented two applications, a transonic compressor rotor and steam turbine nozzle guide vanes. In both cases, the predicted flows were in closer agreement with experimental evidence.

Baralon [8] studied the Euler throughflow model in depth, and his code based on a cellcentered finite volume method with a characteristic upwind scheme of third order. Baralon discussed normal blade blockage and blockage factors, and found a shock occurring in the blade row is equivalent to a normal shock which strength is only depending on the upstream Mach number. What's more, the leading edge singularity problem has been investigated and two different techniques were proposed. Stridh [9] researched all unsteady effects and found in the mixing plane case, the so called deterministic stress terms are missing. Stridh firstly solved the steady state with conventional mixing plane, secondly used this as input to obtain the DST terms and finally used those to corrected the average flow field. Li [10] used the Euler throughflow model to study the performance characteristics of fans, the calculation results are in good agreement with the three-dimensional simulation results. Figure 1 shows the results of rotor 67 by Euler throughflow.

Time Marching Based on Navier-Stokes Model In Euler throughflow model, viscosity loss is usually accounted by introducing entropy increase, and the role of boundary layer is often be ignored. The circumferentially averaged throughflow model based on the Navier-Stokes equation can be used to calculate the boundary layer of the wall, further reducing the dependence on the empirical coefficient.

Simon [11] detailed the development of a throughflow model based on the axial Reynolds Averaged Navier-Stokes equations. Comparisons with an inviscid Euler

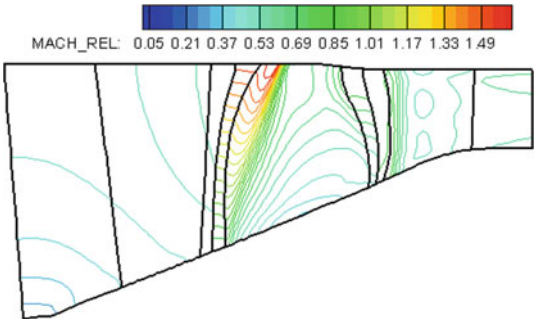

Fig. 1 Flow field of meridional plane calculated by Euler throughflow calculation

model with added entropy production terms allow to judge the improvements provided by the viscous wall treatment. And the improvements showed in the blockage of the flow, the high energy input in rotors and the high level of losses are captured.

Ji [12] of Beijing University of Aeronautics and Astronautics is the first scholar in China to apply the idea of time marching to throughflow calculation. Ji solved the design difficulty of transonic high load turbomachinery by solving the circumferentially averaged Navier-Stokes equation. Compared with the previous throughflow calculation method, it can more correctly consider the influence of boundary layer on wall surface, and the governing equation has unsteady terms, which can be applied in the research of turbomachinery flow stability. Jin [13] derived the governing equation of the throughflow model based on the circumferentially averaged Navier-Stocks equation, and proposed a new blade force model. The governing equation of the fluid was decomposed into the transport effect part and the acceleration effect part of the pressure gradient, and then solved respectively. Furthermore, Jin [13] proposed a new way to calculation averaged flow surface normal vector. Compared with three-dimensional numerical simulation, his solution had high precision. On the original basis, Wan [14] introduced the blockage factors and the mean static pressure, and gave a non-viscous blade force model which could consider the influence of blade profile. Then, the circumferentially nonuniform terms are extracted from the three-dimensional numerical simulation results for analysis, and added them to the circumferentially average flow model as fixed terms. Wu [15] added a blade force model that reflects the compressor design experiences into the numerical method, and proposed a complete throughflow analysis model for off-design conditions. Wu [15] checked the analysis model by a four stages low speed compressor.

3 Blade Force

Although CFD throughflow method has been developed for several decades and has more advantages over traditional throughflow method in theory, it still faces many difficulties to become a mature design method in engineering reality. Yang [16] once

concluded that there are still three biggest difficulties in the largescale application of the current CFD throughflow method in engineering reality. First, the throughflow method is very sensitive to the distribution of blockage factors and flow angles. Besides, blade force model has a decisive influence on the distribution of flow field parameters. The last, leading edge singularity problem still need further research.

One of emergency question is about blade force. The blade force is used to simulate the action of the blade on the fluid in the blade area. Marble [17] provided that it was possible to simulate blade force with distributed volume forces. In general, we divide blade forces into non-viscous blade forces and viscous blade forces in calculation. The non-viscous blade force is parallel to the average flow surface and is used to make the flow turn without entropy increase. Viscous blade force is used to simulate the friction on the blade surface, and loss is introduced into the calculation.

3.1 Non-viscous Blade Force

There are two main ways to simulate the non-viscous blade force.

In the first case, there is no need to solve the circumferentially momentum equation in the blade area, which is used to derive the circumferentially blade force in the form of volume force. According to the condition that the direction of blade force is tangent to the average flow surface, first by the axial velocity calculate circumferentially velocity, and according to the circumferentially momentum equation to calculate the circumferentially blade force. By projecting the circumferentially blade force, the components in all directions can be obtained. Finally, the new blade force is used to calculate the new axial velocity, and iterate the flow field parameters until converged. Dawes [7] and Damle [18] both used this way to simulate the blade force model.

In the second case, the blade force is regarded as an unknown parameter related to time and the non-viscous blade force is calculated by solving a time dependent differential equation. Compared with the former, this method has better convergence. This method, first proposed by Baralon [8], can be understood as a pressure gradient that occurs when the blade force and the flow surface are not tangent. Simon [11] improved on this. Jin [13] pointed out that constant C has a great influence on the convergence in the actual calculation, and proposed a large particle method for the nonviscous blade force model. Wan divided a time step into two steps. The first step did not consider the non-viscous blade force, and the second step only considered the non-viscous blade force. After spatial dispersion, the final iterative relation was obtained. Persico and Rebay [19] proposed a blade force model on penalty formulation based on tangent condition of flow surface. This model can be understood as applying the tangential condition to the elastic blade, and the stiffness of the blades is the penalty factor K. The advantage of using this model is that no additional equations need to be solved. In addition, the parameter K can be adjusted during the calculation process to prevent divergence.

3.2 Viscous Blade Force

The elliptic property of viscous flux makes its discrete process relatively simple. Bosman [20] proposed the famous loss distribution model. It assumed that the loss is caused by a dissipative force which opposes the relative velocity vector. The dissipative force D was assumed to be caused by the flow relative to some surface, such as a blade or an annulus wall, and the coordinate system was chosen to move with this surface. The dissipative force D then opposes the relative velocity W in the coordinate system moving with the surface which is associated with the loss.

4 Establishment and Application of Throughflow Calculation Model

Based on the above analysis, this throughflow calculation program bases on time marching methods and compares the Euler model with the N-S model, adopts the finite volume method, simultaneous the conservation form law above continuity equation, momentum equation and energy equation.

4.1 Spatial Discretization

No matter which kind of numerical schemes of the solution of the Euler equations, the majority thought is a sperate discretization of time and space. Structured finite volume scheme is naturally based on structure grid. And the grid generation is based on: firstly the domain is completely covered by the grid, secondly there is no free space left between the grid cells and the grid cell do not overlap each other.

The difficult of throughflow grid generate is how to simplify three-dimensional blade shape to two-dimensional calculation area. Usually, the camber surface of the blade is extracted approximately as the calculation area of the entire flow path. It should be noted that the camber surface of the blade is defined as the line connecting the center of each tangent circle on the blade profile. At the same time, the calculation as a quasi-3d problem, is expanded in cylindrical coordinate system and take placed in radial and axial direction. Taking Rotor 67 as an example, the original blade shape is showed on the left hand side and the generated grids showed in right hand side (Figs. 2 and 3).

Discretization of Convective Fluxes In transonic compressor, the shock wave has a great influence on the calculation accuracy. The low-dissipated flux splitting scheme (LDFSS) proposed by Edwards is used in this throughflow calculation model because of its strong shock wave capture capability. At the same time the MUSCL (Monotone Upstream Centered Scheme for Conservation Laws) interpolation has to be enhanced by the so-called limiter function or limiter, if the flow region contains strong gradients.

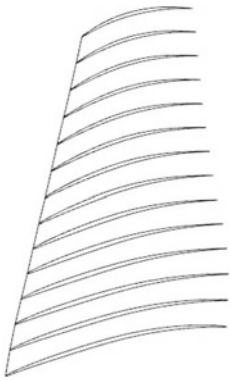

Fig. 2 Blade shape of Rotor 67

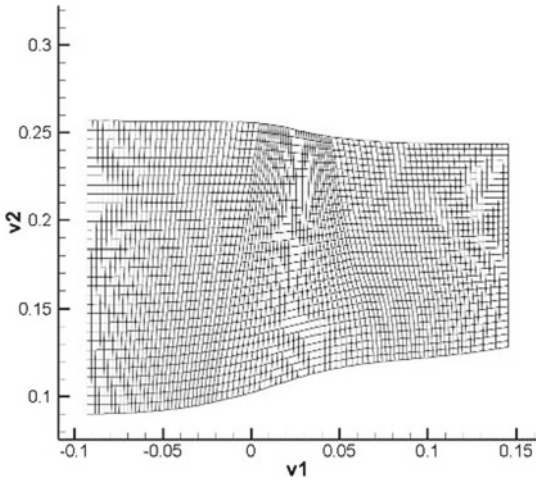

Fig. 3 Quasi 3-d grids of Rotor 67

Discretization of Viscous Fluxes Cell-centered scheme apply Green's theorem relates the volume integral of the first derivative to the surface integral. In order to evaluate the first derivative at the face we have to integration the corresponding flow variables over the boundary of the auxiliary control volume which can be obtained by simple arithmetic averaging.

4.2 Temporal Discretization

Time marching is a method to solve the steady flow field by using unsteady equations. The initial field is usually obtained by radial equilibrium equation. And the initial is usually uniform. Because the flow field is only controlled by groveling equation and boundary condition, so the result is steady. This throughflow calculation model

uses explicit time stepping schemes. Four steps Runge-Kutta method combined with multiple grid can obviously improve the convergence speed. CFL number in this program equals to 2.

4.3 Boundary Condition

Initial value is calculated by radial equilibrium equation. Inlet condition I used total pressure, total temperature and the direction of gas. For the outlet condition we just need one static pressure at one point. Because the distribution along the spreading direction can be calculated by radial equilibrium equation. For the hub and shroud, we usually define no slip boundary condition. At the rotor tip area, because we can't simulation the distance between the blade and the shroud, the result here will has some error. At the interface between the rotating region and the stationary region, we need to set up two layers of virtual grid, which can guarantee the continuity of the calculation region on one hand, and guarantee the same spatial precision at the boundary and inside the calculation region on the other hand.

4.4 Numerical Examples Validation

In order for the model to be used in the aerodynamic design of fans/compressors, it is necessary to evaluate the predictive ability of the model, analyze the causes of errors, and provide suggestions for the improvement of the model. In this section, the high load transonic fan R67 is used as an example to analyze the program results. NASA Rotor 67 is a stage 1 fan Rotor in a multistage compressor designed and tested by NASA in the late 1980s. Due to its relatively detailed experimental data, this example is widely used to verify the accuracy of CFD software. The basic design parameters of NASA Rotor 67 are as follows: design rotating speed is 16043 RPM, tip relative Mach number is 1.38, design pressure ratio is 1.63 and design mass flow rate is 33.25 kg/s.

Euler Throughflow Results for Rotor 67 Because of the limitations of the throughflow calculation program itself, the calculation program can only maintain a certain degree of accuracy at the design point, and there is a large error at the non-design point, and it is needs to establish an additional connection between backward angle and loss at the non-design point. The backward angle and loss have a crucial effect on the aerodynamic performance of the compressor. At present, the backward angle and loss correlation of non-design points are mainly based on empirical formula. Miller proposed a correlation method, but the results show that there are still some errors in the position far from the design. So, this article just compares the program performance at the design point.

The distribution of the axial × radial points in the grid for throughflow calculation is: 32×33 (the channel area before the blade) +30×33 (the blade area) +32×33 (the channel area after the blade). The grid is shown as Fig. 4. For the boundary condition, total temperature at the inlet is 288.15 k and total pressure is 101325 pa. Outlet back pressure is given at the position of hub. The wall surface adopts impermeable boundary condition. Using throttling process to get close to design point. The original back pressure is 70000 pa, and with the process of increase back pressure, the mass flow rate decrease at the exit. And we choose the 107500 pa back pressure condition as the contrast working condition, and the mass flow rate equals to 37.77 kg/s. The efficiency of this rotor calculated by throughflow program is 89.07%. And the relative Mach number distribution of cloud is showed as Fig. 5.

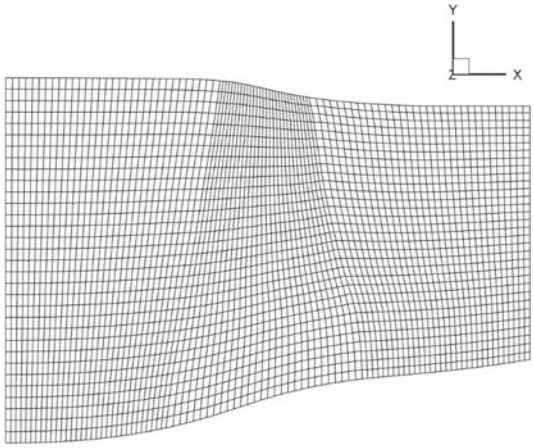

Fig. 4 Grids of Euler throughflow

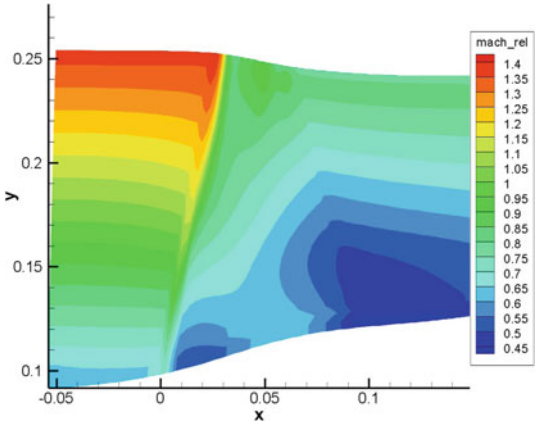

Fig. 5 Mach number distribution by Euler throughflow calculation

As can be seen from the above figure, the distribution of Mach number cloud image is basically reasonable. As a transonic compressor, Rotor 67 shows subsonic flow at the leading edge of the blade near the hub and supersonic flow at the leading edge of the blade near the casing. And the flow calculation model successfully captures the shock wave at the leading edge of the blade, which is consistent with the design state of transonic. However, a slight distortion can also be seen at the leading and trailing edges of the blade, due to the sudden emergence of blade forces at the junction of the blade and bladeless regions resulting in a break in the numerical simulation. At the position where the trailing edge of the blade is close to the casing, a region of low speed flow will appear. The formation of this region is the result of the combined action of distortion and no-tip clearance model.

N-S Throughflow Results for Rotor 67 The turbulence model adopts S-A turbulence model. The influence of fluid viscosity and boundary layer should be considered for N-S throughflow, so the mesh is needed to be encrypted at the wall surface. Since the blade's effect on the fluid is replaced by the blade force model in the two-dimensional throughflow calculation, the blade is not directly simulated physically, and no additional axial grid is needed at the junction between the blade and the pipe. Keep the axial grid density unchanged, the distribution of the axial × radial points in the grid for N-S throughflow calculation is: 32×45 (the channel area before the blade) +30×45 (the blade area) +32×45 (the channel area after the blade). The grid is shown as Fig. 6. The boundary condition is same with Euler throughflow calculation except for N-S method, the wall surface used adiabatic boundary condition without slip. Under the same back pressure of 107500 pa, the mass flow rate calculated by the N-S throughflow method is 37.64 kg/s. Efficiency of this blade is 89.86%. The relative Mach number distribution of cloud is showed as Fig. 7.

The mass flow rate and efficiency of N-S throughflow calculation are lower than that of Euler method, because the N-S throughflow model takes into account the influence of ring wall boundary layer, and the blocking and viscosity loss of ring

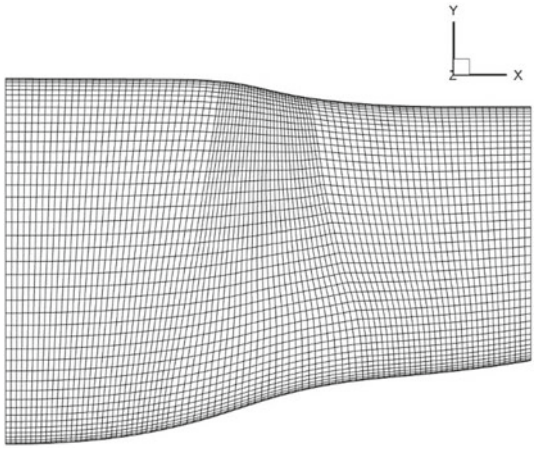

Fig. 6 Grids of N-S throughflow

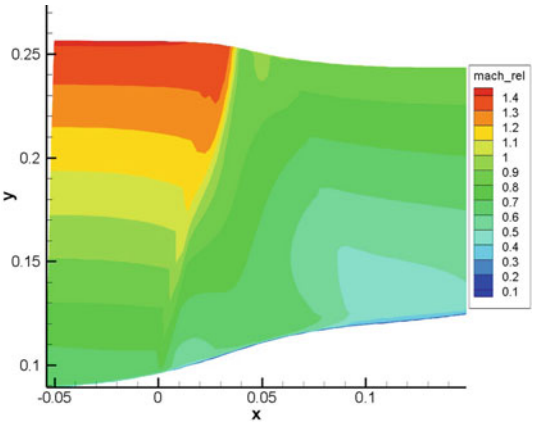

Fig. 7 Mach number distribution by N-S throughflow calculation

wall boundary layer cause the value to drop. At the same time, due to the lack of tip clearance model, there is also a Mach number gap in the tip part and a parameter distortion in the leading and trailing edges of the blade.

By comparing the Mach number distribution cloud map, it can be found that the cloud map of the Mach number distribution calculated by N-S throughflow is basically the same as the Euler throughflow result. The low-energy fluid can be obviously seen near the wall of the N-S model, and this low-energy fluid is the viscous boundary layer, which is also consistent with the experience.

CFX Results for Rotor 67 CFX calculate mesh is generated by software Turbo-Grid, total grids number is large than 1 million and S-A turbulence model was used for numerical calculation. Tip clearance control is 0.356 mm. As a control group, CFX was calculated under the same initial conditions. The rotor speed is 16043RPM and the back pressure is 107500 pa. Periodic boundary conditions are given for the circumferential boundary. The calculated flow rate under this working condition is 34.03 kg/s. Efficiency of this blade is 92.06%. Also, the relative Mach number distribution of cloud is showed as Fig. 8. It can be seen that the Mach number distribution are in relatively agreement with the results of the throughflow calculation. At the leading and trailing edges of the blade and the hub and casing, the 3d calculation program performs better without obvious parameter distortion and data discontinuity, at the cost of more computing resources and computing time. And the mass flow rate is more closed to the design point. Efficiency is obviously higher than other models because of the influence of the precise calculation of viscous boundary layer in 3d operation.

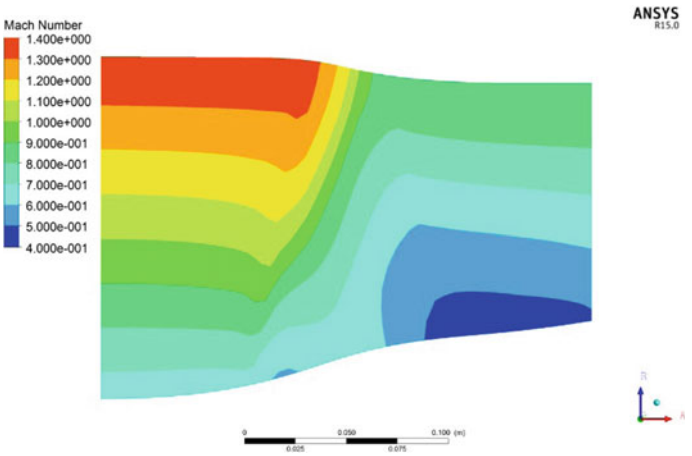

Fig. 8 Mach number distribution by CFX

5 Conclusion

In this paper, three calculating throughflow methods on the S2 stream surface are summarized. Compared with streamline curvature approach and matrix method, time marching method has been widely used because of its good transonic adaptability, shock capture ability and blockage calculate adaptability. The circumferentially averaged throughflow model based on N-S equation can consider the effects of boundary layer better, and has been widely studied.

At the same time, this throughflow calculation program based on time marching is also written, which is solved by finite volume method. Compared N-S results and Euler results with CFX results, analyze the differences between their results and the reasons for the differences. We used this program to get the steady state design point of the flow field, and the results are close with the CFX results.

Although throughflow calculation technology has developed rapidly in the past few decades, there are still several key technologies restricting its development. In this paper, two common methods of blade force simulation are concluded, but it still need further research. In the future, the foundation for the development of higher precision CFD throughflow program is to establish more accurate blade force model, and pay attention to the coupling and matching of each model.

Acknowledgements This investigation is supported by National Natural Science Foundation of China (Grant No. 51976116), Natural Science Fund of Shanghai (grant No. 19ZR1425900), and the Open Research Subject of Key Laboratory (Fluid Machinery and Engineering Research Base) of Sichuan Province(grant No. szjj2019-022).

References

1. Wu ZHR (1952) A general theory of three-dimensional flow in subsonic and supersonic turbomachines of axial-, radial-, and mixed-flow types: NACA TN 2604. Washing-ton, NASA
2. Novak RAJ (1967) Streamline curvature computing procedures for fluid-flow problems. J Eng Power 89(4):478–490
3. Frost GR, Hearsey RM, Wennerstrom AJR (1972) A computer program for the specification of axial compressor airfoils. ARL 72-0171(AD 756879)
4. Marsh HR (1968) A digital computer program for the throughflow fluid mechanics in an arbitrary turbomachine using a matrix method: RM 3509. National Gas Turbine Establishment, London
5. Yuan N, Zhang ZJ, Gu ZHJ (1998) Comparison of three calculation programs of S2 throughflow surface in turbojet compressor. J Propul Technol 19(1):50–56
6. Spurr AJ (1980) The prediction of 3D transonic flow in turbomachinery using a combined throughflow and blade-to-blade time marching method. Int J Heat Fluid Flow 2(4):189–199
7. Dawes WNJ (1992) Toward improved throughflow capability: the use of three-dimensional viscous flow solvers in a multistage environment. J Turbomach 114(1):8–17
8. Baralon S, Eirkson LE, Hall UC (1997) Viscous throughflow modelling of transonic compressors using a time-marching finite volume solver. In: Chattanooga: 13th international symposium on airbreathing engines (ISABE)
9. Stridh M, Eriksson LER (2004) Modeling unsteady flow effects in a 3-D transonic compressor. Ph.D. thesis, Vrije: University Brussel
10. Li XJ, Jin HL, Gui XMJ (2009) Performance numerical investigation of double channel fan/compressor. J Aerosp Power 24(12):2719–2726
11. Simon JF, Thomas JP, Leonard OC (2005) A throughflow analysis tool based on the Navier-Stokes Equations. In: Lille: proceeding of the 6th European turbomachinery conference
12. Lu JC, Meng QG, Zhou SJ (1999) Time-marching method for thoughflow computation of turbomachinery. J Aerosp Power 14(1):23–26
13. Jin HLD (2013) Application of circumferentional average method in multistage axial fan/compressor design and analysis. Ph.D. thesis, Beihang University, Beijing
14. Wan KR (2014) Modeling and application of circumferentially averaged method in turbomachinery: RM 3509. Ph.D. thesis, Beihang University, Beijing
15. Wu DRD (2019) Throughflow modeling and validation of multistage axial flow compressors. Ph.D. thesis, Shanghai Jiao Tong University, Shanghai
16. Yang GJ, Wang CX, Wang DLJ (2017) Time marching based throughflow method: Current status and future development[J]. Acta Aeronautica et Astronautica Sinica 38(09):63–75
17. Marble FJ (1964) Three-dimensional flow in turbomachines. High Speed Aerodyn Jet Propul 10:83–166
18. Damle SV, Dang TQ, Reddy DRJ (1997) Throughflow method for turbomachines applicable for all flow regimes. J Turbomach 119(2):256–262
19. Persico G, Rebay SJ (2012) A penalty formulation for the throughflow modeling of turbomachinery. Comput Fluids 60(10):86–98
20. Bosman C, Marsh HJ (1974) An improved method for calculating the flow in turbomachines, including a consistent loss model. J Mech Eng Sci 16:25–31

Rotating Beamforming in the Frequency Domain for an Incomplete Microphone Array

Mengxuan Li, Wei Ma, and Wei Zhou

Abstract As society developed expeditiously, more attentions have been paid towards harm of noise. Thus beamforming technology based on phased microphone array is widely used in rotating acoustic source localization. In this paper, a ring microphone array is placed parallel to the scanning plane with the array located on the z-axis. However, the microphone and the rotating part are not allowed to be too close for the potential suction danger caused by the rotating part. At present, this problem has not been solved in engineering.

This paper proposes a new method to measure the rotating parts safely by a ring microphone array with a large enough diameter. The diameter of the array is too large more than twice the distance from the array center to the ground. Hence, some microphones cannot be installed. In this paper, the symmetry of the ring array perpendicular to the ground is taken as the center. Moreover, an odd number reduces the number of microphones in turn. Then, the positions and levels of the maximum sound are compared with the previous case which does not reduce the microphones by observing the beamforming result.

When reducing the total number of microphones by less than a quarter, the resolution of the beamforming result decreases gradually while the maximum sound strength increases, and the position of the maximum sound pressure moves slightly. The deviation of the maximum acoustic pressure position can be ignored, and the change of the maximum sound pressure level is very small.

M. Li · W. Ma (✉) · W. Zhou
School of Mechanical and Power Engineering, Shanghai Jiao Tong, University, 800 Dongchuan Road, Shanghai 200240, China
e-mail: mawei@sjtu.edu.cn

School of Aeronautics and Astronautics, Shanghai Jiao Tong University, 800 Dongchuan Road, Shanghai 200240, China

M. Li
e-mail: limengxuan@sjtu.edu.cn

W. Zhou
e-mail: ZW_SJTU@sjtu.edu.cn

Z. Jing and X. Zhan (eds.), *Proceedings of the International Conference on Aerospace System Science and Engineering 2020*, Lecture Notes in Electrical Engineering 680,
https://doi.org/10.1007/978-981-33-6060-0_25

Keywords Rotating acoustic source positioning · Circular array · Symmetrically reducing microphone

1 Introduction

With the development of imaging algorithms, rotating beamforming technology has been widely used in acoustic source recognition as a sound field visualization technology [1]. The current mature rotating beamforming technology includes time domain algorithms [2] and frequency domain algorithms [3]. We know that the motion of the sound source will bring the Doppler effect [2].The frequency domain algorithm solves the Doppler effect by constructing a virtual microphone array that rotates at the same speed as the sound source [4]. The sound pressure of the virtual rotating microphone is obtained by Fourier interpolation which use the sound pressure measured by the real microphone [5, 6]. Frequency domain algorithms are more widely used because of their short computation time [7–10] and their ability to be further combined with deconvolution techniques to improve resolution [11–13]. Although the frequency domain algorithm has great advantages, it requires the ring microphone array center to be directly opposite to the rotating acoustic source center [14, 15]. The rotating part's speed in the project is relatively high, and the suction force generated is very large. Therefore, for safety reasons, it is often not allowed to place the microphone array directly opposite. How to use the ring microphone array to measure the sound pressure to locate the acoustic source has become a problem in the project, and it has not been well solved.

In this article, we use a larger diameter microphone. The microphone arraycenter is still in the right position, but the distance from microphone to the rotating part reaches a safe distance, so the measurement can be use. If the diameter is too large to more than twice the distance from the microphone array center to the ground, then some microphones cannot be installed and the ring microphone array is incomplete. The frequency domain algorithm is used to obtain the beamforming result of the symmetrically deleted microphone.The result obtained by the complete ring microphone array is compared with the deleted microphone in maximum intensity and position of the acoustic source.

The rest of paper is divided into three sections. The Sect. 2 introduces the rotating beamforming algorithm and the cross-complementary matrix using Fourier interpolation. The Sect. 3 introduces the simulation experiment results. The conclusions are given in Sect. 4.

2 Methodology

2.1 Review of Beamforming

As shown in Fig. 1, suppose the total number of microphones is M and the spherical coordinate vector of the microphone is $x_m = (r_{xm}, \varphi_{xm}, \theta_{xm})$, $m = 1, 2, 3, \ldots, M$.The total number of grid points on the scanning plane is S and the spherical coordinate vector of the grid points is $\mathbf{y}_s = (r_{ys}, \varphi_{ys}, \theta_{ys}), s = 1, 2, 3, ..., S$. The sound source rotation angle frequency is Ω and the sound source frequency is ω. Calculate the sound pressure in the frequency domain in a rotating coordinate system:

$$p_\Omega(m, \omega) = \sum_{m_0=-\mathrm{M}/2+1}^{\mathrm{M}/2} p_{m_0}(\omega + m_0\Omega)\mathrm{e}^{\mathrm{i}m_0\varphi_{xm}} \tag{1}$$

$p_{m_0}(\omega+m_0\Omega)$ is the rotational modal coefficient. m_0 is the order of circumferential mode. $p_\Omega(m, \omega)$ represents the sound pressure in the rotating coordinate system of the MTh microphone $\mathrm{i}^2 = -1$.

$$p_{m_0}(\omega) = \frac{1}{M}\sum_{m=1}^{M} p(m, \omega)\mathrm{e}^{-\mathrm{i}m_0\varphi_{xm}} \tag{2}$$

$$p(m, \omega) = \sum_{n=0}^{N_s} p(m, t_n)\mathrm{e}^{-\mathrm{i}\omega t_n} \tag{3}$$

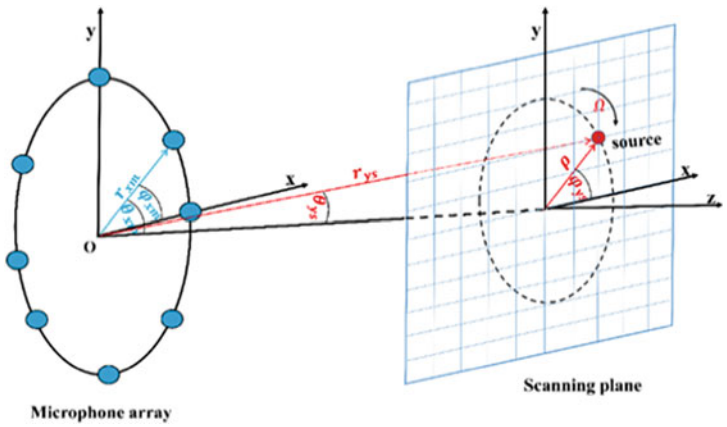

Fig. 1 Schematic

$p(m, \omega)$ and $p(m, t_n)$ respectively represent the frequency and time domain sound pressure collected by the MTh microphone. The range of circumferential modal orders is m_0. t_n is sampling time. N_s indicates the number of samples. Calculate the cross-spectral matrix is $\mathbf{C}_\Omega \in \mathbb{C}^{M\times M}$

$$\mathbf{C}_\Omega = \mathbf{p}_\Omega(\omega)(\mathbf{p}_\Omega(\omega))^{\mathrm{H}} \tag{4}$$

$$\mathbf{p}_\Omega(\omega) = [p_\Omega(1, \omega), \ldots, p_\Omega(m, \omega), \ldots, p_\Omega(M, \omega)]^{\mathrm{T}} \tag{5}$$

Next, calculate the steering vector SV-MD in the rotating coordinate system: regardless of the influence of axial inflow, the free field Green's function of the single-stage in the rotating coordinate system can be obtained by the spherical harmonic function.

$$\begin{aligned} G_\Omega(m, s) = -\mathrm{i} \sum_{m_0=-\infty}^{+\infty} \mathrm{e}^{\mathrm{i}m_0(\varphi_{xm}-\varphi_{ys})} k_{m_0} \\ \sum_{n=|m_0|}^{+\infty} N_{m_0 n}^2 b_n(r_{xm}, r_{ys}) P_n^{|m_0|}(\cos(\theta_{xm})) P_n^{|m_0|}(\cos(\theta_{ys})) \end{aligned} \tag{6}$$

The acoustic wave propagation Green's function matrix $\mathbf{G}_\Omega$ can be written as

$$\begin{aligned} \mathbf{G}_\Omega &= \left[\mathbf{G}_\Omega(1) \cdots \mathbf{G}_\Omega(s) \cdots \mathbf{G}_\Omega(S) \right] \\ &= \begin{bmatrix} G_\Omega(1,1) & \cdots & G_\Omega(1,s) & \cdots & G_\Omega(1,S) \\ \vdots & & \vdots & & \vdots \\ G_\Omega(m,1) & \cdots & G_\Omega(m,s) & \cdots & G_\Omega(m,S) \\ \vdots & & \vdots & & \vdots \\ G_\Omega(M,1) & \cdots & G_\Omega(M,s) & \cdots & G_\Omega(M,S) \end{bmatrix} \end{aligned} \tag{7}$$

Calculate the steering vector matrix

$$\mathbf{W}_\Omega = [\mathbf{W}_\Omega(1) \cdots \mathbf{W}_\Omega(s) \cdots \mathbf{W}_\Omega(s)]^{\mathrm{T}} \tag{8}$$

In the formula

$$\mathbf{W}_\Omega(s) = \frac{\mathbf{G}_\Omega(s)}{\|\mathbf{G}_\Omega(s)\|_2^2} \tag{9}$$

In order to mitigate the interference of irrelevant environmental noise or electromagnetic self-inductance noise in the experiment, it is necessary to remove the diagonal elements of the cross-spectral matrix, thereby improving the dynamic range of sound source recognition. At this time, the corresponding steering vector calculation

formula is

$$\mathbf{W}_{\Omega}(s) = \frac{\mathbf{G}_{\Omega}(s)}{\sqrt{\sum_{(p,q)\in F} |G_{\Omega}(p,s)|^2 |G_{\Omega}(q,s)|^2}} \quad s = 1, 2, 3, \ldots, S \tag{10}$$

where the collection $F = \{(p,q)|1 \le p \le M, 1 \le q \le M, p \ne q\}$.
Finally calculate the beamforming result

$$\mathbf{b} = \left[b(1) \ \ldots \ b(s) \ \ldots \ b(S) \right]^{\mathrm{T}} \tag{11}$$

Among them

$$b(s) = (\mathbf{W}_{\Omega}(s))^{\mathrm{H}} \mathbf{C}_{\Omega} \mathbf{W}_{\Omega}(s) \tag{12}$$

2.2 Review of CSM-MD

The complex sound pressure at the MTh VRA microphone is

$$p_v(m, \omega) = \sum_{m_0 = -\frac{M}{2}+1}^{\frac{M}{2}} Am_0(\omega + m_0\Omega) e^{i m_0 \phi_{xm}} \tag{13}$$

where m_0 is index of mode, $A_{m_0(\omega)}o$ is the spinning mode coefficient and

$$Am_0(\omega) = \frac{1}{M} \sum_{m=1}^{M} p(m, \omega) e^{-i m_0 \phi_{xm}}, \quad -\frac{M}{2} + 1 \le m_0 \le \frac{M}{2}$$

where p(m, ω) is the complex sound pressure at the mth real microphone. The CSM calculated from the pressure in Eq. (13) is denoted by CSM-MD [16].

3 Numerical Simulation

The sound source is a single-stage sub-source.The sound source position coordinates are (9, 30).The-scanning plane is a square of 0.5 m × 0.5 m. The number of grids is 61 × 61. An annular array of 40 microphones distributed uniformly was used to record the pressure of the obtained rotating sound source. The measurement plane

is parallel to the source plane and the distance between them is 1 m. The study was conducted at a sound source frequency of 2780 Hz.

3.1 Array Schematic and Beamforming Results

In a ring microphone array with 40 microphones evenly distributed, the central axis perpendicular to the horizontal plane is used as the axis of symmetry and the microphones are removed at the left and right sides. The number of microphones removed is 1, 3,5,7,9. Obtain the array diagram and beamforming result after removing the microphone in turn. As shown in Fig. 2.

Analysis and comparison of the above results show that as the number of microphones decreases, the resolution of beamforming results decreases and the dynamic performance deteriorates.

3.2 Maximum Sound Pressure Position Coordinates and Sound Pressure

We use the ranks of the grid of the scanning plane where the acoustic source is located as the position coordinates of the loud sound pressure. Take the central axis of the ring microphone array perpendicular to the horizontal plane as the axis of symmetry and remove the microphone at the same time on the left and right sides. The number of microphones removed is 1,3,5,7,9,11. The position coordinates of the maximum sound pressure and the size of the maximum sound pressure are shown in Table 1.

The size of a grid on the scanning plane is 0.0167 m $\times$ 0.0167 m. Rows and columns move within three grids (0.05 m) are all very small changes, it can be ignored. Analyzing the data in the table, it can be seen that as the number of microphones decreases, the coordinates of the maximum sound pressure change, but the change is very small and can be ignored. As the number of microphones decreases, the size of the maximum sound pressure increases gradually and the increase is also a comparative range. To sum up, the reduction of symmetric microphones has little effect on the results of beamforming. The position is negligible, and the size is slightly increased.

4 Conclusion

This article proposes the idea of increasing the diameter of the ring microphone array to a safe distance. This idea solves the safety problem that engineering does not allow the circular microphone array to be placed directly opposite the center of the rotating

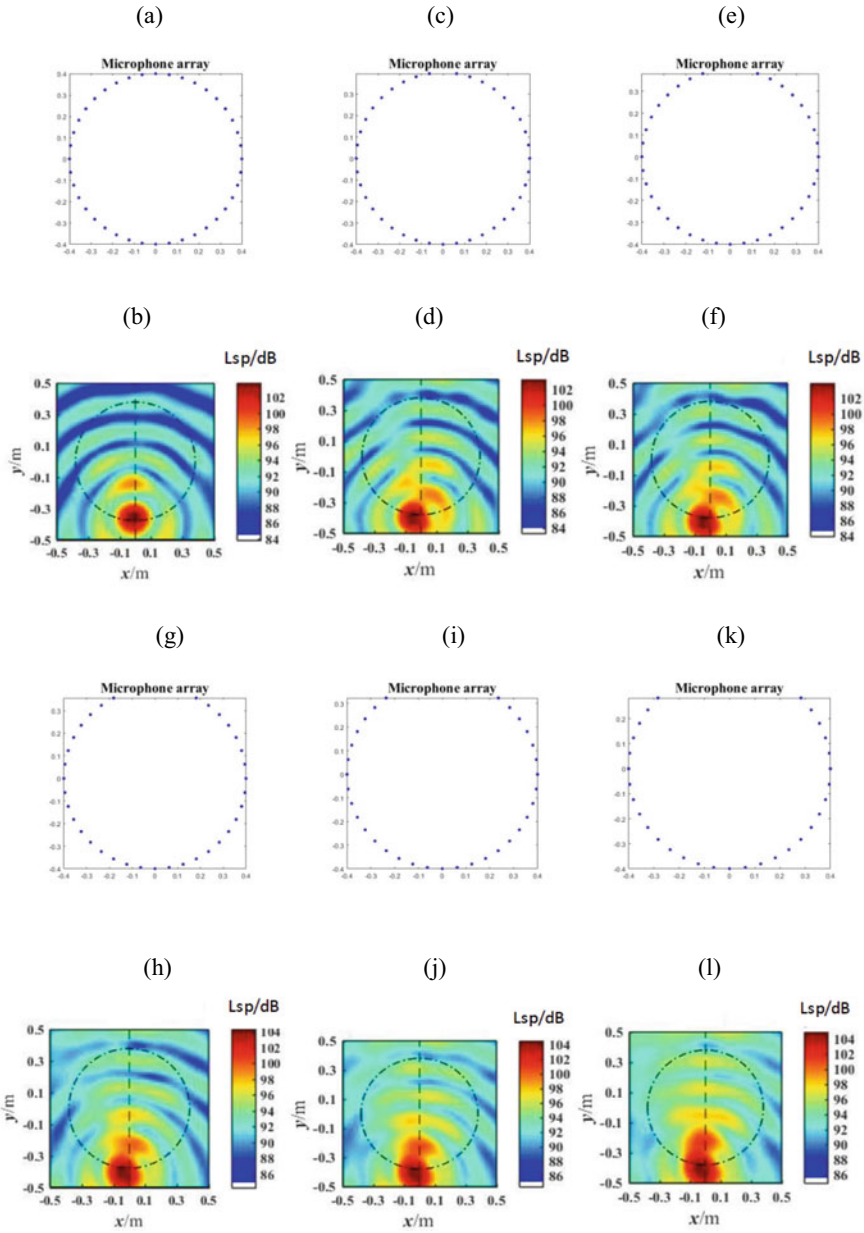

Fig. 2 **a** Microphone array distribution without microphone reduction **b** Beamforming results without microphone reduction **c** Microphone array distribution with one microphone reduction **d** Beamforming results with one microphone reduction **e** Three microphones reduction Microphone array distribution **f** Beamforming results when three microphones are reduced **g** Microphone array distribution when five microphones are reduced **h** Beamforming result when five microphones are reduced **i** Microphone array distribution when seven microphones are reduced **j** Microphone array distribution when reducing nine microphones **k** Beamforming results when reducing nine microphones

Table. 1 Location and maximum pressure changes with decreasing microphones

Reduce the number of microphones	0	1	3	5	7	9	11
acoustic source position coordinates	(9,30)	(7,27)	(6,28)	(6,28)	(6,28)	(6,29)	(6,29)
Maximum sound pressure (dB)	103.8466	103.3418	103.9480	104.3046	104.581	104.9002	105.3650

part. in order to ensure that the ring microphone array is not directly opposed to rotating part center for safety in engineering. Because the ring microphone array diameter is greater than twice the height from the array center to the ground, a ring microphone array is incomplete and some microphones lack symmetry. After calculation, when a ring array with 40 microphones is missing less than 11 microphones, as the number of microphones decreases, the resolution of beamforming decreases, the dynamic performance deteriorates. The location of the localized sound source changes little, so can be ignored. The maximum sound pressure has a slight increase and the increase range is within 2 dB.

References

1. Zeng Y,Hendriks RC (2014) "Distributed delay and sum beamformer for speech enhancement via randomized gossip." IEEE/ACM Trans Audio Speech Lang Process. https://doi.org/10.1109/taslp.2013.2290861
2. Sijtsma P (2010) "Phased array beamforming applied to wind tunnel and fly-over tests." SAE Technical Paper, 0148–7191
3. Pannert W, Maier C (2014) "Rotating beamforming—motion-compensation in the frequency domain and application of high-resolution beamforming algorithms." J Sound Vib. https://doi.org/10.1016/j.jsv.2013.11.031
4. Heo YH, Ih JG, BodénH (2015) "In-duct identification of a rotating sound source with high spatial resolution." J Sound Vib. https://doi.org/10.1016/j.jsv.2015.07.015
5. Lowis CR, Joseph PF (2006) "A focused beamformer technique for separating rotor and stator-based broadband sources."12th AIAA/CEAS aeroacoustics conference AIAA 2006–2710
6. Lowis CR, JosephPF (2006) "Determining the strength of rotating broadband sources in ducts by inverse methods." J Sound Vib. https://doi.org/10.1016/j.jsv.2006.01.031
7. Zhong S, Wei Q, Huang X (2013) "Compressive sensing beamforming based on covariance for acoustic imaging with noisy measurements." J Acoust Soc Am. https://doi.org/10.1121/1.4824630
8. Ma W, LiuX (2018) "Compression computational grid based on functional beamforming for acoustic source localization." Appl Acoust. https://doi.org/10.1016/j.apacoust.2018.01.006
9. Ma W, Liu X (2019) "Phased microphone array for sound source localization with deep learning." Aerosp Syst. https://doi.org/10.1007/s42401-019-00026-w
10. Ma W, LiuX (2017) "Improving the efficiency of DAMAS for sound source localization via wavelet compression computational grid." J Sound Vib. https://doi.org/10.1016/j.jsv.2017.02.005

11. Ma W,Liu X (2017) “DAMAS with compression computational grid for acoustic source mapping.” J Sound Vib. https://doi.org/10.1016/j.jsv.2017.03.027
12. Brooks TF,Humphreys WM (2006) “A deconvolution approach for the mapping of acoustic sources (DAMAS) determined from phased microphone arrays.” J Sound Vib. https://doi.org/10.1016/j.jsv.2005.12.046
13. FischerJ, Doolan C (2017) “Improving acoustic beamforming maps in a reverberanr environment by modifying the cross-correlation matrix.” J Sound Vib. https://doi.org/10.1016/j.jsv.2017.09.006
14. Yu W,Xun H (2018) “Reconstruction of aircraft engine noise source using beamforming and compressive sensing.” IEEE Access. https://doi.org/10.1109/ACCESS.2018.2801260
15. Tóth B, Kalmár-Nagy T, Vad J (2018) “Rotating beamforming with uneven microphone placements.” BeBeC, C D23
16. Ma W, Bao H, Zhang C, Liu X (2020) “Beamforming of phased microphone array for rotating sound source localization.” J. Sound Vib https://doi.org/10.1016/j.jsv.2019.115064

Comprehensive BDS-3 Signal Simulating for Strong Ionospheric Scintillation Studies

Jihong Huang, Xingqun Zhan, and Rong Yang

Abstract The construction of BeiDou Global Navigation Satellite System (BDS-3) is near complete and ready to provide worldwide navigation services soon. As compared to other navigation systems, BDS-3 has superiority that it is the first navigation system fully broadcast triple band signals and utilizes more advanced modulation, i.e. Binary-Offset-Carrier (BOC) modulation to achieve the enhanced accuracy and anti-interference performances. BDS-3 will play an important role in various high precision navigation applications. However, strong ionosphere scintillation will pose a great threat to GNSS accuracy and robustness and BDS-3 has no exceptions. Strong ionospheric scintillations will cause severe signal fluctuations, i.e. simultaneous deep amplitude fading and fast phase fluctuations. It will deteriorate the range measurement accuracy, affect the PNT (positioning, navigation, and timing) performances, and even destroy receiver functioning in some extremely cases. Therefore, the investigation of ionospheric scintillation effects on GNSS signals, especially on novel BDS-3 signals are quite necessary. In this paper, a comprehensive study of a strong scintillation BDS simulator will be carried on the basis of an open source GPS scintillation simulator provided by the SenSe Lab in University of Colorado Boulder using the two-dimensional two-component power-law phase screen theory. The BOC modulation is implemented and integrated in the simulator, so that the raw data of six BDS scintillation signals on three frequency bands, i.e. B1I, B1C (data + pilot), B2a (data + pilot), and B3I are simulated for test. To validate the effectiveness of the signal simulator, the realistic BDS scintillation data was collected, analyzed, and compared with the simulator outputs. The comprehensive simulator presented in this paper will be a tool to facilitate the ionospheric studies as well as advanced GNSS receiver development in future.

J. Huang (✉) · X. Zhan · R. Yang
Shanghai Jiao Tong University, Shanghai, China
e-mail: jihong.huang@sjtu.edu.cn

X. Zhan
e-mail: xqzhan@sjtu.edu.cn

R. Yang
e-mail: rongyang@sjtu.edu.cn

Z. Jing and X. Zhan (eds.), *Proceedings of the International Conference on Aerospace System Science and Engineering 2020*, Lecture Notes in Electrical Engineering 680,
https://doi.org/10.1007/978-981-33-6060-0_26

Keywords Ionospheric scintillation simulator · Phase screen theory · BDS · IF signal simulation · BOC

1 Introduction

Ionospheric scintillation refers to the random amplitude and phase fluctuations observed in radio signals propagating through electron density irregularities in the ionospheric plasma, which most commonly occurs in low-altitude, auroral, and polar regions [1, 2, 24, 12, 14]. These combined effects degrade GNSS receiver carrier tracking performance in terms of increased errors, carrier phase cycle slips, and even loss of lock [13]. Therefore, the investigation of ionospheric scintillation effects on GNSS signals are quite necessary. The intermediate-frequency (IF) data with strong scintillation are required for the study of ionospheric scintillation effects and the development of receivers that can mitigate the ionospheric effects. Although in recent years, the availability of real scintillation IF data collecting is increasing [12, 16, 22], it is still difficult to obtain realistic scintillations with the specific characteristics, because the occurrence of scintillation is difficult to predict. Besides, the cost of real data collection and storage are expensive. Hence, the scintillation simulator will be a useful tool for developing and testing the advanced receiver designs.

Two types of approaches of GPS scintillation simulators have been developed in the past decades, which can be an important guidance for the design of BDS scintillation simulators. The first type is based on the physic models of signal wave propagation through the ionospheric irregularities. The well-known two-component power-law phase screen model (TPPSM) has been studied in [17, 20, 3]. In this theory, the interference to GNSS signal caused by the scintillation is modeled as an extremely thin screen, and the signal phase will be changed after the signal transmit through the screen. To calculate the propagation geometry and the propagation signal's ionospheric piercing point (IPP) scan velocity precisely, a large number of parameters are required for the physics-based models, which bring a cumbersome computational burden. To solve this problem, a compact TPPSM was introduced in [19], where a space-to-time scaling parameter (ρ_F / v_{eff}) was introduced to absorb all dependency on the propagation geometry and IPP scan velocity. The scaling parameter (ρ_F / v_{eff}), together with a strength parameter (U), and three spectral parameters (p_1, p_2, μ_0), form a set of parameters to define the scintillation model. Given a segment of real scintillation data, an irregularity parameter estimation (IPE) method developed in [3, 4] can extract the values of the entire parameter set to generate statistically equivalent scintillation effects. The second type is solely based on the statistics of scintillation signals. Statistical models are parameterized by a small number of scintillation indicators, which simplify the scintillation effects as a stochastic process [5, 10, 11]. This type is straightforward and simple to configure, but there is still room for improvement of simulation accuracy [19]. Recently, the SenSe Lab in University of Colorado Boulder has developed a hybrid simulator that takes advantages of the both types.

It is an open source simulator and can realize the GPS triple frequency scintillation simulation as can be found in [21] (https://github.com/cu-sense-lab/gnss-scintillation-simulator_2-param).

Although the simulator for GPS signal scintillation has been well developed, the BeiDou Navigation Satellite System (BDS) signal scintillation has not been fully investigated in the existing research. The reason is that BDS is a new navigation system built by the Chinese government to provide all-time, all-weather and high-accuracy positioning, navigation and timing services to global users. As of 2020, the construction of BDS-3 system will be finished and start to provide services in worldwide. It is known that BDS-3 is the first navigation system fully broadcast triple band signals i.e., B1, B2, B3. BDS-3 has the specific diversity and novelty on signal structures, navigation bit modulations, satellite operation orbits, etc. BDS has various kinds of orbits, including Middle Earth Orbit (MEO), Geostationary Orbit (GEO) and Inclined Geosynchronous Orbit (IGSO), which extend the service coverage aera. It also applies Complex Binary-Offset-Carrier (BOC) modulation, which can improve the signal quality. It is worthy to build a BDS signal scintillation simulator to study the physical mechanism and effects of ionosphere scintillation so as to develop anti-scintillation receivers and in-depth study of the ionospheric disturbances.

In this paper, a two-parameters, physic-based, strong scintillation BDS-3 signal simulator will be presented based on the routine of GPS scintillation simulator provided by the SenSe Lab with TPPSM scintillation signal simulation. Complex BOC modulation will be implemented and integrated to generate BDS IF signals, and six BDS signals on three frequency bands, i.e. B1I, B1C (data + pilot), B2a (data + pilot), and B3I with scintillation effects will be simulated. To validate the effectiveness of the signal simulator, the realistic BDS scintillation data collected by the SenSe Lab will be analyzed and compared with the simulator outputs.

The organization of this paper is as follows. Section 2 introduces BDS civil signal structures, Sect. 3 describes simulator architecture and phase screen realization, Sect. 4 shows simulation results and results validation, Sect. 5 is the summary and outlook of this paper.

2 BDS Civil Signal Architecture

The knowledge of the signal structure of BDS signals is fundamental to the work covered in this paper. Generating simulated BDS scintillation signals requires the modulation of BDS signal samples using simulated scintillation amplitude and phase realizations. This section summarizes the major structures of the four BDS civil signals, e.g. B1I, B3I, B2a, and B1C that are currently available from the BD satellites. There are mainly three components in transmitted BDS signals: pseudo-range noise (PRN) code sequence, which is unique to each satellite, navigation massage, and RF carrier wave. Only PRN code and RF carrier wave are considered in the current version of simulator. For different civil signals on different bands, the frequencies and

generation methods of three components are different. The following content will elaborate signal constructions on four BDS civil bands. Most details can be found in the interface control documents (ICDs) published at http://www.beidou.gov.cn/.

2.1 BDS B1I Signal

The time domain representation of the signals on B1I is expressed as follows (BDS B1I ICD 2019):

$$S^m_{B1I}(t) = A_{B1I} C^m_{B1I}(t) D^m_{B1I}(t) \cos\left(2\pi f_1 t + \varphi^m_{B1I}\right) \tag{1}$$

where,

superscript m	satellite number;
A_{B1I}	amplitude of B1I;
C_{B1I}	ranging code of B1I;
D_{B1I}	data modulated on ranging code of B1I;
f_1	carrier frequency of B1I;
φ_{B1I}	carrier initial phase of B1I

The nominal carrier frequency of the B1I signal is 1561.098 MHz, the modulation mode is Binary Phase Shift Keying (BPSK), and the signal bandwidth is 4.092 MHz (centered at carrier frequency).

The chip rate of the B1I ranging code is 2.046 Mcps, and the code length is 2046 chips. The range code is generated by truncating a balanced Gold code with the last one chip, and more details of B1I ranging code generation can be found in ICDs (BDS B1I ICD 2019).

2.2 BDS B3I Signal

The time domain representation of the signals on B3I is expressed as follows (BDS B3I ICD 2018):

$$S^m_{B3I}(t) = A_{B3I} C^m_{B3I}(t) D^m_{B3I}(t) \cos\left(2\pi f_3 t + \varphi^m_{B3I}\right) \tag{2}$$

Similarly,

superscript m	satellite number;
A_{B3I}	amplitude of B3I;
C_{B3I}	ranging code of B3I;
D_{B3I}	data modulated on ranging code of B3I;
f_3	carrier frequency of B3I;

φ_{B3I} carrier initial phase of B3I

The nominal carrier frequency of the B3I signal is 1268.520 MHz, the modulation mode is BPSK, and the signal bandwidth is 20.46 MHz (centered at carrier frequency).

The chip rate of the B1I ranging code is 10.23 Mcps, and the code length is 10230 chips. The range code is generated by truncating a Gold code which is the result of truncating and XORing two linear sequences, and more details of B3I ranging code generation can be found in ICDs (BDS B3I ICD 2018).

2.3 BDS B2a Signal

The complex envelope of B2a is expressed as follows (BDS B2a ICD [6]:

$$s_{B2a}(t) = s_{B2a_{data}}(t) + j s_{B2a_{pilot}}(t) \tag{3}$$

where the data component $s_{B2a\_data}(t)$ is generated from the navigation message data $D_{B2a\_data}(t)$ modulated with the ranging code $C_{B2a\_data}(t)$, while the pilot component $s_{B2a\_pilot}(t)$ contains the ranging code $C_{B2a\_pilot}(t)$ only. They both adopt BPSK modulation and have a same carrier frequency at 1176.45 MHz. The power ratio of the data component to the pilot component is 1:1. The expressions of these two components are shown below:

$$s_{B2a_{data}}(t) = \frac{1}{\sqrt{2}} D_{B2a_{data}}(t) \cdot C_{B2a_{data}}(t) \tag{4}$$

$$s_{B2a_{pilot}}(t) = \frac{1}{\sqrt{2}} C_{B2a_{pilot}}(t) \tag{5}$$

where C_{B2a_data} and C_{B2a_pilot} are the ranging code of the corresponding components with the same code length of 10,230, and the chip rate of the B2a ranging code is 10.23 Mbps; D_{B2a_data} is the data modulated on ranging code of data component.

Table 1 shows the components of the B2a signal as well as the modulation, phase relationship and power ratio of each component.

The B2a ranging codes are the tiered codes which are generated by XORing the primary codes with secondary codes. The chip width of the secondary code has the same length as one period of a primary code, and the start of a secondary code

Table 1 Modulation characteristics of the B2a signal (BDS B2a ICD 2017)

Component	Modulation	Phase relationship	Power ratio
$s_{B2a\_data}(t)$	BPSK(10)	0	1/2
$s_{B2a\_pilot}(t)$	BPSK(10)	90	1/2

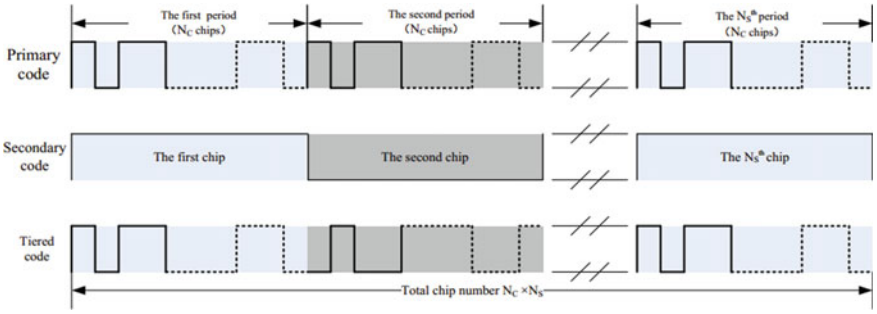

Fig. 1 Timing relationships of the primary code and secondary code (BDS B2a ICD 2017)

Table 2 Characteristics of the B2a ranging codes (BDS B2a ICD 2017)

Signal component	Primary code type	Primary code length (chip)	Primary code period (ms)	Secondary code type	Secondary code length (chip)	Secondary code period (ms)
B2a data component	Gold	10230	1	Fixed sequence	5	5
B2a pilot component	Gold	10230	1	Truncated Weil	100	100

chip is strictly aligned with the start of the first chip of a primary code. The timing relationships are shown in Fig. 1.

The characteristics of the B2a ranging codes are shown in Table 2.

More details of B2a ranging code generation can be found in ICDs (BDS B2a ICD [7]).

2.4 BDS B1C Signal

The complex envelope of B1C is expressed as follows (BDS B1C ICD [8]):

$$s_{B1C}(t) = s_{B1C_{data}}(t) + js_{B1C_{pilot}}(t) \tag{6}$$

where, the $s_{B1C\_data}(t)$ is the data component, which is generated from the navigation message data $D_{B1C\_data}(t)$ and the ranging code $C_{B1C\_data}(t)$ modulated with the sine-phased BOC(1,1) subcarrier $sc_{B1C\_data}(t)$. $s_{B1C\_pilot}(t)$ is the pilot component, which is generated from the ranging code $C_{B1C\_pilot}(t)$ modulated with the QMBOC(6,1,4/33) subcarrier $sc_{B1C\_pilot}(t)$. The power ratio of the data component to the pilot component is 1:3. The expressions of the two components are as follows:

$$s_{B1C_{data}}(t) = \frac{1}{2} D_{B1C_{data}}(t) \cdot C_{B1C_{data}}(t) \cdot sc_{B1C_{data}}(t) \tag{7}$$

$$s_{B1C_{pilot}}(t) = \frac{\sqrt{3}}{2} C_{B1C_{pilot}}(t) \cdot sc_{B1C_{pilot}}(t) \tag{8}$$

where,C_{B1C_data} and C_{B1C_pilot} are the ranging code of the corresponding components with the same code length of 10,230, and the chip rate of the B1C ranging code is 1.023 Mbps; D_{B2a_data} is the data modulated on ranging code of data component.

The B1C data component subcarrier $sc_{B1C\_data}(t)$ is expressed as:

$$sc_{B1C_{data}}(t) = sign\left(\sin\left(2\pi f_{sc_{B1C_a}} t\right)\right) \tag{9}$$

where $f_{sc\_B1C\_a}$ is 1.023 MHz.

The B1C pilot component subcarrier $sc_{B1C\_pilot}(t)$ is the QMBOC (6,1,4/33) composite subcarrier. It is composed of a BOC (1,1) subcarrier and a BOC(6,1) subcarrier, which are in phase quadrature with each other and have a power ratio of 29:4. The expression of $sc_{B1C\_pilot}(t)$ is defined as follows:

$$\begin{aligned} sc_{B1C_{pilot}}(t) = & \sqrt{\frac{29}{33}} sign\left(\sin\left(2\pi f_{sc_{B1C_a}} t\right)\right) \\ & - j\sqrt{\frac{29}{33}} sign\left(\sin\left(2\pi f_{sc_{B1C_b}} t\right)\right) \end{aligned} \tag{10}$$

where $f_{sc\_B1C\_b}$ is 6.138 MHz.

Table 3 shows the components of B1C signal as well as the modulation, phase relationship and power ratio of each component.

The B1C ranging codes are the tiered codes which are generated by XORing the primary codes with secondary codes. The timing relationships of the primary code and secondary code are the same with B2a which has been shown in Fig. 1. The characteristics of the B1C ranging codes are shown in Table 4.

More details of B1C ranging code generation can be found in ICDs (BDS B1C ICD [9]).

Table 3 Modulation characteristics of the B1C signal (BDS B1C ICD 2017)

Component	Modulation		Phase relationship	Power ratio
$s_{B1C\_data}(t)$	Sine BOC(1,1)		0	1/4
$s_{B1C\_pilot\_a}(t)$	QMBOC(6,1,4/33)	Sine BOC(1,1)	90	29/44
$s_{B1C\_pilot\_b}(t)$		Sine BOC(6,1)	0	1/11

Table 4 Characteristics of the B1C ranging codes (BDS B1C ICD 2017)

Signal component	Primary code type	Primary code length (chip)	Primary code period (ms)	Secondary code type	Secondary code length (chip)	Secondary code period (ms)
B1C data component	Truncated Weil	10230	10	N/A	N/A	N/A
B1C pilot component	Truncated Weil	10230	10	Truncated Weil	1800	18000

3 Simulator Architecture and Phase Screen Realization

This section presents the development of the two-parameter scintillation simulator. A brief summary of the scintillation signal simulator routine will be given first, which shows the inputs parameters, architecture and outputs of the simulator. Secondly, a detailed explanation of the phase screen realization step and the wave propagation step in this simulator will be described. Thirdly, this section will show the operation of extracting scintillation generator input parameters from the ground observed scintillation indicators. The work of this section is mainly based on the research of GPS scintillation simulator from SenSe Lab [21], and innovations for BDS signal simulation will be emphasized.

3.1 Scintillation Signal Simulator Routine Description

This subsection describes the architecture of the two-parameters, physic-based scintillation signal simulator. This simulator is developed based on the compact TPPSM theory, which is specified by five parameters $\{U, p_1, p_2, \mu_0, \rho_F/v_{eff}\}$ as mentioned in Sect. 1. In (Carrano and Rino 2016), $\{U, \rho_F/v_{eff}\}$ were shown numerically to be more closely related to the temporal characteristics of the scintillation signals (i.e. $\{S_4, \tau_0\}$) than the three spectral parameters $\{p_1, p_2, \mu_0\}$. In this simulator, three model parameters $\{p_1, p_2, \mu_0\}$ are set to the defaulted as the representative values. U_0 and ρ_F/v_{eff} can be established through numerical evaluation using the user input parameter set $\{S_4, \tau_0\}$. Therefore, the scintillation simulation model can be simplified and only controlled by user-specified expected S_4 and τ_0.

Figure 2 shows the flow chart of the scintillation signal simulator routine. The scintillation signal simulator is mainly consisting of three parts: the user inputs part, scintillation generator part, and baseband signal generator part, which are outlined with blue, red and green respectively. The following content will introduce these three parts in detail.

The user inputs parameters include three categories: ground observed scintillation indicators, propagation geometric parameters, and baseband signal parameters. The static ground observed scintillation indicators are the S_4 index and intensity decorrelation time τ_0, the derivation of these two parameters from scintillation observation

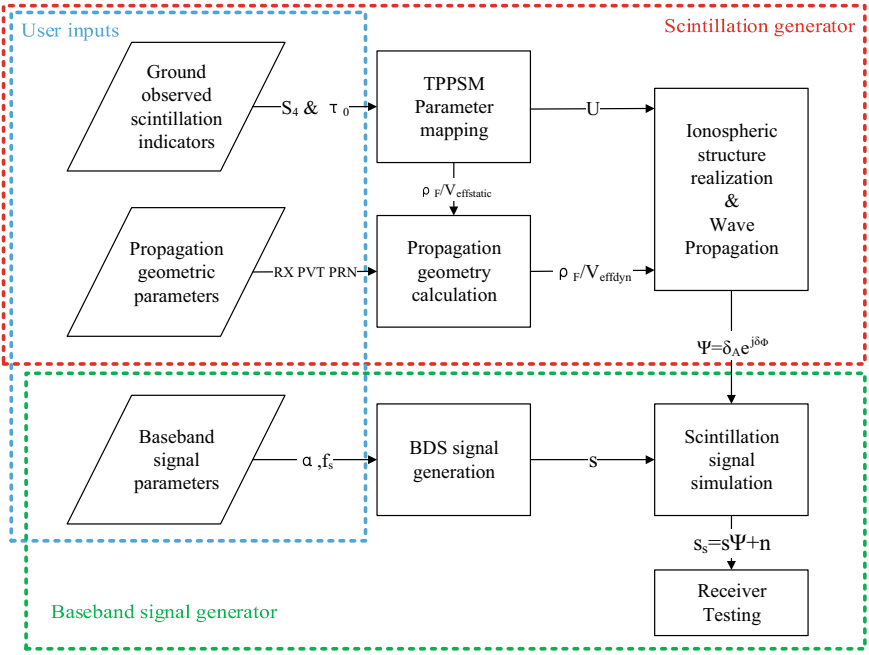

Fig. 2 Flow chart of the scintillation signal simulator (redraw from (Xu 2019))

data will be described in 3.3. The propagation geometric parameters include the platform position, velocity, date and time (PVT), and satellite PRN number. Using the corresponding ephemeris pre-prepared, the satellite orbit is calculated based on the user specified PRN and PVT. The baseband signal parameters are the parameters for a specific BDS signals as mentioned in the Sect. 2, such as carrier frequency, chip rates of ranging code and so on.

The scintillation generator part is outlined with red dashed line in Fig. 2. This is a physics-based, multi-frequency, strong scintillation generator that only require two input parameters: the expected scintillation index S_4 and the intensity decorrelation time τ_0. The user-input $\{S_4, \tau_0\}$ are first converted to $\left\{U, \rho_F/v_{eff_{static}}\right\}$ in the parameter mapping step. The $\rho_F/v_{eff_{static}}$ is the time scaling factor of the static ground observed scintillation and will be used in the propagation geometry calculation step. Both stationary and dynamic receiver platforms can be simulated. For stationary platforms, only the two ground observed scintillation indicators $\{S_4, \tau_0\}$ need to be specified. For dynamics platforms, in addition to the ground observed scintillation indicators, the propagation geometric parameters are also needed to enable the calculation of $\rho_F/v_{eff_{dyn}}$. All the geometric and dynamic dependencies are involved in the calculation of the scaling ρ_F/v_{eff} in the compact TPPSM (Jiao et al. 2018). Then, following the user specified geometry and dynamics embedded in ρ_F/v_{eff}, a plane

wave is propagated through the phase screen realization and the simulated scintillating wave fields at the receiver is $\psi = \delta_A e^{j\delta_\phi}$. More details of the wave propagation step will be given in the next subsection.

The baseband signal generator part modulates the simulated scintillation effects obtained in the last part onto nominal BDS baseband. A general non-scintillating BDS baseband complex signal model can be expressed as the following equation by modifying Eq. (1) [21].

$$s_k = \alpha_k D(k\Delta t - \tau_k) C(k\Delta t - \tau_k) e^{j\phi_k} \tag{11}$$

where k denote the sample number, and Δt stand for the sampling interval. τ_k is the code delay and ϕ_k is the nominal carrier phase delay, respectively? Carrier phase $\phi_k = 2\pi f_{d,k}\Delta t + \phi_{k-1} + \varepsilon_k$, where $f_{d,k}$ is the carrier Doppler frequency, and ε_k is the contribution from various phase noise and error sources except scintillation. Signal amplitude α and sampling rate ($f_s = \frac{1}{\Delta t}$) for the BDS baseband signal generation can be specified. As for the carrier and code phase delays in the baseband signal samples, satellite-receiver geometric range has been yielded to produce them during the propagation geometry calculation. After that the simulated scintillation amplitude ($\delta_{A,k}$) and phase ($\delta_{\phi,k}$) are modulated onto nominal BDS baseband signal s_k to generate scintillation signals as follows [21]:

$$s_{s,k} = s_k \delta_{A,k} e^{j\delta_{\phi,k}} + n_k \tag{12}$$

where n_k represents the thermal noise, which is generated as white Gaussian in this simulator.

In the current version, the simulator ignores the navigation message components and do not considered the scintillation effects on code phase. Therefore, the received scintillation signal samples can then be rewritten as:

$$s_{s,k} = \alpha_k \delta_{A,k} e^{j\delta_{s,k}} + n_k \tag{13}$$

where $\phi_{s,k} = \phi_k + \delta_{\phi,k}$ is the composite carrier phase of the scintillation signal.

3.2 Phase Screen Realization and Wave Propagation

The propagation theory behind the scintillation generator depicted in Fig. 2 was mainly developed in [18] and updated in [19]. This subsection summarizes the fundamental mathematics for the phase screen realization step and the wave propagation step in this simulator. More details can be referred to [18, 19].

As can be seen in Fig. 2, a BDS complex-field scintillation realization can be generated by transforming the inputs parameters $\{S_4, \tau_0\}$ to the TPPSM parameters

$\{U, p_1, p_2, \mu_0, \rho_F/v_{eff}\}$ and the specifying sampling parameters Δt and N. Among the TPPSM parameters, U, μ_0 and ρ_F/v_{eff} are dependent on the signal carrier frequency. The research of [19] show that p_1 and p_2 remain the same for different frequencies, so they can be same for both GPS and BDS signal simulator. To construct the same phase screen for different frequencies, these three parameters can be scaled from one frequency (denoted as the reference frequency f_r) to another (denoted as frequency with scaled parameters f_s) using the following equations [3]:

$$\mu_0(f_s;\, f_r) = \mu_0(f_r)\sqrt{f_r/f_s} \tag{14}$$

$$\frac{\rho_F}{v_{eff}(f_s;f_r)} = \frac{\rho_F}{v_{eff}(f_r)\sqrt{f_r/f_s}} \tag{15}$$

$$U(f_s;\, f_r) = \begin{cases} U(f_r)\left(\frac{f_r}{f_s}\right)^{\frac{1}{2}p_1+\frac{3}{2}}, & if\ \mu_0(f_r) \geq 1, \mu_0(f_s) \geq 1 \\ U(f_r)\mu_0(f_r)^{p_1-p_2}\left(\frac{f_r}{f_s}\right)^{\frac{1}{2}p_1+\frac{3}{2}}, & if\ \mu_0(f_r) < 1, \mu_0(f_s) \geq 1 \\ U(f_r)\mu_0(f_s)^{p_2-p_1}\left(\frac{f_r}{f_s}\right)^{\frac{1}{2}p_1+\frac{3}{2}}, & if\ \mu_0(f_r) \geq 1, \mu_0(f_s) < 1 \\ U(f_r)\left(\frac{f_r}{f_s}\right)^{\frac{1}{2}p_2+\frac{3}{2}}, & if\ \mu_0(f_r) < 1, \mu_0(f_s) \geq 1 \end{cases} \tag{16}$$

More details of Eq. (16) can be referred to (Carrano and Rino [3].

Realistic multi-frequency scintillation with consistent scintillation level and correlated scintillation effects can be generated by the simulator using the Eq. (14) through (16). The inter-frequency consistency of the simulated scintillation is important for the study of multi-frequency scintillation characteristic and the development of multi-frequency receiver algorithms [23].

3.3 *Parameter Estimation*

As mentioned in Sect. 1, IPE technique is used in this paper to extract the TPPSM parameters from real scintillation data. The IPE technique method was developed in [3, 4], and a brief summary is provided as follows.

The IPE technique is essentially an iterative fitting procedure to obtain the TPPSM parameter estimates. The target of this technique is to yield the best match to the intensity spectral density functions (SDF) of the real scintillation data under the least square error criteria. The intensity SDF in the temporal frequency domain theoretically evaluated as follow (Carrano and Rino [3]):

$$\Phi_{I,model}\left(f_D;\, p_1, p_2, \mu_0, U, \frac{\rho_F}{v_{eff}}\right) = I\left(\frac{\mu}{\frac{2\pi\rho_F}{v_{eff}}};\, p_1, p_2, \mu_0, U\right) * \frac{2\pi\rho_F}{v_{eff}} \tag{17}$$

where $I(\mu; p_1, p_2, \mu_0, U) = \int_0^\infty \exp\{-\gamma(\eta, \mu; p_1, p_2, \mu_0, U)\}\cos(\eta\mu)d\eta$ is the intensity SDF observed on the receiver plane, and $\gamma(\cdot)$ is the so-called structure interaction function defined in (Carrano and Rino [3]).

As mentioned earlier, S_4 and τ_0 are the inputs for the simulator. To validate the parameter mappings, S_4 and τ_0 for both model and real data can be calculated from the intensity SDF as [19]:

$$S_4 = \sqrt{2 * \int_{f_{min}}^{f_{max}} \Phi_I(f)df} \tag{18}$$

$$\tau_0 = find\left\{\tau | R_{SI}(\tau) = e^{-1}\right\} \tag{19}$$

where Φ_I is the intensity SDF, $R_{SI}(\cdot)$ is the normalized autocorrelation function (ACF) of the intensity measurements, which can be obtained as the DFT of Φ_I.

4 Simulation Results and Results Validation

In this section, real scintillation data collected by SenSe Lab will be used to validate the simulation results. To obtain the representative values for the TPPSM parameters, IPE is applied to real scintillation data firstly. Then, this study presents the validated results of the simulator using real scintillation data set. The MATLAB implementation of this validation is based on the open source program developed by Rino (ref or website).

4.1 Data Description

The real scintillation BDS data set used in this study were collected at Chile, South America, using a front end with sampling rate at 25 MHz and center frequency at 1.57 GHz. We use the self-developed receiver to track the BDS B1I signal, and the outputs including the receiver location and data will be used for scintillation analysis and simulator verification. By solving the navigation message, the exact geographic location of the receiver is 29.75 ° S, 69.26 ° W (geomagnetic: 20.70 ° S, 1.78 ° E) as shown in Fig. 3-4, which will be used as the geometric propagation inputs for the simulator.

The real data is a 17-minute data collected on March 17, 2017 from Chile with scintillation observed on BDS B1I signal from BDS PRN 14, however, the scintillation only occurs in the last 50 s, as shown in Fig. 5.

According to the top panel of Fig. 5, the scintillation can be divided into two parts. So, the data from 1030th second to 1050th second, which is a 20-second length of

Fig. 3 Real scintillation data receiver location

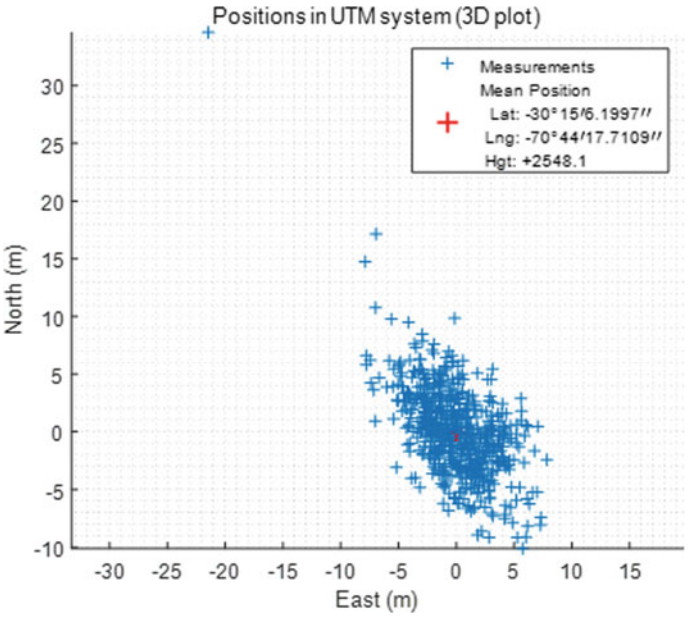

Fig. 4 Real scintillation data positioning results

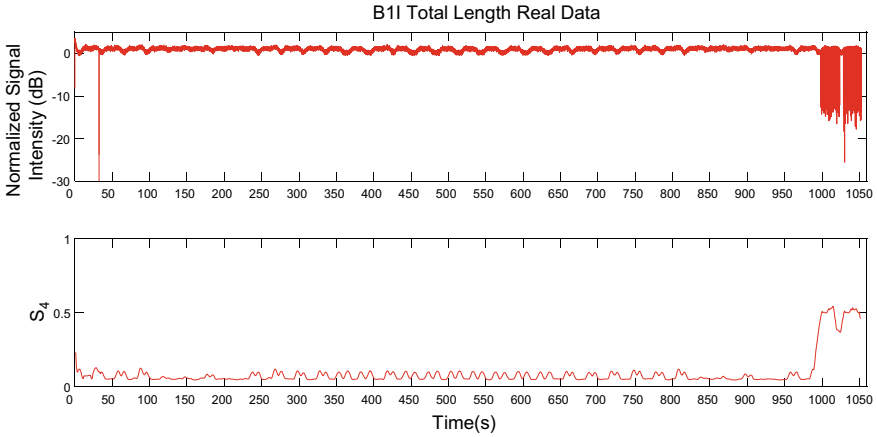

Fig. 5 The real data scintillation characteristics during observation

signal intensity measurement is selected. Figure 6 shows a zoom-in view of the 20-second intensity measurement data. Scintillation with frequency deep fading about 10 dB can be observed in the signal intensity shown on the top panel. The average S_4 index of each segment is plotted in the bottom panel with the center of each 1-second marked as circle.

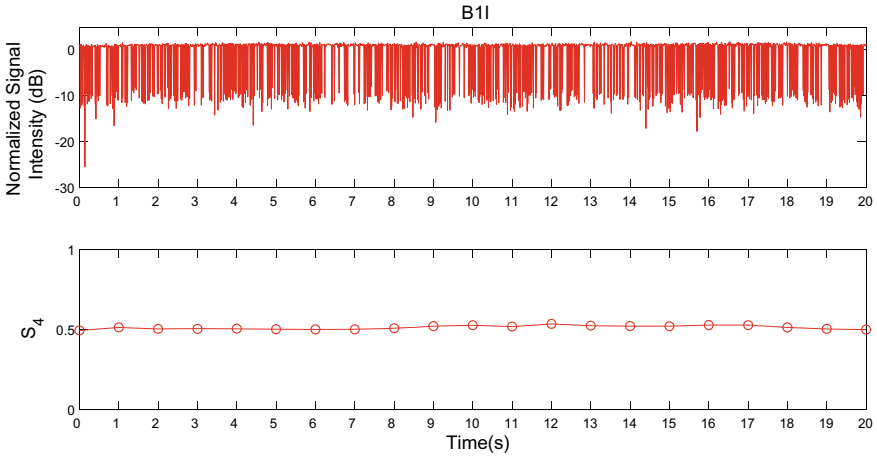

Fig. 6 Selected real data scintillation characterization

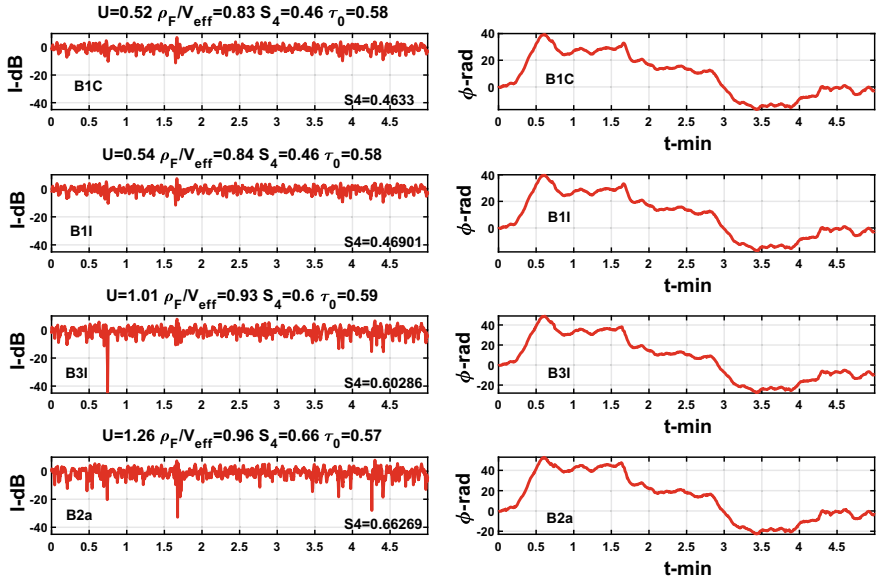

Fig. 7 Scintillation generator results

4.2 Real Data Validation

Using the real data scintillation characterization obtained above, the two inputs parameters $\{S_4, \tau_0\}$ can be extracted with IPE method represented by Eqs. (18) and (19). As shown in Fig. 5, S_4 can be set as 0.5. τ_0 depends on the autocorrelation function (ACF) of the intensity measurements, which can be set as 0.7.

The output of scintillation generator of the simulator is shown in Fig. 7, four signals are simulated including B1I, B1C (data + pilot), B2a (data + pilot), and B3I.

The output of the baseband signal generator is B1I IF signal with a length of 300 s. Scintillation influence is added in the non-scintillation signal after first 30 s. Using this IF signal as input of tracking code, the scintillation characterization for simulation signal can be obtained. Figure 8 shows the comparison of scintillation characterization of real data and simulation result.

From Fig. 8, the effectiveness of two-parameters, physic-based, strong scintillation BDS-3 signal simulator is validated. The normalized signal intensity and S_4 index for real data and simulation results are basically the same. However, there are still a 0.1 gap between the S_4 index of real data and simulation results. More attentions should be paid on this problem in the future.

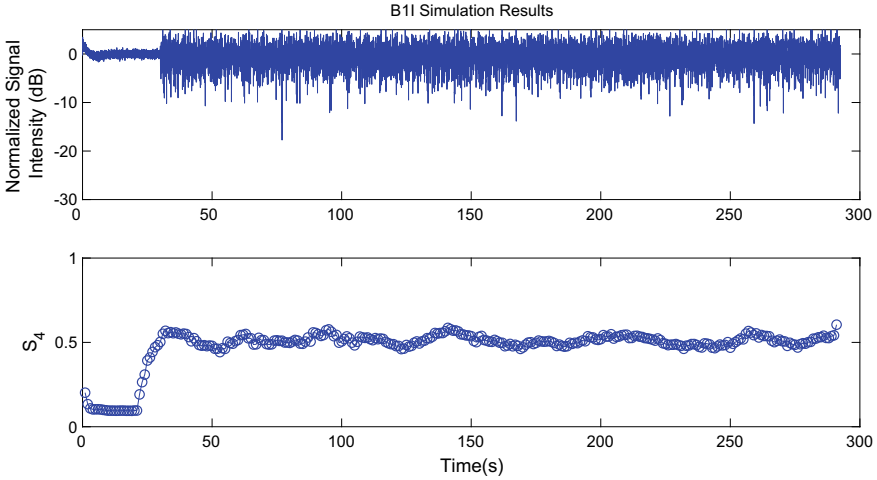

Fig. 8 Simulated results scintillation characterization

5 Summary and Outlook

This paper presented a TPPSM-based scintillation BDS-3 signal simulator that requires only the expected scintillation index S_4 and the intensity decorrelation time τ_0. This simulator can generate six BDS scintillation signals on three frequency bands, i.e. B1I, B1C (data + pilot), B2a (data + pilot), and B3I which are observed on statistical platform or user-defined dynamical platform. A set of strong scintillation data from Chile were processed using IPE to establish the profiles of the model parameters. Based on the profiles of real data, S_4 and τ_0 are extracted and input into the simulator. The results show the real data and simulation results have a very similar characteristics in scintillation and the $\{S_4, \tau_0\}$ values between them are also in a good agreement.

However, there are still a 0.1 gap between the S_4 index of real data and simulation results. More attentions should be paid on this problem in the future. And the current simulator does not generate navigation data bit. In the future, this part will be made up for the investigation on the different navigation modulation during strong ionosphere scintillation.

Acknowledgements The research is supported by the funding from Shanghai Jiao Tong University (WF220541306) and Key laboratory of space microwave technology (6142411193113). The data used in the validation is offered by Professor Yu T. Morton from University of Colorado (CU), Boulder. The reference MATLAB code is from the open source code uploaded by Professor Rino, C. L. Professor Yu T. Morton, and Dr. Xu from University of Colorado (CU), Boulder. The authors also gratefully acknowledge the helpful comments and suggestions of the reviewers, which have improved the presentation.

References

1. Aarons J (1982) Global morphology of ionospheric scintillation. Proc IEEE 70:360–378. https://doi.org/10.1109/PROC.1982.12314
2. Aarons J, Basu S (1994) Ionospheric amplitude and phase fluctuations at the GPS frequencies, Proceedings of the 7th international technical meeting of the satellite division of the institute of navigation (ION GPS 1994), Salt Lake City, UT, pp 1569–1578
3. Carrano CS, Rino CL (2016) A theory of scintillation for two-component power law irregularity spectra: I. Overview Numer Results Radio Sci 51(6):789–813. https://doi.org/10.1002/2015RS005903
4. Carrano CS, Valladares CE, Groves KM (2012a) Latitudinal and local time variation of ionospheric turbulence parameters during the conjugate point equatorial experiment in Brazil. Int J Geophys, Art. No. 103963, https://doi.org/10.1155/2012/103963
5. Cervera MA, Knight MF (1998) Time series modelling of intensity and phase scintillation at GPS frequencies. Acta Geodaetica et Geophsysica Hungarica 33(1):25–40. https://doi.org/10.1007/BF03325520
6. China Satellite Navigation Office (2017) BeiDou navigation satellite system signal in space interface control document open service signal B2a (Version 1.0). http://www.beidou.gov.cn/
7. China Satellite Navigation Office (2017) BeiDou navigation satellite system signal in space interface control document open service signal B1C (Version 3.0). http://www.beidou.gov.cn/
8. China Satellite Navigation Office (2018) BeiDou navigation satellite system signal in space interface control document open service signal B3I (Version 1.0). http://www.beidou.gov.cn/
9. China Satellite Navigation Office (2019) BeiDou navigation satellite system signal in space interface control document open service signal B1I (Version 3.0). http://www.beidou.gov.cn/
10. Hegarty C, El-Arini MB, Kim T, Ericson S (2001) Scintillation modeling for GPS-wide area augmentation system receivers. Radio Sci 36(5):1221–1231, https://doi.org/10.1029/1999rs002425 https://pdfs.semanticscholar.org/1af6/97b5e4b96355174fbd1cce524ebb68f5651c.pdf
11. Humphreys TE, Psiaki ML, Hinks JC, Kintner PM (2009) Simulating ionsphereinduced scintillation for testing GPS receiver phase tracking loops. J Sel Top Sign Process IEEE 3(4):707–715. https://doi.org/10.1109/JSTSP.2009.2024130
12. Jiao Y, Morton Y (2015) Comparison of the effect of high-latitude and equatorial ionospheric scintillation on GPS signals during the maximum of solar cycle 24. Radio Sci 50(9):886–903. https://doi.org/10.1002/2015RS005719
13. Jiao Y, Morton Y, Taylor S, Carroll M (2014b) Characteristics of low-latitude signal fading across the GPS frequency bands. Proc ION GNSS + , Tampa, FL, pp 1203–1212
14. Jiao Y, Morton Y, Taylor S, Pelgrum W (2013a) High latitude ionosphere scintillation characterization, Proc ION ITM, San Diego, CA, pp 579–584
15. Jiao Y, Morton Y, Taylor S, Pelgrum W (2013b) On the correlation between ionospheric scintillation and geomagnetic field activities. Proc ION GNSS + , Nashville, TN, pp 77–83
16. Morton Y, Jiao Y, Taylor S (2015) High-latitude and equatorial ionospheric scintillation based on an event-driven multi-GNSS data collection system. Proc Ionospheric Effects Sym, Alexandria, VA
17. Rino CL, Carrano CS (2013) A compact strong-scatter scintillation model, Proc the international beacon satellite symposium, Bath, U.K. [online] Available at:
18. Rino CL (2011) The theory of scintillation with applications in remote sensing. Wiley, Hoboken, NJ
19. Rino CL, Breitsch B, Morton Y, Jiao Y, Xu D, Carrano C (2018) A compact multifrequency GNSS scintillation model. Navigation 65(4):563–569. https://doi.org/0.1002/navi.263
20. Rino CL, Carrano CS, Roddy P (2014) Wavelet-based analysis and power law classification of C/NOFS high-resolution electron density data. Radio Sci 49(8):680–688. https://doi.org/10.1002/2013RS005272
21. Xu D, Morton Y et al (2019) A two-parameter GPS signal simulator for strong equatorial ionospheric scintillation: modeling and parameter characterization. Navigation

22. Xu D, Morton Y (2015) GPS signal fading and carrier phase variations during strong equatorial ionospheric scintillation. Proc ION ITM, Dana Point, CA
23. Yang R, Xu D, Morton Y (2018) An improved adaptive multi-frequency GPS carrier tracking algorithm for navigation in challenging environments, Proc of IEEE/ION PLANS, Monterey, CA, pp 899–907
24. Yeh CK, Liu CH (1982) Radio wave scintillations in the ionosphere. Proc IEEE 70(4):324–360

Fan Broadband Noise Localization and Mode Identification Technology in Turbofan Engine

Jingnan Chen and Wei Ma

Abstract Microphone array measurement technology is widely used for aeroacoustic measurement, because it has the advantages of being far away from strong mutual interference regions, which can avoid intrusion of the flow field, increasing the size can improve the spatial resolution and increasing the number of microphones can promote dynamic range. As the ducting ratio of civil aeroengine increases, the proportion of fan noise is increasing. In the fan noise, the development of tone noise reduction technology is more mature which makes the problem of broadband noise more prominent. However, the mechanism of broadband noise generation is complicated and signal-to-noise ratio is relatively poor, which make it difficult to control broadband noise. Efficient and accurate in-duct fan broadband sound source localization and mode identification can be realized by arranging a ring or multi-ring microphone array around the duct, which can greatly assist the fan broadband noise reduction technology. This paper summarizes the in-duct rotating broadband noise localization and mode identification technology developed in foreign countries in recent years, namely the in-duct rotating beamforming and the mode beamforming, which use the experimental data provided by the University of São Paulo in Brazil for code verification and compare the calculation results with conventional beamforming and mode decomposition. The results show that the in-duct rotating beamforming has higher source resolution and dynamic range. The mode beamforming with multi-ring array has better radial modal identification capability than the mode decomposition. Finally, the advantages and disadvantages of the new technology and the future improvement direction are expounded.

Keywords Microphone arrar · Fan broadband noiss · Sound source localization · Mode measurement

J. Chen (✉) · W. Ma
Shanghai Jiao Tong University, Shanghai, China
e-mail: chen_jingnan@sjtu.edu.cn

W. Ma
e-mail: mawei@sjtu.edu.cn

Z. Jing and X. Zhan (eds.), *Proceedings of the International Conference on Aerospace System Science and Engineering 2020*, Lecture Notes in Electrical Engineering 680,
https://doi.org/10.1007/978-981-33-6060-0_27

1 Introduction

With the increasing stringency of airworthy noise regulations, the design of lownoise aeroengines has received increasing attention. Under the development trend of low energy consumption and large bypass ratio, the proportion of fan noise in the overall engine noise level has gradually increased [1]. The major components of fan noises are tonal noises and broadband noises. Tonal noises occur at the blade passing frequency (BPF) and its harmonics with concentrated energy, which can be effectively removed by means such as frequency cutoff; while the generation of broadband noises is more complicated. It is currently believed that the dominant broadband noises are due to blade surface pressure differences generated by turbulence and the signal to noise ratio is worse comparing with tonal noises, which makes the development of broadband noises reduction slowly. As the vital technology of noises measurement microphone array is widely used for aerodynamic noise recognition and mode detection. The core of testing technology lies in the development of algorithms for data processing, where beamforming is more popular due to its high computational efficiency and robustness. Fan noise sources are typical rotating noise sources and the primary problem for detecting the rotating noise sources is Doppler effect caused by rotation. Under the free-field model, Sijtsma first proposed the Rotating Source Identifier algorithm (ROSI). It uses time-domain interpolation to construct the de-Dopplerisation spectrum and perform point-by-point scanning to find the position of the sound source [2]; however, the biggest disadvantage of this algorithm is that the calculation efficiency is low, and the resolution will deteriorate rapidly at a low sampling frequency. Pannert et al. proposed a rotating beamforming algorithm under modal decomposition (MD) based on the analytical solution of the free-field rotating sound field proposed by Poletti [3, 4], which is the first extension of rotating beamforming from the frequency domain to the frequency domain greatly improves the resolution of the sound source. However, the calculation efficiency of high-band steering vectors is reduced due to the increase in the number of series expansion terms. Herold uses spatial linear interpolation to construct a virtual rotating array and proposes a virtual microphone rotating array (VRA), which makes the calculation process of rotating beamforming easier and faster. The rotating beamforming technology in the duct was first proposed by Lowis. Based on the Green function of the acoustic wave propagation in the duct obtained from the dipole model of the noise source, it was used as the steering vector to separate the broadband noise in the duct. However, the direct solution of the in-duct Green function to solve the sound source distribution will be seriously affected by the duct wall reflection noise, so the resolution is low. Afterwards, Dougherty proposed to use the duct mode to solve the steering vector on the basis of Lowis, which greatly reduces the influence of the reflected sound of the duct wall on the recognition of broadband noise [5]. Since then, Dougherty and Sutliff etc. have conducted a lot of experimental research on this technology on the NASA Advanced Fan Noise Control (ANCF) bench, and all have obtained good experimental results [6, 7]. Recently, the Caldas team at the University of São Paulo in Brazil conducted a detailed experimental study on the fan

platform (USP Fan Rig) built by Dougherty using the wideband source identification algorithm developed by Dougherty. Compared with the ANCF platform, it has a higher speed and the fan has more stationary blade and the duct has smaller diameters and fewer sensors. Under the more severe experimental conditions, the processing results of the algorithm are still effective [4, 8]. Based on the assumption that the duct broadband noise mode is not coherent, the beamforming algorithm used for sound source recognition can also be applied to mode recognition, and the inherent sidelobe interference characteristics of modal beamforming can also be combined with some deconvolution algorithms, for example (DAMAS [9], CLEAN-SC [10] to clear, so as to obtain a clean main mode distribution map [11–13]. Compared with the traditional Fourier decomposition the advantage is that it can reflect the radial mode distribution, and the arrangement of measuring points is also more convenient to avoid the traditional complex rotating rake array to build radial mode measurements [14]. This article will briefly introduce the currently widely used advanced duct rotating broadband noise beamforming algorithm, and then use the experimental data shared by the team of the University of São Paulo in Brazil for code verification [8], and compare it with conventional beamforming technology (CB) and the results of the free field rotating beamforming technology (ROSI, VRA) are compared, the characteristics of the respective sound source recognition in the duct are analyzed, and then the duct modal beamforming analysis is performed on the shared experimental data, and the calculated results are compared with the results of the traditional Fourier transform, and finally summarize and discuss the advantages and disadvantages of the new broadband noise identification technology and duct modal detection technology and the future work. The main purpose of this article is to analyze advanced aerodynamic noise testing technology, aiming to promote the better development of aerodynamic noise testing technology.

2 Background

2.1 In-Duct Rotating Beamforming

Assume the scanning grid cylindrical coordinates as $\boldsymbol{y}_s = (r_{ys}, \phi_{ys}, z_{ys})$, where grid number $s = 1, 2, 3, \ldots, S$; the cylindrical coordinates for microphone is $\boldsymbol{x}_m = (r_{xm}, \phi_{xm}, z_{xm})$, where microphone numbers are $m = 1, 2, 3, \ldots, M$. The outputs for beamforming corresponding to each grid point are:

$$b(\boldsymbol{y}_s) = \boldsymbol{w}(\boldsymbol{y}_s)^H \bar{\boldsymbol{C}} \boldsymbol{w}(\boldsymbol{y}_s) \tag{1}$$

$$\bar{\boldsymbol{C}} = \boldsymbol{p}\boldsymbol{p}^H - dig(\boldsymbol{p}\boldsymbol{p}^H) \tag{2}$$

where H is conjugate transpose, and the steering vector $\boldsymbol{w}$ can be calculate as:

$$\boldsymbol{w}(\boldsymbol{y}_s) = \frac{g(\boldsymbol{y}_s)}{\sqrt{\sum_{(u,v)\equiv F} |g(\boldsymbol{y}_s, \boldsymbol{x}_u)|^2 |g(\boldsymbol{y}_s, \boldsymbol{x}_v)|^2}} \tag{3}$$

set $F = \{(u, v)|1 \le u \le M, 1 \le v \le M, u \ne v\}$

$$g = [g(\boldsymbol{y}_s, \boldsymbol{x}_1), \ldots, g(\boldsymbol{y}_s, \boldsymbol{x}_m), \ldots, g(\boldsymbol{y}_s, \boldsymbol{x}_M)]^T \tag{4}$$

where T represents transpose, the acoustic wave propagation function under the pipeline boundary conditions can be expressed as

$$g(\boldsymbol{y}_s, \boldsymbol{x}_m) = \sum_{m_0} \sum_{n_0} \frac{\Psi^*_{m_0 n_0}(\boldsymbol{y}_s) \Psi_{m_0 n_0}(\boldsymbol{x}_m)}{\Lambda^2_{m_0 n_0}} \tag{5}$$

where mode shape function is

$$\Psi_{m_0 n_0}(\boldsymbol{y}) = [A J_{m_0}(k^r_{m_0 n_0} r_y) + B Y_{m_0}(k^r_{m_0 n_0} r_y)] e^{i(m_0 \phi_y - k^{\pm Z}_{m_0 n_0} z_y)} \tag{6}$$

where $k^r_{m_0 n_0}$ is radial wavenumber, $k^{\pm z}_{m_0 n_0}$ is axial wavenumber, '+' represents the wave progagates downstream, and '−' means the wave propagates upstream, $\Lambda_{m_0 n_0}$ is mode shape function normalization factor, coefficients A, B are calculated according to the duct shape, J_{m_0} and Y_{m_0} represent the m_0 order Bessel function of the first kind, n_0 is radial mode order [13].

2.2 Mode Beamforming

The sound pressure in the duct can be written as the superimposed form of the duct mode

$$\boldsymbol{p}(\boldsymbol{x}_m) = \sum_{m_0=-\infty}^{+\infty} \sum_{n_0=0}^{+\infty} \boldsymbol{a}_{m_0 n_0} \frac{\Psi_{m_0 n_0}(\boldsymbol{x}_m)}{\Lambda_{m_0 n_0}} \tag{7}$$

where $a_{m_0 n_0}$ is the amplitude of the radial mode (m_0, n_0), $\Psi_{m_0 n_0}$ and $\Lambda_{m_0 n_0}$ are the shape function of the radial mode and its normalization factor respectively. Assuming that the modalities measured by the sensors are not coherent with each other, the modal amplitude $a_{m_0 n_0}$ is that the inherent property of the acoustic site that does not change with the location of the measuring point. Therefore, for all microphone measuring points, Eq. (6) can be written as a matrix:

$$\begin{aligned}\boldsymbol{p} &= \begin{bmatrix} p(x_1) \\ \vdots \\ p(x_m) \\ \vdots \\ p(x_M) \end{bmatrix} = \boldsymbol{G}\boldsymbol{a} \\ &= \begin{bmatrix} g_{m_0^-,0}(x_1) & \cdots & g_{m_0,n_0}(x_1) & \cdots & g_{m_0^+,n_0^+}(x_1) \\ \vdots & \ddots & \vdots & \iddots & \vdots \\ g_{m_0^-,0}(x_m) & \cdots & g_{m_0,n_0}(x_m) & \cdots & g_{m_0^+,n_0^+}(x_m) \\ \vdots & \iddots & \vdots & \ddots & \vdots \\ g_{m_0^-,0}(x_M) & \cdots & g_{m_0,n_0}(x_M) & \cdots & g_{m_0^+,n_0^+}(x_M) \end{bmatrix} \begin{bmatrix} a_{m_0^-,n_0^+} \\ \vdots \\ a_{m_0,n_0} \\ \vdots \\ a_{m_0^+,n_0^+} \end{bmatrix}\end{aligned} \tag{8}$$

$$g_{m_0,n_0}(\boldsymbol{x}_m) = \frac{\Psi_{m_0 n_0}(\boldsymbol{x}_m)}{\Lambda_{m_0 n_0}} \tag{9}$$

where m_0^- and m_0^+ is the lower and upper limits of circumferential mode order respectively, and the magnitude is selected based on the spatial sampling theory; n_0^+ is the upper limit of radial mode order and the value can be selected according to the condition that the axial wave number is real. The problem described by Formula (8) is a typical inverse problem, but the modal propagation matrix G under finite sensors is often non-singular, and the modal amplitude a cannot be obtained by directly inverting the operation. Usually the Tikhonov regularization method can be used directly for the inverse solution. Under the premise that the various modes are not coherent, the beamforming algorithm can also be used to solve.

$$|a_{m_0,n_0}|^2 = \boldsymbol{h}_{m_0,n_0}^H \bar{\boldsymbol{C}} \boldsymbol{h}_{m_0,n_0} \tag{10}$$

$$\boldsymbol{h}_{m_0,n_0} = \frac{g_{m_0,n_0}}{\|g_{m_0,n_0}\|_2^2} \tag{11}$$

$$g_{m_0,n_0} = [g_{m_0,n_0}(\boldsymbol{x}_1), \ldots, g_{m_0,n_0}(\boldsymbol{x}_m), \ldots, g_{m_0.n_0}(\boldsymbol{x}_M)]^T \tag{12}$$

The self-power of each mode can be obtained from Eq. (10). The modal amplitude distribution calculated by beamforming will be affected by the resolution limitation and sidelobe interference. The DAMAS [9] or CLEAN-SC [10] algorithm can be used to further process Eq. (10), which can improve the resolution of the main mode and effectively remove the pseudo mode significantly.

3 Comparative Analysis of Experimental Results

3.1 Introduction of Experimental Equipment and Parameters

Figure 1 shows the test bench used in the experiment, which is mainly composed of three parts, the horn-shaped intake end, which can reduce resistance and reduce the interference of intake noise; the test end which is mainly composed of three rings of microphone sensor and the fan blade of the test; the muffler end of the outlet, which mainly reduces the influence of the exhaust noise at the end of the pipe on the test result. Specific experimental parameters can refer to Table 1.

3.2 Comparison of Broadband Noise Location Methods for Pipeline Rotation

Due to the poor signal-to-noise of broadband noise, it is necessary to extract broadband noise from the collected raw data before locating the broadband noise source, so as to prevent the spectrum leakage of the strong energy single-tone noise from

Fig. 1 São Paulo University fan rig[8]

Table 1 Experiment parameter

Parameters	Value
Duct radius /m	0.3
Blade radius /m	0.25
Number of moving blades	16
Number of stationary blades	14
Speed of fan/rpm	4250
Number of microphones	77
Number of microphone ring	3
Number of microphones in the first ring	33
Number of microphones in the second ring	23
Number of microphones in the third ring	21
Distance from the microphone to the blade plane (first ring) /m	0.86
Distance from the microphone to the blade plane (second ring) /m	0.96
Distance from the microphone to the blade plane (third ring) /m	1.13
Sampling frequency/kHz	51.2
Sampling time/s	30

polluting the broadband noise. The random distribution characteristics of broadband noise can be used to extract, the specific method can refer to [15], this process is called spectrum preprocessing. Figure 2 shows the original spectrum diagram and the spectrum diagram after the separation of the single tone and the broadband. It can be seen that the single tone removal effect is very significant. The blue line represents the discrete tone, and the red line represents the purified broadband.

Figures 3, 4, 5 and 6 show the results of the current beamforming algorithm for sound source localization. The recognition results corresponding to the three analysis frequencies 2.39, 4.2, and 6.5 kHz are given. Since the purpose of this paper is the comparison of the accuracy of the sound source localization, the relative amplitude is uniformly adopted, and the dynamic range is set to 9 dB, the spectrum is estimated using the Welch method [16], the segment length is 2048, and the overlap is 50%. When the sound source frequency is 2.39 kHz, the traditional beamforming results and the free-field rotating beamforming results show the main strong noise areas are roughly located near the wall of the pipe, and only the results of the duct rotating beamforming are located at the blade and the blade root. This is because the first two algorithms are all based on the propagation of sound waves in the free field, and do not consider the reflection of the pipe wall against the sound waves under the boundary conditions of the pipe. When the sound source frequency is 4.2 kHz, the main noise source positions obtained by all algorithms are roughly at the blade and the blade root, but the duct rotating beamforming algorithm has a significant advantage in the distribution rate of the sound source, which can clearly distinguish the leading edges, trailing edges of the blade and the noise source of the blade root. When the sound

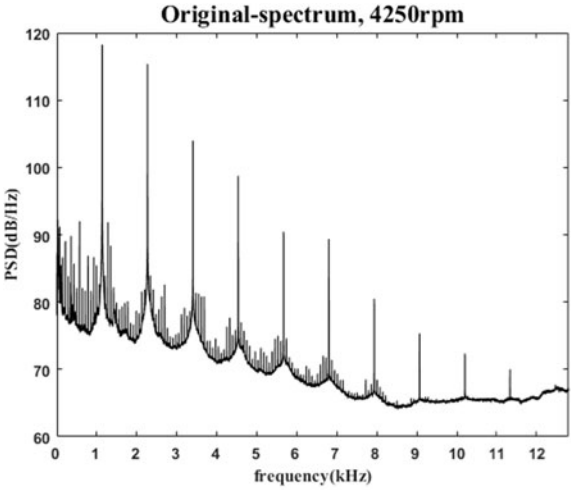

(a) Original power spectral density distribution

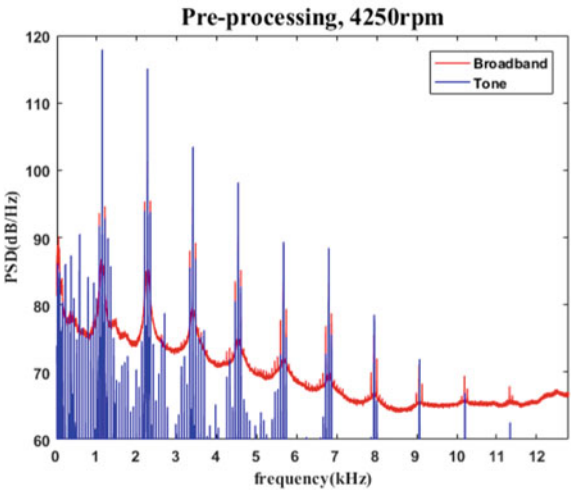

(b) Single tone and broadband separation results

Fig. 2 Fan noise power spectrum distribution

source frequency is 6.5 kHz, the high-frequency side-lobe aliasing will increase, and the traditional wavenumber forming algorithm and ROSI algorithm will fail, and the results will be very confusing; VRA algorithm and duct rotating beamforming algorithm have significant advantages and determine that the sound source is mainly located in the middle area of the blade, where the anti-sidelobe interference of the duct rotating beamforming is outstanding, but the resolution is also impaired and only a blurry circle is distinguished. Figure 7 shows the original experimental results

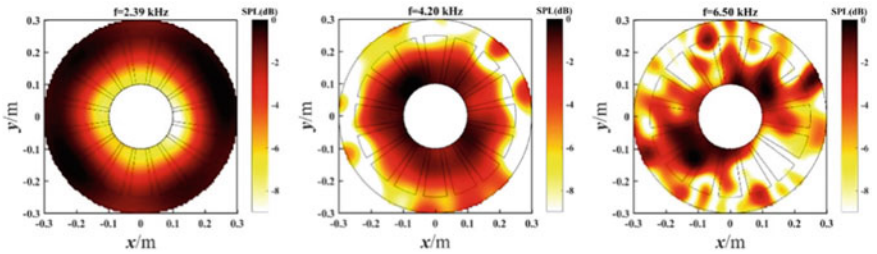

Fig. 3 Conventional beamforming localization result

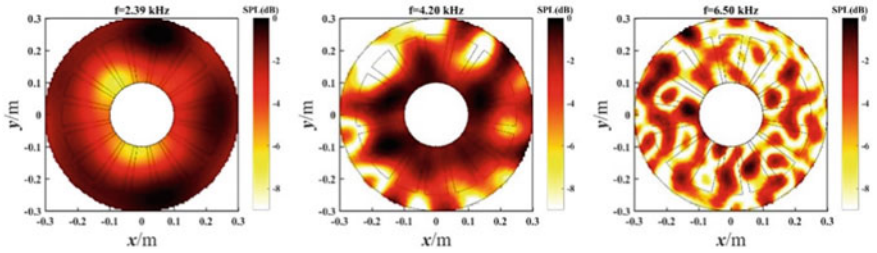

Fig. 4 ROSI localization result

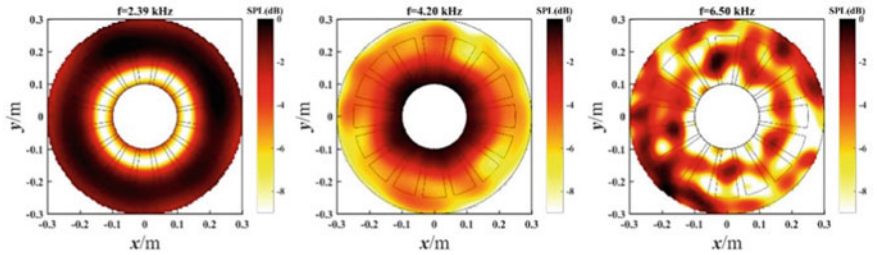

Fig. 5 VRA localization result

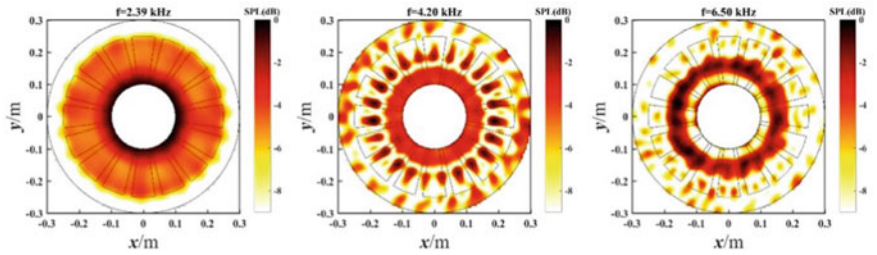

Fig. 6 In-duct beamforming localization result

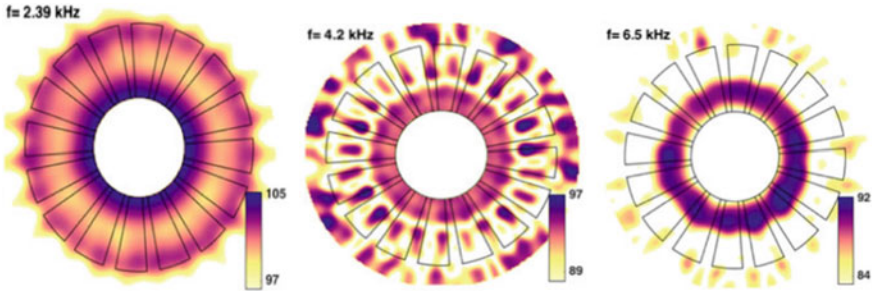

Fig. 7 Localization result in original [8]

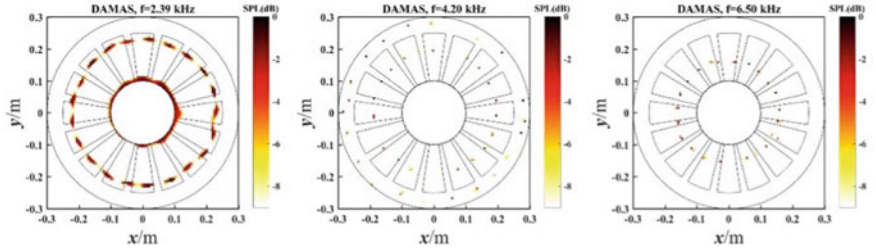

Fig. 8 In-duct beamforming with DAMAS result

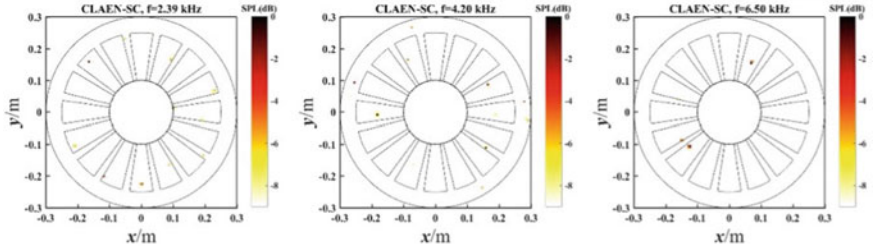

Fig. 9 In-duct beamforming with CLEAN-SC result

of Caldas et al. [8]. By comparison, we can infer that the algorithm repeated in this paper is accurate. Figures 8 and 9 show the results of duct rotating beamforming deconvolution, where Fig. 8 is the DAMAS result and Fig. 9 is the CLAEN-SC result. In comparison, for this experiment the DAMAS result is better than the CLEAN-SC result and is more scientific. DAMAS can extract most of the main noise sources in the duct rotating beamforming results, but there are also failures, such as the noise at the root of the blade corresponding to 4.2 kHz and the occurrence of pseudo noise points at the tip gap source. The root part of the blade is where the blade and the hub are hinged. It is relatively uneven, and the airflow resistance is large, so the aerodynamic noise generated is relatively obvious. However, the results obtained by CLEAN-SC appear to be out of order, which is similar to the results obtained by

Dougherty [11]. This may be related to the strong dependence of CLEAN-SC on the point source hypothesis. However, most of the broadband noise sources generated by actual blades are formed by turbulent pulsations impacting the blades, which have strong randomness and are discrete in space distribution which is quite different from point sources.

3.3 Analysis of Pipeline Modal Beamforming

Using the sound signals collected by 3 ring 77 microphone sensors for duct mode analysis, Fig. 10 shows the mode decomposition based on Fourier transform. The decomposition data is based on the first ting of microphone array, and the main mode corresponding to first order BPF $m = -2$. The main mode corresponding to the second-order BPF is $m = -4$, the main mode corresponding to the third-order BPF is $m = -6$, and the main mode corresponding to the fourth-order BPF is $m = -8$ and 6.

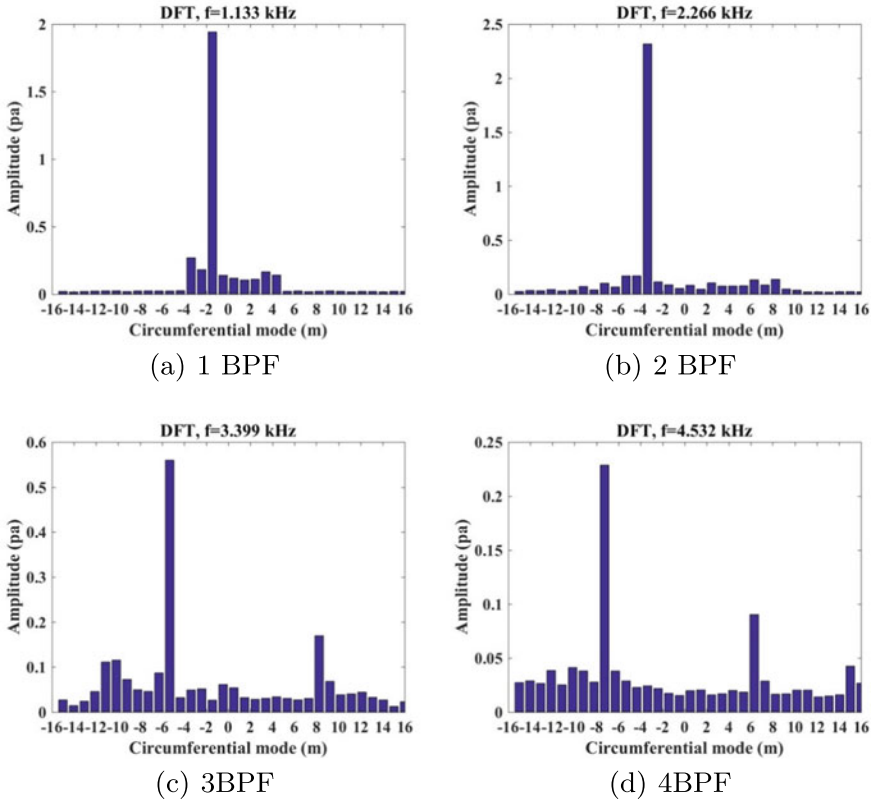

Fig. 10 Fourier mode decomposition results

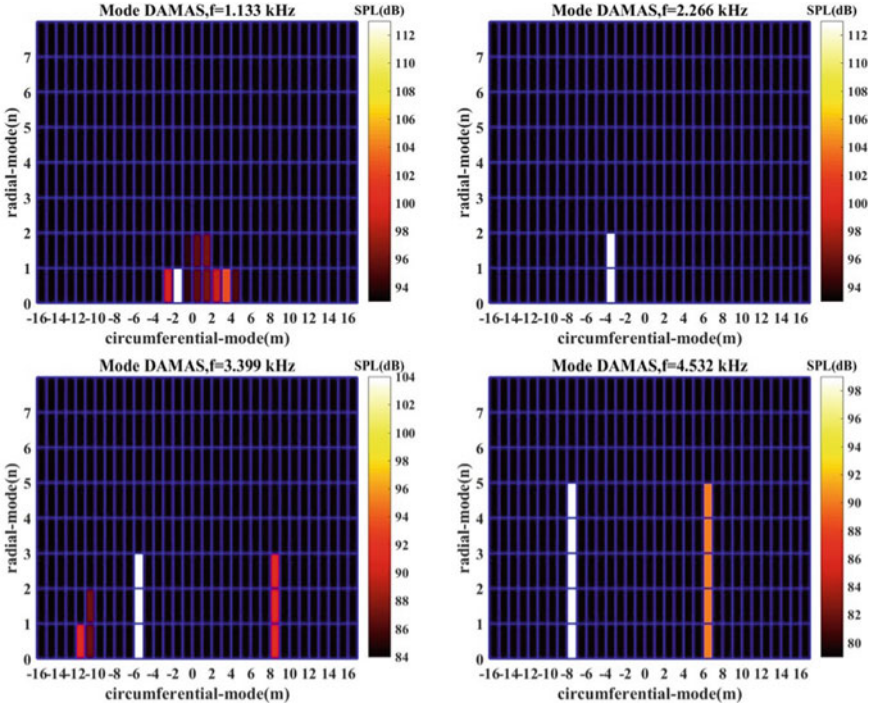

Fig. 11 Mode beamforming results by first ring array

It can be reasonably explained according to Tyler-sofrin's dynamic-static interference theory [17]. Figure 11 shows the results of modal beamforming using the first ring microphone array. From the results, it can be seen that the circumferential mode distribution obtained by using the single ring array processing results is basically consistent with the Fourier method, but the original ability of radial mode recognition is lost. When using a three-ring full array for mode beamforming, the radial mode order can be obtained more clearly and mode detection capabilities have been greatly improved, as shown in Fig. 12. This is because the radial modes contained in the cross sections corresponding to different ring arrays are different. This difference often comes from the phase difference. From the modal shape function Formula (6), it can be known that this phase difference is caused by the axial characteristic distance. Therefore, the axial characteristic length has a certain ability to distinguish between radial modes. Therefore, this feature is widely used to detect radial mode, and it can replace part of the rotating rake method to a certain extent. Commonly used mode beamforming arrays are axial linear arrays and circumferential annular arrays [11, 18].

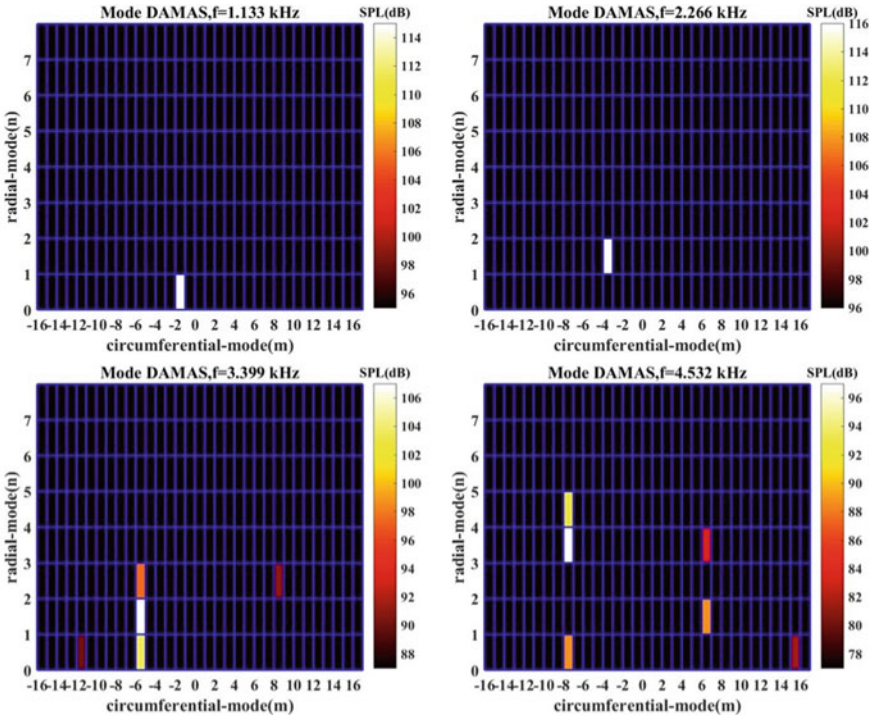

Fig. 12 Mode beamforming results by three-ring array

4 Conclusion

This article focuses on the analysis and comparison of different broadband noise identification techniques and modal detection techniques in the aeroacoustic testing method of duct. Using the experimental data provided by the Caldas team of the University of São Paulo [8], the duct rotating beamforming algorithm was verified and compared with some existing beamforming algorithms, the following conclusions can be drawn:

1. Duct rotating beamforming can better mitigate the effect of reflected sound waves on the wall, and then identify the duct broadband noise source with higher resolution. Traditional beamforming technology and free field rotating beamforming technology have certain effects on noise sources with middle and high frequency but with poor resolution.
2. Using the deconvolution algorithm to post-process the pipeline rotating beamforming results, it is found that the results of DAMAS are better than CLEAN-SC to a certain extent, but DAMAS also has some confusing results. Of course, compared with simple point sound sources, the distribution of the broadband noise source of the blade is much more complicated. The traditional assumption of

independent point sound sources is often untenable, so the traditional deconvolution algorithm for the measurement of complex noise sources in the duct is likely to fail under certain circumstances.

3. The multi-loop mode beamforming algorithm can break through the traditional mode decomposition algorithm to detect the radial mode distribution. However, this method is limited by the assumption of incoherent modalities. Since the mode coherence contained in the broadband noise is low, the results is reasonable to some extent. If the modes are coherent, the credibility of the results obtained by this method will be greatly reduced, for example, without removing the single tone, the radial mode contained in the strong BPF.

References

1. Qiao WY (2010) Aeroengine aeroacoustics. Beijing University of Aeronautics and Astronautics Press, Beijing
2. Sijtsma P, Oerlemans S, Holthusen H, Location of rotating sources by phased array measurements. American Institute of Aeronautics and Astronautics
3. Pannert W, Maier C (2014) Rotating beamforming—motion-compensation in the frequency domain and application of high-resolution beamforming algorithms. J Sound Vibr 333(7):1899–1912
4. Caldas LC, Greco PC, Pagani CC, Baccalá LA, Comparison of different techniques for rotating beamforming at the university of são paulo fan rig test facility. In: 6th Berlin beamforming conference
5. Ym J (2009) Virtual rotating microphone imaging of broadband fan noise
6. Sutliff D, Dougherty R, Walker B (2010) Evaluating the acoustic effect of over-the-rotor foam-metal-liner installed on a low speed fan using virtual rotating microphone imaging
7. Dougherty R, Walker B, Sutliff D, Locating and quantifying broadband fan sources using in-duct microphones. In: 16th AIAA/CEAS aeroacoustics conference, p 3736
8. Caldas LC, Greco PC, Pagani CC, Baccalá LA (2017) Acoustic imaging of in-duct aeroengine noise sources using rotating beamforming and phased arrays. IEEE Trans Comput Imaging 3(3):485–492
9. Brooks Thomas F, Humphreys William M (2006) A deconvolution approach for the mapping of acoustic sources (damas) determined from phased microphone arrays. J Sound Vibr 294(4):856–879
10. Sijtsma P (2007) Clean based on spatial source coherence. Int J Aeroacoust 6(4):357–374
11. Dougherty R, Mendoza J, Nacelle in-duct beamforming using modal steering vectors. In: 14th AIAA/CEAS aeroacoustics conference (29th AIAA aeroacoustics conference), p 2812
12. Caldas L, Baccala LA, Cuenca RG, Queiroz RL, In-duct beamforming noise source estimation mode detection university of são paulo fan rig. In: 21st AIAA/CEAS aeroacoustics conference, p 2233
13. Envia E, Huff D, Morrison C (1996) Analytical assessment of stator sweep and lean in reducing rotor-stator tone noise. In: Aeroacoustics conferences on American institute of aeronautics and astronautics
14. Huo SY, Xu KB, Qiao WY et al (2018) Research of mode identification and error transfer property on fan tonal noise. J Propul Technol 01:185–195
15. Sree D, Stephens DB (2016) Improved separation of tone and broadband noise components from open rotor acoustic data. Aerospace 3(3):29

16. Welch P (1967) The use of fast Fourier transform for the estimation of power spectra: a method based on time averaging over short, modified periodograms. IEEE Trans Audio Electroacoust 15(2):70–73
17. Tyler JM, Sofrin TG (1962) Axial flow compressor noise studies. Report 0148-7191, SAE technical paper
18. Dougherty RP (2016) Mutual incoherence of broadband duct acoustic modes. In: Aeroacoustics conferences on American institute of aeronautics and astronautics
19. Michel U (2006) History of acoustic beamforming
20. Poletti MA, Teal PD (2011) Comparison of methods for calculating the sound field due to a rotating monopole. J Acoust Soc Am 129(6):3513–3520
21. Herold G, Sarradj E (2015) Microphone array method for the characterization of rotating sound sources in axial fans. Noise Control Eng J 63(6):546–551
22. Lowis C, Joseph P, A focused beamformer technique for separating rotor and stator-based broadband sources. In: 12th AIAA/CEAS aeroacoustics conference, p 2710
23. Nelson PA, Yoon SH (2000) Estimation of acoustic source strength by inverse methods: part i, conditioning of the inverse problem. J Sound Vibr 233(4):639–664

Performance Evaluation of Robust GPS Signal Tracking with Moving Horizon Estimation in Urban Environment

Jiawei Xu, Rong Yang, and Xingqun Zhan

Abstract The rise of autonomous drive imposes new challenges in terms of robustness and precision of Global Navigation Satellite Systems (GNSS) technology, especially in the urban environment. The conventional GNSS signal processing usually takes Kalman filter (KF) as the signal parameter estimator to enhance the tracking performance, however, this is not a promising design for the urban navigation application where the signal blockages and severe multipath interferences are frequently occurred. To address this issue, a moving horizon estimator (MHE) will be used to replace KF for the accuracy and robustness improvement. Unlike the KF that highly depends on the accurate modelling of the system and measurement characteristics and cannot afford random outliers and distortions, MHE can incorporate the constraints, e.g., a priori defined variances, to limit threats from the faults, interferences or invalid measurements. Therefore, MHE is less sensitive to the random environmental variations as compared to EKF, which makes it more robust and more applicable to urban environment. The proposed tracking algorithm is verified with a realistic road test near Lujiazui CBD area in Shanghai in post-processing manner. The results confirm the improved accuracy, reliability, and robustness by using MHE method.

Keywords Multipath · Urban environment · Kalman filter · Moving horizon estimator · GNSS signal tracking

J. Xu · R. Yang · X. Zhan (✉)
Shanghai Jiao Tong University, Shanghai, China
e-mail: xqzhan@sjtu.edu.cn

J. Xu
e-mail: xjw000830@sjtu.edu.cn

R. Yang
e-mail: rongyang@sjtu.edu.cn

Z. Jing and X. Zhan (eds.), *Proceedings of the International Conference on Aerospace System Science and Engineering 2020*, Lecture Notes in Electrical Engineering 680,
https://doi.org/10.1007/978-981-33-6060-0_28

1 Introduction

As the development of global navigation satellite system (GNSS), the autonomous driving technology of the unmanned vehicles as well as the intelligent location-based services gradually moved from concept to practice. However, the dense and complicated urban environment pose a great challenge to the GNSS receiver. The high precision and anti-multipath-interference receivers are required for the reliable navigation applications in the urban environment.

Under the urban environment, the complex electromagnetic conditions will cause strong interference to the GNSS signals. For example, reflection and refraction of the signal due to the complex terrain and nearby high-rise buildings, are likely to cause strong amplitude attenuations and rapid phase fluctuations to the received signals. It is the so-called multipath phenomena, which will bring cycle slip or drift in carrier tracking loop, and significantly degrade the positioning accuracy in GNSS receivers. In precise navigation applications, multipath errors dominate the total error budget [1] and the existence of aerial occlusions such as viaducts and tunnels may blocks the direct signals, causing loss of lock, and interruptions of the receivers' navigation functions.

As the most vulnerable part of GNSS receiver, carrier tracking loop is prone to signal attenuations and external interferences. Therefore, the positioning accuracy and anti-interference performance of a GNSS receiver in urban environment is usually limited by the carrier tracking capability.

Phase lock loop (PLL) and frequency lock loop (FLL) are the two ways to accomplish carrier tracking. There are various techniques and designs which serve as their improvements. For example, FLL-PLL cooperative tracking extends the traditional phase and delay locked loop (PLL/DLL) tracking framework to avoid tracking failure due to the change of environment, and is more suitable for tracking under signal attenuation situation [2]. Some researchers utilized vector tracking algorithms to improve the tracking performance in urban environment by performing a joint signal tracking of all the available satellites, rather than independently tracking multiple satellite channels [3].

Multi-sensors fusion is an alternative approach to enhance the navigation performance in urban challenging environment, e.g., [4] integrated multi-constellation and multi-frequency GNSS measurements with IMU and Odometry to mitigate the interferences, like multipath and ionosphere scintillations. [5] proposed two algorithms based on nonlinear least square (NLS) parameter estimation to suppress the multipath interference.

It is found that the advanced filter or estimator can facilitate the carrier tracking loop design for the noise or interference rejections. For example, Kalman filter (KF) has been widely used for carrier tracking as its excellent performance in noise filtering as compared to the traditional proportional integration filter (PIF). [6] has improved GNSS tracking sensitivity and dynamic adaptability with KF tracking implementation. However, KF relies accurate system model. In the urban environment with severe multipath and signal occlusion, the KF-based PLL is sensitive to phase obser-

vations with cycle slips and outliers. Although the KF has been optimized, it still cannot achieve the accuracy and anti-interference as urban road traffic claims.

Moving horizon estimation (MHE) is another widely adopted optimization approach for carrier tracking. The application of MHE is mainly to estimate states of dynamic system. It relies on the minimization of a sum of stage costs subject to a dynamic model [7] and is particularly useful for nonlinear or constrained dynamic systems for which few general methods with established properties are available [8].

Apart from carrier tracking, it also applies to various research and industrial applications. For example, [9] estimates the current states and unmeasured disturbances of an industrial gas phase polymerization reactor, and improves the estimation of unmodeled disturbances. [10] utilizes the robustness of MHE to faulty measurements and conditions that violate process models for industrial process monitoring tools. [11] concludes the feasibility of motion sensorless control based on the frame work of MHE. The associated dynamic optimization problem can be solved in real time, thus highly accurate estimates can be obtained.

Compared with KF, MHE does not require an accurate system model, and can set limits for observations during the optimization process. Therefore, its resistance to environmental interference can be greatly improved, and applicable to the most application scenarios in urban environment. In [12], MHE has been incorporated into vector tracking to prevent contamination in one channel affecting the other satellite channels. [13] integrated the existing estimator with quadratic functions adopted by MHE to improves the estimation performance by gradually increase the content of fusion. In this paper, we will implement the MHE to replace the KF in the PLL design to verify the improvements in urban environment.

The organization of this paper is as follows. Section 2 gives a brief introduction to carrier signal models. Section 3 specifies the design of PLL tracking loop design using KF and MHE respectively. In Sect. 4, in the presence of thermal noise, oscillator error, and receiver platform dynamics, the post-processed navigation satellite signal test data collected on Hongmei Elevated and near Lujiazui CBD area in Shanghai was used to compare the tracking performance of MHE and KF in real urban environments. Section 5 gives the conclusion.

2 Carrier Signal Models

In this section, the signal model will be covered, which comprise of system model and measurement model. The system model for a carrier tracking loop is depicted as below [14]:

$$\mathbf{x}_{k+1} = \mathbf{A}\mathbf{x}_k + \mathbf{n}_k \tag{1}$$

$$\mathbf{z}_k = \mathbf{H}\mathbf{x}_k + \mathbf{v}_k \tag{2}$$

This model is widely used in carrier tracking loop design for it incorporates the platform dynamics, oscillator noise, and thermal noise effect.

2.1 State Model

The state vector $\mathbf{x}_k$, depicting the received signal parameters on dynamic platform at the k^{th} epoch, can be expressed as a 3-dimension vector as follow:

$$\mathbf{x}_k = [\varphi, \omega, \dot{\omega}]_k^T \tag{3}$$

where φ_k is the carrier phase in rad, ω is the carrier frequency in rad/s and $\dot{\omega}$ is the carrier frequency rate in rad/s^2.

The system transient matrix $\mathbf{A}$ is depicted as follow, according to the state vector [14]:

$$\mathbf{A} = \begin{bmatrix} 1 & T & \frac{T^2}{2} \\ 0 & 1 & T \\ 0 & 0 & 1 \end{bmatrix} \tag{4}$$

where T represents the time coherent integration time (usually 1ms for GPS L1 signals).

The system noise vector $\mathbf{n}_k$ normally comprises of oscillator noise in the RF front-end and random walk process due to platform dynamics. Its covariance matrix $\mathbf{Q}$ are dependent on the platform dynamics and is expressed as below:

$$\begin{aligned} \mathbf{Q} &= \begin{bmatrix} \sigma_{\varphi}^2 & \sigma_{\omega\varphi}^2 & \sigma_{\dot{\omega}\varphi}^2 \\ \sigma_{\omega\varphi}^2 & \sigma_{\omega}^2 & \sigma_{\omega\dot{\omega}}^2 \\ \sigma_{\dot{\omega}\varphi}^2 & \sigma_{\omega\dot{\omega}}^2 & \sigma_{\dot{\omega}}^2 \end{bmatrix} \\ &= (2\pi f_L)^2 \begin{bmatrix} Tq_{\varphi} + \frac{T^3}{3}q_{\omega} + \frac{T^5}{20}\frac{q_a}{c^2} & \frac{T^2}{2}q_{\omega} + \frac{T^4}{8}\frac{q_a}{c^2} & \frac{T^3}{6}\frac{q_a}{c^2} \\ \frac{T^2}{2}q_{\omega} + \frac{T^4}{8}\frac{q_a}{c^2} & Tq_{\omega} + \frac{T^3}{3}\frac{q_a}{c^2} & \frac{T^2}{2}\frac{q_a}{c^2} \\ \frac{T^3}{6}\frac{q_a}{c^2} & \frac{T^2}{2}\frac{q_a}{c^2} & T\frac{q_a}{c^2} \end{bmatrix} \end{aligned} \tag{5}$$

where f_L is the GPS L1 carrier frequency (1575.42 MHz), c is the speed of light (3×10^8 m/s), q_{φ} and q_{ω} are the power spectral density of the carrier phase noise and carrier frequency noise due to the local oscillator instability respectively. They can be expressed with the oscillator h-parameters h_0 and h_{-2} as follows:

$$q_{\varphi} = \frac{h_0}{2} \tag{6}$$

$$q_{\omega} = 2\pi^2 h_{-2} \tag{7}$$

the value of oscillator h-parameters depends on the type of oscillator used in the receiver. There are two commomly used type, namely temperature compensate oscillator(TCXO) and oven-controlled oscillator(OCXO). In this paper, we use an OCXO-based front end to collect the raw data, hence, $h_0 = 6.4 \times 10^{-26}(s^2/\text{Hz})$, $h_{-2} = 4.3 \times 10^{-23}(1/\text{Hz})$. q_a represent the power spectrum of the random walk process due to line-of-sight (LOS) platform acceleration with the unit of (m^2/s^6)Hz.

2.2 Measurement Model

The average phase error $\Delta\theta_k$ obtained from the phase discriminator is usually taken as the measurement. It has the following form

$$\Delta\theta_k = \arctan\left(\frac{Q_k}{I_k}\right) \tag{8}$$

where Q_k and I_k are the correlation between the local replica signal and the incoming signal of in-phase and quadrature branch at time epoch k, respectively. The corresponding measurement model can be expressed as:

$$\Delta\theta_k = \mathbf{H}\Delta\mathbf{x}_k + \mathbf{v}_k \tag{9}$$

where $\mathbf{H}$ is the measurement matrix depicted as follow:

$$\mathbf{H} = \begin{bmatrix} 1 & \frac{T}{2} & \frac{T^2}{6} \end{bmatrix} \tag{10}$$

where $\Delta\mathbf{x}_k = \mathbf{x}_k - \hat{\mathbf{x}}_k$. $\Delta\theta_k$ has the information of the error of estimated state vector. Namely, error of estimated phase, carrier frequency and carrier frequency rate. $\mathbf{v}_k$ is the measurement noise and typically assumed as a white Gaussian noise with the variance as:

$$\mathbf{R} = E\left(\mathbf{v}_k\mathbf{v}_k^T\right) = \frac{1}{2TC/N_0}\left(1 + \frac{1}{2TC/N_0}\right) \tag{11}$$

where C/N_0 denotes the carrier-to-noise ratio and is normally above 40dB-Hz for nominal condition.

3 Phase Lock Loop Design

Base on the signal model defined in Sect. 2, two kinds of PLL design with KF and MHE will be constructed in this paper. According to the feedback control system design, the local signal generated by the local reference generator can be expressed as follow:

$$\hat{\mathbf{x}}_{k+1} = \mathbf{A}\hat{\mathbf{x}}_k + \mathbf{B}\mathbf{u}_k \tag{12}$$

where $\mathbf{u}_k$ is a controller and $\mathbf{B}$ is an operator that maps the controller $\mathbf{u}_k$ to the control plant. Subtract equation (12) from (1), we can get the error state:

$$\Delta\mathbf{x}_{k+1} = \mathbf{A}\Delta\mathbf{x}_k - \mathbf{B}\mathbf{u}_k + \mathbf{n}_k \tag{13}$$

The purpose of the carrier tracking is to drive the error state $\Delta\mathbf{x}_{k+1}$ approaching to zero. This can be achieved by taking $\mathbf{u}_k$ as follow:

$$\mathbf{u}_k = \mathbf{K}\Delta\mathbf{x}_k \tag{14}$$

and having the eigenvalues of $\mathbf{A} - \mathbf{BK}$ within the stable region. Usually $\Delta\mathbf{x}_k$ is unknown, therefore we take its estimate to build the controller:

$$\mathbf{u}_k = \mathbf{K}\Delta\hat{\mathbf{x}}_k \tag{15}$$

with $\Delta\hat{\mathbf{x}}_k$ has the following form:

$$\Delta\hat{\mathbf{x}}_{k+1} = (\mathbf{I} - \mathbf{LH})(\mathbf{A} - \mathbf{BK})\Delta\hat{\mathbf{x}}_k + \mathbf{L}\Delta\theta_{k+1} \tag{16}$$

where $\mathbf{L}$ is the estimator gain matrix and can be obtained from PIF and KF design approaches. Finally, the estimation can be put into the local reference generator. Combining equation (16) with (12), (15), the local signal can be generated as follow:

$$\hat{\mathbf{x}}_{k+1} = \mathbf{A}\hat{\mathbf{x}}_k + \mathbf{BK}\Delta\hat{\mathbf{x}}_k \tag{17}$$

equation (17) shows that the state feedback tracking loop design mainly focus on the design of three matrixes, namely the plant input matrix $\mathbf{B}$, the state estimator gain matrix $\mathbf{K}$, and the state feedback gain matrix $\mathbf{L}$. The design of these three matrixes will be introduced briefly below.

3.1 KF-Based Phase Lock Loop Design

The selection of $\mathbf{B}, \mathbf{K}$ should satisfy the controllability and stability of the PLL. According to [14], we use $\mathbf{B} = \mathbf{I}$ and $\mathbf{K} = \mathbf{A}$. Then (17) becomes

$$\hat{\mathbf{x}}_{k+1} = \mathbf{A}\hat{\mathbf{x}}_k + \mathbf{AL}\Delta\theta_k \tag{18}$$

According to the signal models defined in Sect. 2, the KF gain can be obtained as:

$$\mathbf{L} = \mathbf{PH}^T(\mathbf{R} + \mathbf{HPH}^T)^{-1} \tag{19}$$

where $\mathbf{P}$ is the full state estimation variance and can be obtained by discrete algebraic Riccati equation (DARE) below:

$$\mathbf{APA}^T - \mathbf{APH}^T(\mathbf{HPH}^T + \mathbf{R})^{-1}\mathbf{HPA}^T + \mathbf{Q} - \mathbf{P} = \mathbf{0} \tag{20}$$

where system noise matrix $\mathbf{Q}$ and measurement noise $\mathbf{R}$ have been given in equation (5) and (11) respectively.

3.2 MHE-Based Phase Lock Loop Design

The basic idea of Moving Horizon Estimation (MHE) is to reformulate the estimation problem as a Quadratic Programming (QP) problem with a moving, fix-size estimation window [15].

General Formulations Same as the KF, MHE obtain the state vector estimation of $\tilde{\mathbf{x}}_{k+1}$ by equation (17), where $\tilde{\mathbf{x}}_{k+1}$, $\tilde{\mathbf{x}}_k$, $\mathbf{A}$, $\mathbf{B}$ and $\mathbf{K}$ are the same as mentioned in KF. The only difference is that constrained QP is used to obtain the state error estimation $\Delta\tilde{\mathbf{x}}_k$. The QP problem incorporated in MHE can be expressed as follow:

$$\min \; J(\Delta\tilde{\mathbf{X}}_k) = \frac{1}{2}\Delta\tilde{\mathbf{X}}_k^T \mathbf{H}_k \Delta\tilde{\mathbf{X}}_k + \mathbf{f}_k^T \Delta\tilde{\mathbf{X}}_k \tag{21}$$

where

$$\Delta\tilde{\mathbf{X}}_k = [\Delta\tilde{\mathbf{x}}_{k-N+1}^T, \Delta\tilde{\mathbf{x}}_{k-N+2}^T, \cdots \Delta\tilde{\mathbf{x}}_k^T]^T \tag{22}$$

and N is the length of MHE estimation window. The expressions of $\mathbf{H}_k$ and $\mathbf{f}_k$ have the following forms:

$$\mathbf{H}_k = 2(\mathcal{H}^T\mathcal{R}^{-1}\mathcal{H} + \mathcal{A}^T\mathcal{Q}^{-1}\mathcal{A} + \mathbf{G}^T\mathbf{P}^{-1}\mathbf{G}) \tag{23}$$

$$\mathbf{f}_k = -2(\mathcal{H}^T\mathcal{R}^{-1}\Delta\Theta_k - -\mathcal{A}^T\mathcal{Q}^{-1}\mathcal{B}\mathbf{u}_k) \tag{24}$$

Once the QP problem is solved, we will have $\Delta\tilde{\mathbf{X}}_k$, in which contains the $\Delta\tilde{\mathbf{x}}_k$ required in equation (17) to acquire MHE-based PLL state vector estimation $\tilde{\mathbf{x}}_{k+1}$. According to [15], the related variables and matrixes are defined as follow:

$$\mathcal{H} = \mathbf{I}_N \otimes \mathbf{H} \tag{25}$$

$$\mathcal{R} = \mathbf{I}_N \otimes \mathbf{R} \tag{26}$$

$$\mathcal{A} = \begin{bmatrix} -\mathbf{A} & \mathbf{I} & 0 & \cdots & 0 \\ 0 & -\mathbf{A} & \mathbf{I} & \cdots & 0 \\ \vdots & \vdots & \vdots & \ddots & 0 \\ 0 & 0 & \cdots & -\mathbf{A} & \mathbf{I} \end{bmatrix} \tag{27}$$

$$\mathcal{Q} = \mathbf{I}_{N-1} \otimes \mathbf{Q} \tag{28}$$

$$\mathbf{G} = [\mathbf{I}_3, zeros(3, 3(N-1))] \tag{29}$$

$$\Delta\Theta_k = \left[\Delta\theta_{k-N+1}, \Delta\theta_{k-N+2}, \cdots \Delta\theta_k\right]^T \tag{30}$$

$$\mathcal{B} = \mathbf{I}_{N-1} \otimes \mathbf{B} \tag{31}$$

$$\mathbf{u}_k = \mathcal{K}\Delta\tilde{\mathbf{X}}_k(4:3N,1) \tag{32}$$

$$\mathcal{K} = \mathbf{I}_{N-1} \otimes \mathbf{K} \tag{33}$$

Selection of Constrains The purpose of setting constrains is to improve the anti-interference ability of the fragile carrier tracking progress, especially in the urban environment, with the severe multipath interference and frequent signal blockage. Such constrains is set in MHE-based PLL by the nature incorporated linear constrain in QP as:

$$\mathbf{A}_I \Delta\tilde{\mathbf{X}}_k < \mathbf{b}_k \tag{34}$$

where

$$\mathbf{A}_I = \begin{bmatrix} 1 \\ -1 \end{bmatrix}^T \otimes \mathbf{I}_{3N} \tag{35}$$

$$\mathbf{b}_k = \left[ones(1,N) \otimes \Delta\tilde{\mathbf{X}}_{\max}^T, ones(1,N) \otimes \Delta\tilde{\mathbf{X}}_{\min}^T\right] \tag{36}$$

The design of $\Delta\tilde{\mathbf{X}}_{\max}$and $\Delta\tilde{\mathbf{X}}_{\min}$ normally follow the three-sigma rule as bellow:

$$\begin{aligned} \Delta\tilde{\mathbf{X}}_{\max} &= +3\boldsymbol{\sigma} \\ \Delta\tilde{\mathbf{X}}_{\min} &= -3\boldsymbol{\sigma} \end{aligned} \tag{37}$$

where

$$\boldsymbol{\sigma} = \sqrt{diag\left(\mathbf{L}(\mathbf{H}(\mathbf{P} - \mathbf{A}^T\mathbf{P}\mathbf{A})\mathbf{H}^T + \mathbf{R})\mathbf{L}^T\right)^T} \tag{38}$$

Apart from setting as three-sigma, the $\Delta\tilde{\mathbf{X}}_{\max}$and $\Delta\tilde{\mathbf{X}}_{\min}$ could also use the empirical values measured in a nominal environment [15]. The constrains should be tight enough to effectively mitigate the measurement error. However, over tight would damage the robustness in high dynamics condition. There should be a compromised constraint to adapt to the robustness and dynamic response.

4 Experiment Results

The experiment is to compare the performances of the KF-base and MHE-base PLL design in the urban environment. The data used in the experiment was collected on Hongmei Viaduct and in Lujiazui CBD area in Shanghai. The two data sets are named as 'open sky data' and 'urban data' respectively. In 'open sky data' set, GPS L1 C/A PRN 23, 31 are used for analysis. In 'urban data' set, GPS L1 C/A PRN 26 is used. The basic routine is shown in Fig. 1. Specific longitude and latitude of the path for the two data sets are plotted in Figs. 2 and 4. Figures 2 and 5 are the sky plot of all the visible GPS satellites during the test (Fig. 3).

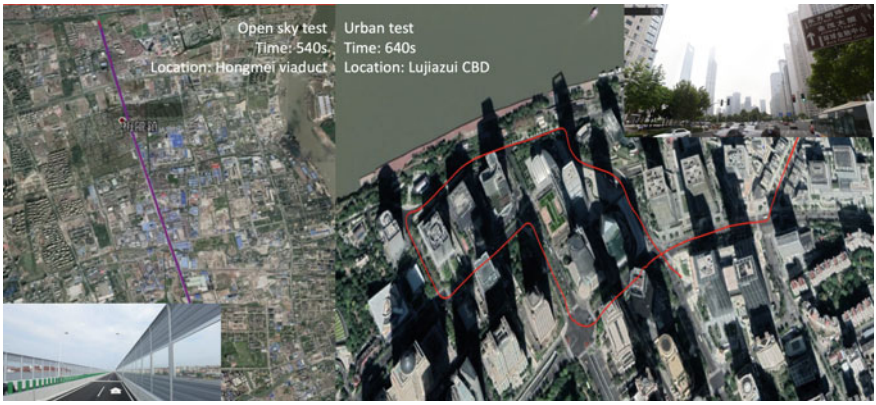

Fig. 1 Basic routes of Open sky and urban data

Fig. 2 Longitute and latitute of Open sky path

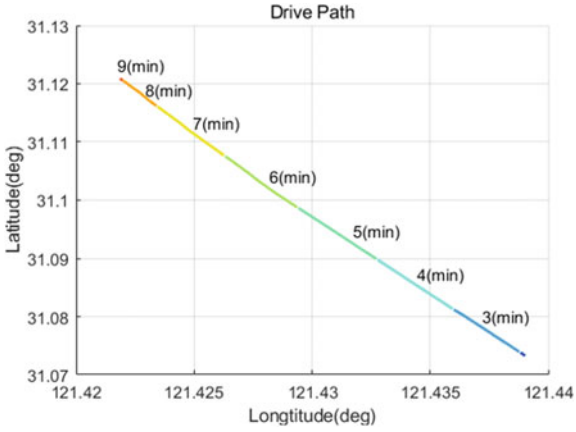

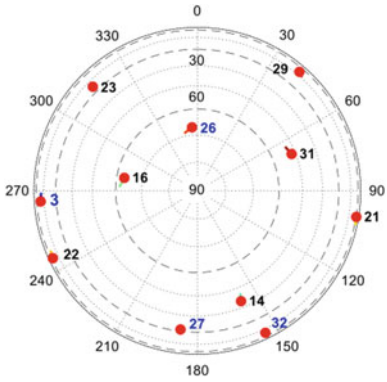

Fig. 3 Sky plot of Open sky

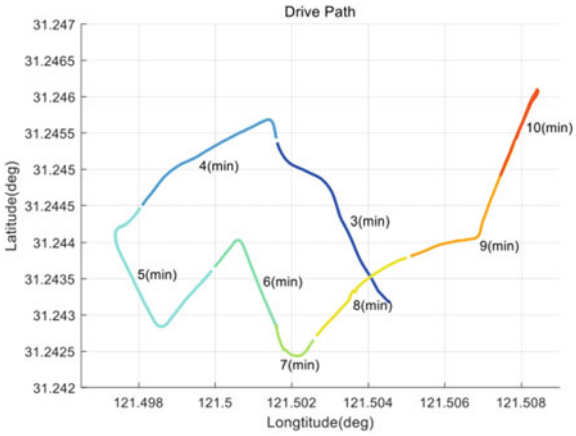

Fig. 4 Longitute and latitute of urban path

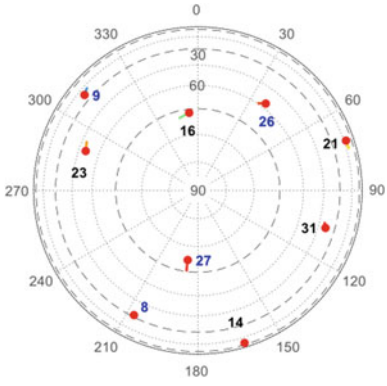

Fig. 5 Sky plot of urban

4.1 The Parameter Settings in PLL Implementation

To process the data, scaler phase tracking loop is implemented in both MHE and KF algorithms in MATLAB. The MHE estimation window length is designed as $N = 2$ and the maximum/minimum of state vector estimation error design follows the three-sigma rule. The integration time is 1 ms for both KF and MHE. To ensure stability of MHE, the PLL is first carried out with KF for $15s$, and then switch to MHE.

4.2 Signal Quality

C/N$_0$ Analysis The CN0 of PRN 23, 31 in Open sky test and PRN 26 in Urban test is shown in Fig. 6. The results are plotted in every second from $0 \sim 5$ minutes for Open sky test and $0 \sim 8$ minutes for Urban test.

Both collect on the viaduct, the PRN 31 gains higher CN0 than PRN 26, which may be caused by the difference in elevation angle. The former has an elevation angle about 50°, while the latter is about 30°. The Urban PRN 26 has an elevation angle slightly smaller than 50°, thus can been seen from Fig. 6 that the peak of its CN0 value also reaches over 45dB-Hz.

Due to the environment difference between Open sky and Uban data, one from the viaduct with few blockages and multipath, and another from CBD area where signal blockage frequently occurs, the Open sky PRN 23, 31 have fewer and less severe CN0 drop, while Urban PRN 26 suffers more obvious CN$_0$ drop (larger than 20dB-Hz) and longer fading duration (longer than 40 s).

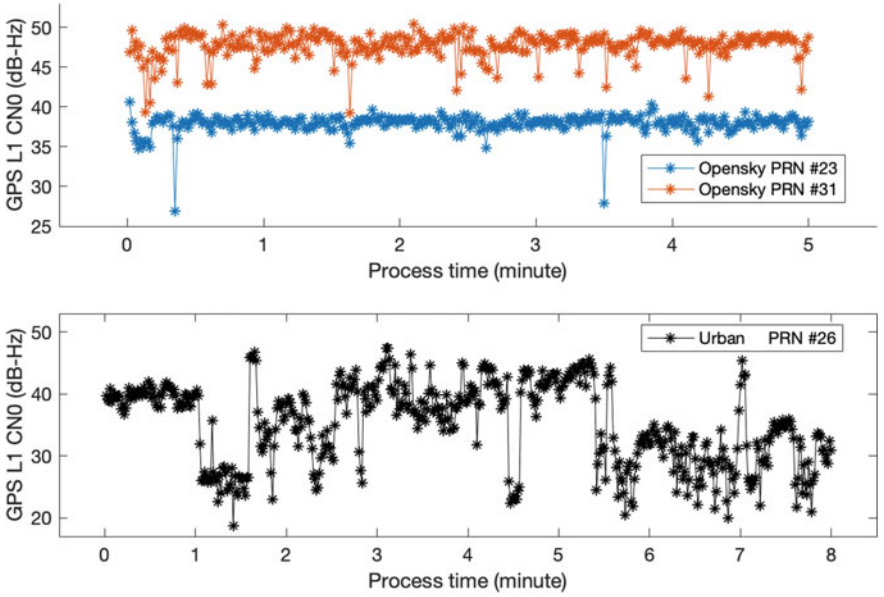

Fig. 6 CN0 of Open sky PRN 23, 31; urban PRN 26

KF-Based Doppler Frequency Analysis Fig. 7 is the doppler frequency of Open sky PRN 23 and 31 from 15 s to 5 min. The doppler frequency was estimated every 1ms.

The ideal Doppler frequency should be a straight line. Seen from Fig. 7, PRN 23 has a stronger fluctuation with the relative low CN_0 at about 39dB-Hz. In idealized situation, doppler frequency is expected to change smoothly and linearly. Signal with a sudden and severe bounce in doppler frequency, normally over 3 Hz back to nominal within 1 s, may suffer from multipath interference or signal blockage.

Figure 8 is the Doppler frequency drawn according to the Urban PRN 26, together with its trend line. Compared with the Open sky data, the frequency deviation from the trend line has risen above 100 Hz, while the former keeps within 10Hz, and causes loss-of-lock after 7 min.

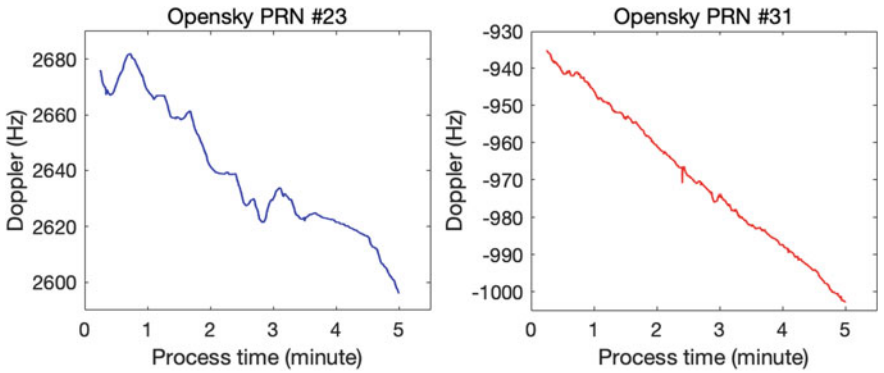

Fig. 7 Doppler of Open sky PRN 23, 31

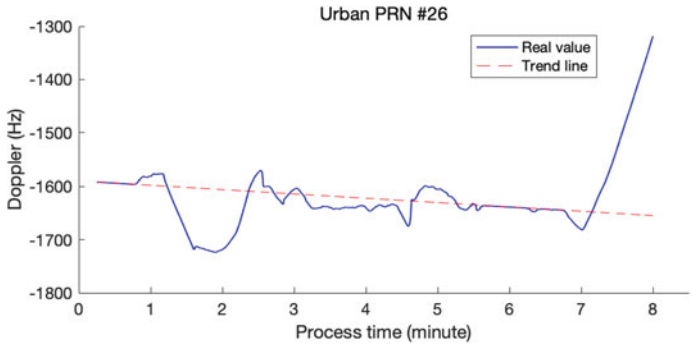

Fig. 8 Doppler of urban PRN 26

4.3 Improvements with MHE

In Figs. 9 and 10, the view in certain part of the Doppler frequency in Fig. 7 are zoomed in, and we add the result processed by MHE for comparison. During 20 ∼ 21 s in Fig. 9, PRN 23 endures a 2.5 Hz bounce, MHE algorithm reduces that error within about 1 Hz. During 144 ∼ 145 s in Fig. 10, PRN31 experiences an even larger bounce over 4 Hz, and MHE mitigated this error with the moving average operation.

Figure 11 is the zoom-in view of Fig. 8 from 60 to 180 s, in which the signal Doppler processed with KF gradually deviates from the trend line with over 120 Hz

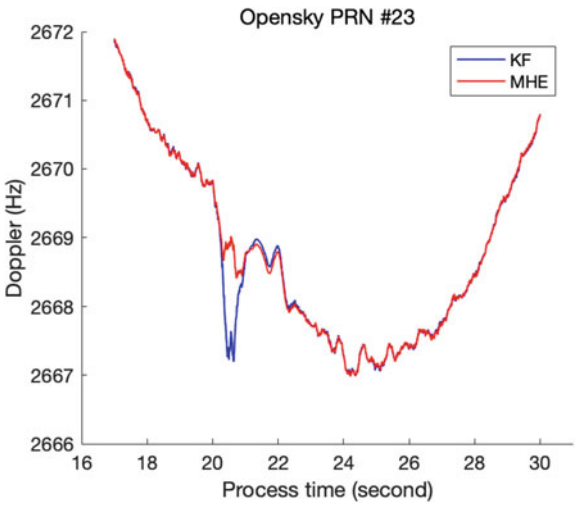

Fig. 9 Partial enlarged view of Open sky PRN 23

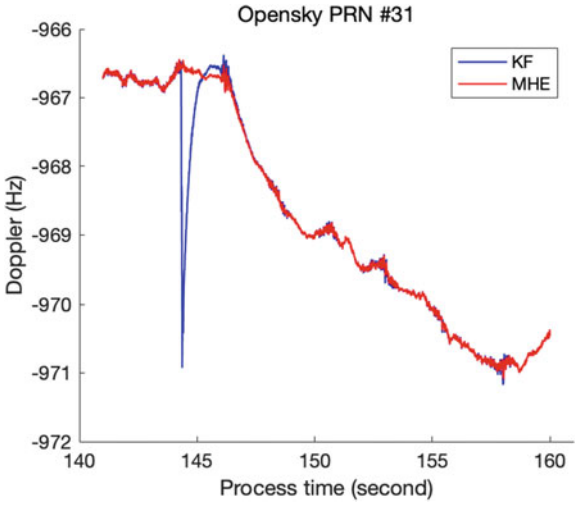

Fig. 10 Partial enlarged view of Open sky PRN 31

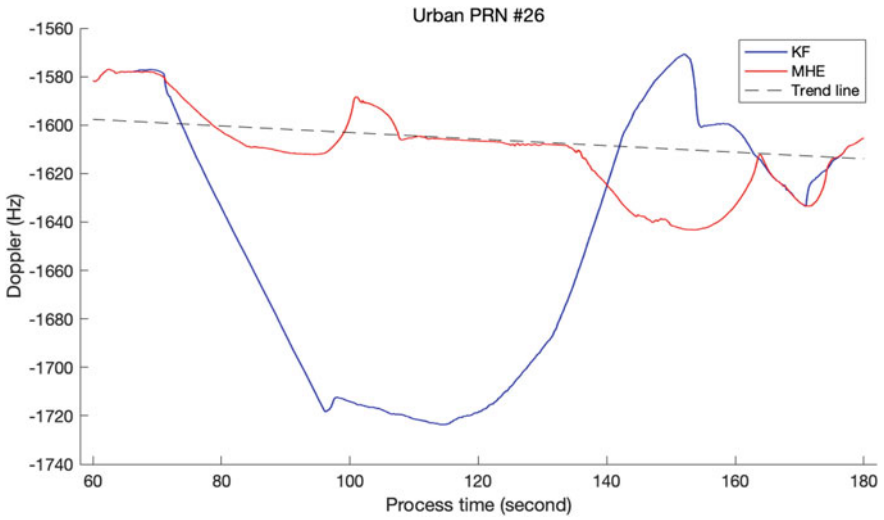

Fig. 11 Partial enlarged view of Urban PRN 26

errors during 70–140 s. Compared with KF, the MHE based tracking loop experienced a slighter degradation, where the MHE can maintain tracking the signals with a smaller frequency fluctuation relative to the trend.

5 Conclusion and Future Work

This paper mainly covers the comparison of performances between KF and MHE algorithm in urban environment. Two sets of real test data are used, one collected on the viaduct and another near CBD area. The former simulates an urban viaduct or suburb road environment with little occlusion and signal reflection, where elevation angle is an important factor to tracking quality. In such condition MHE generally deals with sudden and steep frequency jump that may caused by the multipath (normally within 1 s and over 3 Hz), and can mitigate the frequency errors. Usually MHE performs better in the presence of the intense signal fading or rapid phase changes.

The latter simulates an urban road environment covered by tall buildings and viaducts, where multipath interference and signal blockage dominates. MHE deals with large deviation from trend line (normally lasts over 1 min and exceeds 100 Hz), and can smooth the error within a 15 Hz range to prevent loss-of-lock caused by too much deviation.

In this work, a lot of effort is put into the implement of MHE algorithm. Those parameters in the tracking loop, which is specified for KF algorithm, haven't entirely go through optimization for MHE. For example, the integration time in KF algorithm is set as 1 ms, but considering the estimation window configuration in MHE, the

integration time should be properly extended. As a result, in the urban environment where tracking is difficult, the signal loses lock in the MHE algorithm, thus the comparison between MHE and KF is limited to the optimization in the Doppler frequency and not be able to extend to other aspects normally covered, like normalized signal intensity and detrended phase.

In MHE algorithm itself, some parameters are set as constant, instead of changing according to measurement. One such parameter is the estimation window length N, in this paper, this value is set as 2, a relatively small value which performs better in environment like Open sky but hard to cope with loss-of-lock situation in urban test. The extension of estimation window length could cause delayed response to environmental change, which is a drawback in high dynamics platform. Thus a balance between delay and robustness should be achieved in future. Floating the estimation window length according to the strength of interference might be a better choice. Another parameter is the linear constrain incorporated in QP problem, which is set to follow the three-sigma rule. As mentioned in Sect. 3.2.2, the constrain is recommended to set slightly looser than three-sigma rule, and could be specified to local measurement. A strict limitation to signal measurement did better in Open sky than Urban mainly for this reason.

Acknowledgements The research is supported by the funding from Shanghai Jiao Tong University (WF220541306) and Key laboratory of space microwave technology (6142411193113).

References

1. Smyrnaios M, Schön S, Nicolás ML (2013) Multipath propagation. Characterization and modeling in GNSS, geodetic sciences—observations, modeling and applications, Shuanggen Jin, IntechOpen. https://doi.org/10.5772/54567
2. Liu Y, Yan BZ (2014) A FLL-PLL cooperative GNSS weak signal tracking framework. Appl Mech Mater 551:470–477. Crossref. (Trans Tech Publications, Ltd., May 2014). https://doi.org/10.4028/www.scientific.net/amm.551.470
3. Shytermeja E (2018) Robust GNSS positioning in urban environment. Dogan Ugur Sanli, IntechOpen, Accuracy of GNSS Methods. https://doi.org/10.5772/intechopen.80412
4. Reuper B, Becker M, Leinen S (2018) Benefits of multi-constellation/multi-frequency GNSS in a tightly coupled GNSS/IMU/odometry integration algorithm. Sensors (Basel) 18(9):3052. https://doi.org/10.3390/s18093052
5. Jia QQ, Wu RB, Wang WY, Lu D, Wang L, Li J (2016) Multipath interference mitigation in GNSS via WRELAX. GPS Solutions. https://doi.org/10.1007/s10291-016-0538-9
6. Luo YR, Yu CY, Li J, El-Sheimy N (2019) Performance of Gnss carrier-tracking loop based on kalman filter in a challenging environment. ISPRS—Int Arch Photogramm Remote Sens Spat Inf Sci 42-2/W13:1687-1693. https://doi.org/10.5194/isprs-archives-XLII-2-W13-1687-2019
7. Allan DA, Rawlings JB (2019) Moving horizon estimation. In: Raković S, Levine W (eds) handbook of model predictive control. control engineering. Birkhäuser, Cham
8. Rawlings JB (2013) Moving horizon estimation. In: Baillieul J, Samad T (eds) Encyclopedia of systems and control. Springer, London. https://doi.org/10.1007/978-1-4471-5102-9
9. Ramlal J, Naidoo V, Allsford K, Hedengren J (2007) Moving horizon estimation for an industrial gas phase polymerization reactor. In: Proceedings IFAC symposium on nonlinear control systems design (NOLCOS); 2007]. https://doi.org/10.3182/20070822-3-ZA-2920.00173

10. Spivey B, Hedengren JD, Edgar TF (2010) Constrained nonlinear estimation for industrial process fouling. Indus Eng Chem Res 49(17):7824–7831. https://doi.org/10.1021/ie9018116
11. Andersson A, Thiringer T (2018) Motion sensorless IPMSM control using linear moving horizon estimation with luenberger observer state Feedback. IEEE Trans Transport Electr 4(2):464–473. https://doi.org/10.1109/TTE.2018.2790709
12. Wang Y, Yang R, Ling KV, Poh EK (2015) Robust vector tracking loop using moving horizon estimation. Proceedings of the ION 2015 Pacific PNT meeting, Honolulu, Hawaii, April 2015, pp. 640–648
13. He K, Sukkarieh S (2018) Metamorphic moving horizon estimation. Automatica 97:167–171
14. Yang R, Ling KV, Poh EK, Morton Y (2017) Generalized GNSS signal carrier tracking: part I-modeling and analysis. IEEE Trans Aerosp Electr Syst 53(4):1781–1797. https://doi.org/10.1109/TAES.2017.2673998
15. Wang Y (2016) Modelling and performance analysis of constrained GNSS vector tracking loop using moving horizon estimation. http://hdl.handle.net/10356/66223. Accessed 2016-03-21T01:53:51Z

Feasibility Exploration on Simulation Study Based on Peridynamic for the Bio-Inspired Nacre Nano Composite Against the Impact

Zhiwei Zhou, Shufan Wu, Zhongcheng Mu, Wei Wang, and Ningjing Jiang

Abstract The deformation and failure of materials and structures under high speed impact is a major problem in aerospace, automotive engineering and protection engineering. In this paper, based on peridynamics (PD) model, the deformation and damage mechanism of the bio-inspired nacre nanocomposite against the impact was discussed. According to the existing experiments, the crack evolution and propagation process of "brick-mortar" split-layer microstructure under the impact were approached systematically. According to the result that impact damage only occurs on the top of bio-inspired nacre nanocomposite, it is concluded that peridynamics can be well applied to the analysis of nacre nanocomposites under impact.

Keywords Peridynamics · Bio-inspired nacre nanomaterial · Crack propagation

1 Introduction

The understanding of materials under impact is of great significance in the field of aerospace. In the cosmic environment, micrometeoroid impacts may cause incalculable damage to spacecraft and the international space station. Even the smallest pieces of debris have high relative speeds relative to spacecraft or the international space station, and the highly penetrating impacts they cause can cause problems (Fig. 1).

Under extreme conditions such as the universe, traditional protective engineering materials similar to concrete can no longer meet the requirements of some special environments. In this regard, on the basis of long-term research on traditional materials, scholars from all over the world not only further improve the existing materials from engineering technology, but also learn from nature to imitate and prepare some biomimetic materials with special properties to meet the performance requirements of various special environments.

Z. Zhou · S. Wu (✉) · Z. Mu · W. Wang · N. Jiang
Shanghai Jiao Tong University, Shanghai, China
e-mail: shufan.wu@sjtu.edu.cn

Z. Jing and X. Zhan (eds.), *Proceedings of the International Conference on Aerospace System Science and Engineering 2020*, Lecture Notes in Electrical Engineering 680,
https://doi.org/10.1007/978-981-33-6060-0_29

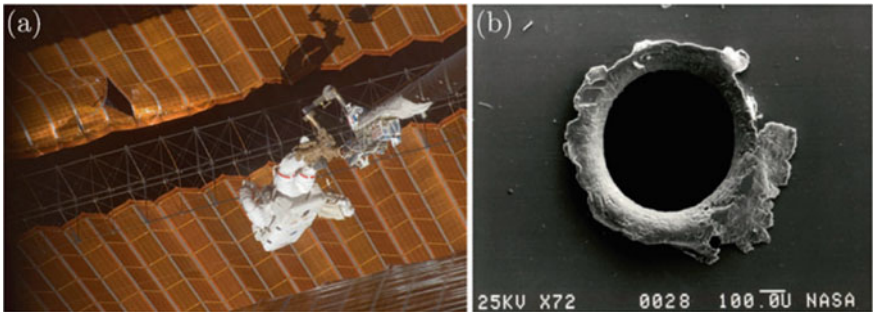

Fig. 1 Damage to the International Space Station by micrometeoroids. **a** Critical repairs were made to the perforated solar wing by astronaut Scott. **b** Image of the hole caused by orbital debris on the panel in the Solar Max experiment. (Images: NASA Orbital Debris Program Office)

More and more researchers are paying attention to hard natural biomaterials because of their various grade structures and excellent mechanical properties. The most famous of these is the nacre, which is the main component of the mollusk protection shell. Its microstructure is mainly composed of microscopic ceramic slices, which are tightly wrapped together by a thin layer of biopolymer, that is, the typical "brick-mortar" split-layer structure with multi-level soft and hard materials combining with each other. It has the characteristics of "weak component, strong composite" and high toughness and strength.

Because of its unique structure, high strength and good toughness and widely followed, preparation of lightweight, high strength, super toughness of layered composite materials has become the model structure, its multiscale, "brick-mortar" staggered-layer microstructure gives its unusual mechanical properties [1–3], especially excellent resistance to impact and mechanical performance, give a new way of thinking for many actual engineering design of high performance impact protective material [4, 5]. However, in the existing public literature, which will be discussed in detail in the second section, most of the research work is focused on the scope of static mechanics. There are only a few literatures that explore the mechanical behavior of nacre materials under high strain rate impact loading, and their research is insufficient. The research scale belongs to the macroscopic scale, and there is no research on the impact property and dynamic toughening mechanism of nacre nanomaterials with smaller scale.

However, bio-inspired nacre nanomaterials have obvious microscale interface effect and under the impact load, the bionic shell nanomaterials problem belongs to the mechanical behavior of discontinuous. It's easy to produce singularity in the process of damage evolution analysis by using the traditional finite element method or finite difference numerical method to simulate and analyze bio-inspired nacre nanomaterials dynamic mechanical behavior of nanometer materials, the analysis will not be accurate and will not be able to further characterize the biomimetic micro interface for crack evolution of the shell. Moreover, the toughening mechanism of biomimetic nacre nanomaterials mainly comes from the microscopic interface effect

between organism and non-organism, and the simulation scale is limited. Therefore, in order to break through the complexity of theoretical analysis and the limitation of limited information acquisition of experimental methods, it is particularly urgent to find a numerical method that can accurately simulate the dynamic mechanical behavior of biomimetic shell nanomaterials.

In recent years, peridynamics (PD) [6–8] has developed rapidly. It combines the advantages of molecular dynamics method and meshless method, and has unique advantages for solving discontinuous problems. It avoids the singularity of traditional macroscopic methods based on continuity hypothesis modeling and solving spatial differential equations in the face of discontinuous problems, and breaks through the limitation of classical molecular dynamics methods in the calculation scale, and shows high solution accuracy and efficiency in the analysis of macro/micro discontinuous mechanical problems. PD method is suitable for dealing with the complex non-planar multi-crack propagation problem in 3D space, and can simulate the entire process of progressive failure of materials. It is mainly used to study the complex mechanical behaviors of dynamic cracks such as propagation and bifurcation in homogeneous and heterogeneous materials [9] and the failure caused by impact damage [10].

Moreover, for the interface layer of heterogeneous materials, PD method can use the force response function of different properties to describe the properties of different materials. Therefore, by comparing the applicable scope of PD numerical simulation method and the microscopic characteristics of biomimetic shell nanomaterials, PD method is an ideal numerical analysis method to analyze and study the dynamic mechanical behavior of bio-inspired nacre nanomaterials.

In this paper, the mechanical behavior of bio-inspired nacre nanomaterials with brick and mud structure in Sect. 2, then PD is introduced in Sect. 3, and the simulation of PD on brittle materials and nacre nanomaterials with brick-mortar structure on impact is introduced in Sect. 4. Finally, it is concluded that PD has a strong applicability in the simulation of brick-mortar structure under impact process.

2 The Bio-Inspired Nacre Nano Composite

At present, the shell nacre's excellent mechanical properties have been verified through a variety of mechanical testing, including tensile testing [11], compression test [12], bending test [13], shearing test [14], indentation test [15] and so on, which caused wide public concern over the excellent tensile properties, the toughness at an astonishing 1.24 kJ/m^2, more than 3000 times that of calcium carbonate ore [15]. Its good mechanical properties are mainly attributed to the multi-level "brick-mortar" split-layer microstructure. Analyzing and studying the toughening mechanism of the multi-level "brick-mortar" split-layer microstructure is the basic and core part to understand the mechanical behavior of shell materials (Fig. 2).

Jager and Fratzl [17] proposed a "shear lag" mechanical model for shell structures, which decomposed the loading deformation into the shear deformation between hard

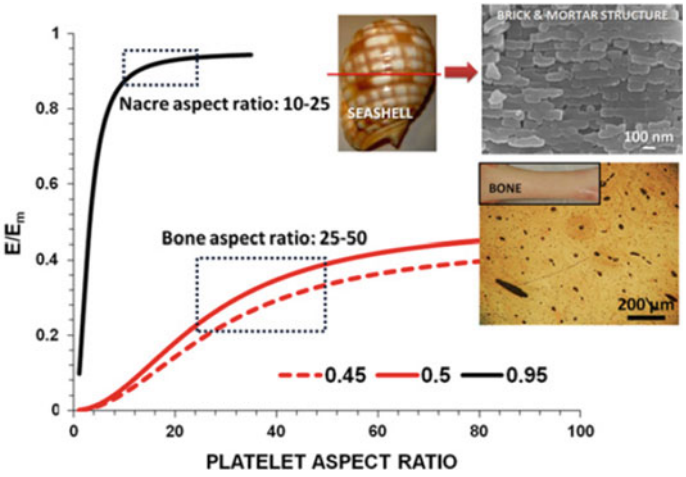

Fig. 2 Dependence of stiffness of bio-composites as a function of aspect ratio of ceramic bricks and volume fraction of ceramic as laid down by Gao et al. [16]. Inset shows the brick and mortar type microstructural arrangement observed in nacre, and microstructure of bone

components and soft components, and the tensile deformation of hard components. Yan [18] proposed a cohesive spring system model, combined with Monte Carlo method, and analyzed the crack cracking process of such "brick-mortar" structure from the perspective of local and global stability analysis. Katti [19] showed through the three-dimensional finite element simulation analysis that the mineral bridge connection between shells is the main factor of high toughness and high strength. Abid [20] used DEM to analyze and study the fracture process of shell materials. Wang [21], Bartelat [22] and Zavattieri [23] analyzed the influence of mechanical behavior on the geometric characteristics of hard components. Djumas [24] carried out topological optimization design on the interface geometry of shell structure based on the feature of "interlock" between layers, and proposed a non-regular interface "brick-mortar" bionic structure. Wang [25] analyzed the influence of a single lamellar layer on the overall damage tolerance of shell through nano-indentation experiment and microscopic detection method.

Ritchie at multi-scale nano and micro to macro perspective, the toughening mechanism of the shellfish as intrinsic to the material damage (internal plastic deformation) and external crack tip shielding mechanisms (external toughening), the result of competition between internal inherent plastic deformation is mainly embodied in the submicron scale, external toughening mechanism mainly on the micron scale, competition between two mechanisms resulting in shellfish structure of macro mechanical properties. Based on the research achievements of previous researchers, Wegst [26] summarized the toughening mechanism of biomimetic shell materials in four aspects:

(i) mineral bridge connection between lamellar connections;
(ii) surface roughness between layers;
(iii) strong adhesion of organic layer;

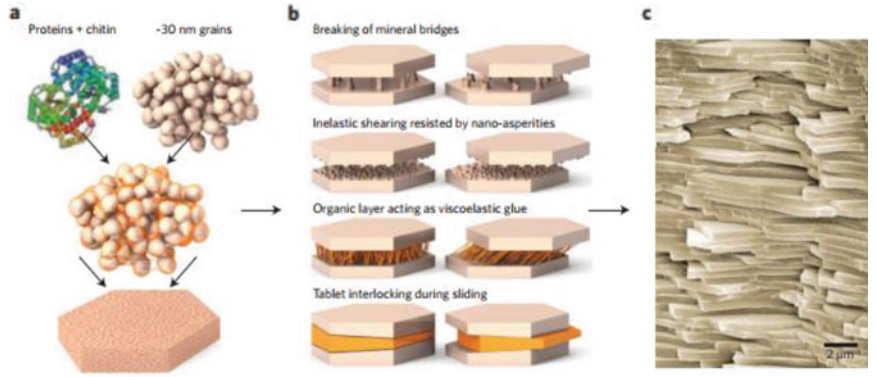

Fig. 3 Toughening mechanism of nacre [25]

(iv) "interlocking" effect of split-level structure.

Four toughening mechanisms are shown in Fig. 3.

The mechanical behavior of split-level microstructure of "brick-mortar" structure of nacre has made a series of outstanding scientific research achievements, but in the existing public literature, most of the research work focuses on static mechanics, the mechanical behavior of literature of exploring the nacre materials under high strain rate impact loading is insufficient and the lack of depth. Wu [24] carried out a drop hammer experimental simulation analysis of shell "brick-mortar" structures by means of three-dimensional finite element numerical simulation analysis method, and the results showed that there was an optimal value of interface strength between the layers, which could promote the best impact resistance performance of nacre structures. Gu [25] made use of 3D printing technology to prepare the biomimetic structure of macroscopical nacres. The drop hammer experiment and numerical simulation analysis show that the cross-laminae is the main factor to improve the anti-impact performance. Yang huiwei [27] used finite element analysis method to analyze and study the basic mechanical properties of nacre "brick-mortar" structure and the dynamic response and penetration resistance of plate and nacre structure under impact. The above research objects are all biomimetic engineering structures, and the research scale belongs to the macroscopic scale, which does not involve the research on the impact performance and dynamic toughening mechanism of bio-inspired nacre nanomaterials with smaller scale.

3 PD Theory

The idea of peridynamicsis a non-local continuum mechanics theory first proposed by professor Silling S.A of Sandia national laboratory [5]. The theory is based on the idea of long-term non-local action, shown in Fig. 4, to establish a mechanical model,

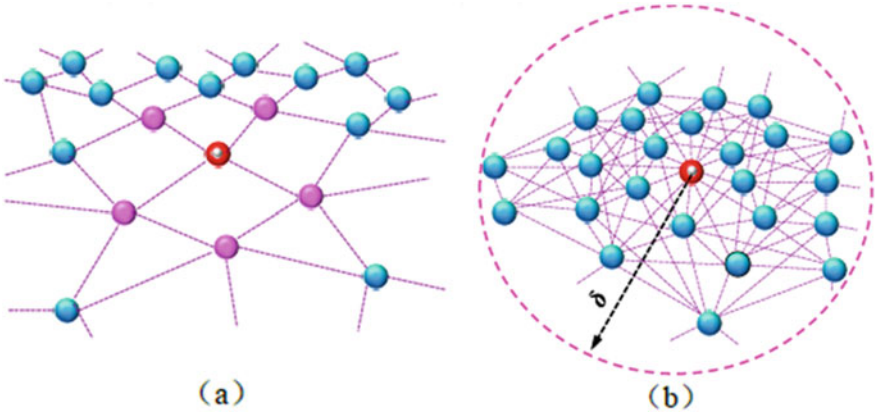

Fig. 4 Diagram of local and nonlocal interactions [5]. **a** Local interaction; **b** Nonlocal interaction

which has the advantages of molecular dynamics (MD), meshless method (MF) and finite element method (FEM).

Different from displacement partial differential equation solution model of traditional local model, the theory is the idea of nonlocal. By solving the space integral type motion equation to describe the material mechanical behavior, the unified description of the mechanical behavior of continuum and non-continuum can be realized, which can completely avoid the displacement derivative. It has a unique advantage to solve the discontinuous problem and can be used to predict failure in the material.

In PD theory, internal forces are expressed by the interaction of non-local forces between particles in a continuum. Each material point interacts with other material points at a limited distance, which is called the horizon.

At the same time, the theory holds that the interaction between any particle in the configuration and other particles in the horizon is generated by "bond", and the pairwise force function is used to describe the magnitude of the force. Thus, the concept of material damage is introduced into PD theory. Since the fracture of the "bond" is irreversible, the deformation, damage initiation, crack propagation and final failure form of the structure can be described by judging the fracture count of the bond, without the help of failure criteria, stress intensity factors or crack propagation rules under complex stress conditions. Therefore, PD can well simulate discontinuous problems such as spontaneous crack initiation and propagation.

Two types of PD equation: bond—based PD and state—based PD are mainly used. The latter is divided into two kinds: ordinary PD and non-ordinary PD. All of these variables have to satisfy the conservation law.

3.1 Bond-Based

The PD equation can be understood as an integral expression of linear momentum balance in continuum mechanics.

The motion equation of particle in elastic material can be expressed as

$$\rho(x)\ddot{u}(x,t) = \int_{Hx} f\left(u' - u, x' - x\right)dV' + b(x,t) \tag{1}$$

where f (u' − u, x' − x) is a pairwise force function in the PD bond that connects material points x', x. And u is the displacement vector field.

PD model was a bond-based model at first. It was deduced by assuming that the density of strain energy in the horizon was equal to the density of traditional strain energy. In the derivation, it is assumed that the interaction forces at the bond-based PD material points is same in magnitude but with opposite direction. No distinction is made between volume deformation and shape deformation of the model. Although the bond-based PD is only applicable to models with specific Poisson's ratio (3D and 2D plane strain models with Poisson's ratio of 1/4, the poisson's ratio of 2D plane stress model is 1/3), but due to its clear physical meaning and simple calculation, it has been rapidly developed and improved.

In 2004, Silling et al. proposed the Prototype Microelastic Brittle (PMB) model [28] based on the theoretical framework of bond-based PD by assuming the linear relationship between constitutive force function and elongation. Then, Silling and Bobaru established the non-linear elastic constitutive model [29]. In PMB model, the material point bond force is constant, which cannot reflect the relationship between the long-range force and the distance between material points. The interaction of material points is similar to the tension and pressure action of spring. In order to reflect the constitutive relation of long range force characteristics between material points, Huang Dan et al. [30–32] improved the original PMB model by introducing nonlinear continuous kernel function into the constitutive force function. An example is given to verify the effectiveness of the improved PMB model. At present, the bond-based PD constitutive function can deal well with the failure process of brittle and quasi-brittle materials, but it is insufficient to deal with the failure of other characteristic materials, such as plastic materials and viscoelastic materials.

The traditional bond PD is only suitable for a specific Poisson ratio. The essence of Poisson's ratio being fixed is that the constitutive force function only considers the axial interaction between material points and ignores the influence of surrounding material points on themselves [33]. In order to solve this problem, Prakash [34], Zhu [35], Zhou [36, 37] et al. considered the rotation Angle between material points by introducing additional tangential stiffness parameters. Breaking through the material Poisson's ratio is fixed limit. Gerstle [38] proposed the Micropolar Peridynamic model, which extended the poisson's ratio limit of the three-dimension and plane strain problem to 0–1/4, and the poisson's ratio limit of the plane stress problem

to 0–1/3 [39]. However, the principle of strain homogenization of the micropole model remains to be further studied [40]. In general, the method of introducing additional parameters only expands the scope of application of Poisson's ratio, but cannot completely break the limit of Poisson's ratio.

3.2 State-Based PD

According to the interaction forces between two material points are assumed to be equal in magnitude and opposite in directions, the original bond-based peridynamic formulation suffers from a limitation on material constants. This problem can be solved by state-based PD. The state is a mathematical concept proposed by Dr. Silling and his collaborators, more specifically it is a mapping from a vector space to a set of tensors. A state can also be considered as an array, and its function is to store information about the parameter of the PD bond associated with a particular material point. For example, a force state stores the PD forces related to a bond. State-based PD is such that the response of a material point depends on the deformation of all the material points within its horizon. Considering the force state, the equation of motion of a material point based on these assumptions above can be written as

$$\rho(x)\ddot{u}(x,t) = \int_{Hx} \left\{ \underline{T}(x,t)\langle x' - x \rangle - \underline{T}(x',t)\langle x - x' \rangle \right\} dV' + b(\mathrm{x} + \mathrm{t}) \qquad (2)$$

where $\underline{T}\langle \cdot \rangle$ represents the force state.

Theoretically, according to the relationship between the direction of the interaction force and the bond deformation, the state-based PD is divided into ordinary and non-ordinary state-based PD. In the ordinary PD, the bond forces between the material points are different in different directions. In the non-ordinary state PD, the bond forces between the material points are unequal in magnitude and the arbitrary in direction. Studies have shown that the ordinary state-based PD can well express the crack development process [41].The zero-energy mode of non-ordinary state-based PD will be exist at the crack tip, which will cause numerical oscillation and lead to inaccurate calculation results [42].In order to solve the numerical oscillation and improve the calculation accuracy, most scholars adopt the data smoothing technology [43, 44] or the method of controlling the parameters of the zero-energy mode [45, 46]. In addition, Breitenfeld [47, 48] et al. defined the concept of PD stress tensor and established the equivalence relation between PD and traditional mechanical parameters. When the distance between adjacent material points in PD horizon region is infinitely close to zero, PD becomes a traditional continuum mechanical model [49–51]. In 2010, Silling proposed the concept of "double States" [52] and "modulus State" [53], which was further improved in the theory of modal PD. Let $\underline{M}$ denote a vector state such that $\underline{M}\langle x - x' \rangle$ is a unit vector pointing from the deformed position of x toward the deformed position of x'. If there's a material which is deformed and

have a scalar state like $\underline{T} = \underline{t}\,\underline{M}$, the material can be called ordinary. If it does not have such property, then it is non-ordinary, the differences are shown in Fig. 3. For a linear elastic isotropic material, the force state is given by

$$\underline{T}(x,t)\langle x' - x\rangle = \left(\frac{2ad\delta}{|x' - x|}\theta(x,t) + bs\right)\frac{y' - y}{|y' - y|} \tag{3}$$

where a, b and d are PD parameters and θ(x, t) is the PD dilatation term. In the non-ordinary state-based PD, this assumption is negligible as long as PD forces in any direction are allowed. It is so critical to make sure that the angular momentum is conserved. Because it won't be transcendental realized compares to the bond-based and ordinary state-based formulations. Therefore, for the non-ordinary state-based PD, the following relationship must hold (Fig. 5)

$$\int_{Hx} \left\{(\mathrm{y}' - \mathrm{y}) \times \underline{T}(x,t)\langle x' - x\rangle\right\}\mathrm{dV}' = 0 \tag{4}$$

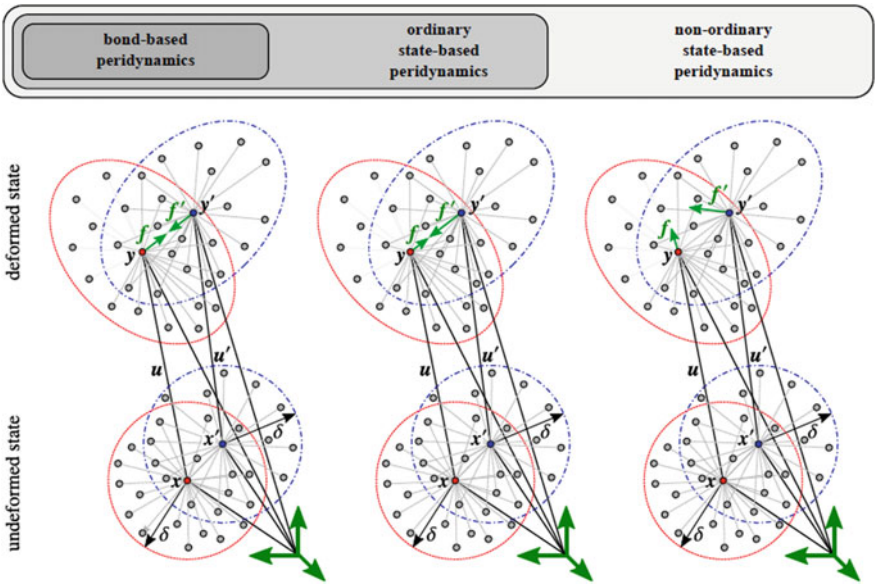

Fig. 5 Illustration of the deformed state and undeformed state of bond-based (left), ordinary state-based (center) and non-ordinary state-based PD formulations (right) [54]

4 PD Model Under Impact

In the impact problem we consider in this section, the object of the material's reaction (an analysis of the impact velocity range and the assumption of isothermal conditions) can be considered to be brittle (i.e., plastic dissipation is negligible). The simplest constitutive model of brittle materials is used in the existing research on brittle materials such as glass. In brick-mortar structure, the impact problem is more complicated because of the combination of hard and soft phases. The purpose of the PD model is to rely on a simple, basic damage mechanism that can contain a variety of failure modes from fine crack to fragmentation and anything in between.

This section first discusses several options for modeling brittle damage with PD, and introduces two kinds of convergence [55, 56]: δ—convergence and m- convergence. For a complete explanation of the complex pattern of how and why cracks arise and propagate during impact on brittle targets. Secondly, based on the impact damage model of brittle materials, the damage of brick-mortar structures under impact is discussed.

4.1 Convergence Study of PD Modeling

In δ-convergence $\delta \to 0$ and m $(= \delta / \Delta x)$ is fixed or increase and δ decrease but at a slower rate. In this case, if the classical solution exists, the numerical dynamic approximation converges to the approximation of the classical solution. The larger m, the closer the approximation.

M—convergence: δ is fixed and m $\to \infty$, approximate numerical PD converge to a given δ exact nonlocal PD solutions.

Material points, an increase in the number of each node and solution convergence Δx becomes smaller and smaller.

4.2 Analysis of Brittle Material and Brick-Mortar Structure Material

In the analysis of the impact process of brittle materials, Florin et al. [57] first used brittle damage in the dynamics model and compared the results with the damage morphology observed in experiments on a seven-layer glass system with polycarbonate layer substrate. Most of the fracture patterns observed in his experimental results can be well reproduced layer by layer by simplified confining dynamic model from the time of contact between the projectile and the glass laminate (Figs. 6 and 7).

Through his research results, it can be found that in the experimental conditions on multi-layer glass blocks, PD model captures some basic damage and fracture

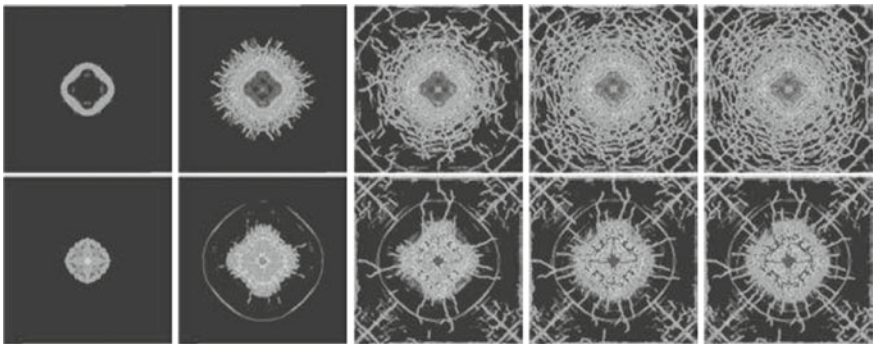

Fig. 6 Time evolution of damage for the first glass layer in the laminate: top row shows the impact face, bottom row shows the back of this first layer. From left to right, snapshots taken at 9, 27, 43, 60, and 127 μs from the time of contact between the projectile and the glass laminate [32]

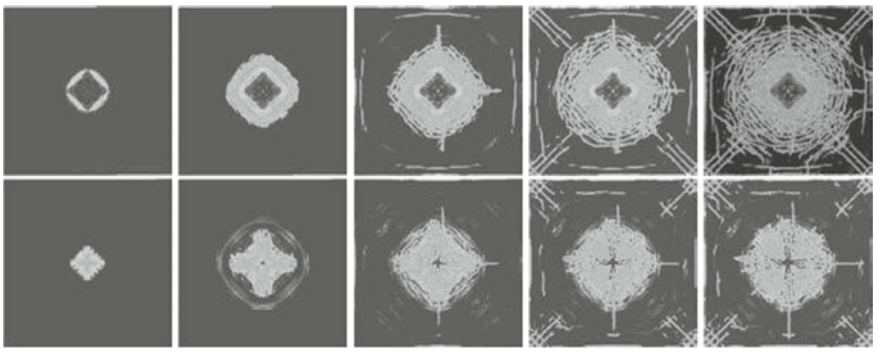

Fig. 7 Time evolution of damage for the last layer of glass (7th) in the multilayered system: top row shows the impact face, bottom row shows the back of the this seventh layer. From left to right, snapshots taken at 36, 50, 79, 110, and 161 μs [32]

characteristics of multi-layer glass system in high-speed collision. It is important to note that the results obtained here do not use any explicit material strain rate correlation. All strain rate dependence in the results are due to wave propagation, damage and fracture dynamics implicit in the brittle multilayered system. The results of his study are in good agreement with the experimental results. It can also be explained that under the strain rate caused by high-speed impact, glass exhibits a very close quasi-brittle material.

Therefore, no explicit strain rate dependence is required to simulate the mechanical behavior under such loading conditions. Sneha Akula [58] studied the impact process of two layers of soft phase and three layers of soft phase with a volume ratio of 20% of brick and mud. His study used an impactor with an initial velocity of 500 m/s to ram all samples, using a uniform time step of 10 ns, which was stable under all test conditions. To make the impactor at least as thick as the sample, he

chose the impactor with a diameter of 9 mm. And the need to change the horizon (delta) and the grid spacing (Δx) for each sample cases, to adapt to the soft phase.

Here are the results of the simulation (Fig. 8, 9, 10 and 11).

The above are the simulation results of time step 66,132,200 μs, and it can be seen that the deformation of the material is very intense in the soft phase. The soft phase deformation is not gradual, appears to be split, and has a hard phase in between. The initial brick has damage, the surrounding soft phase is deformed, limiting the damage to the brick, and the third layer has no damage. This unrealistic deformation is caused by the linear stress-strain relationship of the rubber material model, while in fact the rubber material has nonlinear elastic behavior.

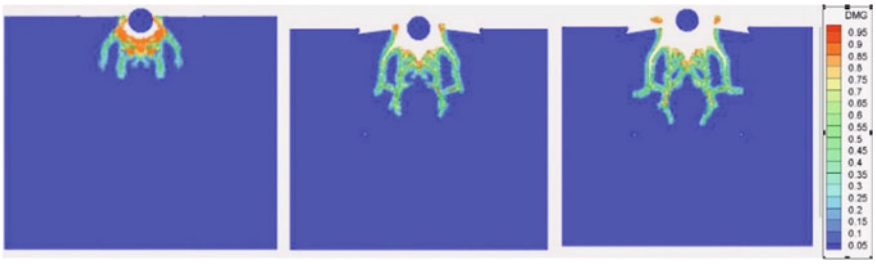

Fig. 8 Damage in the 2 brick-mortar layer structure [33]

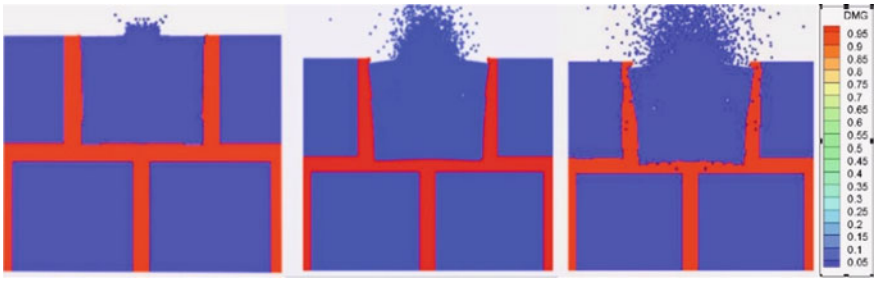

Fig. 9 Material distribution of two brick-mortar layer structure [33]

Fig. 10 Damage profile in 3 brick-mortar layer of structure [33]

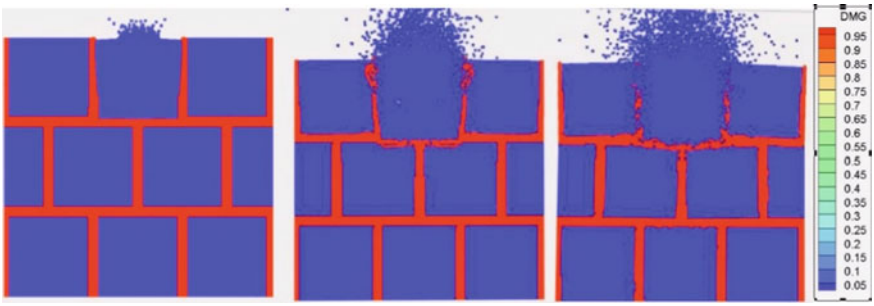

Fig. 11 Material distribution in 3 brick-mortar layer structure [33]

Damage is observed in all different microstructure and is limited to the initial rigid phase. Compared with the linear elastic model, the nonlinear elastic model has stronger actual deformation ability to soft phase.

Further observation shows that the penetration of the material in the soft phase can be observed even with the nonlinear model. Material penetration exists even with a low time step value of 0.1 ns, whereas the current simulation uses a time step of 10 ns. The short-range force has also been increased to 1000 times the current value, and material penetration is still observed.

5 Conclusion

This paper firstly introduces the prospect of bio-inspired nacre nanomaterial with brick-mortar structure in engineering application, and then introduces the PD theory. When the PD model simulates the failure, it is not necessary to make any assumption about the continuity of displacement field, and the concepts of "stress" and "strain" are not needed.

In this paper, the impact of brittle materials such as glass is studied. The dynamic results show that it is possible to obtain the dynamic fracture and damage prediction simulation of multi-layer brittle materials under high-speed impact. The microstructure of two layers of mortar and three layers of mortar with a volume ratio of 20% was also studied. In all cases, it was observed that damage was limited to the effects of the initial brick. And through the study on the deformation of the soft phase in the sample, it is found that the nonlinear model is helpful to observe the soft phase more clearly, but even if the linear elastic model is used, the damage can be accurately expressed. Finally, it can be concluded that the peridynamics method can describe and simulate the failure process of brick-mortar structures under impact.

Although the characteristics of the macro-microscopic combination and non-local integration of PD method have shown strong advantages that other traditional methods do not have when analyzing discontinuous mechanical problems at different scales, PD method, as a new numerical method, also has some shortcomings. When

the elastic deformation problem without damage is simulated, the computational efficiency of PD is significantly lower than that of the traditional finite element method. Most of the existing PD simulation adds modification to describe the constitutive information of materials on the basis of the central action of material point pairs, resulting in the constitutive relationship itself is not accurate, and the application scope is limited. These problems need further study.

References

1. 俞书宏. 仿生纳米结构材料[J]. 功能材料 (2008) 5(5–6):1–10. (Yu S (2008) Biomimetic nanostructured materials [J]. Funct Materi 5(5–6):1–10)
2. 孙 娜,吴俊涛,江 雷. 贝壳珍珠层及其仿生材料的研究进展[J]. 高等学校化学学报, 2011, 10: 2231–2239. (Na S, Jun-Tao W*, Lei J* (2011) Research progress of nacre and biomimetic synthesis of nacre-like materials[J]. Chem J Chinese Univ 32(10):2231–2239)
3. 张以河, 付绍云, 李国耀, 李广涛, 严庆. 聚合物基纳米复合材料的增强增韧. (Zhang Y, Fu S, Li G, Li G, Yan Q (2004) Strengthening and toughening mechanisms of polymer based nanocomposites[J]. 5:99–105)
4. Sun LY, Gibson RF, Gordaninejad F, Suhr J (2009) Energy absorption capability of nanocomposites: a review[J]. Compos Sci Technol 69:2392–2409
5. 杨会伟,路国运. 砌浆层状复合材料珍珠层的应变率效应[J]. 复合材料学报, 2017,34(12):2756–2761.机理[J]. 高技术通讯 (2004), 5:99–105. (Yang H, Lu G (2004) Effect of strain rate on nacre with brick-and-mortar microstructure [J]. Acta Materiae Compositae Sinica 2017(12):2756–2761)
6. Silling SA (2000) Reformulation of elasticity theory for discontinuities and long-range forces[J]. J Mech Phys Solid 48(1):175–209
7. 黄丹, 章青, 乔丕忠, 沈峰. 近场动力学方法及其应用[J]. 力学进展, 2010, 40 (4):448–459. (HUANG D, ZHANG Q et al (2010) A review on peridynamics(Pd)method and its applications [J]. Adv Mech 40(4))
8. 乔丕忠, 张勇, 张恒, 张律文. 近场动力学研究进展[J]. 力学季刊, 2017, 38(01): 1–13. (Qiao PZ, Zhang Y, Zhang H, Zhna LW (2017) A Review on advances in peridynamics[J]. Chinese Q Mech 38(01):1–13)
9. Killic B, Madenci E (2009) Prediction of crack paths in a quenched glass plate by using peridynamic theory[J]. Int J Fract 156(2):165–177
10. Sun CY, Huang ZX (2016) Peridynamic simulation to impacting damage in composite laminate[J]. Compos Struct 138:335–341
11. Currey JD (1977) Mechanical properties of mother of pearl in tension [C]. Proc Royal Soc London 196:443–463
12. Menig R, Meyers MH, Meyers MA et al (2000) Quasi-static and dynamic mechanical response of Haliotis rufescens (abalone) shells [J]. Acta Mater 48:2383–2398
13. Wang RZ, Suo Z, Evans AG et al (2001) Deformation mechanisms in nacre [J]. J Mater Rese 16:2485–2493
14. Li L, Ortiz C (2014) Pervasive nanoscale deformation twinning as a catalyst for efficient energy dissipation in a bioceramic armour [J]. Nat Mater 13:501–507
15. Nukala PK, Simunovic S (2005) A continuous damage random thresholds model for simulating the fracture behavior of nacre [J]. Biomaterials 26:6087–6098
16. Gao H, Ji B, Jäger IL, Arzt E, Fratzl P (2003) Materials become insensitive to flaws at nanoscale: lessons from nature. Proc Natl Acad Sci USA 100:5597–5600
17. Jäger I, Fratzl P (2000) Mineralized collagen fibrils: a mechanical model with a staggered arrangement of mineral particles[J]. Biophys J 79:1737–1746

18. Yan Y, Nakatani A (2019) Stability controlled crack initiation in nacre-like composite materials[J]. J Mech Phys Solid 125:591–612
19. Katti KS, Katti DR, Pradhan SM, Bhosle A (2005) Platelet interlocks are the key to toughness and strength in nacre[J]. J Mater Res 20(5):1097–1100
20. Abid N, Pro JW, Barthelat F (2019) Fracture mechanics of nacre-like materials using discrete-element models: Effects of microstructure, interfaces and randomness[J]. J Mech Phys Solid 124:350–365
21. Wang RZ, Suo Z, Evans AG, Yao N, Aksay IA (2001) Deformation mechanisms in nacre. J Mater Res 16:2485–2493
22. Barthelat F, Li CM, Comi C, Espinosa HD (2006) Mechanical properties of nacre constituents and their impact on mechanical performance. J Mater Res 21:1977–1986
23. Zavattieri PD, Hector LG, Bower AF (2008) Cohesive zone simulations of crack growth along a rough interface between two elastic-plastic solids. Eng Fract Mech 75:4309–4332
24. Wu KJ, Zheng ZJ, Zhang SS, He LH et al (2019) Interfacial strength-controlled energy dissipation mechanism and optimization in impact-resistant nacreous structure[J]. Mater Des 163:1–9
25. Gu GX, Takaffoli M, Buehler MJ (2017) Hierarchically Enhanced Impact Resistance of Bioinspired Composites[J]. Adv Mater 29:1–7
26. Wegst UK, Bai H, Saiz E et al (2015) Bioinspired structural materials [J]. Nat Mater 14:23–36
27. 杨会伟. 浆砌复合结构形式的材料与结构力学行为. 太原理工大学,博士论文.2017. (YANG H (2017) Mechanical behavior of materials and structures in the form of brick and mortar structure. Taiyuan University of Technology, Doctoral thesis)
28. Silling SA, ASKARI A (2004) Peridynamic modeling of impact damage:ASME/JSME pressure vessels and piping conference[C]. Am Soc Mech Eng 197–205
29. Silling SA, Bobaru F (2005) Peridynamic modeling of membranes and fibers[J]. Int J Non-Linear Mech 40(2):395–409
30. 顾鑫,章青,黄丹. 基于近场动力学方法的混凝土板侵彻问题研究[J]. 振动与冲击,2016,35(6):52–58.(Gu X, Zhang Q, Huang D (2016) Peridynamics used in solving penetration problem of concrete slabs[J]. J Vib Shock 35(6):52–58. (in Chinese))
31. 黄丹,卢广达,章青. 准静态变形破坏的近场动力学分析[J]. 计算力学学报,2016,33(5):657–662. (HUANG D, LU G, ZHANG Q (2016) A peridynamic study on quasi-static deformation and failure[J]. Chin J Comput Mech 33(5):657–662. (in Chinese))
32. Huang D, Lu G, Qiao P (2015) An improved peridynamic approach for quasi-static elastic deformation and brittle fracture analysis[J]. Int J Mech Sci 94:111–122
33. 郁杨天,章青,顾鑫. 近场动力学微极模型在求解静力学问题中的应用[J]. 力学季刊,2017(1):50–57. (Yu Y, Zhang Q, Gu X (2017) Application of micropolar peridynamic model in solving static problems[J]. Chin Q Mech (1):50–57. (in Chinese))
34. Prakash N, Seidel GD (2015) A novel two-parameter linear elastic constitutive model for bond based peridynamics[C]. In 56th AIAA/ASCE/AHS/ASC structures, structural dynamics, and materials conference
35. Zhu Q, Ni T (2017) Peridynamic formulations enriched with bond rotation effects[J]. Int J Eng Sci 121(Supplement C):118–129
36. Zhou XP, Shou YD (2016) Numerical simulation of failure of rock-like material subjected to compressive loads using improved peridynamic method[J]. Int J Geomech 17(3):4016086
37. Zhou X, Wang Y, Shou Y, Kou M (2017) A novel conjugated bond linear elastic model in bond-based peridynamics for fracture problems under dynamic loads[J]. Eng Fract Mech
38. Gerstle W, Sau N, Silling S (2007) Peridynamic modeling of concrete structures[J]. Nucl Eng Des 237(12):1250–1258
39. 秦洪远,黄丹,章青. 混凝土复合型裂纹扩展的非局部近场动力学建模分析[J]. 计算力学学报,2017,34(3):274–279.(Qin H, Huang D, Zhang Q (2017) Non-local peridynamic modelling of mixed-mode fracture of concrete[J]. Chin J Comput Mech 34(3):274–279. (in Chinese))
40. Zhu Q, Ni T (2017) Peridynamic formulations enriched with bond rotation effects[J]. Int J Eng Sci 121:118–129

41. Zhou XP, Shou YD, Berto F (2018) Analysis of the plastic zone near the crack tips under the uniaxial tension using ordinary state-based peridynamics[J]. Fatigue Fract Eng Mater Struct 41(5):1159–1170
42. Madenci E, Oterkus S (2016) Ordinary state-based peridynamics for plastic deformation according to von Mises yield criteria with isotropic hardening[J]. J Mech Phys Solid 86:192–219
43. Wu CT, Ren B (2015) A stabilized non-ordinary state-based peridynamics for the nonlocal ductile material failure analysis in metal machining process[J]. Comput Method Appl Mech Eng 291:197–215
44. Becker R, Lucas RJ (2011) An assessment of peridynamics for pre and post failure deformation[R]. Army research lab aberdeen proving ground md weapons and materials research
45. Yaghoobi A, Chorzepa MG (2017) Higher-order approximation to suppress the zero-energy mode in non-ordinary state-based peridynamics[J]. Comput Struct 188:63–79
46. Silling SA (2017) Stability of peridynamic correspondence material models and their particle discretizations[J]. Comput Method Appl Mech Eng 322:42–57
47. Lehoucq RB, Silling SA (2008) Force flux and the peridynamic stress tensor[J]. J Mech Phys Solid 56(4):1566–1577
48. Breitenfeld MS, Geubelle PH, Weckner O, Silling SA (2014) Non-ordinary state-based peridynamic analysis of stationary crack problems[J]. Comput Method Appl Mech Eng 272(11):233–250
49. Silling SA, Lehoucq RB (2008) Convergence of Peridynamics to Classical Elasticity Theory[J]. J Elast 93(1):133
50. Bobaru F, Hu W (2012) The meaning, selection, and use of the peridynamic horizon and its relation to crack branching in brittle materials[J]. Int J Fract 176(2):215–222
51. 谷新保. 近场动力学理论及其在岩石类材料变形破坏过程的数值模拟[D]. 重庆:重庆大学, 2015. (Gu X (2015) Peridynamic theory and its numerical simulation in the deformation and damage process of the rock-like materials [D]. Chongqing: Chongqing University, (in Chinese))
52. Silling SA, Lehoucq RB (2010) Peridynamic theory of solid mechanics[M]. Adv Appl Mech, Aref H, Giessen EVD, Elsevier, 44, pp 73–168
53. Silling SA (2010) Linearized Theory of Peridynamic States[J]. J Elast 99(1):85–111
54. Javili A, Morasata R, Oterkus E, Oterkus S (2019) Peridynamics review. Math Mech Solid 24(11):3714–3739. https://doi.org/10.1177/1081286518803411
55. Bobaru F, Yang M, Alves LF (2009) Convergence, Adaptive refinement, and scaling in 1D peridynamics. Int J Numer Method Eng 77(6):852–877
56. Ha YD, Bobaru F (2010) Studies of Dynamic Crack Propagation and Crack Branching with Peridynamics. Int J Fract 162(1–2):229–244
57. Bobaru F, Xu Z, Wang Y (2016) "Peridynamic modeling of impact and fragmentation", In Handbook of peridynamic modeling
58. Akula S (2018) "Peridynamic modeling of dynamic fracture in bio-inspired structures for high velocity impacts". Mechanical (and Materials) Engineering—Dissertations, Theses, and Student Research, pp 141

An Interface Management Approach for Civil Aircraft Design

Dake Guo, Xinai Zhang, Jiejing Zhang, and Haomin Li

Abstract The interfaces between on-board systems play a very important role for a civil aircraft, which primarily involve the signal, material and energy exchanged between relevant systems in the aircraft. It is believed that a uniform interface management can remove and reduce conflicts between systems in the aircraft integration. It is necessary and essential to perform the interface management in an effective and uniform manner throughout the whole aircraft development life cycle to identify, validate, control, and verify the interfaces to ensure all the sys-tems integrated properly according to the given expectations. An interface management and development approach is proposed, which is composed of four phases, i.e. interface architecture definition, interface identification, documentation and change control. An interface development and management case is pro-vided, which demonstrates that the proposed approach can not only effectively assist system engineers in capturing various types of interfaces, but also can ex-press interfaces in an unambiguous way, which allows engineers to develop a shared understanding about interface requirements. It is also found that the inter-face management approach can control the interfaces in the whole aircraft development life cycle, which is beneficial to aircraft integration.

Keywords Interface management · Interface development · Civil aircraft · Function · Architecture · Integration

1 Introduction

With the increasing demands on civil aircraft with high safety, comfort, environmental friendliness and economics, the functions to be performed by on-board aircraft systems together with their interactions become more and more complex, which brings new challenges to the design, integration and verification of civil aircraft. The design and development of civil aircraft is a high precision, high complexity, and

D. Guo (✉) · X. Zhang · J. Zhang · H. Li
COMAC Shanghai Aircraft Design & Research Institute, Shanghai, China
e-mail: guodake@comac.cc

Z. Jing and X. Zhan (eds.), *Proceedings of the International Conference on Aerospace System Science and Engineering 2020*, Lecture Notes in Electrical Engineering 680,
https://doi.org/10.1007/978-981-33-6060-0_30

highly integrated systems engineering. A civil aircraft is often composed of many systems that can realize different functions, and there are many complex interface relationships between these systems and functions. The interface between on-board systems play an extremely important role in the aircraft development. Typical interface problems include insufficient information flow and lack of communication [1]. Therefore, how to effectively manage the interface development process is a big challenge for system engineers in the civil aircraft industry.

Based on a research into 46 mega projects for analyzing the benefits of interface management, it is showed that projects with systematic interface management tend to have lower mean and less dispersed cost growth, compared with projects without interface management [2]. Several studies also have found that implementing of interface management at the early stages of the project will result in higher performance in terms of scope, time, and schedule [3]. The concept of interface management (IM) within an aerospace project was first proposed using a system engineering approach to analyze the contact points between relatively autonomous interacting organizations, and the corresponding interorganizational problems in 1967 [4]. Nowadays, IM is very popular in high technology industries, such as aerospace and information industries [5].

Nowadays, instead of just simply ensuring that system interfaces should match, interface management is used in the sense of defining systems—organizational, managerial, and technical—and of actively managing their interrelationship [5]. Technology has grown so complex and specialized that no one person possesses the necessary knowledge and experience to know all that is needed. Those professionals that are tasked with managing the design and life-cycle development of today's complex systems and products can only achieve their goals by managing at the interfaces of both people and technology. To develop and manage the interactive information of interfaces is the fundamental to ensure the high safety and reliability in design and development of the aircraft with a controllable cost in the whole life cycle. It is necessary to setup an efficient process to manage and develop interfaces. In this paper, an interface development and management approach is developed for civil aircraft industry.

2 Life Cycle Model of Civil Aircraft

The fundamental systems engineering approach for achieving the desired project objective is use a project life cycle model [5]. The life cycle model gives an approach to divide life cycle into different phases to control the development process. The interface management process shall also meet the phases defined in life cycle model.

HB8525 provides a standard life-cycle model for civil aircraft development including 5 phases, which are requirement and conception demonstration, preliminary design, critical design, test and verification and mass production. The simplified diagram is shown in Fig. 1. For interfaces development, the related design phases and activities including.

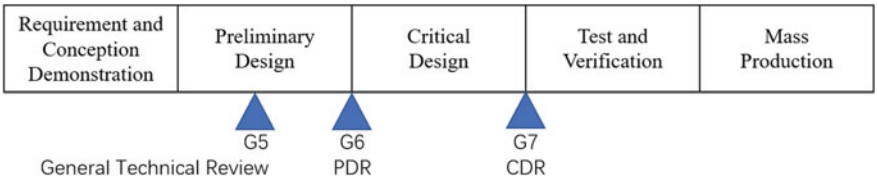

Fig. 1 The life cycle model of civil aircraft development process

At the middle of preliminary design phase, with general technical proposal review at G5, the aircraft level functions shall be defined, all interfaces related to functions shall also be captured.

At G6 stage, i.e. the preliminary design, it is necessary to carry out system function definition and analysis, to capture system interfaces and structural interfaces, and to define system architectures.

At G7 stage, i.e. the critical design, it is necessary to define the system equipment location, and the physical interface implementation in the form of wire and tube allocation.

Since interfaces should be captured in the design phases starting from G5, i.e., preliminary design, critical design, test and verification, all interfaces status shall be monitored, and the related changes shall be controlled.

3 Interface Management

3.1 Classification of Interfaces

To manage the interfaces, it is necessary to define the classifications of interfaces. An interface is the performance, functional and physical attributes required to exist at a common boundary. For a civil aircraft project, there are two types of interfaces: functional interfaces and physical interfaces.

A functional interface defines the purpose of the interface, which is intended to describe what input is needed for a function to operate normally. Functional interfaces only describe the requirements between two elements, no physical implementation information is mentioned.

A physical interface is used to define and control the features, characteristics, dimensions, and tolerances of one design that affects another [6]. Physical interfaces are implementation of functional interfaces. It describes the detail design of the functional interfaces.

3.2 Interface Working Group

Interfaces exist at the common boundary of different parties; single party cannot define the interfaces separately. At the same time, interface definition may be affected by the aircraft architecture integration and tradeoff. The final definition of interfaces needs to be determined by a higher level of design stakeholder's decision. Therefore, to achieve the purpose of managing and developing interfaces efficiently, an interface working group (IWG) shall be established to exercise the management of interfaces and arbitration for issues occur during the interface development. IWG shall consist of chair, and cognizant from all interface parties. The cognizant is generally a higher-level manager to delegate his team.

4 Interface Development

4.1 Interface Architecture Definition

The interface development begins with IWG team to define the architecture for whole aircraft, which is called interface information architecture (IIA), to make sure that the interface development is done with a top-down approach and that each development team is responsible for developing the architecture interfaces assigned to the team. The preliminary task of interface management is to identify the scope of interfaces in a project, to define hierarchy of interfaces, and to determine how different classifications of interfaces are linked between different levels. An architecture of interface for civil aircraft is represented in Fig. 2.

With this architecture, interfaces not only can show the relationship between source and destination, but also can illustrate traceability and allocation among

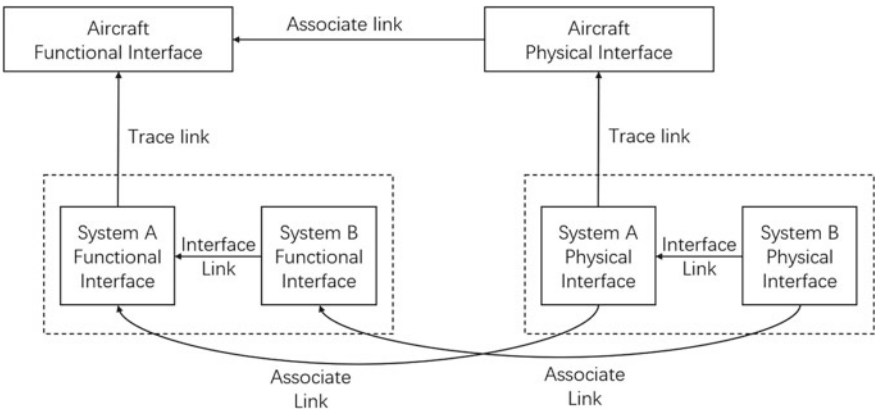

Fig. 2 Interface information architecture

different levels with relationship topology. Interfaces identified by higher level can be assigned to lower level and reviewed by physical architecture design. The interface information architecture can help interface developers to ensure the completeness of interfaces.

The characteristics of interfaces need to be agreed for both sides, only when all involved parties have the same development progress that can achieve this goal. The second task of interface management is to define maturity of different types and levels of interfaces based on aircraft life cycle model. IWG shall monitor and promote interface development status to ensure all parties to capture and define interfaces with the same timeline.

4.2 Interface Identification and Description

Based on the IIA, the first design activity is to identify the interfaces. The identification of interfaces includes two aspects.

On the one hand, systems engineers need to capture the interface relationships between systems, functions, components, and to identify the items (could be signal, material or power) exchanged on interfaces. The necessary attributes also need to be defined, such as bandwidth, data rate, pressure. This activity is performed by analysis and modeling of the functions and architecture for the system of interest. Furthermore, the interfaces also need to be expressed with standard terms in a structured manner, which is specific and unambiguous for stakeholders to understood. For example, the format, *the [Side A] shall send [airspeed] to [Side B]*, is used to describe the publishing side of an interface. The word SHALL is used to illustrate the interface as a requirement for side A. Another example is the format, *the [Side B] will receive [airspeed] from [Side A]*, which can be used to describe the subscribing side of an interface. The word WILL is to state the interface is a commitment for side B to perform.

On the other hand, each item exchanged on an interface shall be defined with a unique name for the whole lifecycle of aircraft, which is necessary for systems engineers to differentiate the items flowing between different system interfaces. For example, it is necessary to have two different item names, height and altitude, when measuring the position of aircraft by radio altimeter and barometric altimeter. Meanwhile, the Weight on Wheel signal and Air/Ground Status signal may also have different meanings when describe the interfaces with proximity sensor. Some additional descriptions may also be needed to explain the detail definition for these items.

4.3 Interface Documentation and Issuing

In this phase, the primary tasks are to negotiate with different parties about the Interface Control Documents (ICD), and then to issue them. After the interfaces are identified on the boundary of a single system, all related parties should review the identified interfaces and negotiate for consistent interfaces. The negotiation should also include examination for the attributes of interfaces. Once the review is done, a link will be built between the commitments of the subscribing sides and the interface requirements of the publishing sides, which means that the interfaces are agreed by both sides. The ICD is a collection of all interface documents agreed by related sides, which records the interfaces with standard format and the related links. ICDs shall be signed and released at a formal platform to show all interfaces conform to the contracts.

4.4 Interface Change Control

Interfaces may change during the whole life cycle of an aircraft. The changes may result from many reasons, such as mistakes found in the integration process or changes of design solution.

Once an interface change occurs, all affected parties should evaluate for interface changes at any point. The interface information architecture provides such a basis. The change impact evaluation can be carried out and ensure the integrity according to the location of the interface in the information architecture. Through the link relationship, it can be evaluated not only the direct related parties of the interfaces, but also the functional and physical architecture of the upper and lower levels. The interface changes can only be implemented after all affected parties have agreed and provided impact analysis. Similarly, the interface change process cannot be closed until all affected parties have completed the implementation of interface changes.

5 Case Study

The development of the fire-alarming interfaces in a cargo is illustrated here as a case to demonstrate the proposed approach. This case shows how the 4-step approach for developing and managing interfaces occurs in a real aircraft development process.

5.1 Functional Interfaces at the Aircraft Level

The process begins with identification of external interfaces of an aircraft. To completely identify the enabling systems and external interfaces, the aircraft is considered as a black box system, and the system concept coming from scenario analysis and stakeholder needs elicitation will be employed to establish aircraft boundaries. The boundaries should delineate where the project has control and responsibility and where the system is interacting with external entities (environments or people) outside the project's control. At this step, it is necessary to identify the characteristic of an interface or a characteristic of what crosses the interface and any variations in the interface.

In the scenario that a cargo bay catches fire, aircraft needs to notify cockpit crew immediately about the emergency, so that the crew members can take necessary steps to suppress the fire. Hereby, the aircraft should be considered as a black box system, which needs to detect air temperature and fire flame to judge whether there is fire or not,and to warn cockpit crew of the fire once the fire condition is true. Based on this analysis, the external interfaces can be established as shown in Fig. 3. Two external interfaces for aircraft are needed in this scenario. One is the fire-detecting interface between the aircraft and the environment, and the other is the fire-alarming interface between the crew and the aircraft.

Based on the above scenario and the function architecture at the aircraft level, the function, to provide hazard protection, should be related to the requirements for fire detection in cargo bay, and the function, to provide information indication, should have a requirement as to provide audio and optic alert to warn pilots. To transfer the fire alarm signal, an interface is captured and identified as:

The function*, to Provide Hazard Protection*, shall send *Cargo Fire Alarming* signal to the function, *to Provide Information Indication.*

In addition, interfaces should be described in a standard writing format mentioned before, which should include source party, destination party and the name of the exchanged item. The word *SHALL* is used to define the interface as a need, desire, or requirement that needs to be satisfied by the system of interest. In this example, the name of the exchanged item, *Cargo Fire Alarm signal*, is unique in whole lifecycle to avoid confusion (Fig. 4).

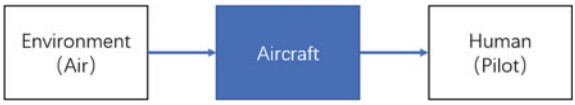

Fig. 3 External interfaces of aircraft

Fig. 4 Functional interfaces at the aircraft level

5.2 *Physical Interfaces at the Aircraft Level*

Once the boundaries are identified and the interface requirements are captured, the IWG team begin to develop detailed interface definitions based on aircraft physical architecture. The definitions are the result of integration design activities and negotiated agreements between the responsible systems. The definitions are the details coming from the design process and they become the successful criteria for interface verification activities. There can be multiple technical aspects to an interface definition, and they can be shared at multiple architectural levels for the same interface.

When the physical composition is considered at aircraft level, the aircraft can be regarded as a combination of multiple systems. Therefore, all aircraft functions need to be allocated to these systems, and system engineering teams will carry out the next step development for each system. To achieve this scope, the aircraft functions need to be decomposed into smaller functions to allocate to single system.

For this case:

(1) The function, *to provide hazard protection*, is decomposed into the function, *to provide fire protection*, which can be allocated to the fire protection system (FPS). The function, *to provide information indication*, which can be allocated to cockpit integration system (CIS) or also allocted to FPS. In this case, it is allocate to CIS based on aircraft architecrure desing.
(2) Another factor that should be considered at this level is that aircraft uses an integration modular architecture (IMA), rather than traditional federal architecture, which means that the cargo fire alarm signal is transferred by IMA BUS network.
(3) As a typical mechnichal system, FPS uses A429 bus to deliver signal. For IMA and CIS which are typical avionic systems, A664 bus are used for main channel of information.

Based on the above analysis, it can be found that the cargo alarm signal is related to three systems shown in Fig. 5. The interactions related to the signal can be stated as: "*FPS* will send *Cargo Fire Alarm* signal to *CIS* via A429 and A664 bus through IMA network". In addition, another requirement related to the above signal can also be derived on the IMA system, which is "Cargo fire alarm signal shall be transmit from A429 to A664."

Since the above description is not a requirement, no "shall" statements should be associated with interface definitions. Instead, the use of "will" is preferred here

Fig. 5 Physical Interfaces at the Aircraft Level

for the writing format of a physical interface. The name of an exchanged item is inherited from functional interface.

5.3 *Functional Interfaces at System Level*

In this phase, the primary task is to define the interfaces from a system function point of view. The definitions in this phase are the result of cooperative (between the interfaces systems) design activities and negotiated agreements between the responsible design teams in IWG.

At the system level, functions should be decomposed into sub-functions, which can further be allocated to items. Based on aircraft structure layout, two cargo bays are needed to meet the commercial payload requirement from stakeholders. Thus, the fire protection system should have two functions to detect fire for the forward cargo and the afterward cargo. Another factor involved in this example is that the fire extinguishing agent shall release to both cargos no matter either of them catches fire. Therefore, the OR logic needs to be performed by a data calculation function to indicate the cargo fire because either of cargo fire need to be alerted. The calculated signal shall be sent to the function, *to provide fire indication*, which is decomposed from the function, *to provide information indication,* at system level for CIS.

Therefore, the internal and external interfaces for fire protection system are shown in Fig. 6 and stated as below:

- The function, *to Detect Forward Cargo Fire,* shall send *FWD Cargo Fire* signal to the function, *to Calculate Data.*
- The function, *to Detect Afterward Cargo Fire,* shall send *AFT Cargo Fire* signal to the function, *to Calculate Data.*
- The function, *to Calculate Data,* shall send *Cargo Fire Alarm* signal to the function, to *Provide Fire Indication.*

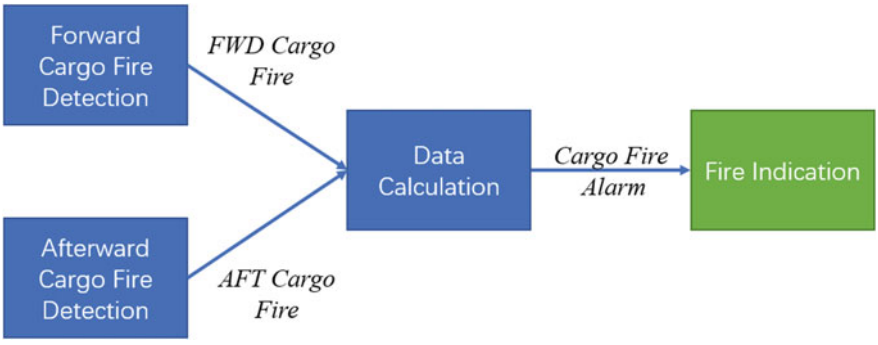

Fig. 6 Functional Interfaces at the System Level

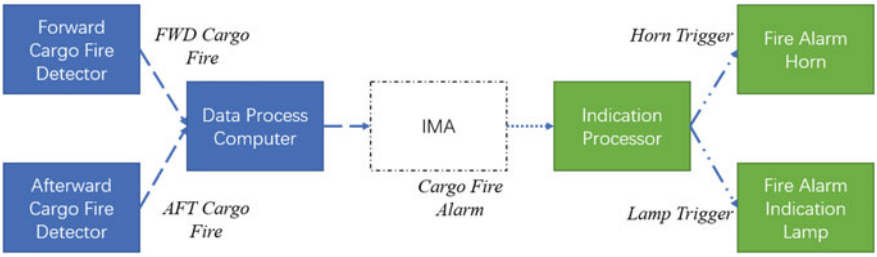

Fig. 7 Physical Interfaces at the System Level

5.4 *Physical Interfaces at the System Level*

The task of system level architecture design is to allocate functions to physical entities. For the fire protection system, a cargo aircraft is required to have several detectors to realize the fire-detecting function. For data calculation function, an integrated computer is needed. For cockpit integrated system, horn is needed to provide sound alarm, and indicator light is used to realize optical alarm. At the same time, according to the system integration, the signal needs to be transformed by IMA, the physical interfaces are defined as shown in the Fig. 7.

- *Forward Cargo Fire Detector* will send *FWD Cargo Fire* signal to *Data Process Computer by A429 BUS*.
- *Afterward Cargo Fire Detector* will send *AFW Cargo Fire* signal to *Data Process Computer* by *A429 BUS*.
- *Data Process Computer* will send *Cargo Fire Alarm* signal to *IMA Network* by *A429 BUS*.
- *IMA Network* will send *Cargo Fire Alarm* signal to *Indication Processor* by *A664 BUS*.
- *Indication Processor* will send *Horn Trigger* signal to *Fire Alarm Horn* by *Hardwire*.
- *Indication Processor* will send *Lamp Trigger* signal to *Fire Alarm Lamp* by *Hardwire*.

5.5 *Change Analysis of Interfaces*

Due to systems integration tradeoffs at aircraft level, all data processing functions are hosted in IMA instead of using separated processors for different systems. Impacted by this change, the fire signal logic of the forward and afterward cargo is executed by hosted function in IMA cabinet instead of the fire protection processor. Therefor the physical interfaces at the system level need to be changed like shown in Fig. 8. The change is only affecting the physical implementation in this case, so no functional interfaces at aircraft level and system level needed to be modified.

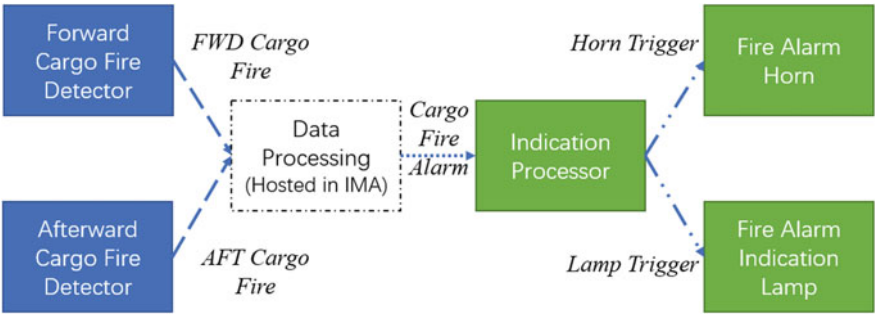

Fig. 8 Changed Physical Interfaces at the System Level

6 Conclusion

A civil aircraft development project is very complex due to its scope, scale, and correlation among many components. The conflicts and problems of interfaces can be caused by different perspectives of definitions and inadequate communication processes between them. Interface management is an effective way to solve these problems. The implementation of interface management at the early stage of the project and the provision of a framework and process for interface development, coordination and management can improve the performance of the project in terms of quality, cost, time, and safety.

An interface management approach has been proposed in this paper. An example of aircraft interface development was presented to show how to define the interfaces based on IIA. According to the proposed approach, the interfaces could be managed by a strong coupling architecture. It also demonstrates that it is necessary to establish a common interface management process throughout the whole aircraft life cycle to ensure the correctness and consistency of the interface definitions and comprehensive analysis of interface changes.

References

1. Topfer A (1995) New products-cutting the time to market. Long Range Plann 28(2):61–78. https://doi.org/10.1016/0024-6301(95)98590-o
2. Shokri S, Ahn S, Lee S et al (2016) Current status of interface management in construction: drivers and effects of systematic interface management. J Construct Eng Manage-ASCE 142(2). https://doi.org/10.1061/(asce)co.1943-7862.0001035
3. Nooteboom U (2004) Interface, management improves on-time, on-budget delivery of megaprojects. J Pet Technol 56(08):32–34. https://doi.org/10.2118/0804-0032-jpt
4. Wren DA (1967) Interface and interorganizational coordination. Acad Manage J 10(1):69–81. https://doi.org/10.5465/255245

5. Morris Peter WG (2008) Project management handbook. In Managing project interfaces-key points for project success
6. Shishko R, Aster R, Chamberlain Robert G et al (1995) NASA systems engineering handbook

Finite Elements Modeling of Randomly Oriented Short Fiber-Reinforced Composite Materials

Daniil Lupachev and Yile Hu

Abstract Randomly oriented short fiber-reinforced composite materials are getting more and more popular due to its manufacturing simplicity and low cost compared with conventional continuous fiber-reinforced composites. Because of the randomization in fiber orientations, it is relatively difficult to simplify and establish its material model for analytically predicting material properties. Therefore, it is important to have a numerical approach to generate computational models and perform analyses. Finite Element (FE) modeling is the most widely and commercially applied modeling technique. It is now a vital and irreplaceable tool in many industries such as automotive, aerospace, defense, consumer products, architecture and many others. This present work demonstrates a FE modeling approach of a Representative Volume Element (RVE) for short fiber-reinforced material. The RVE consists heterogeneous micro-structures for fiber and matrix individually, it is meshed with first-order tetrahedral element. Periodic boundary conditions are applied on the lateral surfaces of RVE in the numerical implementation so that the effective material properties can be obtained.

Keywords Micromechanics of composites · FE modeling · Randomly-oriented · Short fiber · Numerical homogenization

D. Lupachev · Y. Hu (✉)
Aerospace Structure Research Center, School of Aeronautics and Astronautics, Shanghai Jiao Tong University, Shanghai 200240, China
e-mail: yilehu@sjtu.edu.cn

D. Lupachev
e-mail: lupachev.daniil@sjtu.edu.cn

D. Lupachev
Department of Aircraft Engineering, Moscow Aviation Institute, Moscow 125993, Russia

Z. Jing and X. Zhan (eds.), *Proceedings of the International Conference on Aerospace System Science and Engineering 2020*, Lecture Notes in Electrical Engineering 680,
https://doi.org/10.1007/978-981-33-6060-0_31

1 Introduction

Composite materials are getting more and more widely-used. In aircraft and spacecraft industry, composite materials turn out to be vital, some projects just can't be accomplished without composites. In some projects consuming of composite materials allow to save significant amount of weight and fuel.

Randomly oriented short fiber-reinforced composite materials might have pseudo-isotropic elastic properties, therefore, its behaviors are quite similar to the behavior of commonly used materials. That is the reason why randomly oriented short fiber-reinforced composites have huge potential of usage and appliances.

That is important to have an ability to get effective material properties of those materials. To get numerical solution of this problem, Finite Element Method (FEM) was used in the present study. It is the most widely used approach for numerically solving engineering problems based on dividing large system into the smaller subsystems—finite elements. The RVE term was first used by Hill [1] and it can be defined as the smallest material volume element for which the macroscopic constitutive representation is a sufficiently accurate model to represent mean constitutive response [2].

The main purpose of this work is to provide simple and straight forward method to calculate effective elastic properties of randomly oriented short fiber-reinforced composite materials. Meanwhile, this approach can be used to determine effective elastic properties of other types of composite materials such as continuous fiber reinforced composites, multilayered composites, particle reinforced composites etc. In this work for preprocessing/meshing Hypermesh software was used, Abaqus + EasyPBC plugin used for postprocessing/solving.

2 CAD Model of RVE

Generation of the CAD model of randomly oriented short fiber-reinforced composite RVE is a challenging problem. It requires using some modeling algorithms which can provide randomly oriented models of fibers.

The fibers modelled by those algorithms should meet the following criteria:

- Nonoverlapping
- Periodicity.

In this particular work, the CAD model of a RVE for randomly oriented short fiber-reinforced composite from reference [3] was employed as shown in Fig. 1.

The components of fibers and matrix were imported as different solid parts, they are not connected to each other and not sharing any of the surfaces. The first step is to connect matrix and fibers geometry parts. Easiest way to achieve this is to transform the internal boundaries of solid parts to surfaces, and then trim those surfaces with each other.

The trimmed surfaces are organized to three components for mesh generation.:

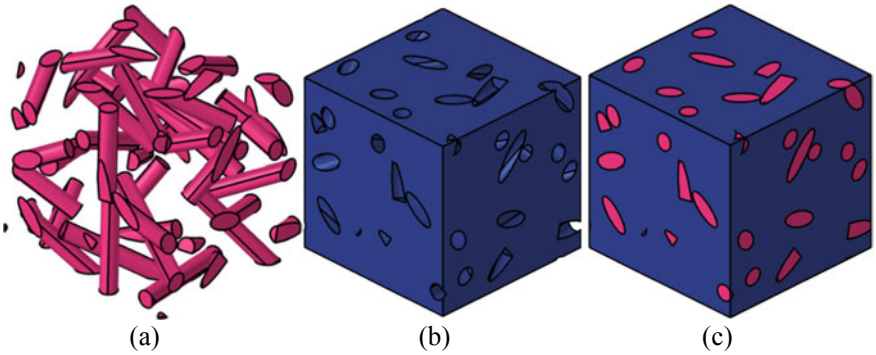

Fig. 1 CAD model of randomly oriented short-fiber reinforced composite RVE. **a** Fibers part **b** Matrix part **c** RVE model

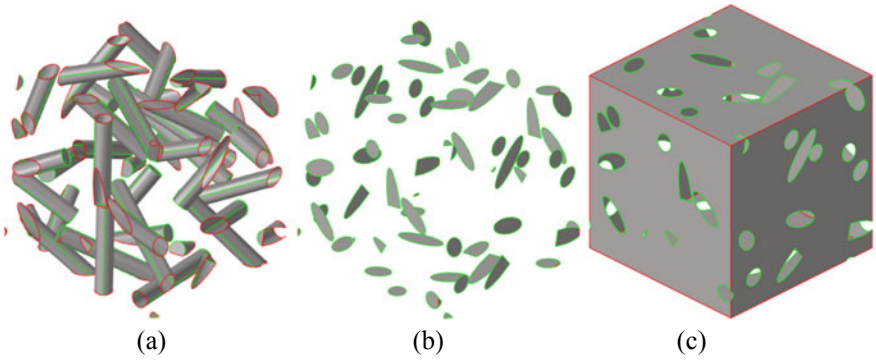

Fig. 2 Topology view of surfaces of RVE model. **a** Internal surfaces of fibers **b** External surfaces of fibers **c** Surfaces of matrix [Red lines- free edges, Green lines—edges connected to other surfaces]

- Surfaces of matrix (separated from each other)
- External surfaces of fibers
- Internal surfaces of fibers (Fig. 2).

3 Finite Elements Model

After acquiring of the relative CAD model, FEM model can be generated. For the external surfaces of the RVE, opposite sides must generate absolutely identical meshes. The meshing process should be starting from generation of 2D periodic mesh. There exist many tools to get mapped (sure about this expression?) mesh on the opposite side such as “Translate”, “Imprint”, “Periodic Mesh”, “Project” etc. In order to apply periodic boundary conditions, the mesh must be mappable on the opposite sides. Thus, “Imprint” and “Project” tools which assign nodes to the geometry

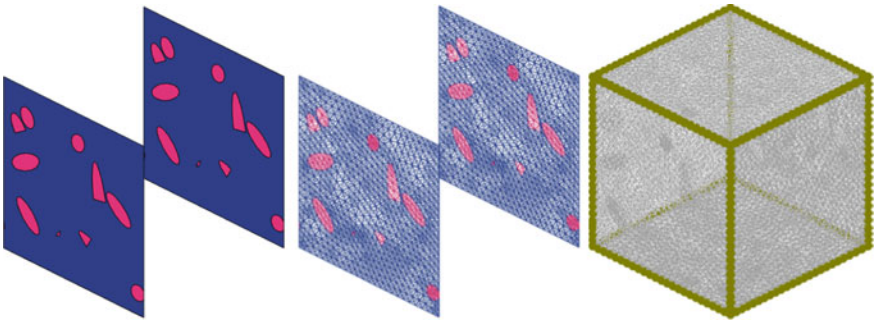

Fig. 3 Translation of the mesh to the opposite side. **a** Opposite surfs (CAD) **b** Original mesh and translated mesh **c** Equivalence of the free edges of the mesh [Real mesh is significantly smaller; this mesh is for demonstration only]

are not suitable in this case because of the imperfections in geometry. The "Periodic mesh" tool creates much more accurate mesh compare to the previous tools and it can be used in this case but because of the assigning mesh to the geometry it still has some imperfections.

The best option in this case is to use "Translation" tool, it makes a copy of the mesh on one side to its opposite side, disregarding the geometry imperfections on these two surfaces.

After repeating this procedure to all of the surfaces, the resulting 2D mesh of the RVE with free edges between surfaces is identical to the topology of the CAD model (Fig. 3a). To eliminate the free edges, the "Equivalence" tool was used with tolerance 10E-8 so that those surfaces are connected without moving nodes.

Next step is meshing of internal fibers component (Fig. 4a) and connect to mesh of external fibers component (Fig. 4b). It is very important that during this process external fibers component (Fig. 4b) cannot be changed to keep periodicity. By using "equivalence" tool, internal fiber-part can be connected to external fiber-part without changing the last one. Some free edges should be equivalent to higher level of tolerance, some elements should be splitted/edited or deleted and some nodes should be replaced manually. After equivalencing of the meshes 2D mesh can be transformed to 3D mesh consisted of first-order tetrahedral element. It is important to keep external nodes as an anchors to apply periodic boundary conditions in the next step.

4 Perioidic Boundary Conditions

Periodic Boundary Conditions (PBC) is mandatory for approximation an infinite system by using RVE (Fig. 5).

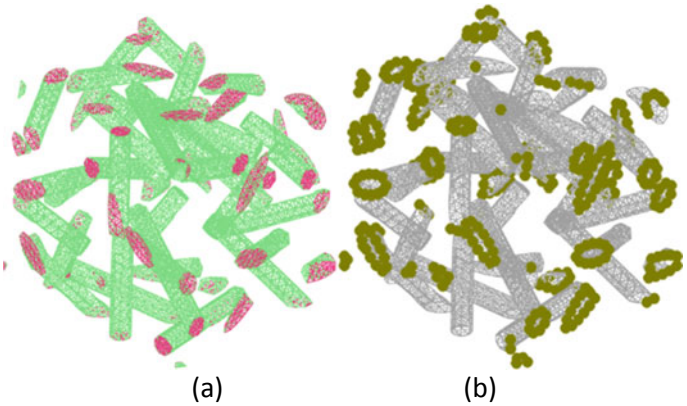

Fig. 4 Meshing fiber part **a** Separate meshes of the fibers components **b** Equivalence of the free edges of the mesh [Real mesh is significantly smaller; this mesh is for demonstration only]

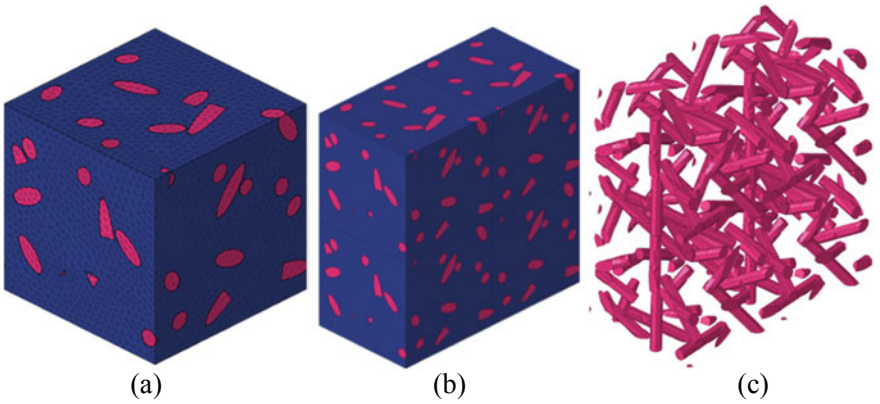

Fig. 5 Representation of PBC by meshed RVE **a** Single meshed RVE **b** 4 periodic meshed RVE **c** 4 periodic meshed fiber parts of RVE [Real mesh is significantly smaller; this mesh is for demonstration only]

On this step constraint equations between opposite nodal parts should be generated. Example of constrain equation from ABAQUS CAE:

$$Set1 : DOF3 - Set2 : DOF1 = 0 \tag{1}$$

It is possible to apply boundary conditions manually with "Constraints-equations" tool in Abaqus but there are more than few thousand constraints need to be applied manually. Easiest way to apply periodic boundary conditions is EasyPBC plugin [2] for Abaqus CAE provided by Sadik L. Omairey.

EasyPBC is an open-source ABAQUS CAE plugin developed to estimate the homogenized effective elastic properties of user created periodic representative volume element (RVE), all within ABAQUS without the need to use third-party software. The plugin automatically applies the concepts of the periodic RVE homogenization method in the software's user interface by categorizing, creating, and linking sets necessary for achieving deformable periodic boundary surfaces, which can distort and no longer remain plane [2].

Constraint equations for deriving elastic properties:

For elastic modulus E11:

$$X_{Front} - X_{Back} = Assigned\ value \tag{2}$$

$$X_{Top,Left} - X_{Bottom,Right} = 0 \tag{3}$$

$$Y_{Top,Front,Left} - Y_{Bottom,Back,Right} = 0 \tag{4}$$

$$Y_{Top,Front,Left} - Y_{Bottom,Back,Right} = 0 \tag{5}$$

For shear modulus G12:

$$X_{front,Left} - X_{Back,Right} = 0 \tag{6}$$

$$Y_{Front} - Y_{Back} = Assigned\ value \tag{7}$$

$$X_{Top} - X_{Bottom} = Assigned\ value \tag{8}$$

$$Y_{Top,Left} - Y_{Bottom,Right} = 0 \tag{9}$$

$$Z_{Front,Top,Left} - Y_{Back,Bottom,Right} = 0 \tag{10}$$

Post-processing stage equations bellow:

$$E = \frac{Stress}{Axial\ strain} \tag{11}$$

$$E11 = \frac{\sum Front\ surface\ nodal\ forces\ in\ 1 - Direction}{\frac{Front\ surface\ area(H \times W)}{\Delta L/L}} \tag{12}$$

$$\nu = \frac{-Transverse\ strain}{Axial\ strain} \tag{13}$$

$$\nu 12 = \frac{\Delta H/H}{\Delta L/L} \tag{14}$$

$$\nu 13 = \frac{\Delta W/W}{\Delta L/L} \tag{15}$$

$$G = \frac{Shear\ stress}{Tensor\ of\ \ shear\ strain} \tag{16}$$

$$G = \frac{\sum Top\ surface\ nodal\ forces\ in\ 1 - Direction}{\frac{Front\ surface\ area(L \times W)}{\Delta 1/H + \Delta 2/L}} \tag{17}$$

Final results in terms of Von-Misses stress can be seen in Fig. 6. Numerical results of the homogenization were compared with results from the literature [3], good correlations can be observed (Table 1).

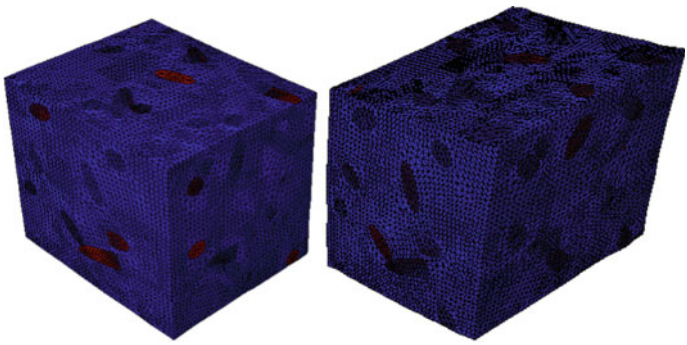

(a) (b)

Fig. 6 Displacements of the RVE. **a** Model for E11 **b** Model for G12 [Real mesh is significantly smaller; this mesh is for demonstration only]

Table 1 Numerical results of the homogenization

Parameters	Example (GMC)	Results
E11 (GPa)	48.7	55.14
E22 (GPa)	48.9	57.31
E33 (GPa)	48.7	54.35
G23 (GPa)	20.5	23.59
G31 (GPa)	20.5	23.52
G12 (GPa)	20.5	23.77
$\nu 21$	0.1792	0.18
$\nu 31$	0.1793	0.18
$\nu 32$	0.1783	0.17

5 Conclusion

Current method provides simple way for determining effective elastic properties of randomly-oriented short fiber-reinforced composite materials. At the same time this method can be applied to different types of composite materials, including continuous fiber reinforced composites, multilayered composites, particle reinforced composites etc. In this particular work such commercial software was used: Hypermesh and Abaqus +EasyPBC plugin, different software can be used to follow this method.

References

1. Hill R (1963) Elastic properties of reinforced solids: Some theoretical principles. J Mech Phys Solids 11(5):357–372. https://doi.org/10.1016/0022-5096(63)90036-X
2. Omairey S, Dunning P, Sriramula S (2018) Development of an ABAQUS Plugin Tool for Periodic RVE Homogenisation. Eng Comput. https://doi.org/10.1007/s00366-018-0616-4
3. Sertse HM, Goodsell J, Ritchey AJ, Pipes RB, Yu W (2017) Challenge problems for the benchmarking of micromechanics analysis: level I initial results. J Compos Mater. https://doi.org/10.1177/0021998317702437

Capturing and Defining Interface Requirements in Commercial Aircraft Development Program

Jiejing Zhang, Xinai Zhang, Haomin Li, Dake Guo, Yong Chen, and Kaili Zhang

Abstract With the increasing customer expectations s and the development of civil aircraft design technology, the functions to be performed by the civil aircraft systems become more and more complex. Meanwhile, those functions will interact deeply with complex logical and physical manners to complete different missions indifferent operation scenarios. Used to describe the information, data, geometry constrains and logic between two interacting functions, interface requirements play an extremely important role in not only the aircraft architecture development process, but also the aircraft integration and verification process. Therefore, it is essential to capture and manage all the interfaces completely and properly to ensure the aircraft as well as the onboard systems to perform the expected functions under some certain operation scenarios. All onboard systems development terms will define their required and provided interface information according to the system architectures and characteristics concurrently. It is required to define an interface development process in order to take on the above challenge, which often results from ambiguous expression of interface requirements, and the difficulty in managing huge amount of data about interface requirements, and in the control frequent changes. Based on the generic aircraft development process, this paper proposes a systematic approach for

J. Zhang (✉) · X. Zhang · H. Li · D. Guo · K. Zhang
COMAC Shanghai Aircraft Design & Research Institute, Shanghai, China
e-mail: zhangjiejing@comac.cc

X. Zhang
e-mail: zhangxinai@comac.cc

H. Li
e-mail: lihaomin@comac.cc

D. Guo
e-mail: guodake@comac.cc

K. Zhang
e-mail: zhangkaili@comac.cc

Y. Chen
Shanghai Jiao Tong University, Shanghai, China
e-mail: mechenyong@sjtu.edu.cn

Z. Jing and X. Zhan (eds.), *Proceedings of the International Conference on Aerospace System Science and Engineering 2020*, Lecture Notes in Electrical Engineering 680,
https://doi.org/10.1007/978-981-33-6060-0_32

capturing and defining interface requirements. The interface development and definition activities throughout the aircraft program life cycle are elaborated in details. The interface classifications and the corresponding interface types and examples are introduced. The interface topology relationship and data model is investigated and defined, which forms the basis for the interface linkage and interface management database development. A case study is carried out to demonstrate the interface requirements development approach proposed here. It is found that the structural interface development process is helpful for engineers to capture the interface together with relevant attributes, which are represented in a uniform and unambiguous format and therefore can serve as the basis for relevant stakeholders to understand the interface definition. A significant advantage of the proposed approach is that it allows systems engineers to arrange the huge amounts interface together with interface attributes according to the interface classifications and types. It also shows that the interface data topology architecture enables engineers to establish traceabilities between interface requirements, which is beneficial to change impact analysis and interface consistent check.

Keywords Interface definition · Interface management · Civil aircraft · Integration

1 Introduction

In the development of civil aircraft, safety, economy, comfort and environmental protection are the goals of aircraft development and operation. The realization of these goals requires many systems to coordinate with each other in order to complete the design, manufacture and installation of millions of parts, and to organize and manage a large number of suppliers and research teams. This process cannot be achieved only by several technological breakthroughs, but also by a comprehensive process of multiple technologies. The relationship among the development activities in many disciplines must be coordinated. The overall performance of the aircraft obtained by this synthesis and coordination is more than the sum of the local performance of simple superposition. Therefore, it is of great significance to apply systems engineering theories and methods to aircraft development.

As more and more functions should be realized in a civil aircraft, the interactions between different functions is becoming more and more complex, and the logic and operation modes of these functions interact with each other deeply. A aircraft often has to operate in different scenarios and complete different tasks. The information and data transmitted between functions and systems are the interface data of the aircraft. Therefore, interface definition is a very important task for aircraft design, and plays an important role in the integration and verification phase.

It is widely acknowledged that the aircraft development process should be well planned with the systems engineering approach, which includes such stages as stakeholder requirements definition, functional analysis, requirement definition, architecture definition, design integration and trade-offs, product integration, verification and validation of aircraft and systems, and final delivery, operation and disposal.

The aircraft interface definition is a technical activity throughout the whole aircraft development process.

Note that there are two types of interfaces for an aircraft, i.e. external interfaces and internal interfaces. Hereby, external interfaces refer to those between the aircraft under development and the environment outside the aircraft, such as those between the aircraft and the control tower, between the aircraft and the ground maintenance equipment. Internal interfaces are the interfaces between aircraft systems, such as those between aircraft systems. Due to limited space, the interface definition process described in this paper primarily deals with internal interface of an aircraft, introduces a method of uncovering capture and management based on aircraft development process, and describes the interface development and management activities of aircraft in the whole life cycle.

2 Civil Aircraft General Development Process

Aircraft is a complex product system, which generally use the hierarchical development method. Since an aircraft development program will usually last for a long time, it is necessary to carry out the requirements-checking process as soon as possible. Otherwise, the errors in the aircraft development process would not be detected and corrected in time, which would result in huge economic losses and even project failure.

Therefore, the whole life cycle model is generally used to divide the development process into multiple stages, set access control in each stage, define the work and deliverables required in each stage in details, and define the maturity of corresponding work. The development process of a civil aircraft can often be divided into five stages: technology and concept demonstration, requirement development, preliminary design, detailed design, trial production and verification, and mass production [1]. During this process, engineers not only need to develop the design solutions to the products intended to perform the operational functions of the system, but also need to establish requirements for the products and services that enable each operational/mission of product in the system architecture. Meanwhile, the technical management processes are used to establish and evolve technical plans for the project, to manage communication across interfaces, to assess progress against the plans and requirements for the system products or services, to control technical execution of the project through to completion, and to aid in the decision-making process [2].

3 Interface Development in Aircraft Program

3.1 Interface Classification

The interfaces including functional interface, physical interface.

Functional interfaces contain logical associations between different functions that allow transmission of a item flow across a boundary. Item flows maybe signal flows, electrical power flows, mechanical force flows, and so on. The interfaces between different functions are often defined in Functional Interface Control Documents (abbreviated as FICDs later). For the development of a civil aircraft, FICDs often involve the FICDs at different levels, e.g. at the aircraft level, and the system level.

Physical interfaces often contain the concrete implementation of interfaces between physical items. Interfaces associated with material contact. Physical interfaces are described in terms of their characteristics such as mechanical, electrical, and environmental [3].

Electrical interface shall contain the detail parameters of electrical wires, which shall be documented in Electrical Interface Control Documents. Electrical Interface Control Documents shall be generated according to Physical Interface Control Documents structure strictly and signal link is not allowed to create only in Electrical Interface Control Documents.

Mechanical Interface shall contain the details of all LRU level Mechanical interface data for a particular supplier, except those details that are more conveniently communicated via a drawing/digital physical model.

3.2 Interface Topology Relationship and Data Model

The development of the system has its own constraints, and the interfaces between functions depends on the development of multiple systems. Therefore, introduction of system maturity index can enhance the quality of the interface definitions.

It is the fact that a system development process cannot achieve full maturity at once for each allocated functional definition. Therefore, a more realistic approach is to define intermediate maturity stages and target dates for all systems, as illustrated in Fig. 1. This allows fitting the systems development constraints (System reviews) and Aircraft global schedule.

The amount of interfaces can increase rapidly as the degree of system complexity goes up. Hence, it is necessary to have the interface development process in aircraft requirements engineering, so that all interfaces and their attributes can be identified and defined properly. Interface development process should include the following steps:

- To identify the relationship between an interface type and the design activities that generate the interface type.

Examples of A/C Functions and target Syst. mat. levels	Syst. X	Syst. Y	Syst. Z	F1	F2	F3	F4	F5
T1: Low Maturity Obj	X	X	X					
T2: Medium Maturity Obj.	X							
T3: Medium Maturity Obj.	X	X	X					
T4: High Maturity Obj.	X	X						
T5: High Maturity Obj.	X	X	X					
Milestone 1				X	X			
Milestone 2				X	X	X	X	
Milestone 3				X	X	X	X	X

Fig. 1 Target dates at aircraft level, including systems maturity objectives

- To identify the relationship between the interface attributes and the design activities that generate these attributes.
- To define the related enabling products.
- To define input, output, necessary contend and attributes at each level.

When the interface definition activities are further refined, the interface design method can be applied to different levels, such as the aircraft level, the system level, and the subsystem part, and finally implemented as each part of the equipment. The aircraft interface definition follows the above-mentioned process and decomposition, and covers the system equipment interface definition at a lower level. Systems and equipment shall have their own interface-defining activities, but at different levels.

Due to different development constraints on and cycles of each system, some differences may exist between interfaces scope of software that supports the target functionality. This issue is depicted in the Fig. 2, where SW and HW are represented in a schematic way. The application implemented in the underlying pieces of equipment of each system should satisfy the expected function.

The necessary conditions for a Function Fx availability are that:

- The software on both sides is able to handle relevant data exchanged supporting the function Fx.
- The interfaces on both sides include at least the data necessary to support Fx.

Hereby, the phrase, *at least*, means that the scope of the interface could be larger (grey color in Fig. 2) than the functional scope of the function Fx but not smaller. Nevertheless, there could be some complex conditions that need to be analyzed, depending on whether the differences between the SW application and interface difference (local or remote) are acceptable or not. The reasons for interface definition scope would be larger than the Equipment SW could be as below:

- The design of the system is too complex, and the operation of the equipment is based on hybrid drives).

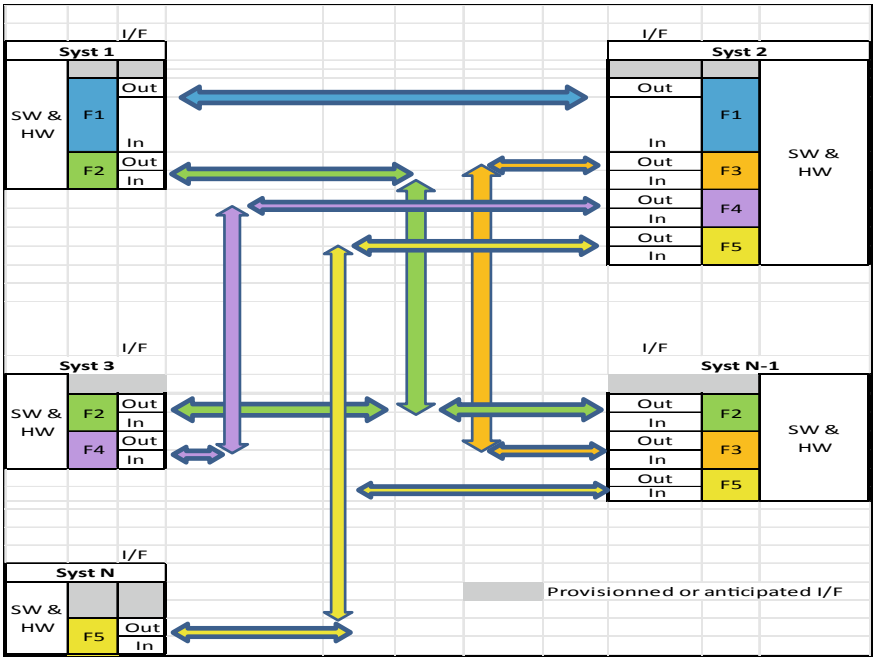

Fig. 2 Relationship between systems development and systems interfaces

- Transparently managed or not by systems on both sides, depending on the system implementation. Whether the boundaries between devices are clearly defined and whether devices are treated as transparent white boxes.

Therefore, it is necessary that SW scope and interface scope should be globally aligned, even if some discrepancy could be accepted in some well managed cases. Then interface definitions are said consistent with the System definition.

As it is elaborated in further details, the progressive system design approach starts from system definition and can be refined into sub-system parts, generally implemented into pieces of equipment. Hence the system interface definition follows this process and decomposition includes the system Equipment interface at a lower level. System and Equipment both contribute to interface definitions but at different and complementary levels.

Furthermore, the interface has to be defined, formalized, checked, published and shared. Indeed, sharing a unique interface definition of equipment with all necessary parties can stop local copies or considering not-updated versions of interface definition.

A key issue associated with the interface definition is how to deal with the data exchanges between emote devices, which are primarily related to the End to End communication. Hence a key topic is the consistency of the definition between each remote pieces of equipment.

Interfaces could be seen as requirements that come from a top-down decomposition, which can further contribute to the integration of systems and aircraft in the bottom-up phase. The challenge is to synchronize multi-levels views together, including aircraft, systems and interfaces. Synchronization and consistency should be ensured for overall Aircraft time schedule, Aircraft key integration steps, functional definitions and systems development schedule.

The number and complexity of interface relationship in a system may increase rapidly with the complexity of the system. Effective management of interface plays an important role in the design and implementation of a complex system. It includes defining and controlling the interface between systems or system elements to ensure that the aircraft and systems can work in a coordinated manner. To implement interface management activities, an interface management plan should be developed first.

The main form of completing the interface management process is to complies and maintain interface control documents. Interface control documents can be divided into several interface control documents according to different activities and purposes.

4 Interface Management Plan

At the very beginning of program, the interface management activities shall be planed based on plan, phases, responsibilities and resources of program. The working plan defines interface management structure, interface information architecture to imply a top-down approach of development that reduce changes. The interface working planning including management process definition, management content identification and development process definition, as shown in Fig. 3.

In the early stage of the project, the interface management activities shall be planned and then the interface management plan documents shall be formed.

Interface management plan is a general plan of interface management work, and the formulation of interface management plan can properly sort out the main activities of interface management in the project. The interface management plan generally

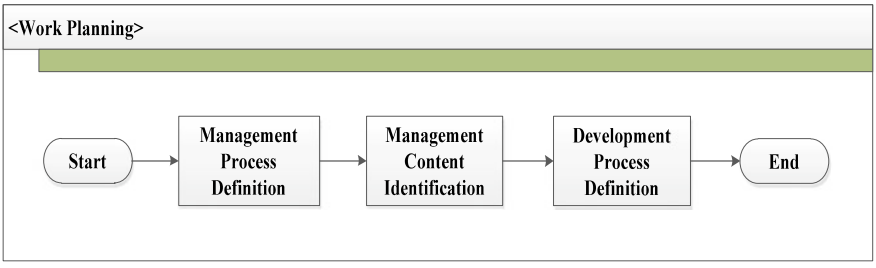

Fig. 3 Interface work planning process

includes the plan of interface data collection, control and management, as well as the template of interface control document, which is used for collection, preparation, change and ICD (Interface Control Document, ICD) management.

The interface management plan shall include the following contents:

- Interface management policy
- Scope of interface management work
- The main activities of interface management (including the requirements for identifying, defining and recording as well as interface control documents)
- Interface change control process
- Main tools of interface management
- Connection with other important processes.

5 Conclusion

Civil aircraft can be regarded as a complex system, and the development of interface requirements for a civil aircraft is based on the level-by-level development of multi-level interfaces. The development of interface requirements involves many related parties, i.e. multiple systems or subsystems. The process of interface requirements development needs to gradually determine the designed functional interfaces and physical interfaces through the recursive iterations between systems or subsystems, so that the correct transfer of functional requirements and the consistency of interfaces among multiple systems, subsystems and equipment can be achieved. The interface definition method described in this paper is based on the concept of system design, and incorporates the interface management technology to carry out the desired method of interface identification and definition, and to implement a unified recursive design process in the process of design and development, which can make the design of interfaces and systems more effectively.

References

1. Development process for civil aircraft. HB 8525–2017
2. Systems Engineering Handbook. NASA. SP-6105 Rev1, 6.3.2
3. Systems engineering-Application and management of the systems engineering process. ISO-IEC 1220–2005

Features of the Use of Damper Supports of Various Designs in a Gas Turbine Engine

N. S. Konoplev, L. V. Farsiian, A. V. Davidov, and M. K. Leontiev

Abstract This article discusses the features of using various designs of elastic-damping devices on GTE supports, including: support with a hydrodynamic damper (with and without an elastic element), support with an elastic ring and support with a plate damper. An analysis of their design is given in terms of the impact on the stiffness and damping of the engine support unit, which allows you to determine the choice of a damping device for solving the complex problem of reducing engine vibrations.

Keywords Damper · Support · GTE · Structure · Vibration · Stiffness · Elastic ring · Plate damper · Hydrodynamic damper

1 First Section

1.1 A Subsection Sample

Please note that the first paragraph of a section or subsection is not indented. The first paragraphs that follows a table, figure, equation etc. does not have an indent, either.

Subsequent paragraphs, however, are indented.

N. S. Konoplev (✉) · L. V. Farsiian · A. V. Davidov · M. K. Leontiev
Institute, Aviation Rocket Engines and Power Plants", Moscow Aviation Institute, Volokolamsk Highway. 4, Moscow 125993, Russia
e-mail: knpprod@yandex.ru

N. S. Konoplev
School of Aeronautics and Astronautics, Shanghai Jiao Tong University, 800 Dongchuan Road, Shanghai 200240, China

Z. Jing and X. Zhan (eds.), *Proceedings of the International Conference on Aerospace System Science and Engineering 2020*, Lecture Notes in Electrical Engineering 680,
https://doi.org/10.1007/978-981-33-6060-0_33

Table 1 Table captions should be placed above the tables

Heading level	Example	Font size and style
Title (centered)	**Lecture Notes**	14 point, bold
1st-level heading	**1 Introduction**	12 point, bold
2nd-level heading	**2.1 Printing Area**	10 point, bold
3rd-level heading	**Run-in Heading in Bold.** Text follows	10 point, bold
4th-level heading	*Lowest Level Heading.* Text follows	10 point, italic

1.1.1 Sample Heading (Third Level)

Only two levels of headings should be numbered. Lower level headings remain unnumbered; they are formatted as run-in headings.

Sample Heading (Forth Level)

The contribution should contain no more than four levels of headings. The following Table 1 gives a summary of all heading levels.

Displayed equations are centered and set on a separate line.

$$x + y = z \tag{1}$$

Please try to avoid rasterized images for line-art diagrams and schemas. Whenever possible, use vector graphics instead (see Fig. 1).

For citations of references, we prefer the use of square brackets and consecutive numbers. Citations using labels or the author/year convention are also acceptable. The following bibliography provides a sample reference list with entries for journal

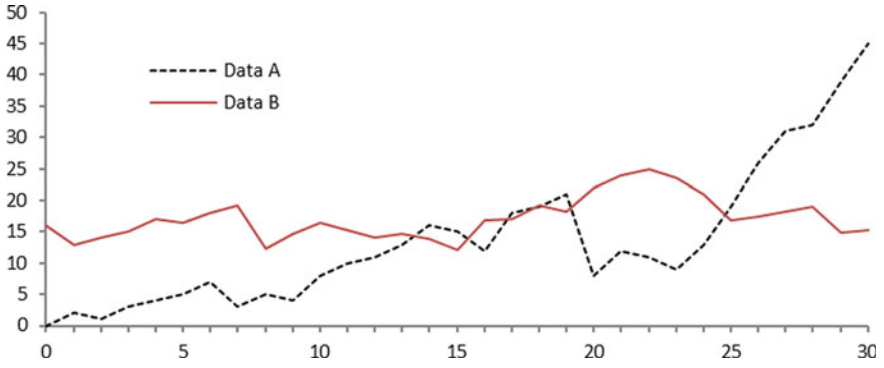

Fig. 1 A figure caption is always placed below the illustration. Short captions are centered, while long ones are justified. The macro button chooses the correct format automatically

articles [1], an LNCS chapter [2], a book [3], proceedings without editors [4], as well as a URL [5].

Acknowledgments. The project is supported by National Natural Science Foundation (Number *********).

2 Introduction

One of the important tasks in the aircraft engine industry is the modernization of existing and the search for new structural means of dealing with increased vibrations caused by rotor imbalances. Designing the supports of GTE rotors with given characteristics of stiffness and damping allows us to solve this problem. To ensure these parameters, special elastic and damping devices are used. Currently, the following ones have become widespread: supports with a hydrodynamic damper, supports with an elastic ring, and multilayer plate damper supports.

When developing a rotary system of promising gas turbine engines, the designer is faced with the task of optimal choice of one or another variant of the damper support, taking into account the possibility of its use in a particular case. The increasing interest in this problem of engineers in other countries confirms the relevance of this topic.

The purpose of the work is to analyze existing modern damper structures, their parameters and determine the selection criteria for damping devices to solve problems with increased vibration in rotor systems.

3 Classification and Features of GTE Damper Supports

The plate damper support or dry friction damper is most convenient for inclusion in the power system of a gas turbine engine, is easy to operate and manufacture, has the ability to work in conditions of high temperatures, aggressive environments and lack of lubrication.

The damper is installed between the bearing housing and the rolling bearing and is an annular package of steel smooth plates ~ 0.5 mm thick, Fig. 2. The scattering of vibrations in this design occurs due to the dry friction forces that arise between the plates.

The state of the surface layers of the samples was analyzed using optical microscopy and roughness measurement in mass production. Using these methods, it was possible to determine the thickness of the modified layer, obtain the microstructure of samples, and also establish the dependence of surface roughness on irradiation modes.

The designer has the ability to several times change the damping properties of such a damper by changing the package layout and changing the magnitude of their interference, without changing the overall dimensions of the damper, which has a positive effect on engine refinement [6]. Damping is characterized by significant

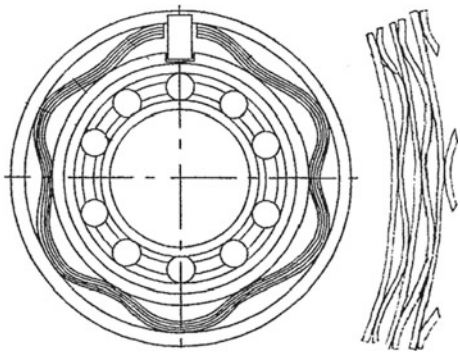

Fig. 2 Plate damper bearing support

stiffness with a rather small damping coefficient compared to other types of dampers [143].

The damper design is well known and described in detail in [6]. For the first time, a multilayer damper was used at the beginning of the 90 s in the high pressure turbine NK-12MV designed by Kuznetsov Design Bureau [7]. Its implementation allowed to reduce the level of vibration by 15 times [6].

There are also designs of multilayer dampers, where the damping package is made in the form of spatial cable elements [8].

Studies [9, 10] of the effect of the constant force of the rotor weight on the elastic-friction characteristics of the corrugated damper showed the need for the introduction of an unloading device into the support structure, which compensates for the weight of the rotor during airplane evolution [11]. The cycle of works by V.I. Ivashchenko and I.D. Eskina [12] is devoted to the creation of a methodology for calculating dampers with corrugated-type unloaders.

The use of such a damper in the support of the gas turbine engine allowed to reduce the amplitude of vibration displacements by 3 times in the working frequency range. [13].

An elastic ring or a throttle damper is a type of hydraulic damper in which vibrations are damped due to the braking of the lubricant in the narrow channels of the damper.

The design is an elastic ring with protrusions along the outer and inner diameters (Fig. 3, b) installed between the rotor housing (Fig. 3, a), the damper is sealed at the ends by rings, the lubricant is throttled through calibrated holes and end slots (Fig. 3, c). During strong vibrations, the oil layer in these protrusions is compressed, and part of the oil flows through the holes, which leads to a loss of energy and a decrease in vibration. For the first time in Russia, such a damper has been designed for the NK-144 [14].

This type of support has the following advantages: high damping ability, small dimensions and the mass of the elastic part of the support, the rotor is centered on the axis of the engine [15], however, it has increased wear of the contacting surfaces and a small resource. The keyway used in the construction for fixing the ring and the subsequently calibrated holes appear cause fatigue cracks. It can be used as an

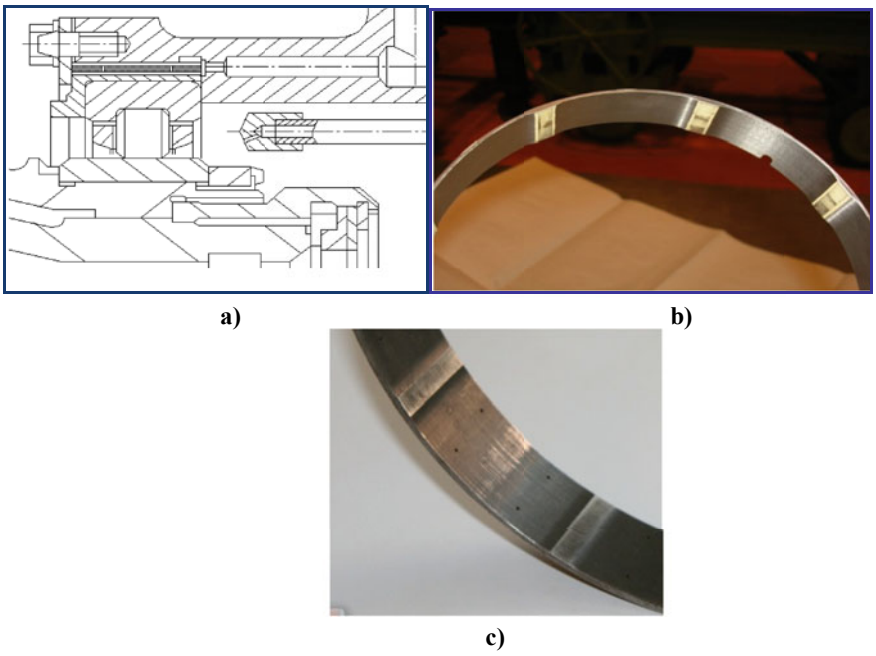

Fig. 3 Elastic ring

alternative if it is impossible to introduce a damper support with an elastic element "squirrel wheel" into the power system of the engine.

The presence of a circumferential throttling groove in the elastic ring [11] increases damping by 1.5 times [16].

The compliance of the ring can vary by a factor of 2–3; during the operation of the damper, the protrusions of the ring can slip relative to the housing [15].

Attempts are currently being made to obtain damping characteristics for an elastic ring using ERSFD (elastic ring squeeze film damper) calculation methods [5, 17]. Due to the fact that the physical effects in the boundary layers of oil flow are poorly presented in mathematical form, and the corresponding mathematical models are practically absent.

Wei Zhang, Qian Ding in their work [18] showed that deformations can occur simultaneously in the inner and outer sections of the elastic ring. The thickness of the internal oil film is affected by the eccentricity of the bearing and the deformation of the elastic ring, while the external only affects the deformation of the elastic ring.

In Russia, supports with an elastic ring are quite widely used and are used in AI-25, TV2-117, AL-31F engines.

The hydrodynamic damper support of a thin compressible film without a centering element is most widely used in foreign and domestic engine manufacturing. In it, the dispersion energy is scattered when a viscous fluid flows over a thin damper gap and the rotor sleeve overcomes external friction in the mates of the damper parts.

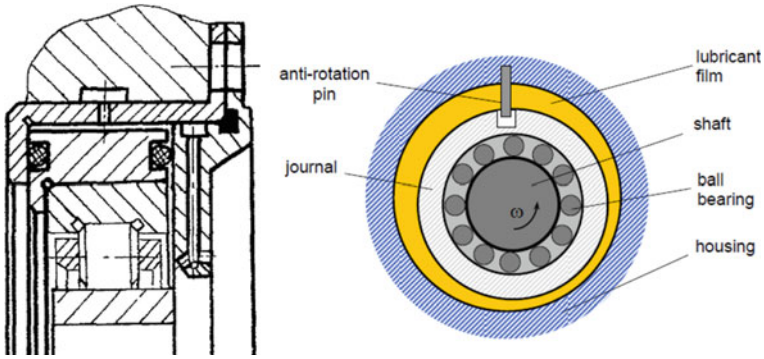

Fig. 4 Hydrodynamic damper

A bearing with a sleeve is installed in a housing with a small gap into which a lubricant responsible for energy dissipation is supplied, Fig. 4. The damping properties depend on the eccentricity and amplitude of the rotor precessional motion inside the oil gap. The detailed design and computational models are well described in [1, 4, 14, 19, 20, 21, 22, 23, 24, 25, 26].

Provided that the parameters are correctly selected, such a damper is most effective for significant rotor oscillation amplitudes that occur mainly at resonant frequencies, that is, the damper parameters are adjusted taking into account the operating rotation frequencies, resonances, and possible rotor unbalances [4].

Analytical models of hydrodynamic damper supports without an elastic element are close to numerical models if they are used within the framework of their basic assumptions [27].

Hydrodynamic damper with an elastic element ("squirrel wheel") - includes an elastic element in the design (Fig. 5a), consisting of a sleeve with a certain number of slots in it, which makes it possible to transfer large axial forces from the bearing to the motor housing, without fear of jamming / skewing of the damper sleeve [28]. The rotor is centered on the axis of the engine. The stiffness of the support is determined by the wall thickness of the sleeve, the width of the slots and the number and length of the rod elements [1]. Misalignment and local bearing load are eliminated, which ensures the reliability of high-speed ball bearings [29]. The elastic element in the structure of the support increases its mass and dimensions, the latter complicates the layout of the support in the engine [25, 30, 31].

The elastic-damper support of the described construction is the most common and widely used in the damper supports of a gas turbine engine. One of the reasons for this spread is the presence of mathematical models confirmed by experimental studies that allow us to design the dynamic behavior of the motor rotor with high accuracy.

A design feature of the elastic elements in the PS-90 engine is the use of dual elastic squirrel-wheel elastic elements(Fig. 5c). This makes it possible to design

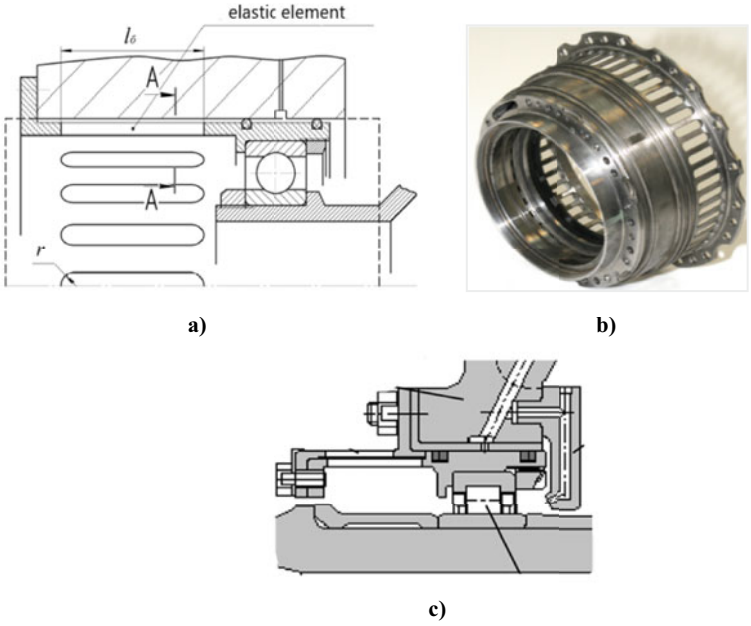

Fig. 5 Hydrodynamic damper with elastic element

supports with the necessary flexibility without increasing the axial dimensions of the structure of the supports [19].

To increase damping, the design of a combined damper is used (Fig. 5b), in which instead of a hydrodynamic damper an elastic ring (throttle damper) is installed [32].

4 Conclusion

The choice of a specific design of an elastic-damper support is always a compromise in which a large number of factors play a role, and the end result is the vibrational behavior of the engine as a whole. This review summarizes the most significant and significant factors that should be paid attention to when choosing one or another design of an elastic-damper support.

Multilayer (plate) dampers are well studied. Their use in aviation gas turbine engines of the « NK » series has shown good efficiency. At the same time, they did not find widespread use in GTE.

Elastic ring throttle dampers currently have a high demand for research. Along with significant advantages (low weight and dimensions), they have significant disadvantages (increased wear and low resource).

Hydrodynamic damper bearings are widely used in foreign practice. But their effectiveness is greatly reduced with not optimal selection of dynamic parameters.

The designers are still faced with the question of creating methods for selecting, calculating and designing the hydrodynamic damper supports of rotors that meet all operating conditions.

References

1. Leontyev MK (1998) Design and calculation of the damper bearings of the rotors of a gas turbine engine: textbook. - M.: Publishing House of the Moscow Aviation Institute
2. Chronin DV, Leontiev MK, Borzdyko EV (1988) The design and design of the elastic damper bearings of the rotor WFD: Textbook. allowance.—M.: Publishing House of the Moscow Aviation Institute, pp 37
3. Vyunov SA, Gusev YI, Corps AV et al (1989) Design and engineering of aircraft gas turbine engines: a textbook for university students with a degree in aircraft engines and power plants, Under the general. Chronin DV(ed). M.: Engineering, p. 368
4. Cookson RA, Kossa SS (1979) The effectiveness of squeeze-film damper bearings supporting rigid rotors without a centralizing spring. Int J Mech Sci 21(11):639–650. https://doi.org/10.1016/0020-7403(79)90043-25
5. Cao L, Gao DP (2007) Damping mechanism of an elastic ring damping film damper, Vib Eng J 584–588
6. Ponomarev YK (1998) Multilayer dampers of aircraft engines [Electronic resource]; Gos. com Grew up. Higher Federation education, Samara. state aerospace. un-t them. SP Koroleva. Samara, Publishing house Samara. state aerospace. University
7. Vilner PD, Ivanov VP, Marinin VB (1962) Plate damper of critical speeds. Technique of the Air Fleet, 4:77–79
8. Ponomarev YK, Antipov VA, Kalakutsky EI. Positive decision on application No. 2001110001/20 of 04/28/01
9. Antipov VA, Ponomarev YK (1983) Computational studies of the anisotropy of the elastic-frictional characteristics of multilayer annular corrugated dampers of turbomachine rotor bearings. Vib Strength Reliab Engines Aircr Syst. Kuibyshev; KuAI ‘, pp 12–19
10. Ponomarev Y (1978) The method of regulating the damping properties of multilayer elements
11. Antipov VA, Berezkin AY, Ponomarev YK, Lapshov YN. Damping device. Chipboard
12. Ivashchenko V, Eskin I (1985) Methodology for calculating the unloading device for rotor support dampers. On Sat Vibrational strength and reliability of engines and aircraft systems. Kuibyshev, KuAI
13. Pronichev Y (2000) “Development of mathematical models and research of perspective designs of multilayer corrugated dampers of aircraft engines”, Samara
14. Eskin ID, Belousov AI, Novikov DK, Vilner PD, Emelyanov MA, Snigirev VN. Hydrodynamic damper, (USSR). No. 2792110
15. Leontiev MK (2011) Study of the characteristics of elastic rings in the supports of rotors of gas turbine engines. Vestn Mai 135–146
16. Diligensky DS, Novikov DK (2015) Calculation of the damping coefficient of elastic rings with a working fluid, SSAU
17. Cao L, Gao DP (2008) Investigation of the critical velocity characteristics of an elastic ring system SFD rotor. J Propul Technol 235–239
18. Zhang W, Ding Q (2015) Elastic ring deformation and pedestal contact status analysis of elastic ring squeeze film damper. J Sound Vib 346:314–327
19. Belousov AI, Balyakin VB, Novikov DK (2002) Theory and design of hydrodynamic dampers of rotor bearings, Belousova AI (ed). Publishing House of the Samara Scientific Center of the Russian Academy of Sciences, Samara, pp. 335

20. Mohan S, Hahn EJ (1974) Design of squeeze film damper supports for rigid rotors
21. Novikov DK, Chaadaev KN (2012) Dynamics of a gas turbine rotor taking into account the nonlinearity of dampers of supports ISSN 1727–0219
22. Novikov DK (1998) Engine vibration reduction NK-12ST
23. Chegodaev DE, Novikov DK, Balyakin VB. Hydrodynamic damper; No. 3280006. pp 25–28
24. Kutakov MN, Degtyarev SA, Leontiev MK (2017) Mathematical models of hydrodynamic dampers in the problems of rotor dynamics of gas turbine engines. Bulletin of Samara University. Aerospace engineering, technology and engineering
25. Sergeev (1959). Damping of mechanical vibrations. M: Fizmatgiz, p 408
26. Zeidan FY, San Andres L, Vance JM (1996) Design and application of squeeze film dampers in rotating machinery. Proceedings of the 25th Turbomachinery Symposium, pp 169–188
27. Kutakov MN, Leontiev MK (2017) The choice of models of hydrodynamic dampers in the problems of rotary dynamics of gas turbine engines
28. Efimenko AV, Polnikova NV, Dotsenko VN (2010) The influence of external friction on the efficiency of the damper bearings of the rotors of aircraft engine turbines and ground-based engines. Engine Engineering Bulletin: Scientific and Technical Journal. N 1, pp 50–52: Fig. Bibliogr. at the end of Art. (3). ISSN 1727-0219
29. Balyakin VB, Barmanov IS (2012) Generalized methodology for calculating and designing elastic-damping bearings of rotors of aircraft gas turbine engines, SSAU
30. Balyakin V, Barmanov I (2009) Improving the methods for calculating the dynamic parameters of elastic elements of gas turbine engines
31. Balyakin V, Barmanov I (2013) Methods for determining the stiffness coefficient of elastic elements of the supports of rotors of aircraft gas turbine engines
32. Belousov AI, Eskin ID, Novikov DK. (USSR). Damper. No. 2575869. pp 25–28; Stated 02/01/78; Publ. 02/28/83
33. Chegodaev DE, Ponomarev YK (1997) Damping. Samara: Publishing House of SSAU, p 134

Research on Integration Technology of Stereoscopic Environment Monitoring System Based on UAV

Weigang An, Liu Liu, Yanping Wang, Wei Zeng, and Le Wang

Abstract In this paper, the researchers built a three-dimensional air pollution monitoring system based on a multi-rotor UAV platform, and did research on the system integration technology. (1) Anti-outflow Field interference measures. We used adjustable speed ducted fans to stabilize the airflow, and set the airway to further improve the intake stability and reduce the interference of the flow field around the drone to the measurement equipment. Optimizing the installation location of the equipment according to the CFD simulation results; (2) Anti-electromagnetic interference treatment. By wrapping the electromagnetic shielding cloth (silver fiber fabric) on the measurement module, the electromagnetic interference generated by the UAV's own device on the sensor module is reduced; (3) Data preprocessing. Before the regional measurement, an airborne control test was carried out, and the data collected by the airborne equipment was corrected using data processing methods. The equipment was equipped with an Internet of Things module and a GPS positioning module, so that the measurement data could be transmitted to the background for analysis in real time. (4) Based on the uniform experimental design method, the UAV inspection points are arranged, and the measurement path of the measurement system is optimized. And carried out on-site measurements in Xi'an, China.

Keywords UAV · Atmospheric monitoring · Uniform experimental design · Area measurement

W. An · L. Liu (✉) · W. Zeng · L. Wang
Northwestern Polytechnical University, Xi'an, China
e-mail: aeroliu@mail.nwpu.edu.cn

Y. Wang
Chengdu Technological University, Chengdu, China
e-mail: wangypcumt@126.com

Z. Jing and X. Zhan (eds.), *Proceedings of the International Conference on Aerospace System Science and Engineering 2020*, Lecture Notes in Electrical Engineering 680,
https://doi.org/10.1007/978-981-33-6060-0_34

1 Introduction

According to the 2018 Report on the State of the Ecology and Environment in China released on May 29, 2019, the ambient air quality in 217 cities exceeded the standard, accounting for 64.2% of the 338 prefecture-level and above cities in China. The air pollution has become a matter of public concern. Currently, air quality monitoring methods include the establishment of ground observation stations, ground-based lidar, professional mobile monitoring vehicles, and satellite remote sensing observations [1, 2] etc. However, these methods have limitations. Such as ground observation stations that can perform long-term monitoring of the area near the stations, but its observation range (height, coverage area, etc.) is limited, and real-time measurement of the designated external area cannot be achieved. Ground-based lidar has high requirements on the working environment, it is suitable for layout in open areas but not the cities. The high price of the equipment has also prevented the working range of that. Satellite monitoring has a long measurement period and high cost. In view of this, some researchers have developed portable measurement equipment. The portable equipment has the advantages of being easy to carry and real-time measurement. However, due to geographical constraints, it is impossible to achieve some areas which are difficult for people to enter or areas at a certain height above ground. In recent years, the rapid development of the UAV industry has made it possible to obtain air quality parameters conveniently, quickly and at low cost [3]. In recent years, some domestic researchers have been working on environmental information monitoring systems based on UAV platforms. For example, Guo Jian of Tianjin University has developed a SIM908-based UAV air room volume detection system [4]. In this paper, the researchers built an air quality monitoring system based on a multi-rotor UAV platform. According to the multi-rotor CFD simulation result [5], we optimized the installation position of the measurement equipment at the drone, and reduced the interference of the surrounding flow field to the equipment measurement. At the same time, the use of certain shielding measures reduces the electromagnetic interference generated by the UAV's own devices. Before the area measurement, an airborne calibration test was carried out, and the data collected by the airborne equipment was corrected through data processing. We used the Median filter to smooth the data and perform regression analysis on the data. The device has built-in IoT module and GPS positioning module, so that the measurement data can be transmitted to the background for analysis in real time. Afterwards, we carried out an area measurement. In the measurement, we adopted a uniform experimental design method to optimized the measurement path of the UAV patrol route, and captured the characteristics of the measurement area.

2 System Components

2.1 UAV Platform

The quality of experimental data directly affected by the choice of aircraft and the installation of equipment. The six-rotor aircraft is a type of multi-rotor aircraft that can take off and land vertically and hover in the air. Compared with a four-rotor drone, six-rotors drone has higher stability and higher safety margin, its load capacity is also higher than the four-rotor UAV. In this experiment, we adopted an industrial-grade UAV with a symmetrical motor wheelbase of 1100 mm and LiPo 6S batteries. It can be mounted on a 5 kg load for more than 15 min. In certain conditions of particulate matter, the scattered light intensity of the particulate matter is proportional to its mass concentration.

2.2 Atmospheric Six Parameter Measurement Equipment

In this paper, we used a light scattering particle counter in the equipment to measure the particle, which is based on the principle that when light is irradiated on particles suspended in the air, scattered light is generated. In conditions of certain particulate matter, the scattered light intensity of the particulate matter is proportional to its mass concentration. By measuring the intensity of the scattered light, the mass concentration conversion factor K value is used to obtain the mass concentration of the particulate matter. Gas measurement includes sulfur dioxide (SO_2), carbon monoxide (CO), nitrogen dioxide (NO_2), ozone (O_3). The gas measurement sensor is a four-electrode electrical sensor. It works according to the principle of electrochemistry. The oxidation process of the gas in the electrolytic cell generates directional moving electrons. By measuring the magnitude of the current, we will get the concentration of the gas according to the proportional relationship between the current and the gas concentration. Since the flow field generated by the six-rotors during flight will interfere the measurement, we wrapped the sensors in a 3D printed resin material box (Fig. 1), and an adjustable speed ducted fan was arranged at the gas port of the box. By adjusting the rotation speed of the fan, the air intake of the measurement module is controlled, which reduces the interference effect of the external airflow. Shen Ao et al. conducted a CFD simulation of the multi-rotor. The increase in the number of rotors and the increase in the wheelbase size will produce a larger quiet wind area under the fuselage. Therefore, we installed the device 10 cm below the fuselage. The airflow at the location is less affected. UAV motors, electronic governors and other devices will cause electromagnetic interference to the equipment. Therefore, we use silver fiber fabric to wrap the outside of the measurement unit to reduce the effect of electromagnetic interference. In the test of anti-interference, one device was hanged on an iron frame at a height of 20 m, and the other device is carried on the drone to a distance of 10 m from the horizontal position of the hanging device at

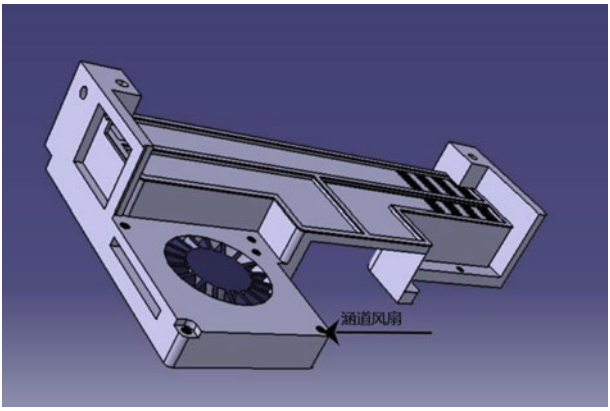

Fig. 1 The design of air passage and ducted fan

the same height. As shown in Fig. 2, the test on the UAV was started after the time 03:33PM (indicated by the green line). We can see that the trend of the sampling values measured by two devices didn't have obvious fluctuation before and after the flight.

3 Data Processing

Due to the inherent characteristics of electrical sensors, original data often has noise problems. If there is a lot of noise in original data, it may affect the precision of the model and ever have a great side effect on the accuracy of the final model [6]. Therefore, data preprocessing is very important before the experimental analysis. When performing air quality analysis on 17 port cities in China, Suling Zhu et al. used data preprocessing techniques to improve the accuracy of the prediction model, Fiuza and Vila [7] used a moving average method to preprocess the data when measuring the oxygen content produced by micro-organisms in the soil. This method increased the availability of the data. In this article, we used median filter to preprocess the original data. The median filter is a non-linear filter. This filter is widely used in image processing [8]. It is useful to reduce the effect of noise. The principle of this filtering method is to use the median of several sample values in the neighborhood of the point to replace the point value. By this way, most of the noise points were eliminated. We assume that the sampling value at time **t** is $\boldsymbol{x_t}$, and the sampling value at time **t-n** is $\boldsymbol{x_{t-n}}$. We reorder all the sampling values from time **t-n** to time **t + n** according to size, these number were $\boldsymbol{x_{i-n}}$, $\boldsymbol{\ldots x_i \ldots}$, $\boldsymbol{x_{i+n}}$ (n is odd), where $\boldsymbol{x_i}$ is the median of this set of data, we use the value of $\boldsymbol{x_i}$ to replace the value of $\boldsymbol{x_t}$. As shown in Fig. 3a–c, after median filtering, the impact of noise and outliers have been reduced.

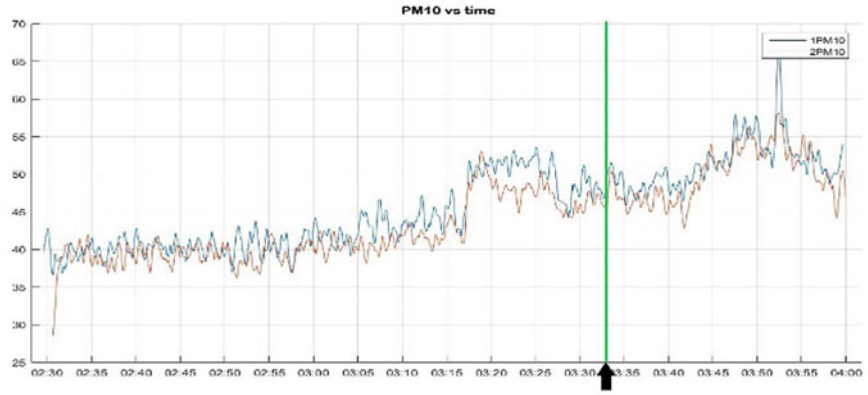

(a) PM10 anti-interference test

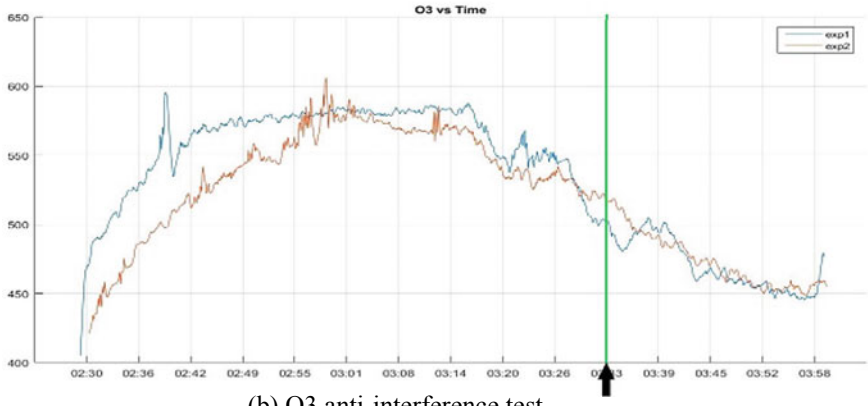

(b) O3 anti-interference test

Fig. 2 Comparison of data stability

Wang et al. [9] used fitting model to evaluate the performance of the portable equipment. They compared the correlation between different devices by data analysis. In this paper, we used the linear fit model to analyze the correlation between the experiment data and the standard values. After the data preprocessing, we compared the experiment data with the standard value of the monitoring station. Since the sampling interval of the measuring device is 5 s and the sampling interval of the monitoring station is 1 min, the length of the vectors is not same. So the data collected by the device will be averaging every 12 data, in this way, we get the experimental data as same as the amount of the monitoring station data in the same time period, and then we performed linear fitting in software, we got the following results (Fig. 3).

We list the results of fitting in Table 1, where p1 is the coefficient of x in the linear equation and p2 is the constant term in the linear equation. Correlation Coefficient is proposed by the famous statistician Carl Pearson. reflects the correlation between the fitted data (x, y). The x represents the standard value, and y here represents the

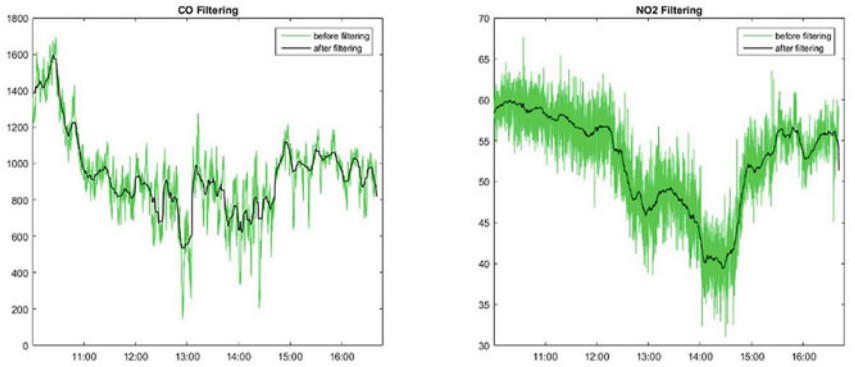

(a)CO (left), $_2$NO (right) Filtering Results

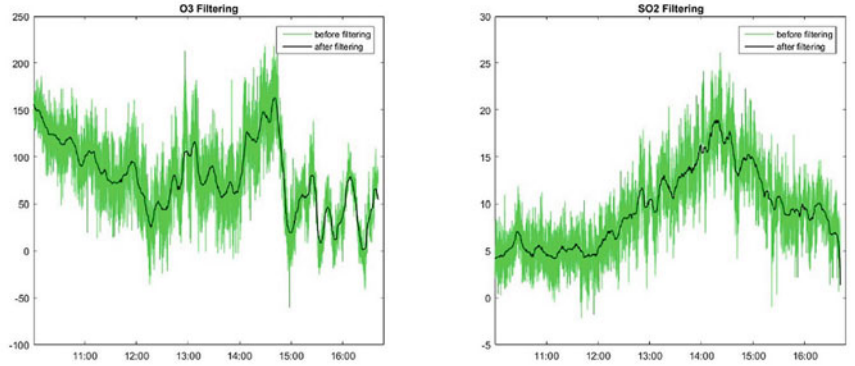

(b) O_3 (left), SO_2 (right) Filtering Results

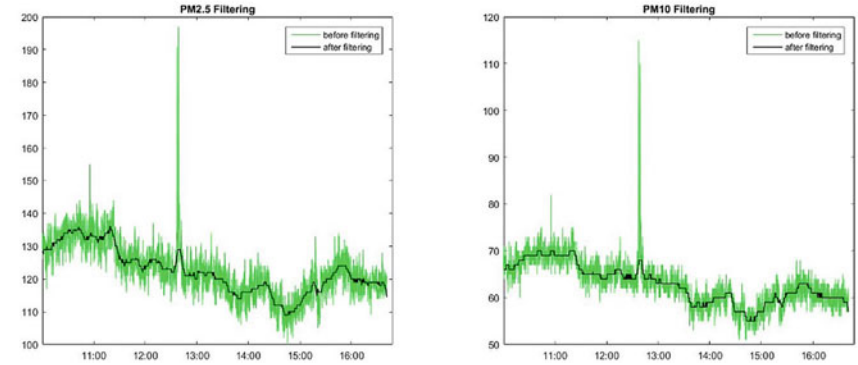

(c) PM2.5 (left), PM10 (right) Filtering Results

Fig. 3 Filtering results of the measurements

Table 1 Fitting results and correlation analysis

Measurements	p1	p2	Correlation coefficient
CO	0.87916	425.1107	75.348%
NO2	0.79669	−11.5327	79.269%
O3	1.0113	35.0771	72.251%
SO2	1.3607	9.8371	56.418%
PM2.5	1.0343	32.0235	89.143%
PM10	0.86001	14.6656	86.298%

experiment value of the airborne equipment. As shown in Table 1, the correlation between the measured values of particle concentration (PM10 and PM2.5) and the standard values had reached more than 80%. In addition to SO-$_2$, the consistency of other measurement values (CO, NO_2, O_3) and standard values had reached more than 70%. Since the concentration of SO_2 in the atmosphere of the normal environment is very small, its relative error is larger than other gases, which results in the calculation of the poor correlation coefficient, but we can see from Fig. 4e that the measurement interval of SO_2 is basically consistent with the standard value. Therefore, we believe that data preprocessing can effectively remove the effects of noise and outliers, and improve the practicality of the data.

4 Field Measurement

Due to the limitation of the endurance of the drone, it is difficult to measure all places in a large area. It means that we need to take some sampling point in this area. We set one point every 50 m in both length and width, so we can get 100 sampling point. In order to pass these 100 points, the drone needs to fly continuously in space for about 6 km according to the Z-shaped route. It is still too long to work on it. The uniform design method is a method to reduce the number of experiments. Through this method, we can make the sampling points spread uniformly in the test range (Fang et al. [10]. Song et al. [11] have studied on the applying of Uniform Experiment Design Method in civil engineering. The results show that by using this method can decrease the required number of experiments remarkably for both physical experiment and numerical experiment and cut down expense, calculation work and time. In this paper, we take the longitude and latitude of the area as 2 experimental factors, and we set the level to 10. Here we used this method to investigate the relations between pollution distribution and spatial position. By referring to the method of uniform design, the 10 sampling points were arranged in 10*10 grids (Fig. 5). According to the sampling points set by us, the route (black broken line) was planned at the ground station. Apparently, the Uniform Design decreased required number of experiments remarkably and deal these problems efficiently.

Based on this measurement system, we took an experiment in Xi'an. We chose a construction site that was located at the campus of Northwestern Polytechnical

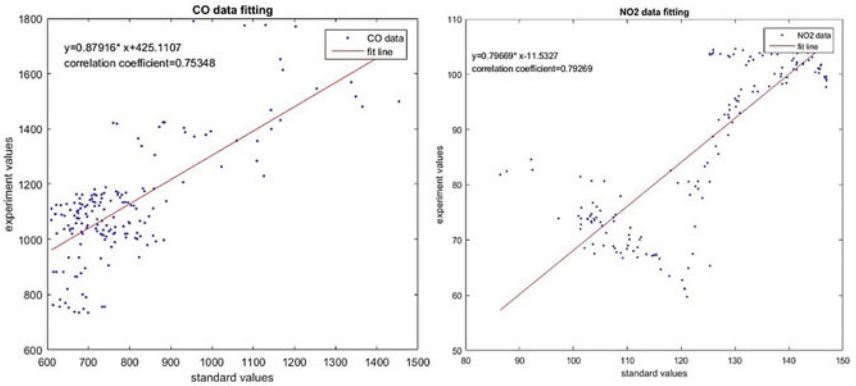

(a)CO (left), NO2 (right) Fitting Rsults

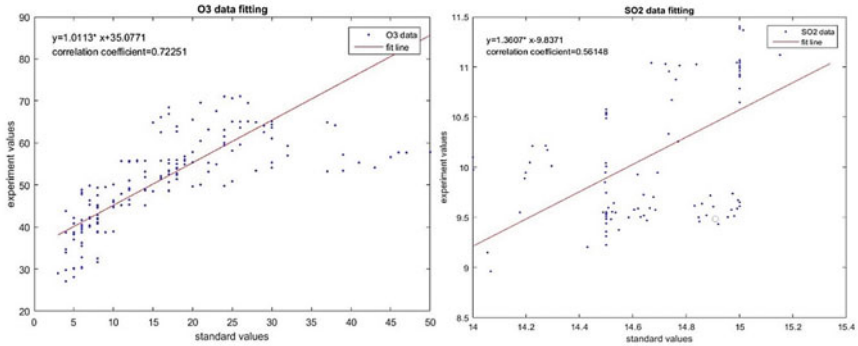

(b)O3 (left), SO2 (right) Fitting Result

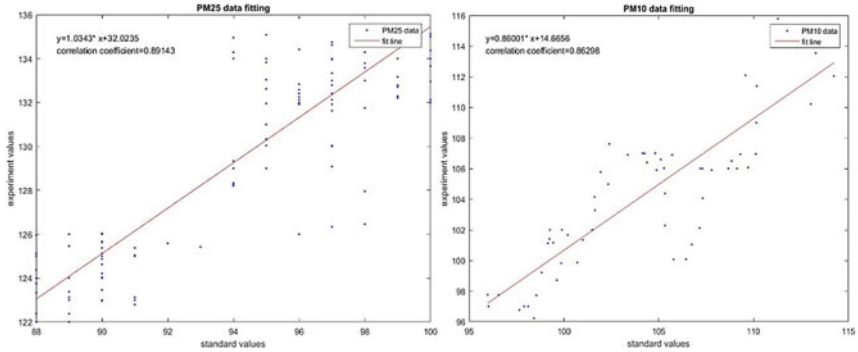

(c)PM2.5 (left), PM10 (right) Fitting Results

Fig. 4 Fitting results of the measurements

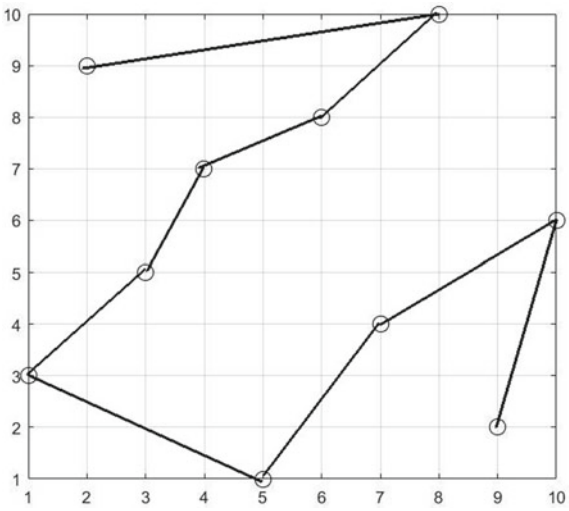

Fig. 5 Path planning of the area

University (Fig. 6). Because of the earth cutting was taken at the construction site, the concentration of the particulate matter should be higher than other area. After the flight measurement, we used Kriging interpolation principles to plot the contour that shows the distribution of PM10 in this field air. In this contour, the deeper of

Fig. 6 Experiment site

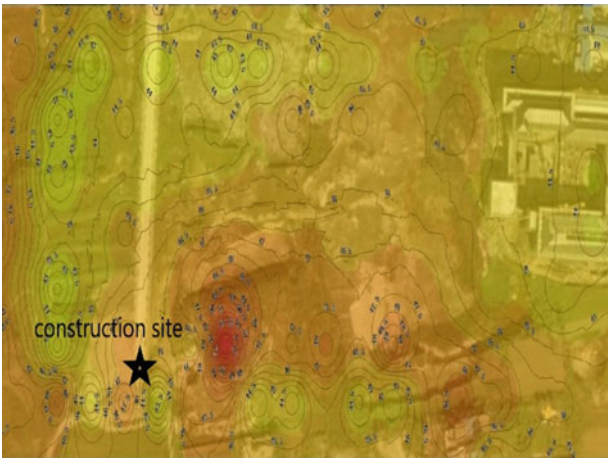

Fig. 7 The distribution of PM10

red color represents the higher value of the PM10 concentration. Because there were wind in the height that the system worked, the maximum of the concentration was not located at the area right above the site. Apparently, the area near the construction had higher PM10 concentration value (Fig. 7). This result confirmed the availability of our working.

5 Conclusion

We studied the atmospheric measurement system on UAV, including anti-electromagnetic interference measures, reducing the interference of the UAV flow field, data pre-processing and fitting analysis, and path optimization of regional measurement. Through the researches above, we have improved the availability of airborne equipment data, reduced the impact of external disturbances on the measurement equipment, and conducted on-site measurements. The measurement results reflected the spatial distribution characteristics of pollutants. This has certain reference value for the tracing of pollutants using drones.

Acknowledgements This work is partially supported by the Key Research and Development Program of Shaanxi (Code: No.2017ZDL-SF-14-4). This work is also sponsored by the Seed Foundation of Innovation and Creation for Graduate Students in Northwestern Polytechnical University (CX2020002). The authors also gratefully acknowledge the helpful comments and suggestions of the reviewers, which have improved the presentation.

References

1. Ackerman SA (1997) Remote sensing aerosols using satellite infrared observations. J Geophys Res pp 17069–17079
2. Zhang B, Wu D, Zhang L, Jiao Q, Li Q (2012) Application of hyperspectral remote sensing for environment monitoring in mining areas. Environ Earth Sci 65(3):649–658
3. Mazeh H, Saied M, Clovis F (2018) Development of a multirotor-based system for air quality monitoring. https://doi.org/10.1109/ebecegc.2018.8357127
4. Jian G (2013) Design and research of air quality monitoring system with UAV based on SIM908. Dissertation, Tianjin University
5. Shen A, Zhou S, Wang M, Peng S, Ren S (2018) Simulation and optimization design of atmospheric detection equipment layout based on UAV. Comput Measure Control 26(02):165–169
6. Zhu S, Sun J, Liu Y, Lu M, Liu X (2020) The air quality index trend forecasting based on improved error correction model and data preprocessing for 17 port cities in China. Chemosphere. https://doi.org/10.1016/j.chemosphere.2020.126474
7. Fiuza A, Vila MC (2005) An insight into soil bioremediation through respirometry. Environ Int 31(2):179–183
8. Chandra E, Kanagalakshmi K (2011) Noise Suppression Scheme using Median Filter in Gray and Binary Images. Int J Comput Appl 26(1):49–57
9. Wang Z, Wang D, Peng Z, Cai M, Fu Q, Wang D (2018) Performance assessment of a portable nephelometer for outdoor particle mass measurement. Environmental Science: Processes & Impacts 20(2):370–383
10. Fang K, Lin DK, Winker P, Zhang Y (2000) Uniform design: theory and application. Technometrics 42(3):237–248
11. Song J, Song Z, Sun R (2012) Study of uniform experiment design method applying to civil engineering. Proc Eng 739–745

Effects of Transition on Aerodynamic Characteristics of Laminar Airfoil Based on CFD

Yanping Zhao, Lianghua Xiao, Yao Chen, and Rui Chen

Abstract Laminar airfoil has extensive application prospect in the civil aviation area as its low drag characteristic. However, the laminar flow is too sensitive to be disturbed and then laminar-turbulent transition location will move forward, which results in a significant increase in drag. Therefore, it is meaningful to obtain the aerodynamic characteristics of laminar airfoil both under natural transition and disturbed transition conditions. This paper focuses on the aerodynamic characteristics of a laminar airfoil named NACA65(1)412. Firstly, numerical simulations of natural transition of the airfoil flow at various angles of attack were carried out using γ-Re_θ model. Secondly, forced transition simulations were taken to imitate the disturbed airfoil flow using k-ω SST model. Results show that, the transition location has a great influence on the aerodynamic characteristics of laminar airfoil, especially on the drag. For the natural transition, as the angle of attack increasing, the natural transition location on the upper surface moves upstream while the one on the lower surface moves the opposite. The upper-surface transition location moves upstream rapidly after the 4° angle of attack. For the forced transition, the drag increases approximately linearly with the transition location for both the upper and lower surface, but the upper-surface behaves much more significant. The lift changes little with the movement of transition locations.

Keywords Laminar airfoil · Aerodynamic characteristics · Laminar-turbulent transition · Forced transition · Numerical simulation

Y. Zhao (✉) · L. Xiao · Y. Chen · R. Chen
AVIC Chengdu Aircraft Industrial (Group) Co. Ltd, Chengdu, China
e-mail: zhaoypbuaa@126.com

L. Xiao
e-mail: xlh0302@126.com

Y. Chen
e-mail: menmen119@126.com

R. Chen
e-mail: cccc_r@126.com

Z. Jing and X. Zhan (eds.), *Proceedings of the International Conference on Aerospace System Science and Engineering 2020*, Lecture Notes in Electrical Engineering 680,
https://doi.org/10.1007/978-981-33-6060-0_35

1 Introduction

Drag reduction is so important in the civil aviation as its influence on the economy and environment pollution. Researches on modern airliners have shown that the friction drag accounts for about 50% of the total drag. So extending the laminar flow region of aircraft is one of the major measures to reduce the drag because the laminar friction drag is much less than the turbulent one. For example, laminar skin friction can be as much as 90% less than turbulent skin friction at the same Reynolds number [1, 2]. Studies have shown that, $150,000 fuel consumption will be saved if the drag reduce by 3% for a long-haul airliner per year [3]. Hence, researches of laminar airfoil/wing become the highlights in aviation field.

Laminar wing technology has been researched by not only Airbus and Boeing, but also Honda [4, 5]. However, studies mainly focus on the design and laminar flow control of laminar airfoil/wing, but rarely mention its practical application, especially the manufacture and maintenance. Roughness, bulges and steps can be found in the practical wing and can promote laminar-turbulent transition [6]. The aerodynamic characteristics would deteriorate sharply. Therefore, it is significant to obtain the aerodynamic characteristics of laminar airfoil both under natural transition and disturbed transition conditions. The study of transition is carried out in this paper, which can help to provide a guide for the design, manufacture, maintenance and flow control of laminar airfoil.

2 Computation Scheme

2.1 Governing Equation and Calculation Method

Reynolds-averaged Navier–Stokes (RANS) equations were adopted in the simulations by using Ansys Fluent (V19.2). The γ-Re_θ transition model and k-ω SST turbulence model were used in the natural transition and forced transition simulations separately. The second order upwind scheme was chosen to discretize the convection term. The diffusion term adopted the central difference scheme, and the SIMPLEC algorithm was used for pressure–velocity coupling.

The γ-Re_θ model is suitable for simulating the natural transition flow, while the k-ω SST model is generally accepted as the most accurate model for turbulent simulation. For detailed information about the calculation models, readers can refer to Fluent (V19.2) user's guides.

2.2 Research Object and Grid Generation

NACA65(1)412 airfoil, with a small leading radius, flat roof, and maximum relative thickness location near to the trailing edge, is one of the representative laminar airfoils. Figure 1 shows the geometry of airfoil and the computational grid. The *X*-axis points to the trailing edge along the chord of the airfoil, and the *Y*-axis is perpendicular to the *X*-axis and points up. The airfoil's maximum relative thickness is 12%, and locates at 40% chord. The maximum relative camber is 2.2%, and locates at 50% chord. The grid was generated by the ICEM software. The up and down boundary is 15c away from the chord. The respective distance of the front and back boundary away from the leading edge and the trailing edge is 15c and 20c. The y^+ was ensured to approximately one. The normal growth rate is 1.1 and the whole mesh contains near one hundred thousand points.

3 Numerical Method Validation

A laminar-flow airfoil, the S809, for horizontal-axis wind-turbine applications, has been designed and analyzed theoretically and verified experimentally in the low-turbulence wind tunnel of the Delft University of Technology Low Speed Laboratory, by Somers [7]. Its results have been widely used for the validation of transition prediction [8]. This paper takes advantage of part of its results to validate. The calculation was simulated at Mach number of 0.107, 0° angle of attack, and Reynolds number based on airfoil chord of 2,500,000.

Figure 2 is the skin friction coefficient (C_f) of S809 airfoil. Taking the upper-surface curve as an example, the C_f becomes negative at the chord location of 50%, which means flow separation. Then the C_f goes to positive again at 56%c, which indicates the flow reattachment. And then the friction drag increases sharply. Combined with the contour of turbulent kinetic energy of upper surface shown in Fig. 3, the transition happens at the 55%c. The flow at the separation point is laminar, and the

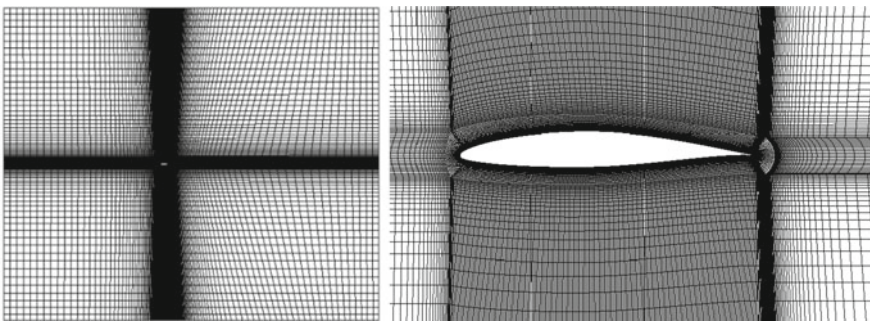

Fig. 1 View of computational grid and geometry of NACA65(1)412 airfoil

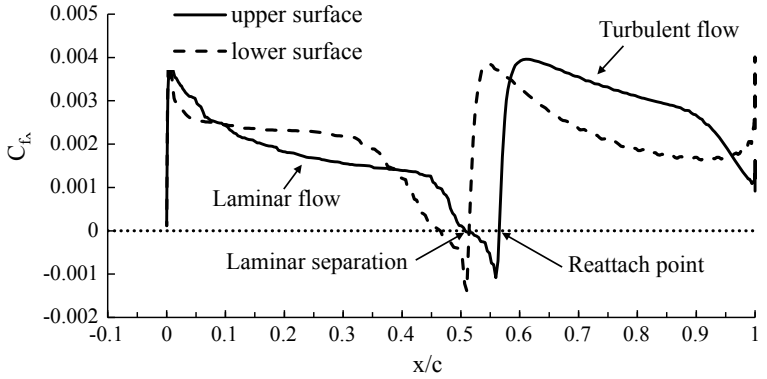

Fig. 2 Skin friction distribution of S809 airfoil

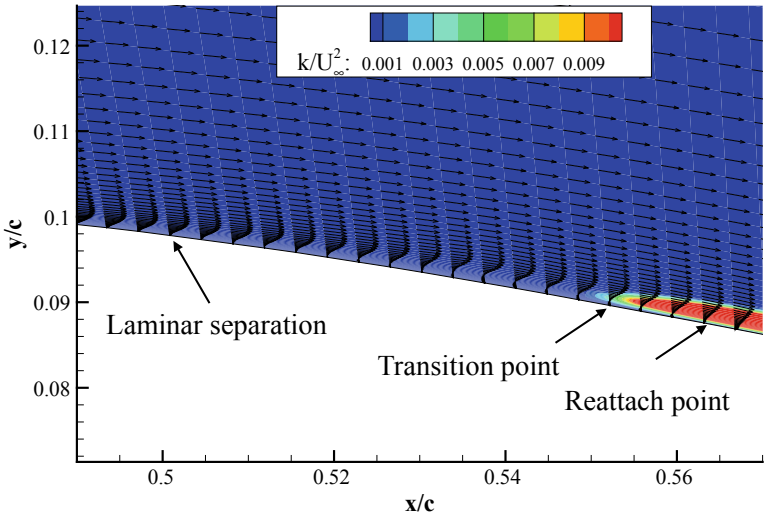

Fig. 3 Contour of turbulent kinetic energy of upper-surface

laminar separation bubble results in the instability of flow, and transition occurs. The boundary layer flow alters from laminar flow to turbulence. The reattachment happens quickly after the flow changing to turbulence. Since the turbulent friction drag is much more than the laminar one, the C_f rises rapidly exceeding the value before separation point. Similarly, the lower-surface transition location is at 50%c.

Figure 4 shows the comparison of the simulated natural transition locations with the experimental data in different angles of attack. As the angle of attack increasing, the natural transition location on the upper surface moves upstream, especially in the vicinity of 6° angle of attack where moves rapidly to the leading edge. The natural transition location on the lower surface moves downstream along with the increasing

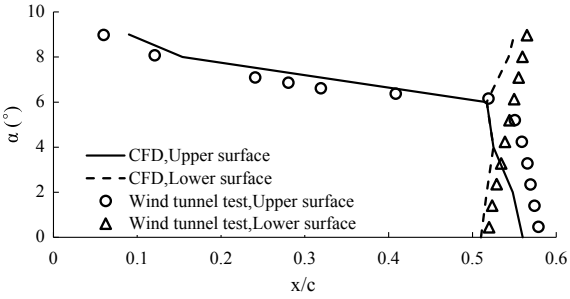

Fig. 4 Comparison of the simulated natural transition locations with the experimental data

of angle of attack, and the total movement is smaller. The simulation results display slightly ahead and are consistent with the experimental data.

Figures 5 and 6 illustrates the comparison of the calculated aerodynamic characteristics including the lift and drag forces with the experimental data of the airfoil, using γ-Re_θ model and k-ω SST model respectively. The drag obtained by γ-Re_θ model is much more accurate than that by k-ω SST model, and the lift is closer with the experimental data. Computation scheme and numerical method conducted by this paper can capture the transition locations precisely, and are reasonable.

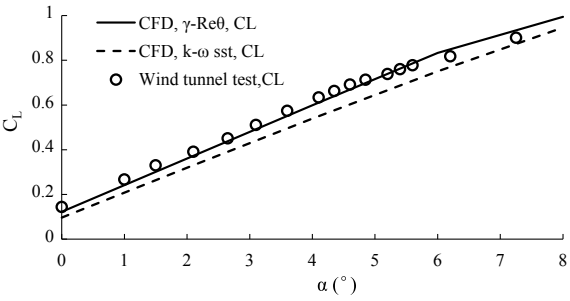

Fig. 5 Comparison of the simulated lift with the experimental data

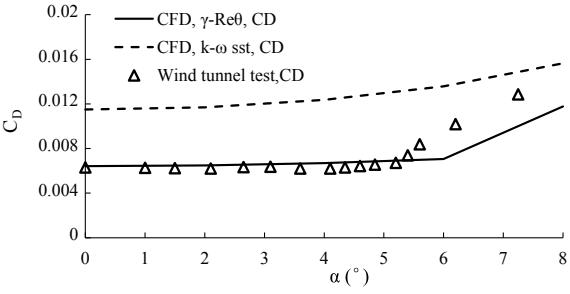

Fig. 6 Comparison of the simulated drag with the experimental data

4 Results and Analysis

4.1 Effects of Natural Transition on Aerodynamic Characteristics of NACA65(1)412 Airfoil

Numerical simulation of natural transition of the NACA65(1)412 airfoil at various angles of attack was carried out, using γ-Re_θ model. The calculation condition is the same as the numerical method validation example.

Figure 7 exhibits the natural transition locations shifting along with the increasing of angles of attack both in upper and lower surfaces of airfoil. At the 0° angle of attack, both the locations are near the 70% chord. As the angle of attack increasing, the upper-surface transition location moves upstream, and the movement speeds up suddenly at 4° angle of attack. The transition location reaches rapidly to the leading edge at the 6° angle of attack, which indicates the boundary layer flow is almost all turbulent. The lower-surface transition location moves downstream slowly along with the increasing of angles of attack, and gets to the trailing edge at the 8° angle of attack, which means no transition occurring and the boundary layer flow is all laminar.

Figure 8 and 9 shows the comparison of the lift and drag curves simulated by γ-Re_θ model and k-ω SST model. It can be seen that, for the k-ω SST model, which

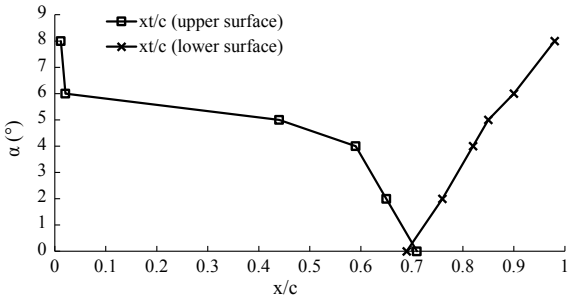

Fig. 7 Natural transition locations of NACA65(1)412 airfoil

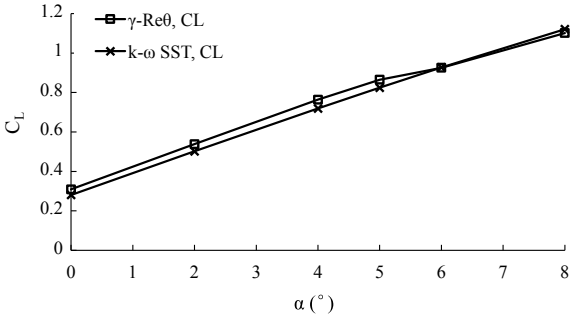

Fig. 8 Comparison of the lift curves of the airfoil simulated by two models

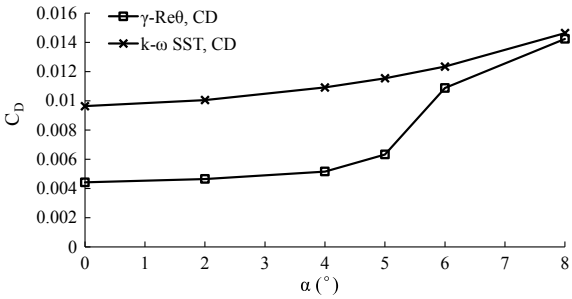

Fig. 9 Comparison of the drag curves of the airfoil simulated by two models

simulates the turbulence, the lift changes linearly with the angle of attack, and the drag varies with the angle of attack in a quadratic curve. For the natural transition simulation, the lift curve is linear in the small angles of attack before 4°. After that the increments of lift slow down and the curve becomes nonlinear, with the rapid rises of drag after the 4° angle of attack. According to the transition locations, the changes of the lift and drag characteristics is caused by the nonlinear forward movement of the transition location on the upper surface after the 4° angle of attack. In fact, the jump of upper-surface transition location will lead to the alteration of boundary layer flow situation, so as to the nonlinear phenomenon of lift curve and a sharp increase of drag.

4.2 Effects of Forced Transition on Aerodynamic Characteristics of NACA65(1)412 Airfoil

Introduction. In engineering, the transition location of airfoil/wing may move ahead by various disturbances. By means of forced transition, the aerodynamic characteristics of disturbed airfoil flow were simulated. The calculation condition is the same as the numerical method validation example, at 0° angle of attack. All simulated transition locations are before the 70%c, as the upper and lower surface natural transition locations of NACA65(1)412 airfoil are both near the 70%c at 0° angle of attack.

Effects of the upper-surface transition. Effects of the upper-transition on aerodynamic characteristics were carried out, while the lower-surface boundary flow is all turbulent. Figure 10 illustrates the lift and drag changing with upper-surface transition locations. As the transition location moves upstream, consequently, the laminar flow region becomes smaller, and the lift decreases as well as the drag rises. In addition, there is a linear relationship between the lift or drag with transition location. The 10% chord movement to the leading edge of upper-surface transition location results in the 1.6% reduction of lift and 7% increase of drag, roughly.

Comparisons of the results of upper-surface transition location at 0% (case 1) and 50% (case 2) chord are demonstrated. Figure 11 shows the comparisons of skin friction coefficient of the two cases. Since the turbulent friction drag is much more

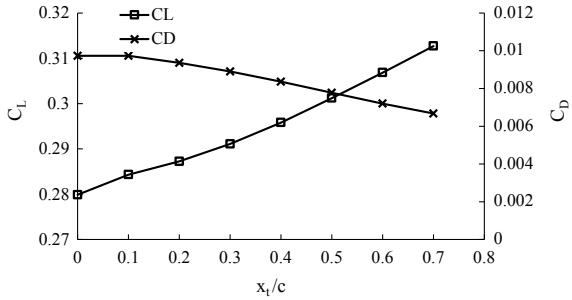

Fig. 10 The lift and drag changing with upper-surface transition locations

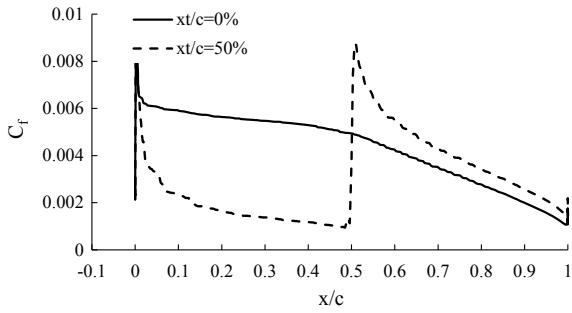

Fig. 11 Comparisons of skin friction coefficient of $x_t/c = 0\%$ with $x_t/c = 50\%$

than the laminar one, it is obvious that the boundary layer is all turbulent in case 1 so that its friction drag is higher than that of case 2, as well as the total drag. Figure 12 is the comparisons of pressure coefficient. The pressure distribution in case 1 contains slightly less area than that in case 2, so its lift is lower.

Effects of the lower-surface transition. Effects of the lower-transition on aerodynamic characteristics were carried out, while the upper-surface boundary flow is all turbulent. Figure 13 illustrates the lift and drag changing with lower-surface transition locations. As the transition location moves upstream, the lift is almost constant

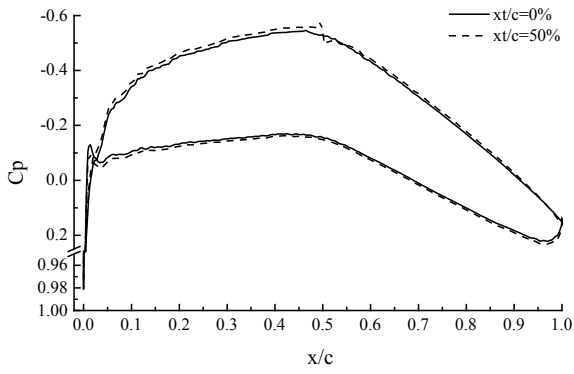

Fig. 12 Comparisons of pressure coefficient of $x_t/c = 0\%$ with $x_t/c = 50\%$

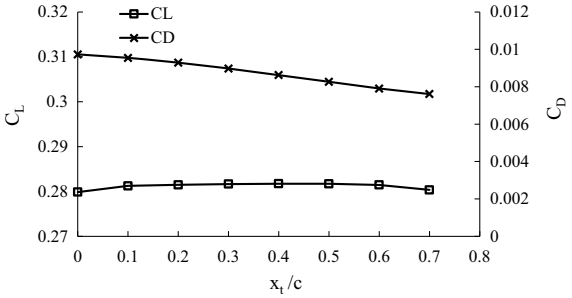

Fig. 13 The lift and drag changing with lower-surface transition locations

while the drag rises. Similarly, there is a linear relationship between the drag and transition location. The 10% chord movement to the leading edge of lower-surface transition location results in the 4% increase of drag, roughly.

In conclusion, it is apparently that the lift is greatly affected by the upper-surface transition location not the lower-surface one. The drag is affected by both the upper and lower surface transition locations in the similar way, and the influence of upper-surface transition location is bigger. Therefore, in laminar airfoil manufacture and maintenance, the surface quality should be guaranteed to avoid the transition occurring ahead of schedule, and the quality of upper-surface should be paid more attention to, particularly.

5 Conclusion

This paper focuses on the aerodynamic characteristics of a laminar airfoil named NACA65(1)412 both under natural transition and disturbed transition conditions. Conclusions can be summarized as follows.

For the natural transition, as the angle of attack increasing, the natural transition location of NACA65(1)412 airfoil on the upper surface moves upstream while the one on the lower surface moving the opposite. The upper-surface transition location will be suddenly move ahead at 4° angle of attack, which will cause the nonlinear phenomenon of lift curve and a sharp increase of drag. The lower-surface transition location moves to the trailing edge gradually and no mutation occurs within the calculated angles of attack.

For the forced transition at 0° angle of attack, as the upper and lower surface transition location moves upstream, the drag increases approximately linearly, and the influence of upper-surface transition location is bigger. The 10% chord movement to the leading edge of upper or lower surface transition location results in the 7 or 4% increase of drag, roughly and respectively. The lift decreases slightly as the upper-surface transition location moving upstream, and is almost unaffected by the lower-surface one.

In laminar airfoil manufacture and maintenance, the surface quality should be guaranteed to avoid the transition occurring ahead of schedule, and the quality of upper-surface should be paid more attention to, particularly. For NACA65(1)412 airfoil, the cruising angle of attack should not be exceed 4°.

Acknowledgements The project is partially supported by Natural Science Foundation of China (Number 11602302).

References

1. Thibert JJ, Reneaux J, Schmitt RV (1990) ONERA activities on drag reduction. In: Proceedings of the 14th congress of ICAS, pp 1053–1064, Bonn
2. Schrauf G (2005) Status and perspectives of laminar flow. Aeronaut J 109(1102):639–644
3. Zhu Z (2011) Aerodynamic design of modern aircraft. National defense industry press, Beijing
4. Fujino M, Yoshizaki Y, Kawamura Y (2003) Natural-laminar-flow airfoil development for a lightweight business jet. J Aircr 40(4):609–615
5. Fujino M (2005) Design and development of the Honda Jet. J Aircr 42(3):755–764
6. Langtry RB (2006) A correlation-based transition model using local variables for unstructured parallelized CFD codes. Dissertation, University of Stuttgart
7. Somers DM (1997) Design and experimental results for the S809 airfoil. NREL/SR-440-6918
8. Chen Y, Gao Z (2009) Application of gamma-theta transition model to flows around airfoils. Acta Aerodyn Sin 27(4):411–418

4D Trajectory and Controller Command Generation Based on Schedule Time of Arrival

Jie Liu, Shuoyan Zhang, and Jizhi Mao

Abstract In order to support the construction of ATC automation system, a four-Dimensional Trajectory (4DT) and controller command generation method based on Schedule Time of Arrival (STA) is proposed. Firstly, four main models of trajectory generation are given: point-mass model, performance model, weather environment and intention model, and the process of trajectory generation is described. Secondly, two methods of generating 4DT according to STA are studied, which are adjusting speed parameters and adjusting command timing. Finally, Guangzhou Baiyun airport is simulated as an example. The result indicates that both optimization methods can meet the requirement of STA, but the command-based method is more consistent with the current control mode, which has a broad application prospect.

Keywords Air traffic management · 4D trajectory generation · Command generation · STA

1 Introduction

The rapid growth of civil aviation flights has brought tremendous pressure to air traffic control (ATC), which causes flight delay and heavy workload to controllers, threatens aviation safety to a certain extent. One of the effective ways to solve this problem is to speed up the construction of ATC automation systems such as controller-assisted decision-making (e.g. AMAN/DMAN), and gradually realize the operation based on 4DT. The implementation of the next-generation ATC automation system is inseparable from the 4DT management technology [1], and the development of 4DT-related

J. Liu (✉) · S. Zhang · J. Mao
China National Aeronautical Radio Electronics Research Institute, Shanghai, China
e-mail: liu_jie_21943@careri.com

S. Zhang
e-mail: zhang_shuoyan@careri.com

J. Mao
e-mail: mao_jizhi@careri.com

Z. Jing and X. Zhan (eds.), *Proceedings of the International Conference on Aerospace System Science and Engineering 2020*, Lecture Notes in Electrical Engineering 680,
https://doi.org/10.1007/978-981-33-6060-0_36

technologies is of great significance for further release the potential of civil aviation transportation.

Research on 4D trajectory prediction has been relatively mature. Wang [2] proposed to use the basic flight model of the aircraft to construct the aircraft's horizontal trajectory, altitude profile, and velocity profile, and then fitted it to obtain a 4D trajectory to achieve aircraft trajectory prediction; Zhang [3] uses aircraft performance model, Ma [4] uses data mining method, and Zhou [5] combines aircraft kinematics model and grey theory, all of them achieve 4D trajectory prediction. Based on 4D trajectory prediction technology, many scholars have carried out a series of researches on improving prediction accuracy [6], minimizing flight costs [7], conflict free [8, 9], energy saving and emission reduction [10], etc. They have achieved remarkable results.

Among them, trajectory generation based on STA can be used for terminal sequencing and conflict resolution, which has a significant effect on alleviating terminal congestion and improving operating efficiency. Soler [11] uses the multi-stage optimal control theory to adjust the speed of the aircraft passing the waypoint so that it reaches the designated position according to the target time; Liu [12] uses a variable flight route to modify the flight distance, which could also change the landing time of the aircraft. However, subject to the current software and hardware resources of ground-to-air communication, the 4DT of ground planning in the above studies could not be well transmitted to the pilot or Flight Management System (FMS), so that makes the optimization result greatly reduced.

According to the current control means, this paper proposes a 4DT generation method based on STA. The trajectory generated by this method considers the aircraft performance and has a clear altitude/velocity change command, which is highly applicable in the current voice control mode.

2 Trajectory Generator

According to the current state, weather environment, flight intention and performance parameters of the aircraft, the trajectory generator uses the Point-Mass Model (PMM) to solve the 4DT of the aircraft in the future. The structure of trajectory generator is shown in Fig. 1.

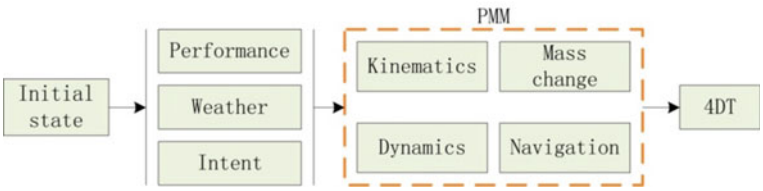

Fig. 1 Structure of 4DT generator of aircraft

2.1 Point-Mass Model

The PMM ignores the complex air flow and rotation characteristics of aircraft in flight, and considers it as a particle for force analysis, including kinematics equation, dynamics equation, mass change equation and navigation equation, which has been widely recognized in the field of civil four-dimensional track. The aircraft Point-Mass Model is built as shown in formula (1):

$$\begin{aligned} \dot{x} &= V_{\mathrm{TAS}} \sin\psi \cos\gamma + W_1 \\ \dot{y} &= V_{\mathrm{TAS}} \cos\psi \cos\gamma + W_2 \\ \dot{h} &= V_{\mathrm{TAS}} \sin\gamma \\ \dot{V}_{\mathrm{TAS}} &= (T - D)/m - g \sin\gamma \\ \dot{\psi} &= g \tan\varphi / V_{\mathrm{TAS}} \\ \dot{m} &= -f_{\mathrm{Fuel}} \end{aligned} \tag{1}$$

where x and y are the horizontal position of the aircraft, h is the vertical position of the aircraft; V_{TAS} represent the aircraft true airspeed; γ, Ψ, φ are flight path angle, heading angle and bank angle respectively; T and D respectively represent the thrust and drag force applied on an aircraft; W_1 and W_2 are the east-trending and north-trending wind velocity components respectively, and f_{Fuel} is fuel flow parameter.

2.2 Performance Parameters

The performance model is used to judge the flight stage, external configuration and other state variables of the aircraft, and also responsible for calculating the control variables such as thrust, drag and fuel consumption. However, in order to improve the accuracy of trajectory calculation, different types of aircraft need to be distinguished. BADA [13] covers the models and parameters required for aircraft performance calculation, which will be cited in this paper.

The aircraft available thrust in different flight stages is the modified value of the maximum climbing thrust in current environment. For a jet aircraft, the maximum climbing thrust in full engine condition is given by formula (2).

$$T_{\max\,\mathrm{climb}} = \mathrm{C}_{\mathrm{Tc},1} \cdot \left(1 - \frac{H_{\mathrm{p}}}{\mathrm{C}_{\mathrm{Tc},2}} + \mathrm{C}_{\mathrm{Tc},3} \cdot H_{\mathrm{p}}^2\right) \cdot \left(1 - \mathrm{C}_{\mathrm{Tc},5} \cdot \Delta T_{\mathrm{eff}}\right) \tag{2}$$

where $T_{\max\,\mathrm{climb}}$ represents the maximum climbing thrust, $\mathrm{C}_{\mathrm{Tc},i}(i = 1, 3, 5)$ is the thrust parameter in BADA, and H_{p} represents the air pressure altitude, ΔT_{eff} is the revision value of thrust calculation when the ambient temperature deviates from the standard atmosphere.

Drag is determined by drag coefficient, true airspeed, air density and wing area, as shown in formula (3).

$$D = \frac{1}{2} C_{\mathrm{D}} \cdot \rho \cdot V_{\mathrm{TAS}}^2 \cdot S \tag{3}$$

where ρ is air density, S is wing area, and C_{D} represents drag coefficient, which is a function of the lift coefficient C_{L}.

The nominal fuel flow f_{nom} for a jet engine is given by thrust and fuel consumption rate η.

$$D = \frac{1}{2} C_{\mathrm{D}} \cdot \rho \cdot V_{\mathrm{TAS}}^2 \cdot S \tag{4}$$

where C_{f1} and C_{f2} are fuel consumption parameter in BADA, and in actual flight the fuel flow is corrected by the nominal fuel flow.

2.3 Weather Environment

Meteorological models are mainly used to estimate atmospheric performance parameters such as air pressure, temperature, air density and speed of sound, as well as to calculate wind direction and speed at different heights in relevant areas. These parameters can be obtained by weather detectors or by numerical interpolation, here is a method of obtaining a weather forecast from the European Centre for Medium-Range Weather Forecasts (ECMWF) and then analyzing the wind field.

The wind field, provided by ECMWF, is in GRIB-II format, which is a concise data format commonly used in meteorology to store the historical and forecast weather data. The data retrieving step includes the determination of region, pressure layers, date, time (0 h 6 h 12 h 18 h UTC), meteorological parameters (u wind, v wind, temperature), and grid resolution ($0.75° \times 0.75°$).

Wind field interpolation is one of the most important links in the meteorological model. The first step of interpolation is to select the two meteorological release times closest to the current time and obtain two sets of wind field data. Then, in each set of data, 8 vertices adjacent to the current point are selected for three-dimensional linear interpolation, as shown in Fig. 2, to obtain the wind field information of the current point. Finally, the wind vector of the current point can be obtained by time linear interpolation of the meteorological wind data obtained at two different time points in the same position.

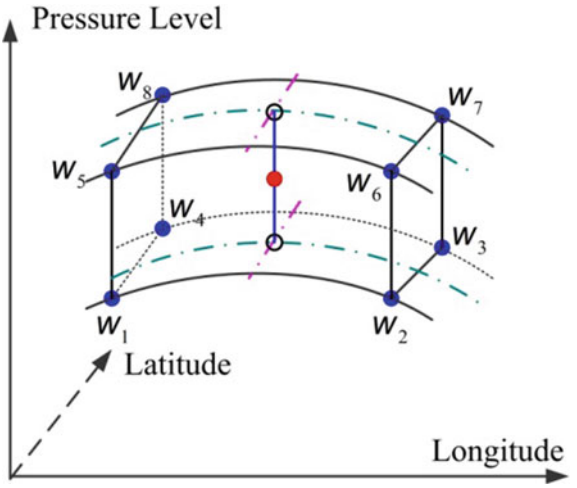

Fig. 2 Three-dimension wind field interpolation diagram

2.4 Flight Intention

Aircraft intent is defined as a set of instructions that are provided as inputs to a computation model in order to specify how the aircraft is to be operated for the 4D trajectory generation. In general, these instructions capture the basic commands and guidance modes at the disposal of the pilot/Flight Management System (FMS) to direct the operation of the aircraft. Table 1 lists the different groups, detailed instructions, constraint categories and affecting parameters of the flight intention model.

Table 1 Flight intention model

Group	Instruction	Category	Parameters
Speed	Hold CAS	Kinematic constraints	V_{CAS}
	Hold Mach		*Mach*
	Hold ROCD		h'
Altitude	Hold altitude	Geometric constraints	h
	Hold flight path		γ
Thrust	Idle, climb, cruise	Kinematic constraints	T
Lateral	Hold track	Geometric constraints	Ψ
	Hold turn rate	Kinematic constraints	φ

3 Trajectory Generation Simulation

A series of software has been developed to support the research of aircraft 4D trajectory, such as the Initial Trajectory Generation Software and the Online Trajectory Prediction Software. The screenshots of some software interfaces are shown in Fig. 3.

In order to verify the accuracy of trajectory generation, the simulated track is compared with the real flight data. Quick Access Recorder (QAR) data of flight CSN3306, B737, on January 20, 2017 is selected, flying from ATAGA to GG404 in Guangzhou Baiyun Airport (ICAO code: ZGGG). Compared with the real data, the following results are obtained. In Fig. 4, the left figure represents the three-dimensional trajectory comparison, while the right figure represents the Calibrated Air Speed (CAS) comparison.

It is not difficult to find that the generated trajectory is basically consistent with the real trajectory in horizontal position, height profile and speed profile, indicating that the trajectory generator can accurately obtain the flight track, which can be used for trajectory prediction, trajectory optimization and other aspects.

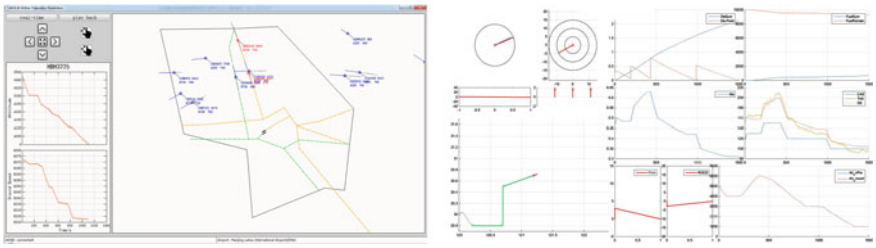

Fig. 3 Trajectory-related software interface

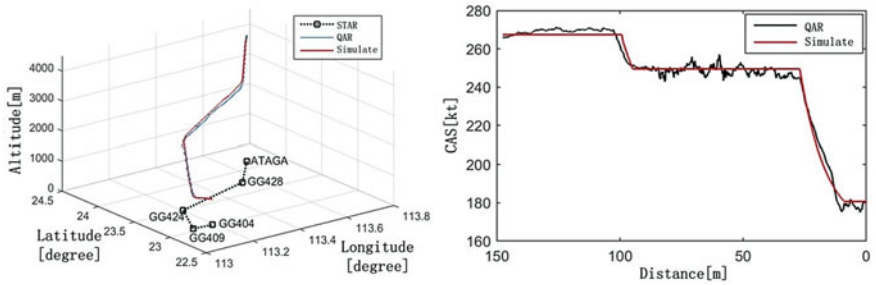

Fig. 4 Trajectory generation results comparison

4 Trajectory Optimization

In fact, trajectory generation based on specific target is an optimization method for aircraft flight path, including trajectory and controller command generation based on STA. If the flight route is not changed, there are two ways to make the aircraft arrive at the waypoint at STA time. One is to constantly adjust the height and speed of the aircraft passing through waypoints, the other is to adjust the timing of the controller's instructions in routine control.

4.1 Adjusting Speed Parameter

The velocity of an aircraft passing the waypoint is between the maximum and minimum range, so the relationship between the passing speed and the speed range can be expressed as a parameter. Suppose *SAP* represents the speed adjustment parameter, t_{ETA} represents the Expected Time of Arrival (ETA), and t_{STA} represents the STA, then the following formula shall be met.

$$\begin{aligned} t_{\mathrm{ETA}}(SAP + \Delta SAP) &\approx t_{\mathrm{ETA}}(SAP) + \frac{\partial t_{\mathrm{ETA}}}{\partial SAP}\Delta SAP \\ &= t_{\mathrm{STA}} \end{aligned} \tag{5}$$

where ΔSAP is the change of velocity adjustment parameter, and $\partial t_{\mathrm{ETA}}/\partial SAP$ is the influence of change of *SAP* on t_{ETA}. According to Way Points (WPs), the horizontal route is divided into several sections, and the ETA is:

$$t_{\mathrm{ETA}} = \sum_{\mathrm{WPs}} \frac{D_{\mathrm{LEG}}}{V_{\mathrm{TAS}}} + t_{\mathrm{Current}} \tag{6}$$

where D_{LEG} is WPs' distance, t_{Current} is current time. Take the derivative of Eq. (6) and substitute it into Eq. (5):

$$\Delta SAP = -(t_{\mathrm{ETA}} - t_{\mathrm{STA}}) \Big/ \sum_{\mathrm{WPs}} -t_{\mathrm{LEG}} \tag{7}$$

where t_{LEG} is flight time of route leg.

4.2 Adjusting Command Timing

Assuming that the starting and ending states of the aircraft in a certain route remain unchanged, according to the aircraft dynamics and performance, the flight time and

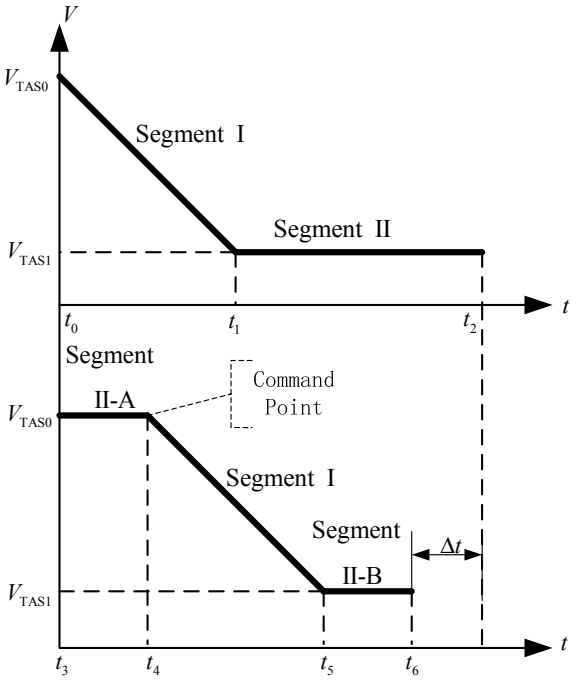

Fig. 5 Adjust vertical section based on timing

flight distance of the aircraft in the process of completing deceleration and descent are fixed, so the timing when the aircraft performs the descent/deceleration operation determines the total flight time in the current segment. The specific implementation steps are as follows.

STEP 1: As shown in Fig. 5, each segment is divided into two sub segments: sub segment I is defined as the completion of deceleration and descent process, and sub segment II is defined as the completion of constant speed-level flight to the next point.

STEP 2: Sub segment II is divided into two sub segments of constant speed-level flight: sub segment II-A before sub segment I, sub segment II-B after sub segment I.

STEP 3: If the time to be adjusted is Δt, the following relationship is satisfied:

$$\begin{aligned} t_0 &= t_3 \\ \Delta t &= t_2 - t_6 \\ t_1 - t_0 &= t_5 - t_4 \end{aligned} \tag{8}$$

the t_i (i = 0, 1, 2, 3, 4, 5, 6) in the formula represents the time of the begin or end of each segment, and the specific meaning refers to the mark in Fig. 5.

STEP 4: Whether before or after optimization, the horizontal distance of the aircraft in each segment is equal, so

$$\int_{t_0}^{t_1} f_1(t)\mathrm{d}t = \int_{t_4}^{t_5} f_2(t)\mathrm{d}t$$
$$\int_{t_0}^{t_2} f_1(t)\mathrm{d}t = \int_{t_3}^{t_6} f_2(t)\mathrm{d}t \tag{9}$$

In the above formula, f_1 represents the speed-time function before optimization, while f_2 represents the speed-time function after optimization.

5 Optimization Verification

This section verifies the difference between the two methods of adjusting speed and adjusting command timing in the trajectory optimization results. When the AMAN optimizes the terminal arrival sequence for Guangzhou Airport, an aircraft, A320, from ATAGA to GG404 is designated for a duration of 1090 s. Different methods are used to optimize the trajectory, and the results are shown in Fig. 6.

It can be seen from Fig. 6 that both methods can meet the STA-based trajectory optimization, and have the same height and speed at the end point GG404. However, in command-based trajectory optimization, the aircraft only has two descent/deceleration processes, and the remaining altitude segments are at the flight level specified by the Chinese RVSM; While speed-based optimization frequently performs deceleration and descent operations, occupying a lot of time and space resources.

6 Discussion

Compared with adjusting the speed parameter, the command-based optimization method has the following advantages:

A. **Less space–time resources occupied by aircraft**

In this case, the aircraft uses the three flight levels specified in the RVSM, namely 4800, 3600 and 1200 m. When the aircraft is flying at these levels, the controller can assign other levels in the nearby airspace to other aircraft. But the method of adjusting the speed parameter cannot do this, which wastes time and space resources.

B. **Controllable for controllers**

Because the trajectory obtained by adjusting the speed parameters has many deceleration/descent processes, it is impossible for the controller to convey this information to the pilot accurately under the existing control conditions; while the optimized trajectory based on the control instruction only needs to issue two commands:

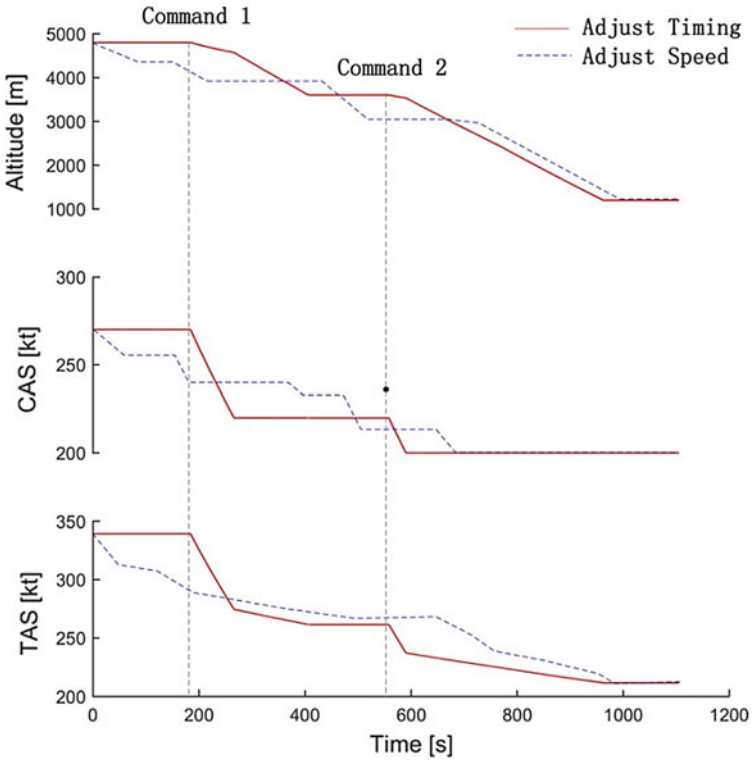

Fig. 6 Trajectory optimization results

Command 1: Descend and maintain 3600, speed 220.
Command 2: Descend and maintain 1200, speed 200.

C. **Operable for pilots**

Without the ability to enter the 4D trajectory into the FMS, it is very difficult for the pilot to achieve the trajectory shown in red lines in Fig. 6. For command-based trajectories, when the controller issues a control instruction, the pilot only needs to select the corresponding altitude and speed targets on the Mode Control Panel (MCP).

7 Prospect

The current air traffic management system requires higher levels of automation and intelligence, and one of the foundations for its upgrade is the optimization of the aircraft 4D trajectory. In an air traffic management decision support system such

as AMAN, STA-based trajectory generation can provide a basis and an implementation approach for AMAN's sequencing and conflict resolution. Future research can consider the operating rules such as the control interval, with safety, environmental protection and other indicators as the optimization goals, to achieve automatic control in the terminal area (including automatic routing, interval maintenance, automatic issuance of instructions), and change the role of the controller from decision to monitor.

Acknowledgements This work is partially supported by Four-Dimensional Trajectory Integrated Surveillance System(4DT ISS) application research project.

References

1. International Civil Aviation Organization (2013) Global Air Navigation Plan (ICAO Doc 9750-AN/963). ICAO
2. Wang C, Guo JX, Shen ZP (2009) Prediction of 4D trajectory based on basic flight models. J Southwest Jiaotong Univ 44(2):295–300
3. Zhang JF, Jiang HH, Wu XG (2014) 4D trajectory prediction based on BADA and aircraft intent. J Southwest Jiaotong Univ 49(3):553–558
4. Ma L, Ma YS (2019) Four-dimensional trajectory prediction method based on ADS-B data mining. J Civil Aviat Univ China 37(4):1–4
5. ZhouZJ, Chen JL, Shen BB et al (2016) A trajectory prediction method based on aircraft motion model and grey theory. In: 2016 IEEE advanced information management, communications, electronics and automation control conference (IMCEC), pp 1523–1527. IEEE, Xi'an, China
6. Zhang JF, Liu J, Hu R et al (2018) Online four dimensional trajectory prediction method based on aircraft intent updating. Aerosp Sci Technol 77:774–787
7. Wang T (2017) Noise annoyance reduction oriented arrival flight track optimization. Civil Aviation University of China
8. Matsuno Y, Tsuchiya T (2015) Near-optimal conflict-free trajectory generation in the presence of uncertainty. In: AIAA guidance, navigation and control conference, AIAA, Kissimmee, Florida, USA
9. Wang ZK, Wu MG, Wen XX et al (2019) Flight collision resolution and recovery strategy based on velocity obstacle method. J Beijing Univ Aeronaut Aeronaut 45(7):1294–1302
10. Yu QD (2019) Performance analysis of continuous descent operation based on 4D trajectory. Civil Aviation University of China
11. Soler M, Olivares A, Staffetti E (2012) Framework for aircraft trajectroy planning toward an efficient air traffic management. J Aircr 49(1):341–348
12. LiuJ, Zhang JF, Dai XM et al (2018) Research on trajectory generation and optimization in continuous descent operations. In: 2018 aviation technology, integration, and operations conference, pp 1–14. AIAA, Atlanta, USA
13. European Experimental Center (2014) User manual for the base of aircraft data (BADA), revision 3.12. EEC

The Mechanisms of Albatrosses' Energy-Extraction During the Dynamic Soaring

Wei Wang, Weigang An, and Bifeng Song

Abstract Albatrosses are the soaring champion among the birds, they can travel 1000 km per day without eating or rest, scientist summarizes this flying style as dynamic soaring. This paper is focusing on the mechanisms of dynamic soaring, by derivation energy harvesting equation, link the basic variables which could infect gliding performance. Through analysis two different energy-extraction equation in two different reference system, this paper finds the key to dynamic soaring and provide a new concept of bionic unmanned aerial vehicle (UAV) design.

Keywords Bionic · Dynamic soaring · Energy-harvesting mechanisms

1 Introduction

Birds always inspired people to achieve flying, back to the Renaissance, Leonardo da Vinci had observed albatrosses for a long time, and it was the first time people linked albatrosses soaring with the wind [1]. Then in the nineteenth century, Lord Rayleigh first used dynamics soaring to refer albatrosses' soaring technique [2, 3], and divided dynamic soaring cycle into four parts: Windward climb, High altitude turn, Leeward descent, Low altitude turn, as shown in Fig. 1. Through experimental measurements, scientists found albatrosses can fly over 13 days during the migration and the energy cost equal to the consumption of 11L gasoline [4]. Sachs found albatrosses' fly speed can achieve 70 km/h, albatrosses need to generate 80 W energy for that [5]. Based on these charming phenomenon, scientists are interested in the dynamic soaring and studying albatrosses' behavior.

Weimerskirch used GPS to measure four wandering albatrosses' travel distance while they were migrating [6]. The result shows that the albatrosses fly trajectory is

W. Wang · W. An (✉)
School of Aeronautics, Northwestern Polytechnical University, Xi'an, China
e-mail: Vulpes.wang@mail.nwpu.edu.cn

B. Song
Research and Development Institute of Northwestern Polytechnical University in Shenzhen, Shenzhen, China

Z. Jing and X. Zhan (eds.), *Proceedings of the International Conference on Aerospace System Science and Engineering 2020*, Lecture Notes in Electrical Engineering 680,
https://doi.org/10.1007/978-981-33-6060-0_37

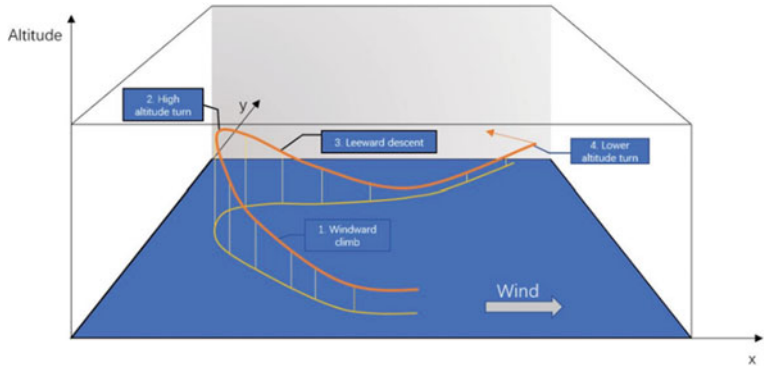

Fig. 1 Typical trajectory of dynamic soaring

related to the wind. Sachs also used GPS and on-bird device to measure the energy change during the dynamic soaring four parts [7, 8].

The scientists also interested in the energy-harvesting mechanisms. Early in 1925 Walkedn had tried using flight dynamics to solve dynamic soaring force problems in 3DOF [9]. Nowadays, researchers in the National University of Defense Technology have done certain work including optimizing dynamic soaring trajectory, albatrosses equations of motion and dynamic soaring force analysis [10, 11].

For the designing of new concept UAV (Unmanned aerial vehicle), the mechanisms of that how albatrosses gain energy during the dynamic soaring is also nonnegligible. The previous research was using Newton's Second Law and energy equation to build the energy change rate during the dynamic soaring. Some scientist focus on the airspeed as a variable of kinetic energy [12–14], others focus on the ground speed [15, 16].

This paper presents the detailed derivation of the 6DOF energy harvesting equation in two reference system: Inertial frame and non-inertial frame. Using known data to draw an energy-time curve to verify the ability of energy harvesting.

2 Energy Harvesting Mechanisms

2.1 Point of View

In flight dynamics, normally there are 4 types of axes system: (1) Inertial Axes System, (2) Earth-Fixed Axes System, (3) Navigational System, (4) Body Axes System. For the dynamic soaring study, scientists always focus on the Earth-Fixed Axes and Body axes system. This paper is using two types of reference frames (Inertial and non-inertial) to deduce the energy harvesting equation, the definition of forces and angles are shown in Fig. 2. In an inertial frame, the speed using in the

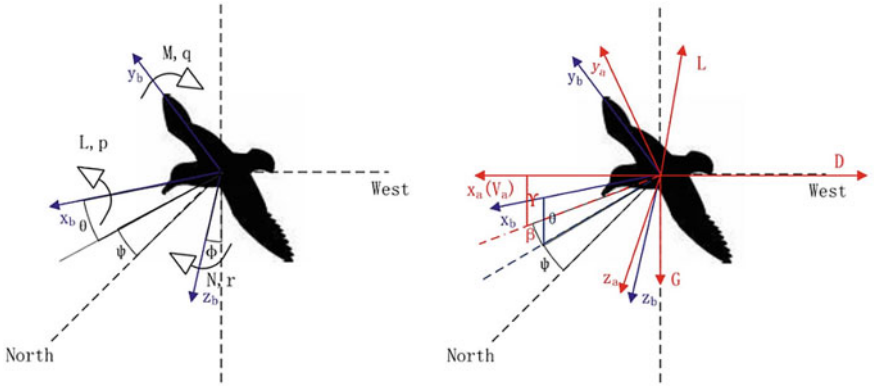

Fig. 2 The axes of two reference frame

Table 1 Differences between two reference frames

Reference frame	Speed of kinetic energy	Newton's second law	Mechanical energy equation
Inertial frame	Ground speed	$\boldsymbol{F} = m\boldsymbol{a}$	$E = 1/2m\left(\dot{x}^2 + \dot{y}^2 + \dot{z}^2\right) + mgz$
Non-inertial frame	Airspeed	$\boldsymbol{F} - m\boldsymbol{a}_0 = m\boldsymbol{a}$	$E = 1/2mV_a^2 + mgz$

equation is inertial speed and in the non-inertial frame, the speed is airspeed. More differences between these two frames are shown in Table 1.

While deducing the energy harvesting equation under the inertial frame, $\left[\theta\ \psi\ \Phi\right]^T$ are the angle to describe the albatross' posture. Meanwhile under the non-inertial frame, not only $\left[\theta\ \psi\ \Phi\right]^T$ but also $\left[\gamma\ \beta\ \psi\right]^T$ are needed. All these variables are shown in Fig. 1.

Considering build the dynamic soaring model, this paper is using the following assumptions:

1. The AOA and the sideslip angle are zero in windless conditions, which means the albatross' head is pointing the direction of speed.
2. Neglect the side force, which means $\mathrm{Y} = 0$.
3. Neglect the rotation, which means $\mathrm{p} = 0, \mathrm{q} = 0, \mathrm{r} = 0$.

After these assumptions, the model can be simplified as follow (Fig. 3).

This paper considering only exist horizontal wind and wind gradient, meanwhile, it parallel to x_E as shown in Fig. 4. Hence, the complex dynamic soaring model can be simplified for mechanisms study.

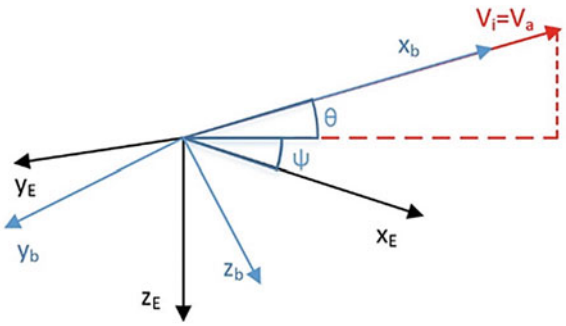

Fig. 3 The simplified model (windless condition)

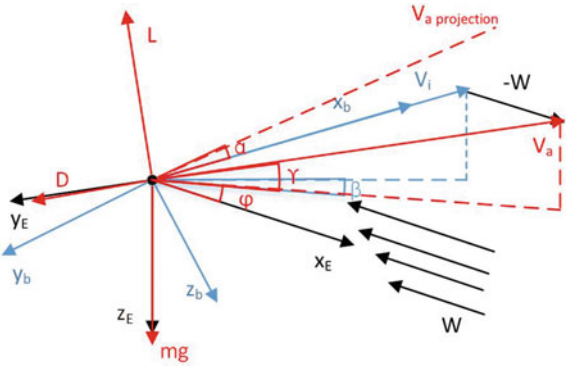

Fig. 4 The simplified model (wind added)

2.2 *Energy Harvesting Equation in Inertial Frame*

The force equation in the body axes system is

$$\begin{bmatrix} F_x \\ F_y \\ F_z \end{bmatrix} = \begin{bmatrix} \cos\alpha\cos\beta & \cos\alpha\sin\beta & -\sin\alpha \\ -\sin\beta & \cos\beta & 0 \\ \sin\alpha\cos\beta & \sin\alpha\sin\beta & \cos\alpha \end{bmatrix} \begin{bmatrix} -D \\ 0 \\ -L \end{bmatrix} + mg \begin{bmatrix} -\sin\theta \\ 0 \\ \cos\theta \end{bmatrix} \quad (1)$$

Focus on the x-direction (head direction), the force equation is shown as (2), then using Newton's Second Law, derived following equation:

$$F_x = -D\cos\alpha\cos\beta + L\sin\alpha - mg\sin\theta \quad (2)$$

$$m\frac{dV_i}{dt} = -D\cos\alpha\cos\beta + L\sin\alpha - mg\sin\theta \quad (3)$$

Now turn to the energy part, recall energy equation in the inertial frame. Let E_m represents energy per mass (E/m). Using the energy change rate to monitor energy harvesting.

$$E_m = \frac{1}{2}V_i^2 + gh \tag{4}$$

$$\frac{dE_m}{dt} = V_i\frac{dV_i}{dt} + g\frac{dh}{dt} \tag{5}$$

Using Eq. (3) to substituting the left side of Eq. (5), and the height-time change rate can be replaced by vertical ground speed, then can be replaced by $V_i \sin\theta$. The energy harvesting equation is as follows.

$$\frac{dE_m}{dt} = -\frac{D}{m}V_i \cos\alpha \cos\beta + \frac{L}{m}V_i \sin\alpha \tag{6}$$

The first term is energy loss costing by drag, the second term is energy gaining by lift. Once the second term greater than the first term, the energy harvesting soaring will be realized.

2.3 Energy Harvesting Equation in Non-inertial Frame

The equation in the non-inertial frame is built on the airspeed as illustrated before. The Newton Second Law in this system is

$$m\frac{dV_a}{dt} = -D - mg\sin\gamma + m\dot{V}_w \cos\gamma \cos\varphi \tag{7}$$

$$\dot{V}_w = \frac{dV_w}{dh}\frac{dh}{dt} = V_f \times V_a \sin\gamma \tag{8}$$

Recall energy equation and simultaneous with Eq. (7), deducing the energy harvesting equation (V_f is gradient wind):

$$E_m = \frac{1}{2}V_a^2 + gh \tag{9}$$

$$\frac{dE_m}{dt} = -\frac{D}{m}V_a + V_f V_a^2 \sin\gamma \cos\gamma \cos\varphi \tag{10}$$

The first term is as similar as the inertial frame, but the second term is different, scientists named this term as dynamic soaring thrust [17].

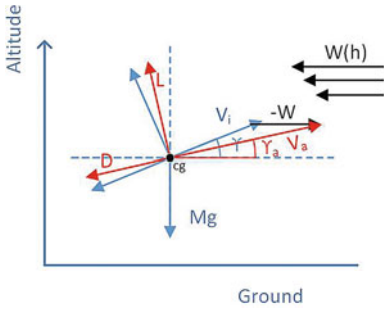

Fig. 5 The wind changes lift direction

3 Result and Discussion

It is obviously the reason why energy changed during the dynamic soaring is different between two points of view. In the inertial frame, the energy harvesting is relied on the lift acting, while in the non-inertial frame, the contribution is from the wind gradient.

Scientists are arguing about rather the gradient wind is vital for dynamic soaring or only wind is enough. This paper stands for the opinion which gradient wind is needed, the detail will be discussed as follow.

It is easy to understand the energy harvesting mechanisms in the inertial frame, the horizontal wind changes the direction of airspeed and makes lift generating force component at the direction of inertial speed, details are seeing in Fig. 5, there has a force ($L\sin(\gamma - \gamma_\alpha)$) work on the direction of inertial speed. Hence the kinetic energy gained. While in the non-inertial frame, the energy comes from the work dynamic soaring thrust has done.

The problem is what dynamic soaring defines needs continuous motion. The derivation in the inertial frame only got wind as a variable, no matter it is a gust or a continuously changing wind. In other words, a flying bird faces a gust that can gain energy, but this definition cannot actually expose the concept of dynamic soaring.

The reason why this divergence arising is that dynamic soaring is actually a continuous motion, however, no matter in the inertial frame or the non-inertial frame, the derivation only calculates certain moments, ignoring the continuity. Link the derivation and above discussion can determine the wind gradient is vital for dynamic soaring.

4 Verification

In order to simulate the energy change during the dynamic soaring, this paper is using simple iteration to calculate the airspeed, energy change during the dynamic soaring windward climb section. First, the mentioned equations need to transform in

order to control the variable. Use C_D to represent the drag in Eq. (10) and build the energy changes-airspeed Eq. (11).

$$\frac{dE_m}{dt} = -\frac{1}{2}\frac{\rho V_a^2 S C_D}{m} V_a + V_f V_a^2 \sin\gamma \cos\gamma \cos\varphi \tag{11}$$

There have many types of gradient wind that geographers have summarized. For the dynamic soaring study, scientists using the exponential wind field as shown as follow (Fig. 6).

$$V_W = V_{ref}\left(\frac{h}{h_{ref}}\right)^p \tag{12}$$

V_{ref} is normally related to h_{ref}. The value of V_{ref} is around 10–25 m/s, and the value of h_{ref} is around 20 m. p is land surface roughness, usually around 0.1–0.143 [18, 19]. Take the derivative of V_W and h, the gradient wind (V_f) can be explained as Eqs. (13, 14). Further, simultaneous Eqs. (11) and (14), shown below.

$$V_W = 20\left(\frac{h}{20}\right)^{0.12} \tag{13}$$

$$\frac{dV_W}{dh} = 0.12\left(\frac{h}{20}\right)^{-0.88} \tag{14}$$

$$\frac{dE_m}{dt_{wind}} = -\frac{1}{2}\frac{\rho V_a^2 S C_D}{m} V_a + 0.12\left(\frac{V_a \sin\gamma}{20}\right)^{-0.88} V_a^2 \sin\gamma \cos\gamma \cos\varphi \tag{15}$$

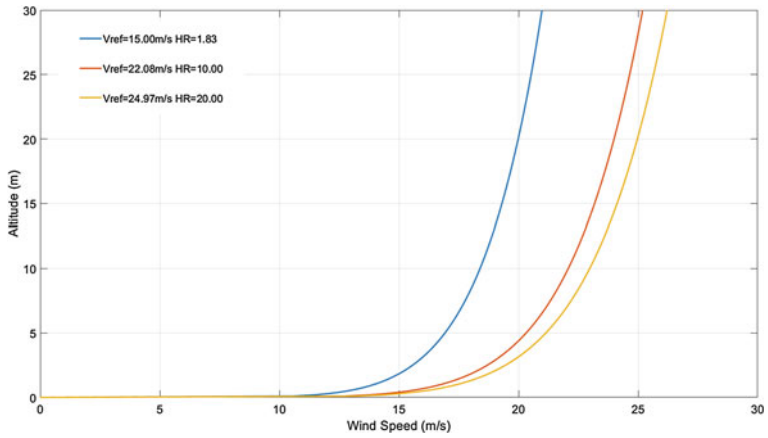

Fig. 6 The wind profile of exponential wind field

Table 2 The initial conditions

Air speed	Wind speed	Start altitude	C_L	L/D
11 m/s	10.5 m/s	0.1 m	1.45	20
Load	γ	φ	Wind aera	Mass
2.8	5°	0°	0.65 m^2	9 kg

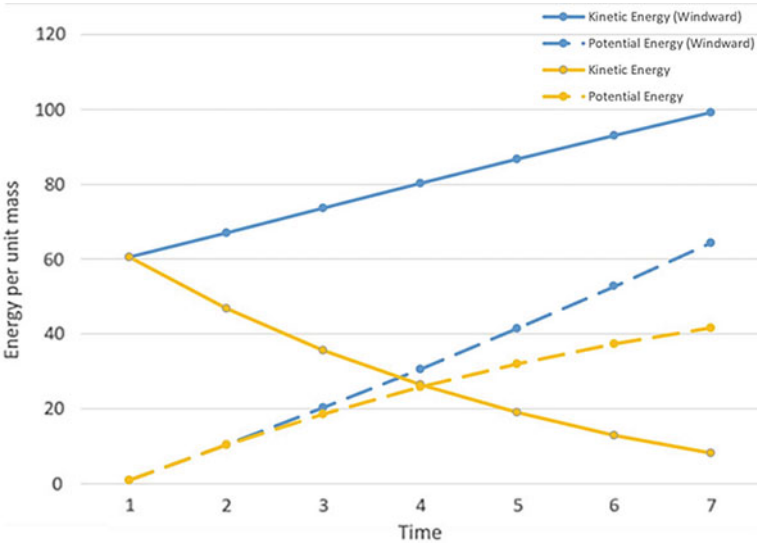

Fig. 7 The energy changes in two conditions

$$\frac{dE_m}{dt_{windless}} = -\frac{1}{2}\frac{\rho V_a^2 S C_D}{m} V_a \tag{16}$$

The initial conditions are referenced as scientists' conclusions and summarized in the Table 2, Fig. 7. Take 0.1 as the time step size.

After calculation, the result is shown in Table 3.

Summarize these data and draw the climb profile (Fig. 7) can clearly show that the energy albatross reached in the wind condition is higher than windless conditions.

This result is also can be verified through Table 3, which can be noticed in the end both airspeed and altitude in wind conditions are higher than another.

5 Conclusion

Dynamic soaring is a classic bionic case that scientists learned from albatrosses then tried to implement in the engineering field. For UAV, dynamic soaring can extend

Table 3 Simulation result

	Wind			Windless		
t	(ΔE_m/kg)	Air speed (m/s)	Altitude (m)	(ΔE_m/kg)	Air speed (m/s)	Altitude (m)
0	–	11.00	0.10	–	11.00	0.10
1	16.04	11.58	1.06	−4.26	9.68	1.06
2	16.53	12.14	2.07	−2.90	8.44	1.90
3	16.95	12.67	3.13	−1.92	7.28	2.64
4	17.27	13.17	4.23	−1.23	6.17	3.27
5	17.53	13.64	5.38	−0.75	5.1	3.81
6	17.71	14.08	6.57	−0.42	4.06	4.25

their cruising time which accord with the environmental friendly design concept. The energy harvesting mechanisms is a key point of dynamic soaring while scientists are studying for a while. However, the previous result always focuses on one point of view, ignoring the difference between inertial frame and non-inertial frame. This paper simultaneous deduces the energy harvesting equation and points out the difference.

The result shows clearly that in the inertial frame the lift will influence the energy harvesting rate but in the non-inertial frame is not. Summarize the above discussion, the energy harvesting equation deducing in the non-inertial frame can expound the mechanisms of dynamic soaring. The source of energy is the gradient wind, which can generate a dynamic soaring thrust to work on kinetic energy.

For dynamic soaring UAV design, the key to maintain efficient energy gaining is reducing the drag. Another considerable aspect is the wind field detected device. Wind direction is vital as dynamic soaring relied on the wind, so this is also a challenge for dynamic soaring realization. In further study, not only the devices organization but also trajectory optimizing, flight control needs to be done.

Acknowledgements This work is supported by the Key Research and Development Program of Shaanxi (Program No.2017ZDL-SF-14-4). And sponsored by the Seed Foundation of Innovation and Creation for Graduate Student in Northwestern Polytechnical University (CX2020002). The authors also gratefully acknowledge the reviewers' beneficial advice, which has improved the presentation.

References

1. Richardson PL (2018) Leonardo da Vinci's discovery of the dynamic soaring by birds in wind shear. Notes Rec Roy Soc J Hist Sci (20180024)
2. Lord Rayleigh F (1883) The soaring of birds. Nature 27(1883):534–535
3. Raspet F, August S (1960) Biophysics of bird flight. Science 132(3421):191–200
4. Croxall JP et al (2005) Global circumnavigations: tracking year-round ranges of nonbreeding albatrosses. Science 307(5707):249–250

5. Sachs F, Gottfried S et al (1960) Flying at no mechanical energy cost: disclosing the secret of wandering albatrosses. PLoS One 7(9):e41449
6. Weimerskirch F, Henri S et al (2002) GPS tracking of foraging albatrosses. Science 295(5558):1259–1259
7. Sachs F, Gottfried S et al (2013) Experimental verification of dynamic soaring in albatrosses. J Exp Biol 216(22):4222–4232
8. Sachs F, Gottfried S (2016) In-flight measurement of upwind dynamic soaring in albatrosses. Prog Oceanogr 142:47–57
9. Walkden F (1925) Experimental study of the "soaring" of albatrosses. Nature 116(2908):132
10. Shan S (2017) Force balance in dynamic soaring of aerial vehicle. J Nat Univ Defense Technol 39(4):15–20
11. Shan S (2015) Dynamic modeling of dynamic soaring and energy gaining from the wind gradient. J Nat Univ Defense Technol 37(4):45–49
12. Richardson F, Philip S (2015) Upwind dynamic soaring of albatrosses and UAVs. Prog Oceanogr 130:146–156
13. Richardson F, Philip S (2011) How do albatrosses fly around the world without flapping their wings? Prog Oceanogr 88(1–4):46–58
14. Zhu B, Hou Z (2015) Transformation in dynamic soaring of unmanned aerial vehicles. J Nat Univ Defense Technol 37(1):78–83
15. Bower F (2011) Boundary layer dynamic soaring for autonomous aircraft: design and validation. Dissertation, Stanford University
16. Bonnin F (2020) From albatross to long range UAV flight by dynamic soaring. Dissertation, University of the West of England
17. Deittert F, Markus S (2009) Engineless unmanned aerial vehicle propulsion by dynamic soaring. J Guidance, Control, Dyn 32(5):1446–1457
18. Sukumar F, Selig S (2013) Dynamic soaring of sailplanes over open fields. J Aircr 50(5):1420–1430
19. Deittert F, Richards S, Toomer T (2009) Dynamic soaring flight in turbulence. In: AIAA guidance, navigation, and control conference AIAA 2009-6012

Aerodynamic Design and Optimization of Bionic Wing Based on Wandering Albatross

Weigang An, Fuzhen Shi, Shibei He, Wei Wang, Hang Zhang, and Liu Liu

Abstract The aerodynamic characteristics of the wing largely determine the flight performance of the aircraft. In studies of nature, it has been found that albatrosses can travel thousands of miles over the sea, with little flapping of their wings, because of their lift-and-drag properties. In order to further study the aerodynamic performance of albatross wings, this paper extracts the mathematical model of bionic wing according to the shape parameters of a wandering albatross, and selects GOE 174 airfoil as the airfoil of bionic wing by 2D aerodynamic analysis, and finally designs and establishes the three-dimensional model of bionic wing. Considering the individual size differences of wandering albatross and the wing deformation during dynamic flying, the Genetic Algorithm(GA) and Vortex Lattice Method(VLM) were used to optimize the size parameters of wing shape with the lift-drag ratio as the optimization objective. The bionic wings with and without optimization were compared with the flat wings with the same wingspan, wing area and wing type. Vortex Lattice Method and 3D-Panel were used for aerodynamic calculation under the same flight conditions to obtain the relationship between the lift coefficient, drag coefficient, lift-drag ratio of the wings and the Angle of attack, as well as the wing pressure, lift, viscosity and induced drag distribution, respectively. The results show that the bionic wing with optimization has excellent lift-drag characteristics. When the Angle of attack is 7 degrees, the lift coefficient, drag coefficient and lift-drag ratio of the bionic wing with optimization are 0.667, 0.025 and 26.768, respectively. Compared with the bionic wing without optimization and the rectangular wing, the lift-drag ratio increases by 5.71 and 7.87%, respectively.

Keywords Albatross wings · Bionic design · Aerodynamic optimization

W. An · F. Shi (✉) · W. Wang · H. Zhang · L. Liu
School of Aeronautics, Northwestern Polytechnical University, Xi'an, China
e-mail: sfzmwq@mail.nwpu.edu.cn

S. He
School of Automobile and Transportation, Chengdu Technological University, Chengdu, China

Z. Jing and X. Zhan (eds.), *Proceedings of the International Conference on Aerospace System Science and Engineering 2020*, Lecture Notes in Electrical Engineering 680,
https://doi.org/10.1007/978-981-33-6060-0_38

1 Introduction

There is growing demand for small, electric, fixed-wing uavs in both the military and civilian sectors, and much attention is being paid to improving their performance. The Unmanned Aircraft Systems Road Map 2005–2030, released by the U.S. department of defense in 2005, proposed that uav endurance is a key factor in uav performance (US Department of Defense [1]. With the study of nature since 1990, it has been discovered that the albatross (Fig. 1) has excellent gliding abilities and can fly thousands of miles across the ocean with very little flapping of its wings [2]. As early as in 1883, British scientists Lord Rayleigh have put forward the "dynamic soaring" in the journal of NATRUE to explain the flying mode of the albatross [3], in recent years, researchers have discovered that the albatross's ability to stay aloft is not only due to its ability to extract energy from sea breezes by dynamic soaring, but also due to the aerodynamic properties of its wings, which are superior to conventional wing and other bird wings [4]. Therefore, through the research and bionic analysis of albatross wings, the aerodynamic characteristics of the wings can be improved, which has great guiding significance for improving the endurance performance of uav and even aircraft.

In 2014, professor Hou of the National University of Defense Technology set up an albatross wings shape model to study the feasibility of highly maneuverable aircraft and their control strategies [5]. In 2018, Gerardo Sanchez and Ryan Salazar et al. studied the lift coefficient, drag coefficient and lift-drag ratio of an albatross wings under different wingspans and aspect ratios. At the same time, different airfoils were selected for comparative analysis of lift coefficient, drag coefficient and lift-drag ratio. Based on the comparison results, Gerardo et al. proposed an inclined wing uav with a aspect ratio of 6.8, a wingspan of 2.2 m and an airfoil of AG26 [6]. In the same year, Adam Stempeck and Mostafa Hassanalian et al. modeled albatross wings, and used 3D-Panel and Horseshoe Vortex Lattice to calculate the aerodynamic performance of other standard geometric wings (rectangular, oval and triangular) and other migrating birds' model wings (tern, golden eagle, pelican, swan, etc.) under

Fig. 1 A wandering albatross in flight

the same aerodynamic environment. The results show that the lift-to-drag ratio of the albatross wings is the largest when the Angle of attack is 5 degrees, and the lift-to-drag ratio in the range of −2 to 3 degrees is better than other conventional geometric wings and migrating birds' wings [4].

The above research shows that albatross wings have excellent aerodynamic characteristics, but the current research has the following deficiencies: First, according to an analysis of albatross flying videos, albatrosses do not have perfectly horizontal wings when they soar, but most of the current research is based on bionic modeling of the two-dimensional shape of albatross wings when they are horizontal, there has been no further study of the three-dimensional shape of albatross wings in flight. Second, most of the current studies directly take the statistical average of albatross wings for modeling analysis, although this shows that albatross wings have a high lift-to-drag ratio, without taking into account changes in aerodynamic performance caused by individual differences in albatross wing size and the influence of wing size parameters on the aerodynamic performance of albatross wings.

In this paper, the flying video of albatross is decomposed and analyzed frame by frame to establish the parameter model of bionic wing and extract the soaring state of albatross wing. Then compare and analyze the bionic airfoil and the low-speed airfoil to select the airfoil of the bionic wing and get the preliminary model of the bionic wing. Then, using the Genetic Algorithm (GA) as the optimization algorithm, and using the Vortex Lattice Method (VLM) for aerodynamic calculation, and the length size of albatross wings and the dihedral and sweep angles of albatross wings in flight were used as the optimization variables, and the maximum lift-to-drag ratio was used as the optimization objective to optimize the bionic wings. Finally, to verify the aerodynamic performance of the bionic wing, in this paper, a rectangular wing model with the same wingspan, wing area and wing type is established. The 3D-panel and Vortex Lattice Method (VLM) were used for aerodynamic calculation and analysis of the bionic wings with and without optimization.

In this paper, there are five chapters. The second chapter introduces the extraction process of albatross wing size parameters and the modeling process of bionic wing. In the third chapter, according to the existing albatross wing size parameter range and the change range of the wing dihedral angle and the sweep angle during flying, the optimized parameter setting and results are introduced. The fourth chapter is the aerodynamic calculation and comparative analysis of the bionic wing. Finally, the last chapter will summarize the work of this paper.

2 Modeling of Albatross Wing Parameters and Bionic Wings

2.1 Extraction of Size Parameters of Albatross Wings

About 20 species of albatross are known, and their wingspan and other parameters vary with the species [7]. For example, the common black-backed albatross has a wingspan of between 1.95 and 2.15 m, while the largest wandering albatross has an average wingspan of 3.1 meters. Gerardo Sanchez and Ryan Salazar et al. studied the lift coefficient, drag coefficient and lift-drag ratio of the wing of the albatross under different wingspan and aspect ratio, and found that with the increase of the aspect ratio, the lift coefficient of the bionic wing increases, the drag coefficient decreases, and the lift-drag ratio increases accordingly [6]. Therefore, taking the wandering albatross as the bionic prototype and considering the actual uav's wingspan parameters, the bionic wing model with wingspan of 3 meters was established and optimized.

The wandering albatross, known to have the largest wingspan of any bird, has a wingspan of up to 3.7 m and an average wingspan of 3.1 m. Its huge wingspan gives the wandering albatross a good gliding ability, and researchers using GPS tracking found that it can use ocean winds to sail 8,000 km in 24 days [8]. In order to intuitively describe the size parameters and shape characteristics of albatross wings, as shown in Fig. 2, the significant changes of albatross wings according to the sweep angle of

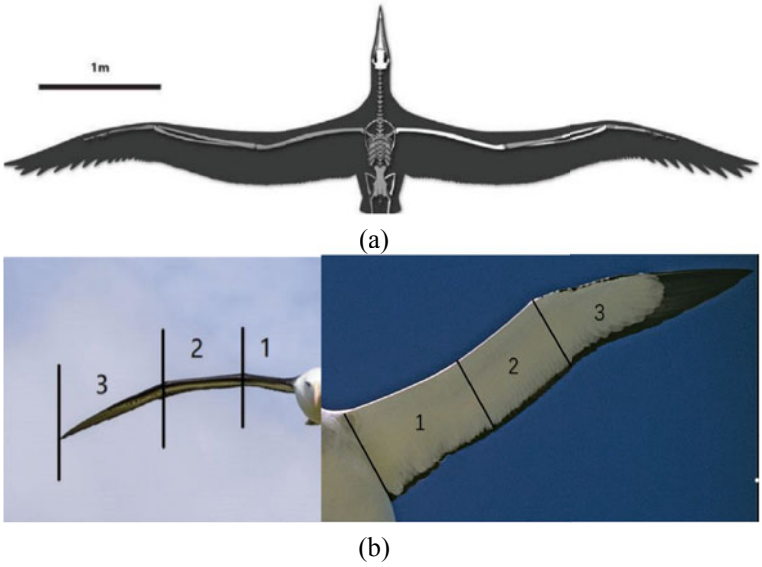

Fig. 2 Wandering albatross wing bone **a** and segments **b**

Fig. 3 The front view of the abdomen of the wandering albatross

their bones are simplified into 3 segments, from the fuselage outward are No. 1, No. 2 and No. 3 segment.

The wing is usually described by such parameters as the span length, the chord length, the sweep Angle and the dihedral Angle. Therefore, the length of the span and chord is defined and extracted according to the segment of the wing firstly. As shown in the figure, according to the simplified wing segment, the span length of wing segments 1, 2 and 3 are defined as No. 1 span, No. 2 span and No. 3 span in turn, and the chord of wing segments 1, 2 and 3 near the fuselage are defined as no.1 chord, no. 2 chord and no. 3 chord in turn. The average wingspan of the wandering albatross is about 3.1 m [9], therefore, the wandering albatross with a wingspan of 3.11 m was selected as the research object in this paper. For lack of specimens of the wandering albatross's wings, in order to extract the parameters of albatross wings, the front view of the abdomen of the wandering albatross when the wings were horizontally spread was selected for measurement. As shown in Fig. 3, the measured wingspan in the figure is 208.5 mm, the distance between the right wing tip and the longitudinal axis of the fuselage is 95 mm, and the distance between the left wing tip and the longitudinal axis of the fuselage is 94 mm, that is, the absolute error of the measurement of the left and right wings is 1.06%, which is within the acceptable range. Table 1 shows the measured values of No. 1, No. 2, No. 3 span length and chord length. Due to errors in the picture, the measured parameters of the left and right wings are not exactly the same. Therefore, the average value of the measured values of the left and right wings is taken as the reference measurement value of the dimension parameters.

After obtaining the measured values of albatross wing parameters, it is considered to convert them into the actual parameters of the albatross wing. Wingspan is one of the most important overall parameters of the wing, and because of the large wingspan value, using wingspan as a molecule for transformation can reduce the error caused by transformation, and when the wingspan changes, the parameters of each wing segment can change according to the proportion. Therefore, wingspan was selected as the scaling factor, and the measured value was converted by the ratio of wingspan to the length parameters of each wing section. Meanwhile, the ratio of the length parameters of each wing segment to the wingspan is taken as the parameter model to describe the bionic wing, as shown in Table 1.

Table 1 Measurement and actual size of wandering albatross wings

The length of the parameter		The measured value	Actual wing size after conversion/mm	Conversion factor	The proportion of the sections
The wing span of segment	No.1 span	28	417.65	7.44643	13.43%
	No.2 span	22	328.15	9.47727	10.55%
	No.3 span	44.5	663.76	4.6854	21.34%
The wing chord of segment	No.1 chord	21	313.24	9.92857	10.07%
	No.2 chord	16.75	249.84	12.44776	8.03%
	No.3 chord	16.25	242.4	12.83	7.80%

Next, the Angle parameters of albatross wings were analyzed. Because the angle of albatross wings will change in the process of flying, to extract the angle parameters of albatross wings, we need to start from the flying process of albatross. Considering that most of the current uav's cruise is dominated by flat hovering, the wandering albatross in the flat flying attitude shown in Fig. 4 is selected as the research object of angle parameters. The measured values of the sweep angle and the dihedral angle of each wing segment are shown in Table 2. Due to the error in the Angle of the left and right wings, the measurement angle of the left and right wings is not exactly the same. Therefore, the average of the measured values of both wings is used as the reference measurement value of the wing parameters.

Therefore, according to the above span length and chord length conversion data as well as the measurement data of dihedral angle and sweep angle, and considering the actual aircraft wing, the initial design of the wingtip chord length is 50 mm. The 2D parametric model of the bionic wing with 3-meter wingspan was established, as shown in Table 2.

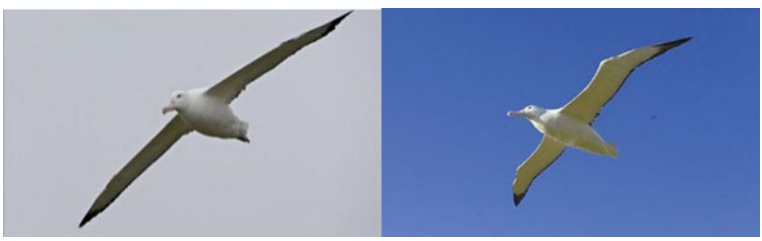

Fig. 4 The wandering albatross in the flat flying attitude

Table 2 The 2D parametric model of the bionic wing with 3 m wingspan

Parameter	No.1 segment	No.2 segment	No.3 segment
The span length/mm	403	317	640
The chord length/mm	302	241	234
The sweep angle/degree	15	−3.5	23.5
The dihedral angle/degree	9.5	−3.5	−20

2.2 Extraction of Size Parameters of Albatross Wings

Due to errors in the picture itself, the process of the measurement and the extraction, in this paper, the extracted two-dimensional parameter model of wing was tested. Shaffer [9] investigated and counted the tarsal bone, beak peak, weight, shoulder width, maximum circumference, maximum forehead area, body size index, wingspan, wing area, average aerodynamic chord length, wing load, aspect ratio and other data of 24 males (16 adults, 8 chicks) and 32 females (20 adults, 12 chicks) wandering albatross.

Due to the large individual differences between chicks and females, the statistical data of adult male albatross were selected as the reference size for the geometric parameters of wandering albatross. According to the literature, the statistical sizes of the overall parameters such as wingspan, aspect ratio, average aerodynamic chord length and wing area of albatross wings could be obtained, as shown in Table 3.

The wing span of the albatross used in this paper is 3110 mm. The ratio of parameters previously obtained is used to calculate the span length and chord length of each wing segment according to the wingspan, so as to calculate the wing area, average aerodynamic chord length and aspect ratio of the albatross wing. As shown in Table 4, the calculated data were compared with the statistical mean value of the wandering albatross wing given in the literature. It can be seen that the relative errors of the converted values of albatross wing parameters, such as wing area, average aerodynamic chord length and aspect ratio, and the statistical values in literature are 0.60%, 0.21% and 0.38%, respectively, within the acceptable range. That is to say, the method has a certain feasibility, and the parameters of albatross wings are quite accurate by measuring them with pictures.

Table 3 The wing parameters of wandering albatross given in the literature

The important parameters	Wingspan	Mean aerodynamic chord	Aspect ratio	Wing area
Parameter values of albatross wings	3110 ± 40 mm	201 ± 8 mm	15.5 ± 0.6	6226 ± 270 cm^2

Table 4 Error comparison of albatross wing parameters

The important parameters	Conversion data of albatross wings	The statistical average of albatross wings	The relative error
Wingspan	3110 mm	3110 mm	0.00%
Wing area	6263.4 cm^2	6226 cm^2	0.60%
Mean aerodynamic chord	201.42 mm	201 mm	0.21%
Aspect ratio	15.44	15.5	0.38%

2.3 Airfoil Selection and Establishment of Bionic Wing Model

After extracting the shape parameters of albatross wings, the appropriate airfoil was selected to build the three-dimensional model of the bionic wing. GOE 174 is an airfoil derived from albatross wings [10, 11, 12]. In addition, GOE 173 and GOE 176 are bionic airfoils based on albatross wings. In order to make the comparative analysis more comprehensive, some low-speed airfoils commonly used in uav design are considered to be added, and the airfoil with better aerodynamic performance is selected for the bionic wing through 2D analysis of the bionic airfoil and the conventional low-speed airfoil.

First, the Reynolds number is determined according to the actual flying environment of the albatross. Because researchers have observed that wandering albatrosses often fly at altitudes of 15–20 m over the ocean, they have never been seen flying above 30 m [13, 14, 15, 16]. Therefore, taking the sea surface temperature as the standard, the aerodynamic viscosity at 15 degree centigrade is $1.78*10^{-5}$Pa·s, and the air density is 1.225 kg/m^3. For airspeed, although the airspeed of albatross is constantly changing in the dynamic soaring, with the analysis and calculation of the albatross flying process, the researchers found that the average airspeed of albatross in the whole flying process is about 20 m/s [17, 18, 19]. The average aerodynamic chord length of the wandering albatross of Shaffer statistics is taken as the characteristic length L. From the formula of Reynolds number calculation:

$$\mathrm{Re} = \rho \, \mathrm{vL}/\mu \approx 2.8 * 10^5 \tag{1}$$

According to the Reynolds number calculated from (1), firstly, 2D aircraft analysis is used to calculate the aerodynamic parameters of the bionic airfoil, as shown in Fig. 5. The lift-drag ratio and C_m of each airfoil under Re = 250,000 and Re = 300,000 are calculated respectively. It can be seen that compared with the other two airfoils, GOE 174 has a stable and high lift-to-drag ratio in a larger scale of attack range. In addition, the C_m of GOE 174 is also relatively small. Therefore, among the albatross airfoils, GOE 174 has the best performance.

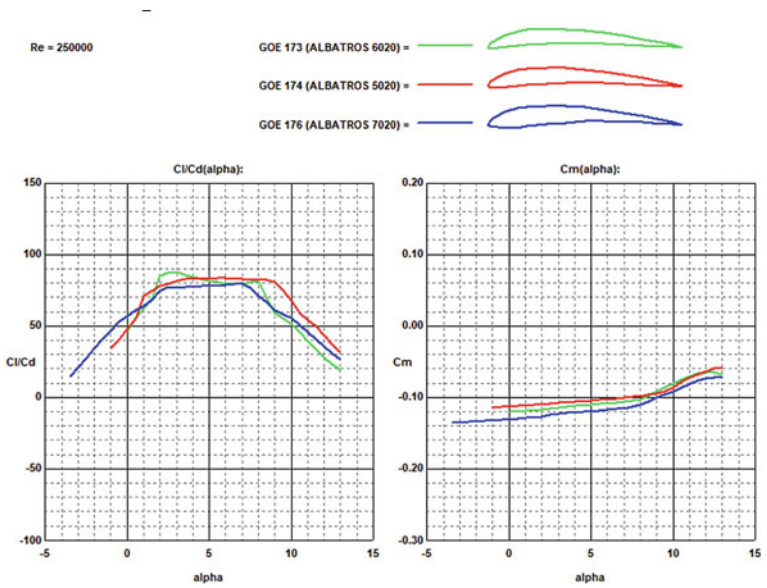

(a)

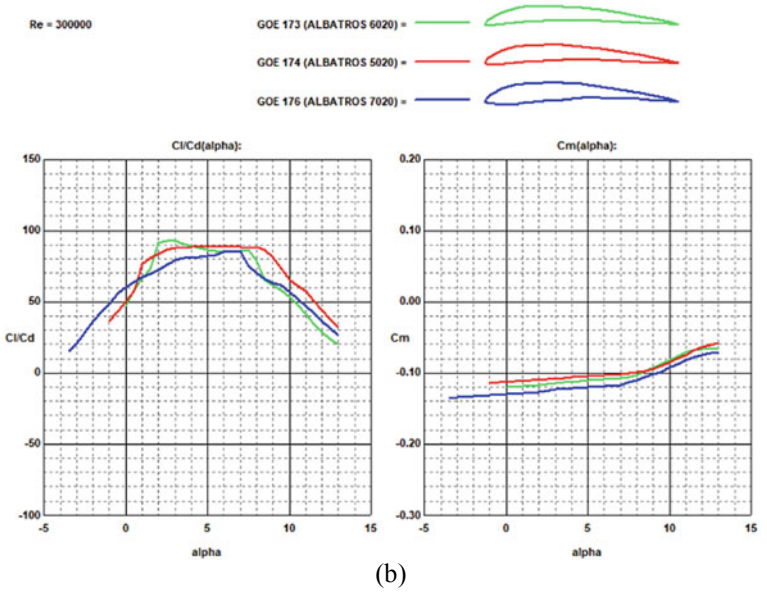

(b)

Fig. 5 2D aerodynamic analysis of bionic airfoil under Re = 250,000 **a** and Re = 300,000 **b**

Next, the aerodynamic performance of GOE 174 was compared with that of conventional low-speed airfoil. In this paper, SD7084, S4083, CLARK YM-15 and NACA 6409 were selected as the possible low-speed airfoil for bionic wing, and 2D aerodynamic analysis was conducted for the above five airfoil. The lift-drag ratio and C_m of each airfoil under Re = 250,000 and Re = 300,000 were calculated respectively. As shown in Fig. 6, it can be seen from the calculation results that NACA 6409 is the optimal lift-to-drag ratio, followed by GOE 174, and SD7084 is the worst. Correspondingly, the C_m is opposite. According to the comprehensive results, the absolute value of C_m of GOE 174 is relatively large, about 0.1, within the acceptable range, and it has excellent lift-drag ratio characteristics. Therefore, this paper selects GOE 174 as the airfoil of bionic wing.

In summary, this paper chooses GOE 174 as the airfoil of the bionic wing. With the parameters given in Table 2 as the design size of the bionic wing, the bionic wing model was finally established. In this paper, XFLR 5 is used to achieve parametric modeling, as shown in the Fig. 7, the middle fuselage of the wing is replaced by a flat wing section.

3 Optimization of Bionic Wing Parameters Based on Maximum Lift-Drag Ratio

3.1 Definition and Description of Optimization Problem

The bionic wing has previously been designed and modeled based on the albatross's flat wing shape. However, on the one hand, the individual difference of wandering albatross makes the wing sizes of different individuals different, and the aerodynamic performance of the wings will vary with the length parameters. On the other hand, since the fixed-wing aircraft cannot achieve the complex angle parameter changes like albatross wings, and the current wing deformation technology is not mature. Therefore, it is necessary to further study the parameters of the bionic wing with the best aerodynamic performance in the flat flight attitude.

The lift-drag ratio is an important parameter to reflect the aerodynamic performance of a wing. Therefore, in this paper, the maximum lift-drag ratio is considered as the optimization objective, and the optimization algorithm is adopted to optimize the size parameters of each bionic wing segment. The design variables are the span length (x), chord length (y), upper inverse Angle (α) and sweep Angle (β) of each wing segment, as shown in Eq. (2), and the footnote is the wing segment number.

As for the constraints of the optimization variables, the constraints of length parameters according to the wingspan and chord interval of albatross by Shaffer statistics, and according to the previous proportional model of wing segment length parameters based on wingspan, the corresponding optimization interval is obtained. Among them, for the span length, since the bionic wing with 3 m wingspan needs to be designed, the span length of the wing segment needs to be restrained. After removing

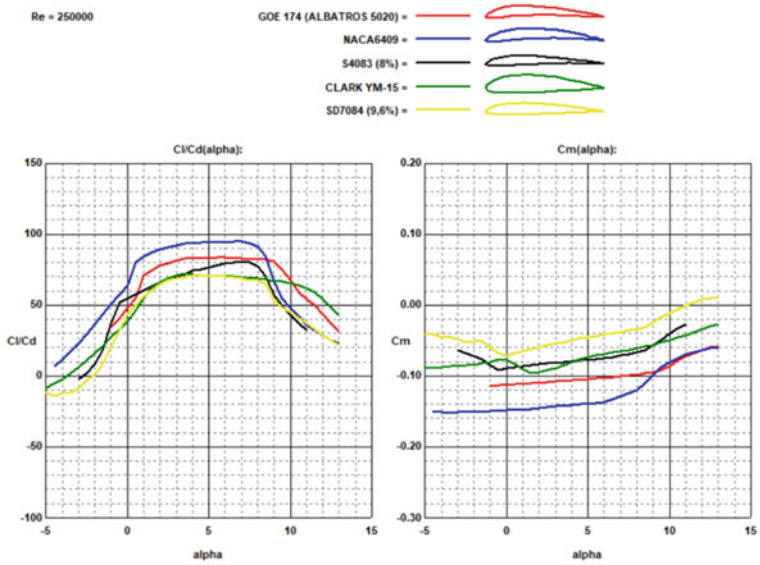

(a)

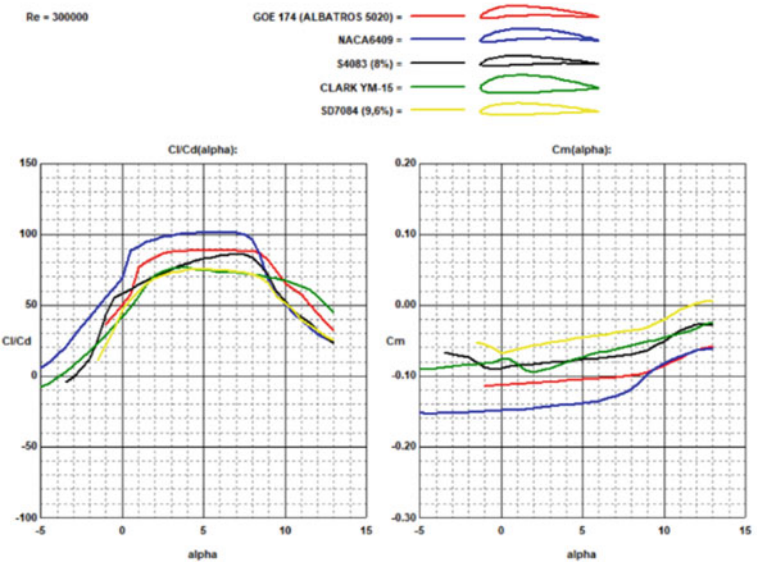

(b)

Fig. 6 2D aerodynamic analysis of GOE 174 and other conventional low speed airfoil under Re = 250,000 **a** and Re = 300,000 **b**

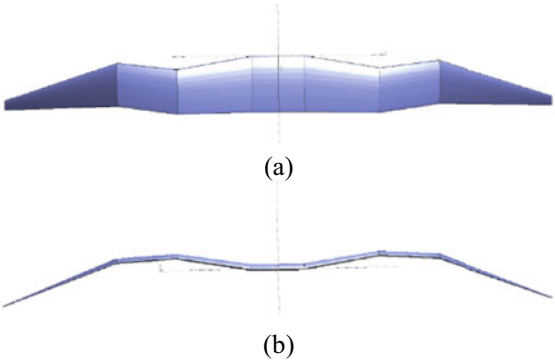

Fig. 7 Elevation and top view of 3D model of the original bionic wing

the fuselage width of the albatross, the total span length of the three wing segments is 1360 mm. For the chord length, a reasonable optimization interval is defined for the chord length at the wing tip considering the conventional wing design.

In terms of angle parameters, this paper extracted the angle changes of albatross wing during dynamic soaring through the decomposition and frame-by-frame analysis of several albatross flying videos, and thus determined the optimization interval of angle parameters. Finally, on the basis of the literature statistics and video analysis of albatross, the optimization interval was expanded appropriately. On the one hand, the interval boundary is taken as an integer, which is easy to express. On the other hand, by taking a certain amount of redundancy, the influence of size parameters on lift-drag ratio of the bionic wing can be analyzed more intuitively according to the optimization results. The optimization mathematical equation is shown in (2). In the optimization equation, lower and upper represent the lower limit and upper limit of the optimization interval of corresponding optimization variables, and the specific values are given in Table 5:

$$\begin{gathered}
\text{Maximize}\, u = f_{C_L/C_D}(x, y, \alpha, \beta) \\
Subject\ to \\
x_i^{lower} \le x_i \le x_i^{upper}, 1 \le i \le 3 \\
y_j^{lower} \le y_i \le y_i^{upper}, 1 \le j \le 4 \\
\alpha_m^{lower} \le \alpha_m \le \alpha_m^{upper}, 1 \le m \le 3 \\
\beta_n^{lower} \le \beta_n \le \beta_n^{upper}, 1 \le n \le 3 \\
\sum_{i=1}^{3} x_i = 136\ \text{cm}
\end{gathered} \tag{2}$$

In order to perform aerodynamic calculations, in addition to the wing parameters as optimization variables, the flight environment needs to be set. According to the research, the average airspeed of albatross is about 20 m/s during the whole flying process, and the air density calculated above is1.225 kg/m^3, and the Reynolds number is 2.8*10^5. In addition, to calculate the lift-drag ratio of the wing, it is necessary to determine the angle of attack of the bionic wing. According to the change trend of

Table 5 The specific optimization interval of the optimization variable

Optimization variables	The lower limit	The upper limit
x_1 (cm)	35	50
x_2 (cm)	30	40
x_3 (cm)	60	80
y_1 (cm)	25	40
y_2 (cm)	20	30
y_3 (cm)	20	30
y_4 (cm)	1	10
α_1 (degree)	−10	10
α_2 (degree)	−10	10
α_3 (degree)	−60	60
β_1 (degree)	−15	10
β_2 (degree)	−15	10
β_3 (degree)	−60	60
Airspeed (m/s)	20	
AOA (degree)	5	

lift-drag ratio of GOE 174 airfoil with the Angle of attack, it can be seen that when the Angle of attack is 5 degrees, the lift-drag ratio of GOE 174 tends to be stable and reaches the peak, so the bionic wing with the angle of attack at 5 degrees is selected for aerodynamic calculation.

3.2 The Settings of Optimization and the Analysis of the Optimization Results

According to the optimization mathematical model, the parameter optimization of the wing has high complexity and strong nonlinearity, and it is difficult for the traditional optimization algorithm to converge from the local optimal to the global optimal. Therefore, intelligent optimization algorithm is considered to solve the problem. According to the principle of optimization, intelligent optimization algorithms include Simulated Annealing algorithm, Genetic Algorithm, Tabu Search algorithm, Particle Swarm Optimization algorithm and Ant Colony algorithm. Among them, the Simulated Annealing algorithm has poor parallelism, the Tabu Search algorithm relies on the setting of initial parameters, and the Ant Colony algorithm itself is complex, which is prone to stagnation in the calculation process. PSO is easy to fall into the local optimal solution when the objective function is multi-peak curve, and will not improve with the increase of population size. Compared with other optimization algorithms, although GA has a large amount of computation, for the complex

optimization problem of wing parameters, GA computes the stability and uniformity, and can ensure the global optimal solution when the population size increases to a certain value. Therefore, GA was selected to optimize the parameters of the bionic wing.

To optimize wing parameters with GA, the function of lift-drag ratio should be determined at first. During aerodynamic calculation of the wings, due to the large amount of CFD calculation, the convergence speed was slow. Vortex Lattice Method was used to estimate the lift-to-drag ratio of the bionic wings in the optimization process. Tomas[18] verified the considerable accuracy and feasibility of Vortex Lattice Method by comparing various aerodynamic calculation methods. For this optimization problem, the computational efficiency and convergence speed can be improved without affecting the optimal solution.

GA starts the search process from a group of randomly generated initial solutions. Therefore, in addition to the objective function, only the range of design variables needs to be set before optimization. In the previous section, the interval of the optimization variable has been given. Since the angle parameter is a two-digit number, in order to make the optimization result more intuitive, the length parameter takes the centimeter as the unit, that is, as a two-digit number. According to the variable interval given by the optimization mathematical model, the optimization Settings are shown in Table 5.

Table 6 shows the results of the optimization. The optimization results show that the bionic wing has better aerodynamic performance when it has a certain lower dihedral angle and sweep angle. In addition, it can be seen from the optimal solution that the No. 1, No. 2 span and No. 1, No. 2 and No. 3 chord tend to be lower bound of the optimization interval, which may mean that the further reduction of these length size parameters can lead to higher lift-drag ratio.

Table 6 The results of optimization

Parameter	Result
x_1 (cm)	35.8
x_2 (cm)	30.8
x_3 (cm)	69.4
y_1 (cm)	28
y_2 (cm)	20.7
y_3 (cm)	21.2
y_4 (cm)	4.6
α_1 (degree)	-3.7
α_2 (degree)	0.1
α_3 (degree)	−13.9
β_1 (degree)	−11.4
β_2 (degree)	−10.5
β_3 (degree)	−21.4

4 Analysis and Comparison of Aerodynamic Characteristics of Bionic Wing

By rounding the optimization results, new bionic wing parameters can be determined, as shown in Table 7. Figure 8 is a new 3D bionic wing model established by XFLR 5 according to the optimized bionic wing parameters.

In order to study the aerodynamic performance and optimization effect of the bionic wing, the aerodynamic model of the rectangular wing with the same wingspan, wingspan and wing area as that of the bionic wing was established in this paper. XFLR 5 and MATLAB program were used to calculate the lift coefficient, drag coefficient and lift-drag ratio of the bionic wing and the rectangular wing under the same flight conditions. The relationship between aerodynamic parameters and angle of attack of each wing is calculated and analyzed by Vortex Lattice Method, and they are compared. The lift coefficient, drag coefficient and lift-drag ratio are shown in the Fig. 9. It can be seen from the Fig. 9c that the lift-drag ratio of the bionic wing with optimization is always the highest. When the angle of attack is 7 degrees, the lift-drag ratio of the three wings reaches the maximum. Among them, the maximum

Table 7 Parameters of the bionic wing with optimization

Parameter	No. 1 Segment	No. 2 Segment	No. 3 Segment
The span length/mm	358	308	694
The chord length/mm	280	207	212(46)
The sweep angle/degree	11.5	10.5	21
The dihedral angle/degree	-4	0	-14

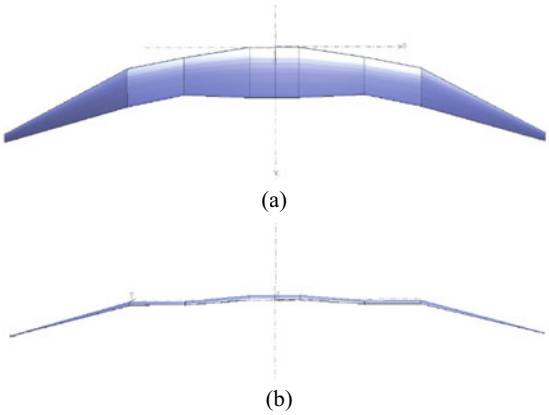

Fig. 8 Elevation and top view of 3D model of the bionic wing with optimization

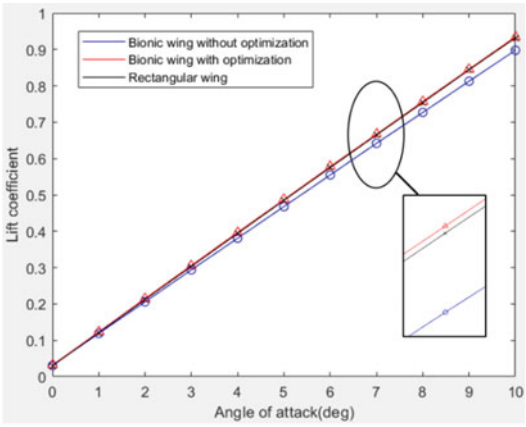

(a)

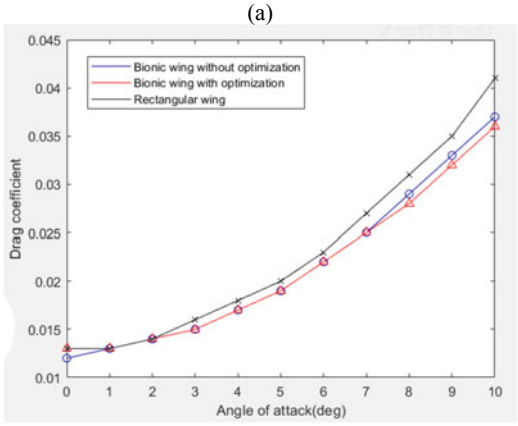

(b)

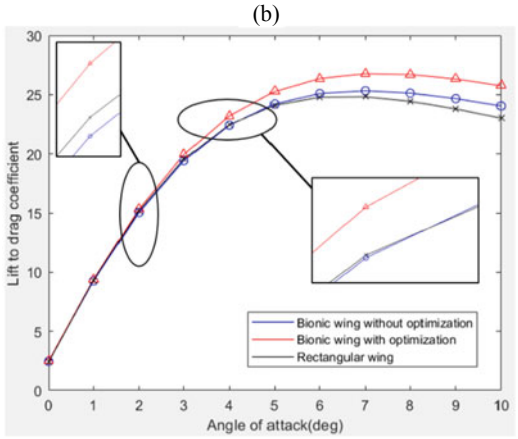

(c)

Fig. 9 The relationship between the lift coefficient **a**, drag coefficient **b**, lift-drag ratio **c** of three wings and angle of attack

lift-to-drag ratio of the bionic wing with optimization is 26.768, and the maximum lift-to-drag ratio of the bionic wing without optimization and rectangular wing is 25.322 and 24.816, respectively. Therefore, compared with the rectangular wing, the maximum lift-to-drag ratio of the bionic wing with optimization increased by 7.87%. The maximum lift-drag ratio of the bionic wing was increased by 5.71% through optimization.

In addition, it can be seen that the lift-to-drag ratio of the rectangular wing is higher than that of the bionic wing without optimization in the range of 0 to 4 degrees of attack. In the range of 4 to 10 degrees, the result is the opposite. Figure 9a shows that the lift coefficient of the rectangular wing is higher than that of the bionic wing without optimization, and the optimization improves the lift coefficient of the bionic wing, making it exceed that of the rectangular wing. The Fig. 9b shows that the drag coefficient of the bionic wing is always lower than that of the rectangular wing except in the range of 1 to 2 degrees angle of attack, and the drag coefficient of the bionic wing is effectively reduced in the range of 7–10 degrees angle of attack though optimization.

In summary, the bionic wing has a low drag coefficient and a high lift-drag ratio. Optimization can effectively improve the lift coefficient and reduce the drag coefficient, so as to improve the lift-drag ratio of the bionic wing.

According to the aerodynamic parameters calculated above, 3D surface element method is adopted to calculate the pressure, lift, viscosity and induced drag distribution of the bionic wing and the rectangular wing when the angle of attack is 7 degrees, as shown in the Fig. 10. It can be seen that compared with the rectangular wing, the bionic wing has a higher area of low pressure, and when extending to both sides of the wing tip along the wingspan, the drag decreases significantly compared with the rectangular wing.

5 Conclusion

In this paper, the bionic wing with wingspan of 3 m was designed by parameterizing the wings of wandering albatross, and the optimization variables and intervals were determined based on the statistical data of wandering albatross and the flying process, and the bionic wing was optimized by Genetic Algorithm and Vortex Lattice Method. The excellent aerodynamic performance and optimization effectiveness of the bionic wing are verified by the Vortex Lattice Method. Calculation results show that the preliminary design of the bionic wing lift coefficient is lower than the rectangular wing, and after over 4 degrees angle of attack, the drag coefficient and lift-to-drag ratio of bionic wings is better than rectangular wings. The optimization improves the lift coefficient and lift-drag ratio of the bionic wing, reduces the drag coefficient of the bionic wing, and makes the aerodynamic performance of the bionic wing better than that of the rectangular wing. Among them, when the angle of attack is 7 degrees, the lift coefficient and the drag coefficient and the lift-to-drag ratio of the bionic wing with optimization is 0.667, 0.025, and 26.768. Compared with

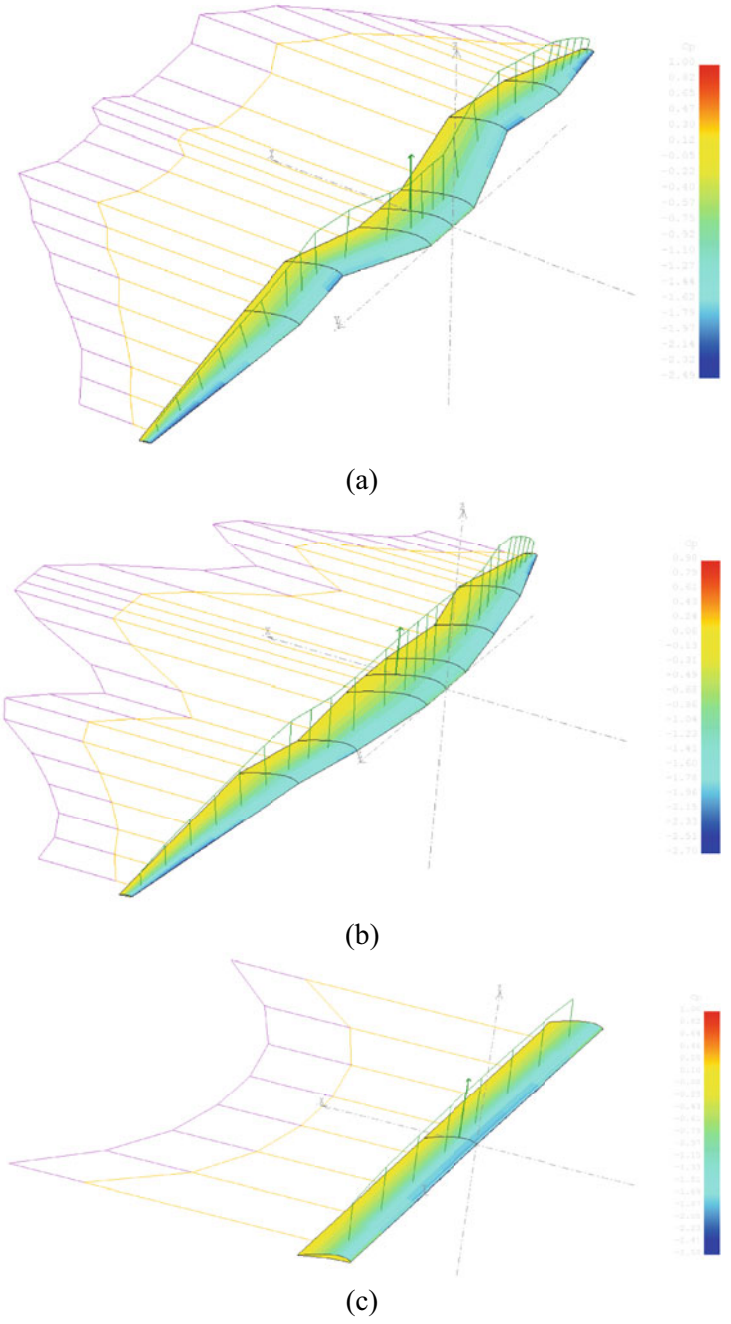

Fig. 10 The pressure, lift, viscosity and induced drag distribution of the bionic wing without optimization **a**, the bionic wing with optimization **b** and the rectangular wing **c**

the bionic wing without optimization and rectangular wing, the lift-to-drag ratio increases by 5.71% and 7.87%, respectively. Therefore, the albatross wing shape contains excellent aerodynamic performance, and the aerodynamic optimization can further improve the lift and drag characteristics of the bionic wing, which provides an important reference for the improvement of aircraft endurance performance.

Acknowledgements This work is partially supported by the Key Research and Development Program of Shaanxi (Code: No.2017ZDL-SF-14-4).

References

1. US Department of Defense: Unmanned Aircraft Systems Road Map 2005–2030 (2005), p. 51
2. Wilson JA (1975) Sweeping flight and soaring by albatrosses. Nature 257(5524):307–308
3. Rayleigh L (1883) The Soaring of Birds. Nature 27(701):534–535
4. Stempeck A, Hassanalian M, Abdelkefi A (2018) "Aerodynamic performance of albatross-inspired wing shape for marine unmanned air vehicles", In 2018 aviation technology, integration, and operations conference, p 3899
5. Zhaowei L, Zhongxi H, Juntao Z (2014) The very flexible aircrafts and albatross flight: 29th Congress of the international council of the aeronautical sciences
6. Sanchez, G, Salazar RD, Hassanalian M et al (2018) Sizing and performance analysis of albatross-inspired tilt-wing unmanned air vehicle: AIAA
7. Leaser J (2008) On the Wings of the Albatross. National Geographic
8. Jouventin P, Weimerskirch H (1990) Satellite tracking of wandering albatrosses. Nature 343(6260):746–748
9. Shaffer SA, Weimerskirch H, Costa DP (2001) Functional significance of sexual dimorphism in wandering albatrosses, diomedea exulans. Funct Ecol 15(2):203–210
10. Hassanalian M, Throneberry G, Ali M, Ben Ayed S, Abdelkefi A (2017) Role of wing color and seasonal changes in ambient temperature and solar irradiation on predicted flight efficiency of the albatross. J Therm Biol. S0306456517304175
11. Broderick M (2017) Flying like a bird: second stage feasibility. Dissertation, University of Queensland
12. Pellerito V, Hassanalian M, Sedaghat A (2019) Performance analysis of a bioinspired albatross airfoil with heated top wing surface: experimental study AIAA propulsion and energy
13. CJ, Pennycuick (1982) The flight of petrels and albatrosses (procellariiformes), observed in south georgia and its vicinity. Philosophical Transactions of the Royal Society B Biological Sciences
14. Richardson PL (2011) How do albatrosses fly around the world without flapping their wings? Prog Oceanogr 88(1–4):46–58
15. Sachs G, Traugott J, Holzapfel F (2011) Progress against the wind with dynamic soaring: results from in-flight measurements of albatrosses. Aiaa Guidance, Navigation, & Control Conference & Exhibit
16. Sachs G, Traugott J, Nesterova AP, Bonadonna F (2013) Experimental verification of dynamic soaring in albatrosses. J Exp Biol 216(22):4222–4232
17. Spear LB, Ainley DG (1997) Flight speed of seabirds in relation to wind speed and direction. Ibis 139(2):234–251
18. Richardson, Philip L (2015) Upwind dynamic soaring of albatrosses and uavs. Prog Oceanogr 130:146–156
19. Richardson PL, Wakefield ED, Phillips RA (2018) Flight speed and performance of the wandering albatross with respect to wind. Mov Ecol 6(1):3

Effect of Aspect Ratio on Wake Patterns and Thrust Characteristics of Pitching Wings

Dechuan Ma, Zhan Qiu, Gaohua Li, and Fuxin Wang

Abstract Recently, flapping wing has attracted much attention due to its potential application prospect in the design of bionic Micro Aerial Vehicles(MAVs). As one of simplified propulsors developed to understand the thrust generation mechanisms of flapping wing, the pitching wing did not raised enough concern in previous studies because of its relatively poor propulsion performance. In particular, the aspect ratio effect and its physical mechanism in thrust generation need to be further clarified. In this paper, three-dimensional numerical simulations on a rectangular wing operating in a pure pitching motion are carried out to investigate the effect of aspect ratio on the vortex structures and thrust performance. For the governing parameters considered, the results indicate that both thrust and the critical Strouhal number(St) of drag-to-thrust transition are not significantly affected by the aspect ratio until St is beyond about 0.5, after which a greater thrust can be acquired for a higher aspect ratio. It's believed that there exists a critical aspect ratio corresponding to the transition from the bifurcation wake to the deflection wake, above which the effect of aspect ratio on vortex structures can be neglected. To reveal the underlying mechanism of aspect ratio effect, a force estimation method based on finite control volume is used to establish a relationship between flow field and thrust. Three flow mechanisms are found that are responsible for the aspect ratio effect on thrust generation: for a higher aspect ratio, a more intense momentum surplus field and a more intense vorticity field are the mechanisms that generate greater thrust while a more pressure reduction

D. Ma · Z. Qiu · G. Li · F. Wang (✉)
School of Aeronautics and Astronautics, Shanghai Jiao Tong University,
No.800, Dongchuan Road, Shanghai 200240, China
e-mail: fuxinwang@sjtu.edu.cn

D. Ma
e-mail: cdma123@sjtu.edu.cn

Z. Qiu
e-mail: qiuzhan1995@sjtu.edu.cn

G. Li
e-mail: liqueen@sjtu.edu.cn

Z. Jing and X. Zhan (eds.), *Proceedings of the International Conference on Aerospace System Science and Engineering 2020*, Lecture Notes in Electrical Engineering 680,
https://doi.org/10.1007/978-981-33-6060-0_39

field is the mechanism that generates greater drag. The aspect ratio effect on thrust generation actually results from the competition of these flow mechanisms. This work is expected to improve awareness for principles of flapping-wing propulsion.

Keywords Pitching wings · Aspect ratio · Thrust characteristics · Vortex structures · Flow mechanisms

1 Introduction

Military and civilian demand for the Micro Aerial Vehicles(MAVs) has prompted researchers to pay more attention to flapping wing flight in nature [1]. Several simplified models such as pure pitching, pure plunging as well as combined pitching and plunging wings were developed in previous studies to understand the thrust generation mechanisms of flapping wings, of which the pitching wing did not raised enough concern because of its relatively poor propulsion performance comparing with the other two [2].

Most of previous work has been carried out based on two dimensional approximation. In the 1930s, Theodorsen [3] and Garrick [4] proposed a liner theory that theoretically derived an analytical solution to the mean thrust of a 2D pitching plate, which indicated the dependence of thrust performance on kinematic parameters. The numerical investigation by Das et al. [5] showed that the mean thrust was proportional to the square of Strouhal number. Senturk and Smits [6] studied the scaling law of thrust with respect to Strouhal number, Reynolds number, the pitching amplitude as well as the thickness of airfoil. Tian et al. [7] addressed that the location of pitching axis had evident effect on the thrust performance.

Different wake vortex patterns were observed by flow field visualization in both experimental and numerical investigations [8–10]. It has been widely accepted that the evolution of vortex patterns relate to the propulsion performance. Von Karman [11] indicated that the jet-like field induced by the reverse Bénard-von Kármán(rBvK) vortex street could generate thrust for a thin plate in transverse oscillations. In 1989, Koochesfahani [8] experimentally measured the wake flow field of NACA0012 pitching airfoil at $Re = 12000$ and estimated thrust from wake by momentum integral equation. He demonstrated that the momentum surplus or the jet flow caused by reverse Bénard-von Kármán vortex street produced a net thrust while the momentum deficit caused by Bénard-von Kármán(BvK) vortex street corresponded to a net drag. The numerical investigation by Deng et al. [12] suggested that there was an another wake transition line after which some three dimensional features appeared in wake of NACA0015 pitching airfoil. They believed that this 2D-3D wake transition line was the boundary of maximum propulsion efficiency. Most of later research has been conducted based on the "jet" theory although some challenges still remain for it. For example, the drag-to-thrust transition was found to lag significantly behind the transition from BvK vortex street to rBvK vortex street when the Strouhal number

increasing [13]. Ashraf et al. [14] attributed this lag phenomenon to the fact that the momentum surplus was offset by the pressure reduction caused by the airfoil motion.

In contrast, investigations on the three dimensional pitching wing are quite limited. King et al. [15] experimentally observed a vortex chain consisting of alternating linked streamwise and spanwise vortex tubes for a trapezoidal pitching plate, which experienced a spanwise compression when convecting downstream. A similar wake structure was visualized for a low-aspect-ratio pitching panel by Buchholz and Smits [16, 17], who also found that the thrust production increased with the aspect ratio increasing($AR = 0.54 \sim 2.38$). Reference [18] further indicated that this vortex chain could bifurcate into two deflected jet-like flow for large Strouhal number and the wake bifurcation point moved upstream when the Strouhal number increasing. The finite-time Lyapunov exponent field was used to performed a Lagrangian analysis for the flow field evolution of a pitching trapezoidal plate in [19], which suggested that the Lagrangian saddles released from the trailing edge were related to extreme of thrust. Some scaling laws of thrust and propulsion efficiency were proposed to evaluate the aspect ratio effect by Green and Smits [20] and Ayancik et al. [21]. Hemmati and Smits [22] indicated that the thrust production of a pitching plate with convex trailing edge was significantly affected by the Reynolds number($Re = 1000 \sim 10000$) while the wake structures not. In addition, the effect of trailing edge shape on thrust performance was also investigated [23, 24].

Although the wake structures and thrust characteristics of pitching wings have been well elucidated in previous studies, it's still an open question that how they interact with each other. In particular, the aspect ratio effect and its physical mechanism in thrust generation need to be further clarified. In this paper, three-dimensional numerical simulations on a rectangular pitching wing are conducted to investigate the effect of aspect ratio on the vortex structures and thrust performance. To reveal the underlying mechanism of aspect ratio effect, a force estimation method based on finite control volume is used to establish a relationship between flow field and thrust production. We organize this paper as follows: Sect. 2 introduces the kinematics definition, solver setting and validation, and the aerodynamics decomposition method. The results and discussions can be acquired in Sects. 3 and Sect. 4 is the conclusion.

2 Numerical Methods

2.1 Kinematics Definition

We consider a rectangular wing with NACA0012 profile operating in a simple harmonic pitching motion around its quarter chord defined as

$$\alpha = \alpha_0 \sin(2\pi f t) \tag{1}$$

where α_0 is the pitching amplitude and f is the pitching frequency. There are some important nondimensional parameters which dominate the propulsion performance and the wake dynamics of the flapping wings such as the nondimensional amplitude (A_D), Strouhal number (St), Reynolds number (Re) and the aspect ratio (AR). The nondimensional amplitude and the Strouhal number are formulated as follows

$$A_D = A/D = 1.5c\sin(\alpha_0)/D \quad \text{and} \quad St = fA/U_\infty \tag{2}$$

in which c and D are the chord length and maximum thickness of airfoil; U_∞ is the freestream speed; A is the peak-to-peak amplitude of trailing edge.

In this paper, Re = 1000 is specified as the Reynolds number effect on thrust production is small when Re is beyond 1000 [5]. The aspect ratio is chosen to be 2,4 and 6 covering the low, medium and high aspect ratios of insects [25], and an infinite aspect ratio (2D) is also considered for comparison. For each aspect ratio, the pitching frequency varies between 1 and 5 Hz while the pitching amplitude is fixed at 10deg, which correspond to a Strouhal number range of $St = 0.178 \sim 0.892$ and a single nondimensional amplitude of $A_D = 2.17$. These nondimensional parameters are determined within typical kinematics of flapping flight in nature.

2.2 Solver Setting and Validation

The computational domain is a cylinder zone as shown in Fig. 1, whose radius and height are 50c and 100c, respectively. The pitching wing lies in the center of the cylinder and its pitching axis coincides with the axis of the cylinder. The O-type grid is adopted to discrete the flow domain. To improve the grid resolution for capturing the wake structures, the flow domain is divided into two blocks by an interior surface which is 5c away from the wing surface. The inner block has $301 \times N \times 121$ ($N = 121 \sim 281$ for each AR) nodes in circular, spanwise and radical direction,

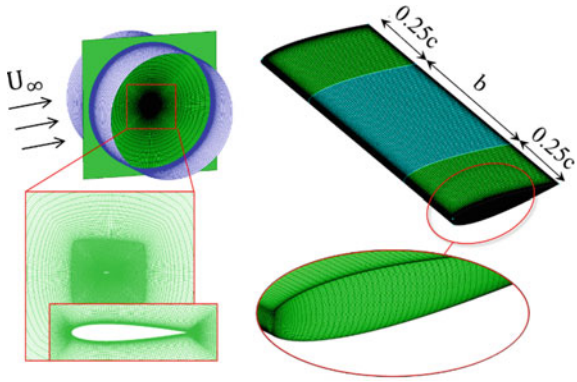

Fig. 1 Computational model and grids

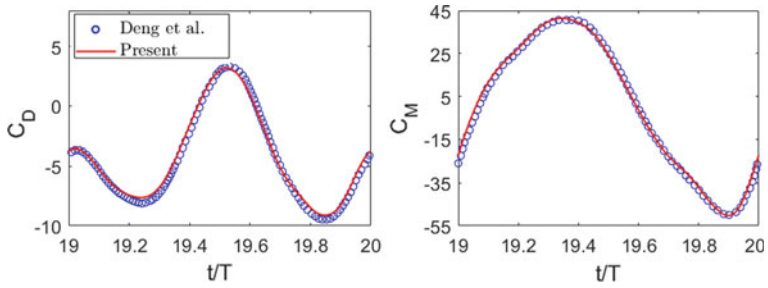

Fig. 2 Comparison with literature

respectively. The radial grid growth rate of the block is 1.1, and the thickness of first layer grids is 0.001c which satisfies that the y^+ value is less than one. The grids on the wing surface are arranged such that the outboard wing (0.25c) has more refined grids close to the wingtip while the inboard wing (b) has uniform grids (Fig. 1) .The outer block is a coarse grid region with a large grid growth rate in radical direction. The total grid number of the two blocks increases from 8 million to 16 million with the aspect ratio increasing.

The incompressible Navier-Stokes equations are numerically solved using the pressure based solver of fluent 17.2. We choose the laminar model as the Reyn-olds number is small (Re = 1000). For the boundary conditions, the no-slip wall and the constant velocity inlet ($U_\infty = 0.146$) are applied on the wing and the far field, respectively; the circle planes of the cylinder are set as symmetry boundary. The whole flow domain undergoes the same rigid motion as the pitching wing which is specified by the user defined function (UDF) file. The pressure-velocity coupled scheme is selected as SIMPLEC algorithm. There are 360 time steps with 25 inner iterations per pitching cycle. To obtain the convergent solutions, the computation is performed until the relative error of the cycle average thrust coefficient is less than 0.5% in consecutive pitching cycles.

We conduct a validation for the solver setting in the 2D case because it's not easy to obtain 3D aerodynamic data for comparison from references. Figure 2 compares aerodynamic forces of NACA0015 pitching airfoil at Re = 1700 ($A_D = 2$, $St = 0.5$) with results of Deng et al. [12] by CFD. It's shown that both drag and moment coefficients agree well with those of Deng et al.

2.3 Aerodynamics Decomposition Method

For incompressible viscous flow, according to Newton's second law, the aerodynamics acting on the pitching wing is

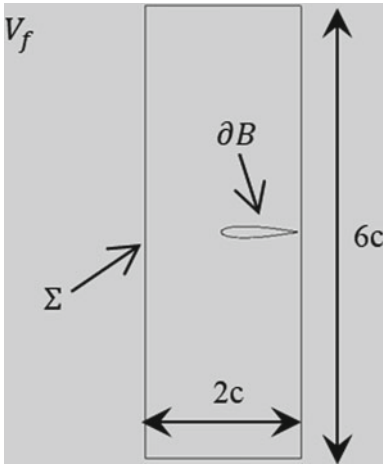

Fig. 3 Schematic diagram of control volume

$$\boldsymbol{F} = -\oiint_{\partial B}(-p\boldsymbol{n} + \boldsymbol{\tau})dS \tag{3}$$

$$= -\rho \iiint_{V_f} \boldsymbol{a}dV + \oiint_{\Sigma}(-p\boldsymbol{n} + \boldsymbol{\tau})dS \tag{4}$$

in which p, $\boldsymbol{\tau}$ and ρ are static pressure, shear stress and fluid density; $\boldsymbol{a} = d\boldsymbol{u}/dt$ is the fluid acceleration, $\boldsymbol{u}$ is the fluid velocity; V_f is the finite control volume surrounding the wing whose inner boundary is the wing surface ∂B and outer boundary is Σ; $\boldsymbol{n}$ is the unit normal vector (Fig. 3). Equation (3) is a commonly used method for directly integrating aerodynamics on the wing surface. In contrast, Eq. (4) is an indirect one which evaluates aerodynamics based on the flow field around the wing and thus could be helpful for analyzing the flow mechanism behind aerodynamics generation.

From Eq. (4), Wang et al. [26] further derived that

$$\begin{aligned}\boldsymbol{F} = &\underbrace{\rho \iiint_{V_f} \boldsymbol{u} \times \boldsymbol{\omega} dV}_{\text{(1)vortex force(V)}} \underbrace{-\rho \iiint_{V_f} \frac{\partial \boldsymbol{u}}{\partial t} dV}_{\text{(2)local fluid acceleration(A)}} \underbrace{-\oiint_{\partial B}(\rho|\boldsymbol{u}|^2/2)\boldsymbol{n}dS}_{\text{(3)virtual fluid occupied by wing(B)}} \\ &\underbrace{-\oiint_{\Sigma}(\rho|\boldsymbol{u}|^2/2)\boldsymbol{n}dS}_{\text{(4)momentum induced(M)}} \underbrace{-\oiint_{\Sigma} p\boldsymbol{n}dS}_{\text{(5)pressure induced(P)}} + \underbrace{\oiint_{\Sigma}\boldsymbol{\tau}dS}_{\text{(6)shear stress(S)}}\end{aligned} \tag{5}$$

where $\boldsymbol{\omega}$ is the vorticity. The first term in Eq. (5) is vortex force; the second and third terms are the contributions of the local fluid acceleration caused by the unsteady inertial effect of wing motion and the virtual fluid occupied by the wing to the aerodynamics and the sum of them is called added mass force; the last three terms

are momentum induced, pressure induced and friction forces acting on the outer surface of the control volume. The shear stress on outer surface is usually small and thus the last term is neglected in present paper. The initial letters are used to represent these terms as shown in Eq. (5), for example, "V" represents vortex force.

3 Results and Discussion

3.1 *Effect of Aspect Ratio on Vortex Structures and Thrust*

Figure 4 compares the thrust coefficients for various aspect ratios. For a given Strouhal number, there are two greater peak values in time history curve of thrust coefficient for a higher aspect ratio as shown in Fig. 4a–c. Figure 4d indicates that both the cycle average thrust coefficient and the critical Strouhal number corre-sponding to the drag-to-thrust transition are not nearly influenced by the aspect ratio until St is beyond

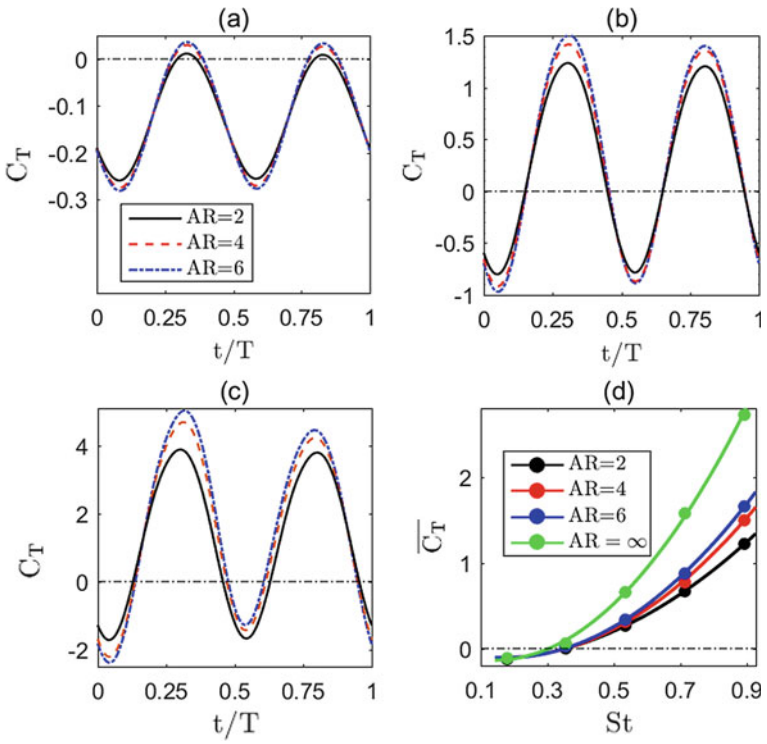

Fig. 4 Thrust coefficients for various aspect ratios: time history of thrust coefficients at **a** $St = 0.178$, **b** $St = 0.535$ and **c** $St = 0.892$; **d** cycle average thrust coefficients

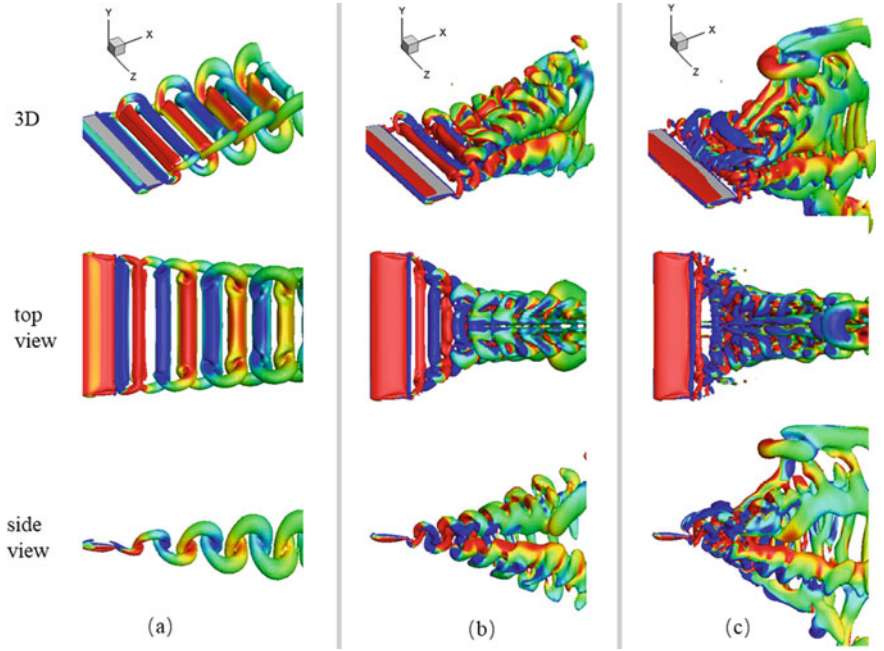

Fig. 5 Vortex structures colored by spanwise vorticity for AR = 4 ($Q = 0.1$): **a** $St = 0.178$; **b** $St = 0.535$; **c** $St = 0.892$

above 0.5, after which a greater thrust can be obtained for a higher aspect ratio. In particular, the cycle average thrust coefficient of two dimensional pitching airfoil ($AR = \infty$) is significantly greater than the finite-span wing, which demonstrates that the two dimensional simplification could overestimate the thrust of pitching wings.

The wake vortex structures for medium aspect ratio ($AR = 4$) are visualized based on Q-criterion as shown in Fig. 5. There is a vortex ring shedding from trailing edge per pitching cycle which evolves into some complex vortex structures when moving downstream. When St is small, the vortex rings shedding in several consecutive pitching cycles are connected by wingtip vortex tubes and form a vortex chain whose side view looks like the Bénard-von Kármán vortex street (Fig. 5a). The spanwise length of the vortex chain gradually decreases in streamwise direction, which is called spanwise compression or shrinkage phenomenon as observed by King et al. [15]. When St increases, the spanwise vortex tubes become closer with each other, which strengthens their interaction (Fig. 5b). It's difficult to find a complete vortex ring because the skeletons of the vortex chain are very dense. The side view shows that the vortex chain splits into two branches in transverse direction, one extends upwards and the other downwards. This phenomenon is called the wake bifurcation which can be described by the bifurcation angle defined as the angle between these two branches. The spanwise shrinkage of the vortex chain becomes severe. For a larger

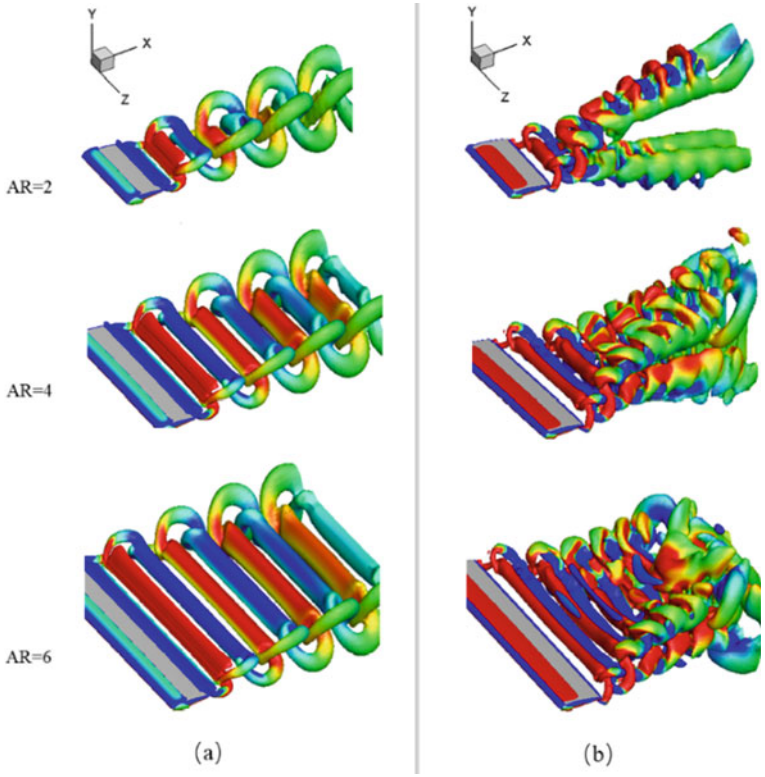

Fig. 6 Vortex structures colored by spanwise vorticity for various aspect ratios ($Q = 0.1$): **a** $St = 0.178$; **b** $St = 0.535$

St, it's even impossible to distinguish vortex rings with each other (Fig. 5c). The bifurcation angle increases, which indicates that the degree of the wake bifurcation is enhanced.

Figure 6 illustrates the aspect ratio effect on vortex structures. The vortex chains look similar except that the spanwise length is greater for a higher aspect ratio when St is small (Fig. 6a). When St increases, the aspect ratio effect is evident. Specifically, the bifurcation angle decreases and the wake bifurcation becomes insignificant as the upward branch tends to disappear when the aspect ratio increasing (Fig. 6b). The leaving downward branch of the vortex chain looks like the wake deflection phenomenon seen in two dimensional pitching airfoil. Therefore, we believe that there exist a critical aspect ratio corresponding to the transition from bifurcation wake to the deflection wake, above which the effect of aspect ratio on wake vortex structures for pitching wings can be neglected.

3.2 *Thrust Evaluation Based on Finite Control Volume*

As discussed in Sect. 3.1, the flow field induced by pitching wing motion is complex and it's not convenient to reveal the underlying flow mechanism behind aspect ratio effect on thrust production. Therefore, we turn our eyes to the cross sections of pitching wings. Figure 7 compares the cycle average thrust coefficients at midspan and wingtip sections. It's indicated that the difference of thrust coefficients with respect to Strouhal number for various aspect ratio is evident at midspan (Fig. 7a). However, the thrust coefficients are not nearly affected by aspect ratio and their biggest difference is less than 0.05 at wingtip (Fig. 7b). Therefore, we only consider the midspan section in following discussion. Figure 7b also shows that the wingtip produces negative thrust and thus is a big source of drag production. The drag production increases rapidly with the increasing of St, which explains why the two dimensional pitching airfoil has a more outstanding thrust performance comparing with the pitching wing for large St as shown in Fig. 4d.

To relate the thrust generation with the flow field past pitching wing, the force decomposition method based on finite control volume introduced in Sect. 2.3 is adopted for midspan section. The control volume chosen is shown in Fig. 3. A uniform grid with 100 nodes per chord is used for interpolation and integration. The integral rough data is fitted using polynomial fitting method to reduce the numerical error. Figure 8 shows that the integral thrust coefficients (Eq. (5)) agree well with the results by CFD although there are some differences in the peak values of time-varying thrust coefficient and the cycle average thrust coefficient for large St.

Figure 9 gives the components of thrust coefficient at midspan for medium aspect ratio (AR $= 4$), in which $\overline{C_T^{(V)}}$, $\overline{C_T^{(M)}}$ and $\overline{C_T^{(P)}}$ represent the vortex thrust coefficient, the momentum induced thrust coefficient and the pressure induced thrust coefficient, respectively; $\overline{C_T^{(A)}}$ ($C_T^{(A)}$) and $\overline{C_T^{(B)}}$ ($C_T^{(B)}$) are the contributions of the local fluid acceleration caused by the unsteady inertial effect of wing motion and the virtual fluid occupied by the wing to thrust coefficient, respectively. Note a minus sign is added

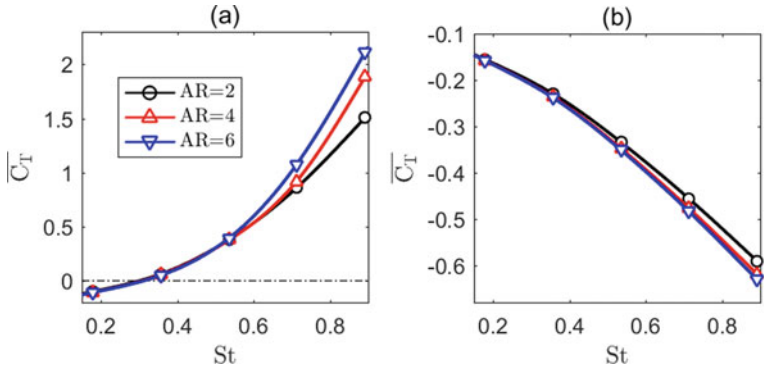

Fig. 7 Cycle average thrust coefficients for different cross sections: **a** midspan; **b** wingtip

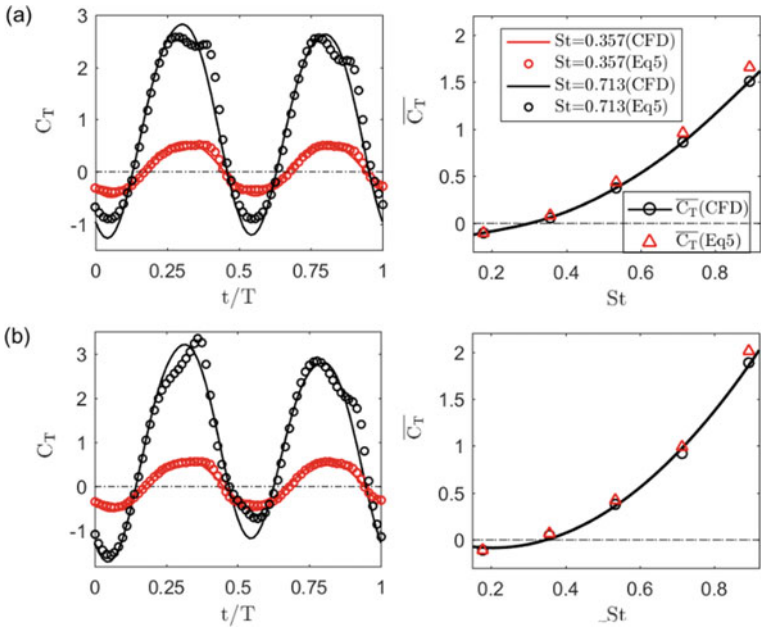

Fig. 8 Comparison of thrust coefficients by CFD with results from integration based on finite control volume at midspan: **a** AR = 2; **b** AR = 4

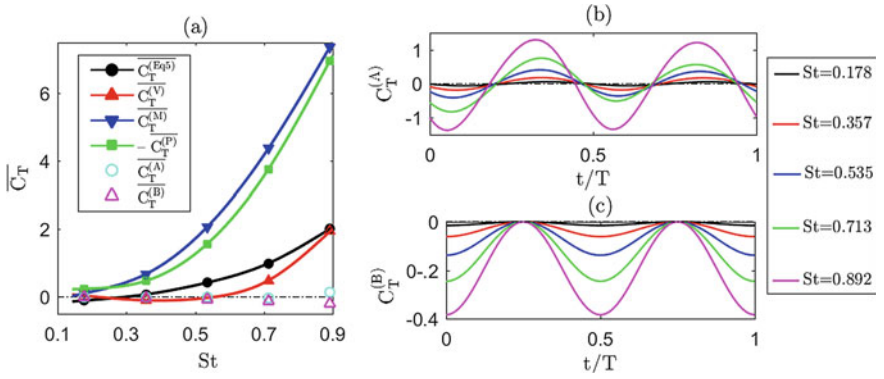

Fig. 9 Components of thrust coefficients at midspan for AR = 4: **a** cycle average thrust coefficients; **b** contribution of local fluid acceleration to thrust; **c** contribution of virtual fluid occupied by wing to thrust

to the pressure induced thrust in Fig. 9a. It's shown that the contribution of local fluid acceleration to the cycle average thrust coefficients ($\overline{C_T^{(A)}}$) is very small and can be neglected (Fig. 9a). For the reasons, the upward and the downward motions of the pitching wing are symmetrical which produce a symmetrical inertial force in Fig. 9b.

The virtual fluid occupied by the wing produces a small drag ($-\overline{C_{\mathrm{T}}^{(\mathrm{B})}}$) as shown in Fig. 9a,c because the airfoil volume itself is very small comparing with the control volume as shown in Fig. 3. Therefore, the dominant terms are vortex thrust ($\overline{C_{\mathrm{T}}^{(\mathrm{V})}}$), momentum induced thrust($\overline{C_{\mathrm{T}}^{(\mathrm{M})}}$) and pressure induced thrust ($\overline{C_{\mathrm{T}}^{(\mathrm{P})}}$).

3.3 *Flow Mechanisms of Aspect Ratio Effect*

For the rectangular control volume as shown in Fig. 3, the momentum induced thrust and the pressure induced thrust can be derived from Eq. (5)

$$\boldsymbol{T}_M = \frac{\rho}{2}\iint_{S_R}(|\boldsymbol{u}_R|^2 - |\boldsymbol{u}_L|^2)dS_R \quad \text{and} \quad \boldsymbol{T}_P = \iint_{S_R}(p_R - p_L)dS_R \tag{6}$$

where the subscripts "L" and "R" represent the left and right boundaries of the control volume. Equation 6 indicates that a net momentum induced thrust and a net pressure induced thrust can be obtained only if a momentum surplus field ($|\boldsymbol{u}_R| > |\boldsymbol{u}_L|$) and a pressure surplus field ($p_R > p_L$) exist. This condition is actually not true for flapping wings. Generally, for a two dimensional pitching airfoil, a BvK vortex street and a rBvK vortex street will induce a momentum deficit field and a momentum surplus field, respectively [8]; there is always a reduction in pressure due to the airfoil motion [14]. Therefore, a pressure induced drag can be always obtained while a momentum induced drag or thrust can be produced depending on the wake patterns.

From discussion in Sect. 3.2, there are only three dominant terms that determine most of thrust, which are compared for various aspect ratios in Fig. 10 and the corresponding vorticity field are given in Fig. 11. As illustrated in Fig. 10b,c, the momentum induced thrust ($\overline{C_{\mathrm{T}}^{(\mathrm{M})}}$) is positive while the pressure induced thrust ($\overline{C_{\mathrm{T}}^{(\mathrm{P})}}$) is negative for different aspect ratios except for $St = 0.178$. Figure 11 shows that when $St = 0.178$, a similar neutral wake (transition from the BvK vortex street to the reverse one) appears in which the vortices are nearly in line, which induces a small momentum deficit field. For other cases, the main characteristics of the reverse BvK vortex street always remains although some complex wake patterns appear for large St such as the bifurcation wake and the deflection wake. Thus a momentum surplus field is formed except for $St = 0.178$, which is responsible for a positive momentum induced thrust ($\overline{C_{\mathrm{T}}^{(\mathrm{M})}}$) generated. A pressure induced drag ($-\overline{C_{\mathrm{T}}^{(\mathrm{P})}}$) is produced due to the pressure reduction caused by the wing motion. As shown in Figs. 10a and 11, a net vortex thrust ($\overline{C_{\mathrm{T}}^{(\mathrm{V})}}$) can be obtained only if the strength of vortex is high enough after the bifurcation wake and the deflection wake appear.

To reveal the aspect ratio effect, we directly compare the thrust components corresponding to the three dominant terms. The momentum field and the pressure field are not shown here because the trend of these fields with respect to aspect ratio is the same as that of thrust produced by them as described by Eq. (6). For a given St,

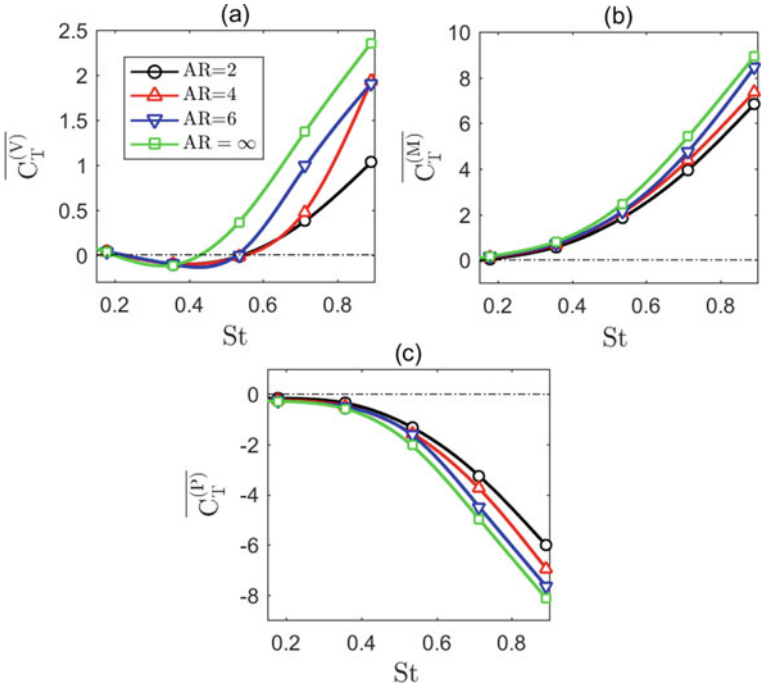

Fig. 10 Effect of aspect ratio on components of cycle average thrust coefficients: **a** vortex thrust; **b** momentum induced thrust; **c** pressure induced thrust

it's shown that both the momentum induced thrust ($\overline{C_{\mathrm{T}}^{(\mathrm{M})}}$) and the pressure induced drag ($-\overline{C_{\mathrm{T}}^{(\mathrm{P})}}$) increase with the aspect ratio increasing, which means a more intense momentum surplus field and a more severe pressure deficit field appear meanwhile. Thus, the more intense momentum surplus and the more pressure reduction in flow field are some of the flow mechanisms which are responsible for the aspect ratio effect on thrust production. In addition, a greater vortex thrust ($\overline{C_{\mathrm{T}}^{(\mathrm{V})}}$) can be obtained for a higher aspect ratio as shown in Fig. 10a. For the reasons, it can be seen in Fig. 11 that there is a weaker vortex interaction which causes less vorticity dissipation in deflection wake comparing with the bifurcation wake for a given St. It's evident that it exists a transition from bifurcation wake to deflection wake for large St when the aspect ratio increases as also discussed in Sect. 3.1. Therefore, a more intense vorticity field is formed for a higher aspect ratio which generates a large vortex force.

From the discussion above, we conclude that a more intense momentum surplus field and a more intense vorticity field are the source of greater thrust while a more pressure reduction field is the source of greater drag for a higher aspect ratio. The effect of the aspect ratio on thrust generation is actually the result of competition of the three flow mechanisms. When comparing Fig. 10b,c, we can find that the momentum induced thrust ($\overline{C_{\mathrm{T}}^{(\mathrm{M})}}$) is close to the pressure induced drag ($-\overline{C_{\mathrm{T}}^{(\mathrm{P})}}$) in

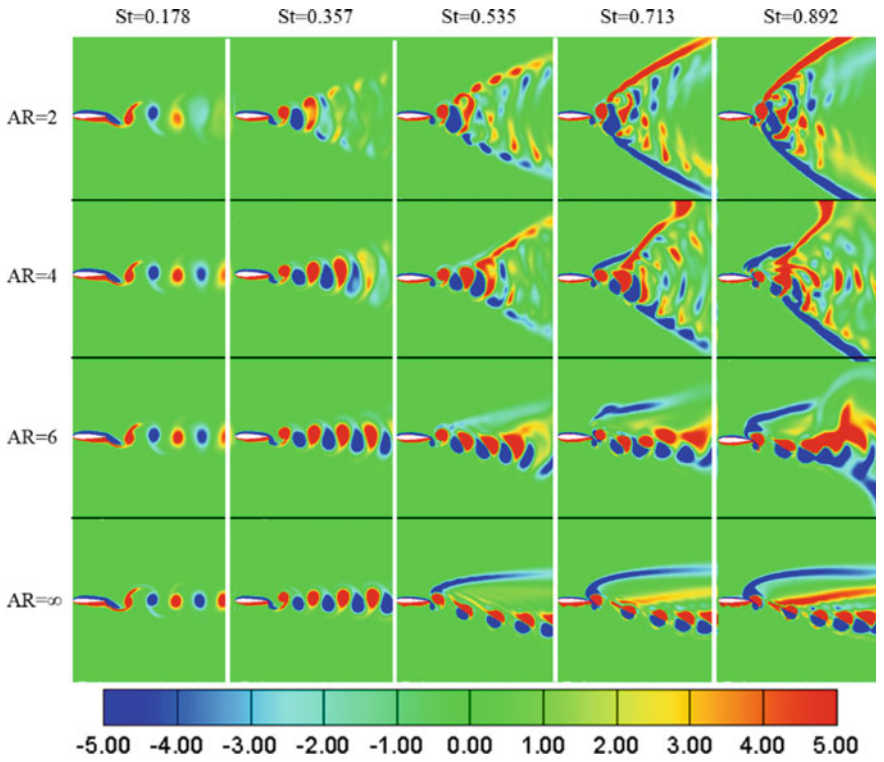

Fig. 11 Contour of spanwise vorticity at midspan

magnitude and they tend to cancel with each other, which means that the vortex thrust ($\overline{C_{\mathrm{T}}^{(\mathrm{V})}}$) determines most of net thrust especially for a large St.

4 Conclusion

This paper numerically investigates the effect of aspect ratio on thrust production and wake vortex structures. A force decomposition method based on finite control volume is used to reveal the flow mechanisms behind the aspect ratio effect. The results are as follows:

(1) For the governing parameters considered, it's shown that both thrust and the critical Strouhal number (St) corresponding to drag-to-thrust transition are not sensitive to the aspect ratio until St is beyond about 0.5, after which a greater thrust can be obtained for a higher aspect ratio.
(2) The bifurcation wake is a special wake pattern for a low-aspect-ratio pitching wing, which gradually evolves into the deflection wake seen in two dimensional

pitching airfoil when the aspect ratio increasing. It's believed that a critical aspect ratio corresponding to the wake transition exists, above which the effect of aspect ratio on vortex structures can be neglected.

(3) Three flow mechanisms are found that are responsible for the aspect ratio effect on thrust generation: for a higher aspect ratio, a more intense momentum surplus field and a more intense vorticity field are the mechanisms that generate greater thrust while a more pressure reduction field is the mechanism that gener-ates greater drag. In fact, the aspect ratio effect on thrust production is the result of competition of these mechanisms.

(4) For a large St, the vortex thrust determines most of net thrust because the momentum induced thrust and the pressure induced drag are close in magnitude and tend to cancel with each other.

It should be noted that the parameter space is limited in this work. It's necessary to examine if these flow mechanisms work for a greater parameter space especially when concerning the effect of Reynolds number, the pitching amplitude as well as the pitching axis, which will be the subject of future study.

References

1. Shi X, Huang X, Zheng Y et al (2016) Effects of cambers on gliding and hovering performance of corrugated dragonfly airfoils. Int J Numer Methods Heat Fluid Flow 26(3/4):1092–1120
2. Rahromostaqim M, Posa A, Balaras E (2016) Numerical investigation of the performance of pitching airfoils at high amplitudes. AIAA J 1–12
3. Theodorsen T (1934) General theory of aerodynamic instability and the mechanism of flutter. NACA Tech Rep 496:413–433
4. Garrick IE (1936) Propulsion of a flapping and oscillating airfoil. Rep Nat Adv Committee Aeronaut NACA Rep 567:419–427
5. Das A, Shukla RK, Govardhan RN (2016) Existence of a sharp transition in the peak propulsive efficiency of a low-Re pitching foil. J Fluid Mech 800:307–326
6. Senturk U, Smits AJ (2019) Reynolds number scaling of the propulsive performance of a pitching airfoil. AIAA J 57(7):1–7
7. Tian W, Bodling A, Liu H et al (2016) An experimental study of the effects of pitch-pivot-point location on the propulsion performance of a pitching airfoil. J Fluids Struct 60:130–142
8. Koochesfahani MM (1989) Vortical patterns in the wake of an oscillating airfoil. AIAA J 27(9):1200–1205
9. Schnipper T, Andersen A, Bohr T (2009) Vortex wakes of a flapping foil. J Fluid Mech 633:411–423
10. Andersen A, Bohr T, Schnipper T et al (2017) Wake structure and thrust generation of a flapping foil in two-dimensional flow. J Fluid Mech 812:R4
11. Von Karman T (1935) General aerodynamic theory-perfect fluids. Aerodynam Theor 2:346–349
12. Deng J, Sun L, Teng L et al (2016) The correlation between wake transition and propulsive efficiency of a flapping foil: a numerical study. Phys Fluids 28(9):094101
13. Godoy-Diana R, Aider JL, Wesfreid JE (2008) Transitions in the wake of a flapping foil. Phys Rev E 77(1):016308
14. Ashraf I, Agrawal A, Khan MH et al (2015) Thrust generation and wake structure for flow across a pitching airfoil at low Reynolds number. Sadhana 40(8):2367–2379

15. King JT, Kumar R, Green MA (2016) Experimental study of the three-dimensional wake of a trapezoidal pitching panel. In: 54th AIAA aerospace sciences meeting, pp 0829
16. Buchholz JHJ, Smits AJ (2006) On the evolution of the wake structure produced by a low-aspect-ratio pitching panel. J Fluid Mech 546:433–443
17. Buchholz JHJ, Smits AJ (2008) The wake structure and thrust performance of a rigid low-aspect-ratio pitching panel. J Fluid Mech 603:331–365
18. Green MA, Rowley CW, Smits AJ (2011) The unsteady three-dimensional wake produced by a trapezoidal pitching panel. J Fluid Mech 685:117–145
19. Kumar R, King JT, Green MA (2018) Three-dimensional pitching panel wake: Lagrangian analysis and momentum distribution from experiments. AIAA J 1–15
20. Green MA, Smits AJ (2008) Effects of three-dimensionality on thrust production by a pitching panel. J Fluid Mech 615:211–220
21. Ayancik F, Zhong Q, Quinn DB et al (2019) Scaling laws for the propulsive performance of three-dimensional pitching propulsors. J Fluid Mech 871:1117–1138
22. Hemmati A, Smits AJ (2019) Reynolds number effects on the wake structure of pitching convex panels. AIAA J 58(3):1–5
23. Van Buren T, Floryan D, Brunner D et al (2017) Impact of trailing edge shape on the wake and propulsive performance of pitching panels. Phys Rev Fluids 2(1):014702
24. Hemmati A, Van Buren T, Smits AJ (2019) Effects of trailing edge shape on vortex formation by pitching panels of small aspect ratio. Phys Rev Fluids 4(3):033101
25. Mao S, Gang DU (2003) Lift and power requirements of hovering insect flight. Acta Mechanica Sinica 19(5):458–469
26. Wang S, Zhang X, He G et al (2013) A lift formula applied to low-Reynolds-number unsteady flows. Phys Fluids 25(9):093605

Research on Negative Turbulent Kinetic Energy Production in Supersonic Channel Flow

Hang Zhou and Fang Chen

Abstract The anomaly of the energy reverse transmission process makes the turbulent kinetic energy production term in the turbulent kinetic energy transport equation negative. The negative production of turbulent kinetic energy (NPTKE) will affect the redistribution of energy in the flow field, and the conventional gradient assumption is not applicable in many flow situations. In this paper, the Reynolds stress turbulence model is used to solve the two-dimensional compressible turbulent kinetic energy transport equation. The commercial software Fluent v19.1 is utilized to numerically simulate the supersonic channel flow with the effect of shock waves. The results indicate that the Reynolds stress model considering flow anisotropy can characterize the NPTKE. The inherent properties of the mean strain rate tensor influence the turbulent kinetic energy production, and the NPTKE is dominated by the stretching factors. The compression caused by the shock wave leads to a constant positive turbulent kinetic energy production at the position, and the local maximum value is approximately obtained.

Keywords Negative production of turbulent kinetic energy · Shock wave · Channel flow

Nomenclature

Π	Turbulent kinetic energy production
u''	Fluctuating velocity of x-direction
v''	Fluctuating velocity of y-direction
w''	Fluctuating velocity of z-direction
U	Velocity component of x-direction

H. Zhou · F. Chen (✉)
Shanghai Jiao Tong University, Shanghai, China
e-mail: fangchen@sjtu.edu.cn

H. Zhou
e-mail: zhou_hang@sjtu.edu.cn

Z. Jing and X. Zhan (eds.), *Proceedings of the International Conference on Aerospace System Science and Engineering 2020*, Lecture Notes in Electrical Engineering 680,
https://doi.org/10.1007/978-981-33-6060-0_40

V	Velocity component of y-direction
W	Velocity component of z-direction
Π_i, Π_{Λ_i}	Component of TKE production
Λ_i^S	Eigenvalue of mean strain rate matrix
$\boldsymbol{\lambda}_{\boldsymbol{i}}^{\boldsymbol{S}}$	Eigenvector of mean strain rate matrix
ρ	Density
$\boldsymbol{S_{ij}}$	Mean strain rate matrix
p''	Fluctuating pressure
δ	Dirac delta function
μ	Viscosity coefficient
φ	The pressure strain term
D	The diffusion term
ε	The dissipation term
S	The source term

1 Introduction

Turbulent kinetic energy production [1] is an important energy source for maintaining turbulent motion, which is closely related to the scalar flux and scalar gradient [2]. The compressible turbulent kinetic energy transport equation [3] describes the mechanical energy transmission behaviour incompressible flows, and one of those terms on the right side of the equal sign is the turbulent kinetic energy production term [4]. The turbulent kinetic energy production term means that the energy is transferred from the mean flow to the turbulence, and its value in the control volume is always positive, but it turns to negative at partial fluid microelements in the fields. This abnormal phenomenon 'energy reversal' was first discovered in a fully developed curved channel flow [5]. This is contrary to the traditional energy cascade theory [6]. The opposite Reynolds stress and shear stress in the flow field results in the emergence of an NTPKE area [7].

The studies found that the asymmetry of the flow field leads to energy imbalance, and there is a greater probability of the NPTKE at rough walls and high turbulence levels [8]. Moreover, local flow field characteristics are also one of the influencing factors, the compressing of material elements causes the positive value, and contrarily the stretching causes the negative [9]. Besides, buoyancy enhances the anisotropy of the flow and promotes the NPTKE [10]. Furthermore, the phenomenon exists not only in curved channels but also in separating and reattaching flow [11], wake flow [12], and Rayleigh-Bénard convection [13].

The researches usually conducted in incompressible low Reynolds number fluid [14] in consideration of the high demands of the equipment and operating difficulties. However, the gas compressibility [15] should not be ignored under actual flight

conditions. The present paper focuses on the variation law of the NPTKE in supersonic situations [16]. The purpose is to discuss the effect of shock waves and inlet parameters on the NPTKE by the commercial software Fluent v19.1 solver.

2 Methodology

2.1 Turbulent Kinetic Energy Production Term

Π represents turbulent kinetic energy production term in two-dimensional transport equation of compressible turbulent kinetic energy, the concrete expression is (1).

$$\begin{aligned}\Pi = &-\overline{\rho}\widetilde{(u''u'')}\frac{\partial \overline{U}}{\partial x} - \overline{\rho}\widetilde{(u''v'')}\frac{\partial \overline{U}}{\partial y} \\ &- \overline{\rho}\widetilde{(u''v'')}\frac{\partial \overline{V}}{\partial x} - \overline{\rho}\widetilde{(v''v'')}\frac{\partial \overline{V}}{\partial y} = \Pi_1 + \Pi_2 + \Pi_3 + \Pi_4\end{aligned} \tag{1}$$

The other form depends on the mean strain rate contribution can be written as follows (2). In general, $\Lambda_1^S > \Lambda_2^S$ is prescribed.

$$\begin{aligned}\Pi &= -\rho u''v''\boldsymbol{S}_{ij} \doteq -\overline{\rho}\widetilde{u''v''}\left[\frac{1}{2}\left(\frac{\partial \overline{U}}{\partial y} + \frac{\partial \overline{V}}{\partial x}\right)\right] \\ &= \underbrace{-\overline{\rho}\Lambda_1^S\overline{u''^2\cos^2\left(\boldsymbol{u}'', \boldsymbol{\lambda}_1^S\right)}}_{\Pi_{\Lambda_1}} \underbrace{-\overline{\rho}\Lambda_2^S\overline{u''^2\cos^2\left(\boldsymbol{u}'', \boldsymbol{\lambda}_2^S\right)}}_{\Pi_{\Lambda_2}}\end{aligned} \tag{2}$$

2.2 Turbulence Model

In this problem, the Reynolds Stress Model (RSM) [17] is used to solve the simplified two-dimensional Reynolds-averaged momentum transport equation for numerical calculation. The modeling process of RSM embodies the anisotropic effect of turbulence [18]. It has stronger modeling ability than the equations of one and two equations and has the potential for higher accuracy prediction of complex flows. The Reynolds-averaged momentum transport equation is shown in Eq. (3),

$$\frac{\partial \rho\overline{u''v''}}{\partial t} + \frac{\partial \rho W\overline{u''v''}}{\partial z} = -\rho\left(\overline{u''w''}\frac{\partial V}{\partial z} + \overline{v''w''}\frac{\partial U}{\partial z}\right) + \overline{p''\left(\frac{\partial u''}{\partial y} + \frac{\partial v''}{\partial x}\right)}$$

$$-\frac{\partial\left[\rho\overline{u''v''w''}+\overline{p'\left(\delta_{kj}u''+\delta_{ik}v''\right)}+\mu\frac{\partial\overline{u''v''}}{\partial z}\right]}{\partial z}$$
$$-2\mu\overline{\frac{\partial u''}{\partial z}\frac{\partial v''}{\partial z}}+Source=\Pi_{ij}+\varphi_{ij}+D_{ij}+\varepsilon_{ij}+S \tag{3}$$

2.3 *Baseline Geometry*

Based on the three-dimensional channel flow model with an airfoil [19], the length of the test section in the physical model is 530 mm, the height is 25 mm, and the 9 mm airfoil is placed on the lower wall surface at 330 mm from the entrance, the specific geometric parameters are shown in Fig. 1, The total pressure of the free stream is 150 kPa, the total temperature is 300 K, and the Mach number is 4 at the standard working condition, according to the experimental standard of the hypersonic wind tunnel laboratory of Shanghai Jiaotong University [20].

3 Numerical Validation

Numerical simulation of the 24° compression corner flow with similar physical properties is performed. Comparing the calculation results with the experimental data [21] and the DNS results [22]. Figure 2 is the experimental and calculated results of the pressure coefficient of the lower wall surface and the velocity profile 4δ downstream of the corner, respectively, in which δ is the boundary layer thickness. It can be seen that the calculation results of the four turbulence models SA, k-ε, SST, and RSM can reflect the changing trend of the flow field parameters, but the calculation results of RSM are in best agreement with the experimental data and DNS results. The error of the calculation results of other turbulence models in the separation and reattachment

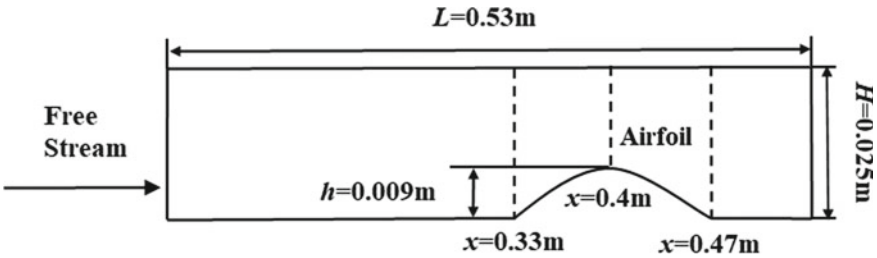

Fig. 1 Geometric parameters of calculation model

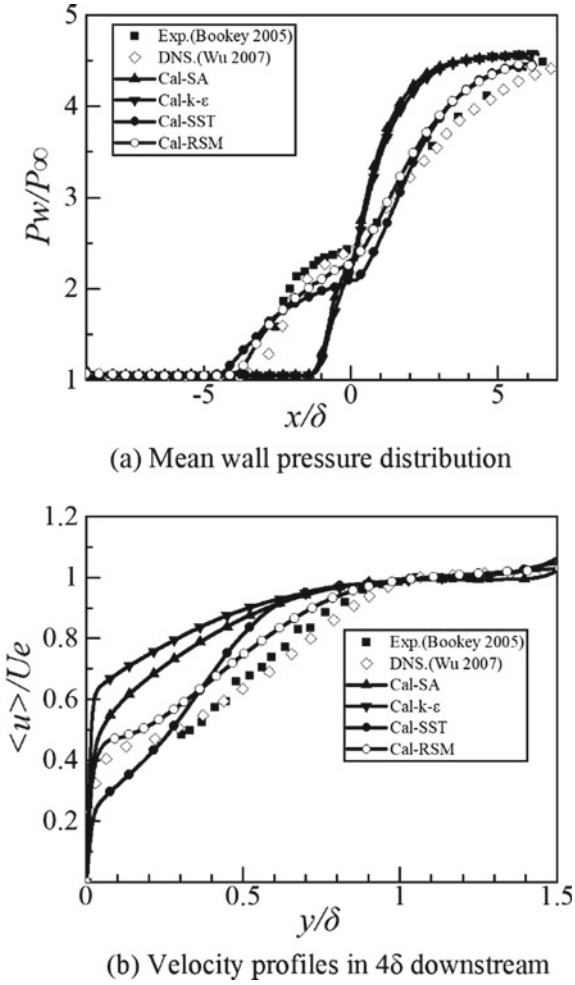

Fig. 2 The comparison of experimental data, DNS data and calculation results

area is slightly larger, indicating that RSM has higher accuracy for the calculation of shock wave area, so the selection of RSM is correct and reliable.

Meanwhile, the grid-independent validation is performed for the calculation examples with grid numbers of 50,000, 150,000, and 300,000, respectively. Figure 3 shows a 50,000-node grid differ greatly from those of the other two numbers of grids, and the grid with 150,000 nodes can meet the requirements of grid independence.

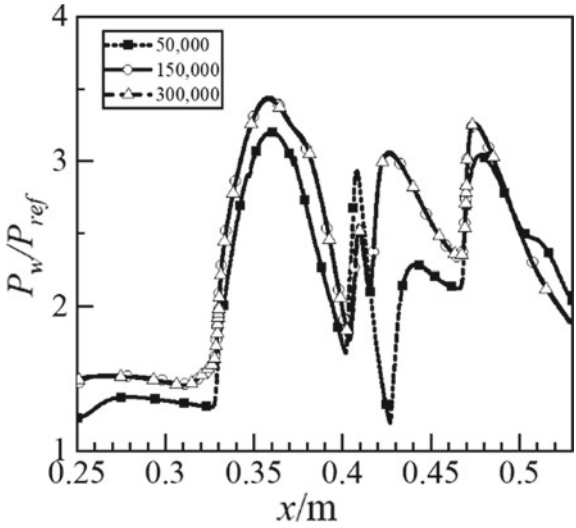

Fig. 3 Validation for grid independence

4 Result and Analysis

4.1 Flow Field Distribution Characteristics

Figure 4 shows pressure and the NPTKE contours of the feature region where the flow direction from $x = 0.32$ m to $x = 0.53$ m, the dashed line represents the shock wave. An oblique shock wave is generated due to the contraction of the lower wall surface at x = 0.33 m. It is determined that the flow situation conforms to the basic law of supersonic flow through a pipe of the variable cross-section by comparing the calculated shock wave angle with the theoretical shock wave angle. The turbulent kinetic energy production near the wall always takes a positive value, and the NPTKE area is concentrated in the center of the inner flow channel. The supersonic fluid is compressible in the case, so $\frac{\partial \overline{U}}{\partial x} \neq -\frac{\partial \overline{V}}{\partial y}$. As a result, different flow direction and normal velocity gradients have different effects on the total turbulent kinetic energy production.

4.2 Shock Wave Effect on the Turbulent Kinetic Energy Production

To analyze the variation law of turbulent kinetic energy production at the shock wave, three feature points A, B and C at the shock wave position in the flow field are selected as shown in Fig. 6, where A (0.36, 0.0140) is located at the incident shock wave, B (0.39, 0.0166) is located at the first reflected shock wave, and C (0.391, 0.0202) is

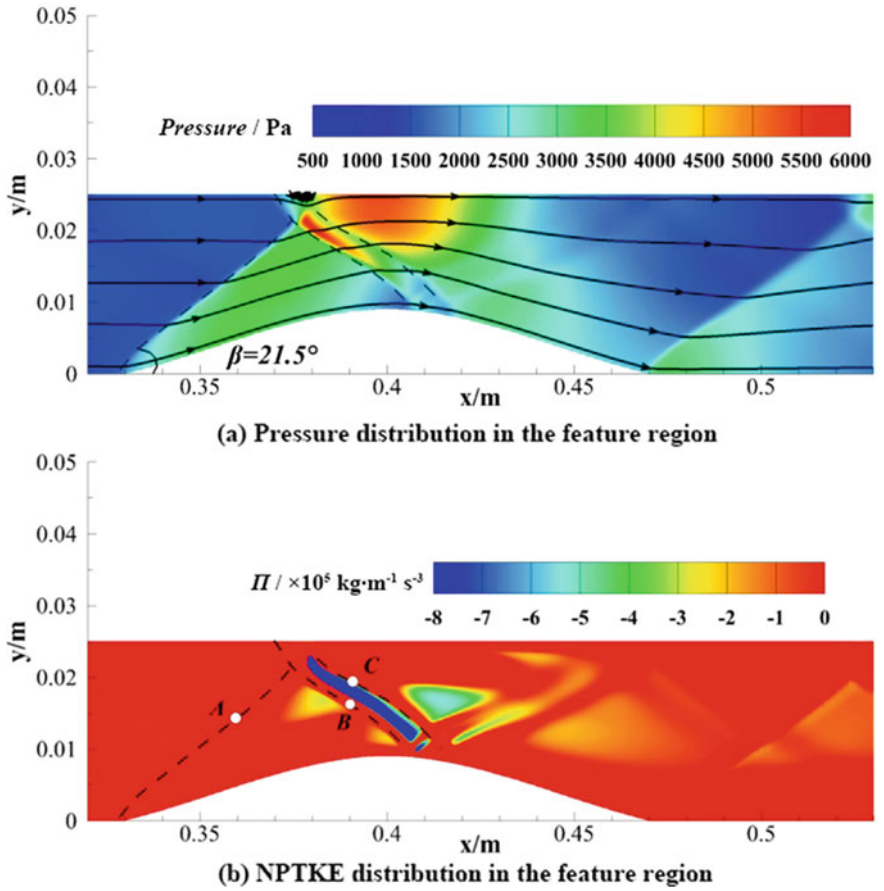

Fig. 4 Pressure and the NPTKE contours in the feature area

located at the second reflected shock wave. Taking the normal direction along with the shock wave as the horizontal axis of coordinates, the half-channel width H/2 is used as the dimensionless length.

It can be seen from Fig. 5 that the pressure gradient at the shock wave is significantly higher than that of the nearby flow field, corresponding to the extreme point of the pressure gradient. The turbulent kinetic energy production at the corresponding position of the shock wave is always positive, and the local maximum value is also approximately obtained at this place. With the dramatic pressure changes, the fluctuating velocity and velocity gradient increase, and the energy transfers from the mean flow to the turbulent flow. When the microelement passes through the oblique shock wave, the pressure increases sharply, the velocity decreases, and the flow direction is deflected toward the shock wave. Since the compression of the shock wave

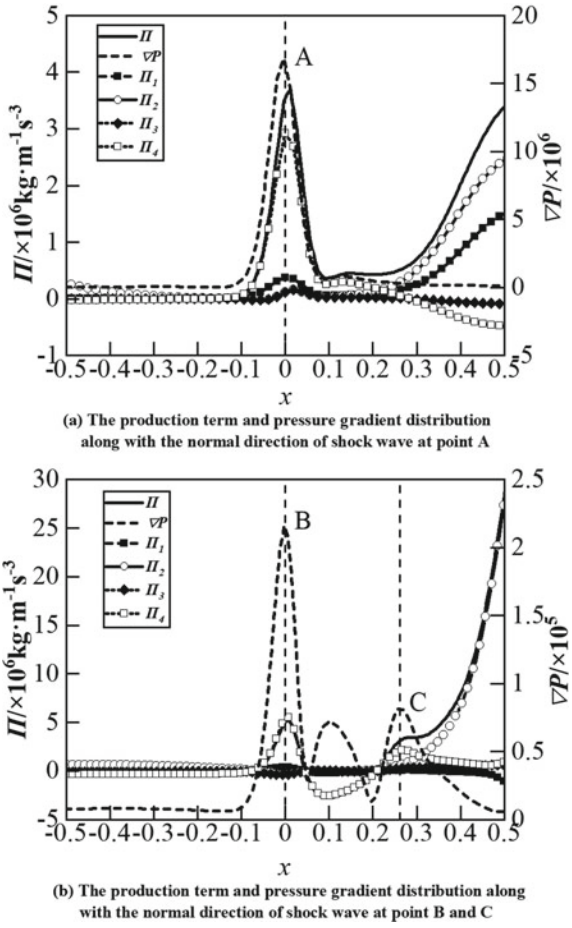

Fig. 5 Turbulent kinetic energy production and pressure gradient distribution at three characteristic points

has a "squeezing" effect on the vicinal microelements so that the process of energy transport is counter gradient.

The turbulent kinetic energy production decomposes into four terms, and the change of $\Pi_4 = -\overline{\rho}\widetilde{v''v''}\frac{\partial \overline{V}}{\partial y}$ in the vicinity of the shock wave is consistent with the total turbulent kinetic energy production. The magnitude is much higher than the other three terms, so the main influence factor of turbulent kinetic energy production can be assumed as the product of normal stress and velocity gradient.

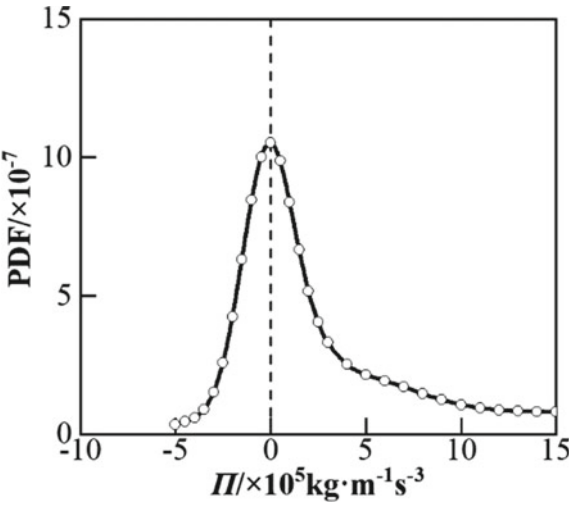

Fig. 6 PDFs of the turbulent kinetic energy production in feature region

4.3 Statistic Distribution of Turbulent Kinetic Energy Production

The statistical method is a useful data post-processing method. Probability density distribution (PDF) is performed on the flow field data in the feature region, as shown in Fig. 6. It shows that although the turbulent kinetic energy production values in the flow field can be positive or negative, the total volume integration always remains positive. By comparison, the NPTKE area increases a lot after the oblique shock wave occurs in the feature region due to the local cross-section variation, and the asymmetry attributes of the area also promote the NPTKE.

Decomposition of the turbulent kinetic energy production term by the strain rate tensor, such as formula (2). The dominant factors affecting the flow field structure are confirmed. Focusing on the analysis of the feature region, the intrinsic contribution value Π_{Λ_k} is shown in (a), (c), (e) in Fig. 7. The legend shows that the compressive eigenvalue term Π_{Λ_2} is the main contribution component in the positive production of turbulent kinetic energy area, whereas the stretching eigenvalue Π_{Λ_1} is the dominant term in the NPTKE area. The distribution of Π_{Λ_k} values in the NPTKE area is closer to zero than that in the positive area.

In order to indicate the cause of the sign change of turbulent kinetic energy production intuitively, separate the $-\overline{\rho u''^2 \cos^2\left(u'', \lambda_k^S\right)}$ item from the expression, and PDF distributions are shown in Fig. 7b, d, f. In general, the $-\overline{\rho u''^2 \cos^2\left(u'', \lambda_k^S\right)}$ distribution in the NPTKE area is more concentrated than that in the positive area. The numerical range of the first term $-\overline{\rho u''^2 \cos^2\left(u'', \lambda_1^S\right)}$ is smaller than the second term $-\overline{\rho u''^2 \cos^2\left(u'', \lambda_2^S\right)}$, regardless of whether the turbulent kinetic energy production value is positive or negative, hence the whole turbulent kinetic energy production is positive during the turbulent process.

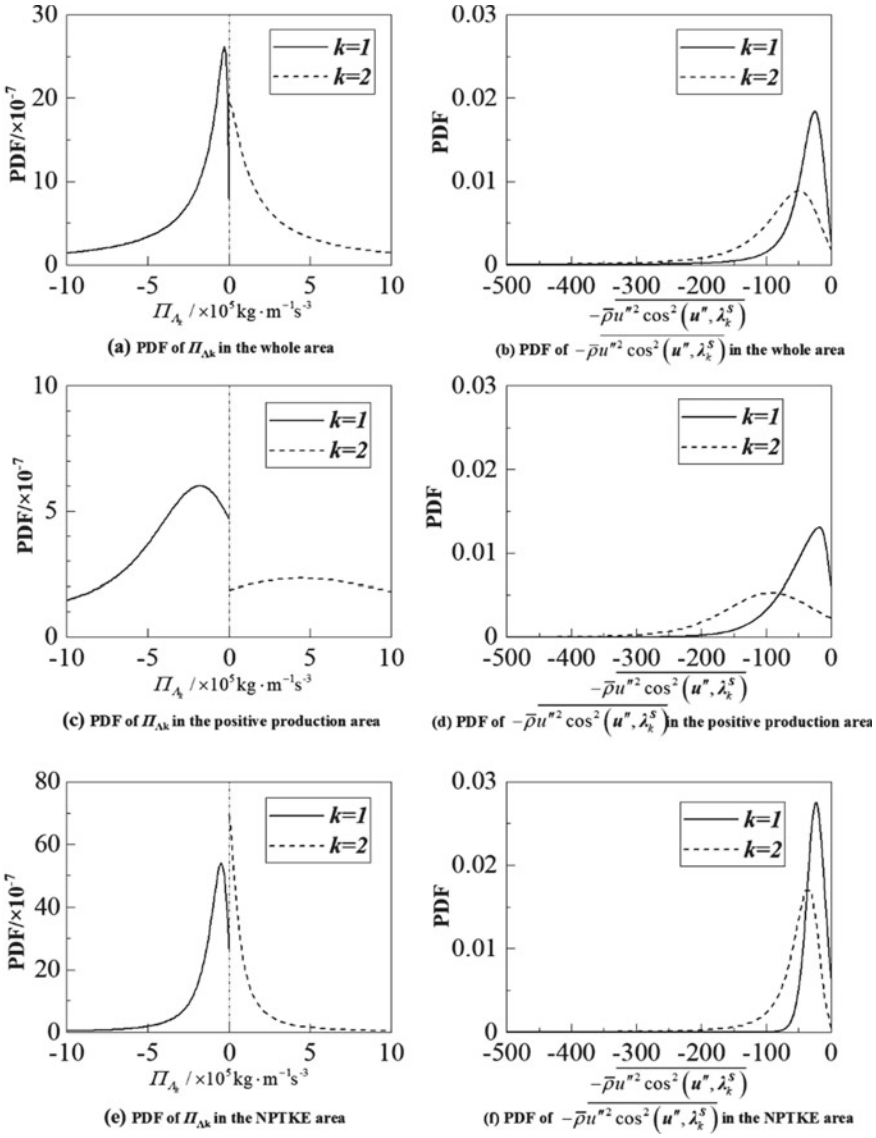

Fig. 7 PDFs of Π_{Λ_k} and $-\overline{\rho u''^2 \cos^2(u'', \lambda_k^S)}$ in the feature region

5 Conclusion

In this paper, the Reynolds stress turbulence model is used to solve the compressible turbulent kinetic energy transport equation, the numerical calculation of the supersonic channel flow is carried out. The main conclusions are as follows:

(1) The inherent properties of the velocity fluctuation and mean strain rate affect the turbulent kinetic energy production. Similar to the subsonic situation, the stretching properties of the flow field lead to $\Pi < 0$, while the compressive properties maintain$\Pi > 0$.
(2) The NPTKE means the appearance of an energy reversal area in the flow field. It's worth noting that the production of turbulent kinetic energy value is always positive in the integral volume.
(3) The production of turbulent kinetic energy at the shock wave position is always positive. The local maximum is approximately obtained, and the product of the normal stress and the gradient is the dominant factor.

Acknowledgements This work is partially supported by the National Natural Science Foundation of China (Grant No. 11672183).

References

1. Laadhari F (2002) On the evolution of maximum turbulent kinetic energy production in a channel flow. Phys Fluids 14:65
2. Rogers MM, Mansour NN, Reynolds WC (1989) An algebraic model for the turbulent flux of a passive scalar. J Fluid Mech 203
3. Victor PS (2010) Transport of kinetic energy in the atmosphere. J Atmos Sci 6:160
4. Holly JO, Pardyjak ER et al (2016) Buoyant turbulent kinetic energy production in steep-slope katabatic flow. Bound-Layer Meteorol 161:405–416
5. Eskinazi S, Erian FF (1969) Energy reversal in turbulent flows. Phys Fluids 12:1988–1998
6. Boffetta G, Celani A, Vergassola M (2000) Inverse energy cascade in two-dimensional turbulence: deviations from gaussian behavior. Phys Rev E 61:29–32
7. Gurka R, Hetsroni G et al (2004) On turbulent energy production in wall bounded flows. Phys Fluids 16:2704
8. Hanjalic K, Launder BE (1972) Fully developed asymmetric flow in a plane channel. J Fluid Mech 51:301–335
9. Cimarelli A, Leonforte A et al (2019) On negative turbulence production phenomena in the shear layer of separating and reattaching flows. Phys Lett A 383:1019–1026
10. Gayen B, Sarkar S (2011) Negative turbulent production during flow reversal in a stratified oscillating boundary layer on a sloping bottom. Phys Fluids 23:101703
11. Park GI (2017) Wall-modeled large-eddy simulation of a high reynolds number separating and reattaching flow. AIAA J 55:3709–3721
12. Palmer MD, Keffer JF (1972) An experimental investigation of an asymmetrical turbulent wake. J Fluid Mech 53:593
13. Liberzon A, LuThi B et al (2005) Experimental study of the structure of flow regions with negative turbulent kinetic energy production in confined three-dimensional shear flows with and without buoyancy. Phys Fluids 17:095110
14. Qiu X, Jiang J, Liu Y (2004) Effects of pressure gradient on turbulent counter-gradient transport phenomena. Acta Mech Sin 36:163–170
15. Rumsey CL (2010) Compressibility considerations for k-ω turbulence models in hypersonic boundary-layer applications. J Spacecraft Rockets 47:11–20
16. Huang W (2016) Transverse jet in supersonic crossflows. Aerosp Sci Technol 50:183–195
17. Yang SL, Siow YK et al (2015) Numerical study of nonreacting gas turbine combustor swirl flow using reynolds stress model. J Eng Gas Turbines Power 125:804–811

18. Alain P, Haitao X, Siggia ED (2016) Small-scale anisotropy in turbulent boundary layers. J Fluid Mech 804:5–23
19. Liu Y, Qiu X (2010) Expermental study of turbulent channel flow with wing. J Shanghai Inst Technol 10:155
20. Zhang Ya, Chen F et al (2013) Research on the relaxation characteristics of PIV tracer particles in supersonic flow. J Exp Fluid Mech 27:70–75
21. Bookey P, Wyckham, C et al (2005) New experimental data of STBLI at DNS/LES accessible reynolds numbers. AIAA paper no. 2005–309
22. Wu M, Martin MP (2007) Direct numerical simulation of supersonic turbulent boundary layer over a compression ramp. AIAA J 45:879–889

Design and Experimental Study of Automatic Docking and Undocking Robot System for Launch Vehicle Propellant Filling

Jiawei You, Yue Huang, and Xiangming Dun

Abstract An automatic docking and undocking robot system was designed for the propellant filling process before the launch of the launch vehicle, instead of manually completing the filling operation. This filling robot system consists of a robot body, a control system and a positioning system. The robot body includes a base, a SCARA manipulator and a gentle docking and withdrawal system. The SCARA manipulator is coordinated to achieve the positioning and tracking of the rocket filling port through the control system and the positioning system, and then the gentle docking and withdrawal system completes the docking of the fill-drain connector and the rocket filling port as the robot's execution end. The positioning system mainly uses a lidar system, which detects the target board to achieve positioning and tracking based on artificial beacons, and uses the arithmetic mean method to perform error compensation. Finally, a large number of experimental studies verify the reliability and stability of the robot system.

Keywords Propellant filling · Automatic docking and undocking robot · SCARA manipulator · Gentle docking and withdrawal · Positioning system

1 Introduction

The filling of the propellant of the launch vehicle is an important part before the launch of the rocket, and it is also a very dangerous part of the launch procedure of the rocket [1, 2]. In the event of an accident, it is very likely to cause casualties. In order to improve safety and reduce the risks caused by manual operation, it is imperative to realize the automation of propellant filling. At present, many countries

J. You (✉) · Y. Huang · X. Dun
Shanghai Jiao Tong University, Shanghai, China
e-mail: mmdhy2940@163.com

X. Dun
e-mail: xmdun@sjtu.edu.cn

Z. Jing and X. Zhan (eds.), *Proceedings of the International Conference on Aerospace System Science and Engineering 2020*, Lecture Notes in Electrical Engineering 680,
https://doi.org/10.1007/978-981-33-6060-0_41

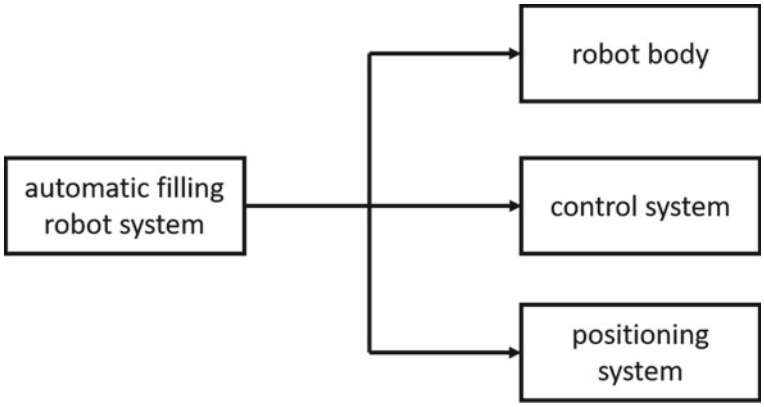

Fig. 1 Robot system framework

in the world such as the United States and Russia have been committed to the research of rocket filling automation, and have achieved certain results [3].

The docking and follow-up technology of "Tower-perch" represented by Russia is simple and reliable in docking and withdrawal. It has a short operation time and has the function of docking after falling off. However, its core belongs to rigid assembly technology, and it is inevitable that it has some shortcomings such as poor environmental adaptability, high requirements for supporting links such as lifting and placement of the rocket body, and large size of the device itself. The "Rocket-perch" docking and follow-up technology, represented by the United States, reduces the difficulty of centering and follow-up due to the shaking of the rocket body during the docking and filling process, but the docking device needs to be manually installed on the rocket body before use. This causes that once the docking device and the docket body are detached, automatic re-docking cannot be achieved [4–6].

This paper designs an automatic filling robot system based on SCARA manipulator [7]. The entire system is composed of robot body, control system and positioning system, as shown in Fig. 1. Through the Lidar positioning system, the target plate at the rocket filling port is positioned and tracked, and then the control system adjusts the position and posture of SCARA mechanical arms. The gentle docking and withdrawal system is used as the execution end to complete the docking and separation of the fill-drain connector and the rocket filling port. The robot has strong adaptability to the environment, small size, high degree of automation and reliability.

2 Mechanical Structure and Function

The mechanical part of the automatic filling robot is mainly the robot body, as shown in Fig. 2. It consists of a base, a SCARA manipulator, and a gentle docking and withdrawal system.

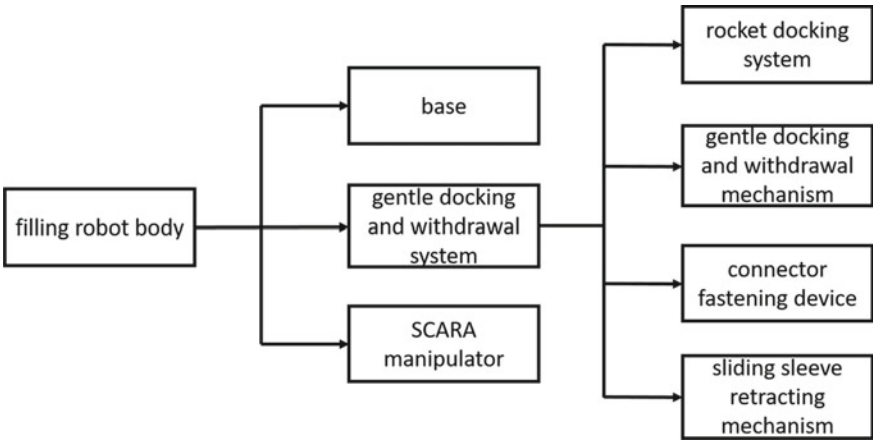

Fig. 2 Mechanical structure

2.1 SCARA Manipulator

The SCARA manipulator is coordinated by the positioning system and the control system to realize the robot's automatic positioning and tracking function for the rocket filling port. It consists of four decoupling joints in series. The first to third joints are rotary joints, and the fourth joint is translational joint. The positioning system detects the relative position of the robot and the rocket filling port in real time, and then three rotating joints adjust the posture of the robotic arms to help complete the docking.

The internal structural layout of the SCARA manipulator is shown in Fig. 3. The rotary joint and the rotary joint are connected by bearings. The servo motor and the reducer are fixed in the hollow shaft of the lower joint. The floating end of the clutch is fixed to the reducer. The clutch is firmly connected to the upper mechanical arm. When the clutch is coupled, the motor can control the movement of the mechanical arm; when the clutch is disconnected, the mechanical arm is in a flexible state and can swing freely. The encoder is located at the end of the joint, which can detect the posture information of the robot arm in real time in order to perform closed-loop control of the robot arm. The fourth joint is mainly driven by a motor through a belt, directly driving the two lead screw modules to cause the floating suspension to move vertically.

2.2 Gentle Docking and Withdrawal System

The gentle docking and withdrawal system belongs to the execution end of the robot. It is mainly used to hold the fill-drain connector and complete the mechanical docking

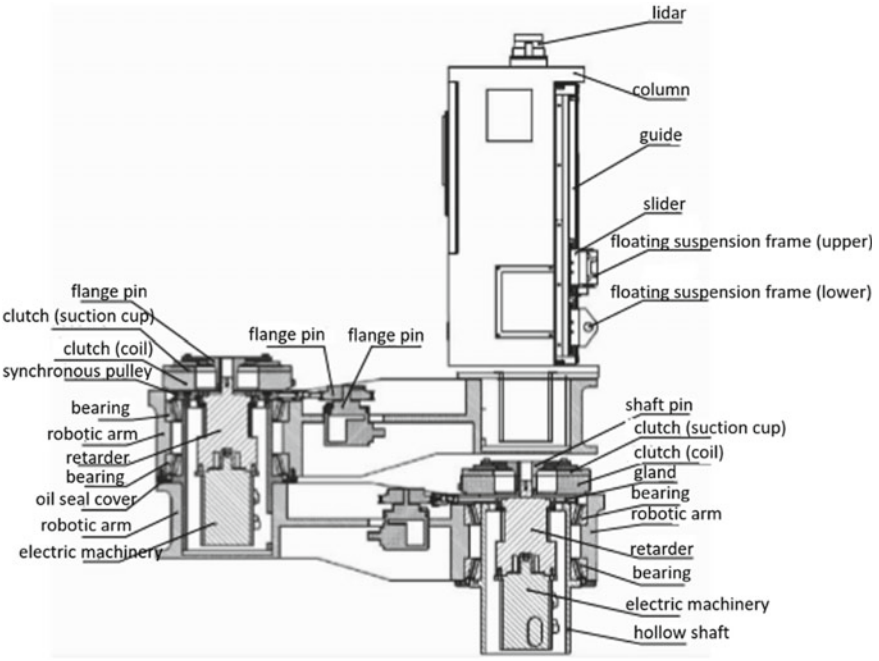

Fig. 3 Internal structure of SCARA manipulator

and withdrawal of the fill-drain connector with the rocket filling port. It consists of a rocket docking system, a gentle docking and withdrawal mechanism, a connector fastening device, and a sliding sleeve retracting mechanism, as shown in Fig. 4.

Rocket docking system. The rocket docking system mainly provides an interface and a locking mechanism for docking with the positioning substrate on rocket. When the robot positioning is basically completed and starting to be up to the rocket, the rocket docking system provides effective docking points and establishes a preliminary connection with the positioning substrate interface. The positioning ball of the positioning substrate enters the positioning hole, and then the cylinder starts to move, pushing the rocker arm mechanism to push out the pin hook which will hook with the ear plate on the positioning substrate. At this time, the link mechanism is a mechanical dead point and the pin hook is locked. The robot and rocket are successfully locked. The structure of rocket docking system is shown in Figs. 5 and 6.

Gentle docking and withdrawal mechanism. The structure of the gentle docking and withdrawal mechanism is shown in Fig. 7. The front end restraint adopts the roller chute structure. When the fill-drain connector enters the rocket interface, the roller chute is pulled by the cylinder, and the roller rolls out of the chute horn. The fill-drain connector will have a pitch margin of $\pm$ 2 mm to achieve a gentle docking and withdrawal. When the docking is completed, the cylinder pulls the chute back and re-constrains the fill-drain connector, so that during the process of propellant

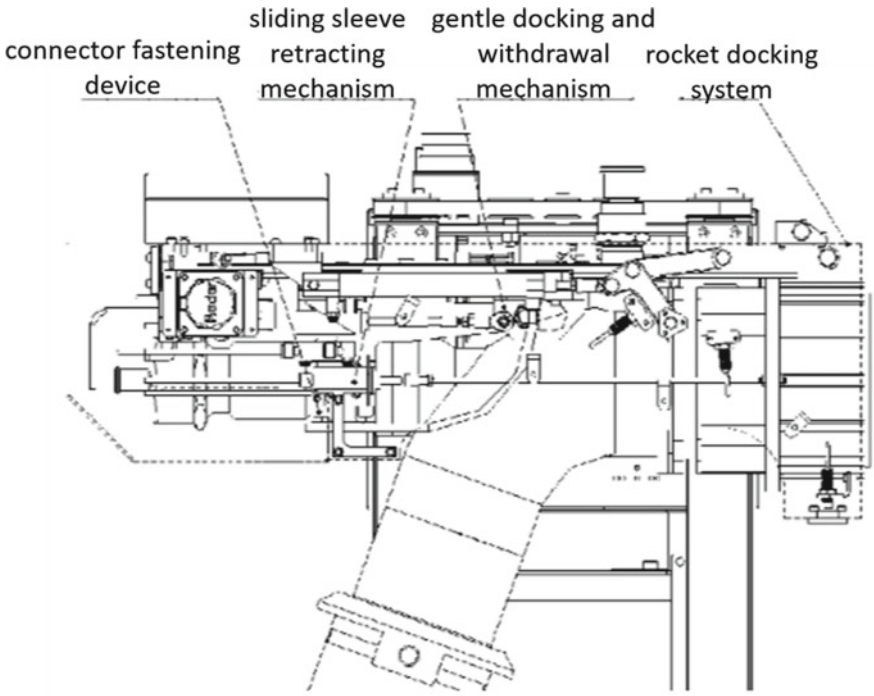

Fig. 4 Gentle docking and withdrawal system

filling, the weight of the fill-drain connector and the propellant in the tube are carried by the rocket docking mechanism to avoid stress on the rocket filling port. The rear cross hinge pin is used to enable the connector fastening device to tilt up and down and swing left and right. The entire gentle docking and withdrawal device is powered by a motor and moves on the guide rail through the slider.

Connector fastening device. The connector fastening device is used for the connection between the gentle docking and withdrawal mechanism and the fill-drain connector. The latching mechanism clamps the outer surface of the connector, and adjusts the locking force by pre-tightening the bolt and nut pair. The connector fastening device is closed with the fixed half by bolt connection, thereby completing the tightening of the fill-drain connector. The mating surface of the latching mechanism and the fill-drain connector is machined to ensure high positioning accuracy and tolerate clamping of the fill-drain connector, as shown in Figs. 8 and 9.

Sliding sleeve retracting mechanism. The sliding sleeve retracting mechanism mainly pulls the sleeve of the fill-drain connector back to unlock before the docking of the fill-drain connector, so that the connector can dock with the rocket filling port successfully, as shown in Fig. 10. The main component of the pulling module is a cylinder, which adopts a double-cylinder drive design. Compared with the motor, the advantages are as follows: it is suitable for flammable and explosive situations, and

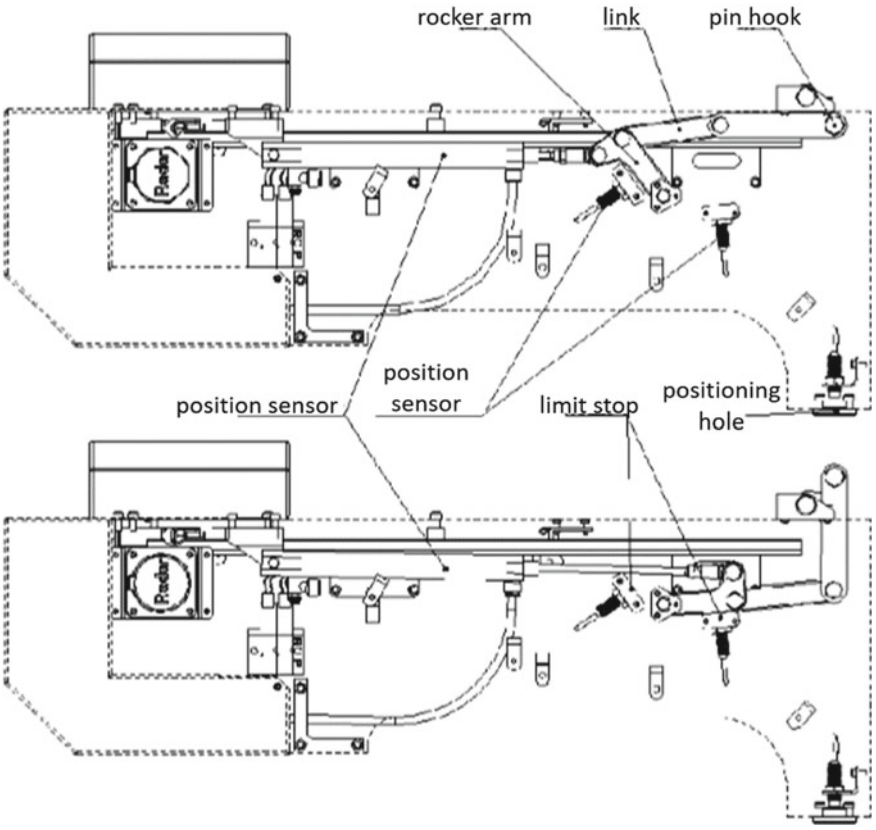

Fig. 5 Rocket docking system

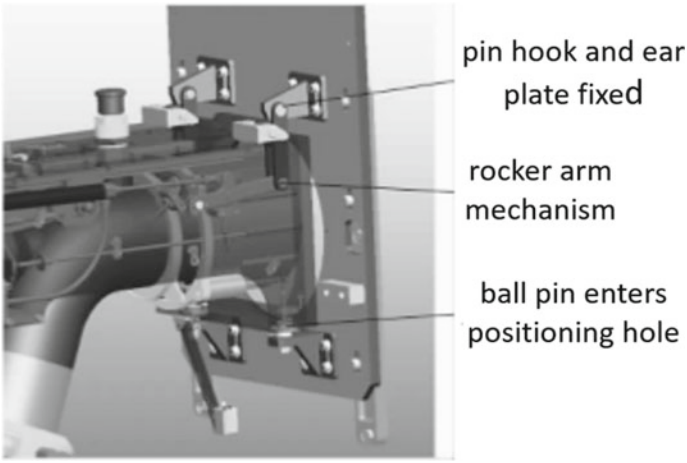

Fig. 6 Locking state

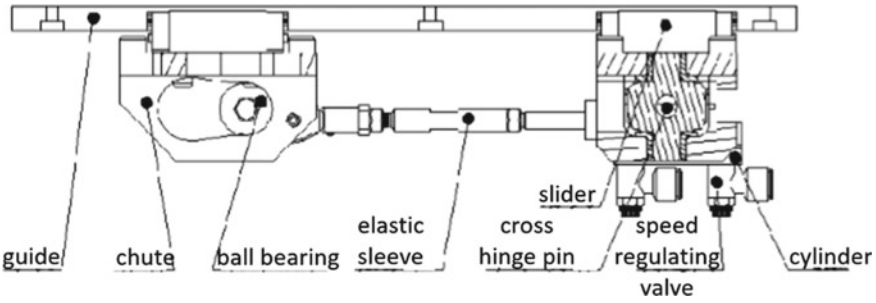

Fig. 7 Gentle docking and withdrawal mechanism

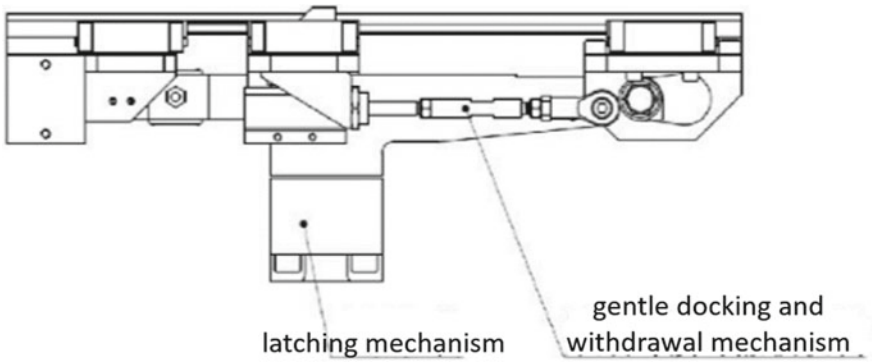

Fig. 8 Connector fastening device

compared with the motor it will not generate electric sparks which has high safety index; the cylinder is flexible, and the air pressure has good compression, which can effectively protect the sleeve and avoid the mechanical stuck or the damage of sleeve during the process of pulling.

3 Control System

The control system uses a dual-controller, dual-position closed-loop, and force servo docking scheme. The dual controller uses two controllers, the remote controller and the field controller, to communicate with each other through the industrial bus to achieve cooperative operation; the dual-position closed-loop is the internal position closed-loop of the arm motor driver and the field controller position closed-loop; the force servo docking is during the docking process, the force sensor installed on the robot arm senses the strength of the docking to achieve the purpose of detecting whether the docking is firm.

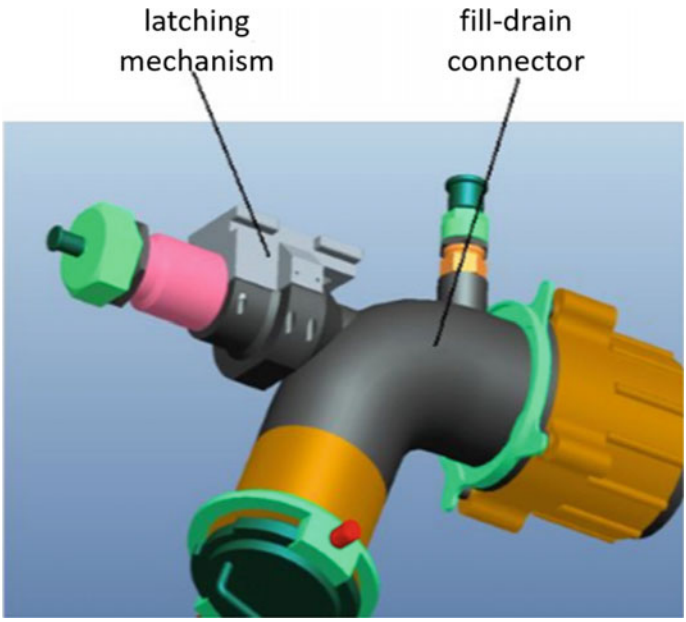

Fig. 9 3D model of connector and locking mechanism

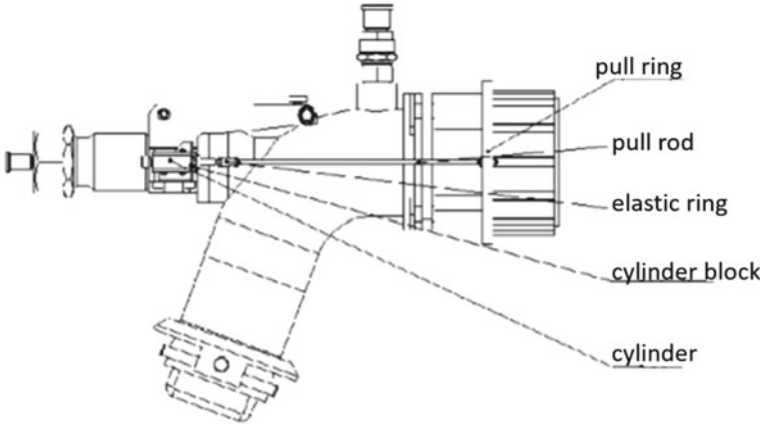

Fig. 10 Sliding sleeve retracting mechanism

As shown in Fig. 11, the main modules of the control system of the filling robot are:

1. Remote controller: placed away from the site, processing sensor data, issuing operating instructions, planning motion paths, and monitoring the operation of the system.

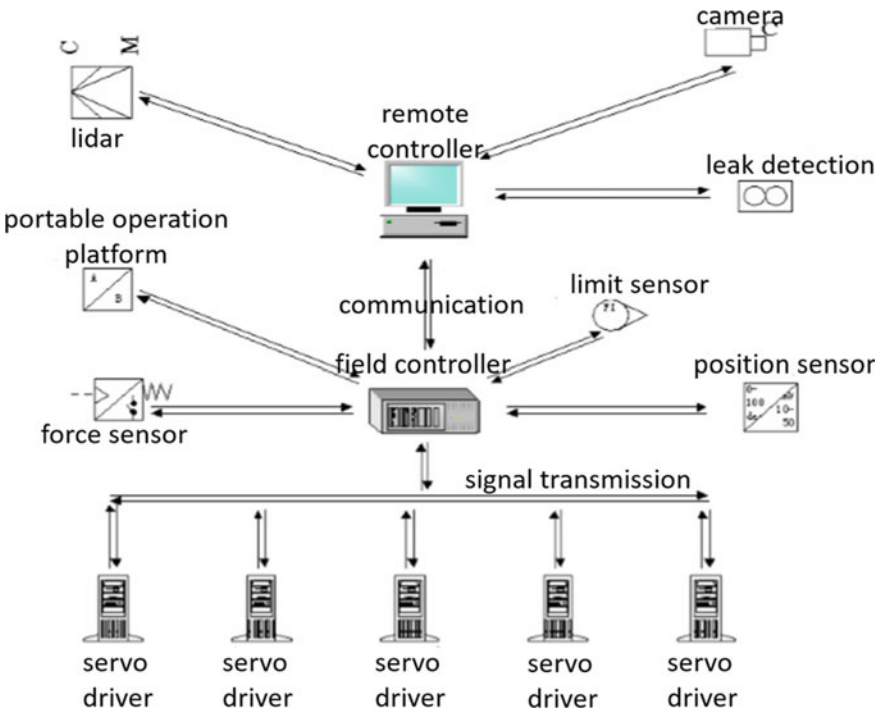

Fig. 11 Control system composition

2. On-site operation and implementation unit: placed on the filling site, and through the coordinated operation of field controllers, sensors, motor drivers and other devices, the mechanism accurately completes the instructions given by the operator. It mainly includes:

   a. Field controller: Give a position movement instruction to the motor driver, and perform position closed loop through position sensor feedback. At the same time, it can communicate with the remote controller.
   b. Camera: Monitor on-site environment.
   c. Lidar: The environmental information is collected by the lidar, and the filling port position is determined through calculation.
   d. Force sensor: Feedback the magnitude of the force during the docking process.
   e. Position sensor: Feedback the current position of each joint to the motor driver and field controller.
   f. Motor driver: Receive the position command of the field controller, drive the joint motion, and perform position closed loop between the driver and the motor through the feedback of the position sensor to precisely control the movement of the arm joint.

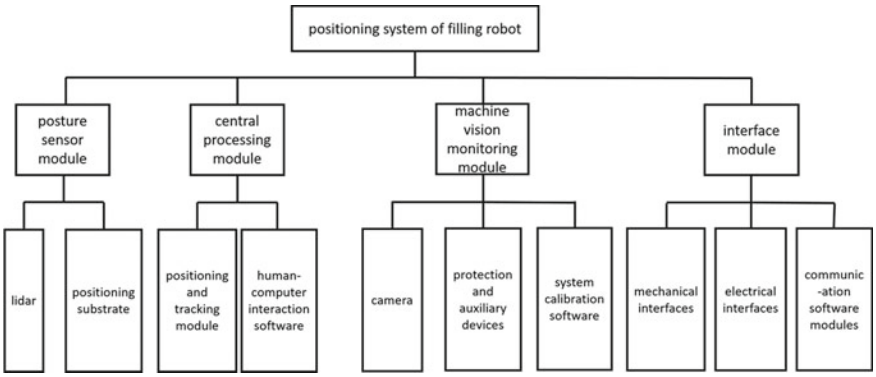

Fig. 12 Framework of positioning system

4 Positioning System

As shown in Fig. 12, the positioning system belongs to the main execution system of the up-to-rocket working phase of the filling robot. It contains the following four sub-modules, which are the lidar sensor module, the data processing control module, the field safety monitoring module, and the software and hardware interface composition. Among them, the lidar sensor module is composed of a lidar and a positioning substrate. The combination of the lidar and the positioning substrate provides a reference for the posture of the robot arm.

The design idea of posture estimation based on lidar detection in this system is to fix a detachable target plate with a special shape on the rocket body. Then rely on lidar to detect two-dimensional environmental information, and use the detection and recognition algorithm to extract environmental information and calculate the position of the target plate. So as to determine the relative position between the fill-drain connector and the rocket filling port. Combined with the specific path motion planning, from coarse positioning to fine positioning, the robot gradually approaches the target to finally realize the filling robot and rocket filling port's precise docking. Considering the misjudgment of positioning caused by posture data fluctuations, the arithmetic mean method is used for error compensation.

5 Performance Index

The performance indicators of the designed automatic docking and undocking robot are as follows:

1. Fine adjustment of body posture: 4 degrees of freedom posture adjustment, the maximum speed is not less than 3 mm/s;
2. Displacement range in any direction: $\not<30$ mm;

3. Maximum docking force: $\leqslant$1000 N;
4. Effective docking distance: $\leqslant$60 mm;
5. The body weight: less than 200 kg;
6. Anti-corrosion performance: able to resist the corrosion of combustion agents and oxidants;
7. Force servo cycle: < 400 ms;
8. Docking motion accuracy: 1 mm;
9. Robot tower installation time: less than 45 min;
10. Working environment temperature adaptability: 5–30 °C;
11. Storage room temperature adaptability: −34–50 °C;
12. Altitude adaptability: 1100 m.

6 Experimental Study

Taking the entire system of the filling robot as the object of inspection, including automatic positioning of the robot, rocket body swing adaptation, gentle docking, and loading hoses, etc. A large number of repeated experiments have verified that the filling robot system achieves various functions and the performance design index. The stability, reliability and security of the system have been also verified. Table 1 records the experimental situation for the comprehensive performance of the robot; Table 2 records the design indicators of the filling robot system and the actual values of the experimentally obtained index parameters. It can be seen from the table that the actual values of the system performance index parameters meet the designed index requirements, indicating the feasibility of the filling robot.

7 Conclusion and Prospect

7.1 Conclusion

Aiming at the realization of automation of launch vehicle propellant filling, this paper designs a kind of automatic docking and undocking robot combining the SCARA manipulator and gentle docking and withdrawal system, which is based on lidar detection and positioning. A series of automated processes such as positioning and tracking of the rocket filling port, docking, filling, and withdrawal have been realized The SCARA manipulator is coordinated to achieve the positioning and tracking of the rocket filling port through the control system and the positioning system, and then the gentle docking and withdrawal system completes the docking of the fill-drain connector and the rocket filling port as the robot's execution end. The positioning system mainly uses a lidar system, which detects the target board to achieve positioning and tracking based on artificial beacons, and uses the arithmetic

Table 1 Experimental situation

Experiment content/purpose	Location	Propellant	Rocket body
Verify that the filling robot system works properly	China Jiuquan Satellite Launch Center	Nothing	Simulated rocket body
Verify the stability of the robot's positioning and tracking under the condition of dinitrogen tetroxide leakage	China Jiuquan Satellite Launch Center	Nothing	Simulated rocket body
Verify the basic functions of the robot, such as rocket body swinging adaptation, gentle docking, loading hose and so on	China Jiuquan Satellite Launch Center	Nothing	Simulated rocket body
The actual rocket body docking test verified the matching of the robot's various mechanical interfaces with the rocket interface. The stability and reliability of the positioning and tracking algorithm are verified	Shanghai 149 Factory	Nothing	CZ-2D rocket body
Use water instead of propellant to verify the stability of robot operation	China Jiuquan Satellite Launch Center	Water	Simulated rocket body
The real propellant filling experiment simulated the real filling environment, which verified the stability of the robot when it was filled with the real propellant, and also verified the robot's anti-corrosion and explosion-proof performance	China Jiuquan Satellite Launch Center	Dinitrogen tetroxide	Simulated rocket body
Under the real rocket environment, the stable working performance of the robot is verified	China Jiuquan Satellite Launch Center	Nothing	CZ-2D rocket body

Table 2 System performance index verification

Index name	Index requirement	Experimental actual value	Remark
Scope of robot operation	≮100 mm	600 mm	In view of the interference of the filling hose with the movement of the column, the effective working radius is only in the front right
Radar positioning accuracy	±6 mm	±4 mm	
Flexible adaptation angle of the rocket docking system	≮0.5°	1°	Adapt to horizontal angle from rocket swing
Horizontal follow-up range	≮30 mm	300 mm	Adapt to horizontal displacement of rocket
Vertical follow-up range	≮30 mm	162 mm	Adapt to vertical displacement caused by rocket ascent and subsidence
Driving force of sleeve	≮60 N	200 N	
Docking force of connector	≮1000 N	1949 N	
Compliant angle of fill-drain connector	≮0.5°	0.8°	Adapted to the problem that the rocket port is not perpendicular to the rocket surface due to the welding process
Docking stroke of fill-drain connector	≮60 mm	142 mm	
Maximum pressure of reserve gas cylinder	0.8 MPa	20 MPa	

mean method to perform error compensation. Finally, a series of experiments verified the reliability and stability of the system.

7.2 Prospect

The automatic docking and undocking robot system described in this article still has some limitations and room for further development.

1. The rear part of the fill-drain connector is a long and heavy metal hose. When the gentle docking and withdrawal system holds the fill-drain connector, it will

withstand greater gravity, and dragging the metal hose also needs to overcome greater resistance. Therefore, a pipeline robotic arm structure can be considered, that is, the robotic arm is designed into a pipe shape, and the fill-drain connector is the end effector of the robotic arm. The propellant is filled directly into the rocket through the pipeline robotic arm, thereby avoiding the drag of the metal hose. The swivel joint will be used as the rotary joint, and the posture of the pipeline robot arm can be adjusted by the motor-gear-belt transmission.

2. It is necessary to install a special shaped target board on the rocket body to help the lidar realize positioning and tracking. We can consider scanning the three-dimensional point cloud and let the lidar directly scan and identify the three-dimensional features of the rocket filling port to achieve positioning and tracking. At the same time, a guide cone and a guide hole can be used to assist positioning. A six-dimensional force sensor can be installed at the bottom of the guide cone to feedback the force.

Acknowledgements This work is partially supported by Robot Research Institute of Shanghai Jiao Tong University and China Jiuquan Satellite Launch Center. The authors also gratefully acknowledge the helpful comments and suggestions of the reviewers, which have improved the presentation.

References

1. Uda RT (1976) Space shuttle tail service mast concept verification. NASA 76-28273[R]. NASA, USA
2. Zhao J (2007) Enlightenment from the command of the rescue organization for the major leakage accident of XX rocket propellant. In: National disaster medicine conference and “watson cup” disaster medicine outstanding academic paper review conference
3. Wang R (2002) Discussion on umbilical connector of launch vehicle. Space Launch Technol 2002(3):1–15
4. Wang L (2003) Analysis of Russian rocket automatic docking technology. Space Launch Technol 2003(1):45–50
5. Dandage SR, Herman NA, Godfrey SE et al (1979) Design and development of the space shuttle tail service masts. NASA 79-21357[R]. NASA, USA
6. Wen J, Dun X, Dun Y et al (2010) Research on the status and development trend of propellant filling automatic docking and undocking robot technology. Robot Technol Appl 2010(6):20–23
7. Jasim WM (2011) Solution of inverse kinematics for SCARA manipulator using adaptive NeuroFuzzy network. Int J Soft Comput 2(4):5966

Adaptive Fading Factor Unscented Kalman Filter with Application to Target Tracking

Peng Gu, Zhongliang Jing, and Liangbin Wu

Abstract One purpose of target tracking is to estimate the states of targets, and Unscented Kalman filter(UKF) is one of the effective algorithms for estimating in the nonlinear tracking problem. Considering the characteristics of complex maneuverability, it is easy to reduce the tracking accuracy and cause divergence due to the mismatch between the system model and the practical target motion-model. Adaptive fading factor is an effective counter to this problem, having been instrumental in solving accuracy and divergence problems. Fading factor can adaptively adjust covariance matrix online to compensate model mismatch error. Moreover, fading factor not only improves the filtering accuracy, but also automatically adjusts the error covariance in response to the different situation. The simulation results show that the adaptive fading factor Unscented Kalman filter(AFUKF) has more advantages in target tracking and it can be better applied to nonlinear target tracking.

Keywords Adaptive fading factor · Target tracking · UKF · Accuracy

1 Introduction

Kalman filter algorithm can derive the optimal estimation of state under conditions involving linear-Gaussian assumption, which is based on the known system model, observation model and statistics of noises. When they are inconsistent with target behavior model, the estimation error will increase. Singer model can express the acceleration of maneuver as a time-dependent process [1], which conforms to actual

P. Gu (✉) · Z. Jing
School of Aeronautics and Astronautics, Shanghai Jiao Tong University, Shanghai, China
e-mail: gpszseu@163.com

Z. Jing
e-mail: zljing@sjtu.edu.cn

P. Gu · L. Wu
AVIC Leihua Electronic Technology Research Institute, Wuxi, China
e-mail: lbwu0105@126.com

Z. Jing and X. Zhan (eds.), *Proceedings of the International Conference on Aerospace System Science and Engineering 2020*, Lecture Notes in Electrical Engineering 680,
https://doi.org/10.1007/978-981-33-6060-0_42

target motion. By adjusting the frequency coefficient of maneuvering to achieve better tracking effect, it has been widely used for nonlinear system [2, 3]. The "current" statistical model was proposed as a representative of adaptive tracking algorithm [4]. In this model, the acceleration noise is assumed to be Rayleigh distribution, and the distribution of state noise is updated in real time through mean value of acceleration.

In the process of target tracking, if the system model deviate from their actual values by unknown random bias, the virtual noise is usually used to reduce confidence level of the filter to the system model, but it is difficult to determine how much virtual noise to be added. At this time, we should consider abandoning the previous observation data, and pay more attention to the newly generated observation value, so that the filter has better performance. In this paper, the fading factor is integrated into unscented Kalman filter to form adaptive fading factor unscented Kalman filter (AFUKF). In general, we can put weight of fading factor on the prediction covariance matrix, so that the output value of the estimation is closer to the actual value. Meanwhile, the adaptive method of the fading factor is described in detail throughout this paper.

2 The Unscented Kalman Filter

For the general nonlinear maneuvering target tracking, techniques for nonlinear filtering typically involve classic estimation methods such as extended Kalman filter (EKF) [5] and Quadrature Kalman filter (QKF) [6] which is approximated by Gauss Hermite quadrature criterion. When the nonlinearity of the system is too severe, piecewise linear application of EKF degrades performance to the nonlinear tracking problem. The extended Kalman filter (EKF) propagates mean value through the linearization of the nonlinear conditions. As the EKF uses the first-order terms as an approximation, linearization errors will rise if neglected higher-order terms begin to dominate. However, sampling points of QKF will grow exponentially as the spatial dimension increases. Thus, QKF is certainly not suitable for high-dimensional cases.

The core of UKF is UT transformation, which is a method for calculating the statistics value of random variable to avoid nonlinear transformation [7, 8]. The fundamental idea is founded on the intuition that it is easier to approximate the probability distribution and statistical variables with finite variables than it is to approximate a nonlinear transformation [9, 10]. The principle of UT transformation is that a set of points (sigma points) are selected according to a certain rule in the original state distribution. This makes the mean and covariance of these points equal to the mean and covariance of the original state distribution. When the sigma points are put into state equation and observation equation, the statistics can be obtained from small scale nonlinear transformations. The optimal state estimates and their covariance matrix can be derived using the statistics of the transformed points [11]. The estimation process is summarized in Table 1 for one cycle.

Table 1 The Unscented Kalman filter

Prediction Stage:
For $i = 1 : \mathrm{L}$
$\hat{x}_i(k\|k-1) = f(\hat{x}(k-1) + \Gamma_i\sqrt{(n+\lambda)P_i(k-1)})$
End
$\hat{x}(k\|k-1) = \sum_{i=0}^{2N} W_i\hat{x}_i(k\|k-1)$
$P(k\|k-1) = \sum_{i=0}^{2N} W_i(\hat{x}_i(k\|k-1) - \hat{x}(k\|k-1))(\hat{x}_i(k\|k-1) - \hat{x}(k\|k-1))^T + Q_k$
Update Stage:
For $i = 1 : \mathrm{L}$
$\hat{x}_i(k\|k-1) = \hat{x}(k\|k-1) + \Gamma_i\sqrt{(n+\lambda)P(k\|k-1)}$
$\zeta_i(k\|k-1) = h(\hat{x}_i(k\|k-1))$
End
$\hat{z}(k\|k-1) = \sum_{i=0}^{2N} W_i\zeta_i(k\|k-1)$
$P_{zz}(k\|k-1) = \sum_{i=0}^{2N} W_i(\zeta_i(k\|k-1) - \hat{z}(k\|k-1))(\zeta_i(k\|k-1) - \hat{z}(k\|k-1))^T + R_k$
$P_{xz}(k\|k-1) = \sum_{i=0}^{2N} W_i(\hat{x}_i(k\|k-1) - \hat{x}(k\|k-1))(\zeta_i(k\|k-1) - \hat{z}(k\|k-1))^T$
$K(k) = P_{xz}(k\|k-1)P_{zz}^{-1}(k\|k-1)$
$\hat{x}(k\|k) = \hat{x}(k\|k-1) + K(k)(z(k) - \hat{z}(k\|k-1))$
$P(k\|k) = P(k\|k-1) - K(k)P_{zz}(k\|k-1)K(k)^T$
Repeating the cycle for the next time, the current state estimation and covariance matrix are obtained as input sources to the estimation processes

3 Adaptive Fading Filter Method

3.1 Fading Memory Method

When the system model is not accurate or mismatch arises between system model and reality, the current observations only play a small role in correcting the estimation. While the previous observations cause the tracking error and filter divergence, the fading memory algorithm is to redistribute the current observation and improve the robustness of the filter.

$$P_{xz}(k|k-1) = \alpha \sum_{i=0}^{2N} W_i(\hat{x}_i(k|k-1) - \hat{x}(k|k-1))(\zeta_i(k|k-1) - \hat{z}(k|k-1))^T + Q_k = \hat{P} + Q_k \quad (1)$$

Assume that α=1, the fading memory algorithm is equivalent to the Unscented Kalman filter, where $\hat{P}$ is the state error covariance in the ideal situation where the system model completely matches the moving target, i.e., with Q_k=0. At this time, the fading factor can alter the coefficient of the state covariance according to the current observation data. The deviation of higher degree between the system model and actual target state can make the coefficient larger. In order to compensate for the estimation error caused by the model mismatch, the observations must be given a higher degree of confidence level. When α is too large, the estimation eventually converges to the observation value which may cause the loss of accuracy of the state estimation.

3.2 *Adaptive Fading Factor Method*

Compared to the linear Kalman filter, the fading factor are introduced into Unscented Kalman filter, where ρ is a prior coefficient,α_k calculation involves the following formula [12]:

$$S_{k+1} = \begin{cases} v_1 v_1^T \, k = 0 \\ \frac{\rho S_k + v_{k+1} v_{k+1}^T}{1+\rho} k \geq 1 \end{cases} \quad (2)$$

$$N = S_{k+1} - R, \; M = P_{zz} - R \quad (3)$$

$$\lambda_k = \frac{trace(N)}{trace(P_{zz}(k|k-1))} \quad (4)$$

$$\alpha_k = \begin{cases} \lambda_k \; \lambda_k \geq 1 \\ 1 \; \lambda_k < 1 \end{cases} \quad (5)$$

Covariance P_{zz} can be used as evaluation criterion to judge the uncertainty of state prediction in the process of filtering. Meanwhile, v_{k+1} is prediction residual error that can be obtained from observation, corresponding to the error of state estimation. It can be seen that whether covariance divergence is likely to occur can be determined by the value of α_k. It demonstrates that the real-time covariance of state estimation is larger than the covariance of state prediction when $\alpha_k > 1$. At this time, we need to make some adjustments to the system model. The weight of the current observation can be increased by the fading memory algorithm. According to the property description

of S_{k+1}, adaptive method of fading factor for UKF called AFUKF algorithm can be established to diminish error covariance when the estimation error caused by model mismatch.

4 Simulation

The proposed AFUKF is applied to the target tracking system as compared to given UKF algorithm and Sage-UKF algorithm. The radar observation station is set at the origin of coordinate in space of two-dimensional scenario, where the target makes the approximate S-type maneuver. The nonlinear system equation and observation equation of the target motion are described as follows:

$$x_{k+1} = \begin{pmatrix} 1 & T & (\alpha T - 1 + e^{-\alpha T})/\alpha^2 \\ 0 & 1 & (1 - e^{-\alpha T})/\alpha \\ 0 & 0 & e^{-\alpha T} \end{pmatrix} x_k + Q_k \tag{6}$$

$$z_k = \begin{bmatrix} \sqrt{x_k^2 + y_k^2} \\ arc\tan(y_k/x_k) \end{bmatrix} + \begin{bmatrix} v_k^r \\ v_k^a \end{bmatrix} z_k = \begin{bmatrix} \sqrt{x_k^2 + y_k^2} \\ arc\tan(y_k/x_k) \end{bmatrix} + \begin{bmatrix} v_k^r \\ v_k^a \end{bmatrix} \tag{7}$$

where x_k and y_k represents the horizontal position and vertical position of the target, v_k^r and v_k^a represent position noise and azimuth noise of the observation, respectively, Q_k is the process noise.

$$Q_k = 2\alpha\sigma^2 \begin{pmatrix} q_{11} & q_{12} & q_{13} \\ q_{21} & q_{22} & q_{23} \\ q_{31} & q_{32} & q_{33} \end{pmatrix} \tag{8}$$

where

$$q_{11} = \frac{1}{2\alpha^5}\left(1 - e^{-2\alpha T} + 2\alpha T + \frac{2\alpha^3 T^3}{3} - 2\alpha^2 T^2 - 4\alpha T e^{-\alpha T}\right)$$

$$q_{12} = q_{21} = \frac{1}{2\alpha^4}\left(1 + e^{-2\alpha T} - 2e^{-\alpha T} + 2\alpha T e^{-\alpha T} - 2\alpha T + \alpha^2 T^2\right)$$

$$q_{13} = q_{31} = \frac{1}{2\alpha^3}\left(1 - e^{-2\alpha T} - 2\alpha T e^{-\alpha T}\right)$$

$$q_{22} = \frac{1}{2\alpha^3}\left(-3 + 4e^{-\alpha T} - e^{-2\alpha T} + 2\alpha T\right)$$

$$q_{23} = q_{32} = \frac{1}{2\alpha^2}\left(1 - 2e^{-\alpha T} + e^{-2\alpha T}\right)$$

$$q_{33} = \frac{1}{2\alpha}\left(1 - e^{-2\alpha T}\right)$$

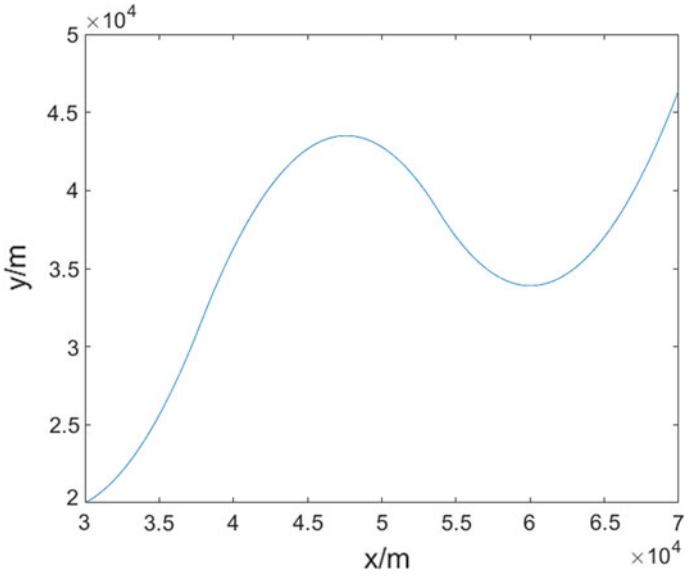

Fig. 1 Real target trajectory

where α is the frequency of maneuvering, T is the sampling period.

As shown in Fig. 1, the flight path is used for simulation analysis. In the rectangular coordinate system, the target position can be regarded as the input state of the system. The vector $s_0 = [x_0, y_0]$ is used to describe the initial target position, where x_k and y_k represent the horizontal position and vertical position of the target, respectively, the initial position of the target is $s_0 = [30000, 20000]$, the initial velocity and acceleration can be derived from the position and time using two-point differencing method.

Root mean square (RMS) tracking error provides a quantitative estimate of how close the target position actually is to the true target position. The performance of each of the algorithms was assessed by using 50 Monte Carlo runs, which are shown in Figs. 2, 3, 4 and 5. The system model deviates so far from the actual motion model when the target turns suddenly, the AFUKF performs better than the traditional methods which rapidly degrade the accuracy of the estimate. This experiment verifies the feasibility of adaptive fading factor Unscented Kalman filter in practical application, and the α_k value changes with the mismatch model error, which can achieve the real-time identification effect.

The AFUKF algorithm proposed in this paper uses the fading factor to adjust the statistical properties of the system noise in real time for estimating target states. It can effectively solve the problem that the estimation error increases due to the mismatch between the system model and the actual model to ensure a quicker convergence and enhance the accuracy of estimation. As shown in Table 2, the RMS errors of position and velocity of the AFUKF algorithm are significantly smaller than those of standard

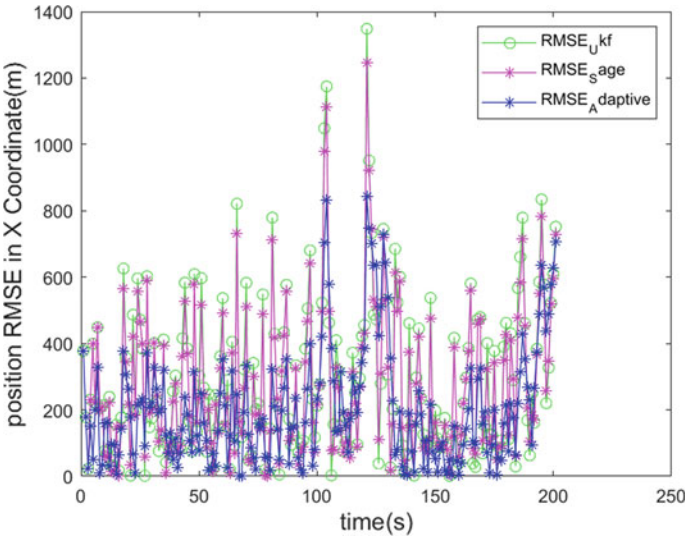

Fig. 2 The position RMSE in X Coordinate for different method over time

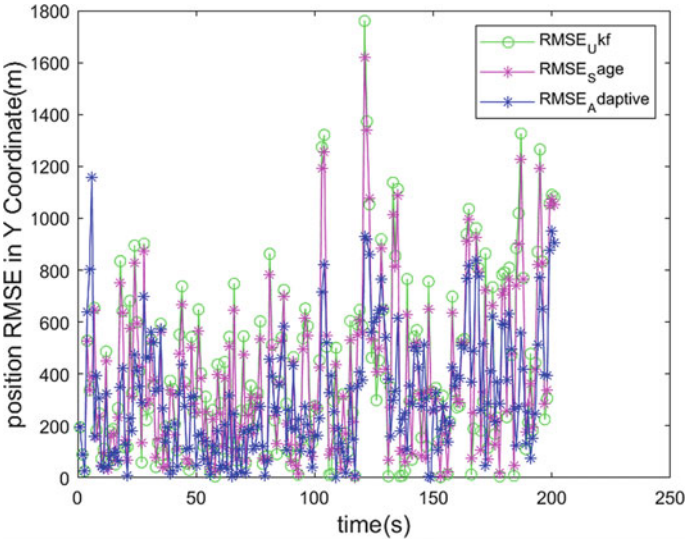

Fig. 3 The position RMSE in Y Coordinate for different method over time

algorithms. Simulation results show that the AFUKF algorithm is significantly better than the standard UKF Algorithm in accuracy and stability of estimation, and the state estimation is also closer to the real target state.

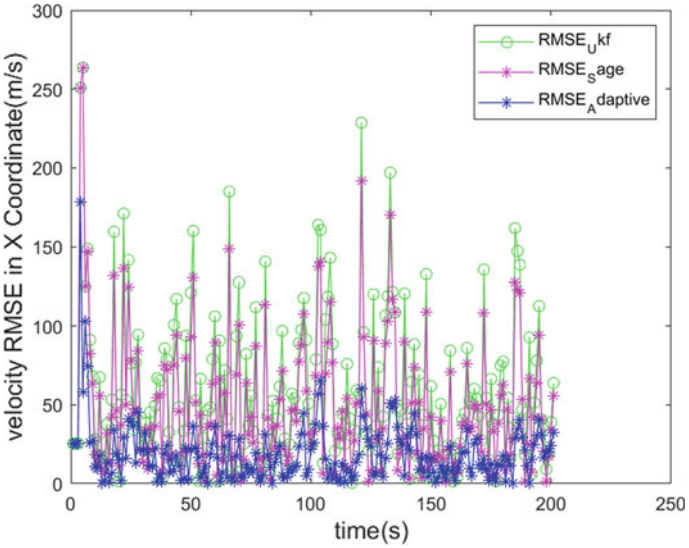

Fig. 4 The velocity RMSE in X Coordinate for different method over time

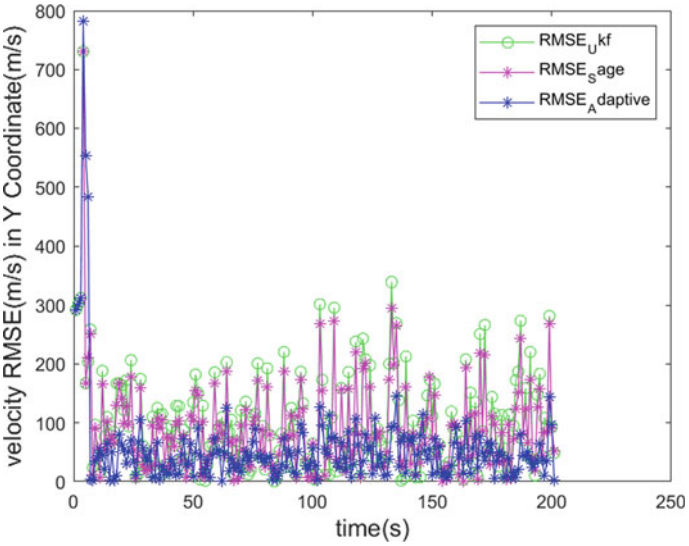

Fig. 5 The velocity RMSE in Y Coordinate for different method over time

Table 2 Comparison of RMS for different methods

Method	Position (m) in X	Position (m) in Y	Velocity (m/s) in X	Velocity (m/s) in Y
UKF	289.99	402.62	60.02	101.46
SAGE-UKF	275.05	383.97	49.60	91.22
AF-UKF	205.45	314.99	18.93	55.89

5 Conclusion

This paper describes the problem of mismatch between the system model and the practical target motion-model when target enters the maneuver in tracking. In order to solve this problem, adaptive fading factor Unscented Kalman filter algorithm is proposed to reduce the errors of estimation. When the system model deviate from the actual model, accurate state estimate can be obtained using the proposed algorithm.In addition, the algorithm demonstrates the feasibility of adaptive fading factor from the perspective of prediction covariance and actual covariance to avoid the calculation of Jacobian matrix of nonlinear and the deviation caused by the first-order linearization. Simulation results show that the proposed method is an effective way to improve the tracking accuracy than the traditional methods.

Acknowledgements This work was supported in part by the National Natural Science Foundation of China under Grant 61673262 and Grant 61175028, and in part by the Shanghai key Project of Basic Research under Grant 16JC1401100.

References

1. Singer RA (1970) Estimating optimal filter tracking performance for Manned Maneuvering Targets. IEEE Trans Aerosp Electron Syst 6(4):473–483
2. Uhlmann JK (1992) Algorithms for multiple target tracking. Am Sci 80(2):128–141
3. Crassidis JL, Markley FL, Cheng Y (2007) Survey of nonlinear attitude estimation methods. J Guid Control Dyn 30(1):12–28
4. Kumar KSP, Zhou H (1984) A "current" statistical model and adaptive algorithm for estimating maneuvering targets. AIAA J Guidance 7(5):596–602
5. Julier SJ, Uhlmann JK (1999) A new extension of the Kalman filter to nonlinear systems. Proc SPIE Int Soc Opt Eng 3068:182–193
6. Closas P, Fernandez-Prades C, Vila-Valls J (2012) Multiple quadrature kalman filtering. IEEE Trans Signal Process 60(12):6125–6137
7. Julier SJ, Uhlmann JK, Durrant-Whyte HF (1995) A new approach for filtering nonlinear systems. In: American control conference, pp. 1628–1632
8. Julier SJ, Uhlmann JK (2003) The spherical simplex unscented transformation. In: American control conference, pp 2430–2434
9. Crassidis JL, Markley FL (2003) Unscented filtering for spacecraft attitude estimation. J Guid Control Dyn 26(3):536–542
10. Rao S, Rajeswari K, Lingamurty K (2009) Unscented Kalman filter with application to bearings—only target tracking. Iete J Res 55(2):63

11. Sorenson HW, Sacks JE (1971) Recursive fading memory filtering. Inf Sci 3(2):101–119
12. Soken HE, Hajiyev C (2011) Adaptive fading UKF with Q-adaptation: application to picosatellite attitude estimation. J Aerosp Eng 26(3):628–636

A Function Analysis Methodology Applied in Civil Aircraft Design

Chao Tang, Xinai Zhang, Haomin Li, Dongsheng Chen, Jian Wang, and Yong Chen

Abstract The functions and requirements play an extremely important role in developing complex systems nowadays. In this paper. A Function Analysis Methodology applied in a civil aircraft program is introduced. The function identification, organization and characterization processes of for a civil aircraft air management system are presented in detail. Furthermore, a function priority approach is taken into consideration. It shows that it is effective to perform functional analysis process to provides benefits to aircraft design: it discourages single-point solutions, and it describes the behaviors that lead to requirements and physical architectures. Function Analysis Methodology provides aircraft system with a functional system description that becomes a framework for developing requirements and physical architectures, and it significantly improves synthesis of design and integration.

Keywords Function analysis · Civil aircraft · System design

1 Introduction

Generally, the airlines prefer an aircraft that can allow them to serve customers in an efficient and profitable manner which is related to the aircraft features that benefits passengers with reliable and affordable travel, and airlines with lower training, operation, maintenance cost [1–4]. A civil aircraft is a typical highly complex system. The aircraft itself includes dozens of high technology systems consisting of millions of parts whose design is highly inter-disciplinary, involving performance-oriented disciplines such as aerodynamics, structures, flight mechanics and control etc. and

C. Tang (✉) · X. Zhang · H. Li · D. Chen · J. Wang
Shanghai Aircraft Design Research Institute, Shanghai, China
e-mail: tangchao1@comac.cc

H. Li · Y. Chen
Shanghai Jiao Tong University, Shanghai, China

Z. Jing and X. Zhan (eds.), *Proceedings of the International Conference on Aerospace System Science and Engineering 2020*, Lecture Notes in Electrical Engineering 680,
https://doi.org/10.1007/978-981-33-6060-0_43

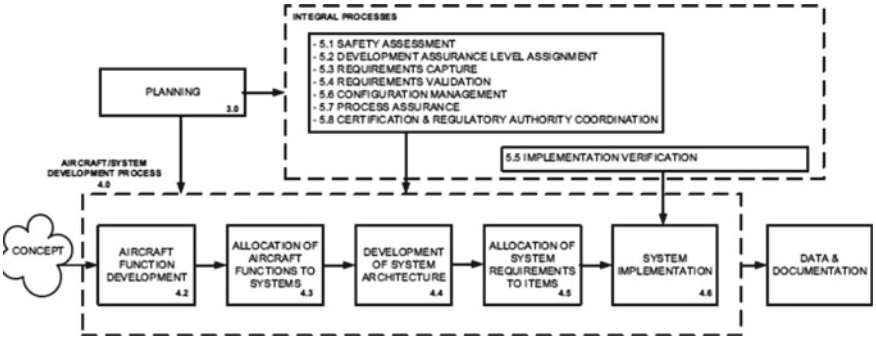

Fig. 1 Aircraft or system development process model from SAE ARP 4754A

the behavior-oriented disciplines such as systems approach to design, manufacture and assembly, system architecture, risk management, reliability and maintenance, cost modeling, supply chain management and so on. With the increased demands on aircraft safety, cost, environmental, security, and comfort performance, the complexity of system functions, interaction between functions, amount of data exchange between systems, and product scale of the civil aircraft is increasing [5, 6].

In order to remain competitive in the international market, aircraft manufacturers need to pay more attention to implementing some new approaches and methodologies in the aircraft development process. It is well known that systems engineering is an effective approach and means to ensure realization of a successful aircraft to satisfy relevant stakeholders needs, by capturing customers' needs and required functionality early in the development stage, documenting requirements and then proceeding with design synthesis considering the operations, cost and schedule, performance and all the other relative factors. It is obvious to find that functions play an extremely important role in a civil aircraft development with the application of systems engineering. SAE International published ARP 4754A which applies the systems engineering principles to provide guidelines for development and certification of complex civil aircraft and systems [7, 8]. The aircraft design starts with identification of aircraft-level functions which are not necessarily associated with a single, physical system implementation (Fig. 1).

2 Function Analysis Methodology

Function Analysis Methodology provides aircraft system with a functional system description that becomes a framework for developing requirements and physical architectures, and it significantly improves synthesis of design and integration. Functional Analysis is the System Engineering process that translates stakeholders' needs into a sequenced and traceable functional architecture [9–11].A typical function analysis methodology can be summarized as below.

2.1 Identify the Function

The goal of function identification process is to describe the final goal of the product completely. In order to describe the product clearly, it is necessary to systematically check the form of each function and check whether it expresses the goal correctly. The definition of function should be clear and simple. Usually, the verb object phrase of "Verb + noun" is used to express the function. The verb should indicate the attribute of the action to meet the needs.

This phase must be detailed, even if there is a risk of proliferation and redundancy when listing functions. By analyzing customer needs and objectives, all functions are exhausted to ensure that all customer needs and objectives are covered.

2.2 Organize the Function

The function set defined by the above process is a relatively loose set of aircraft functions with no fixed logical relationship. It must be combed, integrated, decomposed and expanded to form an aircraft level function list. Function organization first lies in function decomposition, defining function hierarchy. The functional decomposition which usually use function tree and FAST diagram method is to decompose complex functions into several identifiable sub functions.

(a) Function Tree: list the main functions at the first level and the derived functions at the next level.
(b) FAST Diagram: give the root/cause relationship of these functions on the horizontal axis. The function on the right should answer the question "how?", the function on the left should answer the question "why?" The time sequence relationship between these functions is shown on the vertical axis, as shown in Fig. 2.

2.3 Description the Function

Function modeling can be used to describe the function. It is used to analyze the behavior and logic of the function in the operation scenario, develop the functional requirements and functional interface, and effectively guide the subsequent design synthesis and product integration.

Using models is a better way to break down and flow down architecture and requirements because different level developers can have a consistent understanding about the system to be developed. SysML is recommendable for use in functional modeling. A major, but not only, standard is the Systems Modeling Language (SysML) currently hosted by the Object Modeling Group (OMG) [12]. Multiple tools implement SysML as a profile on top of UML, which has many years of software industry investment to leverage.

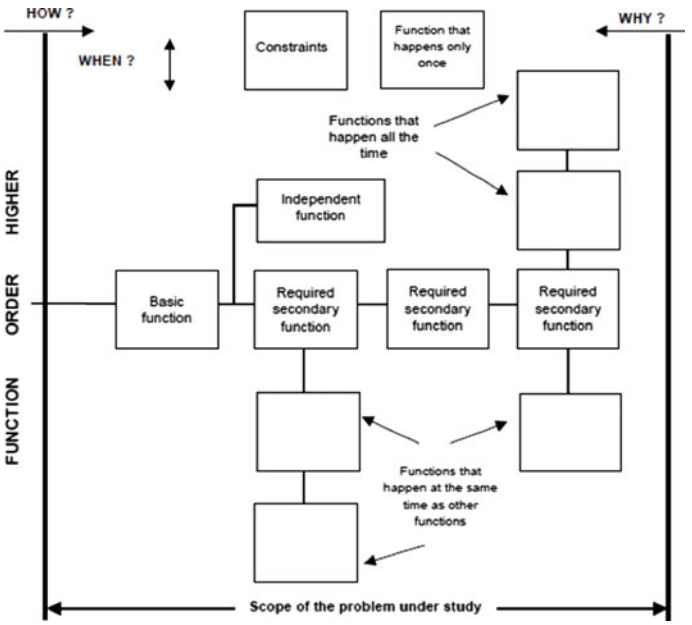

Fig. 2 Example of FAST diagram

2.4 Allocation the Function

The function allocation is based on the result of the process above. Define the internal logic and main sub functions of function realization, comprehensively consider the previous experience and product structure, and allocate the function logic to the corresponding system/subsystem/equipment.

2.5 Prioritize the Functional

Through the previous process, these functions have been identified, organized and characterized. The importance of these functions will be graded according to the importance. This will make the work first focus on the most important functions, of course, all functions must be implemented.

In order to detail the user's expectations, the function evaluation will assign a "weight" to these functions, which is composed of a class of hierarchical quantity values. The best way to measure this weight is to ask customers or other stakeholders directly.

3 Example Study

An example study showing the function analysis methodology in the pressure control system is described. The pressure control system is part of air condition system, which control the cabin pressure in the whole flight phase to ensure pilot and passages have a comfortable environment.

3.1 Identify the Function

Identification scenario. in this stage, different scenarios in the whole life cycle of the aircraft will be given, and the scenarios shall be identified from at least multiple dimensions such as operation stage, environment and failure state. The content of each scenario must be clearly defined to enhance understanding. For the aircraft, typical scenarios are: takeoff, landing, taxiing, maintenance, single engine failure, icing, etc.

Identify stakeholders. Based on the scenario list, identify stakeholders for each scenario, including the people and environment interacting with the scenario.

Define activities. for each stakeholder, determine their specific activities in specific scenarios, appropriately decompose and expand complex activities, and finally form functions.

Function exhaustion. all main functions can be listed by means of environment interaction diagram, exhaustion matrix, etc. In order to ensure that the identified functions correspond to the correct needs and are not redundant, the function list shall be confirmed (Fig. 3).

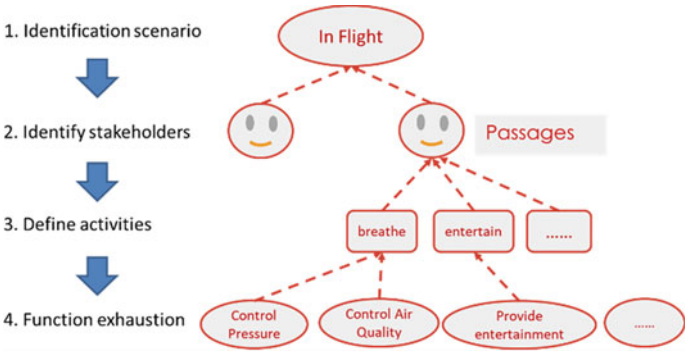

Fig. 3 Function identification process

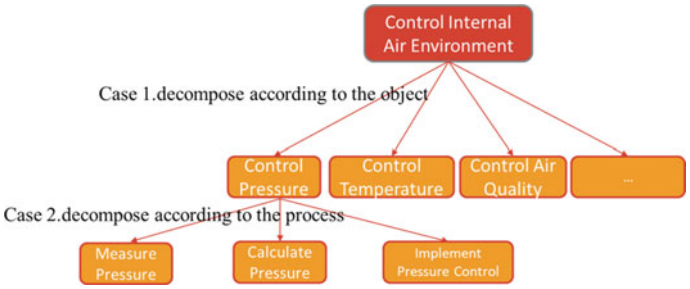

Fig. 4 Function organization process

3.2 Organize the Function

Function organization first lies in function decomposition, defining function hierarchy. The purpose of functional decomposition is to promote design solution, that is, to achieve a group of sub functions respectively, to jointly achieve a total function. Therefore, if the corresponding solution cannot be found according to a subfunction, it needs to be further decomposed until it can correspond to a specific physical implementation scheme. The form of function list mainly includes function tree, FAST, etc.

There are two types of functional decomposition: one is to decompose according to the object type. For example, the function " Control Internal Air Environment" can be divided into sub functions such as "Control Pressure", " Control Temperature" and " Control Air Quality". In this case, these sub functions are relatively independent and have no direct relationship with each other. The other is to decompose the function according to the state change of the object or process scenario. In this case, the sub functions are There is always a logical relationship between functions. It is meaningful to realize some subfunctions first, then other subfunctions. For example, the function of " Control Pressure" can be decomposed into " Measure Pressure", "Calculate Pressure" and "Implement Pressure Control", which have a sequential relationship (Fig. 4).

3.3 Description the Function

For each function listed above, the description of the function and its particular needs is necessary in order to specify the function. Model-based system engineering (MBSE) is a modern engineering method based on model driven approach for complex system integrated design [13] which is widely applied in functional requirements development work. The point is, using the modeling describes graphically the aircraft and system characteristics, including function description. The example of control pressure function modeling shows as below (Fig. 5).

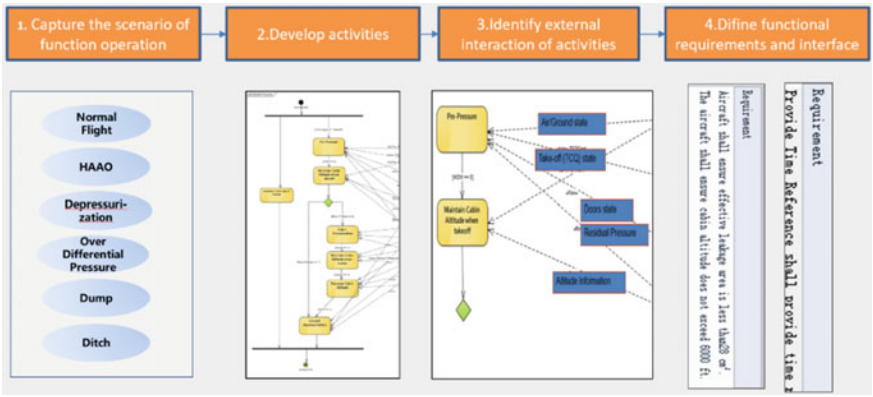

Fig. 5 Function description by functional modeling

Capture the scenario of function operation, The scenario capture should be developed at the aircraft level. First, it is necessary to define the normal behavior of the function in order to achieve the established goal in the whole flight process, which is called normal flight. At the same time, in order to ensure the integrity of requirements as much as possible, it should try to cover all possible scenarios.

Develop activities. The sub function of functional decomposition is the input of activity diagram, through which the system function has been logically constructed to achieve its expected goal. It is necessary to define a work activity diagram for each scenario, and describe the operation process of the function in this scenario in the form of activity flow, that is, to establish the sequence relationship between the sub functions.

Identify external interaction. After identifying the functional operation scenarios, the external interaction objects of the analyzed functions should be defined, that is, the related functions of direct cross-linking with the analyzed functions in any operation scenario, including signal cross-linking and energy flow transfer.

Capture functional requirements and interface. For each activity in the work activity diagram, the activity is transformed into requirement language one by one to generate functional requirements. In the other hand, for each activity element in the activity diagram, analyze whether it needs the cooperation of external functions to complete the overall task. Functional interface will be defined using interface relationship with external interactive functions.

Table 1 Function allocation matrix

Function No.	Aircraft level function	ATA21
XXXX	Control pressure	R

Table 2 Function prioritization table

	Control temperature	Control air quality	Total	%
Control pressure	Control pressure 1	Control pressure 3	4	67%
	Control temperature	Control temperature 2	2	33%
		Control air quality	0	0

3.4 Allocation the Function

According to ARP 4754A, the function allocation step should be done after the steps above. The goal of allocation is to find the solution of problem domain. One function can be allocated to one or more systems and one system can achieve one or more functions as well. Function allocation is always the result of design synthesis and showed in allocation Table 1.

3.5 Prioritize the Function

The best way to prioritize functions is to ask customers or other stakeholders directly. As a special function set, a table should be designed as below, the quantity values represent the importance difference between each two functions, Finally, the weight of each function is obtained by summing, and then the function order is obtained by converting the composite percentage.

The result of this priority work combined with cost analysis will significantly improve function assessment (Table 2).

4 Conclusion

In this paper, a function analysis methodology applied in civil aircraft has been introduced. The function identification, organization and characterization processes of for a civil aircraft system are presented in detail. Function Analysis Methodology provides aircraft system with a functional system description that becomes a framework for developing requirements and physical architectures, and it significantly improves synthesis of design and integration. It has also been demonstrated that it is

necessary to apply this process throughout the whole aircraft life cycle to ensure that customs' needs be transfer into design requirements properly and have an effective solution as well to achieve aircraft development, operation, and commercial success.

References

1. Schaad RG, Hopper JM (1993) The customer influence in 777 design. In: AIAA 93-1139, AIAA/AHS/ASEE aerospace design conference. Irvine, CA, Feb 1993
2. Vigneron Y (2003) Commercial aircraft for the 21st century A380 and beyond. AIAA 2003–2886. In: AIAA/ICAS inrenational air & space symposium and exposition. Dayton, OH, July 2003
3. Cummings TK (2007) Lessons learned from 737 & 787 jet liner programs. In: AIAA 2007–6125, AIAA SPACE 2007 conference & exposition, long beach. California, Sept 2007
4. Loren JR (1992) Design for global competition—the Boeing 777. In: AIAA 92-4190, AIAA aircraft design systems meeting. Hilton Head, SC, Aug 1992
5. Altfeld HH, Tang CH (2013) Commercial aircraft projects—Managing the development of highly complex products. Aviation industry press, Beijing
6. Raghunathan S, Curran R, Kundu AK, Price M, Benard E (2003) Research into integrated aircraft technologies. In: AIAA 2003–6736, AIAA's 3rd annual aviation technology, integration, and operations (ATIO) Tech. Denver, Colorado, Nov 2003
7. Jackson S (2015) Systems engineering for commercial aircraft—a domain-specific adaptation. University of Southern California and Burnham Systems Consulting, ASHGATE, USA
8. "SAE ARP 4754A Guidelines for development of civil aircraft and systems," Society of Automotive Engineers. Dec 2010
9. Cole EL (1998) JR. Cole-Functional analysis-a system conceptual design tool. IEEE Trans Aerosp Electron Syst 34(2) 1998
10. Romli FI (2013) Functional analysis for conceptual aircraft. J Adv Manag Sci 1(4) Dec 2013
11. Nissen HW, Schmitz D, Jarke M, Rose T, Drews P, Hesseler FJ (2009) Evolution in domain model-based requirements engineering for control systems development. In: 2009 17th IEEE international requirements engineering conference
12. "Systems Modeling Language: SysML", www.sysml.org. Accessed Feb 2018
13. Cencetti M, Maggiore P (2013) System modeling framework and MDO tool integration: MBSE methodologies applied to design and analysis of space system. In: AIAA modeling and simulation technologies (MST) conference 2013